

**UCLA**

**UCLA Electronic Theses and Dissertations**

**Title**

Aptamer-Functionalized Field-Effect Transistors For Serotonin and Dopamine Sensing

**Permalink**

<https://escholarship.org/uc/item/97q4d185>

**Author**

Nakatsuka, Nako

**Publication Date**

2017

Peer reviewed|Thesis/dissertation

UNIVERSITY OF CALIFORNIA

Los Angeles

Aptamer-Functionalized Field-Effect Transistors

For Serotonin and Dopamine Sensing

A dissertation submitted in partial satisfaction of the

requirements for the degree Doctor of Philosophy

in Chemistry

by

Nako Nakatsuka

2017

© Copyright by

Nako Nakatsuka

2017

# ABSTRACT OF THE DISSERTATION

Aptamer-Functionalized Field-Effect Transistors

For Serotonin and Dopamine Sensing

by

Nako Nakatsuka

Doctor of Philosophy in Chemistry

University of California, Los Angeles, 2017

Professor Paul S. Weiss, Chair

My thesis work built on over a decade's worth of research in the Andrews and Weiss groups aimed at discovering high-affinity oligonucleotide-based recognition elements called aptamers. Previous work focused on designing and developing solid-phase substrates with surface-tethered small-molecule targets that retained their biological functionality to enable recognition by receptors. I mastered techniques such as chemical lift-off lithography and microfluidics to pattern small-molecules in specific locations to facilitate quantification of *specific* binding relative to background molecules. I demonstrated recognition of surface-tethered dopamine by a previously isolated dopamine aptamer. Specific binding was validated using competitive displacement experiments, which verified that surface-tethered dopamine, despite its reduced degree of freedom, could compete with free dopamine in solution. I addressed one of the shortcomings of



conventional *in vitro* aptamer selection by enabling on-chip determination of equilibrium dissociation constants ( $K_d$ ). Using a novel patterning method to create aptamer concentration gradients on multiplexed substrates, I resolved multiple  $K_d$  values simultaneously. I demonstrated that optimized small-molecule-functionalized substrates were ready to screen for novel neurotransmitter-specific aptamers.

In parallel, however, our collaborators at Columbia University isolated high-affinity (nanomolar  $K_d$ ) aptamers targeting serotonin and dopamine through the use of a solution-phase method. Thus, I advanced our research to the next step by integrating these aptamers onto the semiconducting channels of thin-film field-effect transistors (FETs). Serotonin- and dopamine-functionalized FETs were able to sense target molecules in high ionic-strength, undiluted physiological buffers, as well as in complex environments such as brain tissue. Traditionally, biological FETs have suffered from Debye length limitations under physiological conditions where the effective sensing distance is  $<1$  nm from the surface of the semiconducting channels. We hypothesized that the mechanism that enabled sensitive detection of neurotransmitter targets even in complex fluids was driven by aptamer conformational changes. I read and synthesized every aptamer-FET paper I could find in the literature to understand the current status of the field. I found that mechanistically, there were two emerging lines of thought. The first asserts that electronic signals arise mainly from target-associated charge being brought into close proximity of FETs upon aptamer binding. The second postulates that rearrangement of charged aptamer backbones contributes to aptamer-FET target detection.

I investigated the mechanism of the serotonin and dopamine aptamer-FETs by exploring the influence of divalent cations on aptamer binding. I showed that serotonin and dopamine signal responses behaved differently based on the presence/absence of divalent cations. This meant there were aptamer-specific differences in secondary structure rearrangements upon target capture. I conducted circular dichroism and surface-enhanced Raman spectroscopy to compare alterations in aptamer secondary structures upon target capture, empirically. I demonstrated that these two techniques can be used to track aptamer conformational changes and together, they enabled prediction of sensing capabilities prior to FET incorporation of aptamers. Sensing of a neutral target (glucose) and a zwitterionic species (sphingosine-1-phosphate) further implicated target-induced rearrangement of aptamer charge at the surface of FETs as a key mechanism for small molecule sensing. This mechanism is advantageous as it is generalizable for *any* target of interest regardless of size or charge.

Finally, inspired by recent literature on polydopamine nanoparticles, I fabricated and characterized analogous serotonin-based nanomaterials. I demonstrated that polyserotonin nanoparticles had comparable therapeutic properties to polydopamine nanoparticles such as drug loading efficiency and photothermal capabilities. However, compared to polydopamine, polyserotonin nanoparticles showed reduced protein corona formation on the surface and improved biocompatibilities with three stem cell lines, suggesting their potential for future clinical applications.

The dissertation of Nako Nakatsuka is approved.

Dino Di Carlo

Thomas G. Mason

Anne M. Andrews

Paul S. Weiss, Committee Chair

University of California, Los Angeles

2017

*For my Mom,  
who gave me everything  
to pursue a career so far from home.*

# TABLE OF CONTENTS

List of Abbreviations.....	xv
Acknowledgments .....	xxiii
Vita .....	xxvii
List of Select Publications .....	xxviii

## CHAPTER I

### Next-Generation Biosensors to Monitor Molecules *in Vivo*

I.A. The BRAIN Initiative – Nanotools for Neuroscience.....	2
I.B. Towards Electronic Biosensing <i>in Vivo</i> .....	5
I.B.1. Enzyme- and Antibody-Based Field-Effect Transistors.....	9
I.B.2. Challenges of Debye Lengths in High Ionic-Strength Solutions.....	11
I.C. Aptamer Recognition Elements for Field-Effect Transistors.....	13
I.C.1. Riboswitches and Small-Molecule Aptamers <i>in Vivo</i> .....	16
I.C.2. Challenges of Discovering Aptamers for Small-Molecule Targets .....	17
I.C.3. Selecting Small-Molecule Aptamers in Solution.....	17
I.C.4. Solid-Phase Substrates for Small-Molecule Aptamer Discovery .....	19
References .....	22

## CHAPTER II

### Advancing Biocapture Substrates *via* Chemical Lift-Off Lithography

II.A. Introduction.....	42
II.B. Experimental Methods.....	45
II.B.1. Materials.....	45
II.B.2. Substrate and Stamp Preparation.....	46

II.B.3. Biotin-Streptavidin Patterns .....	47
II.B.4. Side-by-Side Patterning.....	49
II.B.5. Patterning for Membrane-Associated Receptor Capture .....	50
II.B.6. X-Ray Photoelectron Spectroscopy .....	51
II.B.7. Statistical Analyses.....	52
II.C. Results and Discussion .....	53
II.D. Conclusions and Prospects.....	64
Appendix A .....	66
References .....	76

## CHAPTER III

### Controlled DNA Patterning by Chemical Lift-Off Lithography: Matrix Matters

III.A. Introduction.....	86
III.B. Experimental Methods.....	89
III.B.1. Materials.....	89
III.B.2. Substrate and Stamp Preparation.....	90
III.B.3. Patterning Alkanethiol Self-Assembled Monolayer-Modified Substrates <i>via</i> Chemical Lift-Off Lithography. ....	91
III.B.4. Statistical Analyses.....	95
III.C. Results and Discussion .....	96
III.C.1. Chemical Lift-Off Lithography Facilitates Probe DNA Insertion and Target DNA Hybridization.....	96
III.C.2. Oligo(Ethylene Glycol)-Terminated Alkanethiols Reduce DNA Insertion .....	99
III.C.3. Chemical Lift-Off Reduces DNA-Substrate Interactions and Improves DNA Hybridization.....	102
III.C.4. Backfilling Reduces Inserted DNA on Post-Lift-Off Alkanethiol Self-Assembled Monolayers .....	107

III.C.5. DNA Arrays Patterned <i>via</i> Lift-Off Lithography Using Longer Functionalized Alkanethiols .....	109
III.C.6. Spectroscopic Evidence for Lift-Off-Induced Conformation Changes in Oligo(Ethylene Glycol) Moieties. ....	110
III.C.7. Mixed Self-Assembled Monolayers Modulate DNA Surface Coverage.....	114
III.D. Conclusions and Prospects.....	117
Appendix B .....	120
References .....	127

## CHAPTER IV

### Multiplexed Small-Molecule Patterning *via* Pre-Functionalized Alkanethiols

IV.A. Introduction.....	135
IV.B. Experimental Methods.....	138
IV.B.1. Materials.....	138
IV.B.2. Chemical Synthesis.....	140
IV.B.2.a. Fmoc- <i>L</i> -DOPS-OH.....	140
IV.B.2.b. Undec-1-en-11-ylhepta(ethylene glycol) (1).....	140
IV.B.2.c. [1-[(Methylcarbonyl)thio]undec-11-yl]hepta(ethylene glycol) (2).....	141
IV.B.2.d. [1-[(Methylcarbonyl)thio]undec-11-yl]-21-(tosyl)oxy-1,4,7,10,13,16,19-heptaoxaheneicosane (3) .....	142
IV.B.2.e. [1-Mercaptoundec-11-yl]-21-azido-1,4,7,10,13,16,19-heptaoxaheneicosane (4) ....	142
IV.B.2.f. [1-(Pyridin-2-yl)disulfanyl]undec-11-yl]-21-amino-1,4,7,10,13,16,19-heptaoxaheneicosane-amine-hepta(ethylene glycol)-terminated undecane-pyridyl disulfide (7EG-PDS) (5).....	143
IV.B.2.g. Fmoc- <i>L</i> -DOPA-7EG-PDS (6a).....	144
IV.B.2.h. Fmoc- <i>L</i> -5-HTP-7EG-PDS (6b) .....	144
IV.B.2.i. Fmoc- <i>L</i> -His-7EG-PDS (6c) .....	145
IV.B.2.j. Fmoc- <i>L</i> -DOPS-7EG-PDS (6d) .....	146
IV.B.2.k. Fmoc- <i>L</i> -Trp-7EG-PDS (6e) .....	146

IV.B.3. General Procedure for the Coupling of Fmoc-Protected Neurotransmitter (Fmoc-R) to 7EG-PDS Compound (6).....	147
IV.B.4. Substrate Preparation and Chemical Lift-Off Lithography.....	147
IV.B.5. Antibody Binding.....	150
IV.B.6. Statistics.....	151
IV.C. Results and Discussion .....	152
IV.C.1. Synthesis of Pre-Functionalized Molecules .....	152
IV.C.2. Patterning Pre- vs. Post-Functionalized Molecules with Lift-Off Lithography.....	155
IV.C.3. Side-by-Side Comparisons of Pre- vs. Post-Functionalized Approaches .....	161
IV.C.4. Multiplexed Pre-Functionalized Substrates.....	164
IV.D. Conclusions and Prospects.....	169
Appendix C.....	171
References .....	180

## CHAPTER V

### **Aptamer Recognition of Multiplexed Neurotransmitter-Functionalized Substrates**

V.A. Introduction.....	186
V.B. Experimental Methods.....	188
V.B.1. Materials.....	188
V.B.2. Microfluidic Device Fabrication.....	189
V.B.3. Self-Assembled Monolayer Preparation and Patterning.....	190
V.B.4. Aptamer Capture on Small-Molecule-Patterned Substrates.....	191
V.B.5. Image Analysis and Statistics.....	192
V.C. Results and Discussion .....	194
V.C.1. Dopamine Aptamers Recognize Surface-Tethered Dopamine.....	194
V.C.2. Competitive Displacement.....	199
V.C.3. Multiplexed Substrates to Investigate Aptamer Selectivities.....	201



V.C.4. Aptamer Elution from Multiplexed Neurochips.....	206
V.D. Conclusions and Prospects.....	210
Appendix D .....	211
References .....	214

## CHAPTER VI

### **Fabrication of High Performance Ultrathin In<sub>2</sub>O<sub>3</sub> Film Field-Effect Transistors and Biosensors Using Chemical Lift-Off Lithography**

VI.A. Introduction.....	221
VI.B. Experimental Methods.....	224
VI.B.1. Materials.....	224
VI.B.2. Chemical Lift-Off Lithography .....	224
VI.B.3. Fabrication of Field-Effect Transistors and Biosensors.....	225
VI.B.4. Characterization.....	226
VI.C. Results and Discussion .....	227
VI.D. Conclusions and Prospects.....	242
Appendix E.....	243
References .....	255

## CHAPTER VII

### **Aptamer-Field-Effect Transistors Overcome Debye Length Limitations and Enable Small-Molecule Sensing**

VII.A. Introduction .....	263
VII.B. Experimental Methods.....	266
VII.B.1. Materials.....	266
VII.B.2. Aptamer Selection .....	266
VII.B.3. Aptamer Fluorescence Assays.....	267

VII.B.4. Aptamer-Functionalized Field-Effect Transistors.....	267
VII.B.5. Aptamer-Field-Effect Transistor Measurements.....	269
VII.B.6. <i>Ex Vivo</i> Sensing.....	270
VII.B.7. Surface-Enhanced Raman Spectroscopy.....	270
VII.B.8. Circular Dichroism Spectroscopy.....	272
VII.B.9. Statistics.....	272
VII.C. Results and Discussion.....	274
VII.D. Conclusions and Prospects.....	283
Appendix F.....	284
References .....	298

## CHAPTER VIII

### Aptamer-Field-Effect Transistors Mechanistic Investigation

VIII.A. Introduction.....	304
VIII.B. Other Detection Mechanisms of Aptamer-Field-Effect Transistors.....	309
VIII.B.1. Effects of Target Charge in Aptamer-Field-Effect Transistors.....	309
VIII.B.2. Detection of Large Charged Targets by Aptamer-Field-Effect Transistors.....	312
VIII.B.3. Small-Molecule Sensing <i>via</i> Aptamer-Field-Effect Transistors.....	318
VIII.C. Aptamer Conformational Changes .....	321
VIII.C.1. Flexibility of Aptamer Backbones .....	321
VIII.C.2. Extent of Aptamer Conformational Changes .....	323
VIII.C.3. Detecting Aptamer-Target Conformational Changes.....	327
VIII.D. Solution Ion Displacement at Transistor Surfaces .....	331
VIII.E. Conclusions and Prospects .....	335
References .....	338

## CHAPTER IX

### Polyserotonin Nanoparticles as Multifunctional Nanomaterials for Biomedical Applications

IX.A. Introduction.....	350
IX.B. Experimental Methods.....	352
IX.B.1. Materials.....	352
IX.B.2. Serotonin and Dopamine Nanoparticles Synthesis .....	352
IX.B.3. Characterization.....	353
IX.B.3.a. UV-Visible Spectroscopy .....	353
IX.B.3.b. Dynamic Light Scattering and Zeta Potential .....	353
IX.B.3.c. Scanning Electron Microscopy.....	353
IX.B.3.d. Atomic Force Microscopy .....	354
IX.B.3.e. X-Ray Photoelectron Spectroscopy.....	354
IX.B.3.f. Protein Corona .....	354
IX.B.3.g. Cell Viability.....	355
IX.B.3.h. <i>In Vitro</i> Drug Release .....	356
IX.B.3.i. Photothermal Therapy.....	357
IX.B.4. Theoretical Details. ....	358
IX.B.4.a. Quantum Mechanics Computations.....	358
IX.B.4.b. Construction of Serotonin Surfaces .....	359
IX.B.4.c. Molecular Dynamics Simulations .....	360
IX.C. Results and Discussion .....	362
IX.C.1. Synthesis and Characterization of Polyserotonin Nanoparticles.....	362
IX.C.2. Protein Corona.....	366
IX.C.3. Cell Viability.....	369
IX.C.4. <i>In Vitro</i> Drug Release and Photothermal Therapy .....	370
IX.C.5. Molecular and Quantum Dynamics .....	374
IX.D. Conclusions and Prospects.....	378

Appendix G .....	379
References .....	386

## CHAPTER X

### Implementing Aptamer-Field Effect Transistors *in Vivo* – Perspectives

X.A. Introduction.....	395
X.B. Aptamers <i>in Vivo</i> .....	402
X.C. Resolution, Kinetic Measurements, and Multiplexing.....	404
X.D. <i>In Vivo</i> Device Stability and Biocompatibility.....	408
X.E. Conclusions and Prospects.....	411
References .....	412

# LIST OF ABBREVIATIONS

## Acronyms and Symbols

1D	one-dimensional
2-PDS	2,2'-dithiodipyridine
2D	two-dimensional
3D	three-dimensional
5-HT	serotonin
5-HT <sub>1A</sub>	anti-serotonin 1A receptor antibodies
7EG-PDS	hepta(ethylene glycol)undecyl pyridyl disulfide
AA	ascorbic acid
aCSF	artificial cerebrospinal fluid
AEG	(11-mercaptoundecyl) hexa(ethylene glycol)amine
AFM	atomic force microscopy
Ag/AgCl	silver/silver chloride
AIBN	azobisisobutyronitrile
Al <sub>2</sub> O <sub>3</sub>	aluminum oxide
AMPA	$\alpha$ -amino-3-hydroxy-5-methyl-4-isoxazolepropionic acid
ANOVA	analysis of variance
APTMS	(3-aminopropyl)trimethoxysilane
ATP	adenosine triphosphate
Au	gold
BCA	bicinchoninic acid

BEG	biotinylated hexa(ethylene glycol)undecanethiol
BGBC	bottom gate bottom contact
BGTC	bottom gate top contact
Boc	<i>tert</i> -butyloxycarbonyl
Br-C11	11-bromo-1-undecanethiol
BSA	bovine serum albumin
Ca <sup>2+</sup>	calcium ion
CD	circular dichroism
CDCl <sub>3</sub>	deuterated chloroform
CH <sub>3</sub> -C11	1-dodecanethiol
CH <sub>3</sub> COSH	thioacetic acid
CH <sub>3</sub> O-TEG	(11-mercaptoundecyl) tri(ethylene glycol)methyl ether
CLL	chemical lift-off lithography
CNT	carbon nanotube
COOH-HEG	(11-mercaptoundecyl) hexa(ethylene glycol)carboxylic acid
CT	computerized tomography
CV	coefficients of variation
CVD	chemical vapor deposition
D1	anti-dopamine receptor antibodies
DA	dopamine
DCM	dichloromethane
DFT	density functional theory
DIEA	<i>N,N</i> -diisopropylethylamine

DLS	dynamic light scattering
DMEM	Dulbecco's modified eagle medium
DMF	<i>N,N</i> -dimethylformamide
DMSO	dimethyl sulfoxide
DNA	deoxyribonucleic acid
DOPAC	3,4-dihydroxyphenylacetic acid
DOX	doxorubicin
DPSCs	dental pulp stem cells
<i>E.coli</i>	<i>Escherichia coli</i>
EDC	<i>N</i> -(3-dimethylaminopropyl)- <i>N'</i> -ethylcarbodiimide hydrochloride
ELISA	enzyme-linked immunosorbent assay
EnFET	enzyme-modified field-effect transistor
ESP	electrostatic potential
Fab	antigen binding fragment
FET	field-effect transistor
FITC	fluorescein isothiocyanate
Fmoc-Cl	fluorenylmethyloxycarbonyl chloride
FRET	Förster-resonance energy transfer
FSCV	fast-scan cyclic voltammetry
GMSCs	gingival mesenchymal stem cells
hBMMSCs	human bone marrow mesenchymal stem cells
HEG	11-Mercaptoundecyl hexa(ethylene glycol)
HEK293	human embryonic kidney 293 cells

HIV-1	human immunodeficiency virus type 1
HOBt	hydroxybenzotriazole
HPLC	high-performance liquid chromatography
HVA	homovanillic acid
$IC_{50}$	half maximal inhibitory concentration
$I_{DS}$	source-drain current
ImmunoFET	immunologically modified field-effect transistor
$In_2O_3$	indium oxide
$K_d$	dissociation constant
$k_{off}$	dissociation rate constant
$k_{on}$	association rate constant
<i>L</i> -5-HTP	<i>L</i> -5-hydroxytryptophan
<i>L</i> -DOPA	<i>L</i> -3,4-dihydroxyphenylalanine
<i>L</i> -DOPS	<i>L</i> -threo-3,4-dihydroxyphenylserine
<i>L</i> -HD	<i>L</i> -histidine
<i>L</i> -Trp	<i>L</i> -tryptophan
LC-MS	liquid-chromatography mass-spectrometry
MALDI-TOF	matrix-assisted laser desorption ionization-time of flight
MBS	3-maleimidobenzoic acid <i>N</i> -hydroxysuccinimide ester
MCH	6-mercaptohexanol
MCHD	16-mercaptohexadecanol
MCU	mercaptoundecanol
MD	molecular dynamics



MEA	multi-electrode array
MeOH	methanol
Mg <sup>2+</sup>	magnesium ion
MoS <sub>2</sub>	molybdenum disulfide
MRI	magnetic resonance imaging
MTT	3-(4,5-dimethylthiazol-2-yl)-2,5-diphenyltetrazolium bromide
Na <sub>2</sub> CO <sub>3</sub>	sodium carbonate
NaN <sub>3</sub>	sodium azide
NE	norepinephrine
NHS	<i>N</i> -hydroxysuccinimide
NIR	near-infrared
NMR	nuclear magnetic resonance
PA	protective antigen
PBS	phosphate-buffered saline
PCR	polymerase chain reaction
PDA	polydopamine
PDGF	platelet-derived growth factor
PDMS	polydimethylsiloxane
PDS	pyridyl disulfide
PEG	polyethylene glycol
PF-AFM	peak-force atomic force microscopy
Ph <sub>3</sub> P	triphenylphosphine
PMIRRAS	polarization modulation infrared reflection-absorption spectroscopy

PO(OH) <sub>2</sub> -C11	11-mercaptoundecylphosphonic acid
PTMS	trimethoxy(propyl)silane
QM	quantum mechanics
RC	contact resistance
RDF	radial distribution function
RNA	ribonucleic acid
S1P	sphingosine-1-phosphate
SAM	self-assembled monolayer
SELEX	systematic evolution of ligands by exponential enrichment
SEM	scanning electron microscopy
SERS	surface-enhanced Raman spectroscopy
SiNW	silicon nanowire
SPM	scanning probe microscopy
SS	subthreshold swing
Tat	transactivator transcription factor
TEA	triethylamine
TEG	tri(ethylene glycol)
TEG-C <sub>6</sub>	(6-mercaptohexyl) tri(ethylene glycol)
TFA	trifluoroacetic acid
THF	tetrahydrofuran
Ti	titanium
TLMs	transmission-line measurements
ToF SIMS	time-of-flight secondary-ion mass spectrometry

Tph2	tryptophan hydroxylase 2
Trt	trityl
TsCl	4-toluenesulfonyl chloride
TY	tyramine
$V_D$	drain voltage
VEGF	vascular endothelial-derived growth factor
$V_{GS}$	gate bias voltage
XPS	x-ray photoelectron spectroscopy
XRD	x-ray diffraction
XRR	x-ray reflectivity
$\Delta V_{cal}$	calibrated response
$\mu$ CIP	microcontact insertion printing
$\mu_{sat}$	charge carrier mobility

## Units

Å	ångström
aM	attomolar
cm	centimeter
C	Celcius
eV	electronvolt
g	gram
h	hour
Hz	hertz

$k_B$	Boltzmann constant
kDa	kilodalton
MHz	megahertz
mL	milliliter
mm	millimeter
mM	millimolar
mmol	millimole
ms	millisecond
min	minute
$m\Omega$	milliohm
nM	nanomolar
nm	nanometer
pM	picomolar
pmol	picomole
psi	pound-force per square inch
r	radius
s	second
$\mu\text{L}$	microliter
$\mu\text{M}$	micromolar

# Acknowledgments

I would like to start by thanking my family, especially my mother, Chizuru Nakatsuka. I cannot begin to imagine the sacrifices she has made for me to be at this stage in my life. She is my biggest inspiration, raising me as a single mother, teaching me discipline, work ethic, and perseverance, and pushing me to try my best in everything I pursued. As an only child, I have spent almost a decade away from my family, who has never ceased to support me in everything I do. I appreciate my grandmother, Keiko Nakatsuka, my aunt and uncle, Noriko and Ryuichi Utsugi, and my cousin and best friend, Annla Utsugi. I am eternally grateful to my grandfather, Shigetoshi Nakatsuka, who taught me how to design my first rubber-band gun and got me excited about technology and engineering. I wish you were still with us so you could see what a positive influence you had on me.

I would like to show my greatest appreciation towards my advisors, Professors Anne M. Andrews and Paul S. Weiss, for their invaluable mentorship throughout my graduate training. Anne has been an instrumental female role model to me and I continue to be inspired by her passion to achieve a goal she has envisioned for decades. Our extensive discussions on experimental and life strategies over mochas and spending time together at conferences abroad were not only some of my favorite moments, but moments that made me grow. The way I conduct science, disseminate my research, and approach challenging problems has been enriched as a result of her invaluable training. I would not be here today if I had not stumbled into Paul's office five years ago. His charisma and excitement for science was contagious and I dropped everything to come to UCLA. Since then, he has taught me skills that are necessary to becoming a successful researcher

outside of knowing the science. I could not have asked for a better team of brilliant, conscientious, and caring advisors who have had my back for my entire graduate career.

The opportunity to obtain my graduate training at UCLA would have been a mere dream if it were not for the support of my undergraduate research adviser, Ipsita A. Banerjee. She nurtured me from a student who knew nothing about research and gave my love for chemistry a purpose. At UCLA, William M. Gelbart was the first professor I met in the Department of Chemistry and since that day, he has continued to council me with his unrivaled patience and kindness. I am also grateful to my committee members, Thomas G. Mason and Dino Di Carlo, who have been extremely supportive of my research. I would also like to thank Yung-Ya Lin, Johnny W. Pang, Christopher Barrett, and Mary Elizabeth Anderson who have been immensely supportive of me during my time at UCLA.

I am so proud and grateful for my Neurochip family, Wei-Ssu Liao and Huan H. Cao who took me under their wings. Meeting Wei-Ssu was a huge factor in my decision to come to UCLA – his creative mind and love for “crazy” research ideas never failed to motivate me. I was always in awe of Huan’s patience. Not only did he demonstrate how good science was conducted, he was also always there for me for every challenge I faced, from coursework, to the candidacy exam, to my mental breakdowns after my bike crash. I am so grateful to have worked beside these two amazing researchers who are also my lifelong friends.

I am also appreciative of other Andrews and Weiss group members whose expertise and willingness to help me was indispensable for my dissertation research to flourish. Hongyan Yang is an incredible researcher who taught me so much about the area of *in vivo* neuroscience and I am constantly inspired by the way she conducts science. Mahdi Hasani-Sadrabadi played a crucial role in bringing the polyserotonin project to fruition and I am

grateful for his diligence, constant support, and friendship. Xiaobin Xu shared his Raman knowledge with me and I really appreciate all our scientific discussions.

As I became a senior member of the group, I have had the pleasure of working with and mentoring Kevin M. Cheung and Chuanzhen Zhao. I am so happy to entrust the Nanobiosensor project to two smart, driven, and hardworking researchers. I am thankful for Kevin and Chuanzhen always having my back through the good and the bad and I am excited for their future achievements. Moreover, I appreciate all members of the Andrews and Weiss groups for their support and friendship.

I was very fortunate to have the opportunity to work with the best collaborators without whom none of this work would have been possible. I am so grateful to Andrea M. Kasko and Stephanie Deshayes for their instrumental contribution to the Neurochip project, Milan N. Stojanović and Kyung-Ae Yang for the extensive discussions and being so willing to help us to move the aptamer biosensor project forward, and You Seung Rim who patiently showed me the ropes when I first started transistor measurements.

In addition, I would like to gratefully acknowledge funding from the Cal-Brain Neurotechnology Program, Nantworks, Hewlett-Packard, National Institutes of Health (DA045550), and the UCLA dissertation year fellowship, that made all of my research endeavors possible. I also thank the UCLA Department of Chemistry and Biochemistry, the California NanoSystems Institute, and the UCLA Semel Institute for Neuroscience and Human Behavior for the use of their facilities and support of this work.

My graduate life would not have been complete without my friends. Alex M. Mendoza was the first person I met at UCLA. Little did I know then, that I had met a friend who I can rely on, trust, and respect in every aspect of my life. Adam D. Sutton, Colin R.

Rementer, and Joshua T. McGuigan were friends I made my first year and we were inseparable. Six years later even after going our separate ways, the fact that we make the effort to see each other is proof of our strong friendship.

I am also grateful for John D. McMahon and Heidi R. McMahon, whose generosity is immeasurable. They trusted my capabilities as an artist to illustrate an ABC Chemistry book for children and I am really proud of our work. I thank Maureen M. Sampson, Taylor J. Aubry, and Emma K. McCune, three tough and inspiring women, who have helped me tackle new challenges. I also want to recognize my best friend of almost two decades, Louis Persent, without whom I would not be the person I am today.

I would like to thank the UCLA Triathlon Team, in particular, Coach Brady O'Bryan who made me conquer many fears including swimming in open water and getting back to riding after my bike crash. I would never have immersed myself in such hard training if it were not for my then-roommate and friend, Kelly K. O'Neil who encourages me incessantly to become both a better person and athlete.

Finally, I want to thank John M. Abendroth. As my best friend of six years and partner of four, he has supported me unconditionally in the most selfless way in everything I pursue, even through the hardest times. I am fortunate to have someone I trust, respect, and admire to continue to pursue scientific research with, in the next chapter of our lives.



# VITA

I came to the United States of America to attend Fordham University in New York City to pursue an undergraduate degree in chemistry. At Fordham, I joined the research group of Professor Ipsita A. Banerjee in the Department of Chemistry in 2010. My undergraduate research focused on developing peptide-based nanostructures for tissue engineering, drug delivery, and gene therapy applications. At Fordham, I was also a member of the Division I cross country and track and field team, and was on the Atlantic-10 Commissioner's Honor Roll for high academic and athletic performance all four years. I received several academic awards and honors, including the Loret Miller Ruppe Scholarship for International students, the Dean's Scholarship for four years, and a Fordham University undergraduate summer research grant for two years. I published two first-author publications, co-authored five manuscripts and a book chapter, and presented my research at nine conferences, earning my Bachelor of Science in Chemistry in 2012.

Shortly thereafter, I began my graduate work at the University of California, Los Angeles under the mentorship of Professor Anne M. Andrews in the Departments of Psychiatry and Chemistry and Biochemistry, and Professor Paul S. Weiss in the Departments of Chemistry and Biochemistry and Materials Science and Engineering. My dissertation work involved the use of DNA aptamers as artificial receptors integrated into electronic devices for detecting small molecules such as neurotransmitters under physiological conditions. In 2015, I received the Hanson-Dow Excellence in Teaching Award, as well as several travel awards to present my research at conferences both locally (San Diego, CA; San Francisco, CA), within the U.S. (Seattle, WA), and overseas (Gothenburg,

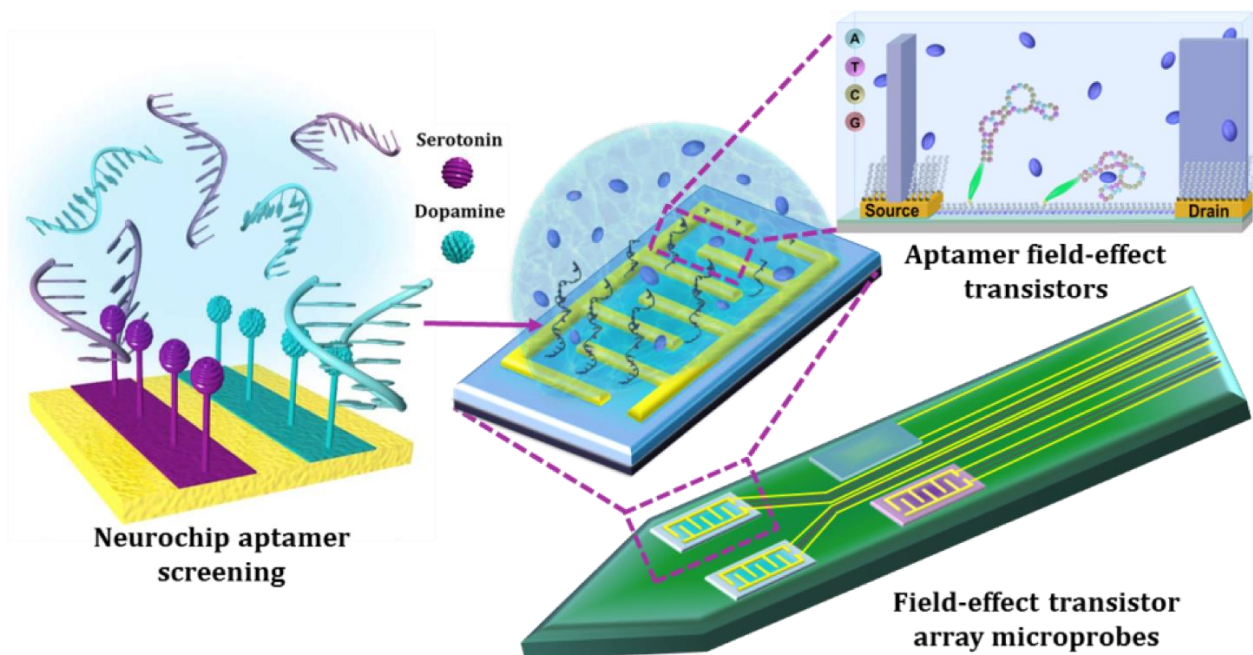
Sweden; Maintenon, France). I won two research pitch contests held at UCLA and was a dissertation year fellow. I was a member of three consecutive National Championship UCLA Triathlon Teams. In 2017, I illustrated a children's ABC book for aspiring chemists, participated in a BuzzFeed x Pfizer video to encourage young kids to get excited about science, and was an invited speaker for the Women in Science, Technology, Engineering, Arts, and Mathematics Conference at the Mirman School for talented children (Santa Monica, CA) to share nanotechnology concepts with five- to ten-year-olds.

## LIST OF SELECT PUBLICATIONS

1. **Nakatsuka N**, Yang KA, Xu X, Abendroth JM, Zhao C, Cheung, KM, Zhu B, Rim YS, Yang Y, Weiss PS, Stojanović MN, and Andrews AM. Aptamer Field-Effect Transistors Overcome Debye Length Limitations and Enable Small-Molecule Sensing, *submitted* (2017).
2. **Nakatsuka N**, Weiss PS, and Andrews AM. Realizing *in Vivo* Biosensors: Aptamer-Functionalized Field-Effect Transistors, *invited review for Chemical Reviews, in preparation* (2017).
3. **Nakatsuka N**, Cao HH, Deshayes S, Kasko AM, Weiss PS, and Andrews AM. Aptamer Recognition by Multiplexed Neurotransmitter-Functionalized Substrates, *in preparation for ACS Chemical Neuroscience* (2017).
4. **Nakatsuka N**, Hasani-Sadrabadi MM, Cheung KM, Young TD, Bahlakeh G, Moshaverinia A, Weiss, PS, Andrews AM. Serotonin Nanoparticles as Multifunctional Nanomaterials for Biomedical Applications, *in preparation for ACS Applied Materials and Interfaces* (2017).
5. **Nakatsuka N** and Andrews AM. Differentiating Siblings: The Case of Dopamine and Norepinephrine, *ACS Chemical Neuroscience* 8, 218-220 (2017).
6. **Nakatsuka N** and Andrews AM. Nanoscale Neurochips to Enable High Resolution *in Vivo* Neurotransmitter Sensing, *Neuropsychopharmacology Reviews* 41, 378-379 (2016).

# Chapter I

## Next-Generation Biosensors to Monitor Molecules *in Vivo*



## **I.A. The BRAIN Initiative – Nanotools for Neuroscience**

On April 2<sup>nd</sup> 2013, President Barack Obama announced the Brain Research through Advancing Innovative Neurotechnologies (BRAIN) Initiative aimed at revolutionizing our understanding of the enigmatic human brain. It was an ambitious call for collaborative efforts to accelerate the design and development of novel nanotools to map dynamic brain function at high density.<sup>1</sup> The capacity to measure brain signaling pathways quantitatively at the length and time scales pertinent to information encoding would enable scientists to discover novel treatments and preventative approaches for psychiatric and neurodegenerative diseases such as depression, post-traumatic stress disorder, and Alzheimer's and Parkinson's diseases.

The complexities of brain function arise from the emergent properties of neural circuits and networks. Individual neurons form synaptic and extrasynaptic contacts with thousands of other neurons. Thus, information gained by neurophysiological techniques such as single-electrode recordings that monitor single to a few neurons do not reflect the overall connectivity of neural networks.<sup>2</sup> Furthermore, neuronal plasticity results in dynamic rearrangements of neural connections and their relative strengths.

To address the challenges incumbent in the BRAIN Initiative, researchers have proposed to record every action potential from every neuron within a circuit, simultaneously.<sup>3</sup> Ironically, this focus on electrophysiology is reminiscent of the questions that defined the War of the Soups and the Sparks<sup>4</sup> in the 1930s. The latter was a debate between the rapidly advancing fields of neuropharmacology (soups) and electrophysiology (sparks) about how neurons communicate across synaptic gaps. While massively parallel electrical recordings would presumably map neural circuits to some extent, they will

ultimately *not* represent information processing in brains that occurs *via* complex synaptic chemistries involving signaling molecules called neurotransmitters. Without considering the complex information inherent in the chemical diversity residing in interneuronal signaling pathways occurring within dynamic changes in neurotransmitter fluxes, we will be unable to fully understand brain function.<sup>5</sup>

Thus, to map human (and experimental animal) brains fully, both dynamic voltage activities associated with neuronal firing *and* chemical neurotransmission associated with numerous neurotransmitters must be considered.<sup>6</sup> If mapped in total, this endeavor would involve an estimated 85 billion neurons, 100 trillion synapses, and 100 chemical neurotransmitters in the human brain.<sup>7</sup> Regarding neurochemical mapping, currently, there are approaches for *in vivo* neurochemical sensing. The first is an indirect approach largely encompassing microdialysis sampling coupled to analytical methods like high-performance liquid chromatography or mass spectrometry.<sup>8</sup> The second involves direct-sensing implantable biosensors.<sup>9-11</sup> While these methods are powerful for studying dynamic neurochemistry, their limitations in terms of temporal and spatial resolution, and chemical selectivity, significantly impede progress toward understanding brain function.

For example, while microdialysis enables multiplexing and dialysate sampling times are decreasing,<sup>12-16</sup> the spatiotemporal resolution is still not well suited to reveal the properties of complex neural circuits. Fast-scan cyclic voltammetry (FSCV), which is a direct-measurement method, has been widely successful for the investigation of dopamine dynamics.<sup>17-20</sup> However, voltammetry is difficult, if not impossible, to generalize to other neurotransmitters and to multiplex. Similarly, enzyme-based amperometric microsensors have been used to measure glucose<sup>21,22</sup> glutamate,<sup>23-25</sup> and acetylcholine.<sup>26-28</sup> While this

approach has enabled much to be learned about neurotransmitter signaling in the context of behaviorally relevant stimuli, it is not widely generalizable because highly selective redox enzymes are nonexistent for many neuropeptides, neurosteroids, and neurolipids.

In light of these collective disadvantages, to answer the call of the BRAIN Initiative, the next generation of nanotools for neuroscience must address chemical sensors that are *small* to record at the level of synapses or local intracellular spaces (tens of nanometers), *fast* to correspond to  $\sim 1$  Hz or better time frames to differentiate neurochemical release/reuptake, *selective* to distinguish between structurally similar small molecule precursors and metabolites present in the extracellular space, as well as closely structured neurotransmitters, and *multiplexed* to enable recording of multiple neurochemicals simultaneously. Our vision is to use aptamer-functionalized field-effect transistor biosensors for direct, simultaneous, dynamic, and spatially resolved measurements of a wide range of chemical signaling molecules in the highly heterogeneous brain extracellular milieu.

## **I.B.      Towards Electronic Biosensing *in Vivo***

To advance the state-of-the-art for *in vivo* biosensing of neurochemicals, we have integrated biomolecular recognition with direct electronic signal detection. Realization of *in vivo* next-generation neurochemical biosensors is built on foundational breakthroughs involving several technologies that when combined, will enable researchers to overcome current limitations in neurochemical monitoring.

Biosensors are target detection systems that consist of biomolecule recognition elements, such as enzymes, antibodies, or cellular receptors, coupled to transducers that convert target recognition into electrochemical, electronic, optical, or other types of directly measurable signals. In 1962, Leland Clark reported an “enzyme electrode”, the antecedent to today’s widely used blood-glucose analyzer, *i.e.*, glucometer.<sup>29</sup> Clark’s biosensor relied on recognition and enzymatic degradation of glucose by glucose oxidase, coupled to the reduction of oxygen to hydrogen peroxide. Oxygen consumption was measured at an oxygen-sensitive electrode.

When *in vivo* glucose monitors were first evaluated two decades ago,<sup>30,31</sup> the surgical procedure to implant these sensors resulted in adverse subcutaneous reactions, obscuring glucose signals and causing side effects in patients.<sup>32</sup> Barriers that had to be overcome for *in vivo* monitoring of glucose, included lack of sensor accuracy and precision over a wide range of target concentrations, short sensor lifetimes, poor calibration, and instability, all of which led to problems with reproducible detection.<sup>33</sup> Nonetheless, today, implantable sensors are used to monitor glucose levels continuously in real time.<sup>34</sup> As such, glucose biosensors exemplify the challenges of translating *in vitro* sensors to *in vivo* environments. *In vivo* sensors are critical to current needs in neuroscience,<sup>5,6,35-37</sup>

microbiome studies, and many areas of basic<sup>38-40</sup> and biomedical<sup>41-43</sup> research, as well as the practice of medicine.<sup>44-50</sup>

Biosensors developed for use *in vitro* are often not amenable for investigating biological processes in living organisms.<sup>51</sup> *In vivo* measurements regularly involve detecting analytes at lower concentrations and/or over wider ranges than those encountered for *in vitro* applications. Pre-concentration or dilution, as well as clean-up to remove interferents can be employed *in vitro*; these steps are largely infeasible when directly sensing *in vivo*. High temporal resolution is commonly needed *in vivo* to capture dynamic events.<sup>52,53</sup> On the whole, the design and implementation of *in vivo* biosensors must address challenges associated with sensitivity, selectivity, temporal and spatial resolution, and biofouling.<sup>54</sup>

One approach to improving signal transduction for biosensors involves the use of field-effect transistors (FETs). In standard FETs, semiconducting *n*- or *p*-doped channel materials between metal source and drain electrodes are used to sense changes in electric fields above channel surfaces, *i.e.*, changes in surface electric fields alter the resistance to electron flow through the semiconductor. When semiconducting channels are biased with positive or negative voltages, three regimes of surface conductivity may exist. For the case of *n*-type semiconductors, when a positive gate voltage is applied, excess electrons will accumulate at the surface, and the bands proximal to the surface are bent downward (Figure I.1A). In this *accumulation* case, band bending makes the surface more *n*-type than the bulk, resulting in a higher majority carrier density. If instead a small negative voltage is applied, the energy bands near the surface are bent upward, and electron carrier density is decreased, in the so-called *depletion* case (Figure I.1B). Here, the space-charge per unit area



depends on the width of the region of charge depletion. Finally, in the *inversion* case, if a large negative voltage is applied to the channel, the energy bands are bent upward even further and the intrinsic level crosses the Fermi level (Figure I.1C). Excess positive carriers are then induced at the surface. Thus, the excess surface conductivity, and direction of current, depends on the applied surface potential.<sup>55</sup> In the case of *p*-type semiconductors, the same three regimes at different surface potentials exist, but band bending occurs in opposite directions. Further, the presence of adsorbates on semiconductor surfaces can change the conductance, which can be attributed to the effects of band bending.

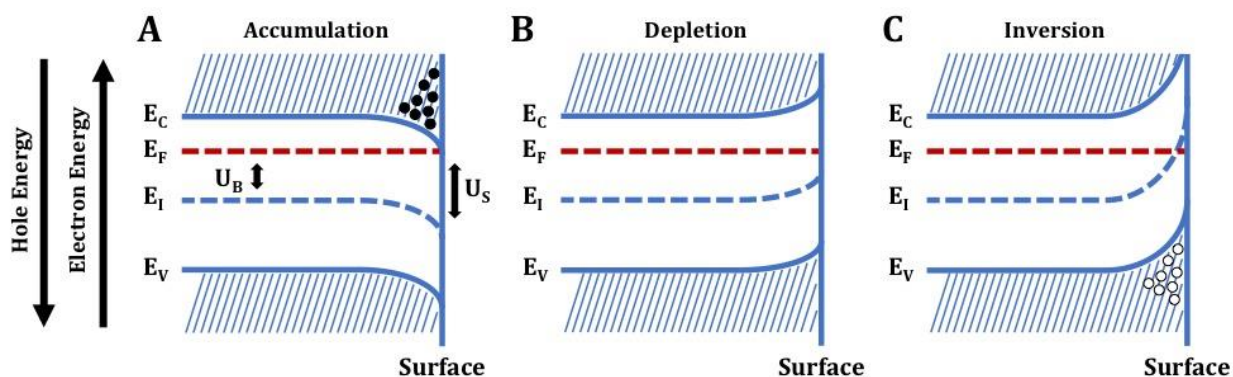


**Figure I.1.** Energy level diagrams and charge distributions of an *n*-type semiconductor showing band bending at the surface. Shown from left to right are the three charge transport regimes described by the (A) accumulation, (B) depletion, and (C) inversion cases.  $E_C$ : conduction band energy,  $E_V$ : valence band energy,  $E_F$ : Fermi energy,  $E_i$ : intrinsic energy level,  $U_B$ : bulk potential,  $U_S$ : surface potential. Electrons (majority carriers) are illustrated as solid circles and holes, (minority carriers) are illustrated as open circles.

The channels of FETs can be functionalized with molecular recognition elements that bind to targets. Target recognition gates channels by shifting surface potentials controlling carrier populations in the channels.<sup>55-64</sup> Associated changes in transconductance serve to amplify target detection significantly, just as transistors are used in common electronic amplification circuits with voltage-controlled gates. Thus,

charge at channel surfaces, as well as in the nearby surrounding medium, is critical to the function of FETs.

In conventional electronic devices, FETs are encapsulated to avoid the effects of charged molecules on their surfaces, whereas in biosensors this effect is used simultaneously for detection and amplification. Channels constructed of nanometer-thin films,<sup>65</sup> or one-dimensional<sup>66-74</sup> or two-dimensional materials<sup>75,76</sup> (*vide infra*) are particularly advantageous because the effects of shifts in surface potential penetrate the entire material, increasing device sensitivity.

The use of FETs in biosensing couples high sensitivity and real-time, label-free measurements with electronic output.<sup>77,78</sup> This strategy for electronic readout enables measurements where dense or opaque tissue precludes or complicates optical approaches.<sup>2,3,79</sup> The availability of a range of physical and chemical patterning methods facilitates FET scaling down to appropriate sizes to match native biological compartmentalization (micro- to nanoscale) enabling physiological measurements.<sup>80</sup> Furthermore, FET architectures have prospects for lower-cost production using conventional, soft, or hybrid lithographies.<sup>81-87</sup>

Surface chemistries employed to tether recognition elements to FET devices are critical to reducing nonspecific binding of interferents, which contributes to reduced sensitivity and poor concentration responses.<sup>88</sup> Detectable changes in FET conductance associated with target binding have been reported to occur at femtomolar and even attomolar analyte concentrations.<sup>89-93</sup> Even low occupancy of tethered recognition elements may be sufficient to produce measureable signals since small perturbations due to reorganization of the ionic double layer disturbs carrier distributions in semiconducting

layers. Consequently, FETs can be used to detect targets at lower and over larger concentration ranges compared to equilibrium sensing devices, which are typically limited to detection within an order of magnitude in either direction of recognition element dissociation constants ( $K_d$ ).

To establish a conceptual framework, I briefly discuss the emergence of biological field-effect transistors (bioFETs) beginning with the use of enzymes or antibodies as molecular recognition elements. Due to limitations of enzyme- and antibody-FETs, particularly when translating to *in vivo* applications, I then focus on nucleic-acid (aptamer) recognition motifs and coupling to FETs.

### **I.B.1. Enzyme- and Antibody-Based Field-Effect Transistors**

Following Clark's development of a glucose biosensor, others capitalized on native enzymes that produce byproducts readily detectable by FETs. The enzyme-FET (enFET) concept was proposed in 1976 by Janata and Moss.<sup>94</sup> This design was realized in 1980 by Caras and Janata who produced an enFET where the conversion of penicillin to penicilloic acid by the enzyme penicillinase was monitored *via* the concomitant generation of protons detected at pH-sensitive FETs.<sup>95</sup> Other examples of enFETs have been utilized to monitor glucose in blood serum<sup>96</sup> or urine,<sup>97</sup> and urea in serum<sup>98,99</sup> or hemodialysis fluids.<sup>100</sup> However, analytes detectable by enFETs are limited because native enzymes that can be coupled with FET signal transduction do not exist for many targets. Accordingly, there was a need to develop molecular recognition elements for other important targets and broadly applicable strategies for doing so.

As an alternative, antibodies can be raised to recognize a wide variety of targets. This capability has led to the development of biosensors based on known antibody-antigen interactions for molecular recognition and FETs for signal transduction, termed immunoFETs.<sup>101,102</sup> Antibodies are most often available for protein targets with molecular weights greater than 5 kD.<sup>103</sup> However, cross-reactivities, which cannot be addressed during antibody selection, interfere with selective sensing.<sup>104</sup> Further, antibody affinities are difficult to modify.<sup>105</sup> Concentrations of analytes *in vivo* can vary significantly requiring affinities of recognition elements to be tunable. Alternately, multiple recognition elements with differing affinities can be used.<sup>106-108</sup>

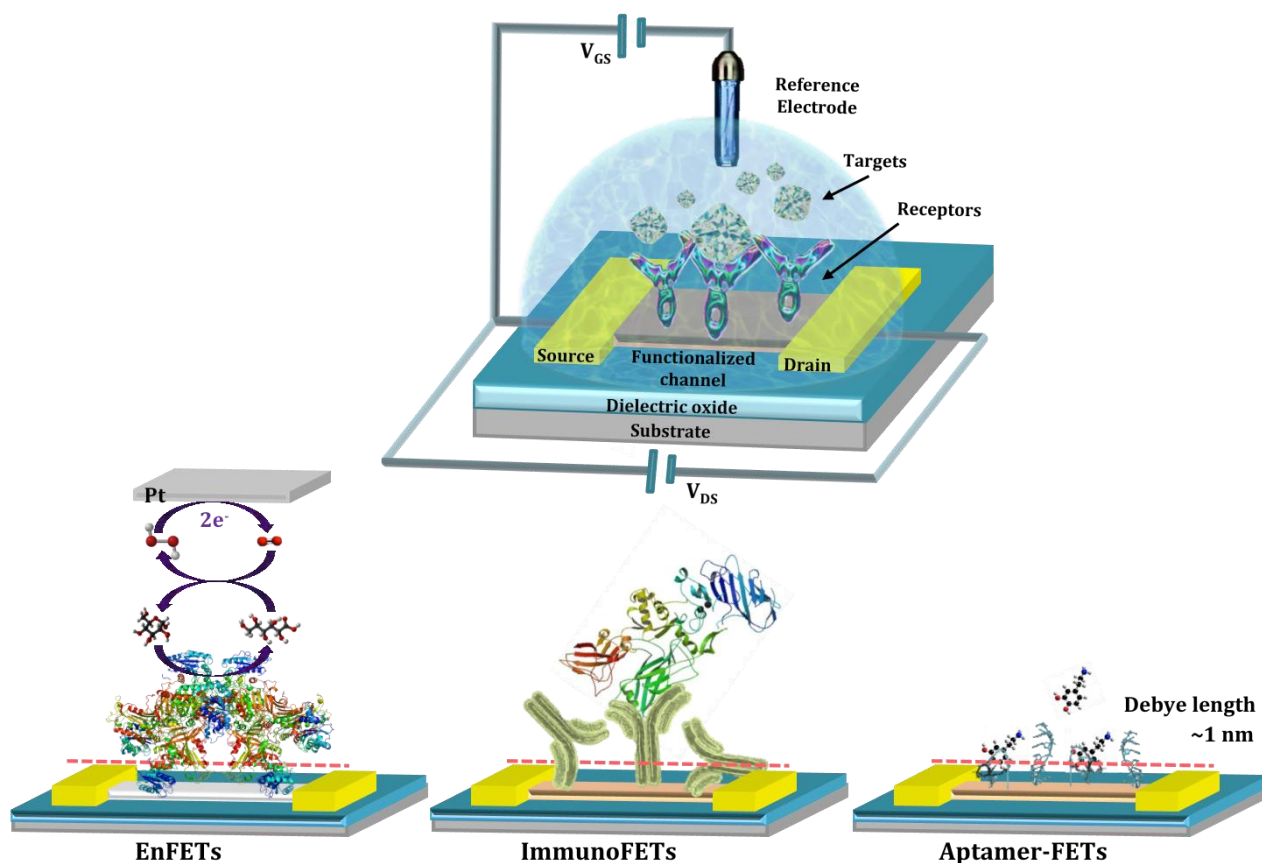


**Figure I.2. (Top)** Schematic of bioFET device architecture with the source, drain, and gate (channel) electrodes shown. **(Bottom)** Relative size differences of recognition elements for enzyme-functionalized FETs (enFETs), antibody-functionalized FETs (immunoFETs), and aptamer-functionalized FETs illustrating the proximity of target binding to FET surfaces in relation to a typical Debye length of ~1 nm in physiologically relevant solutions.

### **I.B.2. Challenges of Debye Lengths in High Ionic-Strength Solutions**

Gating semiconducting channels in FET devices in solution is such that only changes in charge close to device surfaces are detectable with effective sensing distances dependent on the Debye length,<sup>109</sup> *i.e.*, the screening length for charge carriers in solution. In the context of FETs, the Debye length is the distance from a channel surface beyond which the effects of changes in local electric fields decrease rapidly in terms of their ability to shift surface potentials and thereby gate charge carriers in the semiconductor channels.<sup>110</sup> Debye lengths become particularly limiting in the presence of biologically relevant salt concentrations, *i.e.*, high ionic strength environments encountered *in vivo*.<sup>111</sup>

ImmunoFETs have been hypothesized to detect antibody-antigen interactions due to both components, *i.e.*, target and molecular recognition element, being charged.<sup>112</sup> Binding events are theorized to lead to conformational changes in antibodies and also, in protein targets. These conformational changes are proposed to drive changes in potentials at FET surfaces.<sup>113</sup> However, the dimensions of antibodies are tens of nanometers, as opposed to physiological Debye lengths, which are  $\sim 1$  nm (or less), in extracellular or intracellular fluids, or blood, serum, or urine (Figure I.2).<sup>92,114-116</sup> Consequently, capture (or release) of analytes from antibodies has been hypothesized to occur at distances from FET surfaces that are significantly greater than biological Debye lengths such that changes in semiconductor surface charge are largely shielded by solution counterions.<sup>117,118</sup>

Gupta *et al.* discussed ideas about immunoFET limitations associated with Debye lengths, including common misconceptions about antibody structure and surface functionalization.<sup>109</sup> Antibodies immobilized on substrates *via* adsorption are not uniformly oriented with their binding domains pointing away from substrates but are

instead randomly oriented. Antibodies are also flexible, particularly in their hinge regions. Moreover, polyclonal antibodies that recognize different epitopes on a single target bind target molecules in various orientations resulting in changes in charge at varying distances from FET surfaces. Thus, these authors posited that some portion of target binding is expected to occur within or near physiological Debye lengths. By way of example, they reported detection of clinically relevant levels of a biotinylated inflammatory chemokine in physiological salt solution ( $\sim 150$  mM  $\text{Na}^+$ ).<sup>119</sup> Casal *et al.* extended this idea by demonstrating that immunoFETs can be used to detect both human and murine chemokines in physiologically relevant buffers.<sup>120</sup>

One approach to address Debye length limitations involves the use of antibody binding fragments.<sup>121</sup> For instance, while an antibody is  $\sim 10$ - $15$  nm, Okamoto *et al.* used a 3-nm antigen-binding fragment- (Fab) targeting heat-shock protein to conduct sensing in a 10 mM buffer solution with a Debye length of  $\sim 5$  nm.<sup>122</sup> Similarly, Elnathan *et al.* used antibody fragments to detect cardiac troponin I myocardial infarction biomarker with picomolar sensitivity in serum without desalting.<sup>123</sup>

### **I.C. Aptamer Recognition Elements for Field-Effect Transistors**

Aptamers are single-stranded, short DNA, RNA, or nucleic-acid analog oligomers (typically <100 nucleotides) that fold into compact three-dimensional (3D) structures. Aptamers targeting viruses,<sup>124-126</sup> proteins,<sup>127-129</sup> peptides,<sup>130-132</sup> small molecules,<sup>133-136</sup> and ions<sup>137-139</sup> have been identified. Most, if not all aptamers undergo some form of conformational change upon target recognition, *i.e.*, adaptive binding. Compared to antibodies, aptamers are smaller and lack large nonbinding fragment crystallizable (Fc) regions (Figure I.2). As such, aptamers are hypothesized to undergo binding-induced conformational changes closer to sensor surfaces, and potentially, with more significant charge rearrangement occurring within physiological Debye lengths. Moreover, because aptamer phosphodiester backbones are highly negatively charged, conformational changes lead to larger net charge rearrangements in close proximity to semiconductors, even when binding targets that are themselves uncharged.

Aptamers have a number of other potential advantages for bioFET applications and may represent a generalizable strategy for molecular recognition when integrated with FETs.<sup>140-142</sup> Because they are relatively short sequences, aptamers are chemically synthesized with minimal batch-to-batch variation.<sup>143</sup> They can be chemically stabilized for use *in vivo*.<sup>144</sup> Among other methods, aptamers have been modified by conjugation to carrier molecules, such as polyethylene glycol, to slow renal clearance<sup>145-149</sup> or capped at their 3'- and/or 5' ends to enhance nuclease resistance.<sup>150-152</sup> Alternately, nuclease recognition can be prevented by introduction of modified bases, including the use of enantiomeric nucleic acids, or Spiegelmers, where appropriate.<sup>153-155</sup>

Aptamers are isolated by combinatorial approaches that circumvent *de novo* design and result in diverse pools of candidates to evaluate for unique properties. The process of directed evolution, originally termed systematic evolution of ligands through exponential enrichment (SELEX; Figure I.3A),<sup>156-158</sup> has produced aptamers for a variety of applications including *in vitro* diagnostics and biosensor technologies, biomarker discovery, and targeted therapies.<sup>159,160</sup> Advances in SELEX, as well as solution-phase selection approaches<sup>161</sup> have been used to identify aptamers even for challenging targets.<sup>162-166</sup> Aptamers have been demonstrated to have tunable properties when it comes to dynamic responses to changes in analyte concentrations over biologically meaningful time scales.<sup>105,167</sup> As such, aptamers adapted to analytical applications have given rise to aptamer-based biosensors.<sup>168,169</sup>

Another key feature of *in vitro* selection methods is that counter-selection (negative selection) can be incorporated to exclude nucleotide sequences with high affinity for cross-reactive agents (Figure I.3B,C).<sup>162,170,171</sup> Counter-SELEX improves aptamer selectivity towards target molecules vs. structurally similar target analogs including target precursors and metabolites, and high concentration matrix constituents.<sup>172</sup> Aptamers also provide opportunities for tunability where manipulation of primary base sequences controls folding kinetics and binding affinities.<sup>173,174</sup>



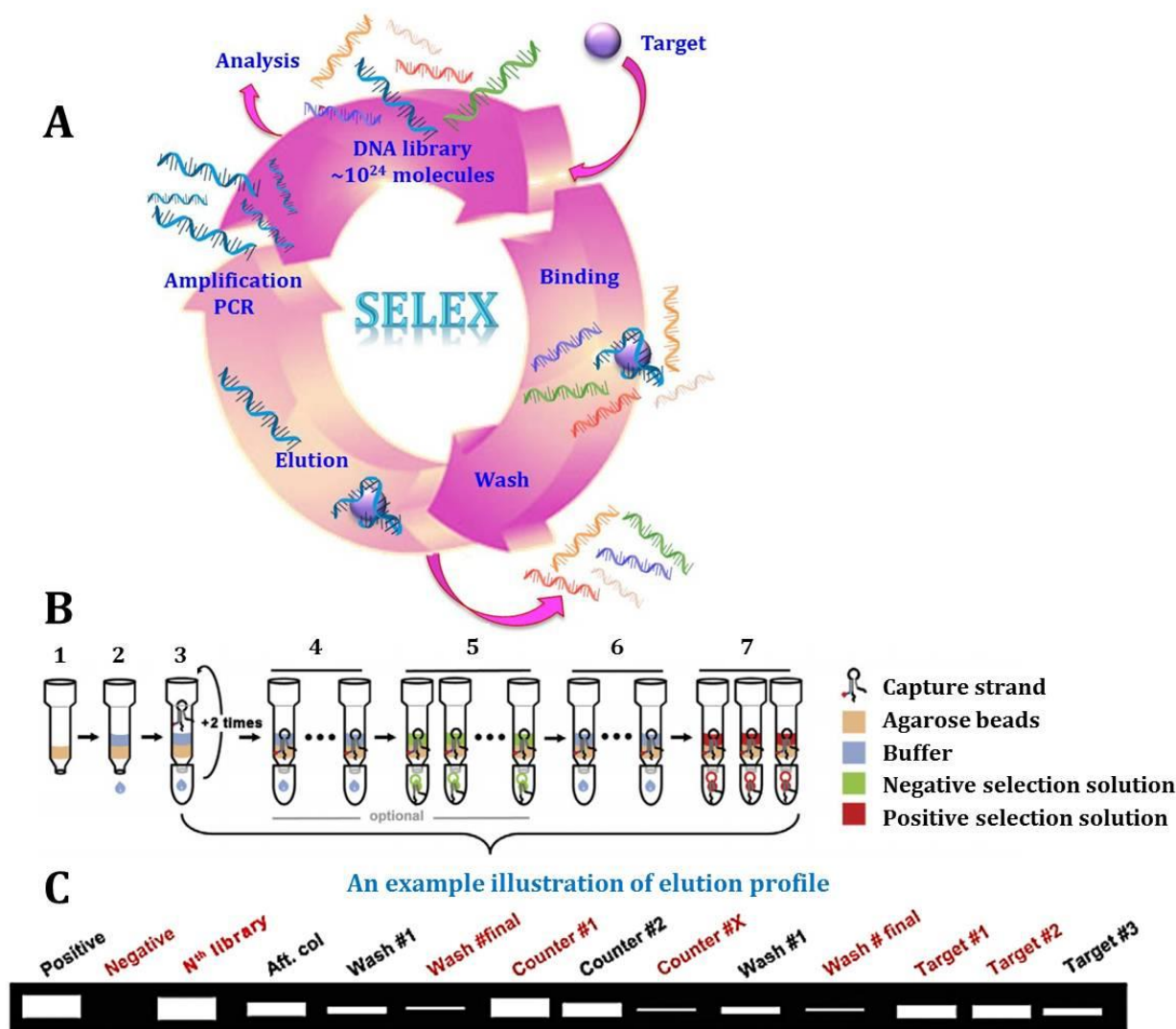


**Figure I.3.** Schematics of SELEX and counter-SELEX. **(A)** Targets immobilized on beads are incubated with a DNA library. Beads are then washed to remove unbound DNA sequences. Bound sequences are eluted and amplified *via* PCR for subsequent rounds of more stringent selection. **(B)** Solution-phase selection procedure: (1) Agarose bead addition, (2) Beads are washed with SELEX buffer for equilibration. (3) Addition of nucleotide library. The eluent is collected and re-applied to the column to maximize capture. (4) The column is washed with SELEX buffer ~10 times to remove low-affinity library elements. Numbers of washes can be adjusted based on the desired selection stringency. (5) Negative/counter selection to remove less specific library elements that bind to molecules that compete with the desired target. (6) Additional washes to remove residual sequences from negative selection step. (7) Positive selection where incubation occurs with free target molecules in solution; the red-labeled fractions are collected. **(C)** An example illustrating elution profiles. The collected eluents are compared through small-scale PCR. Adapted with permission from ref. 162. Copyright 2016 Elsevier.

### **I.C.1. Riboswitches and Small-Molecule Aptamers *in Vivo***

Naturally occurring riboswitches have been discovered that recognize small molecules and ions with remarkably high sensitivity and selectivity.<sup>194</sup> Riboswitches are noncoding messenger RNA domains that control gene expression *via* small-molecule effector recognition and conformational switching.<sup>195-197</sup> A riboswitch for guanine was discovered having  $K_d \approx 5$  nM.<sup>198</sup> A thiamine pyrophosphate-sensing riboswitch was identified having picomolar target affinity.<sup>198,199</sup> The existence of riboswitches suggests substantial potential for synthetic aptamers to be identified that recognize small molecules specifically and with affinities appropriate for *in vivo* sensing applications.

In addition to naturally occurring riboswitches, some synthetic aptamers recognizing small molecules exist and have demonstrated capabilities for monitoring small-molecule targets *in vivo*. For example, recognition of adenosine and associated changes in aptamer secondary structure have been exploited to induce self-assembly of gold nanorods, which in turn, enhanced plasmon resonance for the detection of adenosine (4-80 nM) in the brains of rats.<sup>200</sup> Graphene oxide, which adsorbs nucleic acids and has super fluorescence quenching efficiencies, was coupled to an ATP-specific aptamer-based two-photon fluorescent nanoprobe for the detection of intracellular ATP in HeLa cells and *in vivo* in zebrafish.<sup>201</sup> Aptamer sensors coupled to fluorescein in proximity to binding motifs and immobilized on living cells were used to detect gliotransmitters, which control synaptic activity in the brain.<sup>202</sup> While these cases show the potential of isolating synthetic aptamers and employing them *in vivo*, they are extremely limited, leading to a discussion of the challenges associated with discovering aptamers for diverse physiologically important small-molecule targets.

### **I.C.2. Challenges of Discovering Aptamers for Small-Molecule Targets**

Small molecules play important roles in biological signaling pathways throughout the body.<sup>203</sup> In the brain, numerous small molecules, including neurotransmitters, neuromodulators, and neurohormones are critical targets for mapping complex extracellular chemistries to understand brain function.<sup>5,6</sup> Aptamers for small molecules with affinities needed to investigate inter- and intracellular signaling molecules over physiologically relevant concentration ranges (pM to  $\mu$ M) upon incorporation into biosensors, while plausible, have otherwise proven difficult to identify.<sup>204</sup> Binding affinities of most reported small-molecule aptamers are in the micromolar range.<sup>205</sup> Moreover, some reported aptamers display cross-reactivity with structurally similar molecules encountered *in vivo*. For example, dopamine aptamers cross-react with norepinephrine, another neurotransmitter that differs from dopamine by a single hydroxyl moiety.<sup>206-210</sup> The scarcity of new high-affinity small-molecule aptamers has been attributed to the complexity in targeting molecules with low molecular mass and rotatable bonds.<sup>211,212</sup>

### **I.C.3. Selecting Small-Molecule Aptamers in Solution**

Recent breakthroughs circumvent difficulties associated with solid-phase SELEX,<sup>213,214</sup> specifically those posed by identifying aptamers for small molecules.<sup>144,250</sup> Several groups have used modified SELEX approaches to identify aptamers for small-molecule, low-epitope targets that obviate the need to tether targets.<sup>166,215-217</sup> Stojanović and co-workers have used short DNA strands complementary to one arm of a stem sequence in a stem-loop motif for immobilization to a column *via* biotin-streptavidin linkage.<sup>218</sup> A library of DNAs having variable nucleotides in key locations in a three-way junction motif was then

immobilized *via* base pairing to the complementary strand. Target molecules in relevant buffers were flowed through the column. Sequences with high-affinity target recognition were released due to conformational changes associated with target binding. This strategy has enabled the discovery of aptamers that undergo substantial target-binding induced conformational changes that can serve as candidates for coupling to FET platforms.

Target association drove stem formation displacing aptamer candidates from the complementary sequence and thus, the column. Liberated sequences were then enriched in subsequent rounds of selection.<sup>140</sup> The critical advantage of this approach involves the use of small molecules unmodified and in solution, *i.e.*, as they exist during *in vivo* signaling.<sup>162</sup> Using untethered small-molecule targets during selection maximizes interactions with oligonucleotides increasing the likelihood of identifying aptamers with high target affinity. Further, the ability to tune counter-selection protocols minimizes cross-reactivity with similarly structured analytes enhancing aptamer selectivity (Figure I.3B).<sup>171</sup>

A different solution-phase aptamer discovery strategy involved a method inspired by phage display<sup>157</sup> that takes advantage of the ability to carry out PCR amplification in water/oil emulsions.<sup>139</sup> An aptamer library was dispersed such that each droplet in an emulsion contained on average, one unique DNA sequence. These droplets, termed “aptamer particles”, were sorted by fluorescence-activated cell sorting based on target-binding affinities. Instead of fluorescently labeling small-molecule targets, which alters their structures, two different fluorescently labeled reporter strands were hybridized to short constant regions incorporated into each sequence of the DNA library. Upon target binding, one reporter was released, reducing its specific fluorescence in an affinity-

mediated manner. This design enabled direct measurement of metal ion binding to individual aptamer particles without labels, solid supports, or modifications.

#### **I.C.4. Solid-Phase Substrates for Small-Molecule Aptamer Discovery**

In parallel to solution-phase selection, solid-phase screening substrates have the potential to isolate small-molecule aptamers with the advantage of exerting molecular level control of surface parameters to optimize surface environments for biorecognition (Figure I.4).<sup>36,219-221</sup> Chemical patterning and functionalization approaches have been developed to endow biocapture surfaces with recognition and sorting capabilities demonstrated using antibodies<sup>222</sup> and native G-protein coupled receptors.<sup>223</sup> To immobilize targets without using their limited functional group moieties for tethering, modified small-molecule neurotransmitters having an extra functional group have been used for linking chemistries.<sup>220</sup> This strategy enabled small molecules functionalized to capture substrates to mimic free (solution) target molecules. Furthermore, neurotransmitter targets were patterned using microfluidics, which enabled multiplexing and interrogation of specific binding vs. a reference (nonspecific) background when quantifying dissociation constants.<sup>224</sup>

Solid substrates for small-molecule aptamer screening will be complementary to newer solution-phase selection methods,<sup>132,162,163,171</sup> yet with advantages associated with spatial target control. For example, the extent of specific binding relative to matrix recognition can be investigated using target-patterned substrates (Chapter II).<sup>225</sup> Solid substrates enable fine-tuning of target surface densities and reduction of nonspecific binding by manipulating matrix molecule chemistries (Chapter III).<sup>220-223</sup> Multiplexed

patterning of similarly structured targets *via* microfluidics or other types of chemical patterning can be used for counter-selection (Chapter IV).<sup>226</sup> Furthermore, *relative* aptamer binding affinities can be quantified using small-molecule-functionalized substrates (Chapter V).<sup>226</sup>

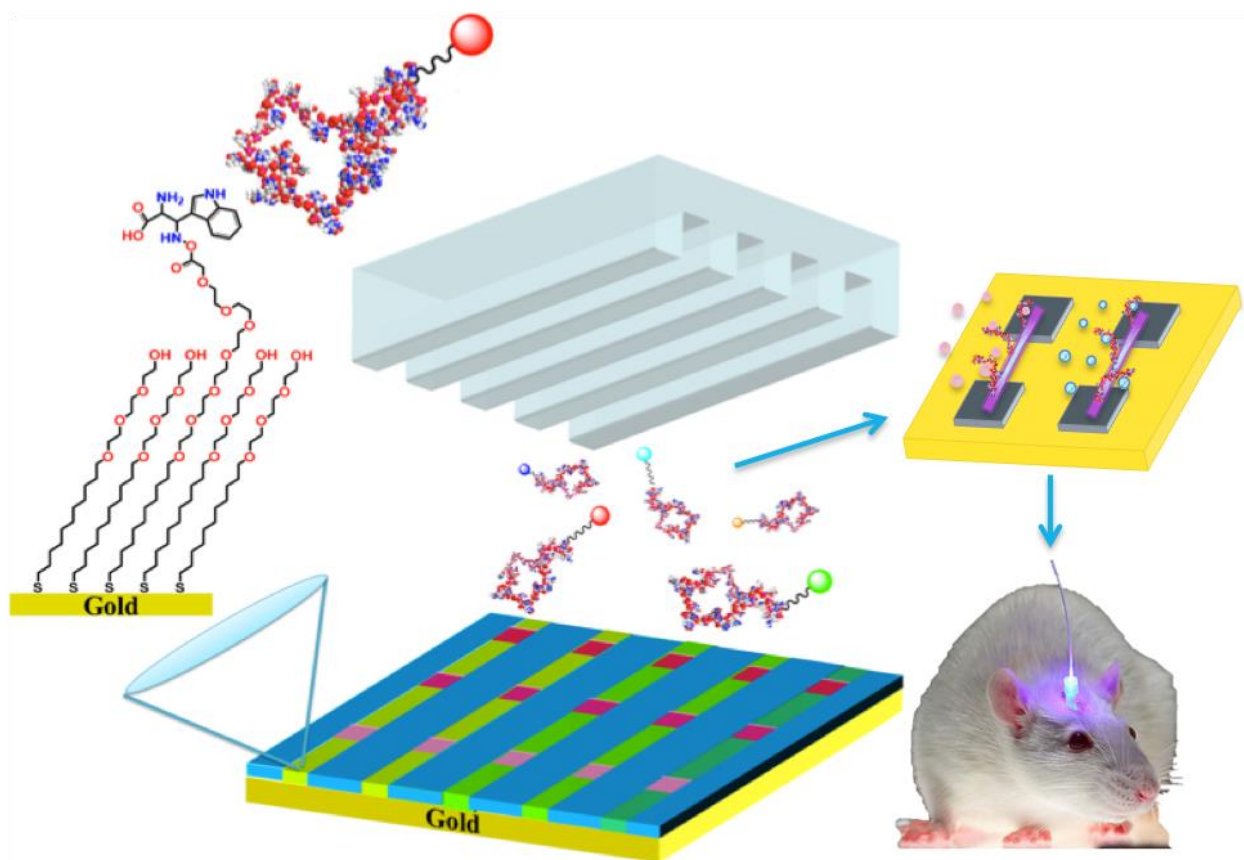


**Figure I.4.** Schematic showing the chemistry, patterning, and use of solid-phase substrates to identify aptamers for use as neurotransmitter recognition elements in novel sensing devices to monitor chemical neurotransmission. **(Left)** The chemistry of self-assembled alkanethiols on gold substrates is shown. A small fraction of these molecules is functionalized with 5-hydroxytryptophan (or other precursors/amino acids) to mimic free serotonin (or other neurotransmitters). **(Middle)** A substrate patterned orthogonally *via* microfluidics devices is shown. These neurochips can be used to screen large libraries of chemically synthesized nucleic acids to identify aptamer sequences that selectively recognize neurotransmitters. **(Right)** Identified aptamers are then coupled to field-effect transistors. Reproduced with permission from ref. 36. Copyright 2016 Nature Publishing Group.

Prior to isolating high-affinity aptamers that can differentiate similarly structured molecules, I immobilized a previously identified dopamine aptamer<sup>227</sup> onto the semiconducting channels of field-effect transistors to conduct biosensing (Chapter VI).<sup>81</sup> Upon discovery by collaborators of aptamers targeting serotonin and dopamine with high specificity and selectivity *via* solution-phase SELEX,<sup>166,171</sup> I was able to sense small-molecule neurotransmitters with unprecedented detection limits over wide concentration ranges even *ex vivo* in brain tissue (Chapter VII).<sup>228</sup> One of my goals was to examine potential mechanisms behind highly sensitive aptamer-based field-effect transistor sensing by analyzing the existing literature critically (Chapter VIII). Elucidating aptamer-FET target recognition mechanisms will enable generalization of sensors designed initially with the goal of *in vivo* neurochemical sensing, to target diverse biomarkers that are difficult to detect in physiological conditions.

## References

1. Insel, T. R.; Landis, S. C.; Collins, F. S. The NIH BRAIN Initiative. *Science* **2013**, *340*, 687-688.
2. Alivisatos, A. P.; Chun, M. Y.; Church, G. M.; Deisseroth, K.; Donoghue, J. P.; Greenspan, R. J.; McEuen, P. L.; Roukes, M. L.; Sejnowski, T. J.; Weiss, P. S.; Yuste, R. The Brain Activity Map. *Science* **2013**, *339*, 1284-1285.
3. Alivisatos, A. P.; Chun, M. Y.; Church, G. M.; Greenspan, R. J.; Roukes, M. L.; Yuste, R. The Brain Activity Map Project and the Challenge of Functional Connectomics. *Neuron* **2012**, *74*, 970-974.
4. Valenstein, E. S. The War of the Sparks and the Soups. *Brain and Cognition* **2002**, *48*, 244-244.
5. Andrews, A. M. The BRAIN Initiative: Toward a Chemical Connectome. *ACS Chem. Neurosci.* **2013**, *4*, 645-645.
6. Alivisatos, A. P.; Andrews, A. M.; Boyden, E. S.; Chun, M.; Church, G. M.; Deisseroth, K.; Donoghue, J. P.; Fraser, S. E.; Lippincott-Schwartz, J.; Looger, L. L.; Masmanidis, S.; McEuen, P. L.; Nurmikko, A. V.; Park, H.; Peterka, D. S.; Reid, C.; Roukes, M. L.; Scherer, A.; Schnitzer, M.; Sejnowski, T. J.; Shepard, K. L.; Tsao, D.; Turrigiano, G.; Weiss, P. S.; Xu, C.; Yuste, R.; Zhuang, X. W. Nanotools for Neuroscience and Brain Activity Mapping. *ACS Nano* **2013**, *7*, 1850-1866.
7. Azevedo, F. A. C.; Carvalho, L. R. B.; Grinberg, L. T.; Farfel, J. M.; Ferretti, R. E. L.; Leite, R. E. P.; Jacob, W.; Lent, R.; Herculano-Houzel, S. Equal Numbers of Neuronal and Nonneuronal Cells Make the Human Brain an Isometrically Scaled-up Primate Brain. *J. Comp. Neurol.* **2009**, *513*, 532-541.
8. Kennedy, R. T. Emerging Trends in *in Vivo* Neurochemical Monitoring by Microdialysis. *Curr. Opin. Chem. Biol.* **2013**, *17*, 860-867.
9. Robinson, D. L.; Hermans, A.; Seipel, A. T.; Wightman, R. M. Monitoring Rapid Chemical Communication in the Brain. *Chem. Rev.* **2008**, *108*, 2554-2584.
10. Hascup, K. N.; Hascup, E. R. Electrochemical Techniques for Subsecond Neurotransmitter Detection in Live Rodents. *Comp. Med.* **2014**, *64*, 249-255.
11. Muller, A.; Joseph, V.; Slesinger, P. A.; Kleinfeld, D. Cell-Based Reporters Reveal *in Vivo* Dynamics of Dopamine and Norepinephrine Release in Murine Cortex. *Nat. Methods* **2014**, *11*, 1245-1252.



12. Liu, Y. S.; Zhang, J.; Xu, X. M.; Zhao, M. K.; Andrews, A. M.; Weber, S. G. Capillary Ultrahigh Performance Liquid Chromatography with Elevated Temperature for Sub-One Minute Separations of Basal Serotonin in Submicroliter Brain Microdialysate Samples. *Anal. Chem.* **2010**, *82*, 9611-9616.
13. Song, P.; Hershey, N. D.; Mabrouk, O. S.; Slaney, T. R.; Kennedy, R. T. Mass Spectrometry "Sensor" for *in Vivo* Acetylcholine Monitoring. *Anal. Chem.* **2012**, *84*, 4659-4664.
14. Zhang, J.; Liu, Y. S.; Jaquins-Gerstl, A.; Shu, Z.; Michael, A. C.; Weber, S. G. Optimization for Speed and Sensitivity in Capillary High Performance Liquid Chromatography. The Importance of Column Diameter in Online Monitoring of Serotonin by Microdialysis. *J. Chromatogr. A* **2012**, *1251*, 54-62.
15. Yang, H. Y.; Thompson, A. B.; McIntosh, B. J.; Altieri, S. C.; Andrews, A. M. Physiologically Relevant Changes in Serotonin Resolved by Fast Microdialysis. *ACS Chem. Neurosci.* **2013**, *4*, 790-798.
16. Yang, H. Y.; Sampson, M. M.; Senturk, D.; Andrews, A. M. Sex- and Sert-Mediated Differences in Stimulated Serotonin Revealed by Fast Microdialysis. *ACS Chem. Neurosci.* **2015**, *6*, 1487-1501.
17. Phillips, P. E. M.; Stuber, G. D.; Heien, M. L. A. V.; Wightman, R. M.; Carelli, R. M. Subsecond Dopamine Release Promotes Cocaine Seeking. *Nature* **2003**, *422*, 614-618.
18. Stuber, G. D.; Klanker, M.; de Ridder, B.; Bowers, M. S.; Joosten, R. N.; Feenstra, M. G.; Bonci, A. Reward-Predictive Cues Enhance Excitatory Synaptic Strength onto Midbrain Dopamine Neurons. *Science* **2008**, *321*, 1690-1692.
19. Kishida, K. T.; Sandberg, S. G.; Lohrenz, T.; Comair, Y. G.; Saez, I.; Phillips, P. E. M.; Montague, P. R. Sub-Second Dopamine Detection in Human Striatum. *PLoS One* **2011**, *6*.
20. Ostlund, S. B.; LeBlanc, K. H.; Kosheleff, A. R.; Wassum, K. M.; Maidment, N. T. Phasic Mesolimbic Dopamine Signaling Encodes the Facilitation of Incentive Motivation Produced by Repeated Cocaine Exposure. *Neuropsychopharmacology* **2014**, *39*, 2441-2449.
21. Lugo-Morales, L. Z.; Loziuk, P. L.; Corder, A. K.; Toups, J. V.; Roberts, J. G.; McCaffrey, K. A.; Sombers, L. A. Enzyme-Modified Carbon-Fiber Microelectrode for the Quantification of Dynamic Fluctuations of Nonelectroactive Analytes Using Fast-Scan Cyclic Voltammetry. *Anal. Chem.* **2013**, *85*, 8780-8786.
22. Kiyatkin, E. A.; Wakabayashi, K. T. Parsing Glucose Entry into the Brain: Novel Findings Obtained with Enzyme-Based Glucose Biosensors. *ACS Chem. Neurosci.* **2015**, *6*, 108-116.

23. Tolosa, V. M.; Wassum, K. M.; Maidment, N. T.; Monbouquette, H. G. Electrochemically Deposited Iridium Oxide Reference Electrode Integrated with an Electroenzymatic Glutamate Sensor on a Multi-Electrode Array Microprobe. *Biosens. Bioelectron.* **2013**, *42*, 256-260.
24. Wassum, K. M.; Tolosa, V. M.; Tseng, T. C.; Balleine, B. W.; Monbouquette, H. G.; Maidment, N. T. Transient Extracellular Glutamate Events in the Basolateral Amygdala Track Reward-Seeking Actions. *J. Neurosci.* **2012**, *32*, 2734-2746.
25. Wassum, K. M.; Tolosa, V. M.; Wang, J.; Walker, E.; Monbouquette, H. G.; Maidment, N. T. Silicon Wafer-Based Platinum Microelectrode Array Biosensor for Near Real-Time Measurement of Glutamate *in Vivo*. *Sensors (Basel)* **2008**, *8*, 5023-5036.
26. Parikh, V.; Kozak, R.; Martinez, V.; Sarter, M. Prefrontal Acetylcholine Release Controls Cue Detection on Multiple Timescales. *Neuron* **2007**, *56*, 141-154.
27. Sarter, M.; Lustig, C.; Howe, W. M.; Gritton, H.; Berry, A. S. Deterministic Functions of Cortical Acetylcholine. *Eur. J. Neurosci.* **2014**, *39*, 1912-1920.
28. Sarter, M.; Kim, Y. Interpreting Chemical Neurotransmission *in Vivo*: Techniques, Time Scales, and Theories. *ACS Chem. Neurosci.* **2015**, *6*, 8-10.
29. Clark, L. C.; Lyons, C. Electrode Systems for Continuous Monitoring in Cardiovascular Surgery. *Ann. N. Y. Acad. Sci.* **1962**, *102*, 29-45.
30. Garg, S. K.; Potts, R. O.; Ackerman, N. R.; Fermi, S. J.; Tamada, J. A.; Chase, H. P. Correlation of Fingerstick Blood Glucose Measurements with Glucowatch Biographer Glucose Results in Young Subjects with Type 1 Diabetes. *Diabetes Care* **1999**, *22*, 1708-1714.
31. Tamada, J. A.; Garg, S.; Jovanovic, L.; Pitzer, K. R.; Fermi, S.; Potts, R. O. Noninvasive Glucose Monitoring: Comprehensive Clinical Results. Cygnus Research Team. *J. Am. Med. Assoc.* **1999**, *282*, 1839-1844.
32. Garg, S. K. The Future of Glucose Monitoring. *Diabetes Technol. Ther.* **2016**, *18*, 1-3.
33. Rodbard, D. Continuous Glucose Monitoring: A Review of Successes, Challenges, and Opportunities. *Diabetes Technol. Ther.* **2016**, *18*, 3-13.
34. Garg, S. K.; Schwartz, S.; Edelman, S. V. Improved Glucose Excursions Using an Implantable Real-Time Continuous Glucose Sensor in Adults with Type 1 Diabetes. *Diabetes Care* **2004**, *27*, 734-738.
35. Javey, A.; Weiss, P. S. Mimicking the Human Brain and More: New Grand Challenge Initiatives. *ACS Nano* **2015**, *9*, 10533-10536.

36. Nakatsuka, N.; Andrews, A. M. Neurochips Enable Nanoscale Devices for High-Resolution *in Vivo* Neurotransmitter Sensing. *Neuropsychopharmacology* **2016**, *41*, 378-379.
37. Andrews, A. M.; Schepartz, A.; Sweedler, J. V.; Weiss, P. S. Chemistry and the BRAIN Initiative. *J. Am. Chem. Soc.* **2014**, *136*, 1-2.
38. Jones, A. M.; Grossmann, G.; Danielson, J. A. H.; Sosso, D.; Chen, L. Q.; Ho, C. H.; Frommer, W. B. *In Vivo* Biochemistry: Applications for Small Molecule Biosensors in Plant Biology. *Curr. Opin. Plant Biol.* **2013**, *16*, 389-395.
39. Eckert, M. A.; Vu, P. Q.; Zhang, K. X.; Kang, D. K.; Ali, M. M.; Xu, C. J.; Zhao, W. A. Novel Molecular and Nanosensors for *in Vivo* Sensing. *Theranostics* **2013**, *3*, 583-594.
40. Slomovic, S.; Pardee, K.; Collins, J. J. Synthetic Biology Devices for *in Vitro* and *in Vivo* Diagnostics. *P. Natl. Acad. Sci. U.S.A.* **2015**, *112*, 14429-14435.
41. Hasan, A.; Nurunnabi, M.; Morshed, M.; Paul, A.; Polini, A.; Kuila, T.; Al Hariri, M.; Lee, Y. K.; Jaffa, A. A. Recent Advances in Application of Biosensors in Tissue Engineering. *BioMed Res. Int.* **2014**, *2014*, 1-18.
42. Iverson, N. M.; Barone, P. W.; Shandell, M.; Trudel, L. J.; Sen, S.; Sen, F.; Ivanov, V.; Atolia, E.; Farias, E.; McNicholas, T. P.; Reuel, N.; Parry, N. M.; Wogan, G. N.; Strano, M. S. *In Vivo* Biosensing via Tissue-Localizable Near-Infrared-Fluorescent Single-Walled Carbon Nanotubes. *Nat. Nanotechnol.* **2013**, *8*, 873-880.
43. Liu, Q. J.; Wu, C. S.; Cai, H.; Hu, N.; Zhou, J.; Wang, P. Cell-Based Biosensors and Their Application in Biomedicine. *Chem. Rev.* **2014**, *114*, 6423-6461.
44. Murugaiyan, S. B.; Ramasamy, R.; Gopal, N.; Kuzhandaivelu, V. Biosensors in Clinical Chemistry: An Overview. *Adv. Biomed. Res.* **2014**, *3*, 67-81.
45. Morrison, D. W. G.; Dokmeci, M. R.; Demirci, U.; Khademhosseini, A. Clinical Applications of Micro- and Nanoscale Biosensors. *Biomedical Nanostructures* **2008**, 439-460.
46. Rogers, M. L.; Boutelle, M. G. Real-Time Clinical Monitoring of Biomolecules. *Annu. Rev. Anal. Chem.* **2013**, *6*, 427-453.
47. Weiss, P. S.; Hood, L. A Conversation with Dr. Leroy Hood: Visionary Biologist and Biotechnologist. *ACS Nano* **2007**, *1*, 242-247.
48. Alvarez, M. M.; Aizenberg, J.; Analoui, M.; Andrews, A. M.; Bisker, G.; Boyden, E. S.; Kamm, R. D.; Karp, J. M.; Mooney, D. J.; Oklu, R.; Peer, D.; Stolzoff, M.; Strano, M. S.; Santiago, G. T. D.; Webster, T. J.; Weiss, P. S.; Khademhosseini, A. Emerging Trends in Micro- and Nanoscale Technologies in Medicine: From Basic Discoveries to Translation. *ACS Nano* **2017**, *11*, 5195-5214.

49. Mitragotri, S.; Anderson, D. G.; Chen, X. Y.; Chow, E. K.; Ho, D.; Kabanov, A. V.; Karp, J. M.; Kataoka, K.; Mirkin, C. A.; Petrosko, S. H.; Shi, J. J.; Stevens, M. M.; Sun, S. H.; Teoh, S.; Venkatraman, S. S.; Xia, Y. N.; Wang, S. T.; Gu, Z.; Xu, C. J. Accelerating the Translation of Nanomaterials in Biomedicine. *ACS Nano* **2015**, 9, 6644-6654.
50. Pelaz, B.; Alexiou, C. H.; Alvarez -Puebla, R. A.; Alves, F.; Andrews, A. M.; Ashraf, S.; Balogh, L. P.; Ballerini, L.; Bestetti, A.; Brendel, C.; Bosi, S.; Carril, M.; Chan, W. C. W.; Chen, C. Y.; Chen, X. D.; Chen, X. Y.; Cheng, Z.; Cui, D. X.; Du, J. Z.; Dullin, C.; Escudero, A.; Feliu, N.; Gao, M. Y.; George, M.; Gogotsi, Y.; Grunweller, A.; Gu, Z. W.; Halas, N. J.; Hampp, N.; Hartmann, R. K.; Hersam, M. C.; Hunziker, P.; Jian, J.; Jiang, X. Y.; Jungebluth, P.; Kadhiresan, P.; Kataoka, K.; Khademhosseini, A.; Kopecek, J.; Kotov, N. A.; Krug, H. F.; Lee, D. S.; Lehr, C. M.; Leong, K. W.; Liang, X. J.; Lim, M. L.; Liz-Marzan, L. M.; Ma, X. M.; Macchiarini, P.; Meng, H.; Mohwald, H.; Mulvaney, P.; Nel, A. E.; Nie, S. M.; Nordlander, P.; Okano, T.; Oliveira, J.; Park, T. H.; Penner, R. M.; Prato, M.; Puentes, V.; Rotello, V. M.; Samarakoon, A.; Schaak, R. E.; Shen, Y. Q.; Sjoqvist, S.; Skirtach, A. G.; Soliman, M. G.; Stevens, M. M.; Sung, H. W.; Tang, B. Z.; Tietze, R.; Udugama, B. N.; Van Epps, J. S.; Weil, T.; Weiss, P. S.; Willner, I.; Wu, Y. Z.; Yang, L. L.; Yue, Z.; Zhang, Q.; Zhang, Q.; Zhang, X. E.; Zhao, Y. L.; Zhou, X.; Parak, W. J. Diverse Applications of Nanomedicine. *ACS Nano* **2017**, 11, 2313-2381.
51. Simon, D. T.; Gabrielsson, E. O.; Tybrandt, K.; Berggren, M. Organic Bioelectronics: Bridging the Signaling Gap between Biology and Technology. *Chem. Rev.* **2016**, 116, 13009-13041.
52. Andrews, A. M. The Future of Monitoring Molecules. *ACS Chem. Neurosci.* **2015**, 6, 1-2.
53. Andrews, A. M.; Weiss, P. S. Nano in the Brain: Nano-Neuroscience. *ACS Nano* **2012**, 6, 8463-8464.
54. Daniels, J. S.; Pourmand, N. Label-Free Impedance Biosensors: Opportunities and Challenges. *Electroanalysis* **2007**, 19, 1239-1257.
55. Weiss, P. S.; Trevor, P. L.; Cardillo, M. J. Gas Surface Interactions on InP Monitored by Changes in Substrate Electronic-Properties. *J. Chem. Phys.* **1989**, 90, 5146-5153.
56. Shockley, W. Diffusion and Drift of Minority Carriers in Semiconductors for Comparable Capture and Scattering Mean Free Paths. *Phys. Rev.* **1962**, 125, 1570-1576.
57. Many, A.; Grover, N. B.; Goldstein, Y. *Semiconductor Surfaces*; North Holland Publishing Company: Amsterdam, **1965**.
58. Korotcenkov, G. Metal Oxides for Solid-State Gas Sensors: What Determines Our Choice? *Mat. Sci. Eng. B-Solid* **2007**, 139, 1-23.

59. Eranna, G.; Joshi, B. C.; Runthala, D. P.; Gupta, R. P. Oxide Materials for Development of Integrated Gas Sensors - A Comprehensive Review. *Crit. Rev. Solid State Mater. Sci.* **2004**, *29*, 111-188.
60. Wang, C. X.; Yin, L. W.; Zhang, L. Y.; Xiang, D.; Gao, R. Metal Oxide Gas Sensors: Sensitivity and Influencing Factors. *Sensors (Basel)* **2010**, *10*, 2088-2106.
61. Barsan, N.; Weimar, U. Conduction Model of Metal Oxide Gas Sensors. *J. Electroceram.* **2001**, *7*, 143-167.
62. Sberveglieri, G. Recent Developments in Semiconducting Thin-Film Gas Sensors. *Sensor Actuat. B-Chem.* **1995**, *23*, 103-109.
63. Gopel, W.; Schierbaum, K. D. SnO<sub>2</sub> Sensors - Current Status and Future Prospects. *Sensor Actuat. B-Chem.* **1995**, *26*, 1-12.
64. Krivetskiy, V.; Rumyantseva, M.; Gaskov, A. In *Metal Oxide Nanomaterials for Chemical Sensors*; Carpenter, M. A., Mathur, S., Kolmakov, A., Eds.; Springer-Verlag New York: New York, **2013**, 69-115.
65. Lin, P.; Yan, F. Organic Thin-Film Transistors for Chemical and Biological Sensing. *Adv. Mater.* **2012**, *24*, 34-51.
66. Xiang, J.; Lu, W.; Hu, Y. J.; Wu, Y.; Yan, H.; Lieber, C. M. Ge/Si Nanowire Heterostructures as High-Performance Field-Effect Transistors. *Nature* **2006**, *441*, 489-493.
67. Tian, B. Z.; Cohen-Karni, T.; Qing, Q.; Duan, X. J.; Xie, P.; Lieber, C. M. Three-Dimensional, Flexible Nanoscale Field-Effect Transistors as Localized Bioprobes. *Science* **2010**, *329*, 830-834.
68. Liang, G. C.; Xiang, J.; Kharche, N.; Klimeck, G.; Lieber, C. M.; Lundstrom, M. Performance Analysis of a Ge/Si Core/Shell Nanowire Field-Effect Transistor. *Nano Lett.* **2007**, *7*, 642-646.
69. Greytak, A. B.; Lauhon, L. J.; Gudiksen, M. S.; Lieber, C. M. Growth and Transport Properties of Complementary Germanium Nanowire Field-Effect Transistors. *Appl. Phys. Lett.* **2004**, *84*, 4176-4178.
70. Duan, X. J.; Gao, R. X.; Xie, P.; Cohen-Karni, T.; Qing, Q.; Choe, H. S.; Tian, B. Z.; Jiang, X. C.; Lieber, C. M. Intracellular Recordings of Action Potentials by an Extracellular Nanoscale Field-Effect Transistor. *Nat. Nanotechnol.* **2012**, *7*, 174-179.
71. Kong, J.; Franklin, N. R.; Zhou, C. W.; Chapline, M. G.; Peng, S.; Cho, K. J.; Dai, H. J. Nanotube Molecular Wires as Chemical Sensors. *Science* **2000**, *287*, 622-625.

72. Chen, R. J.; Bangsaruntip, S.; Drouvalakis, K. A.; Kam, N. W. S.; Shim, M.; Li, Y. M.; Kim, W.; Utz, P. J.; Dai, H. J. Noncovalent Functionalization of Carbon Nanotubes for Highly Specific Electronic Biosensors. *P. Natl. Acad. Sci. U.S.A.* **2003**, *100*, 4984-4989.
73. Javey, A.; Guo, J.; Wang, Q.; Lundstrom, M.; Dai, H. J. Ballistic Carbon Nanotube Field-Effect Transistors. *Nature* **2003**, *424*, 654-657.
74. Chen, Y.; Wang, X.; Hong, M. K.; Erramilli, S.; Mohanty, P.; Rosenberg, C. Nanoscale Field Effect Transistor for Biomolecular Signal Amplification. *Appl. Phys. Lett.* **2007**, *91*, 243511-243513.
75. Matsumoto, K.; Maehashi, K.; Ohno, Y.; Inoue, K. Recent Advances in Functional Graphene Biosensors. *J. Phys. D Appl. Phys.* **2014**, *47*, 1-6.
76. Green, N. S.; Norton, M. L. Interactions of DNA with Graphene and Sensing Applications of Graphene Field-Effect Transistor Devices: A Review. *Anal. Chim. Acta.* **2015**, *853*, 127-142.
77. Janata, J. 20 Years of Ion-Selective Field-Effect Transistors. *Analyst* **1994**, *119*, 2275-2278.
78. Rim, Y. S.; Bae, S. H.; Chen, H. J.; Yang, J. L.; Kim, J.; Andrews, A. M.; Weiss, P. S.; Yang, Y.; Tseng, H. R. Printable Ultrathin Metal Oxide Semiconductor-Based Conformal Biosensors. *ACS Nano* **2015**, *9*, 12174-12181.
79. Weiss, P. S. Brain Activity Mapping Project: Applying Advances in Nanoscience and Nanotechnology to Neuroscience. *ACS Nano* **2013**, *7*, 1825-1826.
80. Makowski, M. S.; Ivanisevic, A. Molecular Analysis of Blood with Micro-/Nanoscale Field-Effect-Transistor Biosensors. *Small* **2011**, *7*, 1863-1875.
81. Kim, J.; Rim, Y. S.; Chen, H. J.; Cao, H. H.; Nakatsuka, N.; Hinton, H. L.; Zhao, C. Z.; Andrews, A. M.; Yang, Y.; Weiss, P. S. Fabrication of High-Performance Ultrathin In<sub>2</sub>O<sub>3</sub> Film Field-Effect Transistors and Biosensors Using Chemical Lift-Off Lithography. *ACS Nano* **2015**, *9*, 4572-4582.
82. Saavedra, H. M.; Mullen, T. J.; Zhang, P. P.; Dewey, D. C.; Claridge, S. A.; Weiss, P. S. Hybrid Strategies in Nanolithography. *Rep. Prog. Phys.* **2010**, *73*, 1-40.
83. Fuchs, A.; Bender, M.; Plachetka, U.; Kock, L.; Wahlbrink, T.; Gottlob, H. D. B.; Efavi, J. K.; Moeller, M.; Schmidt, M.; Mollenhauer, T.; Moormann, C.; Lemme, M. C.; Kurz, H. Nanowire Fin Field Effect Transistors via UV-Based Nanoimprint Lithography. *J. Vac. Sci. Technol. B* **2006**, *24*, 2964-2967.
84. Wang, Z.; Yuan, J. F.; Zhang, J.; Xing, R. B.; Yan, D. H.; Han, Y. C. Metal Transfer Printing and Its Application in Organic Field-Effect Transistor Fabrication. *Adv. Mater.* **2003**, *15*, 1009-1012.

85. Granlund, T.; Nyberg, T.; Roman, L. S.; Svensson, M.; Inganas, O. Patterning of Polymer Light-Emitting Diodes with Soft Lithography. *Adv. Mater.* **2000**, *12*, 269-273.
86. Kim, C.; Shtein, M.; Forrest, S. R. Nanolithography Based on Patterned Metal Transfer and Its Application to Organic Electronic Devices. *Appl. Phys. Lett.* **2002**, *80*, 4051-4053.
87. Parashkov, R.; Becker, E.; Riedl, T.; Johannes, H. H.; Kowalsky, W. Microcontact Printing as a Versatile Tool for Patterning Organic Field-Effect Transistors. *Adv. Mater.* **2005**, *17*, 1523-1527.
88. Cheng, S. S.; Hotani, K.; Hideshima, S.; Kuroiwa, S.; Nakanishi, T.; Hashimoto, M.; Mori, Y.; Osaka, T. Field Effect Transistor Biosensor Using Antigen Binding Fragment for Detecting Tumor Marker in Human Serum. *Materials* **2014**, *7*, 2490-2500.
89. Hideshima, S.; Hinou, H.; Ebihara, D.; Sato, R.; Kuroiwa, S.; Nakanishi, T.; Nishimura, S. I.; Osaka, T. Attomolar Detection of Influenza A Virus Hemagglutinin Human H1 and Avian H5 Using Glycan-Blotted Field Effect Transistor Biosensor. *Anal. Chem.* **2013**, *85*, 5641-5644.
90. Basu, J.; Roy Chaudhuri, C. Attomolar Sensitivity of FET Biosensor Based on Smooth and Reliable Graphene Nanogrids. *IEEE Electr. Device Lett.* **2016**, *37*, 492-495.
91. Gong, J. R. Label-Free Attomolar Detection of Proteins Using Integrated Nanoelectronic and Electrokinetic Devices. *Small* **2010**, *6*, 967-973.
92. Kim, D. J.; Park, H. C.; Sohn, I. Y.; Jung, J. H.; Yoon, O. J.; Park, J. S.; Yoon, M. Y.; Lee, N. E. Electrical Graphene Aptasensor for Ultra-Sensitive Detection of Anthrax Toxin with Amplified Signal Transduction. *Small* **2013**, *9*, 3352-3360.
93. Xu, G. Y.; Abbott, J.; Qin, L.; Yeung, K. Y. M.; Song, Y.; Yoon, H.; Kong, J.; Ham, D. Electrophoretic and Field-Effect Graphene for All-Electrical DNA Array Technology. *Nat. Commun.* **2014**, *5*, 1-9.
94. Janata, J.; Moss, S. D. Chemically Sensitive Field-Effect Transistors. *Biomed. Eng.* **1976**, *11*, 241-245.
95. Caras, S.; Janata, J. Field-Effect Transistor Sensitive to Penicillin. *Anal. Chem.* **1980**, *52*, 1935-1937.
96. Dzyadevich, S. V.; Korpan, Y. I.; Arkhipova, V. N.; Alesina, M. Y.; Martelet, C.; El'Skaya, A. V.; Soldatkin, A. P. Application of Enzyme Field-Effect Transistors for Determination of Glucose Concentrations in Blood Serum. *Biosens. Bioelectron.* **1999**, *14*, 283-287.

97. Poghosian, A. S. Method of Fabrication of ISFET-Based Biosensors on an Si-SiO<sub>2</sub>-Si Structure. *Sensor Actuat. B-Chem.* **1997**, *44*, 361-364.
98. Gorchkov, D. V.; Soldatkin, A. P.; Poyard, S.; Jaffrezic Renault, N.; Martelet, C. Application of Charged Polymeric Materials as Additional Permselective Membranes for Improvement of the Performance Characteristics of Urea-Sensitive Enzymatic Field Effect Transistors. *Mat. Sci. Eng. C-Biomim.* **1997**, *5*, 23-28.
99. Boubriak, O. A.; Soldatkin, A. P.; Starodub, N. F.; Sandrovsky, A. K.; Elskaya, A. K. Determination of Urea in Blood-Serum by a Urease Biosensor Based on an Ion-Sensitive Field-Effect Transistor. *Sensor Actuat. B-Chem.* **1995**, *27*, 429-431.
100. Pijanowska, D. G.; Torbicz, W. pH-ISFET Based Urea Biosensor. *Sensor Actuat. B-Chem.* **1997**, *44*, 370-376.
101. Cui, Y.; Wei, Q. Q.; Park, H. K.; Lieber, C. M. Nanowire Nanosensors for Highly Sensitive and Selective Detection of Biological and Chemical Species. *Science* **2001**, *293*, 1289-1292.
102. Zhang, A. Q.; Lieber, C. M. Nano-Bioelectronics. *Chem. Rev.* **2016**, *116*, 215-257.
103. Vo-Dinh, T.; Cullum, B. Biosensors and Biochips: Advances in Biological and Medical Diagnostics. *Fresen. J. Anal. Chem.* **2000**, *366*, 540-551.
104. Lemass, D.; O'Kennedy, R.; Kijanka, G. S. Referencing Cross-Reactivity of Detection Antibodies for Protein Array Experiments. *F1000Res.* **2016**, *5*, 1-11.
105. Drabovich, A.; Berezovski, M.; Krylov, S. N. Selection of Smart Aptamers by Equilibrium Capillary Electrophoresis of Equilibrium Mixtures (ECEEM). *J. Am. Chem. Soc.* **2005**, *127*, 11224-11225.
106. Barry, R.; Soloviev, M. Quantitative Protein Profiling Using Antibody Arrays. *Proteomics* **2004**, *4*, 3717-3726.
107. Reimhult, E.; Hook, F. Design of Surface Modifications for Nanoscale Sensor Applications. *Sensors (Basel)* **2015**, *15*, 1635-1675.
108. Leung, K. C. F.; Ho, H. P.; Kwan, Y. W.; Kong, S. K. Immunoassays Using Polypeptide Conjugate Binders with Tuned Affinity. *Expert Rev. Mol. Diagn.* **2010**, *10*, 863-867.
109. Bergveld, P. A Critical-Evaluation of Direct Electrical Protein-Detection Methods. *Biosens. Bioelectron.* **1991**, *6*, 55-72.
110. Attard, P. Electrolytes and the Electric Double Layer. *Adv. Chem. Phys.* **1996**, *92*, 1-159.
111. Smith, A. M.; Lee, A. A.; Perkin, S. The Electrostatic Screening Length in Concentrated Electrolytes Increases with Concentration. *J. Phys. Chem. Lett.* **2016**, *7*, 2157-2163.



112. Schenck, J. In *US Patent no. 4,238,757* 1980.
113. Park, H. J.; Kim, S. K.; Park, K.; Lyu, H. K.; Lee, C. S.; Chung, S. J.; Yun, W. S.; Kim, M.; Chung, B. H. An ISFET Biosensor for the Monitoring of Maltose-Induced Conformational Changes in MBP. *FEBS Lett.* **2009**, *583*, 157-162.
114. Bergveld, P. The Future of Biosensors. *Sensor Actuat. A-Phys.* **1996**, *56*, 65-73.
115. Vacic, A.; Criscione, J. M.; Rajan, N. K.; Stern, E.; Fahmy, T. M.; Reed, M. A. Determination of Molecular Configuration by Debye Length Modulation. *J. Am. Chem. Soc.* **2011**, *133*, 13886-13889.
116. Stern, E.; Wagner, R.; Sigworth, F. J.; Breaker, R.; Fahmy, T. M.; Reed, M. A. Importance of the Debye Screening Length on Nanowire Field Effect Transistor Sensors. *Nano Lett.* **2007**, *7*, 3405-3409.
117. Landheer, D.; Aers, G.; McKinnon, W. R.; Deen, M. J.; Ranuarez, J. C. Model for the Field Effect from Layers of Biological Macromolecules on the Gates of Metal-Oxide-Semiconductor Transistors. *J. Appl. Phys.* **2005**, *98*, 44701-44716.
118. Poghosian, A.; Cherstvy, A.; Ingebrandt, S.; Offenhausser, A.; Schoning, M. J. Possibilities and Limitations of Label-Free Detection of DNA Hybridization with Field-Effect-Based Devices. *Sensor Actuat. B-Chem.* **2005**, *111*, 470-480.
119. Gupta, S.; Elias, M.; Wen, X. J.; Shapiro, J.; Brillson, L.; Lu, W.; Lee, S. C. Detection of Clinically Relevant Levels of Protein Analyte under Physiologic Buffer Using Planar Field Effect Transistors. *Biosens. Bioelectron.* **2008**, *24*, 505-511.
120. Casal, P.; Wen, X. J.; Gupta, S.; Nicholson, T.; Wang, Y. J.; Theiss, A.; Bhushan, B.; Brillson, L.; Lu, W.; Lee, S. C. ImmunoFET Feasibility in Physiological Salt Environments. *Philos. T. R. Soc. A* **2012**, *370*, 2474-2488.
121. Mazarin de Moraes, A. C.; Kubota, L. T. Recent Trends in Field-Effect Transistors-Based Immunosensors. *Chemosensors* **2016**, *4*, 1-26.
122. Okamoto, S.; Ohno, Y.; Maehashi, K.; Inoue, K.; Matsumoto, K. Immunosensors Based on Graphene Field-Effect Transistors Fabricated Using Antigen-Binding Fragment. *Jpn. J. Appl. Phys.* **2012**, *51*, 1-4.
123. Elnathan, R.; Kwiat, M.; Pevzner, A.; Engel, Y.; Burstein, L.; Khatchtourints, A.; Lichtenstein, A.; Kantaev, R.; Patolsky, F. Biorecognition Layer Engineering: Overcoming Screening Limitations of Nanowire-Based FET Devices. *Nano Lett.* **2012**, *12*, 5245-5254.
124. Kumar, P. K. Monitoring Intact Viruses Using Aptamers. *Biosensors* **2016**, *6*, 1-16.

125. Tuerk, C.; Macdougall, S.; Gold, L. RNA Pseudoknots That Inhibit Human-Immunodeficiency-Virus Type-1 Reverse-Transcriptase. *P. Natl. Acad. Sci. U.S.A.* **1992**, *89*, 6988-6992.
126. Urvil, P. T.; Kakiuchi, N.; Zhou, D. M.; Shimotohno, K.; Kumar, P. K. R.; Nishikawa, S. Selection of RNA Aptamers That Bind Specifically to the NS3 Protease of Hepatitis C Virus. *Eur. J. Biochem.* **1997**, *248*, 130-138.
127. Parashar, A. Aptamers in Therapeutics. *J. Clin. Diagn. Res.* **2016**, *10*, 1-6.
128. Kubik, M. F.; Stephens, A. W.; Schneider, D.; Marlar, R. A.; Tasset, D. High-Affinity RNA Ligands to Human Alpha-Thrombin. *Nucleic Acids Res.* **1994**, *22*, 2619-2626.
129. Soldevilla, M. M.; Villanueva, H.; Pastor, F. Aptamers: A Feasible Technology in Cancer Immunotherapy. *J. Immunol. Res.* **2016**, *2016*, 1-12.
130. Nieuwlandt, D.; Wecker, M.; Gold, L. *In Vitro* Selection of RNA Ligands to Substance P. *Biochemistry* **1995**, *34*, 5651-5659.
131. Williams, K. P.; Liu, X. H.; Schumacher, T. N. M.; Lin, H. Y.; Ausiello, D. A.; Kim, P. S.; Bartel, D. P. Bioactive and Nuclease-Resistant *L*-DNA Ligand of Vasopressin. *P. Natl. Acad. Sci. U.S.A.* **1997**, *94*, 11285-11290.
132. Yang, J.; Zhu, J.; Pei, R.; Oliver, J. A.; Landry, D. W.; Stojanovic, M. N.; Lin, Q. Integrated Microfluidic Aptasensor for Mass Spectrometric Detection of Vasopressin in Human Plasma Ultrafiltrate. *Anal. Methods* **2016**, *8*, 5190-5196.
133. Geiger, A.; Burgstaller, P.; von der Eltz, H.; Roeder, A.; Famulok, M. RNA Aptamers That Bind *L*-Arginine with Sub-Micromolar Dissociation Constants and High Enantioselectivity. *Nucleic Acids Res.* **1996**, *24*, 1029-1036.
134. Connell, G. J.; Illangesekare, M.; Yarus, M. Three Small Ribooligonucleotides with Specific Arginine Sites. *Biochemistry* **1993**, *32*, 5497-5502.
135. Stojanovic, M. N.; de Prada, P.; Landry, D. W. Aptamer-Based Folding Fluorescent Sensor for Cocaine. *J. Am. Chem. Soc.* **2001**, *123*, 4928-4931.
136. Pfeiffer, F.; Mayer, G. Selection and Biosensor Application of Aptamers for Small Molecules. *Front. Chem.* **2016**, *4*, 1-21.
137. Hofmann, H. P.; Limmer, S.; Hornung, V.; Sprinzl, M. Ni<sup>2+</sup>-Binding RNA Motifs with an Asymmetric Purine-Rich Internal Loop and a G-A Base Pair. *RNA* **1997**, *3*, 1289-1300.
138. Rajendran, M.; Ellington, A. D. Selection of Fluorescent Aptamer Beacons That Light up in the Presence of Zinc. *Anal. Bioanal. Chem.* **2008**, *390*, 1067-1075.

139. Qu, H.; Csordas, A. T.; Wang, J. P.; Oh, S. S.; Eisenstein, M. S.; Soh, H. T. Rapid and Label-Free Strategy to Isolate Aptamers for Metal Ions. *ACS Nano* **2016**, *10*, 7558-7565.
140. Nguyen, T. H.; Pei, R. J.; Stojanovic, M.; Lin, Q. Demonstration and Characterization of Biomolecular Enrichment on Microfluidic Aptamer-Functionalized Surfaces. *Sensor Actuat. B-Chem.* **2011**, *155*, 58-66.
141. Stojanovic, M. N.; Kolpashchikov, D. M. Modular Aptameric Sensors. *J. Am. Chem. Soc.* **2004**, *126*, 9266-9270.
142. Stojanovic, M. N.; Semova, S.; Kolpashchikov, D.; Macdonald, J.; Morgan, C.; Stefanovic, D. Deoxyribozyme-Based Ligase Logic Gates and Their Initial Circuits. *J. Am. Chem. Soc.* **2005**, *127*, 6914-6915.
143. Maier, K. E.; Levy, M. From Selection Hits to Clinical Leads: Progress in Aptamer Discovery. *Mol. Ther. Methods Clin. Dev.* **2016**, *5*, 1-10.
144. Kong, H. Y.; Byun, J. Nucleic Acid Aptamers: New Methods for Selection, Stabilization, and Application in Biomedical Science. *Biomol. Ther.* **2013**, *21*, 423-434.
145. Dyke, C. K.; Steinhubl, S. R.; Kleiman, N. S.; Cannon, R. O.; Aberle, L. G.; Lin, M.; Myles, S. K.; Melloni, C.; Harrington, R. A.; Alexander, J. H.; Becker, R. C.; Rusconi, C. P. First-in-Human Experience of an Antidote-Controlled Anticoagulant Using RNA Aptamer Technology - a Phase 1a Pharmacodynamic Evaluation of a Drug-Antidote Pair for the Controlled Regulation of Factor IXa Activity. *Circulation* **2006**, *114*, 2490-2497.
146. Watson, S. R.; Chang, Y. F.; O'Connell, D.; Weigand, L.; Ringquist, S.; Parma, D. H. Anti-L-Selectin Aptamers: Binding Characteristics, Pharmacokinetic Parameters, and Activity against an Intravascular Target *in Vivo*. *Antisense Nucleic A* **2000**, *10*, 63-75.
147. Floege, J.; Ostendorf, T.; Janssen, U.; Burg, M.; Radeke, H. H.; Vargeese, C.; Gill, S. C.; Green, L. S.; Janjic, N. Novel Approach to Specific Growth Factor Inhibition *in Vivo* - Antagonism of Platelet-Derived Growth Factor in Glomerulonephritis by Aptamers. *Am. J. Pathol.* **1999**, *154*, 169-179.
148. Healy, J. M.; Lewis, S. D.; Kurz, M.; Boomer, R. M.; Thompson, K. M.; Wilson, C.; McCauley, T. G. Pharmacokinetics and Biodistribution of Novel Aptamer Compositions. *Pharm. Res.* **2004**, *21*, 2234-2246.
149. Diener, J. L.; Lagasse, H. A. D.; Duerschmied, D.; Merhi, Y.; Tanguay, J. F.; Hutabarat, R.; Gilbert, J.; Wagner, D. D.; Schaub, R. Inhibition of Von Willebrand Factor-Mediated Platelet Activation and Thrombosis by the Anti-Von Willebrand Factor A1-Domain Aptamer ARC1779. *J. Thromb. Haemost.* **2009**, *7*, 1155-1162.

150. Rusconi, C. P.; Roberts, J. D.; Pitoc, G. A.; Nimjee, S. M.; White, R. R.; Quick, G.; Scardino, E.; Fay, W. P.; Sullenger, B. A. Antidote-Mediated Control of an Anticoagulant Aptamer *in Vivo*. *Nat. Biotechnol.* **2004**, *22*, 1423-1428.
151. Wilson, C.; Keefe, A. D. Building Oligonucleotide Therapeutics Using Non-Natural Chemistries. *Curr. Opin. Chem. Biol.* **2006**, *10*, 607-614.
152. Shigdar, S.; Macdonald, J.; O'Connor, M.; Wang, T.; Xiang, D. X.; Al Shamaileh, H.; Qiao, L.; Wei, M.; Zhou, S. F.; Zhu, Y. M.; Kong, L. X.; Bhattacharya, S.; Li, C. G.; Duan, W. Aptamers as Theranostic Agents: Modifications, Serum Stability and Functionalisation. *Sensors (Basel)* **2013**, *13*, 13624-13637.
153. Vater, A.; Klussmann, S. Turning Mirror-Image Oligonucleotides into Drugs: The Evolution of Spiegelmer Therapeutics. *Drug Discov. Today* **2015**, *20*, 147-155.
154. Klussmann, S.; Nolte, A.; Bald, R.; Erdmann, V. A.; Furste, J. P. Mirror-Image RNA That Binds *D*-Adenosine. *Nat. Biotechnol.* **1996**, *14*, 1112-1115.
155. Nolte, A.; Klussmann, S.; Bald, R.; Erdmann, V. A.; Furste, J. P. Mirror-Design of *L*-Oligonucleotide Ligands Binding to *L*-Arginine. *Nat. Biotechnol.* **1996**, *14*, 1116-1119.
156. Ellington, A. D.; Szostak, J. W. *In Vitro* Selection of RNA Molecules That Bind Specific Ligands. *Nature* **1990**, *346*, 818-822.
157. Tuerk, C.; Gold, L. Systematic Evolution of Ligands by Exponential Enrichment - RNA Ligands to Bacteriophage-T4 DNA-Polymerase. *Science* **1990**, *249*, 505-510.
158. Ellington, A. D.; Szostak, J. W. Selection *in Vitro* of Single-Stranded DNA Molecules That Fold into Specific Ligand-Binding Structures. *Nature* **1992**, *355*, 850-852.
159. Holahan, M. R.; Madularu, D.; McConnell, E. M.; Walsh, R.; DeRosa, M. C. Intra-Accumbens Injection of a Dopamine Aptamer Abates MK-801-Induced Cognitive Dysfunction in a Model of Schizophrenia. *PLoS One* **2011**, *6*, 1-8.
160. Weinberg, M. S. Therapeutic Aptamers March On. *Mol. Ther. Nucleic Acids* **2014**, *3*, 1-2.
161. Ozer, A.; Pagano, J. M.; Lis, J. T. New Technologies Provide Quantum Changes in the Scale, Speed, and Success of SELEX Methods and Aptamer Characterization. *Mol. Ther. Nucleic Acids* **2014**, *3*, 1-18.
162. Yang, K. A.; Pei, R.; Stojanovic, M. N. *In Vitro* Selection and Amplification Protocols for Isolation of Aptameric Sensors for Small Molecules. *Methods* **2016**, 58-65.
163. Qu, H.; Csordas, A. T.; Wang, J.; Oh, S. S.; Eisenstein, M. S.; Soh, H. T. Rapid and Label-Free Strategy to Isolate Aptamers for Metal Ions. *ACS Nano* **2016**, *10*, 7558-7565.

164. Kim, J.; Olsen, T. R.; Zhu, J.; Hilton, J. P.; Yang, K. A.; Pei, R.; Stojanovic, M. N.; Lin, Q. Integrated Microfluidic Isolation of Aptamers Using Electrophoretic Oligonucleotide Manipulation. *Sci. Rep.* **2016**, *6*, 1-10.
165. Yang, J.; Bowser, M. T. Capillary Electrophoresis-SELEX Selection of Catalytic DNA Aptamers for a Small-Molecule Porphyrin Target. *Anal. Chem.* **2013**, *85*, 1525-1530.
166. Yang, K. A.; Barbu, M.; Halim, M.; Pallavi, P.; Kim, B.; Kolpashchikov, D. M.; Pecic, S.; Taylor, S.; Worgall, T. S.; Stojanovic, M. N. Recognition and Sensing of Low-Epitope Targets *via* Ternary Complexes with Oligonucleotides and Synthetic Receptors. *Nat. Chem.* **2014**, *6*, 1003-1008.
167. Drabovich, A. P.; Berezovski, M.; Okhonin, V.; Krylov, S. N. Selection of Smart Aptamers by Methods of Kinetic Capillary Electrophoresis. *Anal. Chem.* **2006**, *78*, 3171-3178.
168. Cho, E. J.; Lee, J. W.; Ellington, A. D. Applications of Aptamers as Sensors. *Annu. Rev. Anal. Chem.* **2009**, *2*, 241-264.
169. Mairal, T.; Ozalp, V. C.; Sanchez, P. L.; Mir, M.; Katakis, I.; O'Sullivan, C. K. Aptamers: Molecular Tools for Analytical Applications. *Anal. Bioanal. Chem.* **2008**, *390*, 989-1007.
170. Jenison, R. D.; Gill, S. C.; Pardi, A.; Polisky, B. High-Resolution Molecular Discrimination by RNA. *Science* **1994**, *263*, 1425-1429.
171. Yang, K. A.; Pei, R. J.; Stefanovic, D.; Stojanovic, M. N. Optimizing Cross-Reactivity with Evolutionary Search for Sensors. *J. Am. Chem. Soc.* **2012**, *134*, 1642-1647.
172. Wang, W.; Jia, L. Y. Progress in Aptamer Screening Methods. *Chinese J. Anal. Chem.* **2009**, *37*, 454-460.
173. McConnell, E. M.; Holahan, M. R.; DeRosa, M. C. Aptamers as Promising Molecular Recognition Elements for Diagnostics and Therapeutics in the Central Nervous System. *Nucleic Acid Ther.* **2014**, *24*, 388-404.
174. Armstrong, R. E.; Strouse, G. F. Rationally Manipulating Aptamer Binding Affinities in a Stem-Loop Molecular Beacon. *Bioconjugate Chem.* **2014**, *25*, 1769-1776.
175. Plaxco, K. W.; Soh, H. T. Switch-Based Biosensors: A New Approach Towards Real-Time, *in Vivo* Molecular Detection. *Trends Biotechnol.* **2011**, *29*, 1-5.
176. Gaster, R. S.; Hall, D. A.; Nielsen, C. H.; Osterfeld, S. J.; Yu, H.; Mach, K. E.; Wilson, R. J.; Murmann, B.; Liao, J. C.; Gambhir, S. S.; Wang, S. X. Matrix-Insensitive Protein Assays Push the Limits of Biosensors in Medicine. *Nat. Med.* **2009**, *15*, 1327-1332.

177. Vaisocherova, H.; Brynda, E.; Homola, J. Functionalizable Low-Fouling Coatings for Label-Free Biosensing in Complex Biological Media: Advances and Applications. *Anal. Bioanal. Chem.* **2015**, *407*, 3927-3953.
178. Meyers, S. R.; Grinstaff, M. W. Biocompatible and Bioactive Surface Modifications for Prolonged *in Vivo* Efficacy. *Chem. Rev.* **2012**, *112*, 1615-1632.
179. Rong, G.; Corrie, S. R.; Clark, H. A. *In Vivo* Biosensing: Progress and Perspectives. *ACS Sens.* **2017**, *2*, 327-338.
180. Swensen, J. S.; Xiao, Y.; Ferguson, B. S.; Lubin, A. A.; Lai, R. Y.; Heeger, A. J.; Plaxco, K. W.; Soh, H. T. Continuous, Real-Time Monitoring of Cocaine in Undiluted Blood Serum *via* a Microfluidic, Electrochemical Aptamer-Based Sensor. *J. Am. Chem. Soc.* **2009**, *131*, 4262-4266.
181. Arroyo-Curras, N.; Somerson, J.; Vieira, P. A.; Ploense, K. L.; Kippin, T. E.; Plaxco, K. W. Real-Time Measurement of Small Molecules Directly in Awake, Ambulatory Animals. *Proc. Natl. Acad. Sci. U. S. A.* **2017**, *114*, 645-650.
182. Stojanovic, M. N.; Green, E. G.; Semova, S.; Nikic, D. B.; Landry, D. W. Cross-Reactive Arrays Based on Three-Way Junctions. *J. Am. Chem. Soc.* **2003**, *125*, 6085-6089.
183. Li, L.; Tong, R.; Chu, H.; Wang, W.; Langer, R.; Kohane, D. S. Aptamer Photoregulation *in Vivo*. *Proc. Natl. Acad. Sci. U. S. A.* **2014**, *111*, 17099-17103.
184. Soundararajan, S.; Chen, W.; Spicer, E. K.; Courtenay-Luck, N.; Fernandes, D. J. The Nucleolin Targeting Aptamer AS1411 Destabilizes *Bcl-2* Messenger RNA in Human Breast Cancer Cells. *Cancer Res.* **2008**, *68*, 2358-2365.
185. Reyes-Reyes, E. M.; Teng, Y.; Bates, P. J. A New Paradigm for Aptamer Therapeutic AS1411 Action: Uptake by Macropinocytosis and Its Stimulation by a Nucleolin-Dependent Mechanism. *Cancer Res.* **2010**, *70*, 8617-8629.
186. Soundararajan, S.; Wang, L.; Sridharan, V.; Chen, W.; Courtenay-Luck, N.; Jones, D.; Spicer, E. K.; Fernandes, D. J. Plasma Membrane Nucleolin Is a Receptor for the Anticancer Aptamer AS1411 in MV4-11 Leukemia Cells. *Mol. Pharmacol.* **2009**, *76*, 984-991.
187. Shi, H.; He, X.; Wang, K.; Wu, X.; Ye, X.; Guo, Q.; Tan, W.; Qing, Z.; Yang, X.; Zhou, B. Activatable Aptamer Probe for Contrast-Enhanced *in Vivo* Cancer Imaging Based on Cell Membrane Protein-Triggered Conformation Alteration. *Proc. Natl. Acad. Sci. U. S. A.* **2011**, *108*, 3900-3905.
188. Zhao, W.; Schafer, S.; Choi, J.; Yamanaka, Y. J.; Lombardi, M. L.; Bose, S.; Carlson, A. L.; Phillips, J. A.; Teo, W.; Droujinine, I. A.; Cui, C. H.; Jain, R. K.; Lammerding, J.; Love, J. C.; Lin, C. P.; Sarkar, D.; Karnik, R.; Karp, J. M. Cell-Surface Sensors for Real-Time Probing of Cellular Environments. *Nat. Nanotechnol.* **2011**, *6*, 524-531.

189. Landry, M. P.; Ando, H.; Chen, A. Y.; Cao, J. C.; Kottadiel, V. I.; Chio, L.; Yang, D.; Dong, J. Y.; Lu, T. K.; Strano, M. S. Single-Molecule Detection of Protein Efflux from Microorganisms Using Fluorescent Single-Walled Carbon Nanotube Sensor Arrays. *Nat. Nanotechnol.* **2017**, *12*, 368-377.
190. Ruckman, J.; Green, L. S.; Beeson, J.; Waugh, S.; Gillette, W. L.; Henninger, D. D.; Claesson-Welsh, L.; Janjic, N. 2'-Fluoropyrimidine RNA-Based Aptamers to the 165-Amino Acid Form of Vascular Endothelial Growth Factor (VEGF<sub>165</sub>). Inhibition of Receptor Binding and VEGF-Induced Vascular Permeability through Interactions Requiring the Exon 7-Encoded Domain. *J. Biol. Chem.* **1998**, *273*, 20556-20567.
191. Ng, E. W. M.; Shima, D. T.; Calias, P.; Cunningham, E. T.; Guyer, D. R.; Adamis, A. P. Pegaptanib, a Targeted Anti-VEGF Aptamer for Ocular Vascular Disease. *Nat. Rev. Drug Discov.* **2006**, *5*, 123-132.
192. Sundaram, P.; Kurniawan, H.; Byrne, M. E.; Wower, J. Therapeutic RNA Aptamers in Clinical Trials. *Eur. J. Pharm. Sci.* **2013**, *48*, 259-271.
193. Maier, K. E.; Levy, M. From Selection Hits to Clinical Leads: Progress in Aptamer Discovery. *Mol. Ther. Methods Clin. Dev.* **2016**, *5*, 16014.
194. Breaker, R. R. Riboswitches and the RNA World. *Cold Spring Harb. Perspect. Biol.* **2012**, *4*, 1-15.
195. Winkler, W.; Nahvi, A.; Breaker, R. R. Thiamine Derivatives Bind Messenger RNAs Directly to Regulate Bacterial Gene Expression. *Nature* **2002**, *419*, 952-956.
196. Mandal, M.; Breaker, R. R. Gene Regulation by Riboswitches. *Nat. Rev. Mol. Cell Bio.* **2004**, *5*, 451-463.
197. Coppins, R. L.; Hall, K. B.; Groisman, E. A. The Intricate World of Riboswitches. *Curr. Opin. Microbiol.* **2007**, *10*, 176-181.
198. Mandal, M.; Boese, B.; Barrick, J. E.; Winkler, W. C.; Breaker, R. R. Riboswitches Control Fundamental Biochemical Pathways in *Bacillus Subtilis* and Other Bacteria. *Cell* **2003**, *113*, 577-586.
199. Welz, R.; Breaker, R. R. Ligand Binding and Gene Control Characteristics of Tandem Riboswitches in *Bacillus Anthracis*. *RNA* **2007**, *13*, 573-582.
200. Wang, J. A.; Zhang, P.; Li, J. Y.; Chen, L. Q.; Huang, C. Z.; Li, Y. F. Adenosine-Aptamer Recognition-Induced Assembly of Gold Nanorods and a Highly Sensitive Plasmon Resonance Coupling Assay of Adenosine in the Brain of Model SD rat. *Analyst* **2010**, *135*, 2826-2831.

201. Yi, M.; Yang, S.; Peng, Z. Y.; Liu, C. H.; Li, J. S.; Zhong, W. W.; Yang, R. H.; Tan, W. H. Two-Photon Graphene Oxide/Aptamer Nanosensing Conjugate for *in Vitro* or *in Vivo* Molecular Probing. *Anal. Chem.* **2014**, *86*, 3548-3554.
202. Tokunaga, T.; Namiki, S.; Yamada, K.; Imaishi, T.; Nonaka, H.; Hirose, K.; Sando, S. Cell Surface-Anchored Fluorescent Aptamer Sensor Enables Imaging of Chemical Transmitter Dynamics. *J. Am. Chem. Soc.* **2012**, *134*, 9561-9564.
203. Cho, M. J.; Juliano, R. Macromolecular *versus* Small-Molecule Therapeutics: Drug Discovery, Development and Clinical Considerations. *Trends Biotechnol.* **1996**, *14*, 153-158.
204. Jing, M.; Bowser, M. T. Methods for Measuring Aptamer-Protein Equilibria: A Review. *Anal. Chim. Acta.* **2011**, *686*, 9-18.
205. McKeague, M.; Derosa, M. C. Challenges and Opportunities for Small Molecule Aptamer Development. *J. Nucleic Acids* **2012**, *2012*, 748913.
206. Mannironi, C.; Di Nardo, A.; Fruscoloni, P.; Tocchini-Valentini, G. P. *In Vitro* Selection of Dopamine RNA Ligands. *Biochemistry* **1997**, *36*, 9726-9734.
207. Walsh, R.; DeRosa, M. C. Retention of Function in the DNA Homolog of the RNA Dopamine Aptamer. *Biochem. Bioph. Res. Co.* **2009**, *388*, 732-735.
208. Zheng, Y.; Wang, Y.; Yang, X. R. Aptamer-Based Colorimetric Biosensing of Dopamine Using Unmodified Gold Nanoparticles. *Sensor Actuat. B-Chem.* **2011**, *156*, 95-99.
209. Kim, E.; Paeng, I. R. Advantageous Sensitivity in the DNA Homolog of the RNA Dopamine Aptamer. *J. Immunoassay Immunochem.* **2014**, *35*, 83-100.
210. Park, H.; Paeng, I. R. Development of Direct Competitive Enzyme-Linked Aptamer Assay for Determination of Dopamine in Serum. *Anal. Chim. Acta* **2011**, *685*, 65-73.
211. Pfeffer, P.; Gohlke, H. Drugscore(RNA) - Knowledge-Based Scoring Function to Predict RNA-Ligand Interactions. *J. Chem. Inf. Model.* **2007**, *47*, 1868-1876.
212. Carothers, J. M.; Goler, J. A.; Kapoor, Y.; Lara, L.; Keasling, J. D. Selecting RNA Aptamers for Synthetic Biology: Investigating Magnesium Dependence and Predicting Binding Affinity. *Nucleic Acids Res.* **2010**, *38*, 2736-2747.
213. Ruscito, A.; DeRosa, M. C. Small-Molecule Binding Aptamers: Selection Strategies, Characterization, and Applications. *Front. Chem.* **2016**, *4*.
214. Kim, Y. S.; Gu, M. B. Advances in Aptamer Screening and Small Molecule Aptasensors. *Adv. Biochem. Eng. Biot.* **2014**, *140*, 29-67.
215. Nutiu, R.; Li, Y. Structure-Switching Signaling Aptamers. *J. Am. Chem. Soc.* **2003**, *125*, 4771-4778.

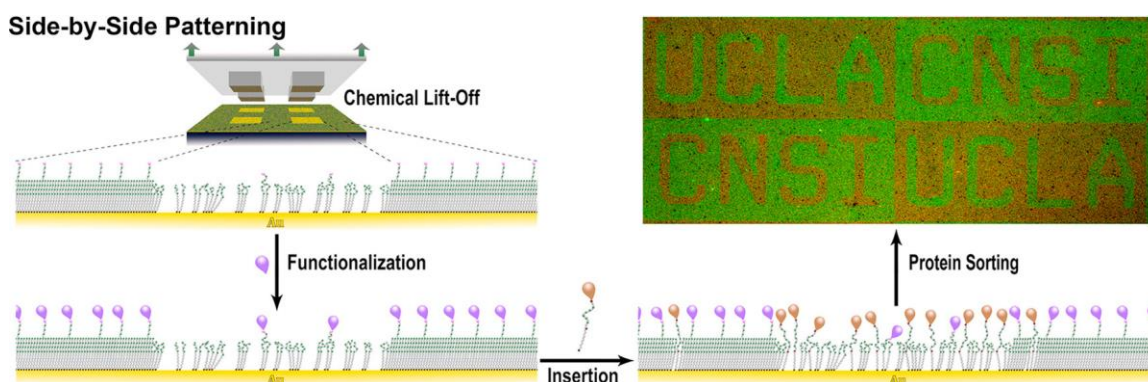


216. Martini, L.; Meyer, A. J.; Ellefson, J. W.; Milligan, J. N.; Forlin, M.; Ellington, A. D.; Mansy, S. S. *In Vitro* Selection for Small-Molecule-Triggered Strand Displacement and Riboswitch Activity. *ACS Synth. Biol.* **2015**, *4*, 1144-1150.
217. Spiga, F. M.; Maietta, P.; Guiducci, C. More DNA-Aptamers for Small Drugs: A Capture-SELEX Coupled with Surface Plasmon Resonance and High-Throughput Sequencing. *ACS Comb. Sci.* **2015**, *17*, 326-333.
218. Yang, K. A.; Pei, R. J.; Stojanovic, M. N. *In Vitro* Selection and Amplification Protocols for Isolation of Aptameric Sensors for Small Molecules. *Methods* **2016**, *106*, 58-65.
219. Andrews, A. M.; Liao, W. S.; Weiss, P. S. Double-Sided Opportunities Using Chemical Lift-Off Lithography. *Acc. Chem. Res.* **2016**, *49*, 1449-1457.
220. Vaish, A.; Shuster, M. J.; Cheunkar, S.; Singh, Y. S.; Weiss, P. S.; Andrews, A. M. Native Serotonin Membrane Receptors Recognize 5-Hydroxytryptophan-Functionalized Substrates: Enabling Small-Molecule Recognition. *ACS Chem. Neurosci.* **2010**, *1*, 495-504.
221. Shuster, M. J.; Vaish, A.; Szapacs, M. E.; Anderson, M. E.; Weiss, P. S.; Andrews, A. M. Biospecific Recognition of Tethered Small Molecules Diluted in Self-Assembled Monolayers. *Adv. Mater.* **2008**, *20*, 164-167.
222. Shuster, M. J.; Vaish, A.; Cao, H. H.; Guttentag, A. I.; McManigle, J. E.; Gibb, A. L.; Martinez, M. M.; Nezarati, R. M.; Hinds, J. M.; Liao, W. S.; Weiss, P. S.; Andrews, A. M. Patterning Small-Molecule Biocapture Surfaces: Microcontact Insertion Printing vs. Photolithography. *Chem. Commun.* **2011**, *47*, 10641-10643.
223. Liao, W. S.; Cao, H. H.; Cheunkar, S.; Shuster, M. J.; Altieri, S. C.; Weiss, P. S.; Andrews, A. M. Small-Molecule Arrays for Sorting G-Protein-Coupled Receptors. *J. Phys. Chem. C* **2013**, *117*, 22362-22368.
224. Araz, M. K.; Tentori, A. M.; Herr, A. E. Microfluidic Multiplexing in Bioanalyses. *JALA* **2013**, *18*, 350-366.
225. Cao, H. H.; Nakatsuka, N.; Serino, A. C.; Liao, W. S.; Cheunkar, S.; Yang, H. Y.; Weiss, P. S.; Andrews, A. M. Controlled DNA Patterning by Chemical Lift-Off Lithography: Matrix Matters. *ACS Nano* **2015**, *9*, 11439-11454.
226. Nakatsuka, N.; Cao, H. H.; Deshayes, S.; Kasko, A. M.; Weiss, P. S.; Andrews, A. M. Aptamer Recognition by Multiplexed Neurotransmitter-Functionalized Substrates. *in preparation* **2017**.
227. Walsh, R.; DeRosa, M. C. Retention of Function in the DNA Homolog of the RNA Dopamine Aptamer. *Biochem. Biophys. Res. Co.* **2009**, *388*, 732-735.

228. Nakatsuka, N.; Yang, K. A.; Xu, X.; Abendroth, J. M.; Zhao, C. Z.; Cheung, K. M.; Zhu, B.; Rim, Y. S.; Yang, Y.; Weiss, P. S.; Stojanovic, M. N.; Andrews, A. M. Aptamer Field-Effect Transistors Overcome Debye Length Limitations and Enable Small-Molecule Sensing. *submitted* **2017**.

## Chapter II

# Advancing Biocapture Substrates *via* Chemical Lift-Off Lithography



The information in this chapter was published in  
*Chemistry of Materials* **2017**, 29, 6829-6839  
and has been reproduced here.

Authors: Cao, H. H.; Nakatsuka, N.; Liao, W. -S.; Serino, A. C.;  
Cheunkar, S.; Yang, H.; Weiss, P. S.; Andrews, A. M.

## II.A. Introduction

To produce multiplexed, functional, biocapture platforms for high-throughput screening or biosensing applications, surface immobilization and patterning strategies are needed to anchor molecules on solid substrates for capturing and sorting respective binding partners from complex mixtures in solution or *in vivo*.<sup>1-11</sup> Although, *in vivo* sensing to date has been based largely on electrochemical<sup>12-14</sup> or enzymatic detection,<sup>15-17</sup> small-molecule biocapture strategies provide gateways to new sensing opportunities.<sup>18</sup> Immobilization of large biomolecules on surfaces requires avoiding denaturation upon surface adsorption and favorable orientation for ligand binding.<sup>19-24</sup> In contrast, surface tethering of small-molecule probes necessitates judicious selection of coupling chemistries and surface dilution to facilitate recognition by large biomolecule binding partners.<sup>22,25-32</sup> For instance, the areal size mismatch on surfaces between small-molecule neurotransmitters or amino acids and large antibody or receptor binding partners is >100 fold.<sup>33,34</sup>

An important goal of small-molecule chemical patterning is site-specific placement of multiple probes on substrates for the interrogation of target binding specificity and selectivity.<sup>32,35-38</sup> However, achieving this objective has been challenging.<sup>39-43</sup> We developed additive methods to pattern small molecules to investigate biomolecule capture *via* relative quantification of binding on functionalized vs. unfunctionalized regions of substrates. Microcontact insertion printing ( $\mu$ CIP) was used to pattern small-molecule neurotransmitters and precursors mimicking endogenous neurotransmitters on alkanethiol self-assembled monolayer (SAM)-modified Au substrates.<sup>44-46</sup> Using this approach, molecular tethers are inserted into pre-formed SAMs and tethers are subsequently functionalized on-substrate with small-molecule probes. To circumvent

problems associated with the sequential surface functionalization chemistries needed for multi-functionalized substrates, we used microfluidics to generate multiplexed substrates.<sup>38</sup> Here, two-component SAMs with low proportions of tether molecules (<10% solution concentration) are produced by co-deposition to achieve dilution of surface tethers. Individual channels are exposed to different small-molecule targets for multiplexed functionalization.

We also developed a subtractive patterning method called chemical lift-off lithography (CLL), where alkanethiol SAM molecules are removed from Au substrates.<sup>47,48</sup> Polydimethylsiloxane (PDMS) stamps are treated with oxygen plasma to generate siloxyl groups on stamp surfaces. Activated stamps are brought into conformal contact with hydroxyl-terminated alkanethiol SAMs (or other suitably terminated monolayers) on Au substrates to produce covalent interactions at stamp/SAM interfaces. Previous studies indicated the lability of Au-Au bonds at substrate-SAM interfaces based on evidence for mobile Au thiolates within SAMs<sup>49-52</sup> and the presence of low-coordination Au adatoms beneath SAMs.<sup>53-55</sup> Zhang *et al.* used thiol-derivatized tips and atomic force microscopy (AFM) to quantify the strengths of isolated Au-S bonds.<sup>56</sup> They showed that Au-S bonds were sufficiently strong such that Au-Au bonds at the outermost Au-substrate layers can be preferentially disrupted. We have shown that stamp/SAM and SAM/Au interfacial interactions in lift-off lithography are stronger than Au-Au substrate bonds as stamp lift-off causes alkanethiols and the outermost layer of the underlying Au atoms to be simultaneously removed.<sup>47,57</sup>

Previously, lift-off regions were patterned with biotin-terminated alkanethiols to capture streptavidin.<sup>47</sup> Lift-off removes a significant portion of the initial monolayer. Yet,

molecules remaining in the contact regions facilitate controlled and favorable insertion of new molecules. For example, DNA probes can be inserted into lift-off regions for highly efficient and tunable hybridization with complementary oligomers.<sup>58</sup> Chemical lift-off lithography has also been combined with sol-gel chemistry to print transistors for small-molecule biosensors.<sup>59</sup>

Here, we advance the understanding, use, and applicability of CLL. We expanded the feature shapes and sizes patterned by lift-off lithography and extend nanoscale patterning by this method to sub-30-nm using a single lift-off step. We produced bifunctional substrates to demonstrate biomolecule recognition and sorting. We used lift-off lithography to produce patterned substrates that capture native protein targets. In addition, alkanethiols with a range of terminal functionalities were investigated to enlarge the molecular library that can be patterned by CLL.

## II.B. Experimental Methods

### II.B.1. Materials

Silicon substrates with 100-nm Au films over 10-nm Ti adhesive layers were purchased from Platypus Technologies (Madison, WI, USA). 6-Mercaptohexanol (MCH), 1-dodecanethiol (CH<sub>3</sub>-C11), *N*-hydroxysuccinimide (NHS), *N*-(3-dimethylaminopropyl)-*N'*-ethylcarbodiimide hydrochloride (EDC), *N,N*-dimethylformamide (DMF), 4-methylpiperidine, bovine serum albumin (BSA), and 0.01 M phosphate buffered saline (PBS) ([NaCl]=138 mM, [KCl]=2.7 mM pH 7.4) were purchased from Sigma-Aldrich (St. Louis, MO, USA). Absolute, 200 proof, anhydrous, ACS/USP grade ethyl alcohol was from PHARMCO-AAPER (Oakland, CA, USA). Deionized water (~18 MΩ) was obtained from a Millipore water purifier (Billerica, MA, USA). The Fmoc-protected biological precursors to serotonin and dopamine, *i.e.*, 9-fluorenylmethyloxycarbonyl-5-hydroxy-*L*-tryptophan (Fmoc-*L*-5HTP) and 9-fluorenylmethyloxycarbonyl-3,4-dihydroxy-*L*-phenylalanine (Fmoc-*L*-DOPA) were purchased from AnaSpec-Eurogentec (Fremont, CA, USA).

(11-Mercaptoundecyl) tri(ethylene glycol) (TEG) and (11-mercaptoundecyl) hexa(ethylene glycol)carboxylic acid (COOH-HEG) were purchased from Toronto Research Chemicals Inc. (Toronto, ON, Canada). 11-Mercaptoundecyl hexa(ethylene glycol)biotin (biotinylated hexa(ethylene glycol)undecanethiol; BEG) was from Nanoscience Instruments Inc. (Phoenix, AZ, USA). 11-Bromo-1-undecanethiol (Br-C11) was obtained from Assemblon Inc. (Redmond, WA, USA). (11-Mercaptoundecyl) hexa(ethylene glycol)amine (AEG), 11-mercaptoundecylphosphonic acid (PO(OH)<sub>2</sub>-C11), and (11-mercaptoundecyl) tri(ethylene glycol)methyl ether (CH<sub>3</sub>O-TEG) were from Prochimia (Sopot, Poland).

Streptavidin antibodies (1 mg/mL) and AlexaFluor® 546 goat anti-mouse IgG (H+L) highly cross-adsorbed antibodies (2 mg/mL) were purchased from Invitrogen (Carlsbad, CA, USA). Mouse polyclonal anti-serotonin<sub>1A</sub> (5-HT<sub>1A</sub>) receptor antibodies (whole antiserum), rabbit polyclonal anti-dopamine D<sub>1</sub> receptor antibodies (whole antiserum), mouse monoclonal anti-*L*-5-HTP antibodies (1 mg/mL), mouse monoclonal anti-*L*-DOPA antibodies (1 mg/mL), and fluorescein isothiocyanate (FITC)-conjugated rabbit polyclonal anti-streptavidin antibodies (10 mg/mL) were purchased from Abcam Inc. (Cambridge, MA, USA). Human 5-HT<sub>1A</sub> receptors (0.8 fmol receptor protein/μg membrane protein; 6.4 μg/μL total protein concentration) from transfected human embryonic kidney 293 (HEK293) cells and untransfected HEK293 cell membranes (10 μg/μL total protein concentration) were from Perkin Elmer, Inc. (Waltham, MA, USA). All antibodies and proteins were used as received and incubated with substrates in 0.01 M PBS pH 7.4 at room temperature. Antibodies not labeled with fluorophores and fluorescently labeled antibodies were diluted 1:200 and 1:100, respectively, in 0.01 M PBS pH 7.4.

### **II.B.2. Substrate and Stamp Preparation**

All Au substrates were hydrogen-flame annealed, followed by incubation with ethanolic solutions of alkanethiols. After monolayer formation, substrates were rinsed thoroughly with fresh ethanol and dried with nitrogen gas. Different feature shapes on polydimethylsiloxane (PDMS) stamps were produced from silicon masters, which were fabricated by standard photolithography. The process of stamp fabrication and details of oxygen plasma treatment are published elsewhere.<sup>38,46,47,58</sup>



Briefly, a 10:1 mass ratio of *SYLGARD* 184 silicone elastomer base and curing agent (Ellsworth Adhesives, Germantown, WI, USA) was mixed thoroughly in a plastic cup, degassed under vacuum, cast onto master substrates in plastic Petri dishes, and cured in an oven at 70°C overnight. Polymerized stamps were removed from masters, cut into usable sizes, and treated with oxygen plasma (Harrick Plasma, power 18 W, and oxygen pressure 10 psi) for 30 s just prior to use to produce hydrophilic reactive PDMS surfaces.<sup>46,47,58</sup>

### **II.B.3. Biotin-Streptavidin Patterns**

Substrates were incubated with ethanolic solutions of 0.5 mM TEG for ~17 h to form SAMs. Oxygen plasma-treated PDMS stamps were placed in conformal contact with substrates for 30 min to enable stamp/substrate contact reactions, which caused SAM molecules and underlying Au atoms to be removed from contact areas once stamps were released from the substrates (Figure II.1A). Stamps with microscale protruding features (~30  $\mu\text{m}$  with ~30-60  $\mu\text{m}$  spacings) or nanoscale protruding or recessed features (200-nm circles with 2- $\mu\text{m}$  pitch or 30-nm lines with 3- $\mu\text{m}$  pitch, respectively) were used for patterning. Post-lift-off substrates were inserted with 80/20 ethanolic solutions of 0.40 mM TEG and 0.1 mM BEG for 1 h. For nanoscale patterning, 100% ethanolic solutions of 0.5 mM BEG were used to maximize BEG insertion into post-lift-off TEG-modified substrates.

Biotinylated substrates were incubated with 10 mg/mL BSA for 5 min to block nonspecific protein adsorption sites, then with 50  $\mu\text{g/mL}$  streptavidin for 20 min, and finally with 100  $\mu\text{g/mL}$  FITC-conjugated rabbit anti-streptavidin antibodies for 20 min to visualize streptavidin binding to surface-tethered biotin (Table SA.1). Copious amounts of deionized water were used to rinse substrates gently after each protein incubation step.

An inverted fluorescence microscope (Axio Observer.D1, Carl Zeiss Microscopy, LLC, Thornwood, NY, USA) was used to image substrates. A 38 HE/high efficiency filter set with excitation and emission wavelengths at  $470 \pm 20$  and  $525 \pm 25$  nm, respectively, was used to image streptavidin-biotin fluorescence patterns. A 43 HE/high efficiency filter set with excitation and emission wavelengths at  $550 \pm 25$  and  $605 \pm 70$  nm, respectively was used to visualize antibody binding to *L*-DOPA or *L*-5-HTP substrates (*vide infra*). Fluorescence images were collected using 10× or 20× objective lenses for microscale or nanoscale patterns, respectively. Exposure times were 100 ms (or longer as needed) to visualize differences in fluorescence between the patterned features and the surrounding background or between regions patterned with different probes. The same exposure times were used to image all test and control samples for each experiment. Auto-optimized contrast images were also collected to maximize visualization of nonspecific recognition on control substrates (see Supporting Information; Appendix A).

Fluorescence intensities (arbitrary units) were determined using AxioVs40 version 4.7.1.0 software (Carl Zeiss MicroImaging, Inc.). Fluorescence line scans were adjusted to be approximately the same sizes as patterned features. On average, five line scans were acquired per image. Fluorescence intensities for bright vs. dark areas were averaged for each line scan and then for each image. For images with more complex patterns, *i.e.*, UCLA/CNSI letter-shaped features, fluorescence intensities were measured in bright vs. dark regions using a histogram function. Fluorescence was quantified from at least three different substrates per condition per experiment.

Streptavidin-biotin nanoscale features were investigated *via* tapping-mode AFM (Dimension 5000, Bruker AXS, Santa Barbara, CA, USA). Topographic AFM images were

collected using Si cantilevers with a spring constant of 48 N/m and a resonant frequency of 190 kHz (Veeco Instruments, Santa Barbara, CA, USA). The resulting images were processed with WSxM 4.0 Beta 6.4 software (Nanotec Electronica, Madrid, Spain).<sup>60</sup>

#### **II.B.4. Side-by-Side Patterning**

Substrates were incubated with 90/10 ethanolic solutions of 0.45 mM TEG and 0.05 mM AEG tethers for ~17 h to create dilute amine-terminated SAMs. Stamps were activated with oxygen plasma and brought into conformal contact with SAM-modified substrates for 30 min to generate stamp/SAM interfacial interactions.

For functionalization with the first probe, which takes place primarily in the unpatterned (non-lifted-off) regions (Figure II.1B), solutions of 20 mM Fmoc-protected *L*-DOPA or 40 mM Fmoc-protected *L*-5-HTP were combined with 20 mM or 40 mM NHS/EDC, respectively, in 60/40 DMF/deionized water. This step activates the carboxyl groups of *L*-DOPA or *L*-5-HTP with NHS esters for subsequent reaction with the amino moieties of AEG SAM molecules to form amide bonds (Scheme II.1). Substrates were incubated with activated *L*-DOPA or *L*-5-HTP solutions for 4 h. To functionalize the second probe, substrates were then incubated with 90/10 ethanolic solutions of 0.45 mM TEG and 0.05 mM BEG for 1 h to insert BEG primarily into the patterned (lifted-off) regions (Figure II.1B).

The Fmoc protecting groups on *L*-DOPA and *L*-5-HTP prevented intermolecular reactions between these NHS-activated probe molecules. After immobilization on substrates, Fmoc protecting groups were removed with 20% 4-methylpiperidine in deionized water for 20 min. After rinsing with deionized water and drying with nitrogen

gas, functionalized substrates were incubated with 10 mg/mL BSA for 5 min, then with mixtures of streptavidin (50  $\mu$ g/mL) and either mouse monoclonal anti-*L*-DOPA primary antibodies or mouse monoclonal anti-*L*-5-HTP primary antibodies for 20 min, and then with mixtures of FITC-conjugated rabbit polyclonal anti-streptavidin antibodies (100  $\mu$ g/mL) and AlexaFluor® 546 goat anti-mouse IgG secondary antibodies (20  $\mu$ g/mL) for 20 min to visualize multiplexed protein patterns (Table SA.1). Imaging was carried out as described above.

#### **II.B.5. Patterning for Membrane-Associated Receptor Capture**

Dilute amine-terminated SAMs were produced by incubating substrates with 95/5 ethanolic solutions of 0.048 mM TEG and 0.025 mM AEG for ~17 h. Substrates were brought into conformal contact for 30 min with the hydrophilic reactive surfaces of oxygen plasma-treated PDMS stamps (25  $\mu$ m  $\times$  25  $\mu$ m square protruding features). Post-lift-off substrates were functionalized with activated *L*-5-HTP and deprotection was carried out using the procedures described in the previous section.

After rinsing with deionized water, substrates were incubated with 10 mg/mL BSA for 5 min to reduce nonspecific protein binding.<sup>38,45</sup> The *L*-5-HTP-modified substrates were then incubated with 100  $\mu$ g/ $\mu$ L 5-HT<sub>1A</sub> receptors for 1 h. The receptor-associated cell membranes were not solubilized to retain native receptor conformations favorable for probe recognition.<sup>24,33,38,61</sup> Previously, we found that primary antibodies recognizing membrane-associated receptors have weak affinity for surface-tethered probes.<sup>38</sup> Thus, after incubating with 5-HT<sub>1A</sub> receptors, functionalized substrates were exposed to anti-dopamine D<sub>1</sub> receptor rabbit polyclonal blocking antibodies for 15 min to reduce

nonspecific binding of anti-5-HT<sub>1A</sub> receptor primary antibodies to surface-tethered *L*-5-HTP. Substrates were incubated with mouse polyclonal anti-5-HT<sub>1A</sub> receptor primary antibodies for 15 min followed by 20 µg/mL AlexaFluor® 546 goat anti-mouse secondary antibodies for 15 min to visualize 5-HT<sub>1A</sub> receptor binding (Table SA.1). Substrates were rinsed with deionized water between protein incubation steps. The 43 HE fluorescence filter set was used to visualize capture of 5-HT<sub>1A</sub> receptors to patterns of surface-tethered *L*-5-HTP as described above.

#### **II.B.6. X-Ray Photoelectron Spectroscopy**

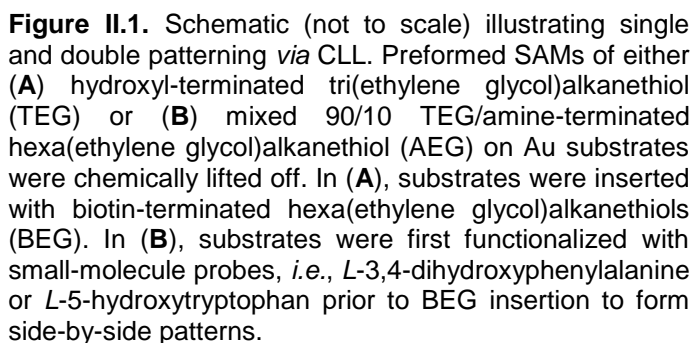
Featureless PDMS stamps were used for the CLL process. All X-ray photoelectron spectroscopy (XPS) data were collected using an AXIS Ultra DLD instrument (Kratos Analytical Inc., Chestnut Ridge, NY, USA). A monochromatic Al K<sub>α</sub> X-ray source (10 mA for survey scans and 20 mA for high resolution scans, 15 kV) with a 200 µm circular spot size and ultrahigh vacuum (10<sup>-9</sup> Torr) was used.<sup>46,47</sup> Spectra were acquired at a pass energy of 160 eV for survey spectra and 20 eV for high-resolution spectra of Au 4f regions (100 scans) using a 200-ms dwell time.

A charge neutralizer (flood gun) was used to obtain XPS signals on PDMS, which is an insulator. As a result, peaks are shifted slightly from their expected regions. For example, the C 1s peak is 4-5 eV lower than its reference peak at 284.0 eV. Because the number of peaks of interest was small (only Au 4f peaks on PDMS samples), and they were well separated (~4 eV); peak shifting did not affect peak identification. No corrections were carried out during data collection to shift peaks back to particular regions or to scale peaks based on reference locations.

### **II.B.7. Statistical Analyses**

Data were analyzed by two-tailed unpaired Student's *t*-tests using GraphPad Prism 5.0 (GraphPad Software Inc., San Diego, USA). Fluorescence intensities were normalized to mean values for control regions and are reported as means  $\pm$  standard errors in relative fluorescence units (RFU) with probabilities  $P < 0.05$  considered statistically significant.

To explore the flexibility of CLL as a patterning method for creating functional small-molecule arrays beyond initial findings,<sup>47,48,62</sup> we investigated substrates patterned with the small-molecule biotin (Figure II.1A) over a wide variety of feature shapes and sizes (Figure II.2). The use of PDMS stamps with different protruding microscale features produced corresponding bright fluorescent patterns (Figure II.2A). Relative quantification of the fluorescence in bright vs. dark areas of each pattern indicated differential recognition of surface-tethered biotin by streptavidin in the patterned vs. unpatterned regions. A lack of measurable fluorescence or patterning was observed when similar substrates were incubated



with FITC-labeled anti-streptavidin antibodies in the absence of streptavidin indicating negligible nonspecific antibody binding (Figure SA.1).

A wide-area, bright nanodot array is shown against a dark TEG background in Figure II.2B, illustrating a streptavidin-biotin recognition pattern with 100-fold smaller features than in Figure II.2A. Nanodot feature sizes measured by tapping-

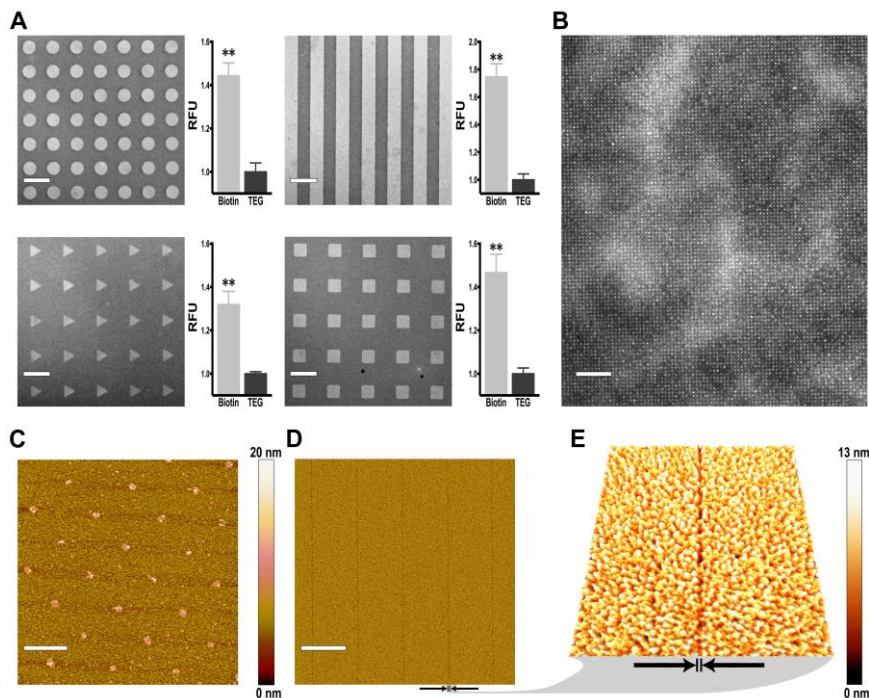


**Figure II.2.** Representative fluorescence and scanning probe images of streptavidin recognition on microscale and nanoscale biotin-patterned substrates. (A) Bright, microscale circular-, striped-, triangular-, or square-patterned regions or (B) nanoscale dots are visualized against a dark surrounding hydroxyl-terminated tri(ethylene glycol)alkaneethiol (TEG) background. Binding of streptavidin to surface-tethered biotin was visualized with fluorescein isothiocyanate (FITC)-labeled anti-streptavidin antibodies (excitation at 495 nm). Fluorescence images were recorded at an emission wavelength of 519 nm. Error bars represent standard errors of the mean [ $N=3$ ;  $**t<0.01$  vs. unpatterned regions] (C) Atomic force microscopy (AFM) topography image to quantify sizes of streptavidin-biotin nanodots shown in (B). The dots are  $215 \pm 3$  nm in diameter. In (D) and (E), AFM topographic images at two different scales are of sub-30 nm wide TEG lines on a streptavidin-biotin background. The arrows help to visualize the locations of single lines. Scale bars are 60  $\mu\text{m}$ , 40  $\mu\text{m}$ , 2  $\mu\text{m}$ , and 3  $\mu\text{m}$  for A, B, C, and D, respectively. The imaged area is 2  $\mu\text{m} \times 2 \mu\text{m}$  in E.

mode AFM were  $215 \pm 3$  nm in diameter (Figure II.2C). Because AFM images were collected under dry conditions, some of the proteins captured on biotin-functionalized dots may have been denatured and/or desorbed contributing to the irregular shapes in Figure II.2C.<sup>63</sup>

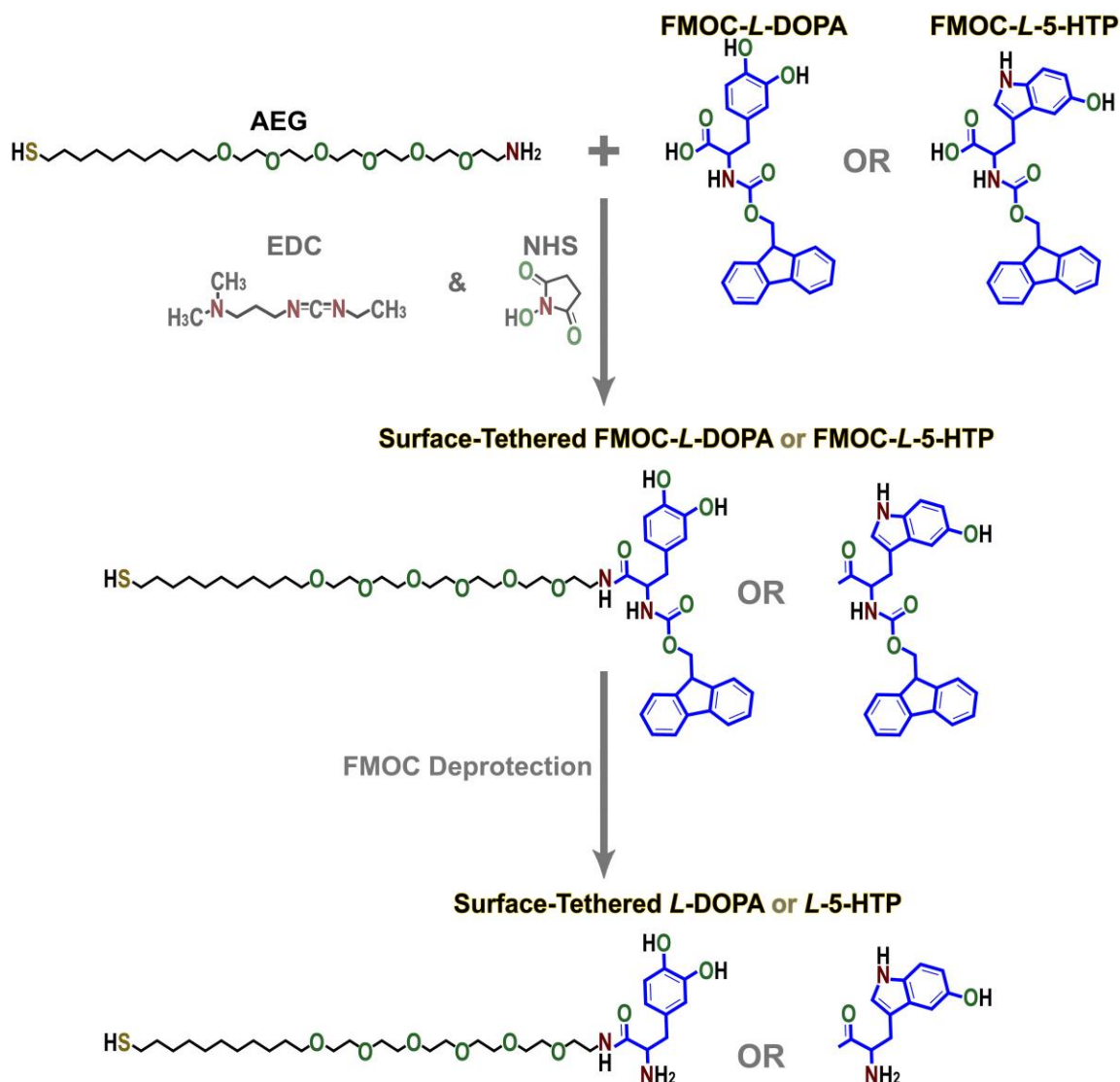


Previously, we used CLL to produce features as small as 40 nm using a single lift-off step; double lift-off lithography was needed to pattern 20-nm features.<sup>47</sup> Here, we achieved sub-30-nm feature resolution with single-step lift-off *via* an inverse patterning strategy, *i.e.*, ultra-small features were produced in the noncontact areas. Creating nanoscale features in contact areas by conventional additive patterning approaches, *e.g.*, microcontact printing,<sup>64</sup> microdisplacement printing,<sup>65,66</sup> microcontact insertion printing,<sup>67,68</sup> as well as by subtractive CLL is difficult because protruding, ultra-small features on PDMS stamps are not mechanically stable during stamp/substrate conformal contact. However, smaller features can be created by deliberately manipulating/distorting stamps.<sup>48,62,69</sup> Employing “hard” PDMS or composite stamp materials and/or hierarchically structured stamps may also enable ultra-small features in contact regions.<sup>62,70,71</sup>

Tapping-mode AFM was needed to visualize the nanoscale patterns in Figure II.2D,E. As shown in Figure II.2D, wide lines ( $\sim 3\ \mu\text{m}$ ) with positive-height topographic features produced by streptavidin recognition of biotinylated (contact) regions are contrasted with narrow TEG features with negative-height topography. Negative features were  $26 \pm 1\ \text{nm}$  wide by AFM (Figure II.2E). Since, narrow line widths are similar to Au grain sizes on 100-nm polycrystalline Au films ( $\sim 20\text{-}50\ \text{nm}$ ), Au graininess increases line-edge roughness and reduces the accuracy of feature size and/or measurement.<sup>72,73</sup> This result suggests further possibilities of using CLL to produce sub-20-nm or even sub-10-nm features *via* ultra-flat Au films on mica substrates.<sup>74-76</sup>

Above and in previous work, CLL was used to remove TEG or other hydroxyl-terminated undecanethiol SAM molecules.<sup>47</sup> Here, we extended the use of CLL to mixed TEG/AEG SAMs. To determine whether stamp contact removes AEG, we used flat PDMS

stamps to carry out lift-off on 100% AEG SAMs. Post-lift-off PDMS stamps contacted with AEG-modified Au substrates showed Au 4f XPS signals (Figure SA.2), indicating that AEG molecules are lift-able.



**Scheme II.1.** Schematic illustrating surface functionalization chemistries. *N*-Hydroxysuccinimide (NHS) and *N*-(3-dimethylaminopropyl)-*N*-ethylcarbodiimide hydrochloride (EDC) were used to create NHS-ester activated carboxyl groups on 9-fluorenylmethyloxycarbonyl (Fmoc)-protected 3,4-dihydroxy-*L*-phenylalanine (*L*-DOPA) or 5-hydroxy-*L*-tryptophan (*L*-5-HTP). The NHS esters were then reacted with the amino moieties on amine-terminated hexa(ethylene glycol)alkanethiol (AEG) to form amide bonds. Protecting groups were removed after probe functionalization on substrates to reveal epitopes necessary for recognition by biomolecule partners.

The AEG in the noncontact regions, as well as any remaining AEG in the contact regions, was functionalized with 3,4-dihydroxy-*L*-phenylalanine (*L*-DOPA) or 5-hydroxy-*L*-tryptophan (*L*-5-HTP) (Scheme II.1). Afterwards, insertion of 90/10 TEG/BEG into the contact regions was carried out to create side-by-side biotin/*L*-DOPA or biotin/*L*-5-HTP bifunctional patterns (Figure II.1B). The BEG and AEG molecules were in low abundance compared to TEG to ensure dilution of surface-tethered biotin and *L*-DOPA or *L*-5-HTP<sup>33,38</sup> in the TEG background matrix for efficient capture of large biomolecule binding partners.<sup>77-79</sup> Moreover, low abundance of functional molecules, *i.e.*, AEG in the original SAM or BEG in the insertion solution, minimized residual cross-contamination of side-by-side patterns.

Bifunctionalized substrates were exposed to solutions containing pairs of binding partners, *i.e.*, biotin and anti-*L*-DOPA or anti-*L*-5-HTP primary antibodies, to investigate site-specific sorting of biomolecules. Substrates were then exposed to solutions containing FITC-conjugated anti-streptavidin antibodies and AlexaFluor® 546 secondary antibodies for sorting and visualization of bound streptavidin or primary *L*-DOPA or *L*-5-HTP antibodies, respectively.

In Figure II.3A, at the fluorescence emission wavelength for FITC-conjugated anti-streptavidin antibodies (519 nm), bright wide channels (~75  $\mu\text{m}$ ) illustrate streptavidin-biotin recognition in stamp-contact regions. In contrast, dark narrow channels (~30  $\mu\text{m}$ ) occur where *L*-DOPA was functionalized in the noncontact areas. Conversely, in Figure II.3B, at the fluorescence emission wavelength for AlexaFluor® 546 secondary antibodies (573 nm), bright narrow channels represent anti-*L*-DOPA antibody recognition

of surface-functionalized *L*-DOPA against dark wide channels where biotin-captured streptavidin occurred.

Similarly, juxtaposed biotin-streptavidin and *L*-5-HTP/anti-*L*-5-HTP antibody patterns are shown in Figure II.3D and II.3E, respectively, corresponding to fluorescence wavelengths of FITC-conjugated anti-streptavidin antibodies (519 nm) and AlexaFluor® 546 secondary antibodies (573 nm), respectively. Bright “UCLA” letters and bright regions surrounding the “CNSI” letters in Figure II.3D indicate biotin-streptavidin recognition. The “CNSI” letters and bright areas surrounding the “UCLA” letters in Figure II.3E indicate *L*-5-HTP/anti-*L*-5HTP-antibody binding on the same substrates shown in Figure II.3D. Low levels or lack of fluorescence occurred when substrates were incubated with solutions containing FITC-conjugated anti-streptavidin antibodies or AlexaFluor® 546 secondary antibodies, respectively, without prior exposure to streptavidin and *L*-DOPA or *L*-5-HTP primary antibodies (Figure SA.3). These findings indicate negligible nonspecific binding of the fluorescently labeled antibodies to bifunctional substrates. Importantly, these results demonstrate that bifunctional patterns produced using CLL could be used to direct capture of neurotransmitter-related biomolecules including receptors (*vide infra*), transporters, and artificial receptors.<sup>6,7,30,33,38</sup>

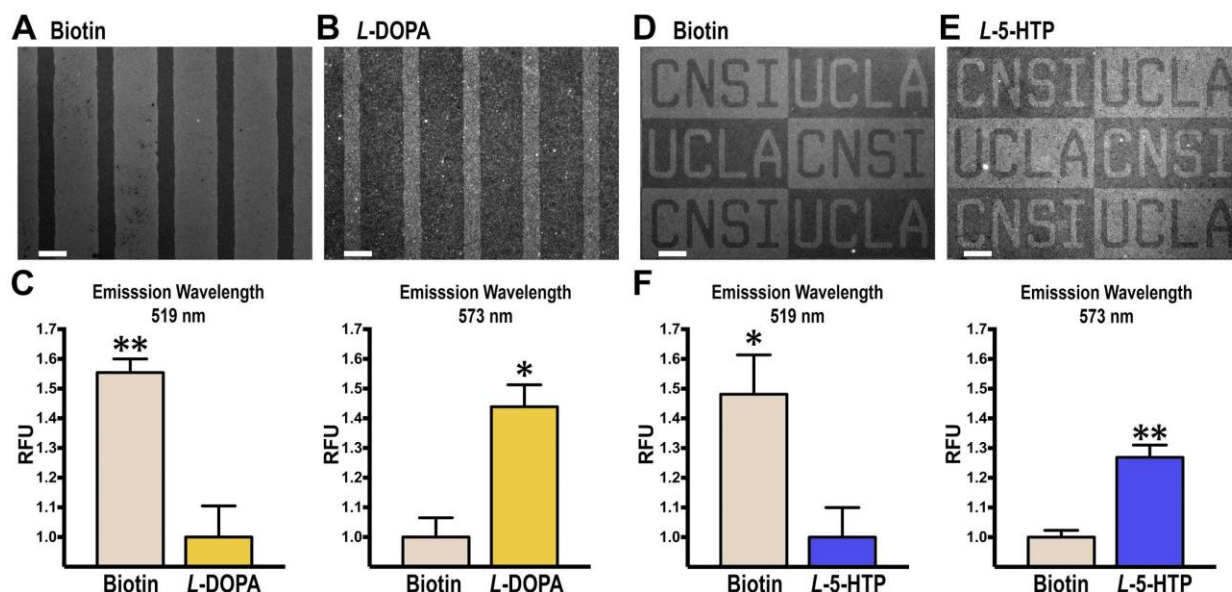


**Figure II.3. Target sorting on bifunctional substrates.** Representative fluorescence images are shown for (A,B) biotin/L-DOPA and (D,E) biotin/L-5-HTP patterned substrates. Substrates were exposed to mixed solutions of streptavidin and anti-L-DOPA or anti-L-5-HTP primary antibodies followed by mixed fluorescein isothiocyanate (FITC)-conjugated anti-streptavidin antibodies (excitation at 495 nm) and AlexaFluor® 546 secondary antibodies (excitation at 556 nm). Substrates were then imaged at (A,D) 519 nm or (B,E) 573 nm emission wavelengths. In (C, left), significantly higher relative fluorescence intensities were measured in the wide-striped biotin-modified regions vs. the narrow-striped L-DOPA-modified regions [ $t(4)=5$ ,  $**P<0.01$ ] at the FITC emission wavelength. While in (C, right), significantly higher relative fluorescence intensities were detected in the L-DOPA-modified narrow-striped regions vs. the wide-striped biotin-functionalized regions [ $t(6)=3$ ,  $*P<0.05$ ] at the AlexaFluor® 546 emission wavelength. Similarly, in (F, left), at the FITC emission wavelength, higher relative fluorescence intensities were observed within the UCLA letters and regions surrounding the CNSI letters [ $t(4)=4$ ,  $*P<0.05$ ], which were biotin-modified vs. surrounding the UCLA letters and within the CNSI letters, which were L-5-HTP-modified regions. In (F, right), opposite fluorescent intensity patterns were quantified at the AlexaFluor® 546 emission wavelength [ $t(6)=6$ ,  $**P<0.01$ ].  $N=3-4$  substrates per group. Scale bars are 50  $\mu\text{m}$ .

Variations in intermolecular interactions in mixed vs. monocomponent monolayers may impact lift-off yields. Nonetheless, we estimate that lift-off removes  $\sim 70\%$  of AEG molecules (similar to the lift-off yield for TEG molecules). If the mixed monolayers used here nominally contained 5-10% AEG, then  $\sim 1.5-3\%$  of the molecules remaining in the contact regions would be AEG and functionalized with L-DOPA or L-5-HTP. As such, a small amount of anti-L-DOPA or anti-L-5-HTP antibody binding likely occurs in the lift-off regions, which are subsequently functionalized with biotin. Similarly, in mono- and

bifunctionalized substrates (Figure II.1), small numbers of BEG molecules insert into native SAM defects in the noncontact regions, in addition to insertion in the contact regions. Previously, we used quartz crystal microbalance gravimetry to estimate insertion of alkanethiol molecules similar to BEG into SAM defects in preformed TEG monolayers.<sup>30</sup> We determined that the degree of solution-phase insertion constituted ~0.5% of the monolayer for 4-h insertion times with 0.2 mM insertion molecules. Here, we inserted BEG into TEG SAMs for 1 h using 0.05-0.1 mM BEG. Thus, the extent of “unintentional” BEG insertion into noncontact region defects is probably <0.5% of the monolayer. Collectively, these effects reduce selective functionalization of contact vs. noncontact regions somewhat. However, they appear to have negligible consequences for relative site-specific target recognition under dilute deposition and insertion conditions (Figure II.3C,F).

We have shown through the use of small-molecule probes with an additional functional group for linking chemistries that we can retain free functional groups needed for native receptor capture and sorting.<sup>33,46</sup> Earlier patterning was by microcontact insertion printing or microfluidics.<sup>33,38,46</sup> Here, lift-off lithography was used to pattern the small-molecule serotonin precursor *L*-5-HTP to investigate capture of native 5-HT<sub>1A</sub> membrane-associated G-protein-coupled receptors. Because 5-HT<sub>1A</sub> receptors play critical roles in regulating serotonin neurotransmission in the central nervous system,<sup>80</sup> they are targets for developing treatments for neuropsychiatric disorders.<sup>81,82</sup>

Subtractive patterning was carried out on 95/5 TEG/AEG mixed SAMs. The AEG molecules were then functionalized with *L*-5-HTP, which has an additional carboxyl moiety compared to serotonin. Anti-5-HT<sub>1A</sub> receptor primary antibodies and AlexaFluor® 546-labeled secondary antibodies were used to visualize *L*-5-HTP/5-HT<sub>1A</sub> receptor recognition. Patterns of 5-HT<sub>1A</sub> receptors appeared in

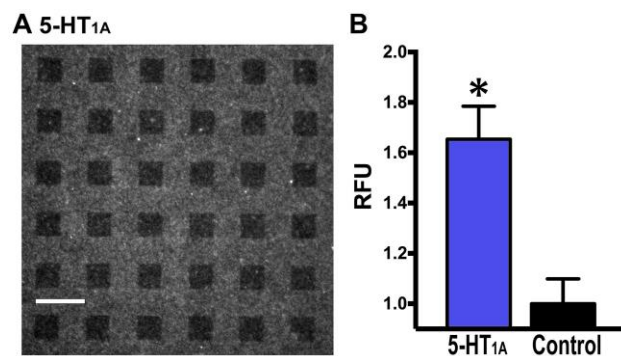


**Figure II.4.** Native receptor capture. (A) Representative fluorescence image of an *L*-5-HTP-modified substrate exposed to HEK293 membranes from cells overexpressing 5-HT<sub>1A</sub> receptors, anti-5-HT<sub>1A</sub> receptor primary antibodies, and AlexaFluor® 546 secondary antibodies (excitation at 556 nm). (B) Mean relative fluorescence intensities were significantly different for stamp-noncontact vs. contact regions [ $t(4)=4$ ,  $*P<0.05$ ]. Scale bar is 50  $\mu$ m.

fluorescence microscopy images as bright areas surrounding arrays of dark TEG squares (Figure II.4A). Relative fluorescence intensities in *L*-5-HTP-functionalized (noncontact) regions were significantly greater than in control (contact) regions (Figure II.4B). Additional experiments were carried out where similarly patterned substrates were exposed to membranes from cells that do not express 5-HT<sub>1A</sub> receptors. Substrates were incubated with anti-5-HT<sub>1A</sub> receptor primary antibodies and AlexaFluor® 546-labeled secondary antibodies. Fluorescent patterns were not detectable (Figure SA.4) indicating negligible nonspecific binding of cell-membranes to patterned *L*-5-HTP.

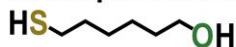
To expand CLL to additional alkanethiols that self-assemble on Au substrates, we investigated lift-off chemistries at stamp/SAM interfaces by varying the terminal functional groups of SAM molecules (Chart II.1). X-ray photoelectron spectroscopy characterization of post-lift-off PDMS stamps (Figure SA.5) and wet chemical etching (Supplemental Information; Appendix A) indicated that generally, hydrophilic terminal groups,

*i.e.*, -OH, -COOH, -NH<sub>2</sub>, and -PO(OH)<sub>2</sub>, are amenable to chemical lift-off, presumably because of their abilities to undergo condensation reactions with activated stamp surfaces. By contrast, hydrophobic moieties, *i.e.*, -CH<sub>3</sub>, -OCH<sub>3</sub>, and -Br, or the small-molecule probe biotin showed no evidence of lift-off. Chain lengths and SAM ordering may influence stamp-SAM reactions and lift-off efficiencies, however, XPS does not have the sensitivity to detect potentially subtle differences in lift-off efficiencies.<sup>58</sup> In any case, a shortcoming of CLL is that not all terminal moieties are amenable to patterning by this method, limiting, to some extent, the on-substrate reactions that can be utilized.

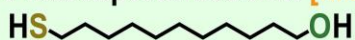


## Lift-Able

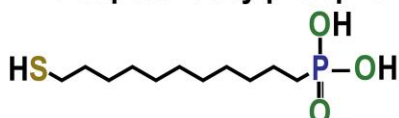
6-Mercaptohexanol [MCH]



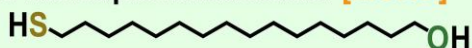
11-Mercaptoundecanol [MCU]<sup>\*,†</sup>



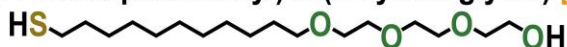
11-Mercaptoundecylphosphonic acid [PO(OH)<sub>2</sub>-C11]



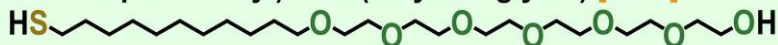
16-Mercaptohexadecanol [MCHD]<sup>†</sup>



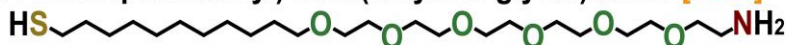
(11-Mercaptoundecyl) tri(ethylene glycol) [TEG]<sup>\*,†</sup>



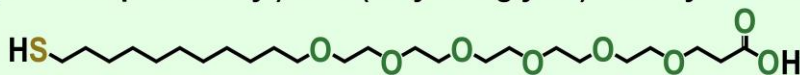
(11-Mercaptoundecyl) hexa(ethylene glycol) [HEG]<sup>†</sup>



(11-Mercaptoundecyl) hexa(ethylene glycol)amine [AEG]



(11-Mercaptoundecyl) hexa(ethylene glycol)carboxylic acid [COOH-HEG]

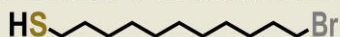


## Non-Lift-Able

1-Dodecanethiol [CH<sub>3</sub>-C11]



11-Bromo-1-undecanethiol [Br-C11]<sup>+</sup>



(11-Mercaptoundecyl) tri(ethylene glycol)methyl ether [CH<sub>3</sub>O-TEG]<sup>\*</sup>



(11-Mercaptoundecyl) hexa(ethylene glycol)biotin [BEG]

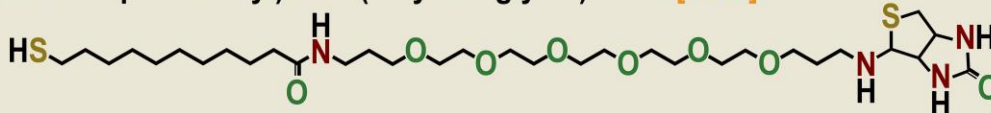


**Chart II.1.** Lift-able and non-lift-able alkanethiols investigated via X-ray photoelectron spectroscopy to detect the presence/absence of Au 4f peaks on post-lift-off polydimethylsiloxane stamps. \*Ref. 47; †Ref. 56; †investigated by wet chemical etching only.

## II.D. Conclusions and Prospects

In summary, we broadened the scope of subtractive patterning *via* CLL by demonstrating a wide variety of feature shapes and sizes, bifunctional substrates, native protein capture, and a large library of lift-able molecules. Sub-30-nm biopatterning *via* a single lift-off step was possible using the noncontact areas to advantage. Small-molecule probes were spatially encoded side-by-side on the same substrates to create multiplexed platforms such that targets were directed to the correct probe locations from solution. Small molecules mimicking endogenous neurotransmitters were patterned by lift-off lithography and captured native receptor targets.

One drawback of using CLL or other stamp-based patterning methods to produce multiplexed substrates involves successive on-substrate probe functionalization steps. Here, we used biotin pre-functionalized molecules, *i.e.*, BEG, to circumvent serial functionalization, which can result in unintended reactions and leaves unreacted surface tethers to contribute to nonspecific target recognition.<sup>83,84</sup> We are investigating the synthesis of a variety of small-molecule pre-functionalized alkanethiols (Chapter IV). Preformed 100% TEG SAMs could then be used for lift-off, in place of mixed SAMs, which would obviate tether molecules remaining in the lift-off regions. Post-lift-off substrates could be functionalized *via* microfluidics to address pre-functionalized molecules to different substrate locations.

Alternately, generating defects by exposing SAM-modified substrates to ultraviolet light or electron irradiation followed by solution deposition of ligand-functionalized molecular substituents could be used to control specific binding of proteins and to generate bifunctional substrates.<sup>85,86</sup> These strategies have been combined with electron-beam

lithography to pattern DNA probes on biorepulsive SAMs.<sup>87,88</sup> Although these approaches can be used to create user-defined features, they are limited in terms of sequential processing and time-consuming tuning of ultraviolet wavelength or electron irradiation doses.<sup>85,89,90</sup>

Ongoing efforts to optimize and to understand CLL mechanistically include collaborative work to characterize and to quantify lift-off and insertion yields further *via* sum frequency generation spectroscopy.<sup>91</sup> Time-of-flight secondary-ion mass spectrometry (ToF SIMS) may also be useful in this regard. However, charge exchange with neighboring molecules is complicated and without detailed information on the ionization efficiencies of each species, quantification, particularly for low abundance species remaining after lift-off or insertion, is not possible by ToF SIMS.<sup>92</sup> Others and we are investigating the basis of variable reactivities of head groups on different substrates (*e.g.*, -SH on Au vs. Ge, or -PO(OH)<sub>2</sub> on In<sub>2</sub>O<sub>3</sub>/SnO<sub>2</sub><sup>93</sup>). We are also determining the unique characteristics of PDMS-supported Au monolayers.<sup>48,57</sup> In general, multiplexed patterning capabilities, nanoscale biopatterns, as well as the fabrication of thin-film field-effect transistor-based biosensors *via* CLL point to the broad applicability of this patterning method.<sup>1,94-96</sup>

## **APPENDIX A**

### **Advancing Biocapture Substrates *via* Chemical Lift-Off Lithography**

#### **Supporting Information**

Experiments were carried out to investigate nonspecific binding associated with fluorescently tagged antibodies, which may contribute to the total fluorescence signals associated with the binding of streptavidin or primary antibodies to biotin-, or 3,4-dihydroxy-*L*-phenylalanine- (*L*-DOPA) or 5-hydroxy-*L*-tryptophan- (*L*-5-HTP) functionalized substrates, respectively. These experiments were performed using the same procedures described in the methods sections in Chapter II with the exception that streptavidin or anti-*L*-DOPA/*L*-5-HTP antibodies were omitted. The results are shown in Figures SA.1 and SA.3. Additionally, control experiments were carried out to investigate nonspecific binding of human embryonic kidney 293 (HEK293)-cell membranes to *L*-5-HTP functionalized substrates. These experiments were performed using the same procedures described in the methods sections in Chapter II with the exception that HEK293 cell membranes from untransfected cells not expressing 5-HT<sub>1A</sub> receptors were used. The results are shown in Figure SA.4.

X-Ray photoelectron spectroscopy (XPS) experiments were performed to investigate removal of (11-mercaptoundecyl) hexa(ethylene glycol)amine (AEG) molecules during CLL. Flat, featureless polydimethylsiloxane (PDMS) stamps were used in place of patterned stamps to maximize the lift-off areas measured with XPS. Previously, the removal of (11-mercaptoundecyl) tri(ethylene glycol) (TEG) SAM molecules *via* CLL was determined from Au 4f XPS signals resulting from Au atoms bound to the lifted-off alkanethiols on flat PDMS stamps. Here, a similar procedure was used to determine whether AEG molecules are removed by CLL (Figure SA.2).

To expand on the types of SAM molecules amenable to CLL, XPS experiments were carried out to investigate alkanethiols terminated with a variety of functional groups. Flat,

featureless, activated PDMS stamps were used to try to remove Au-SAM complexes from Au substrates. Figure SA.5 shows representative XPS spectra of post-lift-off PDMS stamps that were in contact with 6-mercaptohexanol (MCH), 11-mercaptoundecylphosphonic acid ( $\text{PO}(\text{OH})_2\text{-C11}$ ), (11-mercaptoundecyl) hexa(ethylene glycol)carboxylic acid ( $\text{COOH-HEG}$ ), 1-dodecanethiol ( $\text{CH}_3\text{-C11}$ ), (11-mercaptoundecyl) tri(ethylene glycol)methyl ether ( $\text{CH}_3\text{O-TEG}$ ), or (11-mercaptoundecyl) hexa(ethylene glycol)biotin (BEG) SAMs. The presence of Au 4f XPS peaks on MCH,  $\text{PO}(\text{OH})_2\text{-C11}$ , and  $\text{COOH-HEG}$  samples (Fig. SA.5a,b,c) demonstrates that these molecules participate in lift-off chemistries. In contrast, the absence of Au 4f XPS peaks on  $\text{CH}_3\text{-C11}$ ,  $\text{CH}_3\text{O-TEG}$ , or biotinHEG samples (Fig. SA.5d,e,f) shows that these molecules are not amenable to lift-off. The Au 4f XPS peaks associated with MCH are not well resolved compared to the other lift-able alkanethiols. Because MCH molecules have shorter chain lengths compared to the other molecules tested (Chart II.1, Chapter II), intermolecular interactions are weaker leading to more disordered orientations and reduced SAM integrity, which could affect the lift-off chemistry and/or yield.

In most cases, we also used wet chemical etching to characterize lift-off. After contact with PDMS stamps, patterned SAM-modified Au substrates were exposed to aqueous solutions of 20 mM iron nitrate and 30 mM thiourea for 20 min. Post-lift-off exposed Au regions were etched, while the non-lift-off regions were protected by intact SAMs. Etched substrates were rinsed with deionized water and dried with nitrogen gas. If substrates showed clearly visible (by eye) Au patterns, then the SAM molecules were determined to be amenable to lift-off. Otherwise, SAM molecules were deemed not lift-able.

The conclusions reached by wet etching were in agreement with those obtained from XPS experiments.

In one case, *i.e.*, 11-bromo-1-undecanethiol (Br-C11), wet etching was the only method used to test the lift-off chemistry. Since the etched substrates for Br-C11 molecules did not show visible Au patterns, we concluded that this molecule was not lift-able.

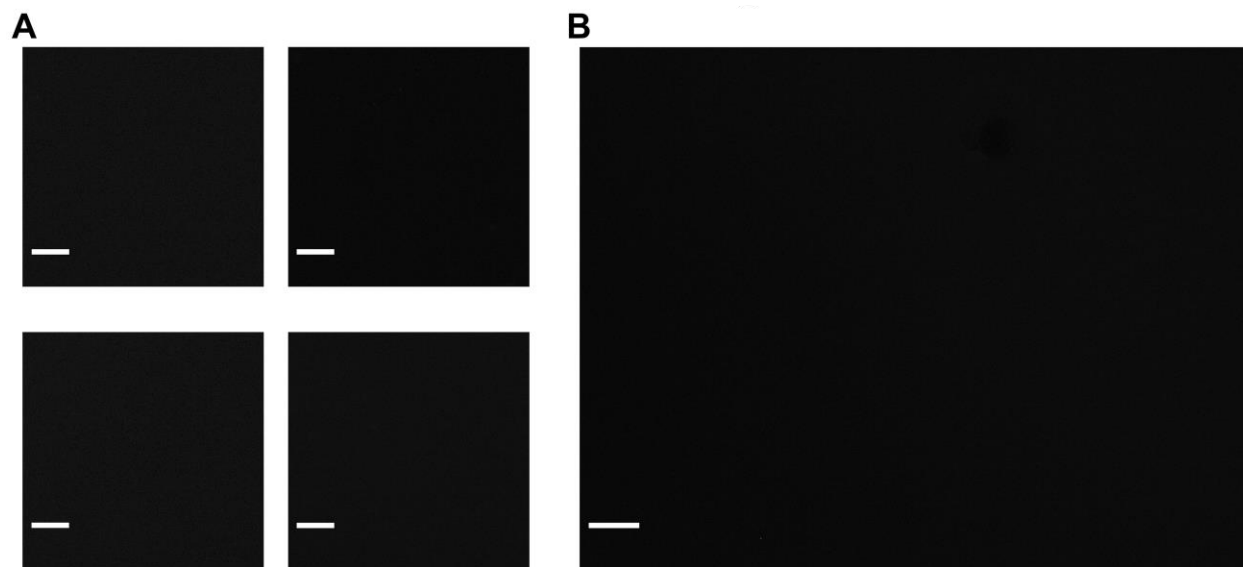
**Table SA.1.** Strategies for visualizing biotin, antibody, and membrane-associated receptor binding to bioselective substrates.

Surface-Tethered Small-Molecule Probe	Protein Targets	Primary Antibodies	Secondary Antibodies
Biotin	Streptavidin	*Rabbit Polyclonal FITC-Conjugated Anti-Streptavidin	N/A
<i>L</i> -5-hydroxytryptophan ( <i>L</i> -5-HTP)	Human 5-HT <sub>1A</sub> Receptors (R) N/A	Mouse Polyclonal Anti-5-HT <sub>1A</sub> -R Mouse Monoclonal Anti- <i>L</i> -5-HTP	<sup>†</sup> AlexaFluor® 546 Goat Anti-Mouse IgG <sup>†</sup> AlexaFluor® 546 Goat Anti-Mouse IgG
<i>L</i> -3,4-dihydroxyphenylalanine ( <i>L</i> -DOPA)	N/A	Mouse Monoclonal Anti- <i>L</i> -DOPA	<sup>†</sup> AlexaFluor® 546 Goat Anti-Mouse IgG

\*Excitation 495 nm; emission 519 nm  
<sup>†</sup>Excitation 556 nm; emission 573 nm



## Same Contrast as Figure II.2



## Auto-Optimized Contrast

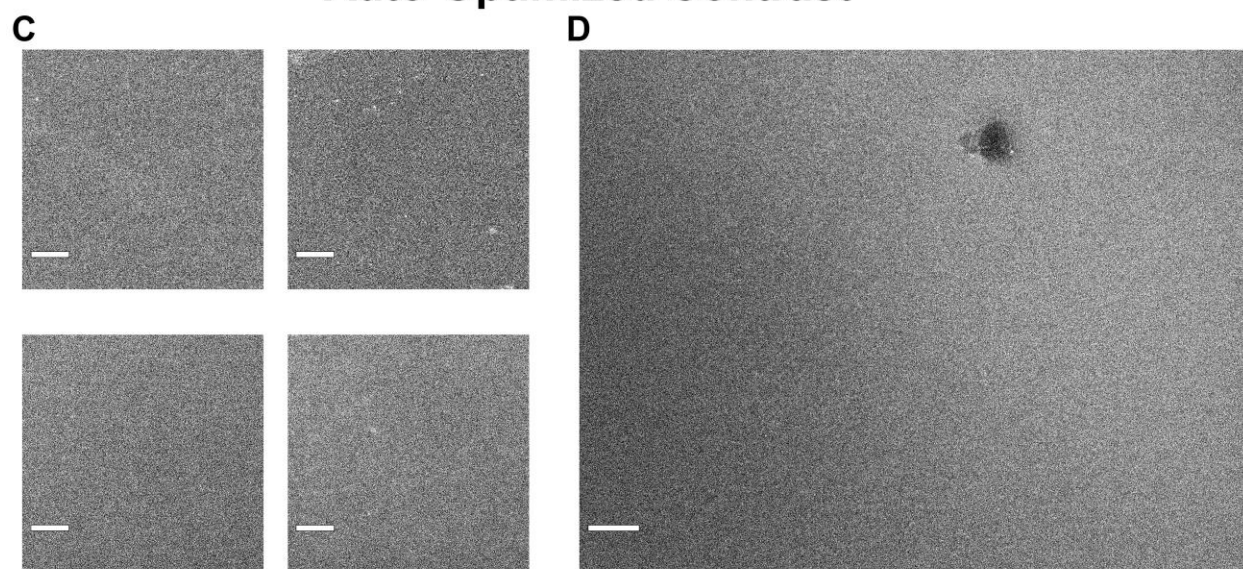


**Figure SA.1.** Control experiments corresponding to Figure II.2 in Chapter II. Representative fluorescence microscopy images showing nonspecific binding of fluorescein isothiocyanate (FITC)-conjugated anti-streptavidin antibodies (excitation at 495 nm) in the absence of streptavidin on **(a)** microscale and **(b)** nanoscale patterns of biotinylated hexa(ethylene glycol)undecanethiol-modified Au substrates. Images were acquired at an emission wavelength of 519 nm. Imaging contrast was maximized to try to detect fluorescent **(c)** microscale and **(d)** nanoscale patterns. Patterns were not detectable in all cases suggesting negligible nonspecific binding of FITC-conjugated anti-streptavidin antibodies to the substrate chemistries. Scale bars are 60  $\mu\text{m}$  in **(a,c)** and 40  $\mu\text{m}$  in **(b,d)**.

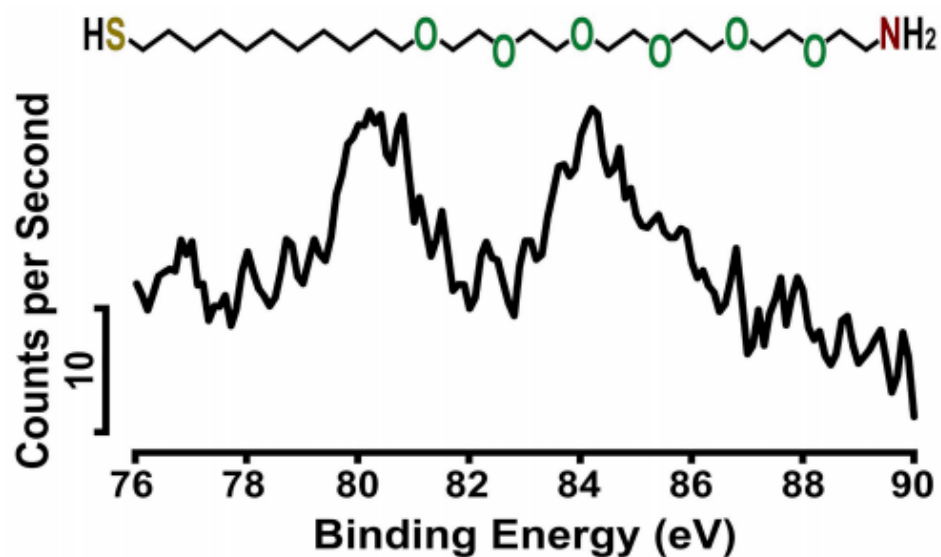
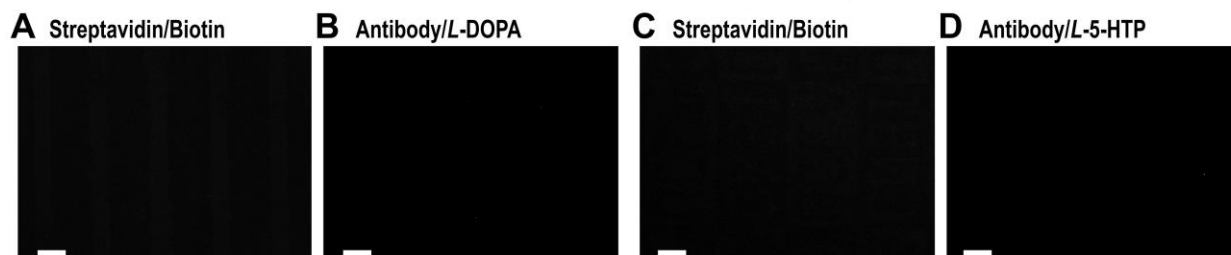


**Figure SA.2.** Representative X-ray photoelectron spectroscopy (XPS) spectra of Au 4f peaks on flat, featureless PDMS stamps used for chemical lift-off on (11-mercaptoundecyl) hexa(ethylene glycol)amine (AEG) self-assembled monolayers (SAMs). The presence of Au 4f XPS peaks at ~80 eV and 84 eV indicates that AEG molecules are amenable to chemical lift-off.

### Same Contrast as Figure II.3



### Auto-Optimized Contrast

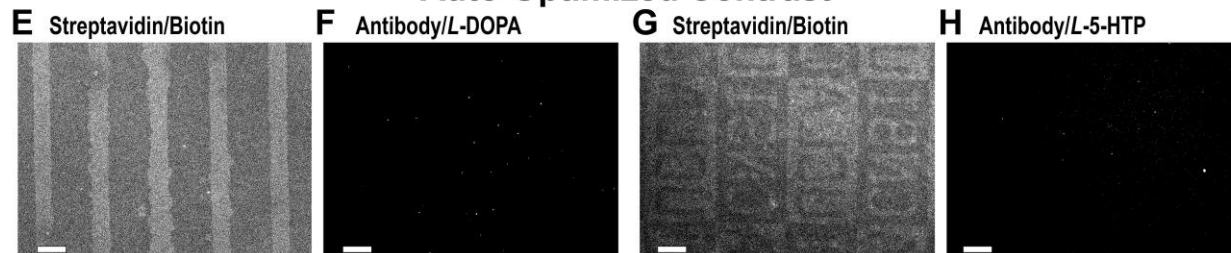


**Figure SA.3.** Control experiments corresponding to Figure II.3 in Chapter II. Fluorescence images of nonspecific binding resulting from substrate exposure to solutions of fluorescein isothiocyanate (FITC)-conjugated anti-streptavidin antibodies (excitation at 495 nm) and AlexaFluor 546<sup>®</sup> secondary antibodies (excitation at 556 nm) in the absence of streptavidin, and anti-L-DOPA or anti-L-5-HTP primary antibodies on **(a,b)** biotin/L-DOPA and **(c,d)** biotin/L-5-HTP patterned surfaces. Substrates were imaged at emission wavelengths of 519 nm **(a,c)** or 573 nm **(b,d)**. Imaging contrast was maximized to try to detect fluorescence patterns in **(e,f)** biotin/L-DOPA and **(g,h)** biotin/L-5-HTP patterned surfaces. Patterns were not observed in **(f,h)** indicating no detectable nonspecific binding of anti-L-DOPA or anti-L-5-HTP primary antibodies. Recognizable patterns were observed in **(e,h)** indicating that at high contrast, a small amount of nonspecific binding of FITC-conjugated anti-streptavidin antibodies to the substrates is observed. Scale bars are 60  $\mu\text{m}$  in **(a,c,e,g)** and 40  $\mu\text{m}$  in **(b,d,f,h)**.

## HEK293/*L*-5-HTP

**A** Same Contrast as Figure II.4



**B** Auto-Optimized Contrast

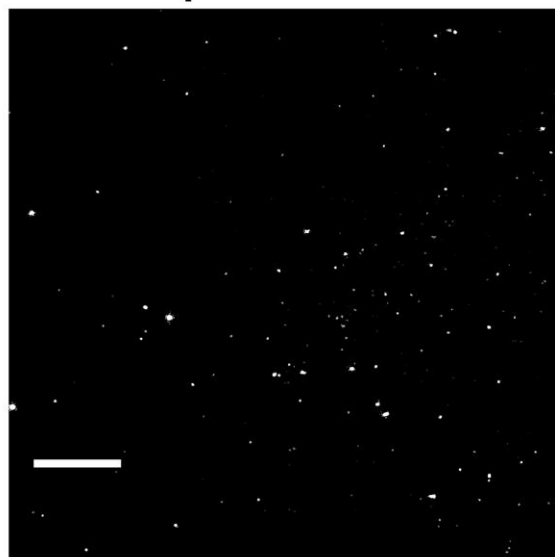


**Figure SA.4.** Control experiments corresponding to Figure II.4 in Chapter II. The lack of observable fluorescence at both levels of contrast suggests negligible nonspecific binding of primary and secondary antibodies to *L*-5-HTP patterned substrates when 5-HT<sub>1A</sub> receptors are not present in HEK293 cell membranes. Fluorescence images were recorded at an emission wavelength of 573 nm. *N*=3 substrates were tested. Scale bars are 50  $\mu$ m.

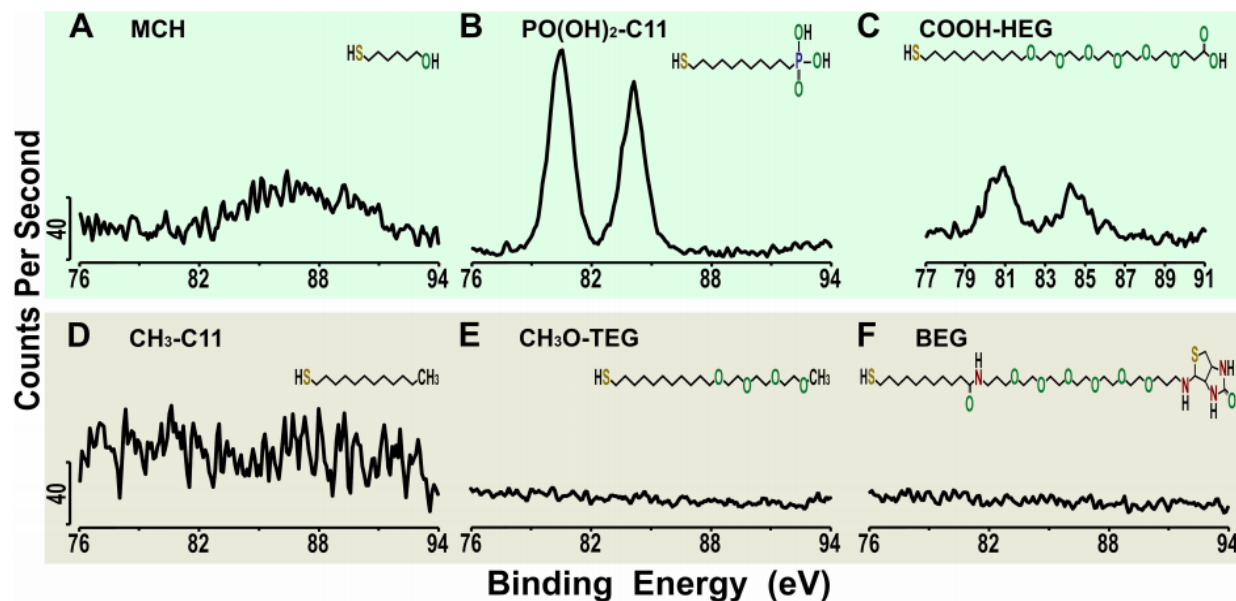


**Figure SA.5.** Representative X-ray photoelectron spectroscopy (XPS) spectra of Au 4f peaks on flat, featureless PDMS stamps subjected to chemical lift-off on (a) 6-mercaptohexanol (MCH), (b) 11-mercaptoundecylphosphonic acid (PO(OH)<sub>2</sub>-C<sub>11</sub>), (c) (11-mercaptoundecyl) hexa(ethylene glycol)carboxylic acid (COOH-HEG), (d) 1-dodecanethiol (CH<sub>3</sub>-C<sub>11</sub>), (e) (11-mercaptoundecyl) tri(ethylene glycol)methyl ether (CH<sub>3</sub>O-TEG), and (f) (11-mercaptoundecyl) hexy(ethylene glycol)biotin (BEG) self-assembled monolayers (SAMs). The presence of a broad Au 4f XPS peak in (a) at ~87 eV and well-resolved Au 4f XPS peaks in (b and c) at ~81 eV and 84 eV indicate that MCH, PO(OH)<sub>2</sub>-C<sub>11</sub>, and COOH-HEG molecules are amenable to chemical lift-off. In contrast, the absence of Au 4f XPS peaks in (d, e, and f) show that lift-off of CH<sub>3</sub>-C<sub>11</sub>, CH<sub>3</sub>O-TEG, and BEG molecules is negligible.

## References

1. MacBeath, G.; Koehler, A. N.; Schreiber, S. L. Printing Small Molecules as Microarrays and Detecting Protein-Ligand Interactions En Masse. *J. Am. Chem. Soc.* **1999**, *121*, 7967-7968.
2. LaFratta, C. N.; Walt, D. R. Very High Density Sensing Arrays. *Chem. Rev.* **2008**, *108*, 614-637.
3. Wittenberg, N. J.; Im, H.; Johnson, T. W.; Xu, X.; Warrington, A. E.; Rodriguez, M.; Oh, S.-H. Facile Assembly of Micro- and Nanoarrays for Sensing with Natural Cell Membranes. *ACS Nano* **2011**, *5*, 7555-7564.
4. Andrews, A. M.; Weiss, P. S. Nano in the Brain: Nano-Neuroscience. *ACS Nano* **2012**, *6*, 8463-8464.
5. Tran, H.; Killops, K. L.; Campos, L. M. Advancements and Challenges of Patterning Biomolecules with Sub-50 nm Features. *Soft Matter* **2013**, *9*, 6578-6586.
6. Alivisatos, A. P.; Andrews, A. M.; Boyden, E. S.; Chun, M.; Church, G. M.; Deisseroth, K.; Donoghue, J. P.; Fraser, S. E.; Lippincott-Schwartz, J.; Looger, L. L.; Masmanidis, S.; McEuen, P. L.; Nurmikko, A. V.; Park, H.; Peterka, D. S.; Reid, C.; Roukes, M. L.; Scherer, A.; Schnitzer, M.; Sejnowski, T. J.; Shepard, K. L.; Tsao, D.; Turrigiano, G.; Weiss, P. S.; Xu, C.; Yuste, R.; Zhuang, X. W. Nanotools for Neuroscience and Brain Activity Mapping. *ACS Nano* **2013**, *7*, 1850-1866.
7. Andrews, A. M. The BRAIN Initiative: Toward a Chemical Connectome. *ACS Chem. Neurosci.* **2013**, *4*, 645-645.
8. Tu, S.; Jiang, H. W.; Liu, C. X.; Zhou, S. M.; Tao, S. C. Protein Microarrays for Studies of Drug Mechanisms and Biomarker Discovery in the Era of Systems Biology. *Curr. Pharm. Des.* **2014**, *20*, 49-55.
9. Andrews, A. M.; Schepartz, A.; Sweedler, J. V.; Weiss, P. S. Chemistry and the BRAIN Initiative. *J. Am. Chem. Soc.* **2014**, *136*, 1-2.
10. Biteen, J. S.; Blainey, P. C.; Cardon, Z. G.; Chun, M.; Church, G. M.; Dorrestein, P. C.; Fraser, S. E.; Gilbert, J. A.; Jansson, J. K.; Knight, R.; Miller, J. F.; Ozcan, A.; Prather, K. A.; Quake, S. R.; Ruby, E. G.; Silver, P. A.; Taha, S.; van den Engh, G.; Weiss, P. S.; Wong, G. C. L.; Wright, A. T.; Young, T. D. Tools for the Microbiome: Nano and Beyond. *ACS Nano* **2016**, *10*, 6-37.
11. Nakatsuka, N.; Andrews, A. M. Neurochips Enable Nanoscale Devices for High-Resolution *in Vivo* Neurotransmitter Sensing. *Neuropsychopharmacology* **2016**, *41*, 378-379.

12. Wassum, K. M.; Ostlund, S. B.; Loewinger, G. C.; Maidment, N. T. Phasic Mesolimbic Dopamine Release Tracks Reward Seeking During Expression of Pavlovian-to-Instrumental Transfer. *Biol. Psychiatry* **2013**, *73*, 747-755.
13. Yang, H. Y.; Sampson, M. M.; Senturk, D.; Andrews, A. M. Sex- and Sert-Mediated Differences in Stimulated Serotonin Revealed by Fast Microdialysis. *ACS Chem. Neurosci.* **2015**, *6*, 1487-1501.
14. Wenzel, J. M.; Rauscher, N. A.; Cheer, J. F.; Oleson, E. B. A Role for Phasic Dopamine Release within the Nucleus Accumbens in Encoding Aversion: A Review of the Neurochemical Literature. *ACS Chem. Neurosci.* **2015**, *6*, 16-26.
15. Wassum, K. M.; Tolosa, V. M.; Tseng, T. C.; Balleine, B. W.; Monbouquette, H. G.; Maidment, N. T. Transient Extracellular Glutamate Events in the Basolateral Amygdala Track Reward-Seeking Actions. *J. Neurosci.* **2012**, *32*, 2734-2746.
16. Sarter, M.; Lustig, C.; Howe, W. M.; Gritton, H.; Berry, A. S. Deterministic Functions of Cortical Acetylcholine. *Eur. J. Neurosci.* **2014**, *39*, 1912-1920.
17. Kiyatkin, E. A.; Wakabayashi, K. T. Parsing Glucose Entry into the Brain: Novel Findings Obtained with Enzyme-Based Glucose Biosensors. *ACS Chem. Neurosci.* **2015**, *6*, 108-116.
18. Andrews, A. M. The Future of Monitoring Molecules. *ACS Chem. Neurosci.* **2015**, *6*, 1-2.
19. Fang, Y.; Frutos, A. G.; Lahiri, J. Membrane Protein Microarrays. *J. Am. Chem. Soc.* **2002**, *124*, 2394-2395.
20. Hodneland, C. D.; Lee, Y. S.; Min, D. H.; Mrksich, M. Selective Immobilization of Proteins to Self-Assembled Monolayers Presenting Active Site-Directed Capture Ligands. *Proc. Natl. Acad. Sci. U. S. A.* **2002**, *99*, 5048-5052.
21. Kwon, Y.; Han, Z.; Karatan, E.; Mrksich, M.; Kay, B. K. Antibody Arrays Prepared by Cutinase-Mediated Immobilization on Self-Assembled Monolayers. *Anal. Chem.* **2004**, *76*, 5713-5720.
22. Christman, K. L.; Enriquez-Rios, V. D.; Maynard, H. D. Nanopatterning Proteins and Peptides. *Soft Matter* **2006**, *2*, 928-939.
23. Wong, L. S.; Khan, F.; Micklefield, J. Selective Covalent Protein Immobilization: Strategies and Applications. *Chem. Rev.* **2009**, *109*, 4025-4053.
24. Fruh, V.; Ijzerman, A. P.; Siegal, G. How to Catch a Membrane Protein in Action: A Review of Functional Membrane Protein Immobilization Strategies and Their Applications. *Chem. Rev.* **2011**, *111*, 640-656.

25. Nehilla, B. J.; Popat, K. C.; Vu, T. Q.; Chowdhury, S.; Standaert, R. F.; Pepperberg, D. R.; Desai, T. A. Neurotransmitter Analog Tethered to a Silicon Platform for Neuro-BioMEMS Applications. *Biotechnol. Bioeng.* **2004**, *87*, 669-674.
26. Smith, R. K.; Lewis, P. A.; Weiss, P. S. Patterning Self-Assembled Monolayers. *Prog. Surf. Sci.* **2004**, *75*, 1-68.
27. Love, J. C.; Estroff, L. A.; Kriebel, J. K.; Nuzzo, R. G.; Whitesides, G. M. Self-Assembled Monolayers of Thiolates on Metals as a Form of Nanotechnology. *Chem. Rev.* **2005**, *105*, 1103-1169.
28. Vu, T. Q.; Chowdhury, S.; Muni, N. J.; Qian, H. H.; Standaert, R. F.; Pepperberg, D. R. Activation of Membrane Receptors by a Neurotransmitter Conjugate Designed for Surface Attachment. *Biomaterials* **2005**, *26*, 1895-1903.
29. Gussin, H. A.; Tomlinson, I. D.; Little, D. M.; Warnement, M. R.; Qian, H. H.; Rosenthal, S. J.; Pepperberg, D. R. Binding of Muscimol-Conjugated Quantum Dots to GABA<sub>A</sub> Receptors. *J. Am. Chem. Soc.* **2006**, *128*, 15701-15713.
30. Shuster, M. J.; Vaish, A.; Szapacs, M. E.; Anderson, M. E.; Weiss, P. S.; Andrews, A. M. Biospecific Recognition of Tethered Small Molecules Diluted in Self-Assembled Monolayers. *Adv. Mater.* **2008**, *20*, 164-167.
31. Wendeln, C.; Singh, I.; Rinnen, S.; Schulz, C.; Arlinghaus, H. F.; Burley, G. A.; Ravoo, B. J. Orthogonal, Metal-Free Surface Modification by Strain-Promoted Azide-Alkyne and Nitrile Oxide-Alkene/Alkyne Cycloadditions. *Chem. Sci.* **2012**, *3*, 2479-2484.
32. Claridge, S. A.; Liao, W.-S.; Thomas, J. C.; Zhao, Y.; Cao, H. H.; Cheunkar, S.; Serino, A. C.; Andrews, A. M.; Weiss, P. S. From the Bottom Up: Dimensional Control and Characterization in Molecular Monolayers. *Chem. Soc. Rev.* **2013**, *42*, 2725-2745.
33. Vaish, A.; Shuster, M. J.; Cheunkar, S.; Singh, Y. S.; Weiss, P. S.; Andrews, A. M. Native Serotonin Membrane Receptors Recognize 5-Hydroxytryptophan-Functionalized Substrates: Enabling Small-Molecule Recognition. *ACS Chem. Neurosci.* **2010**, *1*, 495-504.
34. Claridge, S. A.; Schwartz, J. J.; Weiss, P. S. Electrons, Photons, and Force: Quantitative Single-Molecule Measurements from Physics to Biology. *ACS Nano* **2011**, *5*, 693-729.
35. Ganesan, R.; Kratz, K.; Lendlein, A. Multicomponent Protein Patterning of Material Surfaces. *J. Mater. Chem.* **2010**, *20*, 7322-7331.
36. Wendeln, C.; Rinnen, S.; Schulz, C.; Kaufmann, T.; Arlinghaus, H. F.; Ravoo, B. J. Rapid Preparation of Multifunctional Surfaces for Orthogonal Ligation by Microcontact Chemistry. *Chem. Eur. J.* **2012**, *18*, 5880-5888.



37. Wendeln, C.; Ravoo, B. J. Surface Patterning by Microcontact Chemistry. *Langmuir* **2012**, *28*, 5527-5538.
38. Liao, W. S.; Cao, H. H.; Cheunkar, S.; Shuster, M. J.; Altieri, S. C.; Weiss, P. S.; Andrews, A. M. Small-Molecule Arrays for Sorting G-Protein-Coupled Receptors. *J. Phys. Chem. C* **2013**, *117*, 22362-22368.
39. Bachas, L. G.; Meyerhoff, M. E. Theoretical-Models for Predicting the Effect of Bridging Group Recognition and Conjugate Substitution on Hapten Enzyme-Immunoassay Dose-Response Curves. *Anal. Biochem.* **1986**, *156*, 223-238.
40. Ishikawa, E.; Hashida, S.; Kohno, T. Development of Ultrasensitive Enzyme-Immunoassay Reviewed with Emphasis on Factors Which Limit the Sensitivity. *Mol. Cell. Probes* **1991**, *5*, 81-95.
41. Mrksich, M. Mass Spectrometry of Self-Assembled Monolayers: A New Tool for Molecular Surface Science. *ACS Nano* **2008**, *2*, 7-18.
42. Mrksich, M. Using Self-Assembled Monolayers to Model the Extracellular Matrix. *Acta Biomater.* **2009**, *5*, 832-841.
43. Sanchez-Cortes, J.; Bahr, K.; Mrksich, M. Cell Adhesion to Unnatural Ligands Mediated by a Bifunctional Protein. *J. Am. Chem. Soc.* **2010**, *132*, 9733-9737.
44. Mullen, T. J.; Srinivasan, C.; Hohman, J. N.; Gillmor, S. D.; Shuster, M. J.; Horn, M. W.; Andrews, A. M.; Weiss, P. S. Microcontact Insertion Printing. *Appl. Phys. Lett.* **2007**, *90*, 063114.
45. Shuster, M. J.; Vaish, A.; Cao, H. H.; Guttentag, A. I.; McManigle, J. E.; Gibb, A. L.; Martinez, M. M.; Nezarati, R. M.; Hinds, J. M.; Liao, W.-S.; Weiss, P. S.; Andrews, A. M. Patterning Small-Molecule Biocapture Surfaces: Microcontact Insertion Printing vs. Photolithography. *Chem. Commun.* **2011**, *47*, 10641-10643.
46. Vaish, A.; Shuster, M. J.; Cheunkar, S.; Weiss, P. S.; Andrews, A. M. Tuning Stamp Surface Energy for Soft Lithography of Polar Molecules to Fabricate Bioactive Small-Molecule Microarrays. *Small* **2011**, *7*, 1471-1479.
47. Liao, W.-S.; Cheunkar, S.; Cao, H. H.; Bednar, H. R.; Weiss, P. S.; Andrews, A. M. Subtractive Patterning via Chemical Lift-Off Lithography. *Science* **2012**, *337*, 1517-1521.
48. Andrews, A. M.; Liao, W. S.; Weiss, P. S. Double-Sided Opportunities Using Chemical Lift-Off Lithography. *Acc. Chem. Res.* **2016**, *49*, 1449-1457.
49. Stranick, S. J.; Parikh, A. N.; Allara, D. L.; Weiss, P. S. A New Mechanism for Surface-Diffusion - Motion of a Substrate-Adsorbate Complex. *J. Phys. Chem.* **1994**, *98*, 11136-11142.

50. Yu, M.; Bovet, N.; Satterley, C. J.; Bengio, S.; Lovelock, K. R. J.; Milligan, P. K.; Jones, R. G.; Woodruff, D. P.; Dhanak, V. True Nature of an Archetypal Self-Assembly System: Mobile Au-Thiolate Species on Au(111). *Phys. Rev. Lett.* **2006**, *97*, 166102.
51. Moore, A. M.; Mantooh, B. A.; Donhauser, Z. J.; Yao, Y. X.; Tour, J. M.; Weiss, P. S. Real-Time Measurements of Conductance Switching and Motion of Single Oligo(Phenylene Ethynylene) Molecules. *J. Am. Chem. Soc.* **2007**, *129*, 10352-10353.
52. Han, P.; Kurland, A. R.; Giordano, A. N.; Nanayakkara, S. U.; Blake, M. M.; Pochas, C. M.; Weiss, P. S. Heads and Tails: Simultaneous Exposed and Buried Interface Imaging of Monolayers. *ACS Nano* **2009**, *3*, 3115-3121.
53. Woodruff, D. P. The Interface Structure of *n*-Alkylthiolate Self-Assembled Monolayers on Coinage Metal Surfaces. *Phys. Chem. Chem. Phys.* **2008**, *10*, 7211-7221.
54. Maksymovych, P.; Voznyy, O.; Dougherty, D. B.; Sorescu, D. C.; Yates, J. T. Gold Adatom as a Key Structural Component in Self-Assembled Monolayers of Organosulfur Molecules on Au(111). *Prog. Surf. Sci.* **2010**, *85*, 206-240.
55. Hakkinen, H. The Gold-Sulfur Interface at the Nanoscale. *Nat. Chem.* **2012**, *4*, 443-455.
56. Xue, Y. R.; Li, X.; Li, H. B.; Zhang, W. K. Quantifying Thiol-Gold Interactions Towards the Efficient Strength Control. *Nat. Commun.* **2014**, *5*, 1-9.
57. Slaughter, L. S.; Cheung, K. M.; Kaappa, S.; Cao, H. H.; Yang, Q.; Young, T. D.; Serino, A. C.; Malola, S.; Olson, J. M.; Link, S.; Hakkinen, H.; Andrews, A. M.; Weiss, P. S. Patterning Supported Gold Monolayers *via* Chemical Lift-Off Lithography. *Beilstein J. Nanotechnol., in press* **2017**, *8*.
58. Cao, H. H.; Nakatsuka, N.; Serino, A. C.; Liao, W.-S.; Cheunkar, S.; Yang, H.; Weiss, P. S.; Andrews, A. M. Controlled DNA Patterning by Chemical Lift-Off Lithography: Matrix Matters. *ACS Nano* **2015**, *9*, 11439-11454.
59. Kim, J.; Rim, Y. S.; Chen, H. J.; Cao, H. H.; Nakatsuka, N.; Hinton, H. L.; Zhao, C. Z.; Andrews, A. M.; Yang, Y.; Weiss, P. S. Fabrication of High-Performance Ultrathin In<sub>2</sub>O<sub>3</sub> Film Field-Effect Transistors and Biosensors Using Chemical Lift-Off Lithography. *ACS Nano* **2015**, *9*, 4572-4582.
60. Horcas, I.; Fernández, R.; Gómez-Rodríguez, J. M.; Colchero, J.; Gómez-Herrero, J.; Baro, A. M. Wsxn: A Software for Scanning Probe Microscopy and a Tool for Nanotechnology. *Rev. Sci. Instrum.* **2007**, *78*, 013705.

61. Hong, Y. L.; Webb, B. L.; Su, H.; Mozdy, E. J.; Fang, Y.; Wu, Q.; Liu, L.; Beck, J.; Ferrie, A. M.; Raghavan, S.; Mauro, J.; Carre, A.; Mueller, D.; Lai, F.; Rasnow, B.; Johnson, M.; Min, H. S.; Salon, J.; Lahiri, J. Functional GPCR Microarrays. *J. Am. Chem. Soc.* **2005**, *127*, 15350-15351.
62. Xu, X.; Yang, Q.; Cheung, K. M.; Zhao, C.; Wattanatorn, N.; Belling, J. N.; Abendroth, J. M.; Slaughter, L. S.; Mirkin, C. A.; Andrews, A. M.; Weiss, P. S. Polymer-Pen Chemical Lift-Off Lithography. *Nano Lett.* **2017**.
63. Xia, N.; Shumaker-Parry, J. S.; Zareie, M. H.; Campbell, C. T.; Castner, D. G. A Streptavidin Linker Layer That Functions after Drying. *Langmuir* **2004**, *20*, 3710-3716.
64. Wilbur, J. L.; Kumar, A.; Biebuyck, H. A.; Kim, E.; Whitesides, G. M. Microcontact Printing of Self-Assembled Monolayers: Applications in Microfabrication. *Nanotechnology* **1996**, *7*, 452-457.
65. Dameron, A. A.; Hampton, J. R.; Smith, R. K.; Mullen, T. J.; Gillmor, S. D.; Weiss, P. S. Microdisplacement Printing. *Nano Lett.* **2005**, *5*, 1834-1837.
66. Dameron, A. A.; Hampton, J. R.; Gillmor, S. D.; Hohman, J. N.; Weiss, P. S. Enhanced Molecular Patterning via Microdisplacement Printing. *J. Vac. Sci. Technol. B* **2005**, *23*, 2929-2932.
67. Shuster, M. J.; Vaish, A.; Cao, H. H.; Guttentag, A. I.; McManigle, J. E.; Gibb, A. L.; Martinez, M. M.; Nezarati, R. M.; Hinds, J. M.; Liao, W. S.; Weiss, P. S.; Andrews, A. M. Patterning Small-Molecule Biocapture Surfaces: Microcontact Insertion Printing vs. Photolithography. *Chem. Commun.* **2011**, *47*, 10641-10643.
68. Mullen, T. J.; Srinivasan, C.; Hohman, J. N.; Gillmor, S. D.; Shuster, M. J.; Horn, M. W.; Andrews, A. M.; Weiss, P. S. Microcontact Insertion Printing. *Appl. Phys. Lett.* **2007**, *90*.
69. Zhao, C.; Xu, X.; Yang, Q.; Man, T.; Jonas, S. J.; J., S. J.; Andrews, A. M.; Weiss, P. S. Self-Collapse Lithography. *Nano Lett.* **2017**, *17*, 5035-5042.
70. Odom, T. W.; Love, J. C.; Wolfe, D. B.; Paul, K. E.; Whitesides, G. M. Improved Pattern Transfer in Soft Lithography Using Composite Stamps. *Langmuir* **2002**, *18*, 5314-5320.
71. Qin, D.; Xia, Y. N.; Whitesides, G. M. Soft Lithography for Micro- and Nanoscale Patterning. *Nat. Protoc.* **2010**, *5*, 491-502.
72. Melo, L. L.; Vaz, A. R.; Salvadori, M. C.; Cattani, M. Grain Sizes and Surface Roughness in Platinum and Gold Thin Films. *J. Metastable and Nanocrystalline Mater.* **2004**, *20-21*, 623-628.

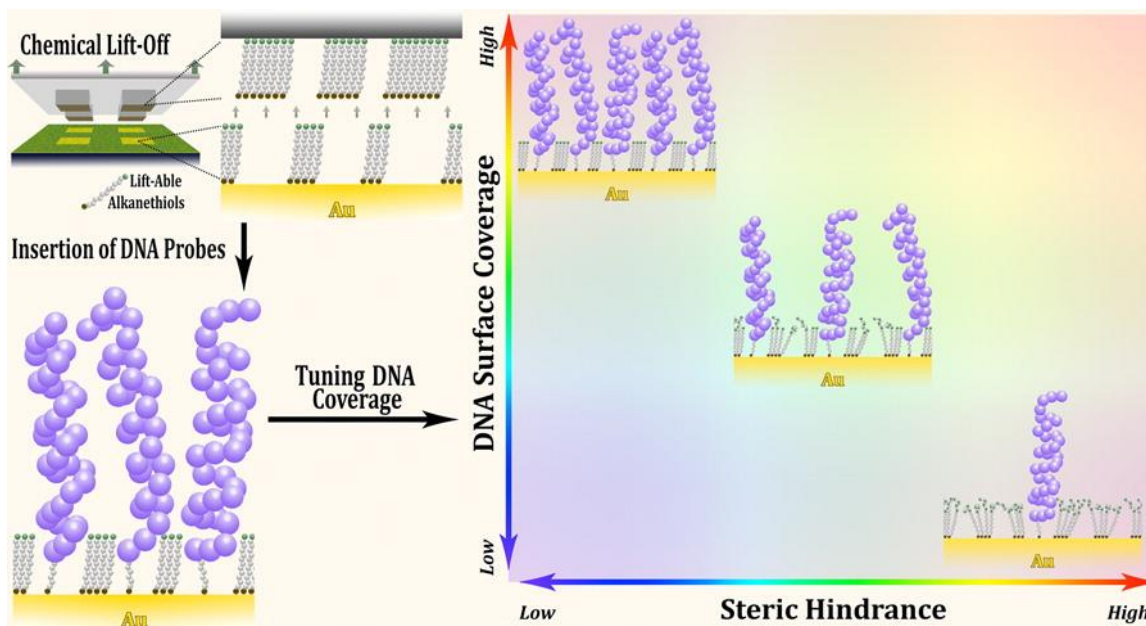
73. Salvadori, M. C.; Melo, L. L.; Vaz, A. R.; Wiederkehr, R. S.; Teixeira, F. S.; Cattani, M. Platinum and Gold Thin Films Deposited by Filtered Vacuum Arc: Morphological and Crystallographic Grain Sizes. *Surf. Coat. Technol.* **2006**, *200*, 2965-2969.
74. Diebel, J.; Lowe, H.; Samori, P.; Rabe, J. P. Fabrication of Large-Scale Ultra-Smooth Metal Surfaces by a Replica Technique. *Appl. Phys. A: Mater. Sci. Process.* **2001**, *73*, 273-279.
75. Ruffino, F.; Torrisi, V.; Marletta, G.; Grimaldi, M. G. Atomic Force Microscopy Investigation of the Kinetic Growth Mechanisms of Sputtered Nanostructured Au Film on Mica: Towards a Nanoscale Morphology Control. *Nanoscale Res. Lett.* **2011**, *6*, 1-13.
76. Tan, C.; Cao, X.; Wu, X. J.; He, Q.; Yang, J.; Zhang, X.; Chen, J.; Zhao, W.; Han, S.; Nam, G. H.; Sindoro, M.; Zhang, H. Recent Advances in Ultrathin Two-Dimensional Nanomaterials. *Chem. Rev.* **2017**, *117*, 6225-6331.
77. Jung, L. S.; Nelson, K. E.; Stayton, P. S.; Campbell, C. T. Binding and Dissociation Kinetics of Wild-Type and Mutant Streptavidins on Mixed Biotin-Containing Alkylthiolate Monolayers. *Langmuir* **2000**, *16*, 9421-9432.
78. Nelson, K. E.; Gamble, L.; Jung, L. S.; Boeckl, M. S.; Naeemi, E.; Golledge, S. L.; Sasaki, T.; Castner, D. G.; Campbell, C. T.; Stayton, P. S. Surface Characterization of Mixed Self-Assembled Monolayers Designed for Streptavidin Immobilization. *Langmuir* **2001**, *17*, 2807-2816.
79. Ballav, N.; Terfort, A.; Zharnikov, M. Fabrication of Mixed Self-Assembled Monolayers Designed for Avidin Immobilization by Irradiation Promoted Exchange Reaction. *Langmuir* **2009**, *25*, 9189-9196.
80. Altieri, S. C.; Garcia-Garcia, A. L.; Leonardo, E. D.; Andrews, A. M. Rethinking 5-HT<sub>1A</sub> Receptors: Emerging Modes of Inhibitory Feedback of Relevance to Emotion-Related Behavior. *ACS Chem. Neurosci.* **2013**, *4*, 72-83.
81. Catapano, L. A.; Manji, H. K. G Protein-Coupled Receptors in Major Psychiatric Disorders. *Biochim. Biophys. Acta, Biomembr.* **2007**, *1768*, 976-993.
82. Richardson-Jones, J. W.; Craige, C. P.; Nguyen, T. H.; Kung, H. F.; Gardier, A. M.; Dranovsky, A.; David, D. J.; Guiard, B. P.; Beck, S. G.; Hen, R.; Leonardo, E. D. Serotonin-1A Autoreceptors Are Necessary and Sufficient for the Normal Formation of Circuits Underlying Innate Anxiety. *J. Neurosci.* **2011**, *31*, 6008-6018.
83. Sigal, G. B.; Bamdad, C.; Barberis, A.; Strominger, J.; Whitesides, G. M. A Self-Assembled Monolayer for the Binding and Study of Histidine Tagged Proteins by Surface Plasmon Resonance. *Anal. Chem.* **1996**, *68*, 490-497.

84. Lahiri, J.; Isaacs, L.; Tien, J.; Whitesides, G. M. A Strategy for the Generation of Surfaces Presenting Ligands for Studies of Binding Based on an Active Ester as a Common Reactive Intermediate: A Surface Plasmon Resonance Study. *Anal. Chem.* **1999**, *71*, 777-790.
85. Jeyachandran, Y. L.; Terfort, A.; Zharnikov, M. Controlled Modification of Protein-Repelling Self-Assembled Monolayers by Ultraviolet Light: The Effect of the Wavelength. *J. Phys. Chem. C* **2012**, *116*, 9019-9028.
86. Jeyachandran, Y. L.; Zharnikov, M. Comprehensive Analysis of the Effect of Electron Irradiation on Oligo(Ethylene Glycol) Terminated Self-Assembled Monolayers Applicable for Specific and Nonspecific Patterning of Proteins. *J. Phys. Chem. C* **2012**, *116*, 14950-14959.
87. Khan, M. N.; Tjong, V.; Chilkoti, A.; Zharnikov, M. Fabrication of ssDNA/Oligo(Ethylene Glycol) Monolayers and Complex Nanostructures by an Irradiation-Promoted Exchange Reaction. *Angew. Chem. Int. Ed.* **2012**, *51*, 10303-10306.
88. Khan, M. N.; Zharnikov, M. Fabrication of ssDNA/Oligo(Ethylene Glycol) Monolayers by Promoted Exchange Reaction with Thiol and Disulfide Substituents. *J. Phys. Chem. C* **2014**, *118*, 3093-3101.
89. Jeyachandran, Y. L.; Weber, T.; Terfort, A.; Zharnikov, M. Application of Long Wavelength Ultraviolet Radiation for Modification and Patterning of Protein-Repelling Monolayers. *J. Phys. Chem. C* **2013**, *117*, 5824-5830.
90. Jeyachandran, Y. L.; Zharnikov, M. Fabrication of Protein Patterns on the Basis of Short-Chain Protein-Repelling Monolayers. *J. Phys. Chem. C* **2013**, *117*, 2920-2925.
91. Cimatu, K.; Baldelli, S. Sum Frequency Generation Microscopy of Microcontact-Printed Mixed Self-Assembled Monolayers. *J. Phys. Chem. B* **2006**, *110*, 1807-1813.
92. Stranick, S. J.; Atre, S. V.; Parikh, A. N.; Wood, M. C.; Allara, D. L.; Winograd, N.; Weiss, P. S. Nanometer-Scale Phase Separation in Mixed Composition Self-Assembled Monolayers. *Nanotechnology* **1996**, *7*, 438-442.
93. Kim, E.; Park, K.; Hwang, S. Electrochemical Investigation of Chemical Lift-Off Lithography on Au and ITO. *Electrochim. Acta* **2017**, *246*, 165-172.
94. Lueking, A.; Horn, M.; Eickhoff, H.; Bussow, K.; Lehrach, H.; Walter, G. Protein Microarrays for Gene Expression and Antibody Screening. *Anal. Biochem.* **1999**, *270*, 103-111.

95. Mishina, Y. M.; Wilson, C. J.; Bruett, L.; Smith, J. J.; Stoop-Myer, C.; Jong, S.; Amaral, L. P.; Pedersen, R.; Lyman, S. K.; Myer, V. E.; Kreider, B. L.; Thompson, C. M. Multiplex GPCR Assay in Reverse Transfection Cell Microarrays. *J. Biomol. Screen.* **2004**, *9*, 196-207.
96. Cao, C.; Zhang, J.; Wen, X.; Dodson, S. L.; Dao, N. T.; Wong, L. M.; Wang, S.; Li, S.; Phan, A. T.; Xiong, Q. Metamaterials-Based Label-Free Nanosensor for Conformation and Affinity Biosensing. *ACS Nano* **2013**, *7*, 7583-7591.

## Chapter III

# Controlled DNA Patterning by Chemical Lift-Off Lithography: Matrix Matters



The information in this chapter was published in  
*ACS Nano* **2015**, 9, 11439-11454  
and has been reproduced here.

Authors: Cao, H. H.; Nakatsuka, N.; Serino, A. C.; Liao, W. -S.; Cheunkar, S.; Yang, H.; Weiss, P. S.; Andrews, A. M.

### III.A. Introduction

Nucleotide microarrays are widely used to identify specific DNA sequences and to investigate large-scale gene expression.<sup>1</sup> To fabricate arrays, probe nucleotides are immobilized on solid substrates for hybridization with complementary targets from solution. Tethering strategies include covalent binding, electrostatic interaction, biotin-streptavidin linkage, and thiolated nucleotide self-assembly.<sup>2,3</sup> Alkanethiol SAMs on Au have been utilized to regulate surface-probe densities and probe-substrate interactions, thereby enhancing specific recognition of tethered DNA targets and minimizing nonspecific binding.<sup>4-8</sup> As such, the use of alkanethiol SAMs modified with DNA probes has advanced understanding of DNA-SAM and DNA-substrate interactions to improve and to optimize the performance of nucleotide-functionalized substrates.<sup>9-15</sup>

Tarlov *et al.* illustrated the importance of alcohol-terminated alkanethiols on Au substrates to facilitate target DNA hybridization.<sup>4,16,17</sup> Here, alkanethiol-DNA was self-assembled and then backfilled with mercaptohexanol (MCH) to dilute the DNA and to prevent direct interactions between DNA probes and substrates.<sup>4,18</sup> Backfilling with alkanethiols also lowers quenching of fluorescently labeled DNA by preventing DNA molecules from lying flat on metal substrates.<sup>12,19</sup> In addition to MCH, mercaptoundecanol (MCU) and oligo(ethylene glycol)-terminated alkanethiols have been used as diluents.<sup>6,7,20-22</sup> The presence of the latter reduces nonspecific interactions with proteins and other biomolecules.<sup>9,23,24</sup> For example, Choi *et al.* demonstrated that DNA substrates created by backfilling with hydroxyl- and carboxyl-terminated oligo(ethylene glycol)-containing alkanethiols and functionalized with cell-adhesion peptides simultaneously promoted peptide-selective cell adhesion and DNA hybridization.<sup>25</sup>

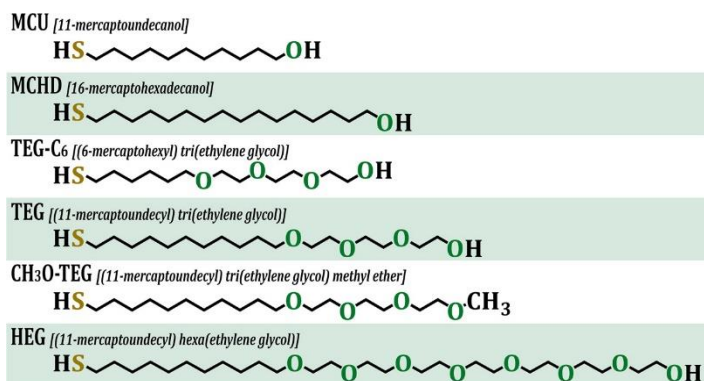


In lieu of backfilling, thiolated DNA can be inserted into preformed alkanethiol SAMs.<sup>6,26,27</sup> Insertion is advantageous for a number of reasons. Instead of exposing surface-bound DNA to ethanolic alkanethiol solutions during backfilling, which causes DNA condensation and precipitation, alkanethiols are assembled first, followed by insertion of DNA dissolved in aqueous buffers.<sup>28,29</sup> Insertion also prevents phase separation.<sup>23,30-33</sup> A recent study of DNA hybridization on Au electrodes demonstrated that surface hybridization was reduced because DNA probes tended to aggregate into domains after backfilling with alcohol-terminated alkanethiols.<sup>34</sup> In contrast, tethered DNA molecules inserted into defect sites in preformed SAMs produced dilute coverage wherein individual probe strands were isolated from each other.<sup>34,35</sup> A low-density environment for surface-bound DNA not only improved hybridization by providing better access for target DNA but it enabled investigation of DNA-substrate interactions at the single-molecule level.<sup>34-37</sup>

Insertion-directed chemistries are also beneficial because they can be combined with surface patterning methods.<sup>38-40</sup> We developed  $\mu$ CIP for substrate patterning<sup>38</sup> and have used this technique to produce dilute coverage of surface-tethered small-molecule ligands on preformed oligo(ethylene glycol)-terminated alkanethiol SAMs.<sup>23</sup> However, using  $\mu$ CIP for DNA patterning will require tuning stamp surface chemistries to facilitate insertion of alkanethiol-functionalized DNA into SAMs.<sup>41</sup> Alternately, we illustrate how patterning characterized by dilute DNA surface coverage and reduced DNA-substrate interactions can be achieved straightforwardly using CLL.<sup>42</sup> Lift-off lithography takes advantage of the strong interactions formed during stamp-substrate contact between the siloxyl groups on oxygen plasma-treated PDMS stamps and hydroxylterminated alkanethiol SAMs. Boxer and co-workers have used similar strategies to remove molecules from lipid

bilayers.<sup>43-45</sup> In lift-off lithography, terminally ( $\omega$ -) functionalized alkanethiol molecules are removed when stamps are lifted from substrates. Here, we investigated how retained alkanethiols in the contacted regions interact with DNA probes to modulate surface properties. A range of alkanethiols terminated with hydroxyl or oligo(ethylene glycol) functional groups were studied (Scheme III.1).

We find that following lift-off lithography, hydroxyl-terminated alkanethiol SAMs enable DNA probes greater access to Au substrates compared to oligo(ethylene glycol)-terminated SAMs. Notably, alkanethiol-



**Scheme III.1.** Abbreviations, names, and molecular structures of the alkanethiols used in these studies.

functionalized DNA inserted into post-lift-off hydroxyl-terminated alkanethiol SAMs showed increased surface hybridization compared to DNA monolayers assembled by backfilling. Moreover, alkanethiol backfilling following patterning *via* lift-off lithography did not improve DNA hybridization efficiency. We discovered that the lift-off process induces conformational changes in oligo(ethylene glycol) moieties resulting in steric effects that limit DNA-probe access to Au surfaces. As such, we varied hydroxyl-/oligo(ethylene glycol)-terminated alkanethiol SAM ratios *via* co-deposition prior to lift-off to tune the amounts of inserted tethered DNA. Ultimately, CLL, in combination with variable matrix compositions, provides a facile means to regulate and to optimize DNA surface coverage, which is essential for controlling hybridization efficiency and the thermodynamic/kinetic behavior of nucleic acids on surfaces.<sup>5,46,47</sup>

### III.B. Experimental Methods

#### III.B.1. Materials

Silicon substrates coated with 100-nm-thick Au films overlaying 10-nm-thick Ti adhesive layers were purchased from Platypus Technologies (Madison, WI, USA). 11-Mercaptoundecyl tri(ethylene glycol) (TEG) was purchased from Toronto Research Chemicals Inc. (Toronto, ON, Canada). 11-Mercaptoundecanol (MCU) and 0.01 M phosphate buffered saline (PBS) ([NaCl] = 138 mM, [KCl] = 2.7 mM, and [MgCl<sub>2</sub>] = 5 mM, pH 7.4) were purchased from Sigma-Aldrich (St. Louis, MO, USA). 16-Mercaptohexadecanol (MCHD) was purchased from Dojindo Molecular Technologies (Rockville, MD, USA). 11-Mercaptoundecyl hexa(ethylene glycol) (HEG), (6-mercaptohexyl) tri(ethylene glycol) (TEG-C<sub>6</sub>), and 11-mercaptoundecyl tri(ethylene glycol) methyl ether (CH<sub>3</sub>O-TEG) were purchased from ProChimia Surfaces (Sopot, Poland). Absolute ethanol was purchased from Decon Laboratories, Inc. (King of Prussia, PA, USA). Deionized water (~18 M $\Omega$ ) was obtained from a Millipore water purifier (Billerica, MA, USA).

Short single-stranded DNA thiolated at the 5' end with a hexyl linker (thioMC6-D) (5'-/5-thioMC6-D/GCA CGA AAC CCA AAC CTG ACC TAA CCA ACG TGC T-3' with molecular weight 10647.2 g/mol and melting temperature 67.2°C), long thiolated single-stranded DNA (5'-/5ThioMC6-D/TTT TTT TTT TTT TTT TTT TTT TTT TTT TTT TTT GCC GGG CGC GGC GCC GGG GCG CCG TTT TTT TTT TTT TTT TTT TTT TTT TGT GGT TTG GTT GTG TGT G-3' with molecular weight 31111.2 g/mol and melting temperature 72.0 °C), Alexa 488 fluorophore-conjugated complementary single-stranded DNA molecules (5'-/5-Alex488N/AGC ACG TTG GTT AGG TCA GGT TTG GGT TTC GTG C-3' with molecular weight 11262.5 g/mol and melting temperature 67.2 °C), and Alexa 488 fluorophore-conjugated

noncomplementary, scrambled, single-stranded DNA sequences (5'-/5-Alex488N/CAT GAA CCA ACC CAA GTC AAC GCA AAC GCA TCA A-3' with molecular weight 11031.4 g/mol and melting temperature 65.3 °C) were purchased from Integrated DNA Technologies (Coralville, IA, USA). All DNA solutions were 100  $\mu$ M as received and were diluted with 0.01 M PBS pH 7.4 to specific concentrations as needed for each experiment.

### III.B.2. Substrate and Stamp Preparation

Silicon substrates with Au films were hydrogen-flame annealed. To prepare SAMs, hydroxyl-terminated alkanethiols (MCU, MCHD), hydroxyl tri(ethylene glycol)-terminated alkanethiols (TEG, TEG-C<sub>6</sub>, HEG), or methoxy tri(ethylene glycol)-terminated alkanethiol (CH<sub>3</sub>O-TEG) in ethanolic solutions (0.5 mM) were self-assembled on Au substrates for 16-18 h. For controlling DNA surface densities, mixed MCU/TEG SAMs were created by varying the ratios of MCU to TEG in solution concentrations as follows (in mM): 1:0, 0.75:0.25, 0.5:0.5, 0.25:0.75, and 0:1. Following self-assembly, substrates were rinsed thoroughly with ethanol and blown dry with nitrogen gas.

Square (25  $\mu$ m  $\times$  25  $\mu$ m or 2  $\mu$ m  $\times$  2  $\mu$ m), protruding features on PDMS stamps were fabricated *via* standard photolithography-processed masters. Details on stamp fabrication and oxygen plasma treatment of PDMS stamps have been published previously. Briefly, 10:1 mass ratios of SYLGARD 184 silicone elastomer base and curing agent (Ellsworth Adhesives, Germantown, WI, USA) were mixed thoroughly in a plastic cup, degassed under a vacuum, cast onto master substrates in a plastic Petri dish, and then cured in an oven at 70 °C overnight. The polymerized stamps were removed from the masters, cut into appropriate sizes, rinsed with ethanol, and blown dry with nitrogen gas. Stamps were then

exposed to oxygen plasma (Harrick Plasma, power 18 W, and oxygen pressure 10 psi) for 30 s, yielding hydrophilic, reactive PDMS surfaces. After lift-off, PDMS stamps were rinsed with ethanol, wiped with Kimberly-Clark tissues soaked in ethanol, and dried with nitrogen gas. Cleaned stamps were sealed to clean glass slides for storage before additional use.

### **III.B.3. Patterning Alkanethiol Self-Assembled Monolayer-Modified Substrates *via* Chemical Lift-Off Lithography**

Oxygen plasma-treated PDMS stamps were brought into conformal contact with SAM-modified substrates for ~6 h for single lift-off. The contact reactions at the stamp-SAM interfaces caused SAM molecules to be removed specifically in the contact regions once the PDMS stamps were released from the substrates. After patterning, substrates were rinsed with ethanol and dried with nitrogen gas.

Double lift-off on TEG SAMs involved a combination of flat (featureless) and patterned PDMS stamps. The first lift-off step was carried out using flat stamps for 3 h to remove molecules from the entire surface. In the second lift-off step, patterned stamps were sealed to the post-lift-off substrates for another 3 h to remove molecules only in the contact regions between the stamp features and the surfaces. The shorter stamp/substrate contact times (3 h vs. 6 h) were selected to expedite DNA pattern generation.

For fluorescence experiments, substrates were incubated in solutions of 1  $\mu$ M DNA probes in 0.01 M PBS pH 7.4 for ~17 h to insert DNA into the post-lift-off exposed Au areas.<sup>8</sup> After incubation, substrates were rinsed thoroughly with deionized water and blown to dryness with nitrogen gas. To visualize DNA hybridization, substrates were exposed to solutions of 1  $\mu$ M target DNA in 0.01 M PBS pH 7.4 for ~1 h. Substrates were

processed in pairs for MCU and TEG SAMs. One substrate was incubated with target DNA and the other with noncomplementary DNA as a control. Each experiment was repeated at least three times over a minimum of three different days. Variations in fluorescence intensities across experiments can arise due to the sensitivity of DNA hybridization to  $\text{Mg}^{2+}$  concentrations in incubation buffers. However, this factor should affect all substrates processed in parallel equally within each experiment. Thus, it is important to process samples in parallel as much as possible and to include appropriate control samples (*e.g.*, hybridization to noncomplementary DNA) in all sample runs.

Deionized water was used to rinse the substrates gently before imaging under an inverted fluorescence microscope (Axio Observer.D1, Carl Zeiss MicroImaging, Inc., Thornwood, NY, USA) using a fluorescence filter set (38 HE/high efficiency) having excitation and emission wavelengths of  $470 \pm 20$  nm and  $525 \pm 25$  nm, respectively. Fluorescence intensity was measured with the line profile function in AxioVs40 version 4.7.1.0 software (Carl Zeiss MicroImaging, Inc., Thornwood, USA). The widths of the fluorescence line scans were made to be approximately the same as that of the square patterned features (*i.e.*, 25  $\mu\text{m}$ ). On average, three to four fluorescence line scans were acquired per image. Fluorescence intensity was averaged for each line scan and then for each image. Alternately, for substrates without patterns, fluorescence intensity was measured using a histogram function and similarly defined areas across all fluorescence images. In all cases, three fluorescence measurements were made per substrate. Specific fluorescence intensities measured on post-lift-off substrates are the differences between the DNA hybridization regions (square features) and the alkanethiol backgrounds (absence of DNA probes).

Backfilling experiments following CLL were performed using the same procedures as those described above with the exception that after DNA probe incubation, substrates were further incubated with 0.5 mM MCU diluted with 0.01 M PBS pH 7.4 to make 10  $\mu$ M MCU solutions for backfilling MCU/DNA SAMs for 30 min. Similarly, solutions of 0.5 mM TEG were diluted with 0.01 M PBS pH 7.4 to make 50  $\mu$ M TEG solutions for backfilling after CLL. The traditional backfilling method was carried out by incubating hydrogen-flame annealed Au substrates with 1  $\mu$ M DNA-probe solutions for  $\sim$ 17 h followed by backfilling with 10  $\mu$ M MCU solution for 30 min. Dilution with PBS was used to minimize the deleterious effect that ethanol can have on DNA probes assembled on surfaces.<sup>28</sup>

For AFM and XPS experiments, post-lift-off substrates were incubated with solutions of 1  $\mu$ M long (100 base) or short (34 base) DNA probes in 0.01 M PBS pH 7.4 for  $\sim$ 17 h, rinsed gently with deionized water and blown dry with nitrogen gas.<sup>8</sup> Tapping mode AFM (Dimension 5000, Bruker AXS, Santa Barbara, CA, USA) was used to characterize height differences on DNA/alkanethiol mixed monolayers on the post-lift-off substrates. Topographic AFM images were collected using Si cantilevers with a spring constant of 48 N/m and a resonant frequency of 190 kHz (Veeco Instruments, Santa Barbara, CA, USA).

For XPS experiments, featureless PDMS stamps were used for the CLL process. All XPS data were collected using an AXIS Ultra DLD instrument (Kratos Analytical Inc., Chestnut Ridge, NY, USA). A monochromatic Al KR X-ray source (10 mA for survey scans and 20 mA for high resolution scans, 15 kV) with a 200  $\mu$ m circular spot size and ultrahigh vacuum ( $10^{-9}$  Torr) were used. Spectra were acquired at a pass energy of 160 eV for survey spectra and 20 eV for high resolution spectra of C 1s, O 1s, N 1s, P 2p, S 2p, and Au 4f regions using a 200 ms dwell time. Different numbers of scans were carried out depending

on the difficulty of identifying each peak vs. background, ranging from 20 scans for C 1s to 100 for Au 4f. All XPS peaks for each element on Au substrates were referenced to the Au 4f signal at 84.0 eV. Atomic percentages were calculated from peak areas.

Because PDMS is an insulator, a charge neutralizer (flood gun) was used to obtain signals from each element on PDMS stamps. As a result, peaks are shifted slightly from their expected regions (for C 1s this is 4-5 eV lower than the reference at 284.0 eV). Because the number of peaks of interest was small (only Au 4f peaks on PDMS samples), and they were well separated ( $\sim 4$  eV), peak shifting did not affect identification. No corrections were carried out during data collection to shift peaks back to particular regions or to scale peaks based on reference locations.

Featureless PDMS stamps were also used for the CLL process for infrared spectroscopy experiments. Polarization modulation infrared reflection-absorption spectroscopy (PMIRRAS) was carried out using a Thermo Nicolet 8700 Fourier transform infrared spectrometer (Thermo Electron Corp., Madison, WI, USA) in reflectance mode using infrared light incident at  $80^\circ$  relative to the surface normal. Spectra with 1024 scans and a resolution of  $4\text{ cm}^{-1}$  were collected in all cases. Each PM-IRRAS experiment was carried out at least four times. Polarization modulation infrared reflection-absorption spectroscopy was used to investigate the removal of molecules due to lift-off by monitoring the peak areas of the O-H stretching band associated with hydroxyl terminal groups. This spectroscopic method was also used to detect the conformational changes of oligo(ethylene glycols) in TEG, TEG-C<sub>6</sub>, HEG, and CH<sub>3</sub>O-TEG alkanethiols.



### III.B.4. Statistical Analyses

Data from fluorescence microscopy, XPS atomic percentage, and AFM topography experiments were initially analyzed by one-way or two-way analysis of variance as appropriate, followed by Tukey's multiple group comparisons. *A priori* individual group comparisons for fluorescence microscopy data were also analyzed by two-tailed unpaired Student's t-tests. All statistics were carried out using GraphPad Prism (GraphPad Software Inc., San Diego, USA). Data are reported as means  $\pm$  standard errors of the means with probabilities of  $P < 0.05$  considered statistically significant.

### III.C. Results and Discussion

#### III.C.1. Chemical Lift-Off Lithography Facilitates Probe DNA Insertion and Target DNA Hybridization

Following self-assembly, oxygen-plasma-treated PDMS stamps were used to remove alkanethiols terminated with hydroxyl moieties from Au substrates within the stamp-substrate contact areas.<sup>42</sup> Previously, we found that ~70% of MCU molecules are removed from the contact regions after lift-off.<sup>42</sup> Further, we showed that inserting biotin hexa(ethylene glycol)-terminated alkanethiols into the contact areas enabled streptavidin recognition in the biotin-patterned regions with features as small as 40 nm for a single lift-off step and 20 nm for two lift-off lithography steps. The precision of these features reached 2 nm and later results showed that we have not yet reached the resolution limits of the method. We reasoned that alkanethiol residues remaining in the contact areas after lift-off would act as diluents when inserting thiolated single-stranded DNA probes.

The CLL process is illustrated in Figure III.1. Negative features in SAMs were generated using PDMS stamps with arrays of protruding square-shaped posts. Patterned SAMs were incubated with alkanethiol-functionalized DNA probe solutions to enable insertion into the post-lift-off areas. Substrates were then exposed to fluorescently labeled target DNA. Experiments were carried out using ~17 h (overnight) insertion times. Short insertion times (*i.e.*, <2 h) were associated with linearly increasing hybridization efficiencies, whereas DNA insertion over longer times resulted in near saturation of hybridization efficiency (Figure SB.1).

A representative fluorescence image of a DNA array formed on a patterned MCU SAM following hybridization with complementary DNA is shown in Figure III.2A. Specificity

of target DNA hybridization is indicated by the lack of a fluorescence pattern when a similar substrate was challenged with noncomplementary target DNA (Figure III.2B). The DNA arrays on post-lift-off TEG- SAMs showed faint yet discernible fluorescent patterns compared to MCU SAMs (Figure III.2C) and similarly lacked detectable fluorescence when hybridized with noncomplementary target DNA (Figure III.2D). These results illustrate that hydroxyl-terminated (MCU) and tri(ethylene glycol)-terminated (TEG) molecules in the lift-off regions act as diluting matrices to enable tethered DNA probe insertion and specific hybridization with target DNA, albeit with different efficiencies.

Prior infrared spectral analysis indicated ~70% liftoff yields for MCU.<sup>42</sup> Here, we compared lift-off efficiencies for

MCU vs. TEG, which were not significantly different (MCU  $64 \pm 7\%$  vs. TEG  $73 \pm 2\%$ ;  $N=3$ ;  $t(4) = 1$ ;  $P>0.05$ ). Thus, DNA insertion into post-lift-off MCU and TEG SAMs was anticipated

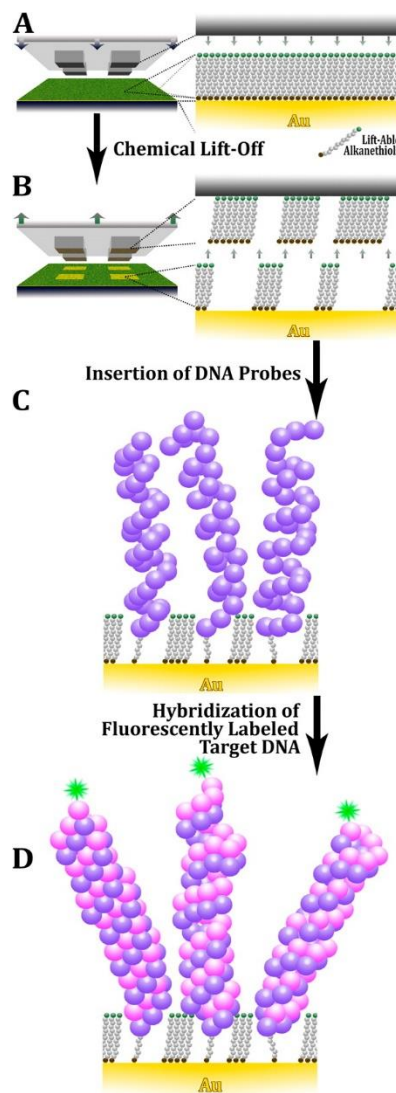


**Figure III.1.** Schematic illustration of CLL/DNA-insertion patterning. (A) Oxygen plasma-treated polydimethylsiloxane stamps are brought into conformal contact with alkanethiol self-assembled monolayers (SAMs) terminated with functional groups that are reactive toward CLL. (B) As a result of the strong interactions at stamp-substrate interfaces, stamp removal causes lift-off of functionalized alkanethiols, albeit incompletely, from Au substrates. (C) The exposed lift-off regions are then insertion-functionalized with alkanethiol-functionalized DNA probes, (D) followed by surface hybridization with fluorescently labeled target DNA.

to occur at similar levels. Nonetheless, fluorescence signals from DNA surface hybridization on TEG SAMs were substantially lower than those detected on MCU SAMs (Figure III.2E).

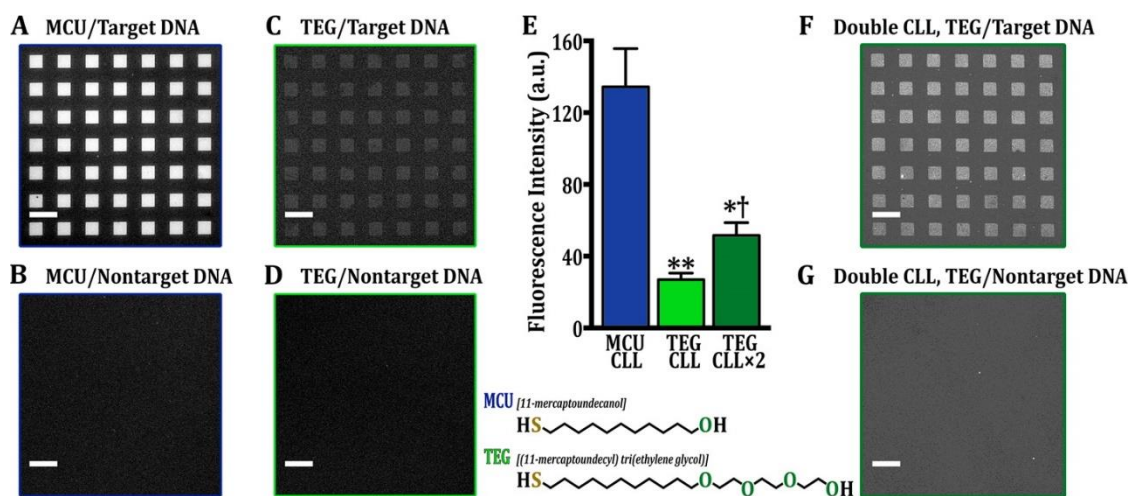


**Figure III.2.** Representative fluorescence images displaying (A,C,F) hybridization of surface-bound DNA probes (34 bases) with fluorescently labeled complementary target DNA or (B,D,G) hybridization with noncomplementary DNA (scrambled 34-base sequences). Post-lift-off self-assembled monolayers (SAMs) are (A,B) hydroxyl-terminated alkanethiols (MCU) or (C,D,F,G) tri(ethylene glycol)-terminated (TEG) alkanethiols. The fluorescence patterns in (F,G) represent double lift-off regions against a post-single-lift-off background. Fluorescence patterns in (A,C,F) compared to their absence in (B,D,G) indicate specific hybridization between Alexa Fluor 488-labeled target DNA (excitation at 495 nm) and tethered probe DNA. (E) Patterned specific fluorescence intensities resulting from DNA hybridization on post-lift-off MCU SAMs were higher than those observed on post-lift-off TEG SAMs. (F) Patterned specific fluorescence intensity was increased on post-double-lift-off TEG SAMs. Fluorescence images were taken with the same exposure times of 5 s at an emission wavelength of 517 nm. Stamp features are (25  $\mu\text{m}$   $\times$  25  $\mu\text{m}$ ). Error bars represent standard errors of the means with  $N=3$  samples per group. Mean intensities were significantly different across groups [ $F(2,6)=18$ ;  $P<0.01$ ]. \* $P<0.05$  and \*\* $P<0.01$  vs. MCU/CLL; † $P<0.05$  vs. TEG/CLL. Scale bars are 50  $\mu\text{m}$ .

We have used sequential lift-off steps to produce substrate features smaller than actual stamp features in doubly contacted regions.<sup>42</sup> Here, we employed double lift-off lithography to investigate whether additional TEG molecules could be removed from SAM substrates to improve DNA insertion and hybridization. First, flat stamps were used to lift-off TEG across entire substrates. Patterned PDMS stamps were next employed to remove additional TEG molecules only in the regions contacted by the stamp features. Alkanethiol probe DNA was then inserted followed by exposure to either fully complementary (Figure III.2F) or noncomplementary (Figure III.2G) fluorescently labeled target DNA.

Hybridization was specific and greater DNA insertion and/or surface hybridization occurred on post-double-lift-off TEG SAMs compared to post-single-lift-off TEG SAMs (Figure III.2E). Patterned fluorescence intensities after double lift-off lithography were twice those following single lift-off (Figure III.2E) and notably, are the differences between DNA hybridization in post-double-lift-off regions vs. the single-lift-off background.

### **III.C.2. Oligo(Ethylene Glycol)-Terminated Alkanethiols Reduce DNA Insertion**

The findings in Figure III.2 suggest that ethylene glycol moieties in TEG hinder the numbers of tethered DNA probes inserted into the lift-off regions of patterned substrates. Alternately, the flexible ethylene glycol segments might interfere with tethered probe DNA surface orientations so as to disfavor hybridization. Both scenarios could lower hybridization efficiency. Several studies have found that although oligo(ethylene glycol)-terminated alkanethiols are longer than comparable hydroxyl-terminated alkanethiols, the ethylene glycol moieties do not interfere with DNA orientations favorable for surface hybridization.<sup>6,21,22,25</sup> In light of this understanding and the double-lift-off findings above, we posited that the ethylene glycol moieties in TEG reduce DNA access to post-lift-off regions during insertion thereby lowering DNA-probe surface densities.

To test this hypothesis, thiolated DNA inserted into post-lift-off MCU vs. TEG SAMs was compared using atomic force microscopy (AFM). After lift-off, MCU and TEG SAMs displayed similar negative-height topographic features where PDMS stamps had contacted SAMs (Figure III.3A,B, respectively). Following incubation with DNA probes, positive-height topographic features protruding beyond SAM backgrounds were observed for MCU SAMs ( $1.5 \pm 0.06$  nm, Figure III.3C), indicating that DNA had been inserted. Significantly smaller

height increases were observed for DNA inserted on TEG SAMs ( $0.34 \pm 0.02$  nm, [ $t(8)=19$ ;  $***P<0.001$ ], Figure III.3D) suggesting that fewer DNA probe molecules had been inserted compared to MCU SAMs.

Although we observed differences in AFM topographic heights between thiolated DNA inserted into post-lift-off MCU vs. TEG SAMs, height differences alone do not conclusively indicate that fewer DNA probes were present on post-lift-off TEG SAMs. Because TEG molecules are longer than MCU molecules, upon insertion, the observed height difference between DNA molecules and the TEG SAM background is expected to be smaller than that observed with the MCU SAM background. Additional AFM experiments were carried out using longer thiolated single-stranded DNA probes (100 bases) to increase AFM topographic contrast over insertion of the 34-base DNA probes. An increase in height was observed on post-lift-off MCU SAMs indicating insertion of long DNA probes ( $2.1 \pm 0.07$  nm, Figure III.3E). Observable, yet smaller height increases were found for post-lift-off TEG SAMs ( $0.78 \pm 0.05$  nm, Figure III.3F). Mean topographic heights of MCU/DNA SAMs were significantly different from TEG/DNA SAMs [ $t(6) = 16$ ;  $P<0.001$ ].

The apparent height differences between the patterned and unpatterned regions in Figure III.3F substantiate DNA-probe insertion on TEG SAMs. However, similar to short DNA, differences in AFM topographic heights where long DNA was inserted into post-lift-off MCU (Figure III.3E) vs. TEG SAMs (Figure III.3F) might still be due to the smaller height differences between DNA molecules and TEG vs. MCU molecules. Assuming a 0.34 nm distance between DNA bases,<sup>48</sup> fully extended 34- and 100-base single-stranded DNA molecules would be ~12 and 34 nm long, respectively. The protruding features on post-lift-off MCU and TEG SAMs (Figure III.3C-F) are substantially smaller than the extended DNA

lengths. Since AFM images were collected under dry conditions and the DNA molecules constitute only a fraction of each monolayer, the segments of the inserted DNA that protrude beyond the matrices were unlikely to be fully extended. Thus, the relative height differences observed on post-lift-off MCU vs. TEG SAMs do not reflect absolute DNA heights relative to SAMs, but instead indicate relative differences in the numbers of inserted molecules. Below, we use these results to estimate the fractions of monolayers associated with inserted DNA. Beyond these estimates, any potential effects of DNA probe lengths on insertion efficiency into SAMs<sup>49</sup> cannot be straightforwardly differentiated by AFM.

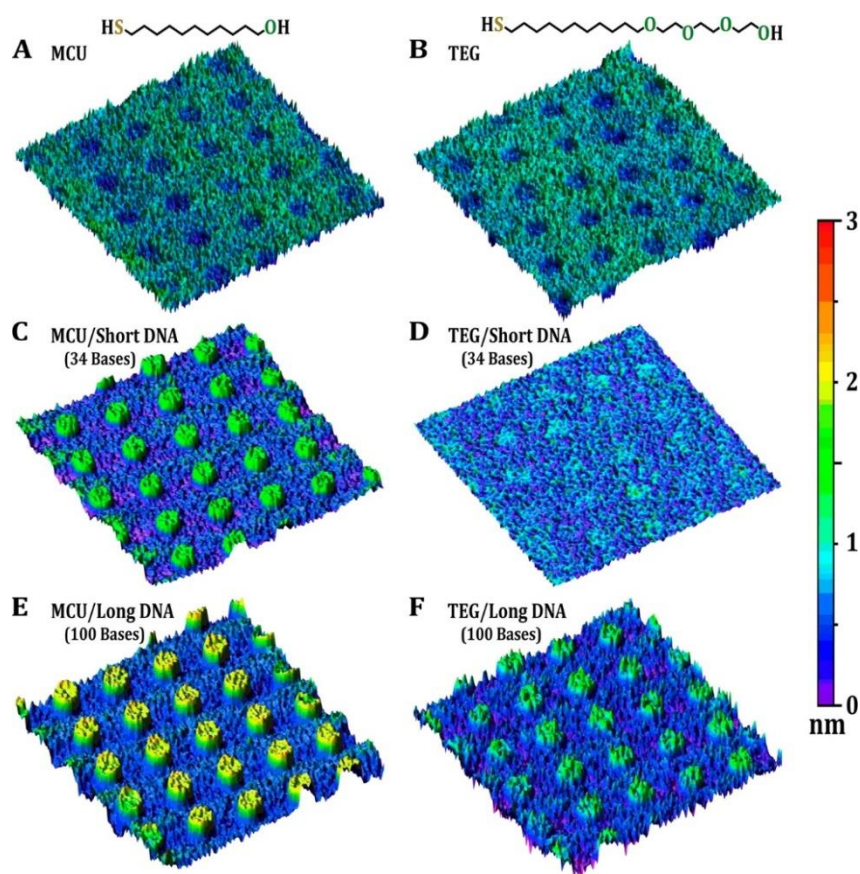


**Figure III.3.** Atomic force microscopy images before and after insertion with short or long DNA. Negative SAM features resulting from CLL of (A) hydroxyl-terminated alkanethiol self-assembled monolayers (SAMs) or (B) tri(ethylene glycol)-terminated SAMs indicate similar degrees of lift-off. After short (34-base) or long (100-base) thiolated DNA was inserted into the lift-off areas, protruding features were observed on MCU SAMs (C,E), while lower-contrast DNA features appeared on TEG SAMs (D,F). Differences in topographic heights between (C) vs. (D) and (E) vs. (F) suggest that fewer DNA probe molecules were inserted into the post-lift-off areas of TEG SAMs, regardless of DNA length. Images are representative of  $N=4-5$  samples per condition. Dimensions are  $20\ \mu\text{m} \times 20\ \mu\text{m}$ .



### III.C.3. Chemical Lift-Off Reduces DNA-Substrate Interactions and Improves DNA Hybridization

We used XPS to quantify DNA-associated nitrogen and phosphorus signals on MCU vs. TEG patterned surfaces. Since we were interested in probe DNA inserted into post-lift-off regions,

featureless PDMS stamps were used with CLL for these experiments to maximize lift-off areas. In addition, because we focused on investigating the XPS fingerprints of DNA, only the N 1s and P 2p XPS data are discussed here. The complete

elements	atomic percentage	
	N 1s	P 2p
DNA (predicted)	18.1	4.7
DNA (experimental)	15.6 ± 0.4	3.6 ± 0.1
DNA/MCU Backfill	13.2 ± 0.3 <sup>*</sup>	3.1 ± 0.2
MCU/DNA Insertion	6.9 ± 0.4 <sup>*,†</sup>	2.0 ± 0.1 <sup>*,†</sup>
TEG/DNA Insertion	N/D (1.0) <sup>*,†</sup>	N/D (0.3) <sup>*,†</sup>
MCU	N/D	N/D
TEG	N/D	N/D

**Table III.1.** X-ray Photoelectron Spectroscopy Atomic Percentages. Predicted XPS atomic percentages for undiluted DNA were calculated using the numbers of nitrogen and phosphorus atoms in DNA probe molecules. Atomic percentages for undiluted thiolated DNA monolayers (experimental) and mixed monolayers of hydroxyl- (MCU) and tri(ethylene glycol) (TEG)-terminated alkanethiol/DNA on Au substrates were calculated from XPS peak areas ( $N=3-6/\text{group}$ ). Not detectable XPS signals are indicated by “N/D”. Atomic percentages in parentheses are hypothetical lower limits are based on XPS detection limits of 1% and a P/N ratio of 0.3 and are used for statistical purposes. Entries are means (standard errors of the means. Nitrogen and phosphorus atomic percentages were significantly different across groups ( $[F(3,14)=280; P<0.001]$  and  $[F(3,14)=135; P<0.001]$ , respectively). <sup>\*</sup> $P<0.01$  vs. DNA (experimental). <sup>†</sup> $P<0.001$  vs. DNA/MCU Backfill.

XPS data can be found in the Supporting Information, Appendix B (Table SB.1). The bottom curves in Figure III.4 indicate that N 1s and P 2p peaks were not present on post-lift-off MCU and TEG SAMs in the absence of DNA probes (*i.e.*, incubation with 0.01 M PBS), as expected. Both N 1s and P 2p peaks corresponding to 6.9 atomic % and 2.0 atomic %, respectively (Table III.1), were observed for thiolated DNA inserted into post-lift-off MCU SAMs (lower-middle curves, Figure III.4A,C). By contrast, these peaks were not detected for DNA inserted into post-lift-off TEG SAMs (middle curves, Figure III.4B,D).



The absence of nitrogen and phosphorus peaks associated with post-lift-off TEG SAMs suggests that DNA insertion into post-lift-off TEG SAMs was either absent or below the XPS detection limit. We conclude the latter case is correct in light of the detectable fluorescence microscopy patterns (Figure III.2C) and AFM topographies (Figure III.3D,F) on similar substrates. Consequently, XPS may not be sensitive enough to detect small amounts ( $\leq 1\%$  monolayer, *vide infra*) of DNA-associated nitrogen and phosphorus on post-lift-off TEG SAMs.

The broad N 1s peak for DNA on post-lift-off MCU SAMs

(lower-middle curve, Figure III.4A) arises from nitrogen peaks associated with heteroaromatic DNA nitrogen at 399.8 eV, and C(=O)-N, N-C(=O)-N and C(=O)-N-C(=O) moieties at 401.6 eV.<sup>50</sup> These nitrogen peaks were at higher binding energies ( $\sim 1$  eV)

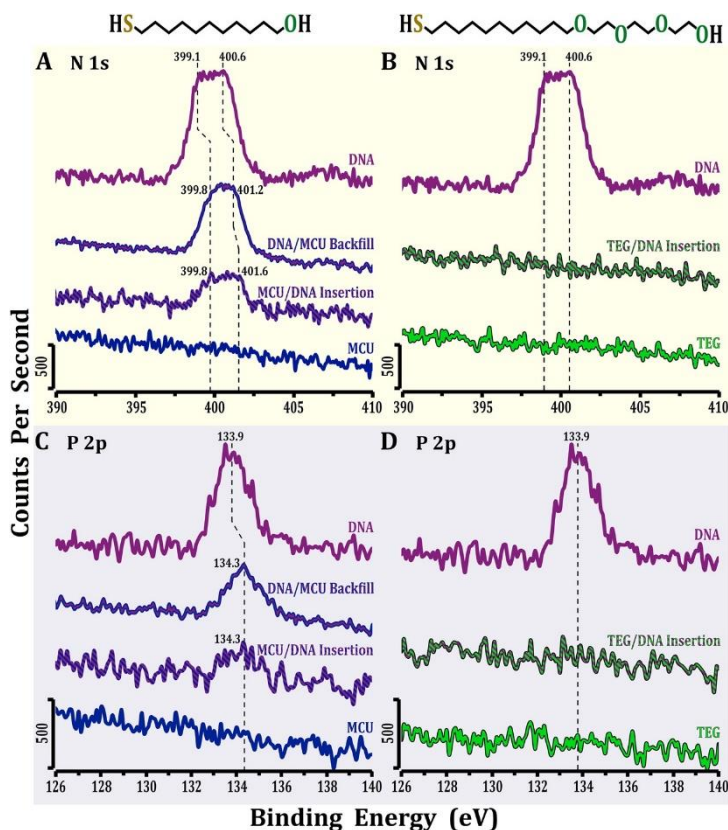


**Figure III.4.** Representative X-ray photoelectron spectra of N 1s and P 2p peaks associated with (A,C) hydroxyl-terminated (MCU) and (B,D) tri(ethylene glycol)-terminated (TEG) alkanethiol self-assembled monolayers (SAMs). All bottom curves represent post-lift-off SAMs incubated with 0.01 M phosphate buffered saline devoid of thiolated DNA probes, hence the absence of nitrogen and phosphorus peaks in these curves. The large N 1s and P 2p peaks from pure DNA monolayers (all top curves) are in contrast to the smaller peaks (all middle curves) from MCU/DNA and TEG/DNA mixed SAMs indicating dilute DNA coverage on MCU-backfilled (upper middle curves A,C) and post-lift-off MCU (lower middle curves A,C) SAMs. The apparent shift to lower energies in N 1s ( $\sim 0.6$ – $1$  eV) and P 2p ( $\sim 0.4$  eV) peaks on pure DNA SAMs compared with alkanethiol/DNA SAMs is attributed to greater DNA–substrate interactions associated with the pure DNA SAMs. Spectra are displaced vertically for ease of visualization.

compared to undiluted tethered DNA monolayers (top vs. lower middle curves in Figure III.4A). Previous studies have shown that heteroaromatic nitrogen in undiluted DNA monolayers interacts with Au substrates, resulting in lower N 1s binding energies compared to the same nitrogen species in DNA bases that are free from substrate interactions.<sup>7,21,51</sup> Additionally, the P 2p peaks from post-lift-off MCU/DNA SAMs were at a higher binding energy ( $\sim 0.4$  eV) than for pure DNA monolayers (top vs. lower middle curves, Figure III.4C). Nitrogen and phosphorus XPS peaks shifted to higher energies indicate that DNA base-substrate interactions are reduced in the presence of post-lift-off MCU molecules suggesting that DNA bases are more available to hybridize with complementary bases in target DNA. In contrast, the thiolated DNA molecules in pure DNA monolayers tend to lie down on metal surfaces such that bases interact with Au substrates disfavoring hybridization with target DNA.

We also prepared substrates using the backfilling method wherein thiolated DNA SAMs were subsequently exposed to MCU solutions (upper-middle curves, Figure III.4A,C). Backfilling was carried out for 30 min because previous studies showed that this incubation time results in DNA-probe orientations that favor hybridization.<sup>7</sup> Similar to DNA inserted in post-lift-off MCU SAMs, nitrogen and phosphorus XPS peaks were at higher binding energies ( $\sim 0.4$  eV for N 1s and  $\sim 0.6$  eV for P 2p) for MCU-backfilled DNA SAMs compared to undiluted DNA monolayers indicating reduced DNA base-substrate interactions.

Prior studies have shown that differences in N 1s and P 2p binding energies between undiluted DNA monolayers and DNA/alkanethiol SAMs not only indicate reduced DNA-substrate interactions in the latter but also upright orientation of DNA probes.<sup>7,15,21</sup>

For example, near-edge X-ray absorption fine-structure spectroscopy has been used to show that shifts to higher binding energies for the N 1s and P 2p XPS signals associated with DNA/alkanethiol monolayers are accompanied by upright probe orientations on Au surfaces.<sup>7,21,52</sup> The N 1s and P 2p peak areas (Table III.1) from post-lift-off MCU/DNA SAMs (6.9 atomic % nitrogen and 2.0 atomic % phosphorus) vs. those of MCU-backfilled DNA SAMs (13.2 atomic % nitrogen and 3.1 atomic % phosphorus) and undiluted DNA monolayers (15.6 atomic % nitrogen and 3.6 atomic % phosphorus; Figure III.4A,C) indicate lower surface coverages of DNA probes on post-lift-off MCU SAMs. Compared with pure DNA monolayers, DNA probes are diluted by ~50% on post-lift-off MCU SAMs, in agreement with previous studies.<sup>6,7,21</sup> These surface coverage estimates, however, are only relative because XPS signals are affected not only by the numbers of molecules on the substrates but also by X-ray attenuation lengths.<sup>51</sup>

Since the XPS data in Figure III.4 show that various methods result in different amounts of surface-assembled DNA, we investigated whether this translated into differential DNA hybridization. Fluorescence resulting from target DNA hybridization on substrates prepared using lift-off lithography followed by probe-DNA insertion was significantly greater than fluorescence intensities from hybridization on undiluted DNA monolayers (Figure III.5A). Moreover, there was greater fluorescence on post-lift-off MCU SAMs compared to MCU-backfilled DNA SAMs. Considering that post-lift-off MCU SAMs had the lowest numbers of DNA probe molecules compared to pure DNA monolayers and MCU-backfilled DNA SAMs (Table III.1 and Figure III.4A,C), these results indicate improved DNA hybridization efficiency associated with the CLL-DNA insertion approach (Figure III.5B), in agreement with studies using other insertion methods.<sup>34,35</sup> Notably, the coefficients of

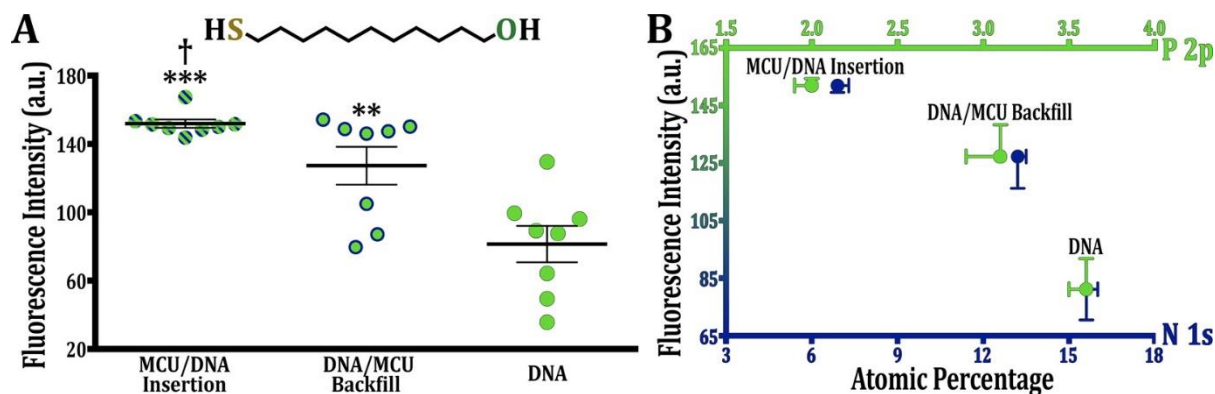


**Figure III.5.** (A) Fluorescence intensities resulting from hybridization of surface-bound DNA probes and fluorescently labeled complementary DNA target strands on post-lift-off hydroxyl-terminated alkanethiol (MCU) self-assembled monolayers (SAMs) (MCU/DNA Insertion), MCU-backfilled DNA SAMs (DNA/MCU Backfill), and pure DNA SAMs (DNA). Mean fluorescence intensities were significantly different across groups [ $F(2,21)=16$ ;  $***P<0.001$ ].  $**P<0.01$  and  $***P<0.001$  vs. DNA;  $†P<0.05$  vs. DNA/MCU Backfill. Error bars represent standard errors of the means with  $N=8$  substrates per group. (B) Correlations are between fluorescence resulting from DNA hybridization vs. X-ray photoelectron spectroscopy atomic percentages [N 1s (bottom/blue x-axis)/P 2p (top/green x-axis)]. Higher fluorescence intensities were correlated with lower DNA probe numbers. Thus, hybridization efficiencies were MCU/DNA Insertion > DNA/MCU Backfill > DNA alone.

variation (%CV) for hybridization were significantly lower for the lift-off-insertion approach signifying improved reproducibility (Figure III.5A; 4.5% MCU/DNA insertion, 25% DNA/MCU backfill, 37% undiluted DNA).

Hybridization efficiencies on Au films and nanoparticles have been determined by various quantification methods including fluorescence-based methods,<sup>7,53,54</sup> electrochemical techniques,<sup>16,49,55,56</sup> “quantitative” XPS,<sup>51</sup> neutron reflectivity measurements,<sup>17</sup> radiometric assays,<sup>57</sup> and surface plasmon resonance spectroscopy.<sup>5,6,21,46</sup> Here, because quantification from fluorescence images and XPS atomic percentages do not provide absolute numbers of DNA probes and targets, we examined relative relationships *via* correlation analysis (Figure III.5B) and determined that improved hybridization efficiency is associated with the lift-off lithography-based DNA insertion approach compared to undiluted DNA monolayers and MCU-backfilled DNA SAMs.

### III.C.4. Backfilling Reduces Inserted DNA on Post-Lift-Off Alkanethiol Self-Assembled Monolayers

Backfilling with MCU or TEG has been shown to increase target DNA hybridization for Au substrates functionalized first with thiolated probe DNA (Figure III.5B).<sup>6,7,21</sup> Here, we investigated the effects of backfilling following lift-off and DNA insertion on MCU and particularly, TEG SAMs. After lift-off and insertion of thiolated DNA probes, we exposed MCU/DNA or TEG/DNA SAMs to additional MCU or TEG molecules, respectively, *via* solution deposition. Backfilling was hypothesized to reduce any remaining DNA-substrate interactions and to increase fluorescence due to greater

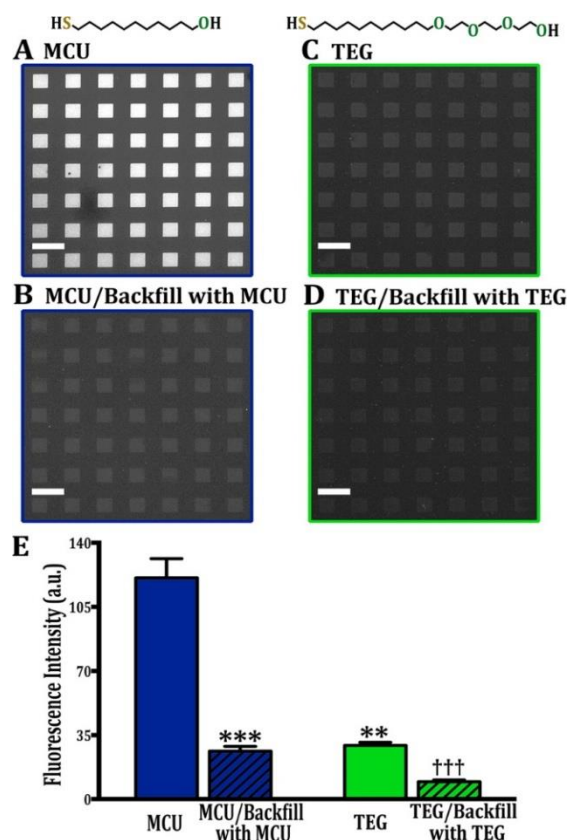


**Figure III.6.** Representative fluorescence images displaying hybridization of thiolated single-stranded DNA probes with Alexa Fluor 488-labeled target DNA (excitation at 495 nm) on (A,B) hydroxyl-terminated alkanethiol (MCU) or (C,D) tri(ethylene glycol)-terminated alkanethiol (TEG) self-assembled monolayers (SAMs) after lift-off lithography and without or with backfilling with additional respective alkanethiol molecules following probe DNA insertion. After exposing post-lift-off MCU/DNA SAMs to additional MCU, fluorescence was decreased in (B) compared to (A) suggesting that thiolated DNA is displaced by subsequent exposure to additional MCU. Similarly, a weaker fluorescent pattern (D) was observed for backfilled post-lift-off TEG/DNA SAMs compared to the pattern after hybridization on a post-lift-off-alone TEG SAM (C). Fluorescence images (shown with the same exposure times of 5 s) were taken at an emission wavelength of 517 nm. (E) Mean intensities were significantly different for post-lift-off MCU vs. TEG surfaces without backfilling (A,C) again indicating significant differences with respect to target hybridization (independent replication vs. Figure III.2, two-way ANOVA interaction term [ $F(1,4)=37$ ,  $P<0.01$ ]). Error bars represent standard errors of the means with  $N=3$  samples per group. \*\* $P<0.01$  and \*\*\* $P<0.001$  vs. MCU; ††† $P<0.001$  vs. TEG. Scale bars are 50  $\mu\text{m}$ .

surface hybridization. On the contrary, we observed decreases in the fluorescence intensities of patterns on both post-lift-off MCU (Figure III.6A,B) and TEG (Figure III.6C,D) SAMs after additional backfilling suggesting that DNA probes were instead removed from substrates.

Removal of DNA probes by backfilling with alkanethiols has been reported.<sup>6,7,21</sup> The purpose of alkanethiol backfilling is to reduce steric interactions between DNA probes and to decrease DNA-substrate interactions. However, when substrates are exposed to alkanethiol backfilling solutions for extended times (>1 h), DNA molecules are displaced and fluorescence decreases due to reduced numbers of surface-bound DNA molecules. Studies by others have shown that DNA probes on MCU-backfilled SAMs diluted by ~50% from pure DNA monolayers required >5 h of backfilling.<sup>7,57</sup> The XPS data above (Table III.1, Figure III.4A vs. III.4C) indicate ~50% dilution of post-lift-off MCU/DNA vs. undiluted DNA monolayers. Thus, DNA surface coverages on post-lift-off substrates might be in the regime where additional alkanethiol backfilling removes inserted DNA probes instead of reducing DNA-substrate interactions, which are already presumably minimized. Decreases in fluorescence after backfilling (Figure III.6E) suggest that additional incorporation of MCU or TEG molecules reduced the numbers of DNA probe molecules. For TEG, the already low numbers of DNA probes on post-lift-off DNA/SAM-modified substrates were further reduced with additional TEG solution exposure. Therefore, we conclude that alkanethiol backfilling is not advantageous when patterning DNA on Au substrates *via* CLL.

### III.C.5. DNA Arrays Patterned *via* Lift-Off Lithography Using Longer Functionalized Alkanethiols

Three terminal ethylene glycol units differentiate TEG from MCU molecules. The additional molecular length of TEG vs. MCU might reduce DNA access to Au surfaces. Alternately, the presence of the ethylene glycol moieties might have a greater influence on alkanethiol-DNA insertion. To differentiate these possibilities, molecules longer than MCU and TEG, namely MCHD and HEG were investigated (Scheme III.1). The alkyl backbone of MCHD is five carbon atoms longer than MCU, whereas HEG has the same alkyl backbone as TEG but contains three additional ethylene glycol units.

Previously, we showed by XPS that oxygen plasma treatment of PDMS stamps is needed to lift-off alkanethiols terminated with hydroxyl or amine tail groups.<sup>42</sup> Because interactions at stamp-SAM and SAM-Au interfaces are stronger than Au-Au substrate bonds, post-lift-off PDMS stamps showed Au 4f XPS signals. In contrast, PDMS stamps following conformal contact with relevant SAMs in the absence of oxygen plasma pretreatment did not show Au 4f XPS signals. Here, the CLL process was carried out on MCHD and HEG SAMs. Post-lift-off PDMS stamps from these SAMs showed Au 4f signals in the XPS spectra (Figure SB.2a,b) indicating that MCHD and HEG are liftable molecules. While intense fluorescent patterns were observed for MCHD/DNA SAMs (Figure SB.3a), such patterns were indiscernible for HEG/DNA SAMs (Figure SB.3b). Thus, although MCHD and HEG molecules are each longer than the corresponding MCU and TEG molecules, respectively, the thicker SAMs formed by MCHD did not hinder DNA probes from accessing Au surfaces. Since the principal differences between MCHD and HEG are the ethylene glycol moieties in the latter, the important finding is that differences in physical lengths between

SAM molecules do not by themselves underlie variations in the numbers of tethered DNA probes inserted into post-lift-off regions and associated target DNA hybridization. Instead, ethylene glycol moieties appear to play key roles in limiting the numbers of DNA molecules on post-lift-off oligo(ethylene glycol)-terminated alkanethiol-modified Au surfaces.

### **III.C.6. Spectroscopic Evidence for Lift-Off-Induced Conformation Changes in Oligo(Ethylene Glycol) Moieties**

Together, information gleaned from investigating the various hypotheses above suggests that steric hindrance originates from the ethylene glycol moieties of TEG (and HEG). To explore the origin of this effect, PM-IRRAS was used to monitor the characteristic vibrational feature of ethylene glycol moieties, namely the C-O-C vibrational stretch, before and after CLL. Similar to the XPS experiments above, featureless PDMS stamps were used to maximize lift-off areas. For alkanethiols with (ethylene glycol)<sub>n</sub> ( $n \leq 4$ ), the C-O-C vibrational band is the dominant IR feature characterizing ethylene glycol moieties.<sup>58</sup> As shown in Figure III.7A, the C-O-C vibrational band displayed a strong, sharp peak at  $\sim 1138 \text{ cm}^{-1}$  for pristine TEG SAMs (top curve), indicating a predominantly all-*trans* conformation for the ethylene glycol moieties.<sup>59</sup> However, after lift-off, the C-O-C peak was shifted to  $\sim 1132 \text{ cm}^{-1}$  and the peak area was decreased (Figure III.7A, bottom curve). Infrared absorption spectra are affected by surface coverage and molecular conformations.<sup>59</sup> While the reduced peak area is likely the result of decreased surface coverage due to the removal of TEG molecules, which is known to occur (*vide supra*), the peak shift is potentially the result of conformational changes in SAM molecules following lift-off. Studies have shown that a C-O-C band at  $\sim 1140 \text{ cm}^{-1}$  is attributable to a predominantly all-*trans* conformation,



whereas red shifts in the C-O-C stretch indicate transitions to disordered helical conformations.<sup>59,60</sup> The spectroscopic shift from 1138 to 1132 cm<sup>-1</sup> suggests that TEG molecules undergo rearrangement from ordered nearly all-*trans* to disordered helical conformations following lift-off (Figure III.8A), which would reduce DNA probe access to Au surfaces. In contrast, such conformational changes do not occur for MCU SAMs post-lift-off due to the absence of oligo(ethylene glycol) moieties (Figure III.8B).

As an additional test that CLL induces

conformational changes in oligo(ethylene glycol) moieties, we investigated TEG-C<sub>6</sub> SAMs using infrared spectroscopy before and after lift-off. The TEG-C<sub>6</sub> molecules are similar to

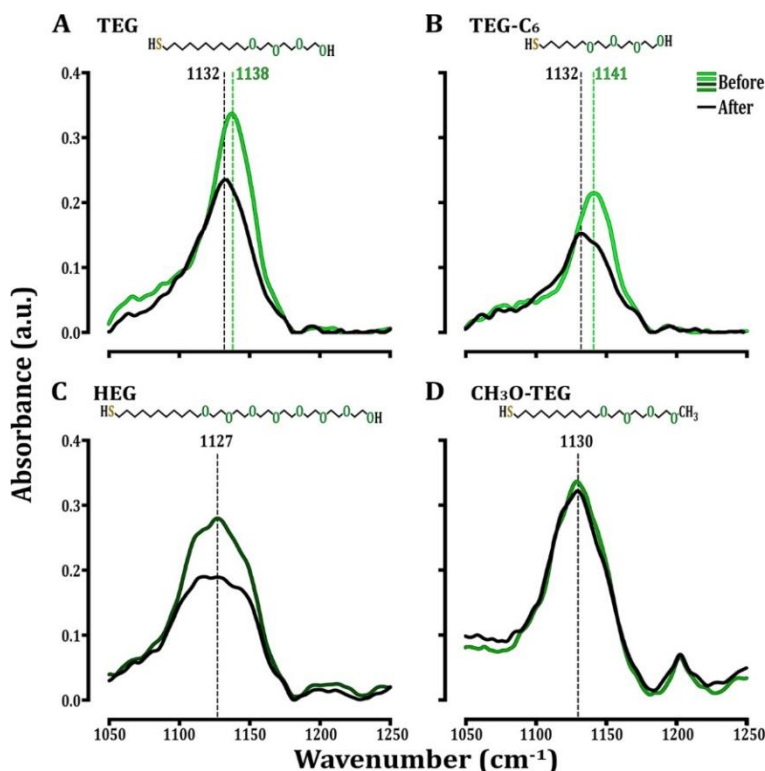


**Figure III.7.** Representative polarization modulation infrared reflection-absorption spectra of (A) tri(ethylene glycol) undecane-thiol (TEG), (B) tri(ethylene glycol) hexanethiol (TEG-C<sub>6</sub>), (C) hexa(ethylene glycol) undecanethiol (HEG), and (D) methoxy tri(ethylene glycol) undecanethiol (CH<sub>3</sub>O-TEG) self-assembled monolayers (SAMs) before (top curves) and after (bottom curves) contact with fully oxidized PDMS stamps. Strong C-O-C vibrational bands at 1138 cm<sup>-1</sup> and 1141 cm<sup>-1</sup> are characteristic of ordered all-*trans* tri(ethylene glycol) conformations in (A) TEG and (B) TEG-C<sub>6</sub> SAMs prior to lift-off, respectively. (C) A broad C-O-C vibrational band at ~1127 cm<sup>-1</sup> is characteristic of disordered helical hexa(ethylene glycol) moieties in HEG SAMs after self-assembly and prior to lift-off. (D) A strong C-O-C vibrational band at 1130 cm<sup>-1</sup> characteristic of amorphous helical tri(ethylene glycol) moieties is also seen with CH<sub>3</sub>O-TEG SAMs. Peak-area decreases in (A, B, and C) indicate the removal of alkanethiol molecules due to lift-off. (D) Because methoxy groups are not lift-able, the peak area of the C-O-C stretch of CH<sub>3</sub>O-TEG SAMs remains the same before and after lift-off. The post-lift-off C-O-C bands in (A) and (B) appear shifted from pre-lift-off positions at 1138 cm<sup>-1</sup> and 1141 cm<sup>-1</sup> for TEG and TEG-C<sub>6</sub>, respectively, to a new position at 1132 cm<sup>-1</sup> indicating conformational changes in tri(ethylene glycol) moieties to disordered helical conformations.

TEG except their aliphatic backbones consist of 6 vs. 11 carbons (Scheme III.1). As shown in Figure III.7B, a C-O-C band was observed at  $\sim 1141\text{ cm}^{-1}$  for pristine TEG-C<sub>6</sub> SAMs (top curve). The peak area was reduced after lift-off and shifted to  $\sim 1132\text{ cm}^{-1}$  (bottom curve). Similar to TEG SAMs, these results show that alkanethiols were removed from Au surfaces (smaller peak area). Moreover, the shifted C-O-C band observed with TEG-C<sub>6</sub> is characteristic of conformational changes in oligo(ethylene glycol) from pre-lift-off ordered *all-trans* to post-lift-off disordered helical conformations.

For HEG molecules, a broad C-O-C stretch for pre-lift-off SAMs (Figure III.7C, top curve) was observed at  $\sim 1127\text{ cm}^{-1}$ , which indicates initial predominantly disordered helical conformations for alkanethiols with six or greater ethylene glycol units, in agreement with previous studies.<sup>60,61</sup> After lift-off, the C-O-C peak area decreased due to removal of SAM molecules (Figure III.7C, bottom curve). Notably, the C-O-C band did not show a redshift similar to TEG and TEG-C<sub>6</sub>. This result suggests that HEG SAMs retain the same relative conformation after lift-off. Although HEG molecules did not show conformational changes associated with lift-off lithography, the disordered helical conformation restricted DNA insertion (Figure SB.3b).

To investigate whether PDMS contact with oligo(ethylene glycol)-terminated SAMs itself produces disordered ethylene glycol conformations, we monitored the C-O-C stretch arising from CH<sub>3</sub>O-TEG SAMs with infrared spectroscopy before and after conformal contact with oxygen plasma-treated PDMS stamps. The CH<sub>3</sub>O-TEG molecules were selected because they are identical to TEG except for the terminal methoxy group (Scheme III.1), which prevents subtractive patterning.<sup>42</sup> A sharp C-O-C band was observed at  $\sim 1130\text{ cm}^{-1}$  for pristine CH<sub>3</sub>O-TEG SAMs, suggestive of initial helical conformations<sup>60</sup> (top curve,

Figure III.7D). Neither the peak position nor the peak area changed post-lift-off (bottom curve, Figure III.7D). The lack of a decrease in peak area indicates that CH<sub>3</sub>O-TEG molecules were not removed from Au surfaces by contact with activated PDMS stamps. The invariant peak position implies that conformal contact with activated PDMS stamps by itself did not change the conformation of the ethylene glycol moieties. However, the peak position at 1130 cm<sup>-1</sup> indicates that the CH<sub>3</sub>O-TEG molecules adopted helical conformations in both pre- and post-lift-off SAMs. Thus, CH<sub>3</sub>O-TEG SAMs are not ideally suited to testing whether stamp contact alone (vs. lift-off) underlies the shift from all-*trans* to helical oligo(ethylene glycol) conformations. We have yet to identify oligo(ethylene glycol) alkanethiols best suited for isolating the effects of stamp contact vs. actual lift-off. These molecules would possess a terminal group not amenable to lift-off yet oligo(ethylene glycol) moieties would adopt an all-*trans* conformation after surface assembly.

The overriding observation from the spectral studies of oligo(ethylene glycol)-terminated alkanethiols is that CLL induces conformational changes in ethylene glycol segments from ordered to disordered states when the former exist following self-assembly. For TEG and TEG-C<sub>6</sub>, ordered all-*trans* conformations were converted to disordered helical conformations after lift-off. For HEG, the helical conformation remained the same before and after liftoff. For CH<sub>3</sub>O-TEG, no conformational or lift-off-related changes occurred. The results of this study as a whole lead to the conclusion that disordered states of oligo(ethylene glycol) existing either prior to lift-off (HEG) or as a result of lift-off (TEG, TEG-C<sub>6</sub>) are associated with steric hindrance so as to reduce (TEG, TEG-C<sub>6</sub>) or to prevent (HEG) thiolated DNA insertion into post-lift-off SAMs. Furthermore, greater numbers of ethylene glycol units appear to interfere to a greater extent with DNA insertion following

patterning by lift-off lithography. Conversely, increased DNA insertion and/or hybridization can be achieved on TEG SAMs *via* double-lift-off lithography (Figure III.2F).

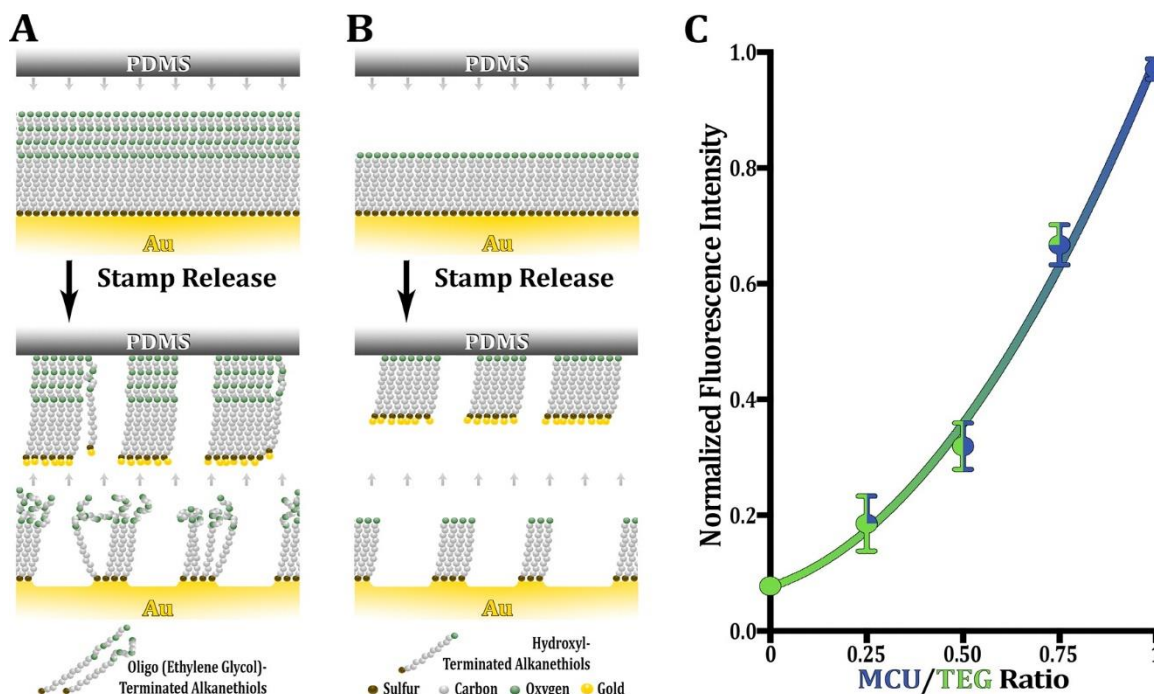


**Figure III.8.** Schematic (not to scale) illustrating changes in self-assembled monolayers (SAMs) of (A) tri(ethylene glycol)-terminated (TEG) or (B) hydroxyl-terminated (MCU) alkanethiols following conformal contact between oxygen plasma-treated stamps and SAM-modified substrates. The spectroscopic evidence in Figure III.7 suggests that ethylene glycol moieties of TEG SAMs undergo conformational changes from ordered all-*trans* conformations prior to CLL to disordered helical conformations afterward, limiting DNA probe access to Au substrates. In contrast, these conformational changes do not occur for post-lift-off MCU SAMs due to the lack of ethylene glycol moieties. (C) Normalized fluorescence intensities arising from surface hybridization of thiolated DNA probes with fluorescently labeled target DNA vs. ratios (prior to self-assembly) of MCU molecules in mixed solutions with TEG molecules. The best-fit curve ( $R^2 > 0.97$ ) indicates that by varying the nominal concentration ratios, steric effects resulting from ethylene glycol moieties are controlled to tune surface probe densities and thus, DNA hybridization. Error bars represent standard errors of the mean with  $N=3$  samples per ratio.

### III.C.7. Mixed Self-Assembled Monolayers Modulate DNA Surface Coverage

Since DNA surface densities are affected differently by MCU vs. TEG due to the ethylene glycol units in the latter, we examined whether variable combinations of these two types of molecules could be used to advantage to tune DNA access to Au substrates. Mixed

composition SAMs have been used to create dilute surface coverages wherein surface tethers are separated and exposed for subsequent chemical modifications, instead of phase segregated.<sup>10,23,39,41,62</sup> As shown in Figure III.8C, fluorescence due to surface hybridization between tethered DNA probes and DNA targets increases with respect to solution concentration ratios of MCU vs. TEG. This relationship indicates that as the fraction of MCU in monolayers increases, steric hindrance from the ethylene glycol moieties in TEG decreases, enabling greater DNA access to the Au surfaces. These results are consistent with the hypothesis that oligo(ethylene glycol) moieties are key factors in regulating DNA surface coverage on post-lift-off SAMs. They further demonstrate that the steric effects resulting from CLL-induced conformational changes in oligo(ethylene glycol) can be used judiciously to control DNA probe surface coverages.

Fluorescence in Figure III.8C resulted from DNA hybridization between surface-bound probes and fluorescently labeled target-DNA. Notably, fluorescence intensities may not directly reflect the actual numbers of surface-bound DNA probes associated with different mixed SAM compositions. Probes already hybridized with target strands may preclude hybridization of additional DNA targets from solution. As such, DNA hybridization may require extended amounts of time (>1 h) to reach saturation at higher probe densities. Also, because we investigated complementary strands with complete base-pair match, some target strands could have cross-hybridized with two DNA probes at higher probe densities.<sup>63</sup> In such a case, part of a target strand hybridizes with the top segment of one DNA probe and the bottom segment of a neighboring probe. Nonetheless, the data in Figure III.8C indicate the dependence and general trends of DNA hybridization on mixed SAM compositions.

Using the MCH backfilling method, Peterson *et al.* reported a DNA surface density of  $3 \times 10^{12}$  molecules/cm<sup>2</sup> on Au surfaces.<sup>5</sup> Furthermore, Lee *et al.* have reported values of  $1.7 \times 10^{13}$  molecules/cm<sup>2</sup> and  $3.6 \times 10^{13}$  molecules/cm<sup>2</sup> for backfilled MCH and oligo(ethylene glycol)-terminated alkanethiols, respectively.<sup>7,21</sup> In contrast, by inserting thiolated DNA into preformed MCH SAMs, Murphy *et al.* and Josephs *et al.* reported low surface densities of  $1.1 \times 10^{10}$  molecules/cm<sup>2</sup> and  $9.5 \times 10^{10}$  molecules/cm<sup>2</sup>, respectively.<sup>34,35</sup> The extent of insertion depends strongly on the preparation of the matrix into which molecules are placed.<sup>33,38,62</sup> We have previously targeted and reached surface densities between  $\sim 2 \times 10^{12}$  molecules/cm<sup>2</sup> and  $8 \times 10^{13}$  molecules/cm<sup>2</sup> *via* insertion.<sup>38,39</sup> In comparison to the backfilling method, correlation analysis of XPS atomic percentages and fluorescence hybridization intensities showed improved hybridization efficiency associated with lower DNA probe surface coverages when using the insertion approach. Thus, we expect that the numbers of DNA probes inserted into post-liftoff MCU or MCHD SAMs are below the upper limit determined for backfilling. Estimations using volume fractions in AFM measurements (shown in Figure III.3), with all of the caveats described above, indicate that the tri(ethylene glycol)-terminated (TEG) and hydroxyl-terminated (MCU) SAMs, as prepared and under the conditions described, lead to tethered DNA densities of  $3\text{-}4 \times 10^{12}$  molecules/cm<sup>2</sup> (5-7 pmol/cm<sup>2</sup>) and  $0.8\text{-}2 \times 10^{13}$  molecules/cm<sup>2</sup> (10-30 pmol/cm<sup>2</sup>), respectively. These values are consistent with what others and we have observed for insertion of other molecules into SAM matrices.<sup>31,33,64</sup>

### III.D. Conclusions and Prospects

Subtractive patterning by CLL relies on strong interactions at stamp-substrate interfaces to remove preassembled alkanethiol SAM molecules from Au substrates. A fundamental advantage of this patterning method is that not all alkanethiol molecules are removed after lift-off within the contacted areas. The remaining molecules create an optimized environment for subsequent insertion and assembly of thiolated DNA probes such that undesirable interactions with substrates are reduced and surface hybridization with target DNA is favored. The extent to which oligonucleotide surface densities are modulated by post-lift-off SAM molecules depends on specific matrix chemistries and in some cases, the conformations of the terminal SAM moieties.

By creating mixed MCU/TEG SAMs, the surface densities of alkanethiol-DNA probes were tuned according to the nominal concentrations of the two-component SAMs. While post-lift-off TEG SAMs represented the lower limits of tethered DNA surface coverages (with HEG appearing to have negligible DNA inserted), post-lift-off MCU (and to a greater extent MCHD) SAMs represented the upper limits of DNA coverages for the range of SAM molecules investigated here. Expansion of additional parameters such as employing alkanethiols with a wider range of terminal functional groups, altering lengths of ethylene glycol moieties or DNA linkers, and tuning alkanethiol surface coverages and/or packing densities, may enable even greater control of DNA insertion into post-lift-off SAMs. This could broaden the upper and lower limits of DNA surface densities while maintaining highly efficient hybridization.

It is noteworthy that conformational changes in ethylene glycol moieties have been shown to vary with hydration, chain-length, temperature-driven processes, packing

densities, surface coverage, and storage conditions.<sup>59,65-67</sup> Our findings show that ethylene-glycol-terminated alkanethiol conformational changes in SAMs can also be induced by the CLL process. Moreover, ionic strength, salt concentration, pH, multipoint binding dendrimers, alkyl linkers, and nucleotide-block spacers have been reported to influence thiolated DNA probe coverage.<sup>8,13,63,68</sup> Here, we show that CLL, in combination with tunable mixed SAM compositions, provide a facile means by which to regulate DNA surface densities.

Probe DNA inserted into native MCH SAM defects has been reported to produce more uniformly distributed DNA monolayers vs. surface-bound DNA back-filled with MCH.<sup>35</sup> However, it was difficult to achieve high DNA surface densities for practical sensing purposes using insertion alone because of the limited numbers of intrinsic SAM defects. Here, we show that by using CLL, large-area, high-density DNA patterns can be fabricated by inserting alkanethiol-functionalized DNA probes into post-lift-off alkanethiol SAMs. These findings advance DNA insertion methods toward more practical applications for creating DNA-based sensors. While a single lift-off step removes a large fraction of the preformed SAM molecules, multiple lift-off steps presumably remove additional SAM molecules and/or create additional defects providing greater surface availability for insertion compared to intrinsic SAM/substrate defects.<sup>42</sup> Thus, “artificial defects” introduced into the post-lift-off regions beyond intrinsic defects are key to a highly feasible and advantageous DNA insertion method.

The “artificial defects” created by CLL appear to comprise a new class of defect site that is serendipitously optimized for insertion and biorecognition. In the future, molecular-resolution information about the post-lift SAM regions will enable a deeper understanding



of their structure. This type of information will also shed light on potential limitations and improve control. The use of scanning probe microscopies to interrogate these SAM structures will be difficult because of their molecular lengths, corrugation, degree of disorder, and association with water molecules under ambient conditions.<sup>69-72</sup> A more precise quantification of the SAM molecules remaining in the stamp-contact regions is feasible using electrochemical reductive desorption, which is sensitive to domain sizes and interaction strengths with different molecules desorbing at different electrochemical potentials.<sup>73-75</sup> Electrochemical reductive desorption measurements will also be useful for determining the numbers and arrangements of alkanethiol molecules remaining on substrates after multiple lift-off steps. Because lift-off lithography patterning reduces DNA-substrate interactions, when coupled with automated processes for generating arrays, this technique should be applicable for fabricating high-throughput platforms to study aptamer-ligand interactions.<sup>76,77</sup> Notably, the ability to control the surface properties of DNA, the sub-40 nm nanopatterning capabilities of CLL, and the ability to fabricate high-performance field-effect transistor-based biosensors also *via* lift-off lithography (Chapter VI) will render single-molecule DNA nanoarrays feasible for bioelectronics and other applications.<sup>78-82</sup>

## **APPENDIX B**

### **Controlled DNA Patterning by Chemical Lift-Off Lithography: Matrix Matters**

#### **Supplementary Information**

Experiments were carried out to determine optimal DNA insertion times. Similar to the conditions in the experimental procedures in Chapter III, chemical lift-off was carried out on MCU SAMs followed by thiolated DNA probe insertion for 0 min, 0.5 min, 2 min, 5 min, 40 min, 120 min (2 h), or 1020 min (17 h). Surface DNA probes were hybridized with fluorescently tagged complimentary DNA. Normalized fluorescence intensities for DNA hybridization vs. DNA insertion times are shown in Figure SB.1.

Atomic percentages determined from XPS peak areas for carbon, oxygen, sulfur, nitrogen, and phosphorus are shown in Table SB.1. With the exception of nitrogen and phosphorus, which are XPS fingerprints for DNA molecules, XPS signals from carbon, oxygen, and sulfur are present in both DNA and matrix molecules. Moreover, X-ray attenuation lengths further complicate the interpretation of the XPS signals. Thus, while reported in Table SB.1 for completeness, these peak areas are not suitable for determining relative surface coverages of DNA probes.

Additionally, XPS experiments were carried out to determine whether hydroxyl-terminated hexadecanethiol (MCHD) and hexa(ethylene glycol)-terminated undecanethiol (HEG) molecules were removed from Au surfaces by chemical lift-off. We showed previously that alkanethiol SAM molecules removed by lift-off resulted in Au 4f XPS signals on post-lift-off PDMS stamps indicating that Au atoms bound to alkanethiols are also removed. Here, Au 4f XPS signals were observed on post-lift-off PDMS stamps, as shown in Figures SB.2a (MCHD) and SB.2b (HEG). Control experiments were carried out wherein oxygen plasma-treated PDMS stamps were not contacted with MCHD and HEG SAMs. Here, no Au 4f signals were observed, as shown in Figure SB.2c. Similar to other XPS experiments in this study, featureless PDMS stamps were used for these experiments.

Additional fluorescence microscopy experiments were carried out to explore an alternative mechanism regarding steric effects of ethylene glycol moieties in TEG molecules induced by the CLL process. Because TEG molecules are longer than MCU molecules by three ethylene glycol units, it is possible that thicker TEG SAMs might hinder DNA probes from accessing Au surfaces. Therefore, if longer alkanethiols, such as hydroxyl-terminated hexadecanethiol (MCHD) and hexa(ethylene glycol)-terminated undecanethiol (HEG) are used, one would expect that the resulting thicker SAMs would obstruct DNA probes from reaching Au surfaces to a greater extent compared to MCU and TEG SAMs, respectively. For example, if SAM thickness alone blocked DNA probes from accessing Au surfaces, then weaker fluorescence patterns would be expected following DNA surface hybridization on either MCHD or HEG SAMs vs. MCU or TEG SAMs, respectively. Similar to the conditions in the Chapter III experimental procedures, CLL was carried out on MCHD and HEG SAMs followed by DNA probe insertion and hybridization with fluorescently tagged complimentary DNA. Representative fluorescence microscopy images are shown in Figures SB.3a (MCHD/DNA SAMs) and SB.3b (HEG/DNA SAMs).

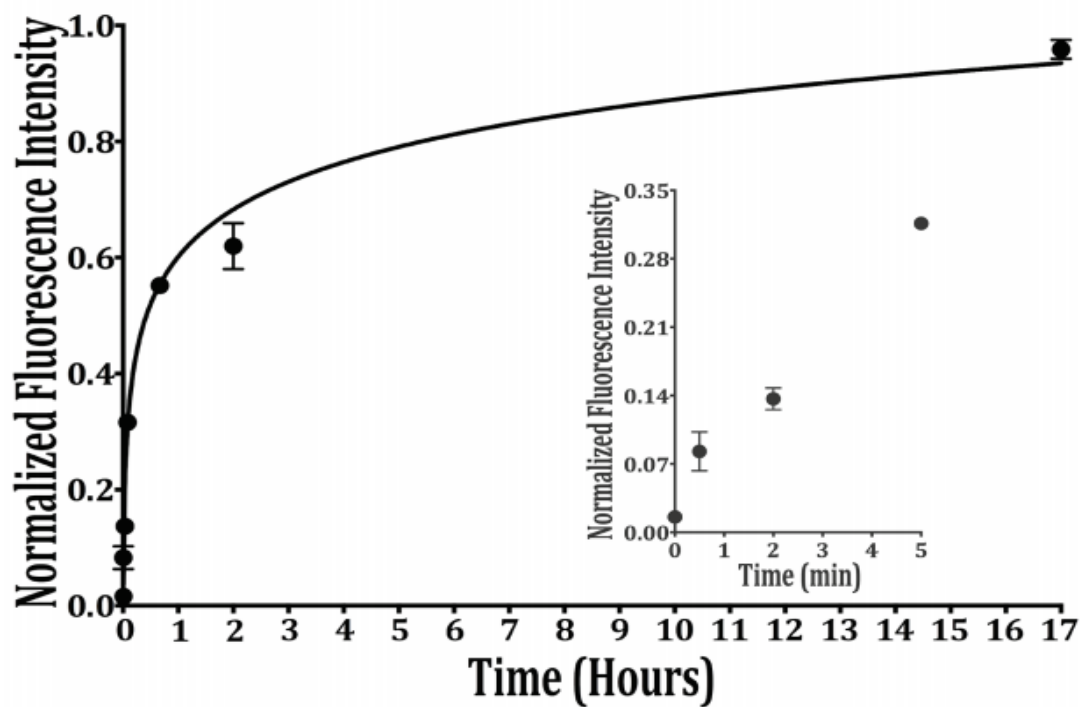


**Figure SB.1.** Normalized fluorescence intensities resulting from target DNA hybridization vs. DNA probe insertion times. An initial sharp increase in hybridization (0- 2 h) was followed by a slow rise in fluorescence intensities, suggesting that DNA probe surface coverages start to approach saturation after 2 h of insertion. The inset shows DNA probe insertion behavior at the early time points.

<b>Elements</b>	<b>Atomic Percentage</b>		
	<b>C 1s</b>	<b>O 1s</b>	<b>S 2p</b>
DNA (predicted)	45.7	31.2	0.3
DNA (experimental)	31.9±0.7	48.8±0.4	N/D
DNA/MCU Backfill	40.7±0.5	41.2±0.2	1.7±0.2
MCU/DNA Insertion	52.7±1.5	35.0±1.3	3.4±0.2
TEG/DNA Insertion	52.4±0.6	44.9±0.7	2.6±0.1
MCU	62.6±3.5	26.4±2.2	5.3±0.4
TEG	51.9±0.5	45.0±1.0	2.6±0.0

**Table SB.1.** Predicted X-ray photoelectron spectroscopy atomic percentages for undiluted DNA were calculated using the numbers of C, O, and S atoms in DNA probe molecules. Atomic percentages for pure DNA monolayers (experimental) and mixed monolayers of hydroxyl- (MCU) and tri(ethylene glycol) (TEG)-terminated alkanethiol/DNA on Au substrates were calculated from XPS peak areas ( $N=3-6/\text{group}$ ). Not detectable XPS signals are indicated by “N/D”. Entries are means  $\pm$  standard errors of the means.

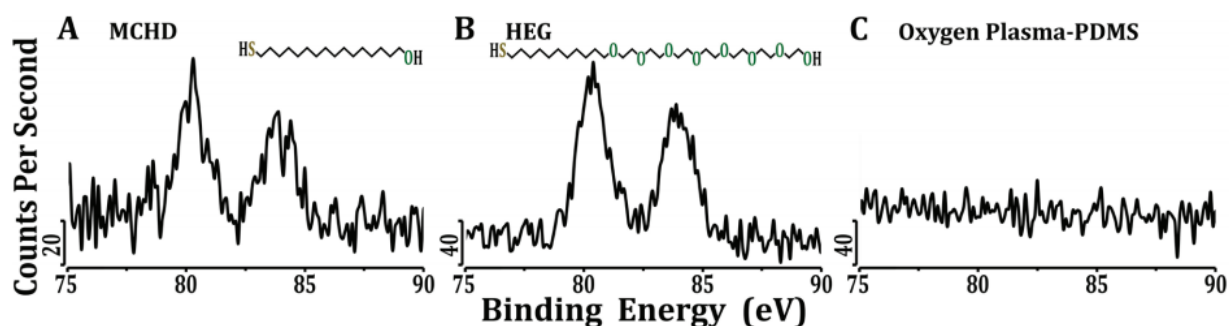


**Figure SB.2.** Representative X-ray photoelectron spectra of Au 4f peaks from post-lift-off oxygen plasma-treated polydimethylsiloxane (PDMS) stamps. Visible Au 4f peaks indicate that (a) hydroxyl-terminated hexadecanethiol (MCHD) and (b) hexa(ethylene glycol)-terminated undecanethiol (HEG) are “lift-able” molecules. (c) A control sample is shown in where the oxygen plasma-treated PDMS stamp was not brought into conformal contact with the SAM and spectroscopy was subsequently carried out.

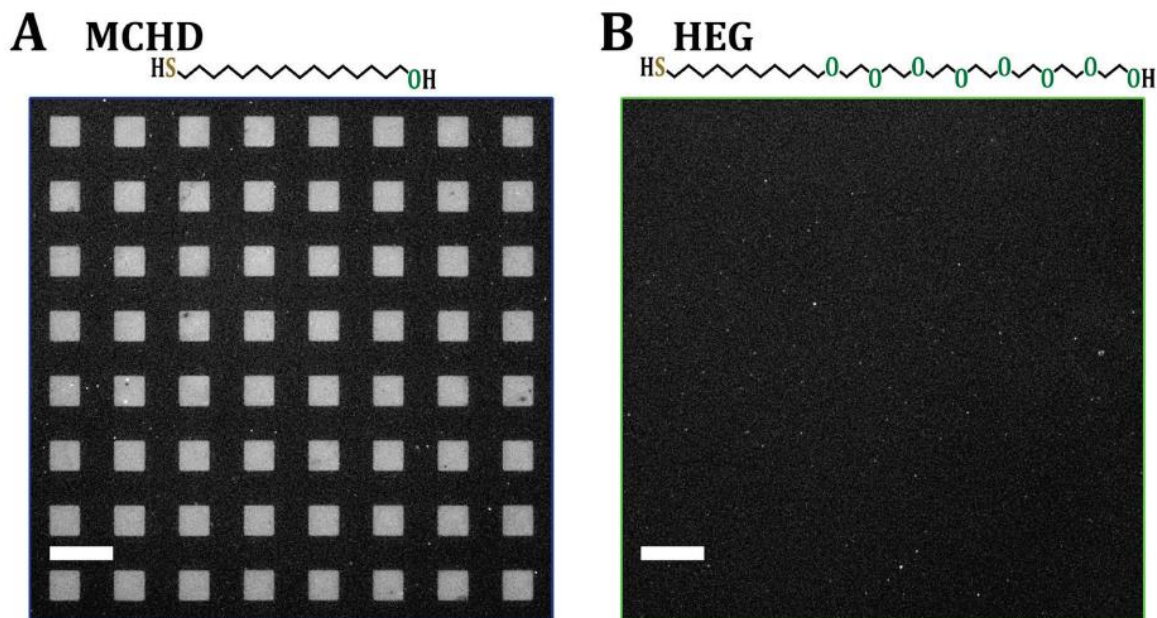


**Figure SB.3.** Representative fluorescence images displaying hybridization of thiolated DNA probes with Alexa Fluor 488 (excitation at 495 nm)-labeled complementary DNA targets on (a) hydroxyl-terminated hexadecanethiol (MCHD) and (b) hexa(ethylene glycol)-terminated undecanethiol (HEG) self-assembled monolayers (SAMs). The bright square patterns in (a) indicate that substantial numbers of DNA probes inserted into the post-lift-off MCHD SAM and were available for hybridization. By contrast, the lack of a discernable pattern in (b) suggests that insertion does not occur to an appreciable extent on HEG SAMs. The fact that a similar fluorescent square pattern is not visible in (b) implies that the increased numbers of ethylene glycol moieties in HEG SAMs impose greater steric hindrance compared to TEG SAMs; HEG molecules are three ethylene glycol units longer than TEG molecules. The fluorescence images (shown with the same exposure time of 5 s) were taken at an emission wavelength of 518 nm. Scale bars are 50  $\mu\text{m}$ .



## References

1. Lockhart, D. J.; Winzeler, E. A. Genomics, Gene Expression and DNA Arrays. *Nature* **2000**, *405*, 827-836.
2. Caruso, F.; Rodda, E.; Furlong, D. N.; Haring, V. DNA Binding and Hybridization on Gold and Derivatized Surfaces. *Sensor Actuat. B-Chem* **1997**, *41*, 189-197.
3. Sassolas, A.; Leca-Bouvier, B. D.; Blum, L. J. DNA Biosensors and Microarrays. *Chem. Rev.* **2008**, *108*, 109-139.
4. Herne, T. M.; Tarlov, M. J. Characterization of DNA Probes Immobilized on Gold Surfaces. *J. Am. Chem. Soc.* **1997**, *119*, 8916-8920.
5. Peterson, A. W.; Heaton, R. J.; Georgiadis, R. M. The Effect of Surface Probe Density on DNA Hybridization. *Nucleic Acids Res.* **2001**, *29*, 5163-5168.
6. Boozer, C.; Chen, S. F.; Jiang, S. Y. Controlling DNA Orientation on Mixed ssDNA/OEG SAMs. *Langmuir* **2006**, *22*, 4694-4698.
7. Lee, C. Y.; Gong, P.; Harbers, G. M.; Grainger, D. W.; Castner, D. G.; Gamble, L. J. Surface Coverage and Structure of Mixed DNA/Alkylthiol Monolayers on Gold: Characterization by XPS, NEXAFS, and Fluorescence Intensity Measurements. *Anal. Chem.* **2006**, *78*, 3316-3325.
8. Day, B. S.; Fieglund, L. R.; Vint, E. S.; Shen, W. Q.; Morris, J. R.; Norton, M. L. Thiolated Dendrimers as Multi-Point Binding Headgroups for DNA Immobilization on Gold. *Langmuir* **2011**, *27*, 12434-12442.
9. Ostuni, E.; Yan, L.; Whitesides, G. M. The Interaction of Proteins and Cells with Self-Assembled Monolayers of Alkanethiolates on Gold and Silver. *Colloids Surf. B* **1999**, *15*, 3-30.
10. Shuster, M. J.; Vaish, A.; Cao, H. H.; Guttentag, A. I.; McManigle, J. E.; Gibb, A. L.; Martinez, M. M.; Nezarati, R. M.; Hinds, J. M.; Liao, W. S.; Weiss, P. S.; Andrews, A. M. Patterning Small-Molecule Biocapture Surfaces: Microcontact Insertion Printing vs. Photolithography. *Chem. Commun.* **2011**, *47*, 10641-10643.
11. Huang, E.; Zhou, F. M.; Deng, L. Studies of Surface Coverage and Orientation of DNA Molecules Immobilized onto Preformed Alkanethiol Self-Assembled Monolayers. *Langmuir* **2000**, *16*, 3272-3280.
12. Rant, U.; Arinaga, K.; Fujita, S.; Yokoyama, N.; Abstreiter, G.; Tornow, M. Structural Properties of Oligonucleotide Monolayers on Gold Surfaces Probed by Fluorescence Investigations. *Langmuir* **2004**, *20*, 10086-10092.

13. Opdahl, A.; Petrovykh, D. Y.; Kimura-Suda, H.; Tarlov, M. J.; Whitman, L. J. Independent Control of Grafting Density and Conformation of Single-Stranded DNA Brushes. *Proc. Natl. Acad. Sci. U. S. A.* **2007**, *104*, 9-14.
14. Kaufmann, R.; Averbukh, I.; Naaman, R.; Daube, S. S. Controlling the Reactivity of Adsorbed DNA on Template Surfaces. *Langmuir* **2008**, *24*, 927-931.
15. Howell, C.; Zhao, J. L.; Koelsch, P.; Zharnikov, M. Hybridization in ssDNA Films - A Multi-Technique Spectroscopy Study. *Phys. Chem. Chem. Phys.* **2011**, *13*, 15512-15522.
16. Steel, A. B.; Herne, T. M.; Tarlov, M. J. Electrochemical Quantitation of DNA Immobilized on Gold. *Anal. Chem.* **1998**, *70*, 4670-4677.
17. Levicky, R.; Herne, T. M.; Tarlov, M. J.; Satija, S. K. Using Self-Assembly to Control the Structure of DNA Monolayers on Gold: A Neutron Reflectivity Study. *J. Am. Chem. Soc.* **1998**, *120*, 9787-9792.
18. Kimura-Suda, H.; Petrovykh, D. Y.; Tarlov, M. J.; Whitman, L. J. Base-Dependent Competitive Adsorption of Single-Stranded DNA on Gold. *J. Am. Chem. Soc.* **2003**, *125*, 9014-9015.
19. Arinaga, K.; Rant, U.; Tornow, M.; Fujita, S.; Abstreiter, G.; Yokoyama, N. The Role of Surface Charging During the Coadsorption of Mercaptohexanol to DNA Layers on Gold: Direct Observation of Desorption and Layer Reorientation. *Langmuir* **2006**, *22*, 5560-5562.
20. Lai, R. Y.; Seferos, D. S.; Heeger, A. J.; Bazan, G. C.; Plaxco, K. W. Comparison of the Signaling and Stability of Electrochemical DNA Sensors Fabricated from 6-or 11-Carbon Self-Assembled Monolayers. *Langmuir* **2006**, *22*, 10796-10800.
21. Lee, C. Y.; Gamble, L. J.; Grainger, D. W.; Castner, D. G. Mixed DNA/Oligo(Ethylene Glycol) Functionalized Gold Surfaces Improve DNA Hybridization in Complex Media. *Biointerphases* **2006**, *1*, 82-92.
22. Boozer, C.; Ladd, J.; Chen, S. F.; Yu, Q.; Homola, J.; Jiang, S. Y. DNA Directed Protein Immobilization on Mixed ssDNA/Oligo(Ethylene Glycol) Self-Assembled Monolayers for Sensitive Biosensors. *Anal. Chem.* **2004**, *76*, 6967-6972.
23. Shuster, M. J.; Vaish, A.; Szapacs, M. E.; Anderson, M. E.; Weiss, P. S.; Andrews, A. M. Biospecific Recognition of Tethered Small Molecules Diluted in Self-Assembled Monolayers. *Adv. Mater.* **2008**, *20*, 164-167.
24. Liao, W. S.; Cao, H. H.; Cheunkar, S.; Shuster, M. J.; Altieri, S. C.; Weiss, P. S.; Andrews, A. M. Small-Molecule Arrays for Sorting G-Protein-Coupled Receptors. *J. Phys. Chem. C* **2013**, *117*, 22362-22368.

25. Choi, S.; Murphy, W. L. Multifunctional Mixed SAMs That Promote Both Cell Adhesion and Noncovalent DNA Immobilization. *Langmuir* **2008**, *24*, 6873-6880.
26. Satjapipat, M.; Sanedrin, R.; Zhou, F. M. Selective Desorption of Alkanethiols in Mixed Self-Assembled Monolayers for Subsequent Oligonucleotide Attachment and DNA Hybridization. *Langmuir* **2001**, *17*, 7637-7644.
27. Aqua, T.; Naaman, R.; Daube, S. S. Controlling the Adsorption and Reactivity of DNA on Gold. *Langmuir* **2003**, *19*, 10573-10580.
28. Fang, Y.; Spisz, T. S.; Hoh, J. H. Ethanol-Induced Structural Transitions of DNA on Mica. *Nucleic Acids Res.* **1999**, *27*, 1943-1949.
29. Kick, A.; Boensch, M.; Kummer, K.; Vyalikh, D. V.; Molodtsov, S. L.; Mertig, M. Controlling Structural Properties of Self-Assembled Oligonucleotide-Mercaptohexanol Monolayers. *J. Electron. Spectrosc.* **2009**, *172*, 36-41.
30. Bumm, L. A.; Arnold, J. J.; Cygan, M. T.; Dunbar, T. D.; Burgin, T. P.; Jones, L.; Allara, D. L.; Tour, J. M.; Weiss, P. S. Are Single Molecular Wires Conducting? *Science* **1996**, *271*, 1705-1707.
31. Cygan, M. T.; Dunbar, T. D.; Arnold, J. J.; Bumm, L. A.; Shedlock, N. F.; Burgin, T. P.; Jones, L.; Allara, D. L.; Tour, J. M.; Weiss, P. S. Insertion, Conductivity, and Structures of Conjugated Organic Oligomers in Self-Assembled Alkanethiol Monolayers on Au{111}. *J. Am. Chem. Soc.* **1998**, *120*, 2721-2732.
32. Shuster, M. J.; Vaish, A.; Gilbert, M. L.; Martinez-Rivera, M.; Nezarati, R. M.; Weiss, P. S.; Andrews, A. M. Comparison of Oligo(Ethylene Glycol) Alkanethiols versus *n*-Alkanethiols: Self-Assembly, Insertion, and Functionalization. *J. Phys. Chem. C* **2011**, *115*, 24778-24787.
33. Claridge, S. A.; Liao, W. S.; Thomas, J. C.; Zhao, Y. X.; Cao, H. H.; Cheunkar, S.; Serino, A. C.; Andrews, A. M.; Weiss, P. S. From the Bottom Up: Dimensional Control and Characterization in Molecular Monolayers. *Chem. Soc. Rev.* **2013**, *42*, 2725-2745.
34. Murphy, J. N.; Cheng, A. K. H.; Yu, H. Z.; Bizzotto, D. On the Nature of DNA Self-Assembled Monolayers on Au: Measuring Surface Heterogeneity with Electrochemical *in Situ* Fluorescence Microscopy. *J. Am. Chem. Soc.* **2009**, *131*, 4042-4050.
35. Josephs, E. A.; Ye, T. Nanoscale Spatial Distribution of Thiolated DNA on Model Nucleic Acid Sensor Surfaces. *ACS Nano* **2013**, *7*, 3653-3660.
36. Josephs, E. A.; Ye, T. A Single-Molecule View of Conformational Switching of DNA Tethered to a Gold Electrode. *J. Am. Chem. Soc.* **2012**, *134*, 10021-10030.

37. Josephs, E. A.; Ye, T. Electric-Field Dependent Conformations of Single DNA Molecules on a Model Biosensor Surface. *Nano Lett.* **2012**, *12*, 5255-5261.
38. Mullen, T. J.; Srinivasan, C.; Hohman, J. N.; Gillmor, S. D.; Shuster, M. J.; Horn, M. W.; Andrews, A. M.; Weiss, P. S. Microcontact Insertion Printing. *Appl. Phys. Lett.* **2007**, *90*.
39. Vaish, A.; Shuster, M. J.; Cheunkar, S.; Singh, Y. S.; Weiss, P. S.; Andrews, A. M. Native Serotonin Membrane Receptors Recognize 5-Hydroxytryptophan-Functionalized Substrates: Enabling Small-Molecule Recognition. *ACS Chem. Neurosci.* **2010**, *1*, 495-504.
40. Saavedra, H. M.; Mullen, T. J.; Zhang, P. P.; Dewey, D. C.; Claridge, S. A.; Weiss, P. S. Hybrid Strategies in Nanolithography. *Rep. Prog. Phys.* **2010**, *73*.
41. Vaish, A.; Shuster, M. J.; Cheunkar, S.; Weiss, P. S.; Andrews, A. M. Tuning Stamp Surface Energy for Soft Lithography of Polar Molecules to Fabricate Bioactive Small-Molecule Microarrays. *Small* **2011**, *7*, 1471-1479.
42. Liao, W. S.; Cheunkar, S.; Cao, H. H.; Bednar, H. R.; Weiss, P. S.; Andrews, A. M. Subtractive Patterning *via* Chemical Lift-Off Lithography. *Science* **2012**, *337*, 1517-1521.
43. Kung, L. A.; Kam, L.; Hovis, J. S.; Boxer, S. G. Patterning Hybrid Surfaces of Proteins and Supported Lipid Bilayers. *Langmuir* **2000**, *16*, 6773-6776.
44. Hovis, J. S.; Boxer, S. G. Patterning Barriers to Lateral Diffusion in Supported Lipid Bilayer Membranes by Blotting and Stamping. *Langmuir* **2000**, *16*, 894-897.
45. Hovis, J. S.; Boxer, S. G. Patterning and Composition Arrays of Supported Lipid Bilayers by Microcontact Printing. *Langmuir* **2001**, *17*, 3400-3405.
46. Peterson, A. W.; Heaton, R. J.; Georgiadis, R. Kinetic Control of Hybridization in Surface Immobilized DNA Monolayer Films. *J. Am. Chem. Soc.* **2000**, *122*, 7837-7838.
47. Rao, A. N.; Grainger, D. W. Biophysical Properties of Nucleic Acids at Surfaces Relevant to Microarray Performance. *Biomater. Sci.* **2014**, *2*, 436-471.
48. Damaschun, G.; Damaschun, H.; Misselwitz, R.; Pospelov, V. A.; Zalenskaya, I. A.; Zirwer, D.; Muller, J. J.; Vorobev, V. I. How Many Base-Pairs Per Turn Does DNA Have in Solution and in Chromatin - an Answer from Wide-Angle X-Ray-Scattering. *Biomed. Biochim. Acta* **1983**, *42*, 697-703.
49. Steel, A. B.; Levicky, R. L.; Herne, T. M.; Tarlov, M. J. Immobilization of Nucleic Acids at Solid Surfaces: Effect of Oligonucleotide Length on Layer Assembly. *Biophys. J.* **2000**, *79*, 975-981.

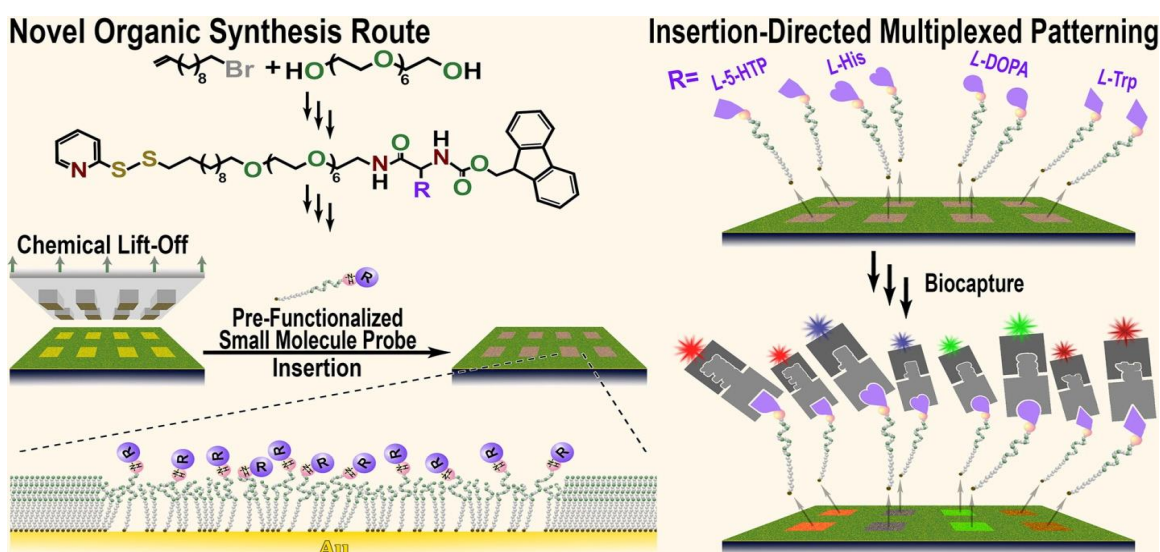
50. May, C. J.; Canavan, H. E.; Castner, D. G. Quantitative X-Ray Photoelectron Spectroscopy and Time-of-Flight Secondary Ion Mass Spectrometry Characterization of the Components in DNA. *Anal. Chem.* **2004**, 76, 1114-1122.
51. Petrovykh, D. Y.; Kimura-Suda, H.; Tarlov, M. J.; Whitman, L. J. Quantitative Characterization of DNA Films by X-Ray Photoelectron Spectroscopy. *Langmuir* **2004**, 20, 429-440.
52. Lee, C. Y.; Nguyen, P. C. T.; Grainger, D. W.; Gamble, L. J.; Castner, D. G. Structure and DNA Hybridization Properties of Mixed Nucleic Acid/Maleimide-Ethylene Glycol Monolayers. *Anal. Chem.* **2007**, 79, 4390-4400.
53. Cederquist, K. B.; Keating, C. D. Hybridization Efficiency of Molecular Beacons Bound to Gold Nanowires: Effect of Surface Coverage and Target Length. *Langmuir* **2010**, 26, 18273-18280.
54. Demers, L. M.; Mirkin, C. A.; Mucic, R. C.; Reynolds, R. A.; Letsinger, R. L.; Elghanian, R.; Viswanadham, G. A Fluorescence-Based Method for Determining the Surface Coverage and Hybridization Efficiency of Thiol-Capped Oligonucleotides Bound to Gold Thin Films and Nanoparticles. *Anal. Chem.* **2000**, 72, 5535-5541.
55. Gorodetsky, A. A.; Buzzeo, M. C.; Barton, J. K. DNA-Mediated Electrochemistry. *Bioconjugate Chem.* **2008**, 19, 2285-2296.
56. Kelley, S. O.; Jackson, N. M.; Hill, M. G.; Barton, J. K. Long-Range Electron Transfer through DNA Films. *Angew. Chem., Int. Ed.* **1999**, 38, 941-945.
57. Gong, P.; Lee, C. Y.; Gamble, L. J.; Castner, D. G.; Grainger, D. W. Hybridization Behavior of Mixed DNA/Alkylthiol Monolayers on Gold: Characterization by Surface Plasmon Resonance and P-32 Radiometric Assay. *Anal. Chem.* **2006**, 78, 3326-3334.
58. Valiokas, R.; Malysheva, L.; Onipko, A.; Lee, H.-H.; Ruzele, Z.; Svedhem, S.; Svensson, S. C. T.; Gelius, U.; Liedberg, B. On the Quality and Structural Characteristics of Oligo-(Ethylene Glycol) Assemblies on Gold: An Experimental and Theoretical Study. *J. Electron Spectrosc. Relat. Phenom.* **2009**, 172, 9-20.
59. Skoda, M. W. A.; Jacobs, R. M. J.; Willis, J.; Schreiber, F. Hydration of Oligo(Ethylene Glycol) Self-Assembled Monolayers Studied Using Polarization Modulation Infrared Spectroscopy. *Langmuir* **2007**, 23, 970-974.
60. Harder, P.; Grunze, M.; Dahint, R.; Whitesides, G. M.; Laibinis, P. E. Molecular Conformation in Oligo(Ethylene Glycol)-Terminated Self-Assembled Monolayers on Gold and Silver Surfaces Determines Their Ability to Resist Protein Adsorption. *J. Phys. Chem. B* **1998**, 102, 426-436.

61. Zorn, S.; Martin, N.; Gerlach, A.; Schreiber, F. Real-Time PMIRRAS Studies of *in Situ* Growth of C<sub>11</sub>Eg<sub>6</sub>OMe on Gold and Immersion Effects. *Phys. Chem. Chem. Phys.* **2010**, *12*, 8986-8991.
62. Weck, M.; Jackiw, J. J.; Rossi, R. R.; Weiss, P. S.; Grubbs, R. H. Ring-Opening Metathesis Polymerization from Surfaces. *J. Am. Chem. Soc.* **1999**, *121*, 4088-4089.
63. Wong, E. L. S.; Chow, E.; Gooding, J. J. DNA Recognition Interfaces: The Influence of Interfacial Design on the Efficiency and Kinetics of Hybridization. *Langmuir* **2005**, *21*, 6957-6965.
64. Smith, R. K.; Nanayakkara, S. U.; Woehrle, G. H.; Pearl, T. P.; Blake, M. M.; Hutchison, J. E.; Weiss, P. S. Spectral Diffusion in the Tunneling Spectra of Ligand-Stabilized Undecagold Clusters. *J. Am. Chem. Soc.* **2006**, *128*, 9266-9267.
65. Valiokas, R.; Svedhem, S.; Ostblom, M.; Svensson, S. C. T.; Liedberg, B. Influence of Specific Intermolecular Interactions on the Self-Assembly and Phase Behavior of Oligo(Ethylene Glycol)-Terminated Alkanethiolates on Gold. *J. Phys. Chem. B* **2001**, *105*, 5459-5469.
66. Zorn, S.; Skoda, M. W. A.; Gerlach, A.; Jacobs, R. M. J.; Schreiber, F. On the Stability of Oligo(Ethylene Glycol) (C<sub>11</sub>EG<sub>6</sub>OMe) SAMs on Gold: Behavior at Elevated Temperature in Contact with Water. *Langmuir*, **2011**, *27*, 2237-2243.
67. Zorn, S.; Dettinger, U.; Skoda, M. W. A.; Jacobs, R. M. J.; Peisert, H.; Gerlach, A.; Chasse, T.; Schreiber, F. Stability of Hexa(Ethylene Glycol) SAMs towards the Exposure to Natural Light and Repeated Reimmersion. *Appl. Surf. Sci.* **2012**, *258*, 7882-7888.
68. Ravan, H.; Kashanian, S.; Sanadgol, N.; Badoei-Dalfard, A.; Karami, Z. Strategies for Optimizing DNA Hybridization on Surfaces. *Anal. Biochem.* **2014**, *444*, 21-46.
69. Esplandiu, M. J.; Hagenstrom, H.; Kolb, D. M. Functionalized Self-Assembled Alkanethiol Monolayers on Au(111) Electrodes: 1. Surface Structure and Electrochemistry. *Langmuir* **2001**, *17*, 828-838.
70. Liu, Y. F.; Yang, Y. C.; Lee, Y. L. Assembly Behavior and Monolayer Characteristics of OH-Terminated Alkanethiol on Au(111): *In Situ* Scanning Tunneling Microscopy and Electrochemical Studies. *Nanotechnology* **2008**, *19*, 065609.
71. Liu, Y. F.; Lee, Y. L. Adsorption Characteristics of OH-Terminated Alkanethiol and Arenethiol on Au(111) Surfaces. *Nanoscale* **2012**, *4*, 2093-2100.
72. Abel, G. R.; Josephs, E. A.; Luong, N.; Ye, T. A Switchable Surface Enables Visualization of Single DNA Hybridization Events with Atomic Force Microscopy. *J. Am. Chem. Soc.* **2013**, *135*, 6399-6402.

73. Mullen, T. J.; Dameron, A. A.; Weiss, P. S. Directed Assembly and Separation of Self-Assembled Monolayers *via* Electrochemical Processing. *J. Phys. Chem. B* **2006**, *110*, 14410-14417.
74. Dameron, A. A.; Mullen, T. J.; Hengstebeck, R. W.; Saavedra, H. M.; Weiss, P. S. Origins of Displacement in 1-Adamantanethiolate Self-Assembled Monolayers. *J. Phys. Chem. C* **2007**, *111*, 6747-6752.
75. Kim, M.; Hohman, J. N.; Serino, A. C.; Weiss, P. S. Structural Manipulation of Hydrogen-Bonding Networks in Amide-Containing Alkanethiolate Monolayers *via* Electrochemical Processing. *J. Phys. Chem. C* **2010**, *114*, 19744-19751.
76. Gao, P.; Cai, Y. G. Aptamer Fiber Anchored on the Edge of a Protein Pattern: A Template for Nanowire Fabrication. *ACS Nano* **2009**, *3*, 3475-3484.
77. Sheng, W. A.; Chen, T.; Tan, W. H.; Fan, Z. H. Multivalent DNA Nanospheres for Enhanced Capture of Cancer Cells in Microfluidic Devices. *ACS Nano* **2013**, *7*, 7067-7076.
78. Wilson, N. A.; Abu-Shumays, R.; Gyarfás, B.; Wang, H.; Lieberman, K. R.; Akesson, M.; Dunbar, W. B. Electronic Control of DNA Polymerase Binding and Unbinding to Single DNA Molecules. *ACS Nano* **2009**, *3*, 995-1003.
79. Yasui, T.; Rahong, S.; Motoyama, K.; Yanagida, T.; Wu, Q.; Kaji, N.; Kanai, M.; Doi, K.; Nagashima, K.; Tokeshi, M.; Taniguchi, M.; Kawano, S.; Kawai, T.; Baba, Y. DNA Manipulation and Separation in Sublithographic-Scale Nanowire Array. *ACS Nano* **2013**, *7*, 3029-3035.
80. Fu, Y. M.; Zeng, D. D.; Chao, J.; Jin, Y. Q.; Zhang, Z.; Liu, H. J.; Li, D.; Ma, H. W.; Huang, Q.; Gothelf, K. V.; Fan, C. H. Single-Step Rapid Assembly of DNA Origami Nanostructures for Addressable Nanoscale Bioreactors. *J. Am. Chem. Soc.* **2013**, *135*, 696-702.
81. Liao, W. S.; Chen, X.; Yang, T. L.; Castellana, E. T.; Chen, J. X.; Cremer, P. S. Benchtop Chemistry for the Rapid Prototyping of Label-Free Biosensors: Transmission Localized Surface Plasmon Resonance Platforms. *Biointerphases* **2009**, *4*, 80-85.
82. Kim, J.; Rim, Y. S.; Chen, H. J.; Cao, H. H.; Nakatsuka, N.; Hinton, H. L.; Zhao, C. Z.; Andrews, A. M.; Yang, Y.; Weiss, P. S. Fabrication of High-Performance Ultrathin In<sub>2</sub>O<sub>3</sub> Film Field-Effect Transistors and Biosensors Using Chemical Lift-Off Lithography. *ACS Nano* **2015**, *9*, 4572-4582.

## Chapter IV

# Multiplexed Small-Molecule Patterning via Pre-Functionalized Alkanethiols



The information in this chapter  
is in preparation for *Chemistry of Materials*  
and has been reproduced here.

Authors: Cao, H. H.; Nakatsuka, N.; Deshayes, S.; Yang, H.;  
Weiss, P. S.; Kasko, A. M.; Andrews, A. M.



#### IV.A. Introduction

For over a decade, we have investigated general design rules for small-molecule surface functionalization to improve recognition by biomolecules.<sup>1-6</sup> In parallel, we have developed readily adoptable small-molecule patterning methods.<sup>2,3,7-10</sup> Patterning enables relative molecular recognition, between functionalized (patterned) and unfunctionalized (unpatterned) regions, to be quantified on the same substrate. We discovered that molecular level patterning *via* insertion-directed self-assembly<sup>11-13</sup> is advantageous for spacing small molecules so that large biomolecule partners have ample access for recognition with minimal steric hindrance.<sup>1,4,6</sup> Controlling surface chemistries to reduce nonspecific substrate interactions is another critical factor that we and others have addressed.<sup>1,3,4,14,15</sup> We demonstrated that linking chemistries employing small molecules where an extra functional group is used for surface-tethering, preserves biomolecule functionality and is essential for recognition.<sup>2,4</sup>

We previously used multiplexed substrates produced using chemical lift-off lithography and microfluidics to sort antibodies or native membrane-associated receptors from mixtures to their cognate small-molecule partners.<sup>2,16</sup> However, the on-substrate conjugation chemistries employed, *e.g.*, NHS-EDC coupling, suffer from incomplete functionalization and possible by-product formation, which likely contribute to surface-to-surface variations and nonspecific recognition.<sup>17-19</sup> On-substrate functionalization is difficult to control and to bring to completion with high yields. The extent of reaction differs with specific probes, contributing to variable specific and greater nonspecific target recognition.<sup>2</sup> Moreover, monodisperse surface-functionalization is challenging due to the

formation of clusters or domains of molecules arising from phase separation of mixed monolayers.<sup>20-22</sup>

In light of these and other shortcomings, we decided to investigate multiplexed and patterned small-molecule substrates using a “pre-functionalized” synthesis approach. Small-molecule oligo(ethylene glycol)-terminated alkanethiols are not generally commercially available. Moreover, synthesis of this type of molecule requires heterobifunctionalization and orthogonal chemistries to couple different small-molecule tail groups. To address these challenges, we developed a novel synthetic route to a library of monodisperse hepta(ethylene glycol)undecyl pyridyl disulfide (7EG-PDS) molecules pre-functionalized with neurotransmitter mimics, *i.e.*, *L*-histidine (*L*-HD), *L*-3,4-dihydroxyphenylalanine (*L*-DOPA), *L*-threo-3,4-dihydroxyphenylserine (*L*-DOPS), *L*-5-hydroxytryptophan (*L*-5-HTP), and *L*-tryptophan (*L*-Trp) (Figure IV.1A).

The small-molecule probes investigated are naturally occurring proximal precursors to biogenic monoamine neurotransmitters, *i.e.*, histamine, dopamine, norepinephrine, and serotonin, respectively. The exception is *L*-tryptophan from which serotonin is synthesized in two enzymatic steps by way of *L*-5-HTP *in vivo*. By using neurotransmitter amino acid *precursors*, as depicted in Figure IV.1A, we introduced an additional carboxyl moiety for tethering, thereby preserving amino groups for biorecognition.<sup>4,23,24</sup> Substrates functionalized with neurotransmitter precursors mimic biologically active (free) neurotransmitters in terms of selective molecular recognition of the corresponding native membrane-associated receptors.<sup>2,4</sup>

Herein, we refer to mimicking precursors as neurotransmitters (unless otherwise noted). We refer to tethers functionalized with neurotransmitters prior to self-assembly as pre-functionalized molecules and tethers that are first self-assembled and then functionalized with neurotransmitters as post-functionalized molecules. Substrates modified with pre-functionalized vs. post-functionalized molecules were patterned *via* chemical lift-off lithography<sup>9,10</sup> (Figure IV.1B,C). Since 7EG-PDS molecules were conjugated with small-molecule probes *prior* to surface assembly and patterning, the need to devise compatible serial functionalization chemistries and to optimize reaction conditions for coupling each neurotransmitter was obviated. We hypothesized that the use of pre-functionalized molecules would improve specific molecular recognition compared to post-functionalization.

## IV.B. Experimental Methods

### IV.B.1. Materials

Silicon substrates with Au films (100-nm-thick overlaying 10-nm-thick titanium adhesive layers) were purchased from Platypus Technologies (Madison, WI, USA). (11-Mercaptoundecyl) tri(ethylene glycol) (TEG) was purchased from Toronto Research Chemicals Inc. (Toronto, ON, Canada). (11-Mercaptoundecyl) hexa(ethylene glycol)amine (AEG) was obtained from ProChimia Surfaces (Sopot, Poland). Threo-3,4-dihydroxyphenylserine (*L*-DOPS or *L*-droxidopa) was purchased from TCI America Inc. (Portland, OR, USA). Fluorenylmethyloxycarbonyl chloride (Fmoc-Cl) was from Oakwood Products (West Columbia, SC, USA). Sodium carbonate ( $\text{Na}_2\text{CO}_3$ ) was purchased from Fisher Scientific. Dichloromethane (DCM) was obtained from Fisher Scientific and distilled over calcium hydride.

9-Fluorenylmethyloxycarbonyl-*L*-3,4-dihydroxyphenylalanine (Fmoc-*L*-DOPA-OH), 9-fluorenylmethyloxycarbonyl-5-hydroxy-*L*-tryptophan (Fmoc-*L*-5-HTP-OH), and *N*- $\alpha$ -(9-fluorenylmethyloxycarbonyl)-*N*-im-trityl-*L*-histidine (Fmoc-*L*-His(Trt)-OH) were from AnaSpec-Eurogentec (Fremont, CA, USA). The *N*- $\alpha$ -(9-fluorenylmethyloxycarbonyl)-*N*-in-*tert*-butyloxycarbonyl-*L*-tryptophan (Fmoc-*L*-Trp(Boc)-OH) and hexa(ethylene glycol) molecules were from ChemPep Inc. (Wellington, FL, USA). 11-Bromo-1-undecene, thioacetic acid ( $\text{CH}_3\text{COSH}$ ), triethylamine (TEA), triphenylphosphine ( $\text{Ph}_3\text{P}$ ), and *N,N*-diisopropylethylamine (DIEA) were purchased from Alfa Aesar (Ward Hill, MA, USA). The NHS, EDC, DMF, 4-methylpiperidine, BSA, 0.01 M PBS (138 mM NaCl, 2.7 mM KCl, 10 mM  $\text{Na}_2\text{HPO}_4$ , 1.8 mM  $\text{KH}_2\text{PO}_4$ , pH 7.4), and azobisisobutyronitrile (AIBN) were purchased from Sigma-Aldrich (St. Louis, MO, USA).

4-Toluenesulfonyl chloride (TsCl), 2,2'-dithiodipyridine (2-PDS), ammonia (7 N in MeOH), and trifluoroacetic acid (TFA) were from Acros Organics (Geel, Belgium). Anhydrous tetrahydrofuran (THF), anhydrous methanol (MeOH), and sodium azide (NaN<sub>3</sub>) were obtained from EMD Chemicals (Gibbstown, NJ, USA). Hydroxybenzotriazole (HOBT) was purchased from CreoSalus Inc. (Louisville, KY, USA). SYLGARD® 184 silicone elastomer kits were from Ellsworth Adhesives (Germantown, WI, USA). Absolute (200 proof) ethanol (EtOH) was purchased from Decon Laboratories, Inc. (King of Prussia, PA, USA). Deionized water (~18 MΩ) was obtained from a Millipore water purifier (Billerica, MA, USA).

Mouse monoclonal anti-*L*-3,4-dihydroxyphenylalanine antibody (ascites), rabbit polyclonal anti-*L*-5-hydroxytryptophan antibody (whole antiserum), rabbit polyclonal anti-*L*-histidine antibody (whole antiserum), and rat polyclonal anti-*L*-tryptophan antibody (pre-adsorbed antiserum) were purchased from Abcam Inc. (Cambridge, MA, USA). AlexaFluor® 546 goat anti-rabbit IgG (H+L) highly cross-adsorbed antibody (2 mg/mL), AlexaFluor® 568 goat anti-rat IgG (H+L) antibody (2 mg/mL), AlexaFluor® 488 goat anti-rabbit IgG (H+L) antibody (2 mg/mL), and AlexaFluor® 488 goat anti-mouse IgG (H+L) highly cross-adsorbed antibody (2 mg/mL) were purchased from Invitrogen (Carlsbad, CA, USA). All primary and secondary antibodies were diluted 1:200 and 1:100, respectively, with 0.01 M PBS pH 7.4 prior to incubation with substrates, unless stated otherwise.

## IV.B.2. Chemical Synthesis

### IV.B.2.a. Fmoc-*L*-DOPS-OH

A solution of 208.5 mg (0.98 mmol, 1 eq.) of *L*-DOPS in 10 mL of a 2:1 mixture of 10% aqueous Na<sub>2</sub>CO<sub>3</sub>/THF was cooled to 0 °C in an ice bath and a solution of Fmoc-Cl (278.9 mg, 1.08 mmol, 1.1 eq.) in THF (3.4 mL) was added dropwise. The reaction was stirred overnight at room temperature. The THF was evaporated under reduced pressure and the compound was extracted with ethyl acetate. The aqueous layer was acidified to pH 2 with 6 M HCl and was then extracted again with ethyl acetate. The organic extract was dried over magnesium sulfate, filtered, and then rotovapped to dryness. The oil was purified by silica gel chromatography (eluent: DCM/ethyl acetate 9:1 to 1:9 and DCM/MeOH 19:1) to give 344 mg of a light brown solid (79%). <sup>1</sup>H NMR (300 MHz, DMSO-*d*<sub>6</sub>, 25 °C): *d* (ppm) = 8.80 (s, 1 H), 8.75 (s, 1 H), 7.88 (d, 2 H, *J* = 7.6 Hz), 7.61-7.71 (m, 2 H), 7.25-7.45 (m, 4 H), 7.07 (d, 1 H, *J* = 9.2 Hz), 6.78 (s, 1 H), 6.62-6.66 (m, 2 H), 4.94 (m, 1 H), 4.05-4.24 (m, 4 H), 3.17 (d, 1 H, *J* = 5.04 Hz). Mass analysis (MALDI-TOF): *m/z* 458.9754 (calculated for C<sub>24</sub>H<sub>21</sub>NNaO<sub>7</sub> [M+Na]<sup>+</sup> *m/z* 458.1210).

### IV.B.2.b. Undec-1-en-11-ylhepta(ethylene glycol) (1)

Undec-1-en-11-ylhepta(ethylene glycol) was synthesized as previously described.<sup>25</sup> Hepta(ethylene glycol) (4.95 g, 15.2 mmol, 3 eq.) was treated with 606 mg of 50% aqueous sodium hydroxide solution (7.6 mmol, 1.5 eq.) for 30 min at 100 °C under argon, and then 11-bromo-1-undecene (1.18 g, 5.05 mmol, 1 eq.) was added. The solution was stirred for 24 h at 100 °C under argon, then cooled down. The organic mixture was extracted with DCM and purified by silica gel chromatography (eluent: ethyl acetate to remove the di-

functionalized molecule, then DCM/MeOH 19:1 to obtain the mono-functionalized molecule, and finally DCM/MeOH 9:1 to recover the non-modified hepta(ethylene glycol) giving 1.51 g of the mono-functionalized compound **1** (colorless oil, 63%).  $^1\text{H}$  NMR (300 MHz, deuterated chloroform ( $\text{CDCl}_3$ ), 25 °C):  $\delta$  (ppm) = 5.74-5.89 (m, 1 H), 4.89-5.04 (m, 2 H), 3.53-3.77 (m, 28 H), 3.44 (t, 2 H,  $J$  = 6.8 Hz), 2.67 (br s, 1 H), 2.04 (q, 2 H,  $J$  = 7.1 Hz), 1.57 (quin, 2 H,  $J$  = 7.0 Hz), 1.22-1.43 (m, 12 H). Mass analysis (MALDI-TOF):  $m/z$  501.2800 (calculated for  $\text{C}_{25}\text{H}_{50}\text{NaO}_8$   $[\text{M}+\text{Na}]^+$   $m/z$  501.3398).

#### IV.B.2.c. [1-[(Methylcarbonyl)thio]undec-11-yl]hepta(ethylene glycol) (**2**)

[1-[(Methylcarbonyl)thio]undec-11-yl]hepta(ethylene glycol) was synthesized as previously described with slight modifications.<sup>25</sup> Compound **1** (587.2 mg, 1.23 mmol, 1 eq.) was dissolved in 4 mL of anhydrous MeOH. Thioacetic acid (351 mL, 4.92 mmol, 4 eq.) and 10 mg of AIBN were added. The mixture was irradiated with a UV lamp (UVP XX-40 BLB, 40-watt, 365 nm) for 24 h. Afterwards, another 10 mg of AIBN was added and the reaction was stirred for an additional 24 h before concentration by rotary evaporation followed by purification by silica gel chromatography (eluent: ethyl acetate, then DCM/MeOH 19:1). Then 618.7 mg of compound **2** (91%) were obtained as a colorless oil.  $^1\text{H}$  NMR (300 MHz,  $\text{CDCl}_3$ , 25 °C):  $\delta$  (ppm) = 3.54-3.78 (m, 28 H), 3.44 (t, 2 H,  $J$  = 6.8 Hz), 2.86 (t, 2 H,  $J$  = 7.3 Hz), 2.77 (br s, 1 H), 2.32 (s, 3 H), 1.50-1.63 (m, 4 H), 1.21-1.41 (m, 14 H). Mass analysis (MALDI-TOF):  $m/z$  577.6519 (calculated for  $\text{C}_{27}\text{H}_{54}\text{NaO}_9\text{S}$   $[\text{M}+\text{Na}]^+$   $m/z$  577.3381).

**IV.B.2.d. [1-[(Methylcarbonyl)thio]undec-11-yl]-21-(tosyl)oxy-1,4,7,10,13,16,19-heptaioxaheneicosane (3)**

To a solution of compound **2** (1.29 g, 2.32 mmol, 1 eq.) in distilled DCM (2 mL), triethylamine (648 mL, 4.64 mmol, 2 eq.) was added. The solution was cooled to 0 °C in an ice bath and TsCl (663 mg, 3.48 mmol, 1.5 eq.) was added. The ice bath was then removed and the solution was allowed to warm to room temperature and react for 24 h. The resultant mixture was diluted in DCM (50 mL) and washed with 2% acetic acid solution and brine. The organic layer was dried with magnesium sulfate and then rotovapped to remove all remaining liquid. The compound was purified by silica gel chromatography (eluent: DCM/ethyl acetate 4:1-1:1). Then 1.26 g of compound **3** (76%) were obtained as a colorless oil. <sup>1</sup>H NMR (500 MHz, CDCl<sub>3</sub>, 25 °C):  $\delta$  (ppm) = 7.80 (d, 2 H, J = 8.1 Hz), 7.34 (d, 2 H, J = 8.1 Hz), 4.16 (t, 2 H, J = 4.9 Hz), 3.69 (t, 2 H, 4.9 Hz), 3.56-3.67 (m, 24 H), 3.44 (t, 2 H, J = 6.9 Hz), 2.86 (t, 2 H, J = 7.1 Hz), 2.45 (s, 3 H), 2.32 (s, 3 H), 1.52-1.62 (m, 4 H), 1.22-1.41 (m, 14 H). Mass analysis (MALDI-TOF): m/z 731.3299 (calculated for C<sub>34</sub>H<sub>60</sub>NaO<sub>11</sub>S<sub>2</sub> [M+Na]<sup>+</sup> m/z 731.3469).

**IV.B.2.e. [1-Mercaptoundec-11-yl]-21-azido-1,4,7,10,13,16,19-heptaioxaheneicosane (4)**

To a solution of compound **3** (1.26 g, 1.77 mmol, 1 eq.) in absolute EtOH (21 mL), NaN<sub>3</sub> (230 mg, 3.54 mmol, 2 eq.) was added. The solution was stirred at 85 °C overnight under argon. Afterward, the solution was cooled to room temperature. The solvent was carefully evaporated under reduced pressure; then the salts were precipitated in ethyl acetate and removed by filtration. The solution was rotovapped to dryness yielding 902.5 mg (94%) of



compound **4** (and its disulfide derivative) as colorless oil. The residue was used as is without further purification. The thioacetate group was cleaved inducing the formation of disulfide bonds (~50%).  $^1\text{H}$  NMR (500 MHz,  $\text{CDCl}_3$ , 25 °C):  $\delta$  (ppm) = 3.49-3.83 (m, 26 H), 3.44 (t, 2 H,  $J$  = 6.7 Hz), 3.39 (t, 2 H,  $J$  = 4.7 Hz), 2.68 (t, 2 H,  $J$  = 7.3 Hz,  $\text{CH}_2\text{-S-S}$ ), 2.52 (q, 2 H,  $J$  = 7.2 Hz,  $\text{CH}_2\text{-SH}$ ), 1.66 (quin, 2 H,  $J$  = 7.3 Hz), 1.57 (quin, 2 H,  $J$  = 7.5 Hz), 1.20-1.40 (m, 14 H). Mass analysis (MALDI-TOF):  $m/z$  560.3625 (calculated for  $\text{C}_{25}\text{H}_{51}\text{N}_3\text{NaO}_7\text{S}$   $[\text{M}+\text{Na}]^+$   $m/z$  560.3345) and  $m/z$  1095.7825 for the disulfide derivative (calculated for  $\text{C}_{50}\text{H}_{100}\text{N}_6\text{NaO}_{14}\text{S}_2$   $[\text{M}+\text{Na}]^+$   $m/z$  1095.6637).

**IV.B.2.f. [1-(Pyridin-2-yl)disulfanyl]undec-11-yl]-21-amino 1,4,7,10,13,16,19 heptaoheneicosane (amine hepta(ethylene glycol)-terminated undecanepyrindyl disulfide (7EG-PDS) (5)**

A solution of compound **4** (902.5 mg, 1.68 mmol, 1 eq.) in anhydrous THF (5 mL) was cooled to 0 °C in an ice bath and triphenylphosphine (818 mg, 3.12 mmol, 1.9 eq.) was added under argon. The ice bath was then removed and the solution was allowed to warm to room temperature and react for 24 h. The solvent was evaporated under reduced pressure and water was added to the mixture. The solution was filtered to remove precipitated triphenylphosphine oxide. The filtrate was then rotovapped to dryness yielding 1.03 g of a crude compound. The residue was dissolved in 20 mL of ammonia solution (7 N in MeOH), and 2-PDS (1.95 g, 8.85 mmol, 5.3 eq.) was added to the mixture under argon. The solution was stirred for 72 h at room temperature. The solvent was removed by rotary evaporation. The resultant mixture was diluted in DCM (100 mL) and washed with water. The organic layer was dried with magnesium sulfate and then

rotovapped to dryness. The compound was dissolved in water, washed with hexane (4 times) and lyophilized. Then 474 mg of compound **5** (45%) were obtained as a colorless oil.  $^1\text{H}$  NMR (500 MHz,  $\text{CDCl}_3$ , 25 °C):  $\delta$  (ppm) = 8.46 (d, 1 H,  $J$  = 4.7 Hz), 7.73 (d, 1 H,  $J$  = 8.2 Hz), 7.64 (t, 1 H,  $J$  = 7.0 Hz), 7.08 (t, 1 H,  $J$  = 6.2 Hz), 3.54-3.76 (m, 26 H), 3.44 (t, 2 H,  $J$  = 6.8 Hz), 2.99 (t, 2 H,  $J$  = 4.1 Hz), 2.79 (t, 2 H,  $J$  = 7.2 Hz), 1.68 (quin, 2 H,  $J$  = 7.2 Hz), 1.56 (quin, 2 H,  $J$  = 6.4 Hz), 1.19-1.45 (m, 14 H). Mass analysis (MALDI-TOF):  $m/z$  621.3679 (calculated for  $\text{C}_{30}\text{H}_{57}\text{N}_2\text{O}_7\text{S}_2$   $[\text{M}+\text{H}]^+$   $m/z$  621.3602).

#### IV.B.2.g. Fmoc-*L*-DOPA-7EG-PDS (**6a**)

Fmoc-*L*-DOPA-OH (88 mg, 0.21 mmol, 1.1 eq.) was coupled to 7EG-PDS compound (**5**) (120 mg, 0.19 mmol, 1 eq.) according to the general procedure described above. Then 81 mg of compound **6a** (42%) were obtained as a colorless oil.  $^1\text{H}$  NMR (300 MHz,  $\text{CDCl}_3$ , 25 °C):  $\delta$  (ppm) = 8.45 (m, 1 H), 7.25-7.76 (m, 10 H), 7.05-7.10 (m, 1 H), 6.56-6.84 (m, 3 H), 6.03 (m, 1 H), 5.70 (m, 1 H), 4.18-4.44 (m, 4 H), 3.51-3.74 (m, 28 H), 3.42 (t, 2 H,  $J$  = 6.8 Hz), 3.04-3.20 (m, 2 H), 2.79 (t, 2 H,  $J$  = 7.2 Hz), 1.68 (quin, 2 H,  $J$  = 7.6 Hz), 1.55 (quin, 2 H,  $J$  = 7.0 Hz), 1.20-1.40 (m, 14 H). Mass analysis (MALDI-TOF):  $m/z$  1022.6145 (calculated for  $\text{C}_{54}\text{H}_{76}\text{N}_3\text{O}_{12}\text{S}_2$   $[\text{M}+\text{H}]^+$   $m/z$  1022.4865).

#### IV.B.2.h. Fmoc-*L*-5-HTP-7EG-PDS (**6b**)

Fmoc-*L*-5-HTP-OH (140.7 mg, 0.32 mmol, 1.1 eq.) was coupled to 7EG-PDS compound (**5**) (179.5 mg, 0.29 mmol, 1 eq.) according to the general procedure described above. Then 133 mg of compound **6b** (44%) were obtained as a colorless oil.  $^1\text{H}$  NMR (500 MHz,  $\text{CDCl}_3$ , 25 °C):  $\delta$  (ppm) = 8.73 (s, 1 H), 8.46 (m, 1 H), 7.19-7.80 (m, 12 H), 7.02-7.09 (m, 2 H), 6.80

(m, 1 H), 6.23 (br s, 1 H), 6.14 (br s, 1 H), 5.87 (m, 1 H), 4.35-4.50 (m, 3 H), 4.23 (t, 1 H,  $J = 7.1$  Hz), 3.45-3.71 (m, 28 H), 3.42 (t, 2 H,  $J = 6.9$  Hz), 3.16-3.40 (m, 1 H), 3.00-3.08 (m, 1 H), 2.78 (t, 2 H,  $J = 7.0$  Hz), 1.68 (quin, 2 H,  $J = 7.3$  Hz), 1.55 (quin, 2 H,  $J = 6.9$  Hz), 1.19-1.41 (m, 14 H). Mass analysis (MALDI-TOF):  $m/z$  1067.5042 (calculated for  $C_{56}H_{76}N_4NaO_{11}S_2$   $[M+Na]^+$   $m/z$  1067.4844).

#### IV.B.2.i. Fmoc-*L*-His-7EG-PDS (**6c**)

Fmoc-*L*-His(Trt)-OH (105.3 mg, 0.17 mmol, 1.1 eq.) was coupled to 7EG-PDS compound (**5**) (97.4 mg, 0.15 mmol, 1 eq.) according to the general procedure described above with a minor change. Before purification by column chromatography, the Trt protecting group was cleaved with 20% trifluoroacetic acid solution in DCM for 1 h at room temperature. The mixture was diluted with DCM, washed with saturated aqueous sodium bicarbonate ( $3 \times$  eq. vol.), dried with magnesium sulfate, and then rotovapped to dryness. The compound was purified by silica gel chromatography (eluent: DCM/ethyl acetate 9:1 to 1:9 and DCM/MeOH 9:1). Then 56.3 mg of compound **6c** (37%) were obtained as a colorless oil.  $^1H$  NMR (300 MHz,  $CDCl_3$ , 25 °C):  $\delta$  (ppm) = 8.46 (m, 1 H), 7.25-7.79 (m, 11 H), 7.07 (m, 1 H), 6.96 (m, 1 H), 6.55 (m, 1 H), 4.57 (m, 1 H), 4.32-4.41 (m, 2 H), 4.22 (t, 1 H,  $J = 7.1$  Hz), 3.46-3.72 (m, 28 H), 3.41 (t, 2 H,  $J = 7.0$  Hz), 3.00-3.34 (m, 2 H), 2.79 (t, 2 H,  $J = 7.1$  Hz), 1.68 (quin, 2 H,  $J = 7.7$  Hz), 1.54 (quin, 2 H,  $J = 6.6$  Hz), 1.17-1.45 (m, 14 H). Mass analysis (MALDI-TOF):  $m/z$  1002.4191 (calculated for  $C_{51}H_{73}N_5NaO_{10}S_2$   $[M+Na]^+$   $m/z$  1002.4691).

#### IV.B.2.j. Fmoc-L-DOPS-7EG-PDS (**6d**)

Fmoc-L-DOPS-OH (94.4 mg, 0.22 mmol, 1.1 eq.) was coupled to **7EG-PDS (5)** (122.6 mg, 0.21 mmol, 1 eq.) according to the general procedure described above. Then 76 mg of compound **6d** (37%) were obtained as a colorless oil. <sup>1</sup>H NMR (300 MHz, CDCl<sub>3</sub>, 25 °C): *d* (ppm) = 8.47 (m, 1 H), 7.25-7.81 (m, 10 H), 7.06-7.15 (m, 2 H), 6.83 (d, 1 H, *J* = 7.9 Hz), 6.65 (d, 1 H, *J* = 7.9 Hz), 6.23 (br s, 1 H), 5.87 (br s, 1 H), 4.99 (m, 1 H), 4.46 (m, 2 H), 4.37 (m, 1 H), 4.24 (t, 1 H, *J* = 6.7 Hz), 3.48-3.78 (m, 28 H), 3.44 (t, 2 H, *J* = 7.0 Hz), 3.25 (m, 1 H), 2.80 (t, 2 H, *J* = 7.3 Hz), 1.63-1.79 (m, 2 H), 1.57 (quin, 2 H, *J* = 7.2 Hz), 1.22-1.42 (m, 14 H). Mass analysis (MALDI-TOF): *m/z* 1060.1505 (calculated for C<sub>54</sub>H<sub>75</sub>N<sub>3</sub>NaO<sub>12</sub>S<sub>2</sub> [M+Na]<sup>+</sup> *m/z* 1060.4634).

#### IV.B.2.k. Fmoc-L-Trp-7EG-PDS (**6e**)

Fmoc-L-Trp(Boc)-OH (106 mg, 0.20 mmol, 1 eq.) was coupled to 7EG-PDS compound (**5**) (125 mg, 0.20 mmol, 1 eq.) according to the general procedure described above with a minor change. Before purification by column chromatography, the Boc protecting group was cleaved with 20% TFA solution in DCM for 1 h at room temperature. The mixture was diluted with DCM, washed with saturated aqueous sodium bicarbonate (3 × eq. vol.), dried with magnesium sulfate, and then rotovapped to dryness. The compound was purified by silica gel chromatography (eluent: DCM/ethyl acetate 9:1 to 1:9 and DCM/MeOH 9:1). Then 129 mg of compound **6e** (63%) were obtained as a colorless oil. <sup>1</sup>H NMR (500 MHz, CDCl<sub>3</sub>, 25 °C): *d* (ppm) = 9.20 (s, 1 H), 8.45 (m, 1 H), 7.25-7.81 (m, 13 H), 7.04-7.21 (m, 2 H), 5.92 (m, 1 H), 5.83 (m, 1 H), 4.35-4.48 (m, 2 H), 4.23 (t, 1 H, *J* = 7.4 Hz), 3.45-3.75 (m, 28 H), 3.44

(t, 2 H, J = 6.8 Hz), 3.03-3.38 (m, 2 H), 2.78 (t, 2 H, J = 7.5 Hz), 1.68 (quin, 2 H, J = 7.5 Hz), 1.55 (quin, 2 H, 7.0 Hz) 1.18-1.42 (m, 14 H). Mass analysis (MALDI-TOF): m/z 1029.6008 (calculated for C<sub>56</sub>H<sub>77</sub>N<sub>4</sub>O<sub>10</sub>S<sub>2</sub> [M+H]<sup>+</sup> m/z 1029.5076).

#### **IV.B.3. General Procedure for the Coupling of Fmoc-Protected Neurotransmitter (Fmoc-R) to 7EG-PDS Compound (6)**

Fmoc-R (1-1.1 eq.) was pre-activated in DCM or DMF (95-105 mM) with DIEA (3 eq.), HOBT (1.2 eq.), and EDC (1.2 eq.) for 30 min under argon. Thereafter, a 95 mM solution of compound **5** in DCM was added to the mixture. The solution was stirred for 24 h under argon at room temperature. The resultant mixture was diluted in DCM and washed with brine. The organic layer was dried with magnesium sulfate and then rotovapped to remove all remaining liquid. The compound was purified by silica gel chromatography (eluent: DCM/ethyl acetate 9:1 to 1:9 and DCM/MeOH 19:1).

#### **IV.B.4. Substrate Preparation and Chemical Lift-Off Lithography**

The Au substrates were hydrogen-flame annealed and then immersed in ethanolic solutions of 0.5 mM TEG for ~18 h for initial SAM formation. After self-assembly, substrates were rinsed with ethanol and blown dry with nitrogen gas. The polydimethylsiloxane (PDMS) stamps were prepared by thoroughly mixing a 10:1 mass ratio of SYLGARD® 184 silicone elastomer base and curing agent, respectively, in a plastic cup. Mixtures were degassed under vacuum to remove bubbles and cast onto photolithographically fabricated silicon master substrates situated in plastic Petri dishes. Elastomeric mixtures and silicon

masters were baked at 70 °C in an oven for ~20 h. Polymerized PDMS stamps were removed from the masters and cut into smaller sizes for easy handling.

To prepare for lift-off lithography, PDMS stamps were exposed to oxygen plasma (power 18 W, oxygen pressure 10 psi, Harrick Plasma, Ithaca, NY, USA) for 40 s to generate reactive siloxyls on stamp surfaces.<sup>9</sup> Activated stamps were brought immediately into conformal contact with TEG-modified Au substrates for ~17 h. After stamp removal, post-lift-off substrates were rinsed thoroughly with ethanol. Preliminary experiments were carried out to investigate the effects of varying incubation (insertion) times (0.25 h-24 h) using *L*-DOPA pre-functionalized thiols (Figure SC.1). Since fluorescence intensities were maximal and did not differ between the 3 h and 24 h time points, patterned substrates were submerged in ethanolic solutions of 0.5 mM pre-functionalized thiols for 3 h for the remainder of the experiments in the study.

For post-functionalization, post-lift-off substrates were submerged in ethanolic solutions of 0.5 mM AEG for 3 h followed by on-substrate neurotransmitter conjugation. To vary the amounts of inserted pre-functionalized thiols or AEG, each was co-incubated in varying proportions with TEG such that total solution concentrations were 1.0 mM. After insertion, substrates were rinsed with ethanol and blown dry with nitrogen gas. Substrates with AEG tethers were incubated with 60/40 DMF/deionized water solutions of 35 mM Fmoc-protected neurotransmitter/NHS/EDC for 3 h. After post-functionalization, substrates were rinsed with ethanol and dried with nitrogen gas.

To generate patterns having two different surface-tethered neurotransmitters, PDMS stamps were used to lift-off TEG SAM molecules twice.<sup>9,10</sup> After the first lift-off step, substrates were inserted with either AEG tethers or pre-functionalized molecules. For the

second lift-off step, PDMS stamps were used to lift-off TEG SAM molecules from spatially non-overlapping regions adjacent to previously patterned regions on the same substrates. The post-double-lift-off substrates were then inserted with either pre-functionalized molecules or AEG tethers, respectively. For post-patterning functionalization, AEG was co-deposited with TEG at a 75%/25% ratio for *L*-5-HTP and 100%/0% AEG/TEG for *L*-DOPA. In both cases, neurotransmitter conjugation was carried out immediately following the AEG insertion steps.

The Fmoc groups used to protect amino moieties during chemical synthesis of pre-functionalized molecules were removed after surface deposition by immersing substrates in 20% 4-methylpiperidine in deionized water for 15 min. Amino moieties of neurotransmitter precursors were also protected by Fmoc to provide protection from competing reactions during post-functionalization. After rinsing with deionized water, all neurotransmitter-modified substrates were incubated with 10 mg/mL BSA for 5 min to reduce nonspecific adsorption of target proteins.<sup>2</sup> Substrates were then completely submerged in deionized water in plastic Petri dishes and gently agitated. This step was repeated using fresh deionized water prior to exposing substrates to antibody solutions. Substrates were always covered with deionized water or antibody solutions. Keeping the substrates wet reduced the likelihood for captured antibodies to denature or to dissociate from substrates.

#### **IV.B.5. Antibody Binding**

Primary and secondary antibodies (Table S1) were diluted 1:200 and 1:100, respectively in 0.01 M PBS. Primary antibodies were incubated with substrates for 20 min, followed by incubation with fluorescently labeled secondary antibodies for 20 min at room temperature.<sup>2</sup> Substrates in plastic Petri dishes were incubated in the dark to reduce photobleaching of dye-labeled secondary antibodies. An inverted fluorescence microscope (Axio Observer.D1) equipped with an AxioCam MRm charged-coupled device camera was used to image substrates (Carl Zeiss MicroImaging, Inc., Thornwood, NY, USA). Two fluorescence filter sets, 38 HE/high efficiency with excitation and emission wavelengths of  $470 \pm 20$  nm and  $525 \pm 25$  nm, respectively, and 43 HE/high efficiency with excitation and emission wavelengths of  $550 \pm 25$  nm and  $605 \pm 70$  nm, respectively, were used to visualize secondary antibody binding on substrates. Fluorescence images were collected using a 10× objective lens.

Fluorescence intensities were determined by performing line scans at a 30-pixel scanning width using AxioVs40 version 4.7.1.0 software (Carl Zeiss MicroImaging, Inc., Thornwood, NY, USA). On average, five line scans were acquired per substrate. All substrates from the same experiment were imaged using the same exposure times to standardize contrast and brightness. Fluorescence intensities were normalized to values for control (unpatterned) regions for each substrate and are reported in relative fluorescence units (RFU) for multiple substrates ( $N=3$  per condition). Fluorescence images shown in the figures are those that most closely represented mean fluorescence intensities. For control experiments where primary antibodies were omitted, representative images were acquired using maximum exposure times to facilitate visualization.



#### **IV.B.6. Statistics**

Differences in relative fluorescence data were evaluated by one-way analysis of variance followed by Tukey's *post hoc* tests (multiple group comparisons) or Student's *t*-tests (two-group comparisons) using Prism Version 5.02 (GraphPad Software Inc., San Diego, USA). Relative fluorescence intensities are reported as means  $\pm$  standard errors of the means with probabilities  $P < 0.05$  considered statistically significant.

## IV.C. Results and Discussion

### IV.C.1. Synthesis of Pre-Functionalized Molecules

The availability of functional oligo(ethylene glycol)-terminated alkanethiols is limited and none of the molecules needed for this study were commercially available. Thus, we devised a novel synthetic route as shown in Scheme IV.1. Hepta(ethylene glycol) was monoetherified with 11-bromo-1-undecene. A large excess of hepta(ethylene glycol) was used to favor monosubstitution,<sup>26</sup> whereas a stoichiometric equivalent of both reagents generally yielded a statistical proportion of unmodified, mono-, and disubstituted molecules. Monoetherification was achieved according to an established protocol<sup>25</sup> using a three-fold excess of hepta(ethylene glycol) compared to 11-bromo-1-undecene with a slight excess of 50% sodium hydroxide to give compound **1** in 63% yield. The terminal olefin then underwent a photoinitiated thiol-ene reaction with thioacetic acid in the presence of AIBN to give compound **2** in good yield (91%). The terminal alcohol was converted to a tosylate leaving group (compound **3**), which was subsequently reacted with sodium azide to provide compound **4** with a yield of 94%.

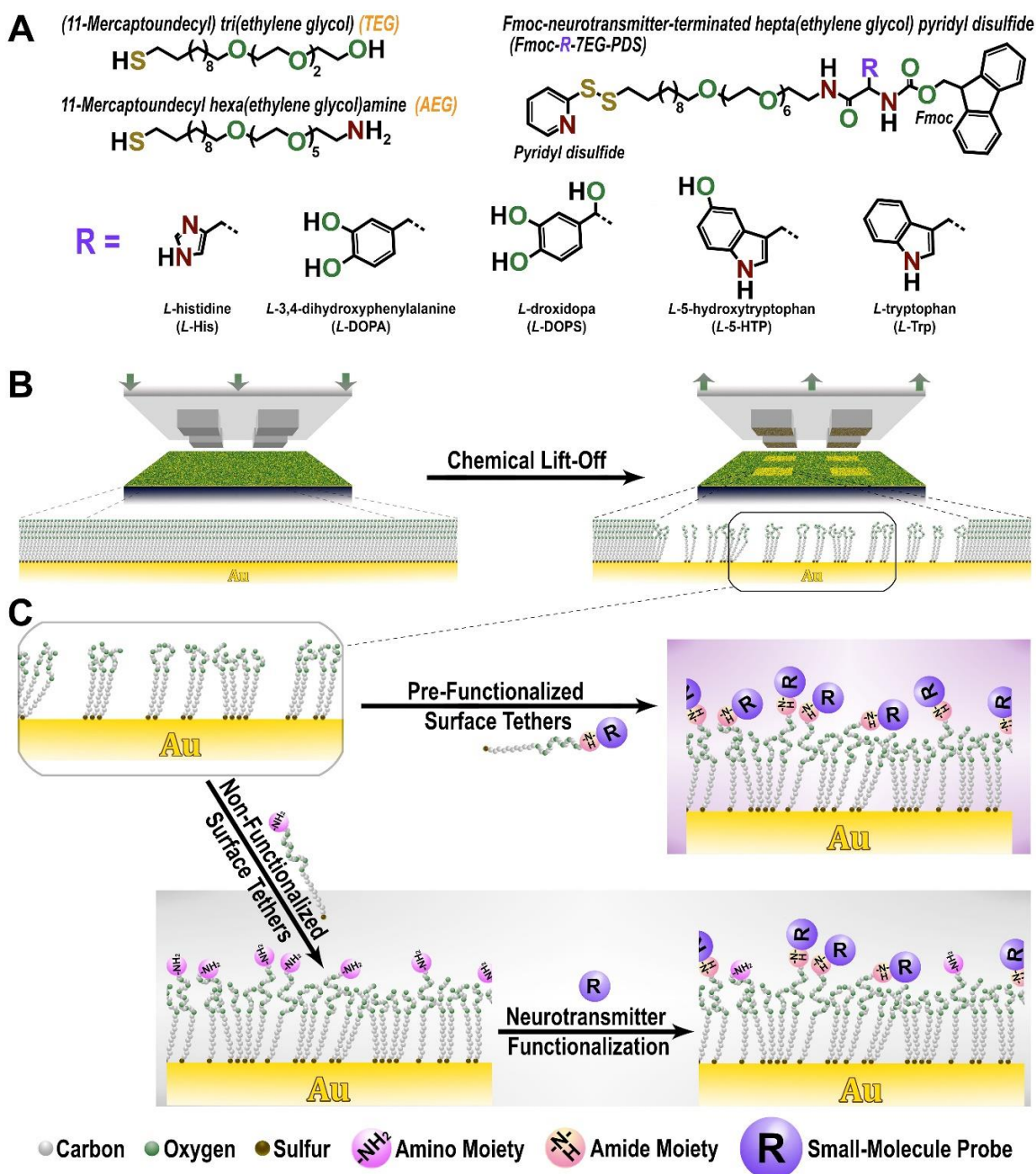


**Figure IV.1.** (A) Chemical structures of oligo(ethylene glycol)alkanethiol tethers (TEG and AEG) and neurotransmitter pre-functionalized molecules (Fmoc-R-7EG-PDS). Pre-functionalized molecules consisted of pyridyl disulfide (PDS) head groups for self-assembly on Au surfaces, hepta(ethylene glycol)undecyl backbones (7EG) to resist nonspecific binding of biomolecule targets, neurotransmitter precursors (R) tail groups for biomolecule capture, and 9-fluorenylmethoxycarbonyl groups (Fmoc) to protect amino moieties during synthesis and self-assembly. The carboxyl groups of the neurotransmitter precursors were linked to 7EG backbones *via* amide bonds. (B) Polydimethylsiloxane stamps were treated with oxygen plasma to generate siloxyl groups for reaction with hydroxyl tri(ethylene glycol)-terminated alkanethiol (TEG) self-assembled monolayers (SAM) on Au surfaces. During stamp/SAM contact, stamps removed ~70% of TEG molecules and associated underlying Au atoms in the contacted areas.<sup>34</sup> (C) Schematics (not to scale) of general patterning and functionalization strategies. Pre-functionalized tethers or tethers amenable to neurotransmitter post-functionalization were inserted into post-lift-off regions.



groups were selected because of their selectivity toward thiols and their reactivity with Au surfaces.<sup>27</sup> Finally, the terminal amine was coupled to Fmoc-R to form an amide bond using standard coupling agents (HOBt and EDC in the presence of DIEA). The side-chain protecting groups of *L*-His and *L*-Trp, trityl (Trt) and *tert*-butyloxycarbonyl (Boc) groups, respectively, were removed with 20% TFA in DCM. The final pre-functionalized molecules (Fmoc-R-7EG-PDS) were obtained in 37-63% yields depending on the neurotransmitter R-group.

Although there are literature reports of the synthesis of oligo(ethylene glycol)-terminated alkanethiols,<sup>25,26,28,29</sup> few studies have reported on pre-functionalization of these tethers with biologically *active* small molecules.<sup>30-33</sup> To the best of our knowledge, pre-functionalization with neurotransmitters or their precursors has not been reported.

#### **IV.C.2. Patterning Pre- vs. Post-Functionalized Molecules with Lift-Off Lithography**

Chemical lift-off lithography was used to pattern TEG SAMs, which functioned as biomolecule-resistant background matrices (Figure IV.1B). Following lithography, which removes ~70% of TEG in the contact regions,<sup>9,16,34,35</sup> pre-functionalized molecules were inserted into the post-lift-off regions (Figure IV.1C). For post-functionalization, AEG tethers were inserted into the post-lift-off regions. Functionalization with Fmoc-protected neurotransmitters (Fmoc-R) *via* amide bond formation was then carried out directly on substrates.<sup>1,2</sup> Prior to biomolecule binding, Fmoc protecting groups were removed from pre- and post-functionalized molecules to reveal epitopes needed for molecular recognition.

Oxygen plasma-treated PDMS stamps patterned with  $25 \times 25 \mu\text{m}^2$  square-shaped protruding features separated by  $25 \mu\text{m}$  spacings were used for lift-off lithography.<sup>9,10</sup> Because SAM molecules are removed only in the stamp-contact regions, patterns of negative, recessed squares were created on Au surfaces. Post-lift-off surfaces were exposed to varying ratios of TEG and pre-functionalized molecules, or TEG and AEG tether molecules followed by post-functionalization. The goal of these experiments was to determine insertion compositions resulting in maximal biomolecule/antibody recognition.

Following patterning, insertion, and surface functionalization (post-functionalized molecules), primary antibodies against each probe were captured on substrates. Primary antibody binding was visualized *via* additional capture of fluorescently labeled secondary antibodies (Table SC.1). Fluorescent square patterns against dark biomolecule-resistant TEG backgrounds resulted from antibody capture (Figure IV.2). As nominal solution ratios of *L*-DOPA or *L*-5-HTP pre-functionalized molecules were increased relative to TEG, fluorescence intensities also increased (Figure IV.2A,B left to right). For pre-functionalized molecules, maximal fluorescence intensities were observed at 100% pre-functionalized molecule ratios for *L*-DOPA and *L*-5-HTP. Substrates exposed to fluorescently labeled secondary antibodies in the absence of primary antibodies showed negligible fluorescence indicating minimal secondary antibody recognition of *L*-DOPA or *L*-5-HTP pre-functionalized molecules (Figure SC.2a,b).

Fluorescence intensities were hypothesized to increase proportionally with increasing fractions of pre-functionalized molecules, assuming equal probabilities of TEG vs. pre-functionalized molecule insertion on post-lift-off substrates. This hypothesis also assumes that primary antibody-probe binding follows a 1:1 stoichiometry such that

fluorescence intensities in Figure IV.2 are representative of surface densities of probe molecules. However, as quantified in Figure IV.3A,B, fluorescence signals were not linearly proportional to increasing fractions of pre-functionalized molecules.

A number of factors likely contributed to this behavior, including differences in the rates of diffusion of the respective molecules to surfaces, steric hindrance arising as the larger pre-functionalized molecules approach surfaces, and differences in miscibility (*i.e.*, pre-functionalized molecules may be less miscible with TEG remaining in the lift-off regions).<sup>16</sup> Additionally, pyridyl disulfides are bulkier and require disulfide cleavage upon adsorption on Au substrates.<sup>27,36</sup> Previous studies of competitive adsorption have shown that adsorption of thiols is about two orders of magnitude faster than adsorption of disulfides.<sup>37,38</sup> In any case, these results demonstrate that co-incubation with TEG is not necessary for maximal insertion and recognition of pre-functionalized molecules; the TEG molecules remaining in the post-lift-off regions appear to provide the dilution needed to achieve maximal antibody binding.



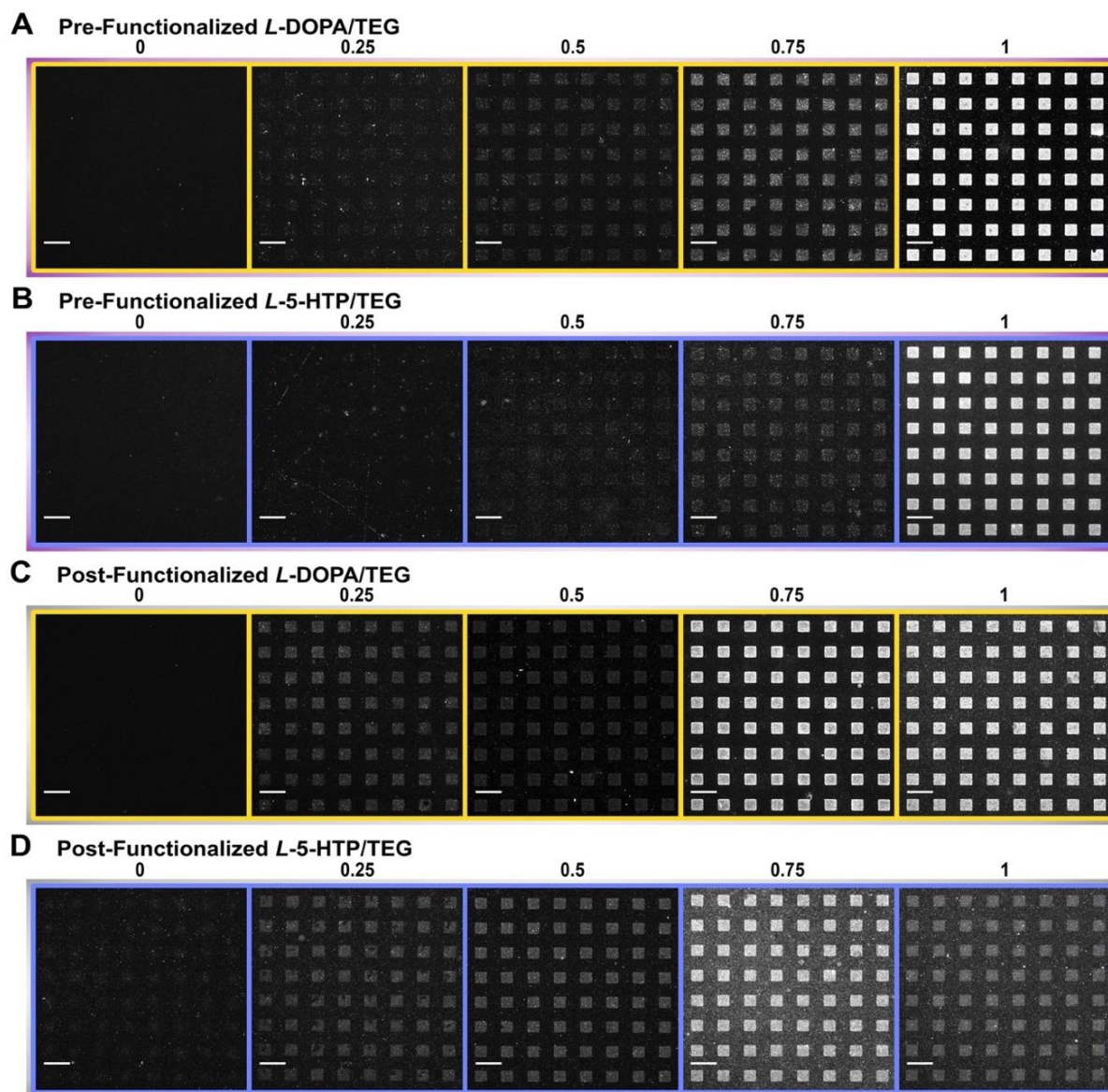


**Figure IV.2.** Representative fluorescence images showing lift-off lithography patterned self-assembled monolayers (SAMs) consisting of (A,B) inserted neurotransmitter (*i.e.*, *L*-3,4-dihydroxyphenylalanine (*L*-DOPA) or *L*-5-hydroxytryptophan (*L*-5-HTP)) pre-functionalized molecules or (C,D) inserted tethers with post-functionalized neurotransmitters. Solution ratios of inserted pre-functionalized molecules or amine-terminated hexa(ethylene glycol)alkanethiol (AEG) tethers vs. hydroxyl-terminated tri(ethylene glycol)alkanethiol (TEG) are shown above each image. Substrates were imaged at an emission wavelength of 525 nm (AlexaFluor® 488 with excitation at 490 nm) to visualize secondary antibodies, which recognize primary antibodies captured on patterned substrates. Scale bars are 50  $\mu$ m.



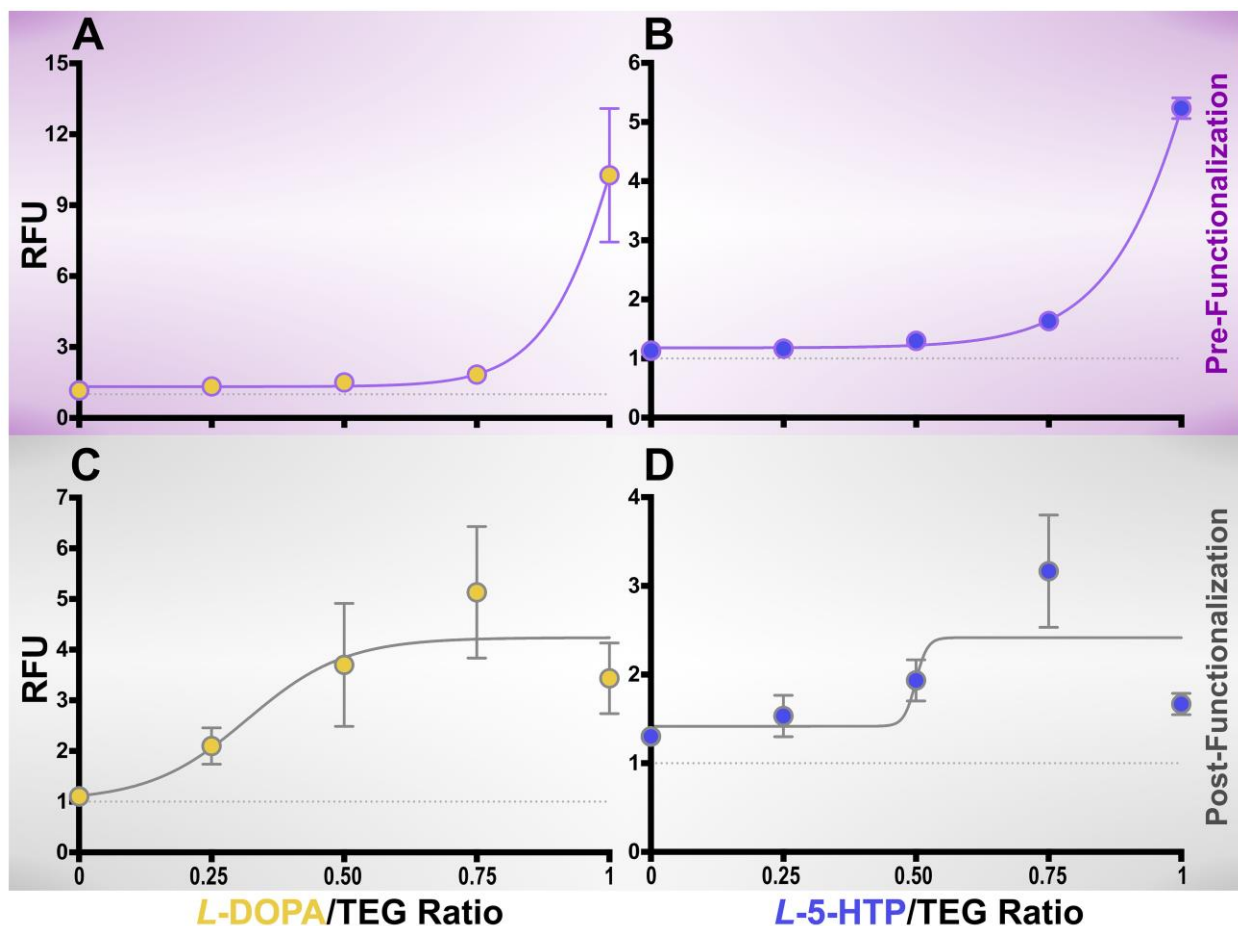


**Figure IV.3.** Relative fluorescence intensities (RFU) vs. solution fractions of (A,B) pre-functionalized and (C,D) post-functionalized molecules relative to hydroxyl-terminated tri(ethylene glycol)alkanethiol (TEG). Data for *L*-3,4-dihydroxyphenylalanine (*L*-DOPA) are shown in (A,C); data for *L*-5-hydroxytryptophan (*L*-5-HTP) are in (B,D). Relative fluorescence intensities rose marginally with increasing fractions of pre-functionalized molecules suggesting preferential adsorption of TEG except where post-lift-off substrates were exposed to 100% pre-functionalized molecules, which resulted in maximal fluorescence intensities. Relatively small standard errors for the data in (A,B) suggest reproducible insertion and antibody recognition of pre-functionalized molecules. By contrast, relative fluorescence intensities for post-functionalized molecules rose less steeply and at lower fractions of tether molecules during self-assembly in (C) for *L*-DOPA and (D) for *L*-5-HTP, where maximal fluorescence intensities were observed at <100% amine-terminated hexa(ethylene glycol)alkanethiol (AEG)/TEG ratios for *L*-DOPA/*L*-5-HTP functionalization. Error bars for replicate samples were comparatively larger for post-functionalized vs. pre-functionalized approaches suggesting greater variability across substrates for post-functionalization. Error bars are standard errors of the means with  $N=3$  samples per datum and are too small to be visualized in some cases.

Similar patterning and antibody capture procedures were carried out in conjunction with post-functionalization (Figure IV.2C,D). Behavior with respect to nominal AEG tether/TEG ratios was different from that observed with pre-functionalized molecules (Figure IV.2A,B). As seen in Figure IV.3C, fluorescence intensities increased at low AEG proportions, approaching a plateau at 50% *L*-DOPA. For *L*-5-HTP (Figure IV.3D), fluorescence intensities peaked at the 25% ratio and reached a plateau. Similar to pre-functionalized substrates, negligible secondary antibody recognition of substrates post-functionalized with *L*-DOPA or *L*-5-HTP was observed (Figure SC.2c,d).

For post-functionalized molecules, neurotransmitters were conjugated to surface tethers after the latter were inserted into post-lift-off regions. As such, antibody binding depends on surface tether densities *and* the efficiency of the NHS/EDC coupling chemistry in attaching *L*-DOPA or *L*-5-HTP to substrates. While we cannot differentiate the contributions of these two factors here, we hypothesize that incomplete on-substrate functionalization is the major contributor to differences in the functionalization strategies for two reasons. First, unlike pre-functionalized molecules, AEG tethers do not possess bulky Fmoc-protected neurotransmitters or pyridyl disulfides. As such, they resemble TEG molecules more closely than do pre-functionalized molecules (Figure IV.1A). Therefore, insertion of AEG was expected to follow solution ratios more closely.

Second, for NHS/EDC surface-coupling, specific conditions including pH, solvents, reagent concentrations, and incubation times must be optimized for individual probes.<sup>19</sup> Side reactions and hydrolysis of NHS esters can result in lower probe conjugation.<sup>17,18</sup> Notably, maximal post-functionalized *L*-DOPA relative fluorescence was only half that observed for pre-functionalized *L*-DOPA. The comparative situation was more striking for

post- vs. pre-functionalized *L*-5-HTP. Together, these observations lead us to tentatively conclude that submaximal functionalization of tethers occurs for post-functionalized substrates. Greater variabilities in post-functionalization efficiencies might also to the larger error terms for post-functionalized substrates (Figure IV.3C,D) vs. pre-functionalized substrates (Figure IV.3A,B).

#### **IV.C.3. Side-by-Side Comparisons of Pre- vs. Post-functionalized Approaches**

A key hypothesis in this study was that pre-functionalizing neurotransmitters to surface tethers prior to self-assembly improves specific recognition by biomolecule targets. To test this idea in a different way, we compared pre- vs. post-functionalization approaches *on the same substrates*. Lift-off lithography was carried out twice, side-by-side on each substrate, resulting in two possible patterning routes. For the first route, neurotransmitter pre-functionalized molecules were inserted into post-lift-off regions first, followed by a second lift-off step in an adjacent region, insertion of AEG tethers, and post-functionalization (Figure IV.4A). The second route involved inserting AEG tethers into post-lift-off substrates followed by probe conjugation. Another lift-off step was performed in an adjacent region on each substrate and neurotransmitter pre-functionalized molecules were inserted into the newly generated post-lift-off areas, *i.e.*, post-functionalization followed by pre-functionalization (Figure SC.3A).

For the first patterning route, *L*-DOPA relative fluorescence intensities were similar for pre- vs. post-functionalization, while *L*-5-HTP relative fluorescence intensities were higher for pre- vs. post-functionalization (Figure IV.4B-D). By contrast, for the reverse, similar relative fluorescence intensities were observed for both neurotransmitters,

regardless of tethering strategy. Capture surfaces exposed to secondary antibodies alone showed negligible fluorescence patterns regardless of patterning order (Figure SC.4).

For the most part, neurotransmitter pre-functionalized molecules displayed consistent levels of antibody binding independent of patterning order. However, while recognition of post-functionalized *L*-DOPA was similar between patterning routes, antibody recognition of *L*-5-HTP post-functionalized molecules was reduced compared to pre-functionalized molecules when the latter were patterned first. (There was a trend toward reduced fluorescence intensity for *L*-5-HTP post-functionalized molecules for the reverse patterning order ( $P < 0.08$ )). These findings support the hypothesis that pre-functionalized molecules can be used to improve/increase specific biomolecule recognition of tethered small molecules. However, they also suggest that improvements depend on specific probes. For example, NHS/EDC coupling chemistry may be more efficient for *L*-DOPA than for *L*-5-HTP. Thus, the levels of antibody binding for *L*-DOPA post-functionalized substrates could not be further improved using pre-functionalized molecules.

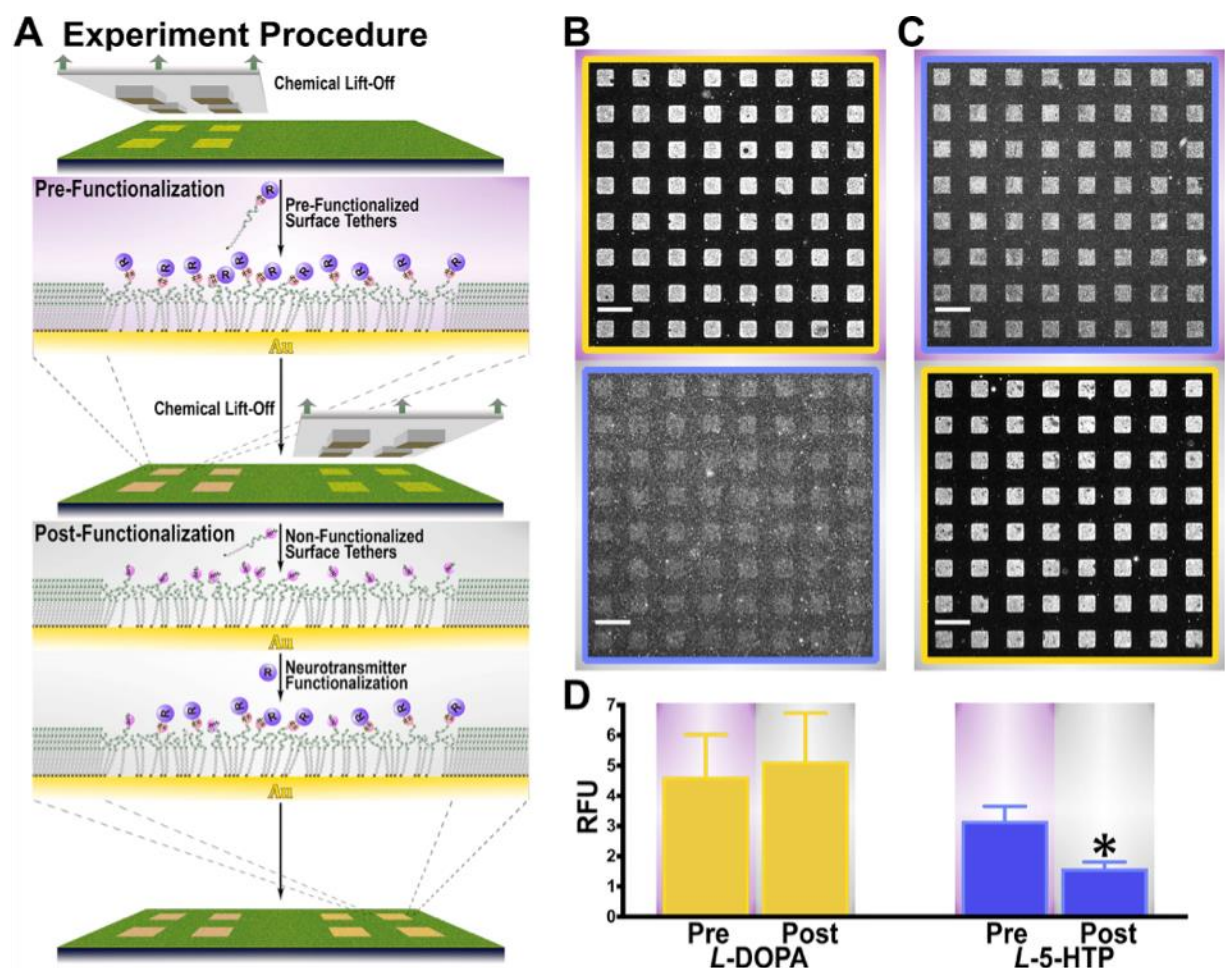


**Figure IV.4.** (A) Schematic illustrating double lift-off patterning of post- followed by pre-functionalized molecules. Tether molecules are inserted after the first lift-off step and post-functionalized followed by insertion of pre-functionalized molecules in an adjacent region after a second lift-off step. (B,C) Representative fluorescence images and (D) relative fluorescence intensities for antibody binding on double patterns of *L*-3,4-dihydroxyphenylalanine (*L*-DOPA) and *L*-5-hydroxytryptophan (*L*-5-HTP). (D) Similar relative fluorescence intensities were observed for *L*-DOPA in pre-functionalized regions compared to post-functionalized regions. By contrast, lower relative fluorescence intensities were observed for *L*-5-HTP in post-functionalized regions compared to *L*-5-HTP in pre-functionalized regions. Substrates were imaged at an emission wavelength of 525 nm (AlexaFluor® 488 with excitation at 490 nm). Error bars are standard errors of the means with  $N=3$  samples per group. Mean intensities are significantly different for *L*-5-HTP  $t(4)=3$  \* $P<0.05$ . Scale bars are 50  $\mu\text{m}$ .

#### IV.C.4. Multiplexed Pre-Functionalized Substrates

Pre-functionalized molecules circumvent the need for sequential and compatible on-substrate coupling chemistries. Thus, we investigated the use of pre-functionalized molecules to create multiplexed neurotransmitter-modified substrates. Side-by-side double lift-off lithography was used to pattern *L*-DOPA and *L*-5-HTP pre-functionalized molecules on the same substrates. Substrates were exposed to primary antibody solutions containing both mouse anti-*L*-DOPA monoclonal antibodies and rabbit anti-*L*-5-HTP polyclonal antibodies. Primary antibody binding was visualized *via* exposure to solutions containing AlexaFluor® 488 (peak emission at 519 nm; “green”) anti-mouse and AlexaFluor® 546 (peak emission at 573 nm; “red”) anti-rabbit secondary antibodies. We hypothesized that primary and secondary antibodies would sort to their respective binding partners so that *L*-DOPA patterned regions would be labeled with green fluorescence and *L*-5-HTP patterned regions labeled with red fluorescence.

Anti-*L*-DOPA antibodies were selective in terms of their recognition of surface-tethered *L*-DOPA vs. *L*-5-HTP (Figure IV.5A-C). By contrast, anti-*L*-5-HTP antibodies recognized surface-tethered *L*-5-HTP and *L*-DOPA similarly (Figure IV.5D-F). Substrates exposed to fluorescently labeled secondary antibodies alone displayed negligible fluorescence (Figure SC.5a-d) leading to the conclusion that anti-*L*-5-HTP primary antibodies cross-react with *L*-DOPA pre-functionalized molecules. Because variabilities in probe functionalization, which affect specific antibody binding, were avoided by using pre-functionalized molecules, the cross-reactivity of polyclonal anti-*L*-5-HTP antibodies likely results from properties of the antibodies themselves.<sup>39,40</sup> Monoclonal antibodies are identical and recognize the same epitope on an antigen. Polyclonal antibodies are

polydisperse recognizing different epitopes on antigens.<sup>41</sup> As such, polyclonal antibodies are known to be more susceptible to cross-reactivity with structurally related epitopes.<sup>22</sup>

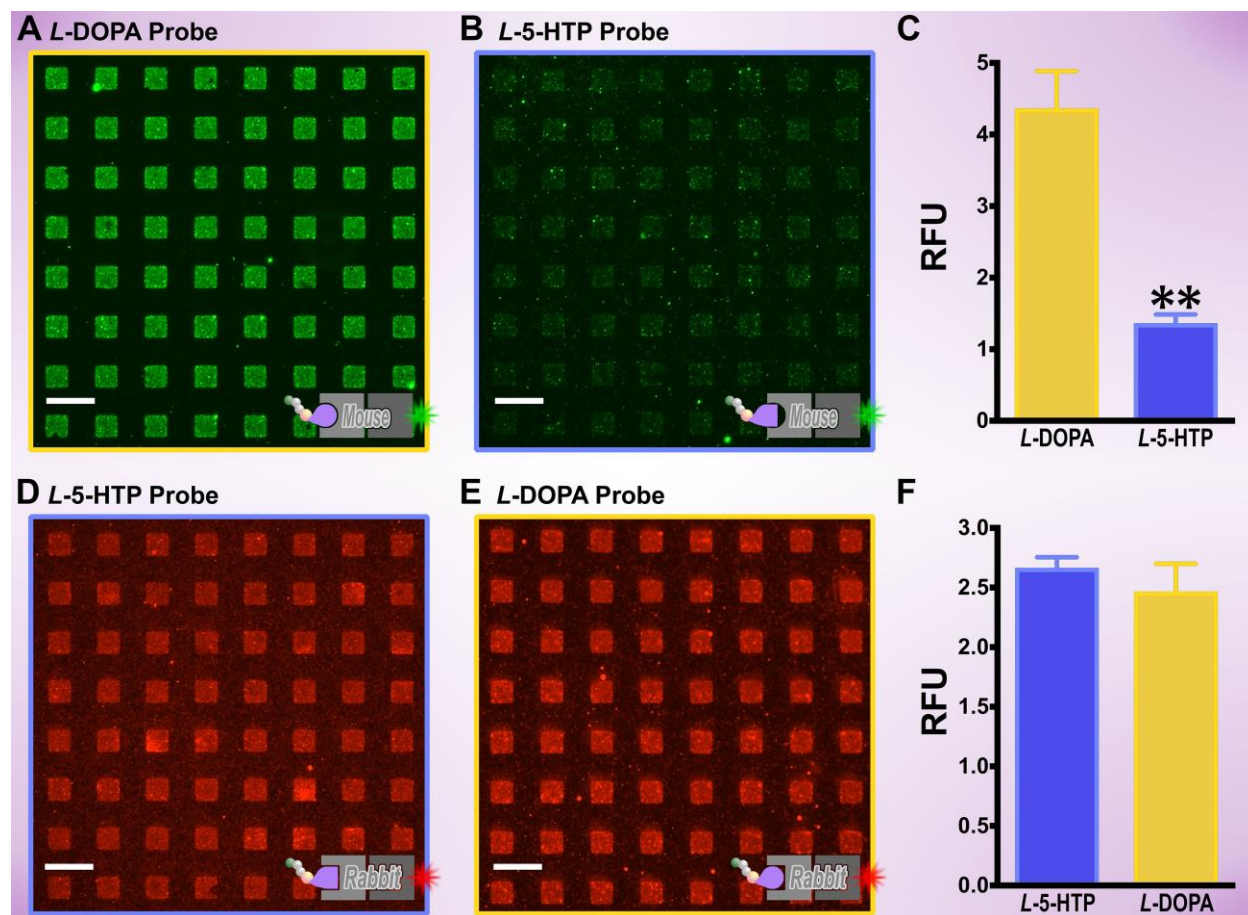


**Figure IV.5.** Representative fluorescence images and relative fluorescence intensity graphs for antibody binding on double lift-off lithography patterns of *L*-3,4-dihydroxyphenylalanine (*L*-DOPA) and *L*-5-hydroxytryptophan (*L*-5-HTP) pre-functionalized molecules. Substrates were imaged at two different emission wavelengths (525 nm (green, **A,B**) and 605 nm (red, **D,E**) for AlexaFluor 488 (excitation at 490 nm) and AlexaFluor 546 (excitation at 556 nm), respectively to visualize recognition of *L*-DOPA vs. *L*-5-HTP by monoclonal anti-*L*-DOPA antibodies in (**A,B,C**). Recognition of *L*-5-HTP vs. *L*-DOPA by polyclonal anti-*L*-5-HTP antibodies is seen in (**D,E,F**). Error bars represent standard errors of the means with  $N=3$  samples per group. Means are significantly different for anti-*L*-DOPA antibody binding  $t(4)=6$   $**P<0.01$ . Scale bars are 50  $\mu\text{m}$ .

The trend for reduced specificity for polyclonal vs. monoclonal antibodies was evident for other pairs of neurotransmitter pre-functionalized molecules on doubly patterned substrates. For example, anti-*L*-DOPA monoclonal antibodies showed selectivity in terms of recognizing *L*-DOPA vs. *L*-His (Figure IV.6A-C) or *L*-Trp (Figure IV.6D-F). By contrast, both anti-*L*-His and anti-*L*-Trp polyclonal antibodies failed to display selective recognition of *L*-His vs. *L*-DOPA (Figure SC.6a-c) and *L*-Trp vs. *L*-DOPA (Figure SC.6d-f), respectively. In fact, these polyclonal antibodies showed greater fluorescence intensities for the wrong target *i.e.*, *L*-DOPA. Anti-*L*-DOPA monoclonal antibodies were not able to distinguish *L*-DOPA vs. *L*-DOPS (Figure IV.6G-I). This pair of probes is the most difficult to differentiate of the substrate pairs investigated here; *L*-DOPA and *L*-DOPS differ by only a single hydroxyl group (Figure IV.1A).<sup>42</sup> In all cases, negligible fluorescence was associated with secondary antibody binding in the absence of primary antibodies (Figure SC.7a-j). We could not identify commercially available antibodies for *L*-DOPS so selectivity experiments focused on differentiating *L*-DOPS from *L*-DOPA could not be carried out.



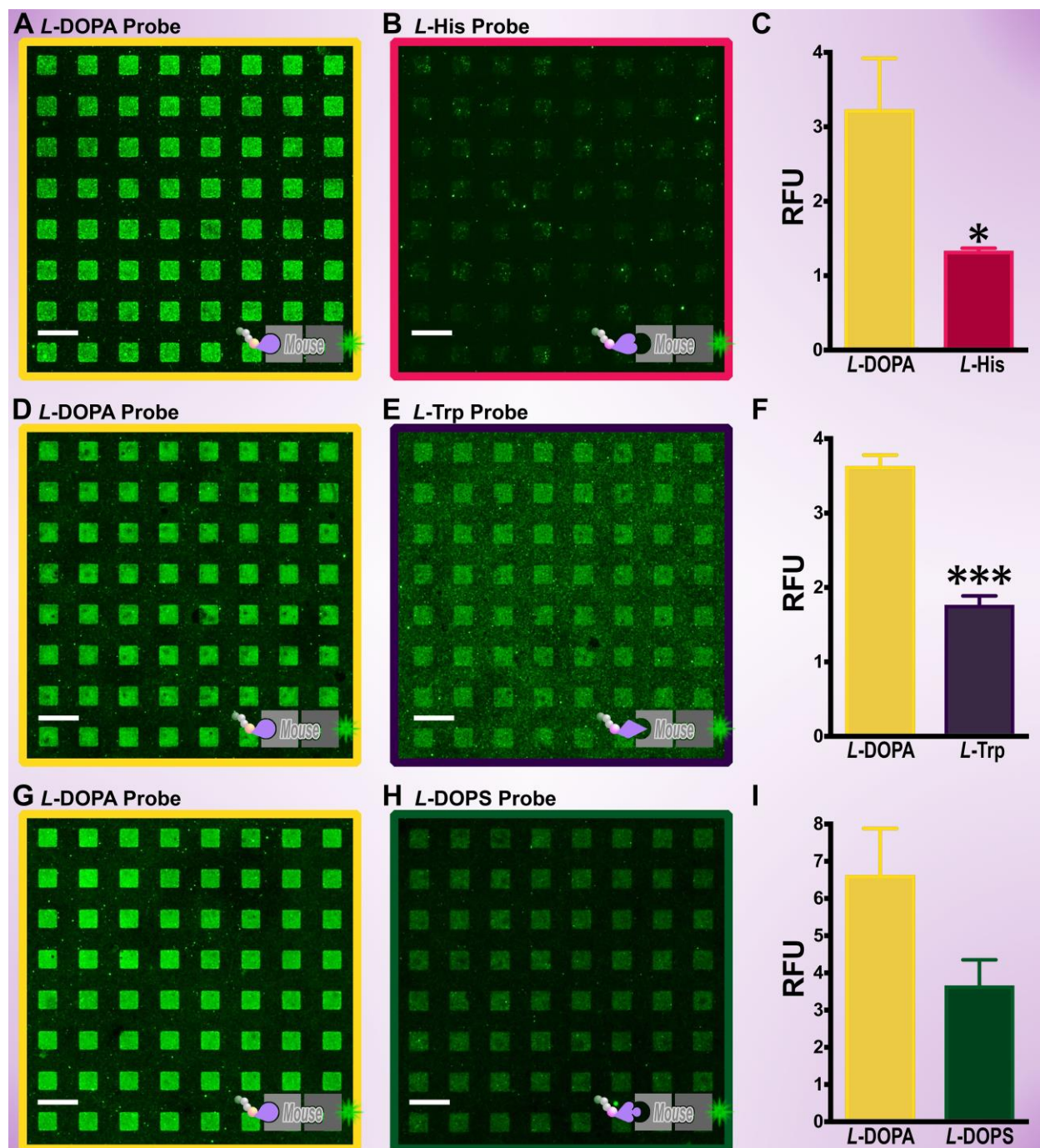


**Figure IV.6.** Representative fluorescence images and intensity graphs for antibody binding on double lift-off lithography patterns of (A,B) L-3,4-dihydroxyphenylalanine (L-DOPA)/L-histidine (L-His), (D,E) L-DOPA/L-tryptophan (L-Trp), and (G,H) L-DOPA/L-droixidopa (L-DOPS) pre-functionalized molecules. Higher relative fluorescence intensities were observed for monoclonal anti-L-DOPA antibody binding to surface tethered L-DOPA vs. (C) L-His and (F) L-Trp, but not (I) L-DOPS. Imaging was via AlexaFluor 488 labeled secondary antibodies (excitation at 490 nm and emission of 525 nm (green)). Error bars are standard errors of the means with  $N=3$  substrates per group. Means are significantly different for (C)  $t(4)=10$  \* $P<0.05$  and (F)  $t(4)=10$  \*\*\* $P<0.001$ . Scale bars are 50  $\mu\text{m}$ .

Together, the results presented herein demonstrate that the pre-functionalized small-molecule tethers are biologically active and have the ability to recognize antibody binding partners. The findings highlight differences in cross-reactivities between monoclonal and polyclonal antibodies, which we used as a test system. Ideally, additional monoclonal antibodies beyond the anti-*L*-DOPA antibody used here could be employed to investigate the hypothesis further that pre-functionalized molecules mimic free neurotransmitters and improve specific and selective recognition. Nonetheless, there are few commercially available monoclonal antibodies for small molecules. We showed that the use of pre-functionalized molecules reduced variability in probe recognition across individual substrates and in some cases, when paired with more selective antibodies, enabled multiplexing. We envision that pre-functionalized molecules bearing probes of interest, in conjunction with capabilities to multiplex substrates *via* facile chemical patterning methods, will enable the identification of novel highly specific and selective biomolecule binding partners targeting neurotransmitters or other critical small-molecule targets.

#### IV.D. Conclusions and Prospects

We have described the synthesis of monodisperse oligo(ethylene glycol)-terminated alkanethiol tethers pre-functionalized with neurotransmitter precursors. The novel synthetic route offers several advantages. First, it enables heterobifunctional tethers to be produced that are otherwise not commercially available. Second, the synthetic routes used here permitted orthogonal coupling chemistries that preserved the integrity of small-molecule probe functional groups. Third, conjugation of a number of different neurotransmitter precursors demonstrated the versatility of this strategy, which should be applicable to other small molecules probes.

We demonstrated that small molecules pre-functionalized to surface tethers displayed more consistent antibody recognition compared to post-patterning functionalization. Pre-functionalized molecules withstood subsequent conditions associated with additional functionalization chemistries. Although multiplexed substrates were indiscriminately recognized by polyclonal antibodies for all neurotransmitter pre-functionalized molecules tested, monoclonal antibodies showed selective recognition of *L*-DOPA vs. other neurotransmitters tested, with the exception of *L*-DOPS, which differs from *L*-DOPA by a single hydroxyl moiety.

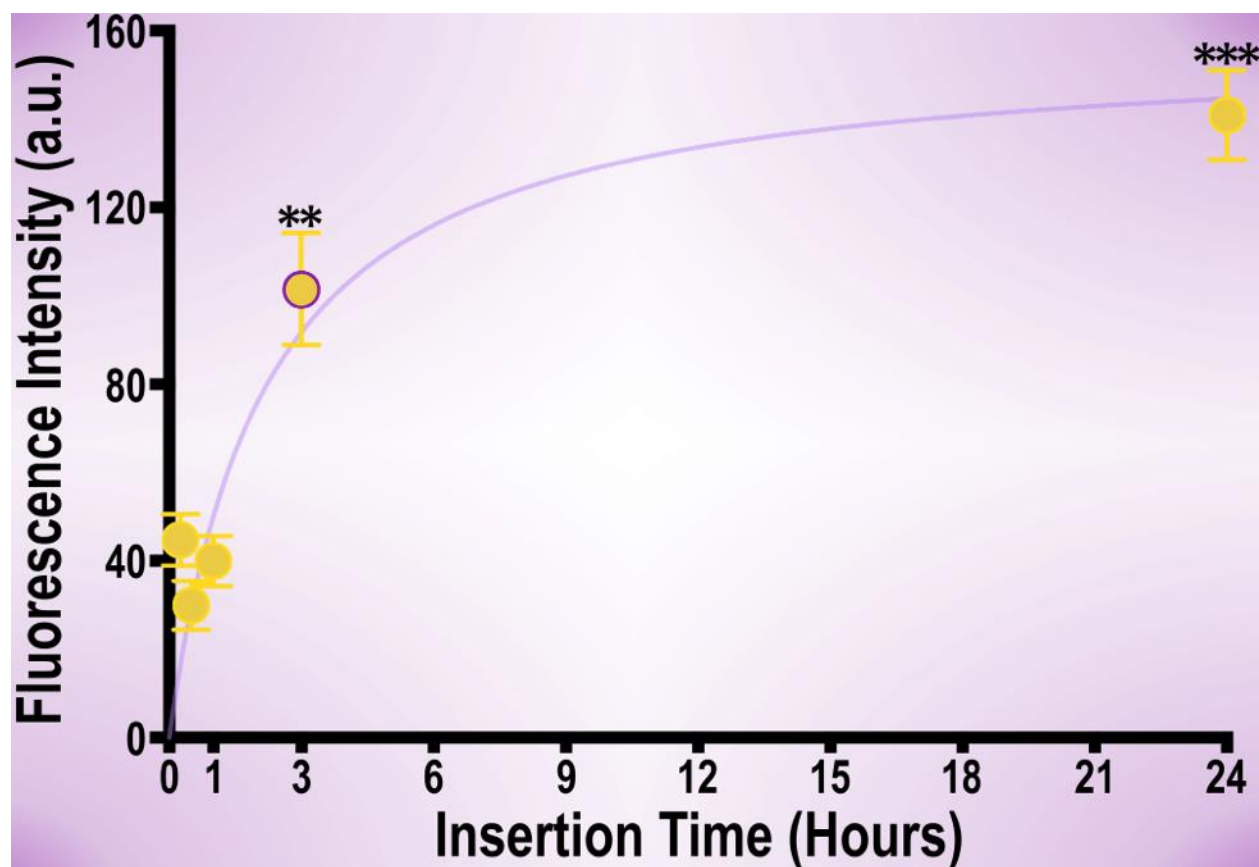
When it comes to finding a solution to cross-reactivity problems associated with biomolecule targets, the ability to reduce nonspecific binding while improving specific binding *via* careful control of surface chemistries appears to be insufficient. That is, the present findings demonstrate that a remaining fundamental limitation lies with the biomolecule receptors themselves; in this case, antibodies that failed to discriminate between small molecule binding partners on chemically defined surfaces. Synthetic

oligonucleotides (aptamers) may have advantages over antibodies.<sup>43-46</sup> Notably, because aptamers are chemically synthesized, their structures are identical and affinities can be tuned by modifying oligonucleotide sequences and thus, binding conformations.<sup>47</sup> Neurotransmitter pre-functionalized molecules and the multiplexing strategy presented here will facilitate the generation of improved substrates for identifying high-affinity aptamers targeting small-molecule neurotransmitters for incorporation into biosensing platforms for neurosensing applications.<sup>43,46,48,49</sup>

## **APPENDIX C**














### **Multiplexed Small-Molecule Patterning *via* Pre-Functionalized Alkanethiols**

#### **Supplementary Information**



**Figure SC.1** Antibody recognition as a function of insertion time. Patterned substrates were imaged at an emission wavelength of 525 nm (AlexaFluor 488-labeled secondary antibodies; excitation at 490 nm) to visualize secondary antibody binding to anti-*L*-DOPA primary antibodies captured on *L*-DOPA functionalized substrates. Error bars are standard errors of the means with  $N=3$  substrates per time point. Fluorescence intensities of captured antibodies were significantly different with respect to insertion times [ $F(4,10)=31.4$ ;  $P<0.001$ ]. \*\* $P<0.01$  and \*\*\* $P<0.001$  vs. 0.25 h, 0.5 h, and 1 h time points. The 3 h time point (purple outline) did not differ from the 24 h time point, thus the former was used for the remainder of the experiments.

**Table SC.1.** Primary antibodies used for molecular recognition of surface-tethered neurotransmitters and fluorescently labeled secondary antibodies for visualization.

Surface-Tethered Small-Molecule Probe	Primary Antibodies	Secondary Antibodies
 <i>L</i> -3,4-dihydroxyphenylalanine ( <i>L</i> -DOPA)	Mouse monoclonal anti- <i>L</i> -DOPA 	AlexaFluor® 488 goat anti-mouse IgG 
 <i>L</i> -5-hydroxytryptophan ( <i>L</i> -5-HTP)	Rabbit polyclonal anti- <i>L</i> -5-HTP 	AlexaFluor® 488 goat anti-rabbit IgG  AlexaFluor® 546 goat anti-rabbit IgG 
 <i>L</i> -histidine ( <i>L</i> -His)	Rabbit polyclonal anti- <i>L</i> -His 	AlexaFluor® 546 goat anti-rabbit IgG 
 <i>L</i> -tryptophan ( <i>L</i> -Trp)	Rat polyclonal anti- <i>L</i> -Trp 	AlexaFluor® 568 goat anti-rat IgG 

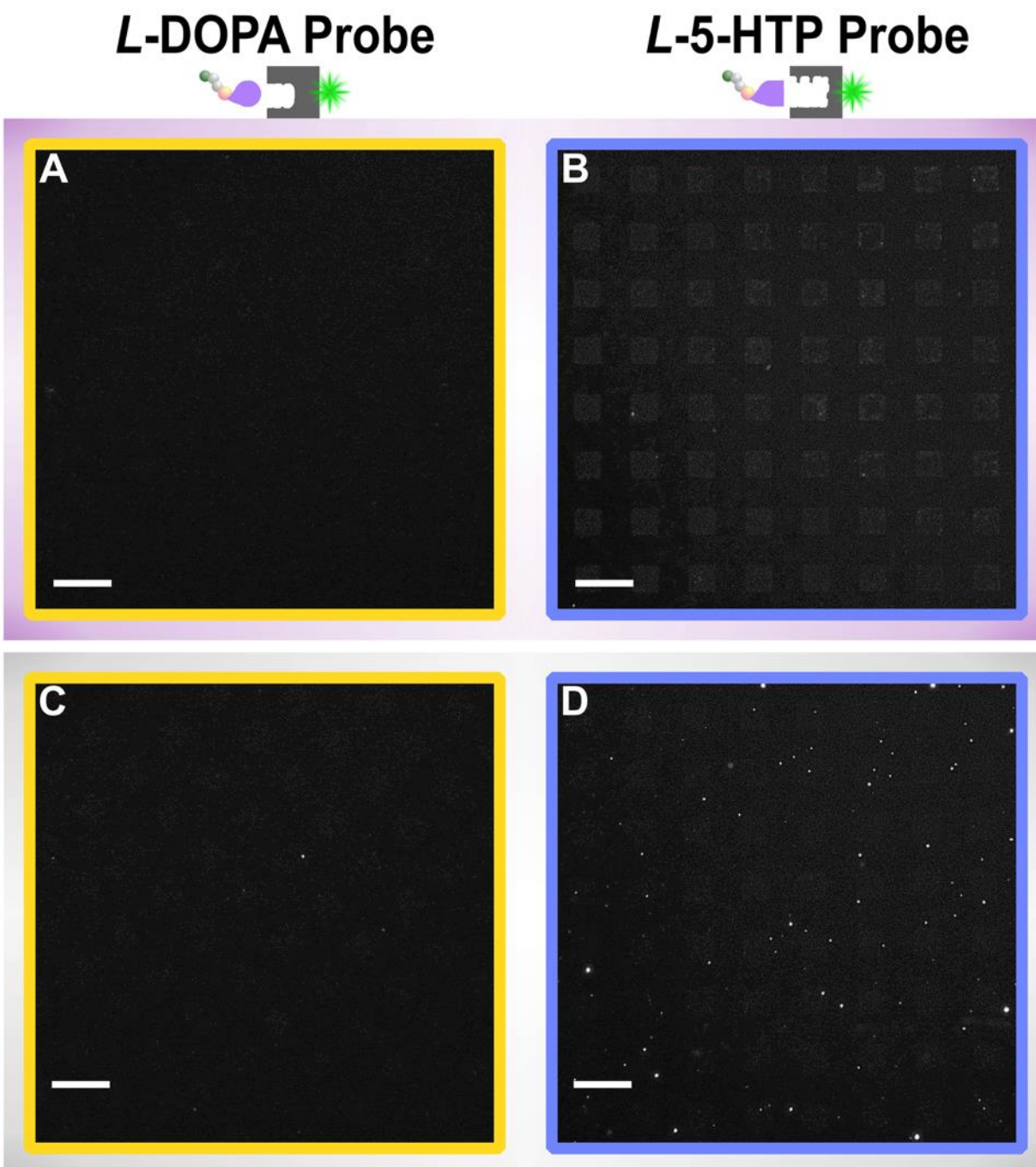


**Figure SC.2.** Representative fluorescence images for control experiments corresponding to Figure IV.2 (Chapter IV). (a) *L*-3,4-Dihydroxyphenylalanine (*L*-DOPA) and (b) *L*-5-hydroxytryptophan (*L*-5-HTP) pre-functionalized molecules; (c) *L*-DOPA and (d) *L*-5-HTP post-patterning functionalization. Patterned substrates were exposed to fluorescently labeled secondary antibodies in the absence of primary antibodies. Imaging contrast was maximized to try to detect fluorescent patterns at an emission wavelength of 525 nm (AlexaFluor 488; excitation at 490 nm). Patterns either were not observed or were faint indicating negligible recognition of surface tethered neurotransmitters by secondary antibodies. Scale bars are 50  $\mu\text{m}$ .



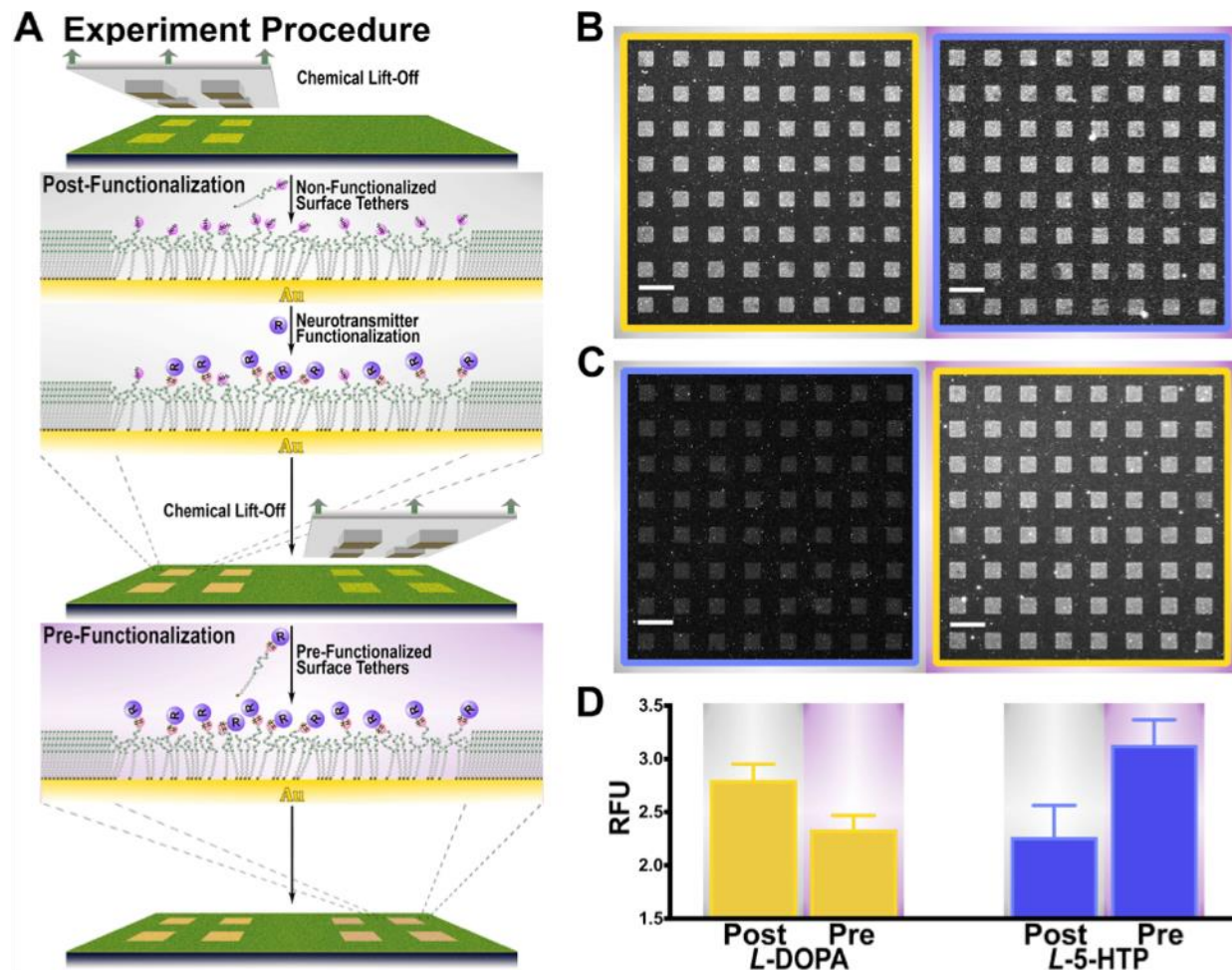


**Figure SC.3.** (a) Schematic illustrating double lift-off patterning of post- followed by pre-functionalized molecules. (b,c) Representative fluorescence images for antibody binding on double patterns of *L*-3,4-dihydroxyphenylalanine (*L*-DOPA) and *L*-5-hydroxytryptophan (*L*-5-HTP). (d) Relative fluorescence intensity graphs showed similar fluorescence signals resulting from antibody binding on *L*-DOPA and *L*-5-HTP post- vs. pre-functionalized substrates. Patterned substrates were imaged at an emission wavelength of 525 nm (AlexaFluor 488; excitation at 490 nm). Error bars represent standard errors of the means with  $N=3$  samples per group.

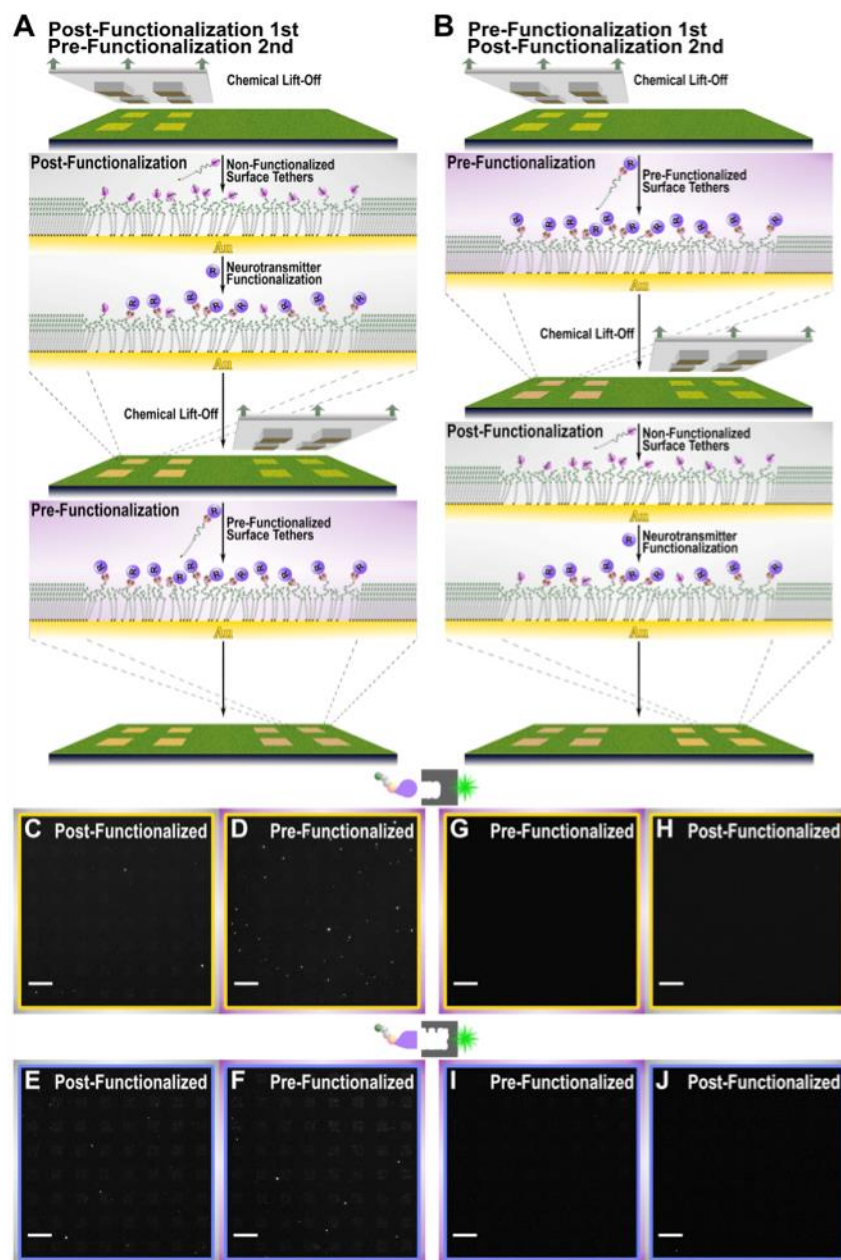


**Figure SC.4.** Control experiments corresponding to Figure IV.4 (Chapter IV) and Figure SC.3. Schematic illustrating double lift-off patterning of (a) post-functionalization followed by pre-functionalization and (b) pre-functionalization followed by post-functionalization. Representative fluorescence images for (c,d,g,h) are patterns of *L*-3,4-dihydroxyphenylalanine (*L*-DOPA) and (e,f,i,j) are patterns of *L*-5-hydroxytryptophan (*L*-5-HTP) on substrates subjected to (c,e) post- followed by (d,f) pre- or (g,i) pre- followed by (h,j) post-functionalization. Substrates were exposed to fluorescently labeled secondary antibodies in the absence of primary antibodies. Fluorescent patterns were not observed even at maximal exposure times at an emission wavelength of 525 nm (AlexaFluor 488; excitation at 490 nm) indicating negligible binding of fluorescently labeled secondary antibodies on patterned substrates. Scale bars are 50  $\mu$ m.

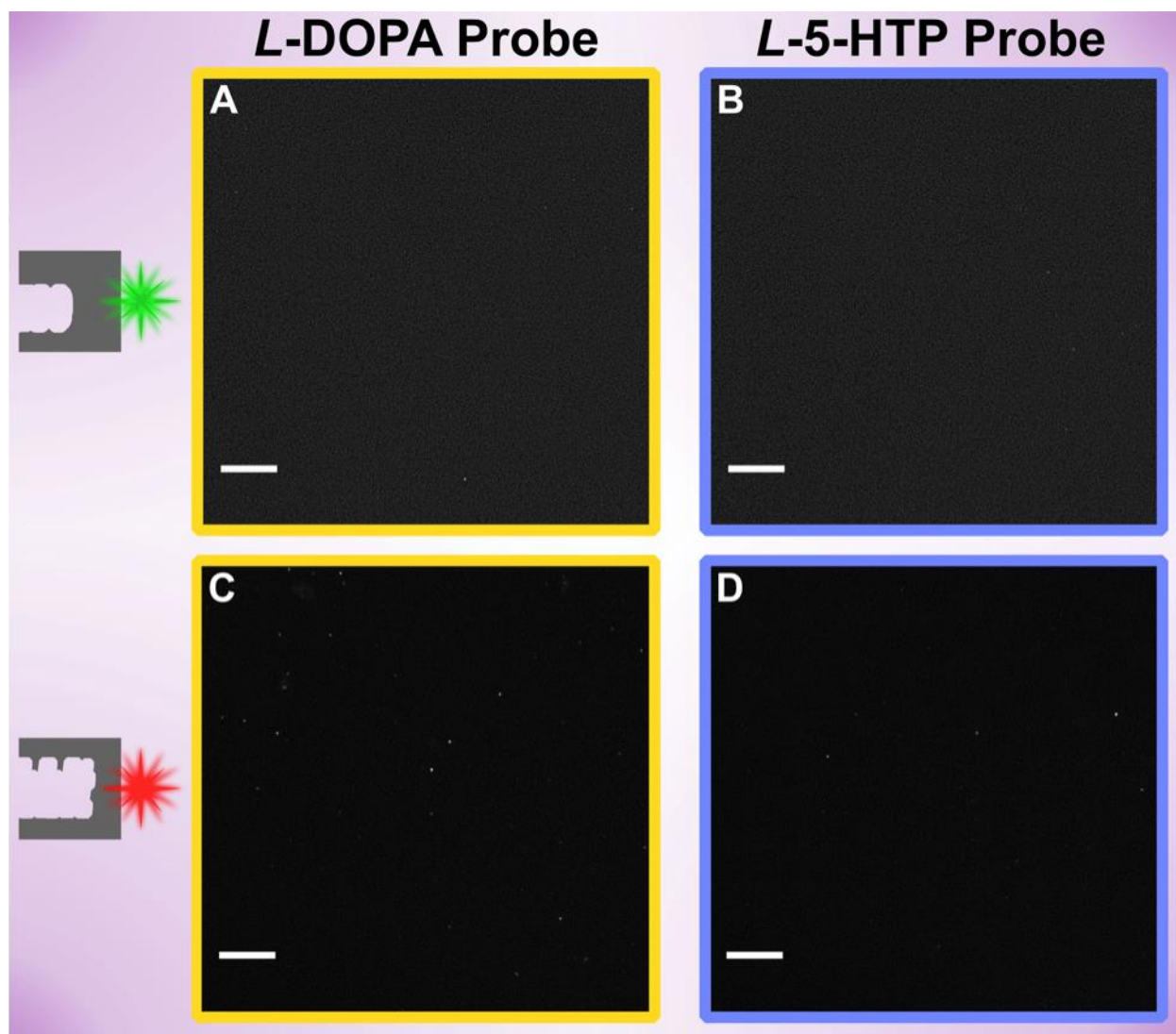


**Figure SC.5.** Control experiments for Figure IV.5 (Chapter IV). Representative fluorescence images for substrates doubly patterned with (a,c) *L*-3,4-dihydroxyphenylalanine (*L*-DOPA) and (b,d) *L*-5-hydroxytryptophan (*L*-5-HTP) pre-functionalized molecules. Patterned substrates were exposed to solutions containing fluorescently labeled secondary antibodies. Negligible fluorescence was observed at each emission wavelength; (a,b) 525 nm (AlexaFluor 488; excitation at 490 nm) and (c,d) 605 nm (AlexaFluor 546; excitation at 556 nm) indicating minimal nonspecific binding of fluorescently labeled secondary antibodies. Scale bars are 50  $\mu$ m.



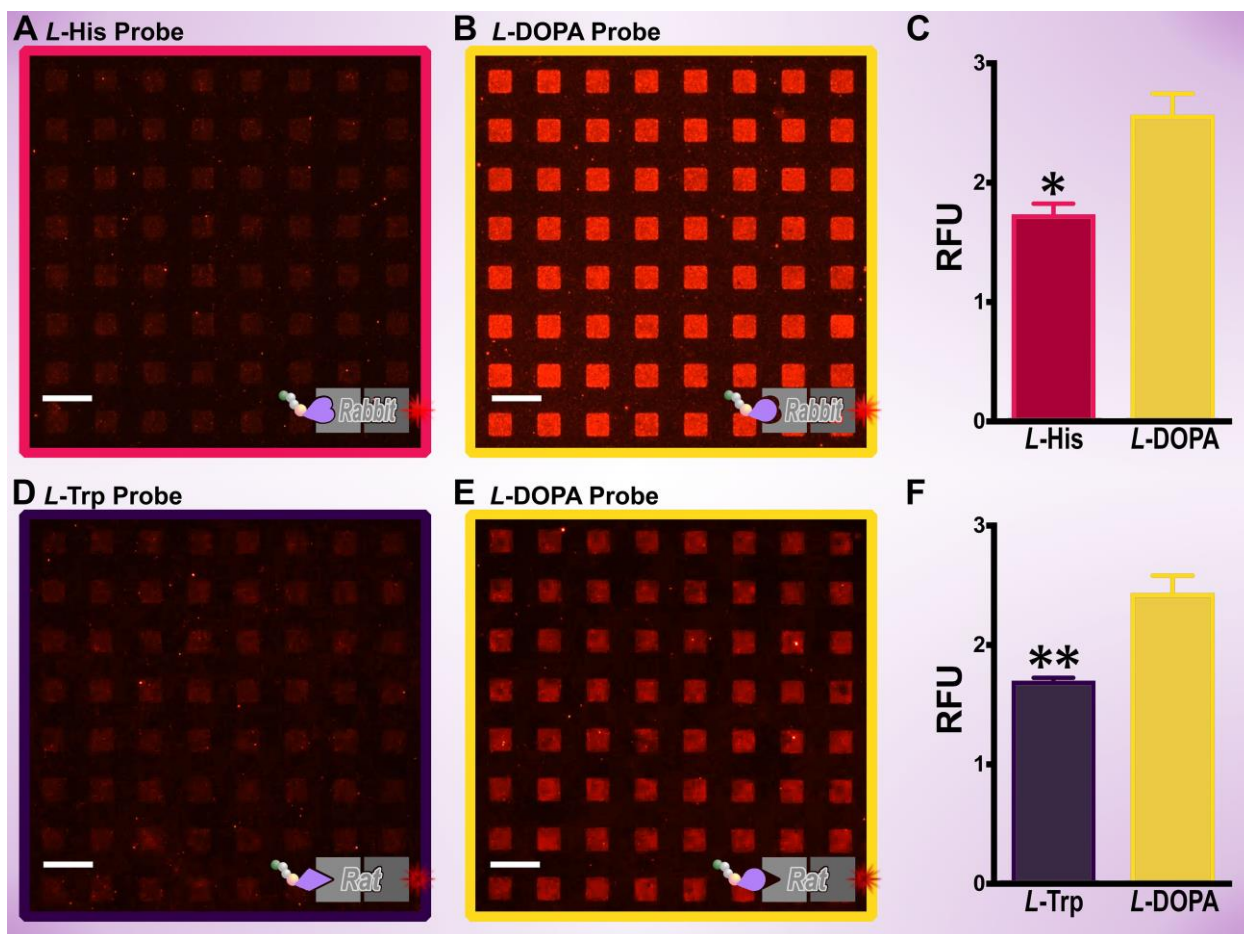


**Figure SC.6.** Complementary experiments for Figure IV.6 (Chapter IV). Representative fluorescence images for substrates doubly patterned with (a,b) *L*-3,4-dihydroxyphenylalanine (*L*-DOPA)/*L*-histidine (*L*-His) and (d,e) *L*-DOPA/*L*-tryptophan (*L*-Trp) pre-functionalized molecules. Patterned substrates were exposed to mixed primary antibody solutions followed by mixed fluorescently labeled secondary antibody solutions. Substrates were imaged at 605 nm (AlexaFluor 546; excitation 556 nm) to visualize primary antibodies captured on (a,b) *L*-DOPA/*L*-His patterns and at 605 nm (AlexaFluor 568 with excitation at 578 nm) to visualize primary antibodies captured on (d,e) *L*-DOPA/*L*-Trp patterns. Images shown here are for red fluorescence to visualize binding of (a,b) anti-*L*-His and (d,e) anti-*L*-Trp primary antibodies. Corresponding images for green fluorescence are shown in Figure IV.6 in Chapter IV. (c,f) Relative fluorescence intensity graphs showed higher binding of anti-*L*-His and anti-*L*-Trp primary antibodies to *L*-DOPA than to *L*-His and *L*-Trp pre-functionalized molecules, suggesting high levels of cross-reactivity of polyclonal antibodies. Error bars are standard errors of the means with  $N=3$  substrates per group. Mean intensities are significantly different in (c)  $t(4)=4$   $*P<0.05$  and (F)  $t(4)=5$   $**P<0.01$ . Scale bars are 50  $\mu\text{m}$ .

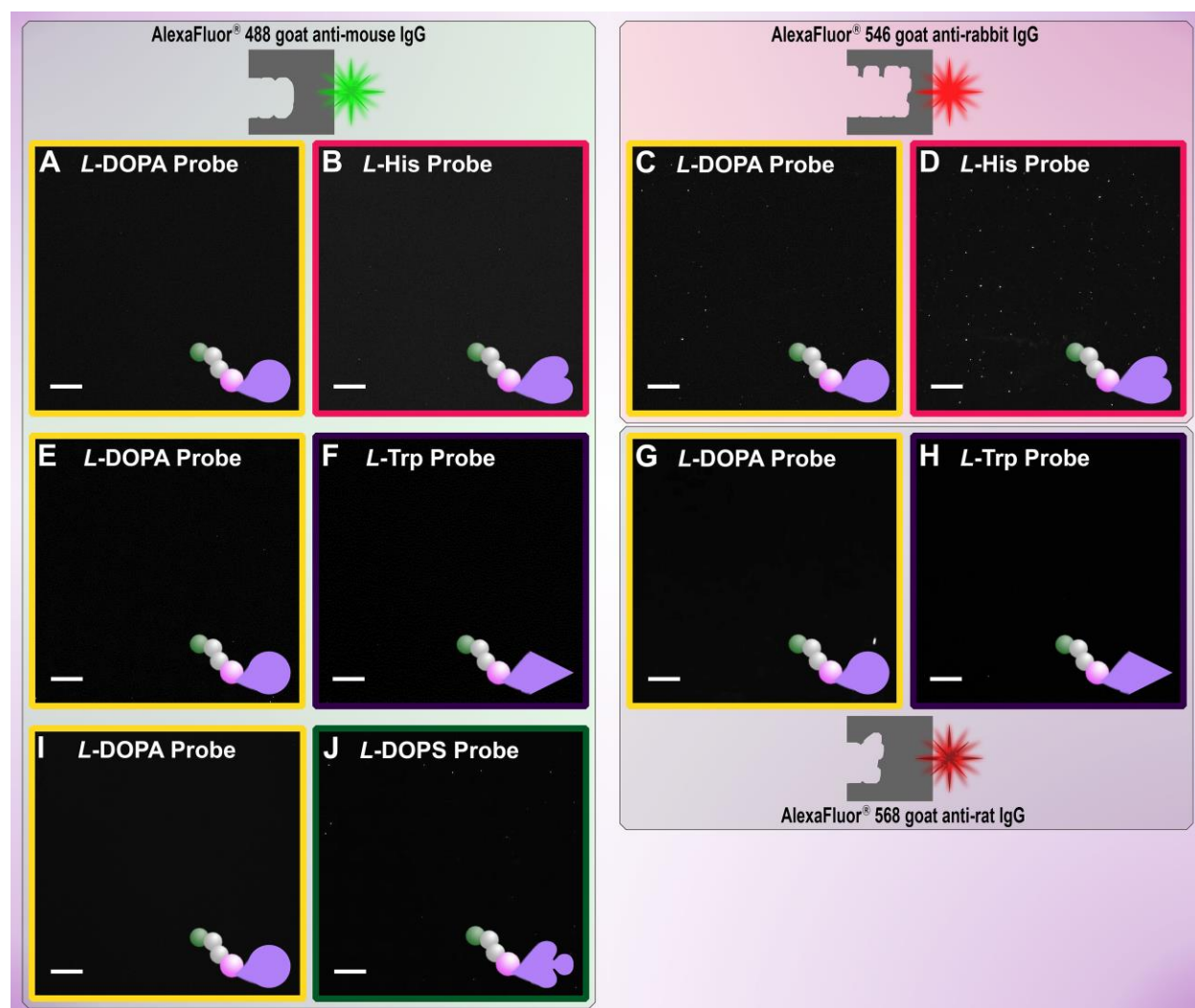


**Figure SC.7.** Control experiments for Figure IV.6 (Chapter IV) and Figure SC.6. Representative fluorescence images for substrates doubly patterned with (a,b,c,d) *L*-3,4-dihydroxyphenylalanine (*L*-DOPA)/*L*-histidine (*L*-His), (e,f,g,h) *L*-DOPA/*L*-tryptophan (*L*-Trp), and (i,j) *L*-DOPA/*L*-droxidopa (*L*-DOPS) pre-functionalized molecules. Patterned substrates were exposed to fluorescently labeled secondary antibodies in (i,j) and with mixed fluorescently labeled secondary antibodies in (a-h). Negligible fluorescence was observed at (a,b) 525 nm (AlexaFluor 488; excitation at 490 nm) or (c,d) 605 nm (AlexaFluor 546; excitation at 556 nm) indicating minimal nonspecific binding of fluorescently labeled secondary antibodies on *L*-DOPA/*L*-His patterns. Similarly, negligible fluorescence patterns occurred at (e,f) 525 nm (AlexaFluor 488; excitation at 490 nm), (g,h) 605 nm (AlexaFluor 568; excitation at 578 nm) and (i,j) 525 nm (AlexaFluor 488; excitation at 490 nm) indicating negligible nonspecific binding of fluorescently labeled secondary antibodies on (e,f,g,h) *L*-DOPA/*L*-Trp and (i,j) *L*-DOPA/*L*-DOPS patterns, respectively. Scale bars are 50  $\mu$ m.

## References

1. Shuster, M. J.; Vaish, A.; Gilbert, M. L.; Martinez-Rivera, M.; Nezarati, R. M.; Weiss, P. S.; Andrews, A. M. Comparison of Oligo(Ethylene Glycol)Alkanethiols *versus* *N*-Alkanethiols: Self-Assembly, Insertion, and Functionalization. *J. Phys. Chem. C* **2011**, *115*, 24778-24787.
2. Liao, W.-S.; Cao, H. H.; Cheunkar, S.; Shuster, M. J.; Altieri, S. C.; Weiss, P. S.; Andrews, A. M. Small-Molecule Arrays for Sorting G-Protein-Coupled Receptors. *J. Phys. Chem. C* **2013**, *117*, 22362-22368.
3. Shuster, M. J.; Vaish, A.; Cao, H. H.; Guttentag, A. I.; McManigle, J. E.; Gibb, A. L.; Martinez, M. M.; Nezarati, R. M.; Hinds, J. M.; Liao, W.-S.; Weiss, P. S.; Andrews, A. M. Patterning Small-Molecule Biocapture Surfaces: Microcontact Insertion Printing vs. Photolithography. *Chem. Commun.* **2011**, *47*, 10641-10643.
4. Vaish, A.; Shuster, M. J.; Cheunkar, S.; Singh, Y. S.; Weiss, P. S.; Andrews, A. M. Native Serotonin Membrane Receptors Recognize 5-Hydroxytryptophan-Functionalized Substrates: Enabling Small-Molecule Recognition. *ACS Chem. Neurosci.* **2010**, *1*, 495-504.
5. Vaish, A.; Shuster, M. J.; Cheunkar, S.; Weiss, P. S.; Andrews, A. M. Tuning Stamp Surface Energy for Soft Lithography of Polar Molecules to Fabricate Bioactive Small-Molecule Microarrays. *Small* **2011**, *7*, 1471-1479.
6. Shuster, M. J.; Vaish, A.; Szapacs, M. E.; Anderson, M. E.; Weiss, P. S.; Andrews, A. M. Biospecific Recognition of Tethered Small Molecules Diluted in Self-Assembled Monolayers. *Adv. Mater.* **2008**, *20*, 164-167.
7. Mullen, T. J.; Srinivasan, C.; Hohman, J. N.; Gillmor, S. D.; Shuster, M. J.; Horn, M. W.; Andrews, A. M.; Weiss, P. S. Microcontact Insertion Printing. *Appl. Phys. Lett.* **2007**, *90*, 063114.
8. Saavedra, H. M.; Mullen, T. J.; Zhang, P. P.; Dewey, D. C.; Claridge, S. A.; Weiss, P. S. Hybrid Strategies in Nanolithography. *Rep. Prog. Phys.* **2010**, *73*, 036501.
9. Liao, W.-S.; Cheunkar, S.; Cao, H. H.; Bednar, H. R.; Weiss, P. S.; Andrews, A. M. Subtractive Patterning *via* Chemical Lift-Off Lithography. *Science* **2012**, *337*, 1517-1521.
10. Andrews, A. M.; Liao, W. S.; Weiss, P. S. Double-Sided Opportunities Using Chemical Lift-Off Lithography. *Acc. Chem. Res.* **2016**, *49*, 1449-1457.
11. Bumm, L. A.; Arnold, J. J.; Cygan, M. T.; Dunbar, T. D.; Burgin, T. P.; Jones, L.; Allara, D. L.; Tour, J. M.; Weiss, P. S. Are Single Molecular Wires Conducting? *Science* **1996**, *271*, 1705-1707.

12. Cygan, M. T.; Dunbar, T. D.; Arnold, J. J.; Bumm, L. A.; Shedlock, N. F.; Burgin, T. P.; Jones, L.; Allara, D. L.; Tour, J. M.; Weiss, P. S. Insertion, Conductivity, and Structures of Conjugated Organic Oligomers in Self-Assembled Alkanethiol Monolayers on Au{111}. *J. Am. Chem. Soc.* **1998**, *120*, 2721-2732.
13. Claridge, S. A.; Liao, W. S.; Thomas, J. C.; Zhao, Y. X.; Cao, H. H.; Cheunkar, S.; Serino, A. C.; Andrews, A. M.; Weiss, P. S. From the Bottom Up: Dimensional Control and Characterization in Molecular Monolayers. *Chem. Soc. Rev.* **2013**, *42*, 2725-2745.
14. Ostuni, E.; Yan, L.; Whitesides, G. M. The Interaction of Proteins and Cells with Self-Assembled Monolayers of Alkanethiolates on Gold and Silver. *Colloids Surf. B* **1999**, *15*, 3-30.
15. Harder, P.; Grunze, M.; Dahint, R.; Whitesides, G. M.; Laibinis, P. E. Molecular Conformation in Oligo(Ethylene Glycol)-Terminated Self-Assembled Monolayers on Gold and Silver Surfaces Determines Their Ability to Resist Protein Adsorption. *J. Phys. Chem. B* **1998**, *102*, 426-436.
16. Cao, H. H.; Nakatsuka, N.; Liao, W. S.; Serino, A. C.; Cheunkar, S.; Yang, H. Y.; Weiss, P. S.; Andrews, A. M. Advancing Biocapture Substrates *via* Chemical Lift-Off Lithography. *Chem. Mater.* **2017**, *29*, 6829-6839.
17. Sam, S.; Touahir, L.; Andresa, J. S.; Allongue, P.; Chazalviel, J. N.; Gouget-Laemmel, A. C.; de Villeneuve, C. H.; Moraillon, A.; Ozanam, F.; Gabouze, N.; Djebbar, S. Semiquantitative Study of the EDC/NHS Activation of Acid Terminal Groups at Modified Porous Silicon Surfaces. *Langmuir* **2010**, *26*, 809-814.
18. Wang, C.; Yan, Q.; Liu, H. B.; Zhou, X. H.; Xiao, S. J. Different EDC/NHS Activation Mechanisms between PAA and PMAA Brushes and the Following Amidation Reactions. *Langmuir* **2011**, *27*, 12058-12068.
19. Xia, N.; Xing, Y.; Wang, G. F.; Feng, Q. Q.; Chen, Q. Q.; Feng, H. M.; Sun, X. L.; Liu, L. Probing of EDC/NHSS-Mediated Covalent Coupling Reaction by the Immobilization of Electrochemically Active Biomolecules. *Int. J. Electrochem. Sci.* **2013**, *8*, 2459-2467.
20. Bumm, L. A.; Arnold, J. J.; Charles, L. F.; Dunbar, T. D.; Allara, D. L.; Weiss, P. S. Directed Self-Assembly to Create Molecular Terraces with Molecularly Sharp Boundaries in Organic Monolayers. *J. Am. Chem. Soc.* **1999**, *121*, 8017-8021.
21. Saavedra, H. M.; Thompson, C. M.; Hohman, J. N.; Crespi, V. H.; Weiss, P. S. Reversible Lability by *in Situ* Reaction of Self-Assembled Monolayers. *J. Am. Chem. Soc.* **2009**, *131*, 2252-2259.

22. Stranick, S. J.; Parikh, A. N.; Tao, Y. T.; Allara, D. L.; Weiss, P. S. Phase-Separation of Mixed-Composition Self-Assembled Monolayers into Nanometer-Scale Molecular Domains. *J. Phys. Chem.* **1994**, *98*, 7636-7646.
23. Congreve, M.; Langmead, C. J.; Mason, J. S.; Marshall, F. H. Progress in Structure Based Drug Design for G Protein-Coupled Receptors. *J. Med. Chem.* **2011**, *54*, 4283-4311.
24. Seeber, M.; De Benedetti, P. G.; Fanelli, F. Molecular Dynamics Simulations of the Ligand-Induced Chemical Information Transfer in the 5-HT<sub>1a</sub> Receptor. *J. Chem. Inf. Comput. Sci.* **2003**, *43*, 1520-1531.
25. Palegrosdemange, C.; Simon, E. S.; Prime, K. L.; Whitesides, G. M. Formation of Self-Assembled Monolayers by Chemisorption of Derivatives of Oligo(Ethylene Glycol) of Structure HS(CH<sub>2</sub>)<sub>11</sub>(OCH<sub>2</sub>CH<sub>2</sub>)<sub>m</sub>-OH on Gold. *J. Am. Chem. Soc.* **1991**, *113*, 12-20.
26. Svedhem, S.; Hollander, C. A.; Shi, J.; Konradsson, P.; Liedberg, B.; Svensson, S. C. T. Synthesis of a Series of Oligo(Ethylene Glycol)-Terminated Alkanethiol Amides Designed to Address Structure and Stability of Biosensing Interfaces. *J. Org. Chem.* **2001**, *66*, 4494-4503.
27. Vazquez-Dorbatt, V.; Tolstyka, Z. P.; Chang, C. W.; Maynard, H. D. Synthesis of a Pyridyl Disulfide End-Functionalized Glycopolymer for Conjugation to Biomolecules and Patterning on Gold Surfaces. *Biomacromolecules* **2009**, *10*, 2207-2212.
28. Prime, K. L.; Whitesides, G. M. Adsorption of Proteins onto Surfaces Containing End-Attached Oligo(Ethylene Oxide) - A Model System Using Self-Assembled Monolayers. *J. Am. Chem. Soc.* **1993**, *115*, 10714-10721.
29. Tolstyka, Z. P.; Richardson, W.; Bat, E.; Stevens, C. J.; Parra, D. P.; Dozier, J. K.; Distefano, M. D.; Dunn, B.; Maynard, H. D. Chemoselective Immobilization of Proteins by Microcontact Printing and Bio-Orthogonal Click Reactions. *ChemBioChem* **2013**, *14*, 2464-2471.
30. Booth, C.; Bushby, R. J.; Cheng, Y. L.; Evans, S. D.; Liu, Q. Y.; Zhang, H. L. Synthesis of Novel Biotin Anchors. *Tetrahedron* **2001**, *57*, 9859-9866.
31. Kleinert, M.; Rockendorf, N.; Lindhorst, T. K. Glyco-SAMs as Glycocalyx Mimetics: Synthesis of *L*-Fucose- and *D*-Mannose-Terminated Building Blocks. *Eur. J. Org. Chem.* **2004**, 3931-3940.
32. Prats-Alfonso, E.; Oberhansl, S.; Lagunas, A.; Martinez, E.; Samitier, J.; Albericio, F. Effective and Versatile Strategy for the Total Solid-Phase Synthesis of Alkanethiols for Biological Applications. *Eur. J. Org. Chem.* **2013**, 1233-1239.

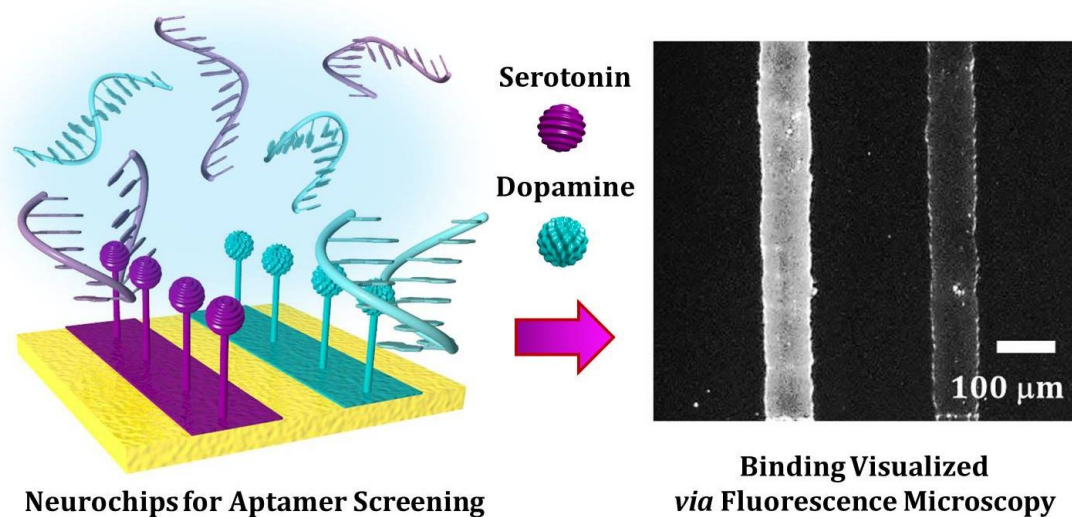


33. Murray, J.; Nowak, D.; Pukenas, L.; Azhar, R.; Guillorit, M.; Walti, C.; Critchley, K.; Johnson, S.; Bon, R. S. Solid Phase Synthesis of Functionalised SAM-Forming Alkanethiol-Oligoethyleneglycols. *J. Mater. Chem. B* **2014**, *2*, 3741-3744.
34. Cao, H. H.; Nakatsuka, N.; Serino, A. C.; Liao, W.-S.; Cheunkar, S.; Yang, H.; Weiss, P. S.; Andrews, A. M. Controlled DNA Patterning by Chemical Lift-Off Lithography: Matrix Matters. *ACS Nano* **2015**, *9*, 11439–11454.
35. Slaughter, L. S.; Cheung, K. M.; Kaappa, S.; Cao, H. H.; Yang, Q.; Young, T. D.; Serino, A. C.; Malola, S.; Olson, J. M.; Link, S.; Hakkinen, H.; Andrews, A. M.; Weiss, P. S. Patterning of Supported Gold Monolayers Via Chemical Lift-Off Lithography. *Beilstein J. Nanotechnol.* **2017**, *8*, 2648-2661.
36. Zareie, H. M.; Boyer, C.; Bulmus, V.; Nateghi, E.; Davis, T. P. Temperature-Responsive Self-Assembled Monolayers of Oligo(Ethylene Glycol): Control of Biomolecular Recognition. *ACS Nano* **2008**, *2*, 757-765.
37. Bain, C. D.; Troughton, E. B.; Tao, Y. T.; Evall, J.; Whitesides, G. M.; Nuzzo, R. G. Formation of Monolayer Films by the Spontaneous Assembly of Organic Thiols from Solution onto Gold. *J. Am. Chem. Soc.* **1989**, *111*, 321-335.
38. Bain, C. D.; Biebuyck, H. A.; Whitesides, G. M. Comparison of Self-Assembled Monolayers on Gold - Coadsorption of Thiols and Disulfides. *Langmuir* **1989**, *5*, 723-727.
39. Prager, E. M. The Sequence-Immunology Correlation Revisited: Data for Cetacean Myoglobins and Mammalian Lysozymes. *J. Mol. Evol.* **1993**, *37*, 408-416.
40. Benjamin, D. C.; Berzofsky, J. A.; East, I. J.; Gurd, F. R.; Hannum, C.; Leach, S. J.; Margoliash, E.; Michael, J. G.; Miller, A.; Prager, E. M.; *et al.* The Antigenic Structure of Proteins: A Reappraisal. *Annu. Rev. Immunol.* **1984**, *2*, 67-101.
41. Lipman, N. S.; Jackson, L. R.; Trudel, L. J.; Weis-Garcia, F. Monoclonal versus Polyclonal Antibodies: Distinguishing Characteristics, Applications, and Information Resources. *ILAR J.* **2005**, *46*, 258-268.
42. Nakatsuka, N.; Andrews, A. M. Differentiating Siblings: The Case of Dopamine and Norepinephrine. *ACS Chem. Neurosci.* **2017**, *8*, 218-220.
43. McKeague, M.; DeRosa, M. C. Challenges and Opportunities for Small Molecule Aptamer Development. *J. Nucleic Acids* **2012**, *2012*, 1-20.
44. Kim, Y. S.; Gu, M. B. Advances in Aptamer Screening and Small Molecule Aptasensors. *Biosensors Based on Aptamers and Enzymes* **2014**, *140*, 29-67.

45. Mei, H. C.; Bing, T.; Yang, X. J.; Qi, C.; Chang, T. J.; Liu, X. J.; Cao, Z. H.; Shangguan, D. H. Functional-Group Specific Aptamers Indirectly Recognizing Compounds with Alkyl Amino Group. *Anal. Chem.* **2012**, *84*, 7323-7329.
46. Kim, J.; Rim, Y. S.; Chen, H. J.; Cao, H. H.; Nakatsuka, N.; Hinton, H. L.; Zhao, C. Z.; Andrews, A. M.; Yang, Y.; Weiss, P. S. Fabrication of High-Performance Ultrathin In<sub>2</sub>O<sub>3</sub> Film Field-Effect Transistors and Biosensors Using Chemical Lift-Off Lithography. *ACS Nano* **2015**, *9*, 4572-4582.
47. Vallee-Belisle, A.; Plaxco, K. W. Structure-Switching Biosensors: Inspired by Nature. *Curr. Opin. Struct. Biol.* **2010**, *20*, 518-526.
48. Alivisatos, A. P.; Andrews, A. M.; Boyden, E. S.; Chun, M.; Church, G. M.; Deisseroth, K.; Donoghue, J. P.; Fraser, S. E.; Lippincott-Schwartz, J.; Looger, L. L.; Masmanidis, S.; McEuen, P. L.; Nurmikko, A. V.; Park, H.; Peterka, D. S.; Reid, C.; Roukes, M. L.; Scherer, A.; Schnitzer, M.; Sejnowski, T. J.; Shepard, K. L.; Tsao, D.; Turrigiano, G.; Weiss, P. S.; Xu, C.; Yuste, R.; Zhuang, X. W. Nanotools for Neuroscience and Brain Activity Mapping. *ACS Nano* **2013**, *7*, 1850-1866.
49. Biteen, J. S.; Blainey, P. C.; Cardon, Z. G.; Chun, M. Y.; Church, G. M.; Dorrestein, P. C.; Fraser, S. E.; Gilbert, J. A.; Jansson, J. K.; Knight, R.; Miller, J. F.; Ozcan, A.; Prather, K. A.; Quake, S. R.; Ruby, E. G.; Silver, P. A.; Taha, S.; van den Engh, G.; Weiss, P. S.; Wong, G. C. L.; Wright, A. T.; Young, T. D. Tools for the Microbiome: Nano and Beyond. *ACS Nano* **2016**, *10*, 6-37.

# Chapter V

## Aptamer Recognition of Multiplexed Neurotransmitter- Functionalized Substrates



The information in this chapter  
is in preparation for *ACS Chemical Neuroscience*  
and has been reproduced here.

Authors: Nakatsuka, N.; Cao, H. H.; Deshayes, S.; Kasko, A. M.;  
Weiss, P. S.; Andrews, A. M.

## V.A. Introduction

Aptamers are single-stranded oligonucleotides that recognize a wide range of targets, including viruses,<sup>1,2</sup> proteins,<sup>3-6</sup> peptides,<sup>7-9</sup> small molecules,<sup>10-17</sup> and ions.<sup>18-20</sup> Isolation of aptamer sequences has most often been carried out through the use of an *in vitro* selection method called the systematic evolution of ligands by exponential enrichment (SELEX).<sup>21,22</sup> In its most commonly used form, SELEX involves covalent modification of solid-phase materials, *e.g.*, sepharose, with target molecules.<sup>21-24</sup> Target-modified substrates are then exposed to combinatorial libraries of large numbers of nucleic acid sequences having variable regions. Only a relatively small number of sequences that bind to targets are isolated.

Compared to antibodies or other biomolecule recognition elements, aptamers possess advantages including the ability to be chemically synthesized and engineered for stability in biological environments.<sup>25,26</sup> Aptamer affinities can be tuned by evolving or mutating recognition sequences.<sup>27-31</sup> As such, aptamers have emerged as candidates for integration into diverse biosensor platforms as recognition elements.<sup>32-35</sup> Understanding relationships between aptamer affinities ( $K_d$ ), conformational dynamics, and binding kinetics ( $k_{on}/k_{off}$ ) will be critical to realizing the potential of aptamers as recognition elements in device architectures, particularly for neurochemical sensing *in vivo*.<sup>36-38</sup>

Once isolated, thermodynamic dissociation constants characterizing aptamer-target binding are typically determined in solution by fluorescence measurements.<sup>16,39-42</sup> Since dissociation constants are directly related to binding kinetics, determining aptamer binding affinities in environments that better mimic those in which sensing is conducted (*i.e.*, on-substrate) is important. Thus, our goal was to develop the capability to determine  $K_d$  values

for aptamers on solid-phase substrates with optimized surface chemistries to enable comparisons of *relative* aptamer-target binding affinities on multiplexed surfaces.

We have developed and characterized neurotransmitter-functionalized substrates. These substrates selectively capture and sort binding partners, including antibodies<sup>43</sup> and native serotonin G-protein-coupled receptors,<sup>44,45</sup> from mixtures to their respective surface-tethered neurotransmitter targets. We have developed patterning methods *via* soft lithography<sup>46</sup> to create regions of high target contrast and to enable visualization and quantification of specific binding of fluorophore-labeled binding partners relative to nonspecific binding on the same substrates *via* fluorescence microscopy. The capability to recognize and to sort multiple G-protein-coupled receptors from mixtures with minimal nonspecific binding suggested that these substrates have the potential to recognize artificial receptors in the form of aptamers, while mimicking target-receptor binding in solution.

Here, we used a previously identified DNA aptamer that recognizes the neurotransmitter dopamine.<sup>13</sup> We investigate whether surface-tethered dopamine can be recognized by this dopamine aptamer and determine binding affinities on-substrate. Using pre-functionalized neurotransmitter-conjugated oligoethylene alkanethiols previously designed and synthesized by us,<sup>47</sup> we produced multiplexed substrates with similarly structured neurotransmitters tethered parallel to one another on the same substrate. Multiplexed substrates enabled the simultaneous determination of *in situ* binding affinities of all surface-tethered small molecules to the dopamine aptamer.

## V.B. Experimental Methods

### V.B.1. Materials

Gold films (100 nm) overlaying titanium (10 nm) on Si substrates were purchased from Platypus Technologies (Madison, WI). Hydroxyl tri(ethylene glycol)-terminated undecanethiol (TEG) and carboxyl hexa(ethylene glycol)-terminated undecanethiol (HEG) were purchased from Toronto Research Chemicals Inc. (Toronto, Canada). *N*-Hydroxysuccinimide (NHS), *N*-(3-dimethylaminopropyl)-*N*'ethylcarbodiimide hydrochloride (EDC), 4-methylpiperidine, and dopamine hydrochloride were purchased from Sigma-Aldrich (St. Louis, MO). *SYLGARD*® 184 silicone elastomer kits were purchased from Ellsworth Adhesives (Germantown, WI). Absolute, 200-proof ethanol was purchased from Decon Laboratories, Inc. (King of Prussia, PA). Deionized water (~18 MΩ) was obtained from a Millipore water purifier (Billerica, MA).

The following fluorescently labeled aptamer sequences were purchased from Integrated DNA Technologies, Inc. (Coralville, IA): AlexaFluor® 546-conjugated single-stranded correct dopamine aptamer: 5'/5Alex546N/-GTC TCT GTG TGC GCC AGA GAC ACT GGG GCA GAT ATG GGC CAG CAC AGA ATG AGG CCC 3' with molecular weight 18,790.9 g/mol and melting point 74.1°C (250 nmol), AlexaFluor® 546-conjugated single-stranded mutated dopamine aptamer (additional base underlined): 5'/5Alex546N/-GTC TCT GTG TGC GCC AGA GAA CAC TGG GGC AGA TAT GGG CCA GCA CAG AAT GAG GCC C 3' with molecular weight 18,926.0 g/mol and melting point 74.2 °C (250 nmol), AlexaFluor® 546-conjugated single-stranded scrambled dopamine aptamer: 5'/5Alex546N/-TGG GTA ACA ATG CGA GCA CTG CGG ACT ATG CAG GAA CTG TGC TGA GCG CGC CAC CGG 3' with molecular weight 18,790.9 g/mol and melting temperature 75.0 °C

(250 nmol), and AlexaFluor® 488-conjugated single-stranded *L*-tryptophan aptamer: 5'/5Alex488N/-AGC ACG TTG GTT AGG TCA GGT TTG GGT TTC GTG C 3' with molecular weight 11,262.5 g/mol and melting point 67.2 °C (250 nmol). Aptamer solutions (100 µM in TE buffer (10mM Tris; 0.1 mM EDTA; pH 8.0) as received from Integrated DNA Technologies, Inc.) were stored at -20 °C and diluted to specific concentrations as needed for each experiment.

### **V.B.2. Microfluidic Device Fabrication**

Polydimethylsiloxane (PDMS) microfluidic devices were prepared by first mixing a 10:1 mass ratio of *SYLGARD*® 184 silicone elastomer base and curing agent. The mixture was then degassed under vacuum until bubbles were no longer visible. The PDMS mixture was cast onto a silicon master substrate with twelve 30 µm wide channels patterned by photolithography. The elastomeric mixture was cured at 60 °C for ~20 h. Polymerized PDMS microfluidic devices were removed from the silicon master and soaked in fresh 95% hexane for 1.5 h three times. These soaking steps removed unpolymerized residues on devices and prevented them from being deposited on substrates, thereby decreasing nonspecific binding.<sup>48</sup> Devices were then rinsed in 50/50 deionized H<sub>2</sub>O/ethanol for 15 min and dried with nitrogen gas.

### V.B.3. Self-Assembled Monolayer Preparation and Patterning

Gold substrates were annealed with a hydrogen flame and submerged in 0.5 mM TEG and 0.125 mM HEG (80:20 ratio) in ethanol for ~16 h to produce mixed self-assembled monolayers.<sup>44</sup> The use of TEG in monolayers minimizes non-specific binding of biomolecules.<sup>43-45,49-51</sup> Substrates were then rinsed thoroughly with ethanol and blown dry with nitrogen gas. For post-self-assembly functionalization and patterning, TEG/HEG SAM-modified gold substrates were incubated for 1 h with an aqueous solution of 35 mM NHS and 35 mM EDC. Substrates were then rinsed thoroughly with deionized H<sub>2</sub>O and blown dry. This step converts the terminal carboxyl groups of HEG to NHS-ester-activated moieties in preparation for amide bond formation with dopamine (Scheme V.1A).<sup>45</sup>

To pattern surface-tethered dopamine molecules, hexane-treated microfluidic devices were sealed to substrates and 35 mM dopamine solutions were injected into all twelve microfluidic channels and incubated for 3 h (Scheme V.1B). Dopamine solutions were prepared in phosphate buffer (10 mM KH<sub>2</sub>PO<sub>4</sub>, 40 mM K<sub>2</sub>HPO<sub>4</sub>, pH 6.7). Following surface conjugation, microfluidic devices were immediately removed from the substrates while submerged in H<sub>2</sub>O to minimize exposure of unfunctionalized substrate regions to dopamine. Substrates were then immersed in fresh deionized H<sub>2</sub>O for 10 min to hydrolyze unreacted NHS-activated carboxyl groups on HEG molecules.<sup>52,53</sup> Post-functionalization, substrates were thoroughly washed in deionized H<sub>2</sub>O and blown dry in preparation for aptamer capture.



#### **V.B.4. Aptamer Capture on Small-Molecule-Patterned Substrates**

Aptamers were diluted 1:100 in binding buffer (10 mM Na<sub>2</sub>HPO<sub>4</sub>, 2 mM KH<sub>2</sub>PO<sub>4</sub>, 2.7 mM KCl, 5 mM MgCl<sub>2</sub>, 500 mM NaCl, pH 7.4) followed by heating at 95 °C in a water bath for 5 min.<sup>54</sup> Post-heat treatment, aptamer solutions were cooled in an ice bath for 20 s before equilibration at room temperature for 10 min. This standard procedure of heating and cooling removes misfolds in aptamer structures and maximizes correctly folded secondary structures. Substrates were then incubated with aptamers for 1 h at room temperature in the dark to prevent fluorophore photobleaching.

For binding affinity measurements, different concentrations of dopamine aptamers (1 μM - 50 μM) were incubated in different channels of microfluidic devices. For competitive displacement assays, microfluidic devices were sealed on dopamine-functionalized substrates and in each channel, the dopamine aptamer (20 μM) was co-incubated with different concentrations of free dopamine (0.1 μM - 50 μM). Solutions of dopamine and the dopamine aptamer were mixed and vortexed for 10 s before injection into microfluidic channels, followed by a 1 h incubation.

For multiplexed patterning, solutions of dopamine or *L*-tryptophan were injected into alternating microfluidic channels and incubated for 3 h. *L*-Tryptophan was dissolved in phosphate buffer (0.73 mM KH<sub>2</sub>PO<sub>4</sub>, 499 mM K<sub>2</sub>HPO<sub>4</sub>, pH 9.5). After microfluidic device removal, functionalized substrates were washed with H<sub>2</sub>O and incubated with a heat-treated mixture of the dopamine and *L*-tryptophan aptamers for 1 h at room temperature. Alternatively, we used oligoethyleneglycol alkanethiols pre-functionalized with neurotransmitters.<sup>47</sup> Here, gold surfaces were flame-annealed and hexane-treated PDMS devices were sealed to substrates. Solutions of 0.5 mM oligoethyleneglycol alkanethiols

pre-functionalized with *L*-3,4-dihydroxyphenylalanine, *L*-threo-3,4-dihydroxyphenylserine, or *L*-5-hydroxytryptophan were injected into separate channels and incubated for 15 min. Use of 100% pre-functionalized molecule ratios was based on maximal fluorescence intensities observed in our previous work.<sup>47</sup>

Microfluidic devices were removed and substrates were rapidly rinsed with ethanol to minimize exposure to incubating chemicals. Substrates were then incubated with 0.5 mM TEG to insert TEG into the areas surrounding the pre-functionalized molecules to minimize nonspecific binding.<sup>55</sup> Following completion of self-assembly, Fmoc groups used to protect amino moieties during the chemical synthesis of pre-functionalized molecules were removed by immersing substrates in 20% 4-methylpiperidine in deionized H<sub>2</sub>O for 15 min. After rinsing with fresh deionized H<sub>2</sub>O, new hexane-treated microfluidic devices were placed on substrates at 90° to original device orientations and aptamer concentration gradients (1  $\mu$ M - 30  $\mu$ M) were injected sequentially into channels and incubated for 1 h.

#### **V.B.5. Image Analysis and Statistics**

Immediately after aptamer binding (and microfluidic device removal where applicable), all substrates were completely submerged in deionized H<sub>2</sub>O and rinsed three times with fresh deionized water. Substrates were carefully removed from the last wash so as to keep their surfaces wet while glass coverslips were mounted. An inverted fluorescence microscope (Axio Observer.D1) with an AxioCam MRm charged-coupled device camera (Carl Zeiss MicroImaging, Inc., Thornwood, NY) was used to visualize aptamer binding on substrates. The microscope was equipped with two fluorescence filter sets, in which one (38 HE/high efficiency) has excitation and emission wavelengths at  $470 \pm 20$  nm and  $525 \pm 25$  nm,

respectively, and the other (43 HE/high efficiency) has excitation and emission wavelengths at  $550 \pm 25$  nm and  $605 \pm 70$  nm. Substrates were imaged using a 10 $\times$  objective lens.

Fluorescence intensities were determined by performing line scans of 30-pixel scanning widths using AxioVs40 Version 4.7.1.0 software (Carl Zeiss MicroImaging, Inc., Thornwood, NY, USA). On average, five line scans were acquired per substrate. Fluorescence intensities were averaged for each line scan and then for each image in patterned (small-molecule-functionalized) and unpatterned (background TEG) areas. All substrates from the same experiment were imaged using the same exposure times to standardize contrast and brightness. Relative fluorescence (units, RFU) were quantified in the patterned vs. unpatterned regions for multiple substrates (ranging from  $N=2$  for controls and  $N=4-6$  for specific experimental conditions). Fluorescence intensities were normalized to mean fluorescence values for background regions.<sup>56</sup> Mean fluorescence intensities of the patterned and unpatterned regions were obtained by normalizing  $\bar{x}_{\text{patterned}}$  and  $\bar{x}_{\text{unpatterned}}$  to the average  $\bar{x}_{\text{unpatterned}}$  value. Relative fluorescence intensities of the patterned regions were calculated by  $\bar{x}_{\text{patterned}}/\bar{x}_{\text{unpatterned}}$ . Fluorescence images shown in the figures are those that most closely represented mean fluorescence intensities.

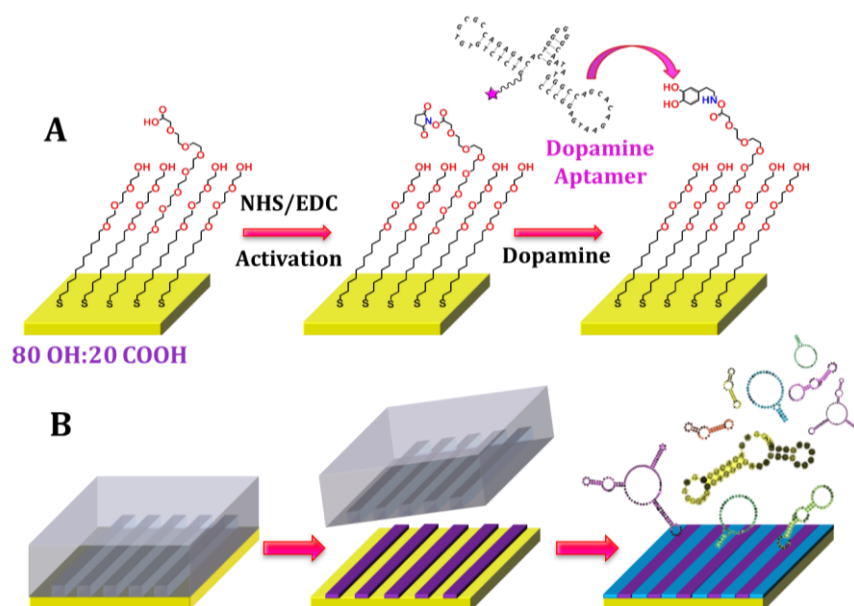
Relative fluorescence intensity data were evaluated by one-way analysis of variance followed by Tukey's multiple group comparisons. All statistics were carried out using GraphPad Prism (GraphPad Software Inc., San Diego). Data are reported as means  $\pm$  standard errors of the means with probabilities  $P < 0.05$  considered statistically significant.

## V.C. Results and Discussion

### V.C.1. Dopamine Aptamers Recognize Surface-Tethered Dopamine

Initially, dopamine-functionalized substrates were used to investigate recognition by nucleic acid aptamers.<sup>13,57-59</sup> The strategy for dilute neurotransmitter-substrate

functionalization is shown in Scheme V.1A.<sup>43,60</sup> Recognition of dopamine by this particular aptamer is thought to involve the



**Scheme V.1.** Schematics (not to scale) of functionalization and patterning strategies. **(A)** Gold substrates were incubated in ethanolic solutions of 80% hydroxyl tri(ethylene glycol)-terminated undecanethiol (TEG) and 20% carboxyl hexa(ethylene glycol)-terminated undecanethiol (HEG). Following NHS/EDC activation, HEG carboxyl groups were conjugated with small molecules such as dopamine, and tested for recognition with aptamers. **(B)** Microfluidics were used to pattern regions with tethered small molecules. Microfluidic devices were sealed onto gold substrates and target solutions (purple) were injected into the channels. After device removal, substrates were incubated with additional TEG (blue) to minimize non-specific binding in non-functionalized regions. Aptamer recognition was evaluated on patterned substrates.

catechol moiety.<sup>59</sup> As such, we hypothesized that immobilizing dopamine *via* its primary amine would permit aptamer binding. Microfluidic devices were used to pattern substrates so that each substrate would have functionalized and unfunctionalized regions to enable relative fluorescence quantification<sup>56,61</sup> (Scheme V.1B). Nonspecific binding was minimized by TEG moieties.<sup>46,62,63</sup>

Aptamer binding was investigated using 5'-fluorophore-tagged nucleic acids (Figure V.1). The “correct” dopamine aptamer sequence was the 57-base DNA homolog of an RNA aptamer originally isolated by *in vitro* selection using dopamine-functionalized agarose affinity columns and a library of  $3.4 \times 10^{14}$  (nominal) RNA sequences by Mannironi and co-workers (Figure V.1A).<sup>59</sup> We also investigated a “mutated” 58-base sequence with an additional adenine at position 21. This added base lies in a recognition loop of the “correct” dopamine aptamer. This mutated sequence was first reported by Walsh and deRosa describing the DNA homolog of an RNA dopamine aptamer (Figure V.1B).<sup>13</sup> We also designed a “scrambled” aptamer sequence, where the same numbers of each nucleotide were retained from the correct 57-base sequence but the primary sequence was changed to generate a significantly different secondary structure (Figure V.1C). Two-dimensional secondary structures shown in Figure V.1 were obtained using the *mfold* program<sup>©</sup>, which generates thermodynamically favorable conformations contingent on base-sequences and external constraints, such as temperature and ionic conditions.<sup>64</sup>

Using dopamine-patterned surfaces, the correct aptamer sequence displayed the highest binding to surface-tethered dopamine (Figure V.1A). By contrast, the mutated sequence showed a large reduction in dopamine-binding-associated fluorescence (Figure V.1B), while the scrambled sequence showed minimal recognition and no detectable pattern (Figure V.1C). Patterning the substrates using microfluidics enabled quantification of relative fluorescence intensities between the dopamine-functionalized and unfunctionalized regions (*i.e.*, background or matrix molecules).

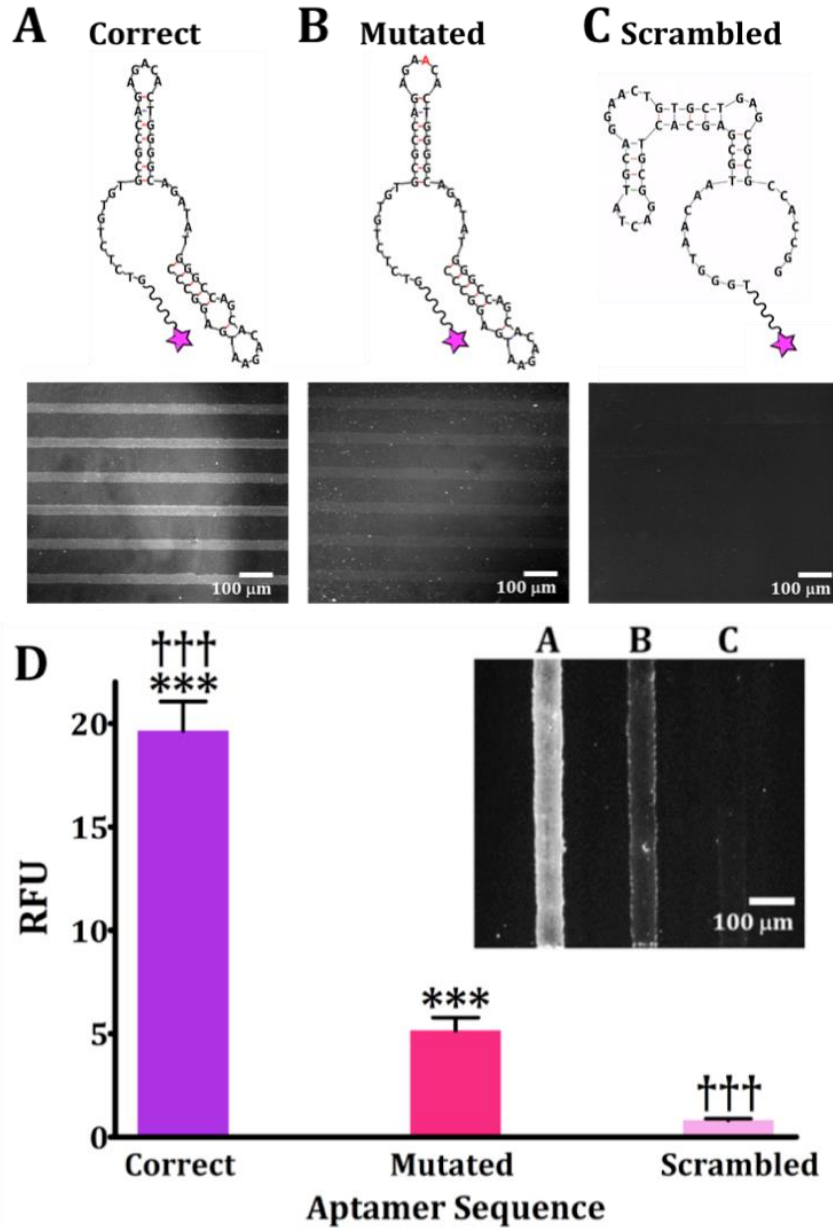


**Figure V.1. (Top)** Dopamine aptamer specificity investigated using microfluidics to pattern dopamine in specified regions on substrates. Representative fluorescence images from  $N=3$  substrates per sequence: (A) 57-base correct dopamine-specific aptamer sequence, (B) a mutated sequence with an extra adenine (red) in a recognition loop, and (C) a scrambled sequence with the same nucleotides as the correct sequence but a different primary sequence to generate a different secondary structure. Substrates were imaged at an emission wavelength of 605 nm for AlexaFluor® 546 (excitation at 556 nm). (D) Relative fluorescence intensities for nucleic acid binding to patterned dopamine substrates. Error bars are standard errors of the means with  $N=3$  samples per group. Means are significantly different for the correct vs. mutated vs. scrambled sequences. The inset shows a representative fluorescence image of all three aptamer sequences captured on the same substrate. Differences in aptamer sequence binding were essentially the same as those determined on separate substrates above. [ $F(2,15)=719$  \*\*\* $P < 0.0001$  vs. scrambled, ††† $P < 0.0001$  vs. mutated by one-way analysis of variance].

To illustrate that differences in relative fluorescence intensities between surfaces incubated with different aptamer sequences were not dominated by surface-to-surface variations, we captured the correct, mutated, and scrambled sequences side-by-side on dopamine-functionalized channels on the *same* substrates (Figure V.1D, inset). Relative differences in aptamer sequence binding were similar to those determined on separate substrates. These results highlight a key advantage of working with target-patterned substrates—binding of different biomolecules can be compared on the same substrates. These results further exemplify that a single base change (addition) in an important target-recognition region alters aptamer-target recognition.<sup>29</sup>

In addition to single aptamer concentrations, we carried out dopamine-

binding measurements on substrates where each channel was exposed to a different aptamer concentration (1-50  $\mu\text{M}$ ) to determine on-substrate thermodynamic dissociation

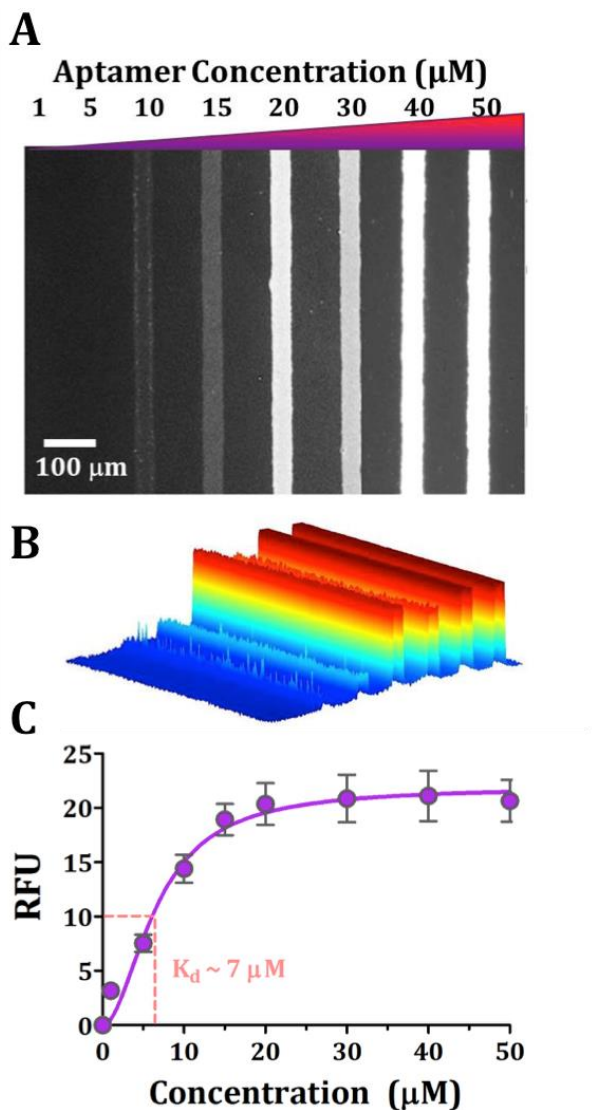


**Figure V.2.** Extracting dopamine aptamer dissociation constant for surface-tethered dopamine. **(A)** Representative fluorescence image from  $N=6$  substrates imaged at fluorescence emission wavelength 605 nm for AlexaFluor® 546 (excitation at 556 nm). Dopamine aptamer recognition was visualized at increasing concentrations of incubated aptamer (1-50  $\mu\text{M}$ ). **(B)** 3-dimensional surface plot of fluorescence image shown in **(A)**. **(C)** The surface binding affinity was obtained ( $\sim 7 \mu\text{M}$ ) by plotting relative fluorescence intensities at increasing aptamer concentrations. Error bars represent standard errors of the means.

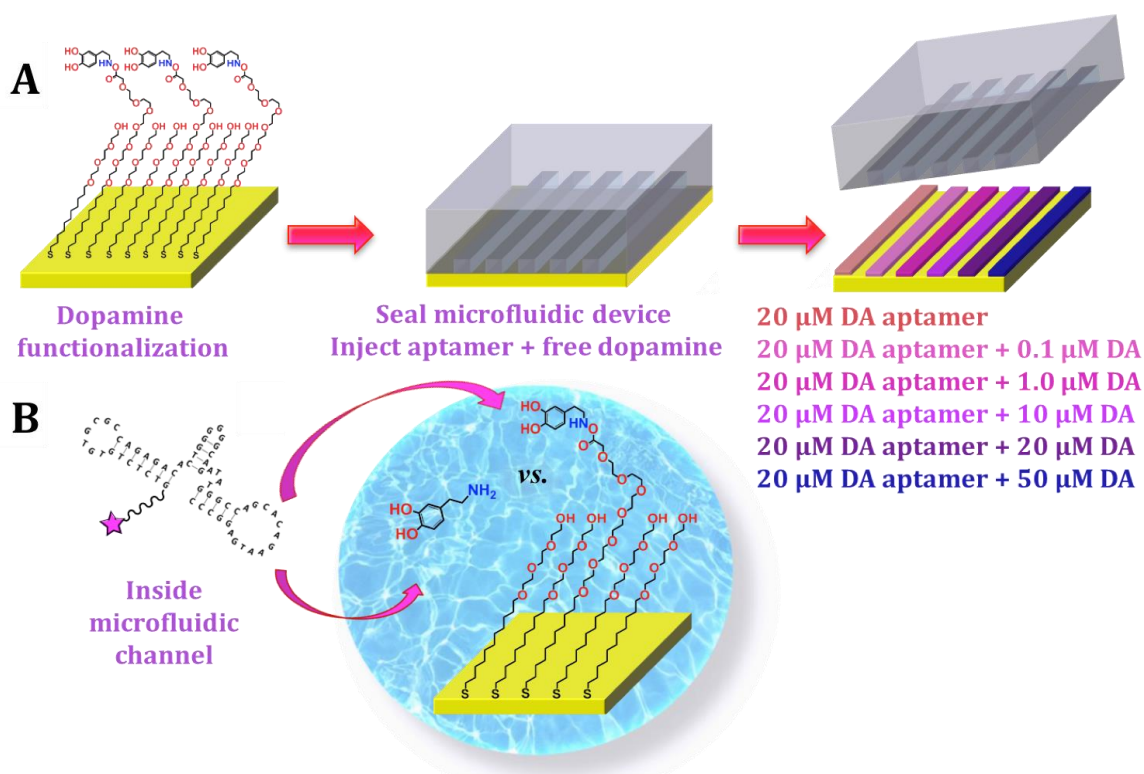
constants ( $K_d$ ) (Figure V.2A,B). A Langmuir isotherm (saturation curve) was generated by plotting increasing aptamer concentrations vs. relative fluorescence intensities (normalized to the background fluorescence of each of six substrates tested). The half-saturation point corresponded to  $K_d$  value of 7  $\mu\text{M}$  (Figure V.2C).

This  $K_d$  value determined for aptamer binding to surface-tethered dopamine was one order of magnitude greater than the  $K_d$  previously reported for this aptamer associating with dopamine in solution (0.7  $\mu\text{M}$ ).<sup>13</sup> Differences in the  $K_d$  values determined on-chip vs. in solution suggest that while surface-functionalized dopamine mimics free dopamine in terms of specificity of biomolecule binding partner capture,<sup>45,65</sup> steric hindrance of surface-bound target capture and/or restricted diffusion may result in a reductions in apparent dissociation constants determined for tethered small-molecule targets. Nonetheless, these results suggest that small-molecule-functionalized and patterned substrates might be used to screen multiple aptamer candidates quickly for relative difference in binding affinities.



## V.C.2. Competitive Displacement

Next, we investigated reversible binding of aptamers to surface-tethered dopamine in the presence of dopamine in solution. We designed competitive assays using substrates patterned with dopamine *via* microfluidics. Substrates were co-incubated with the dopamine aptamer (20  $\mu$ M), a concentration at which dopamine binding was saturated (*vide supra*; Figure V.2C), and different concentrations of free dopamine to vary the degree of competition (Scheme V.2). The concentration range of free dopamine was selected based on the on-chip  $K_d$  value and spanned approximately an order of magnitude above and below this dissociation constant.



**Scheme V.2.** Schematics (not to scale) of competitive displacement in microfluidic channels. **(A)** Dopamine was functionalized on substrates using sequential surface chemistry. Microfluidic devices were sealed on the substrates and a different concentration of dopamine (DA) in solution was co-incubated with a constant concentration of the dopamine aptamer in each channel. **(B)** Within each microfluidics channel, we created competitive environments for surface-tethered dopamine vs. free dopamine for aptamer recognition.

Representative fluorescence images for competitive displacement experiments are shown in Figure SD.1. Sigmoidal behavior of the competitive target-response curves was observed when increasing concentrations of solution dopamine were co-incubated with the dopamine aptamer and surface-tethered dopamine (Figure V.3A). The inhibitory constant,  $K_i$  (*i.e.*, concentration of inhibitor required for 50% inhibition) was calculated to be  $\sim 1 \mu\text{M}$  using the on-substrate  $K_d = 7 \mu\text{M}$  and a fixed aptamer concentration of  $20 \mu\text{M}$ .<sup>66</sup> This indicates that at a concentration of  $\sim 1 \mu\text{M}$ , free dopamine produces half maximal inhibition of the dopamine-aptamer binding to the surface-tethered dopamine.

We carried out further experiments using positive and negative controls. For the negative control condition (Figure V.3B), *L*-tryptophan was surface-tethered instead of dopamine and free dopamine was co-incubated with the dopamine aptamer. We observed negligible fluorescence indicating that

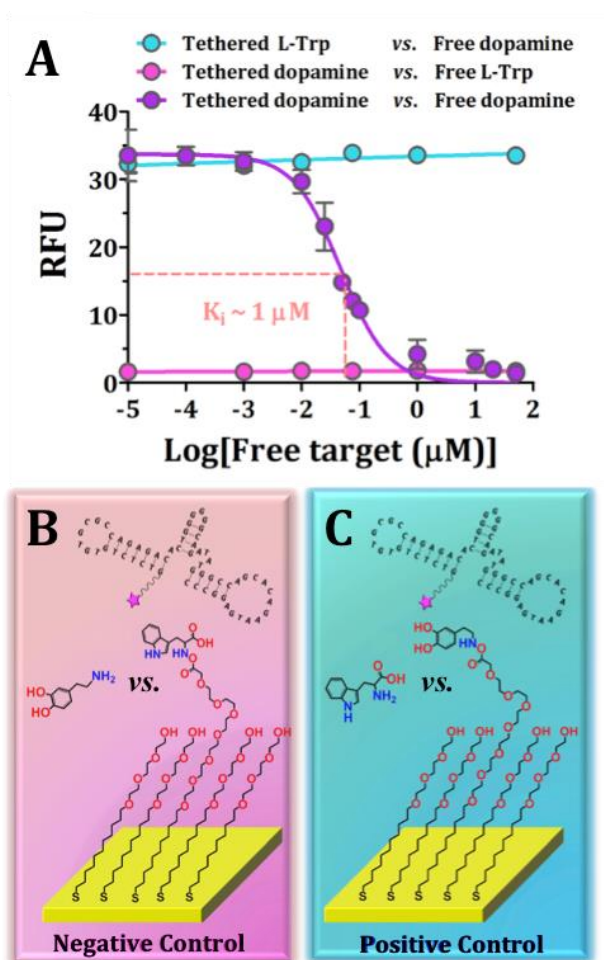


**Figure V.3.** Competitive displacement indicates reversible recognition of surface-tethered dopamine by the dopamine aptamer. **(A)** Inhibitory dose-response curve for surface-tethered dopamine vs. free dopamine. Error bars are standard errors of the means with  $N=4$  substrates for tethered vs. in solution dopamine and  $N=2$  for control conditions. Schematics (not to scale) for the negative control with the incorrect tethered target, *L*-tryptophan **(B)** and positive control with *L*-tryptophan in solution **(C)** are shown.

the dopamine aptamer preferentially bound to free dopamine and was removed during wash post-incubation wash steps from *L*-tryptophan-functionalized substrates.

For the positive control condition (Figure V.3C), we functionalized substrates with dopamine but co-incubated with free *L*-tryptophan in the presence of the dopamine aptamer. In this case, we observed maximal fluorescence across the entire range of *L*-tryptophan concentrations, suggesting negligible competition of *L*-tryptophan with substrate-bound dopamine for dopamine aptamer binding. Together, these data indicate the *selectivity* of the dopamine aptamer to differentiate two endogenous small molecules.

### **V.C.3. Multiplexed Substrates to Investigate Aptamer Selectivities**

We investigated selectivity of the dopamine aptamer by tethering *L*-tryptophan and dopamine molecules on the *same* substrates in alternating channels (Figure V.4A). Yang and co-workers evolved the DNA aptamer into an aptamer that recognizes *L*-tryptophan ( $K_d=1.8\ \mu\text{M}$ ) using *L*-tryptophan immobilized *via* the amino group on epoxy-activated Sepharose beads.<sup>12</sup> Thus, we hypothesized that tethering *L*-tryptophan *via* the same functional group chemistry should enable comparable recognition of the *L*-tryptophan aptamer on our substrates. The *L*-tryptophan aptamer was tagged with Alexa 488, while the dopamine aptamer was tagged with Alexa 546. Using aptamers labeled with different fluorophores allowed us to distinguish binding of each aptamer by visualizing relative fluorescence intensities at different wavelengths.

After incubation of substrates with a mixture of the *L*-tryptophan and dopamine aptamers fluorescence excitation of the dopamine aptamer fluorophore was carried out by excitation at 556 nm. Here, we observed fluorescence only in the dopamine-functionalized

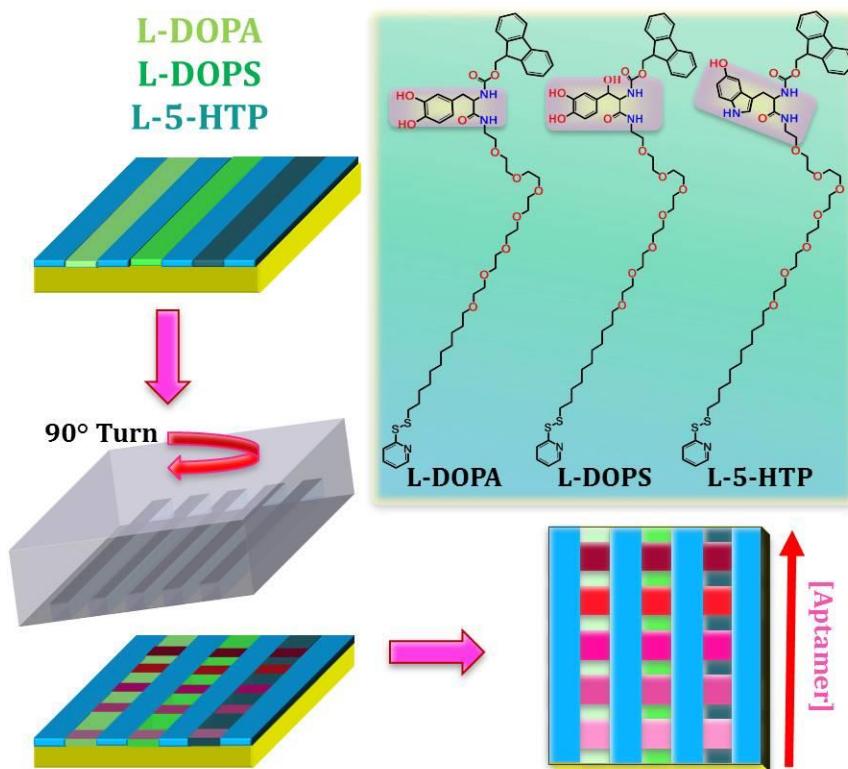


Visualization of sorting and capture of the dopamine aptamer from aptamer mixtures but not the *L*-tryptophan aptamer might result from one of two possibilities. First, the *L*-tryptophan aptamer may be unable to recognize *L*-tryptophan under our specific functionalization conditions. However, prior to investigating multiplexed substrates, recognition of surface-tethered *L*-tryptophan the *L*-tryptophan aptamer in our hands was confirmed (Figure SD.2). Nonetheless, the *L*-tryptophan aptamer yielded significantly lower contrast between regions of functionalized vs. unfunctionalized regions compared to the dopamine aptamer.

The surface functionalization strategy for multiplexing small molecules on substrates *via* microfluidics may cause insufficient *L*-tryptophan to be functionalized for recognition. *L*-Tryptophan typically requires reaction for ~48 h at basic pH for optimal functionalization.<sup>12</sup> By contrast, dopamine has been shown to self-polymerize after only 3 h in solution, coating substrates with dopamine-polymer layers that are tens of nanometers thick.<sup>67</sup> The dopamine used in our experiments was dissolved in pH 6.7 buffer solutions, which slows down but does not completely prevent the process of polymerization.

Thus, multiplexed on-surface functionalization chemistries present challenges for tethering multiple neurotransmitters due to requirements for different incubation times on the same substrate. Above, both small molecules were incubated in the microfluidic channels for 3 h (maximum dopamine incubation time to avoid polymerization), which may have resulted in insufficient *L*-tryptophan functionalization and negligible fluorescence in regions where the *L*-tryptophan aptamer was captured. Nevertheless, aptamer sorting to correctly functionalized substrate regions was demonstrated using the dopamine aptamer.

To tackle the challenge of multiplexed functionalization of structurally similar small molecules and to enable the determination of on-chip  $K_d$  values for multiple targets simultaneously, we investigated pre-functionalized neurotransmitter-conjugated oligoethylene alkanethiols, which we previously designed and



**Scheme V.3.** Schematics (not to scale) of multiplexed patterning of three pre-functionalized molecules (*L*-DOPA, *L*-DOPS, and *L*-5-HTP) on substrates. A new microfluidic device was sealed over all three molecules at a 90° angle to the initial microfluidics device orientation and an aptamer concentration gradient was incubated across different channels. This enabled simultaneous  $K_d$  determinations for all three tethered molecules. The structures of pre-functionalized *L*-DOPA, *L*-DOPS, and *L*-5-HTP are shown on the top right.

synthesized to enable more precise multiplexed patterning of multiple small molecules.<sup>47</sup>

The use of pre-functionalized tethers circumvents the need to meet diverse requirements for incubation times and conditions for attaching different small molecules to precise locations on substrates. Pre-functionalized molecules address limitations associated with incomplete functionalization and side-product formation, and aptamer recognition and binding was hypothesized not to rely on the efficiency of on-substrate coupling chemistries used above (Scheme V.1A).



As shown in Scheme V.3, we devised a method to first pattern multiple pre-functionalized molecules using microfluidics, and then to create an aptamer concentration gradient orthogonal to the original patterns to obtain simultaneous  $K_d$  values for each target neurotransmitter *in situ*. We patterned the tethers pre-functionalized with *L*-3,4-dihydroxyphenylalanine (*L*-DOPA), *L*-threo-dihydroxyphenylserine (*L*-DOPS), and *L*-5-hydroxytryptophan (*L*-5-HTP), which are precursors to the neurotransmitters dopamine, norepinephrine, and serotonin, respectively (Figure V.5A). By tethering the precursors of the neurotransmitters *via* their extra carboxyl groups, the amino and catechol moieties needed for aptamer recognition

were preserved. Comparable fluorescence intensities were observed at different concentrations of the dopamine aptamer incubated with the *L*-DOPA and *L*-DOPS. The calculate  $K_d$  values were 6  $\mu$ M and 8  $\mu$ M, respectively (Figure V.5C).

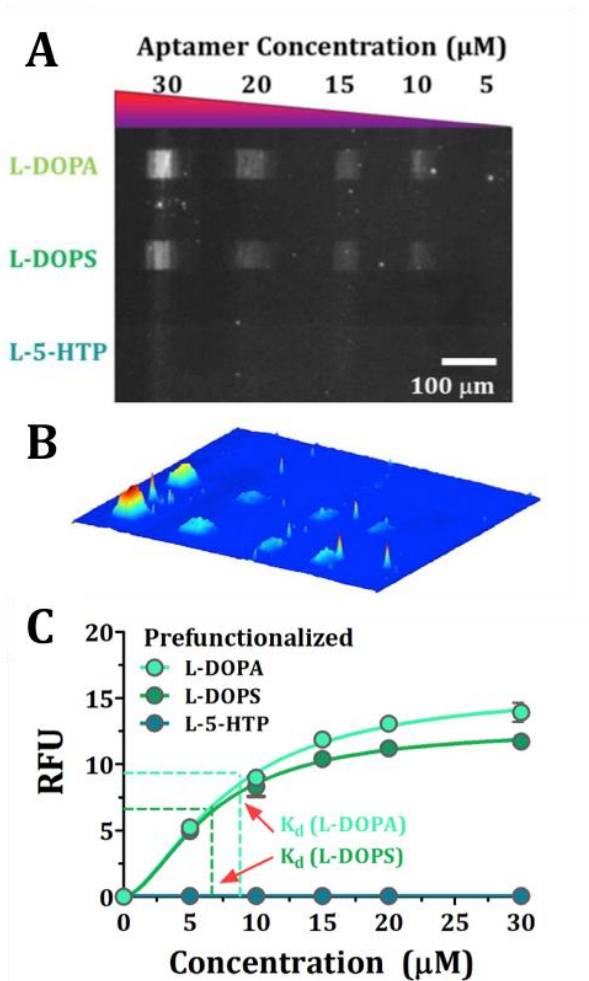


**Figure V.5.** Representative fluorescence image at an emission wavelength of 605 nm for AlexaFluor® 546 (excitation at 556 nm) tested against three pre-functionalized molecules (*L*-DOPA, *L*-DOPS, and *L*-5-HTP). **(B)** 3-dimensional surface plot of fluorescence image shown in **(A)**. **(C)** The surface binding affinity was obtained simultaneously for all three molecules by plotting fluorescence intensities at increasing aptamer concentrations. Error bars represent standard errors of the means with  $N=4$  samples.

Cross-reactivity of the dopamine aptamer towards norepinephrine, which is structurally related to *L*-DOPS, has been reported previously, presumably due to aptamer recognition largely involving the catechol groups present in both norepinephrine and dopamine.<sup>59</sup> Minimal relative fluorescence was observed for the structurally dissimilar *L*-5-HTP. The dopamine aptamer cross-reactivity indicates the difficulty for small molecule aptamers to differentiate between target molecules that differ by a single functional group (in this case, a hydroxyl group).<sup>68</sup> It emphasizes the importance of discovering aptamers that have the capacity to distinguish between physiologically important, structurally similar small molecules. The capacity to measure multiple  $K_d$  values simultaneously on the same substrate allows us to compare *relative* dissociation constants for aptamer binding to specific vs. nonspecific or cross-reactive targets in a facile manner.

#### **V.C.4. Aptamer Elution from Multiplexed Neurochips**

Commonly in SELEX, bound nucleic acid sequences are eluted and amplified by the polymerase chain reaction prior to subsequent rounds of selection.<sup>69</sup> Solid phase selection methods use high pH buffer solutions to elute adsorbed DNA.<sup>70,71</sup> The  $pK_a$ s of guanine and thymine are 9-10. Under highly basic conditions ( $pH > 10$ ), the tertiary amines on these bases become deprotonated to form the negatively charged conjugate bases.<sup>72</sup> Upon deprotonation, intramolecular G/C and A/T hydrogen bonding networks are disrupted, which disrupts nucleic acid secondary structure enabling the elution of sequences that are bound to surface-tethered targets.<sup>73</sup>



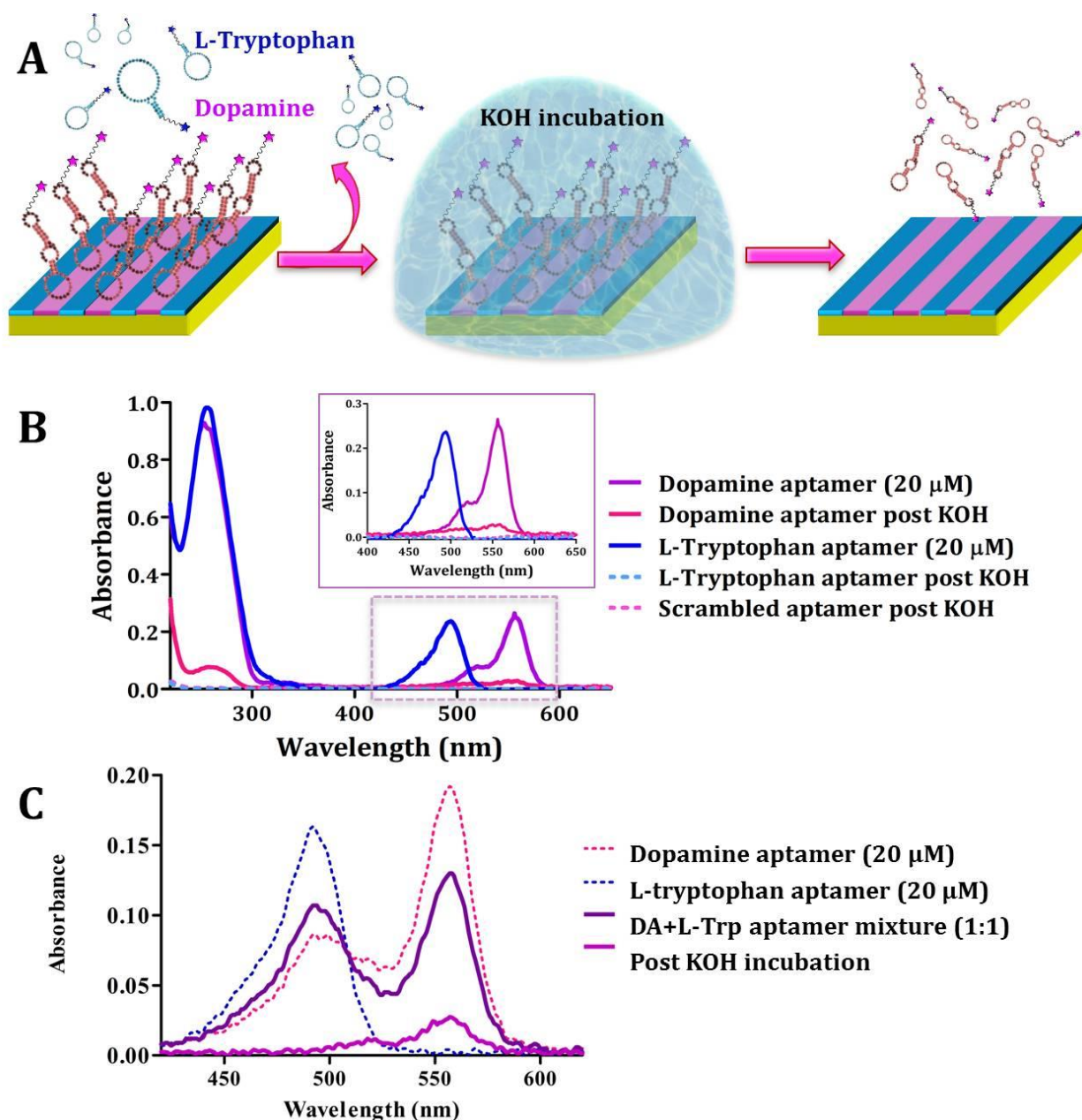


**Figure V.6.** Elution of aptamers after capture on neurochips **(A)** Schematic (not to scale) of incubation of dopamine-functionalized surfaces with a mixture of dopamine and L-tryptophan aptamers. Unbound sequences are rinsed from the substrates. Following KOH treatment, captured aptamers were collected. **(B)** Representative UV-vis spectra ( $N=3$ ) tracking the concentration of aptamers collected after KOH treatment based at AlexaFluor® 546 and AlexaFluor® 488 wavelengths for dopamine and L-tryptophan aptamers, respectively. Control experiments with the scrambled dopamine and L-tryptophan aptamer sequences showed negligible nucleic acid collection. **(C)** Representative UV-vis spectra ( $N=3$ ) for selective elution of dopamine aptamers from a mixture.

We eluted bound aptamers from substrates using a strong base, potassium hydroxide (KOH) (Figure V.6A). Dopamine-functionalized surfaces were incubated with the dopamine aptamer and the initial aptamer concentration was compared to the amount present in post-KOH eluent. Compared to the initial dopamine aptamer concentration of  $20 \pm 0.42 \mu\text{M}$ , the eluent concentration was  $2.6 \pm 0.12 \mu\text{M}$  (Figure V.6B). The captured and eluted dopamine aptamer concentration was an order of magnitude lower than the initial concentration, likely due to low concentrations of substrate-tethered dopamine under dilute self-assembly conditions with TEG needed to minimize steric hindrance. To validate that eluted aptamer concentrations were the result of specific target recognition, we conducted two negative control experiments using the scrambled dopamine aptamer and the *L*-tryptophan aptamer. When dopamine-functionalized substrates were incubated with either of these sequences, we were unable to elute quantifiable amounts of fluorescently labeled nucleic acids (Figure V.6B).

To identify novel aptamers that recognize neurotransmitters of interest, it will be necessary to elute aptamer candidate selectively from mixtures. We performed elutions using mixtures of *L*-tryptophan and dopamine aptamers incubated on dopamine-functionalized substrates, as shown in Figure V.6A. The concentrations of the *L*-tryptophan vs. the dopamine aptamers were distinguished because each aptamer was tagged with different fluorophores that emitted at different wavelengths. Dopamine-functionalized substrates were incubated with 1:1 mixtures of the two aptamers and KOH treatment was used to elute the captured sequences. Only  $0.2 \pm 0.02 \mu\text{M}$  of *L*-tryptophan aptamer was eluted, while  $2.4 \pm 0.13 \mu\text{M}$  of the dopamine aptamer was eluted (Figure V.6C). This latter concentration was comparable to the concentration of the dopamine aptamer recovered

from dopamine-functionalized substrates when the aptamer was incubated by itself (Figure V.6B). The ability to capture neurotransmitter-specific aptamers and to recover them from our neurotransmitter-functionalized substrates illustrates the potential of these substrates for future use in the selection of novel neurotransmitter-specific aptamers.

## V.D. Conclusions and Prospects

Biosensing with aptamers as recognition elements has not reached its full potential due, in part, to a lack of understanding fundamental relationships between aptamer binding affinities ( $K_d$ ) and device sensitivities. Dissociation constants determined in solution differ somewhat from on-substrate aptamer  $K_d$  calculations. We developed solid-phase substrates with highly controlled surface chemistries to tether small molecules mimicking *free* targets in solution for recognition by aptamers. Our results using dopamine and *L*-tryptophan-specific DNA aptamers showed that surface-tethered small molecules were functional for biorecognition by these aptamers. Pre-functionalized molecules, previously shown to display more consistent biomolecule target recognition, were utilized to create multiplexed substrates. The use of pre-functionalized molecules allowed simultaneous determination of on-substrate  $K_d$  values for multiple targets *in situ*, while investigating selectivity for structurally similar small molecules.

The neurotransmitter-functionalized substrates studied here offer the possibility of identifying high affinity neurotransmitter-specific aptamers that have been challenging to isolate *via* conventional solid-phase SELEX. Promising candidate libraries isolated through SELEX can be tested on multiplexed substrates to determine *relative*  $K_d$  values in the presence of nonspecific, similarly structured targets (*e.g.* dopamine *vs.* norepinephrine). Once high-affinity aptamers are discovered and their  $K_d$  values determined *in situ*, our ongoing work will be focused on immobilizing specific aptamers onto biosensors towards the real-time measurement of neurotransmitters in localized brain regions.

## **APPENDIX D**

### **Aptamer Recognition of Multiplexed Neurotransmitter- Functionalized Substrates**

#### **Supplementary Information**

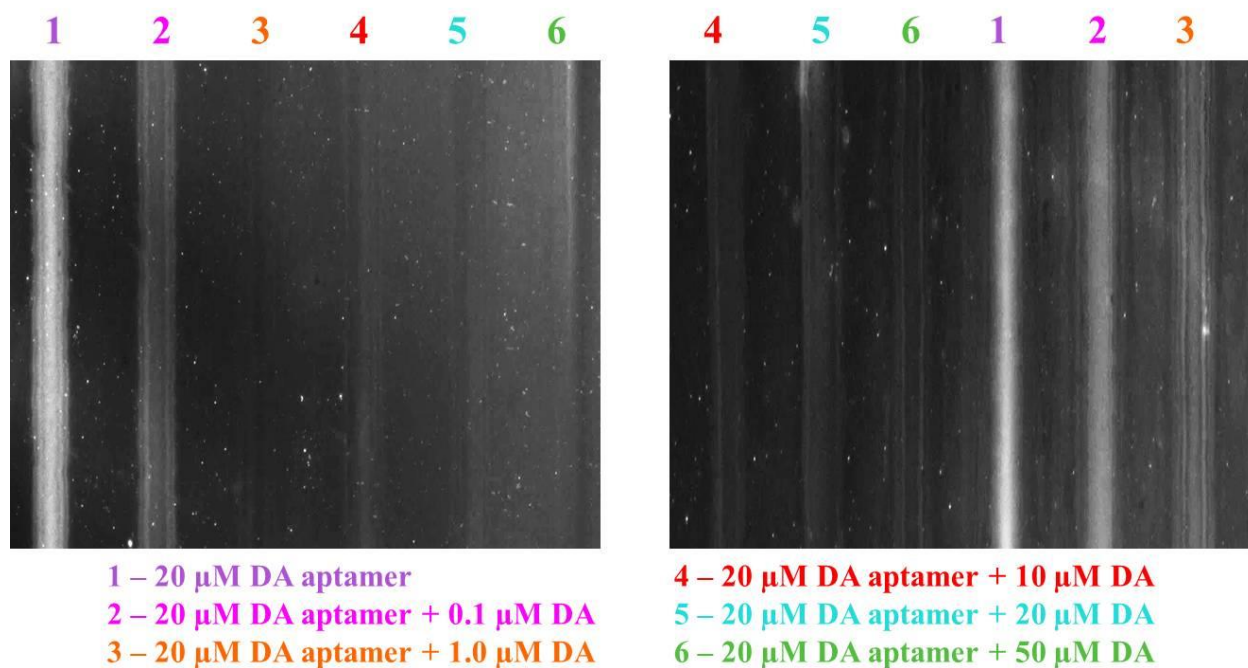


**Figure SD.1.** Representative fluorescence images for competitive displacement to test specific binding between surface-tethered dopamine and the dopamine aptamer. Increasing concentrations of free dopamine was added from 0.1 to 50  $\mu\text{M}$  and quantified in Figure V.3, Chapter V. Alternative channel incubation orders was used for the  $N=4$  trials for unbiased surface patterning and recognition quantification.

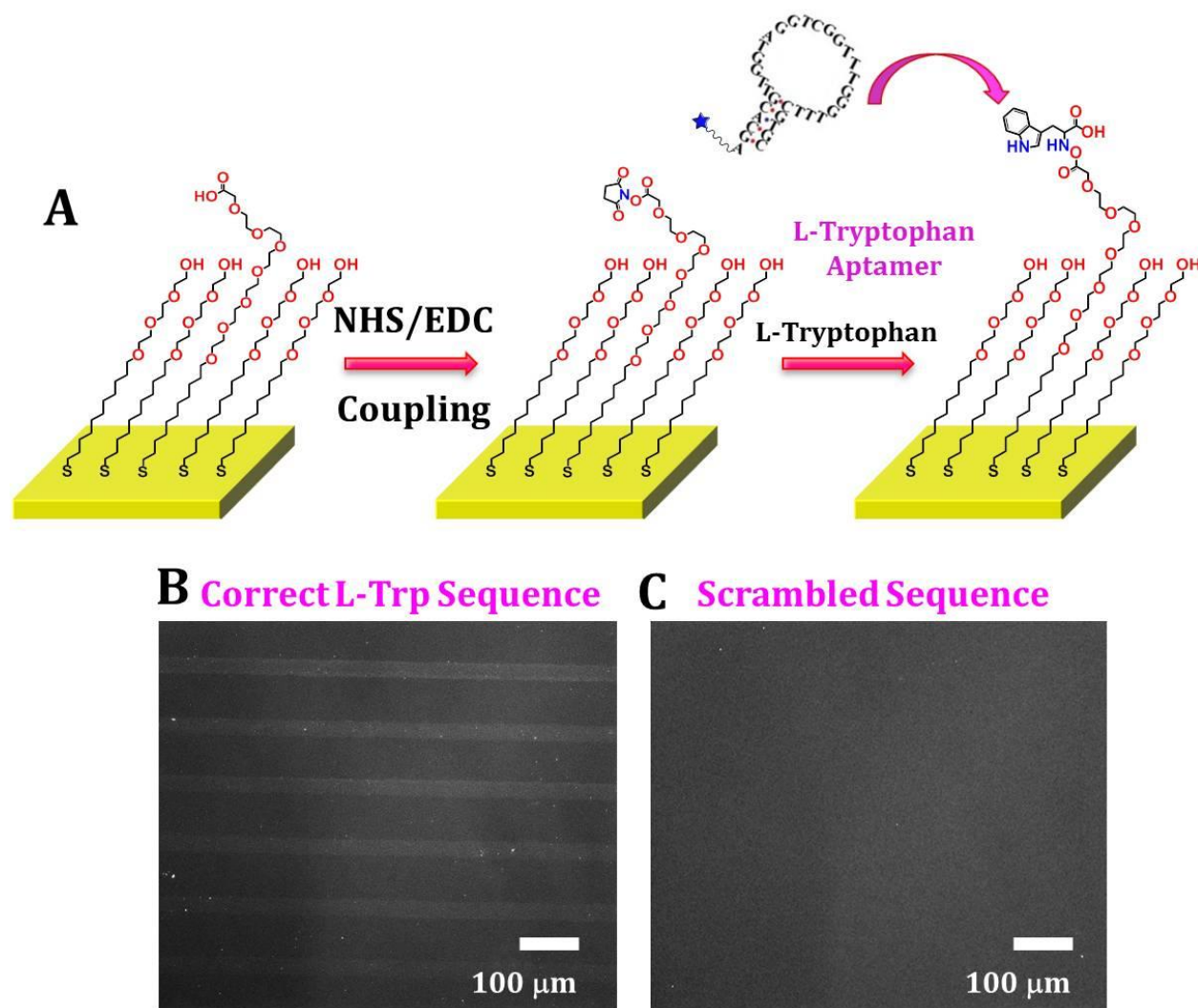


**Figure SD.2.** *L*-Tryptophan aptamer capture on patterned surfaces. **(a)** Schematic (not to scale) of patterning and functionalization of *L*-Tryptophan molecules **(b)** The 34-base *L*-Tryptophan-specific aptamer sequence and **(c)** a scrambled sequence with the same nucleotides conserved as the correct sequence but randomized to generate a different secondary structure. The secondary structures of the aptamers were modeled using *mfold*. Substrates were imaged at an emission wavelength of 525 nm for AlexaFluor® 488 (excitation at 490 nm).

## References

1. Tuerk, C.; Macdougall, S.; Gold, L. RNA Pseudoknots That Inhibit Human-Immunodeficiency-Virus Type-1 Reverse-Transcriptase. *Proc. Natl. Acad. Sci. U. S. A* **1992**, *89*, 6988-6992.
2. Kumar, P. K. R. Monitoring Intact Viruses Using Aptamers. *Biosensors (Basel)* **2016**, *6*, 1-16.
3. Ni, X.; Castanares, M.; Mukherjee, A.; Lupold, S. E. Nucleic Acid Aptamers: Clinical Applications and Promising New Horizons. *Curr. Med. Chem.* **2011**, *18*, 4206-4214.
4. Kubik, M. F.; Stephens, A. W.; Schneider, D.; Marlar, R. A.; Tasset, D. High-Affinity RNA Ligands to Human Alpha-Thrombin. *Nucleic Acids Res.* **1994**, *22*, 2619-2626.
5. Soldevilla, M. M.; Villanueva, H.; Pastor, F. Aptamers: A Feasible Technology in Cancer Immunotherapy. *J. Immunol. Res.* **2016**.
6. Parashar, A. Aptamers in Therapeutics. *J. Clin. Diagn. Res.* **2016**, *10*, Be1-Be6.
7. Williams, K. P.; Liu, X. H.; Schumacher, T. N. M.; Lin, H. Y.; Ausiello, D. A.; Kim, P. S.; Bartel, D. P. Bioactive and Nuclease-Resistant L-DNA Ligand of Vasopressin. *Proc. Natl. Acad. Sci. U. S. A.* **1997**, *94*, 11285-11290.
8. Yang, J.; Zhu, J.; Pei, R.; Oliver, J. A.; Landry, D. W.; Stojanovic, M. N.; Lin, Q. Integrated Microfluidic Aptasensor for Mass Spectrometric Detection of Vasopressin in Human Plasma Ultrafiltrate. *Anal. Methods* **2016**, *8*, 5190-5196.
9. Nieuwlandt, D.; Wecker, M.; Gold, L. *In Vitro* Selection of RNA Ligands to Substance P. *Biochemistry* **1995**, *34*, 5651-5659.
10. Pfeiffer, F.; Mayer, G. Selection and Biosensor Application of Aptamers for Small Molecules. *Front. Chem.* **2016**, *4*, 1-21.
11. Geiger, A.; Burgstaller, P.; vonderEltz, H.; Roeder, A.; Famulok, M. RNA Aptamers That Bind *L*-Arginine with Sub-Micromolar Dissociation Constants and High Enantioselectivity. *Nucleic Acids Res.* **1996**, *24*, 1029-1036.
12. Yang, X. J.; Bing, T.; Mei, H. C.; Fang, C. L.; Cao, Z. H.; Shangguan, D. H. Characterization and Application of a DNA Aptamer Binding to *L*-Tryptophan. *Analyst* **2011**, *136*, 577-585.
13. Walsh, R.; DeRosa, M. C. Retention of Function in the DNA Homolog of the RNA Dopamine Aptamer. *Biochem. Biophys. Res. Co.* **2009**, *388*, 732-735.
14. Ruscito, A.; DeRosa, M. C. Small-Molecule Binding Aptamers: Selection Strategies, Characterization, and Applications. *Front. Chem.* **2016**, *4*, 1-14.



15. Yang, K. A.; Pei, R. J.; Stojanovic, M. N. *In Vitro* Selection and Amplification Protocols for Isolation of Aptameric Sensors for Small Molecules. *Methods* **2016**, *106*, 58-65.
16. Yang, K. A.; Barbu, M.; Halim, M.; Pallavi, P.; Kim, B.; Kolpashchikov, D. M.; Pecic, S.; Taylor, S.; Worgall, T. S.; Stojanovic, M. N. Recognition and Sensing of Low-Epitope Targets *via* Ternary Complexes with Oligonucleotides and Synthetic Receptors. *Nat. Chem.* **2014**, *6*, 1003-1008.
17. Yang, K. A.; Chun, H.; Zhang, Y.; Pecic, S.; Nakatsuka, N.; Andrews, A. M.; Worgall, T. S.; Stojanovic, M. N. High-Affinity Nucleic-Acid-Based Receptors for Steroids. *ACS Chem. Bio.* **2017**, DOI: 10.1021/acschembio.7b00634.
18. Qu, H.; Csordas, A. T.; Wang, J. P.; Oh, S. S.; Eisenstein, M. S.; Soh, H. T. Rapid and Label-Free Strategy to Isolate Aptamers for Metal Ions. *ACS Nano* **2016**, *10*, 7558-7565.
19. Rajendran, M.; Ellington, A. D. Selection of Fluorescent Aptamer Beacons That Light Up in the Presence of Zinc. *Anal. Bioanal. Chem.* **2008**, *390*, 1067-1075.
20. Hofmann, H. P.; Limmer, S.; Hornung, V.; Sprinzl, M. Ni<sup>2+</sup>-Binding RNA Motifs with an Asymmetric Purine-Rich Internal Loop and a G-A Base Pair. *RNA* **1997**, *3*, 1289-1300.
21. Ellington, A. D.; Szostak, J. W. *In Vitro* Selection of RNA Molecules That Bind Specific Ligands. *Nature* **1990**, *346*, 818-822.
22. Tuerk, C.; Gold, L. Systematic Evolution of Ligands by Exponential Enrichment - RNA Ligands to Bacteriophage-T4 DNA-Polymerase. *Science* **1990**, *249*, 505-510.
23. Drolet, D. W.; Jenison, R. D.; Smith, D. E.; Pratt, D.; Hicke, B. J. A High Throughput Platform for Systematic Evolution of Ligands by Exponential Enrichment (SELEX). *Comb. Chem. High Throughput Screen.* **1999**, *2*, 271-278.
24. Stoltenburg, R.; Reinemann, C.; Strehlitz, B. SELEX - A (R)Evolutionary Method to Generate High-Affinity Nucleic Acid Ligands. *Biomol. Eng.* **2007**, *24*, 381-403.
25. Thiviyanathan, V.; Gorenstein, D. G. Aptamers and the Next Generation of Diagnostic Reagents. *Proteom. Clin. Appl.* **2012**, *6*, 563-573.
26. Yuce, M.; Ullah, N.; Budak, H. Trends in Aptamer Selection Methods and Applications. *Analyst* **2015**, *140*, 5379-5399.
27. Pendergrast, P. S.; Marsh, H. N.; Grate, D.; Healy, J. M.; Stanton, M. Nucleic Acid Aptamers for Target Validation and Therapeutic Applications. *J. Biomol. Tech.* **2005**, *16*, 224-234.

28. Imaizumi, Y.; Kasahara, Y.; Fujita, H.; Kitadume, S.; Ozaki, H.; Endoh, T.; Kuwahara, M.; Sugimoto, N. Efficacy of Base-Modification on Target Binding of Small Molecule DNA Aptamers. *J. Am. Chem. Soc.* **2013**, *135*, 9412-9419.
29. Ricci, F.; Valee-Belisle, A.; Simon, A. J.; Porchetta, A.; Plaxco, K. W. Using Nature's "Tricks" to Rationally Tune the Binding Properties of Biomolecular Receptors. *Acc. Chem. Res.* **2016**, *49*, 1884-1892.
30. Vallee-Belisle, A.; Ricci, F.; Plaxco, K. W. Engineering Biosensors with Extended, Narrowed, or Arbitrarily Edited Dynamic Range. *J. Am. Chem. Soc.* **2012**, *134*, 2876-2879.
31. Hasegawa, H.; Savory, N.; Abe, K.; Ikebukuro, K. Methods for Improving Aptamer Binding Affinity. *Molecules* **2016**, *21*.
32. Han, K.; Liang, Z. Q.; Zhou, N. D. Design Strategies for Aptamer-Based Biosensors. *Sensors (Basel)* **2010**, *10*, 4541-4557.
33. Zhou, W. Z.; Huang, P. J. J.; Ding, J. S.; Liu, J. Aptamer-Based Biosensors for Biomedical Diagnostics. *Analyst* **2014**, *139*, 2627-2640.
34. MacKay, S.; Wishart, D.; Xing, J. Z.; Chen, J. Developing Trends in Aptamer-Based Biosensor Devices and Their Applications. *IEEE T. Biomed. Circ. S.* **2014**, *8*, 4-14.
35. Song, S. P.; Wang, L. H.; Li, J.; Zhao, J. L.; Fan, C. H. Aptamer-Based Biosensors. *Trends Anal. Chem.* **2008**, *27*, 108-117.
36. Andrews, A. M. The BRAIN Initiative: Toward a Chemical Connectome. *ACS Chem. Neurosci.* **2013**, *4*, 645-645.
37. Andrews, A. M.; Weiss, P. S. Nano in the Brain: Nano-Neuroscience. *ACS Nano* **2012**, *6*, 8463-8464.
38. Nakatsuka, N.; Andrews, A. M. Neurochips Enable Nanoscale Devices for High-Resolution *in Vivo* Neurotransmitter Sensing. *Neuropsychopharmacology* **2016**, *41*, 378-379.
39. Yang, K. A.; Pei, R. J.; Stefanovic, D.; Stojanovic, M. N. Optimizing Cross-Reactivity with Evolutionary Search for Sensors. *J. Am. Chem. Soc.* **2012**, *134*, 1642-1647.
40. Drees, B. L.; Rye, H. S.; Glazer, A. N.; Nelson, H. C. M. Environment-Sensitive Labels in Multiplex Fluorescence Analyses of Protein-DNA Complexes. *J. Biol. Chem.* **1996**, *271*, 32168-32173.
41. Turgeon, R. T.; Fonslow, B. R.; Jing, M.; Bowser, M. T. Measuring Aptamer Equilibria Using Gradient Micro Free Flow Electrophoresis. *Anal. Chem.* **2010**, *82*, 3636-3641.

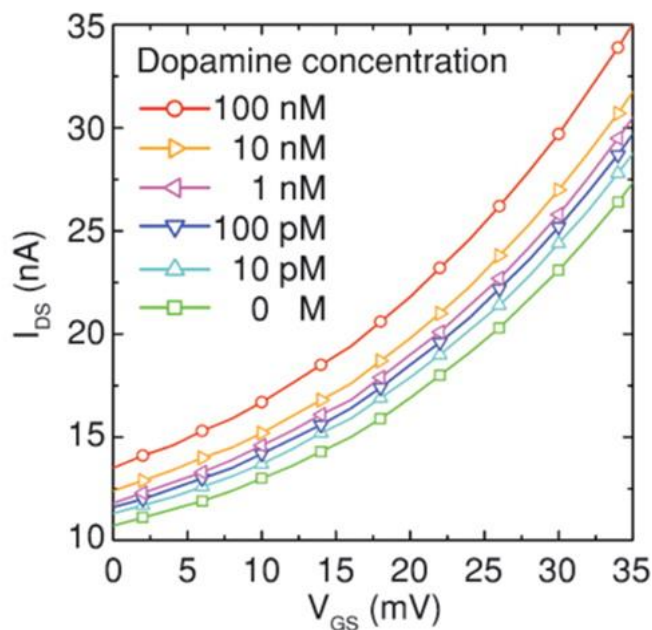
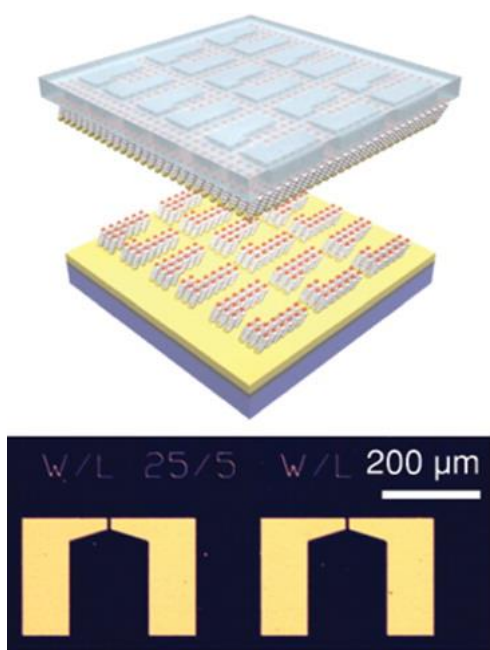
42. Zhang, A. Z.; Chang, D. R.; Zhang, Z. J.; Li, F.; Li, W. H.; Wang, X.; Li, Y. F.; Hua, Q. *In Vitro* Selection of DNA Aptamers That Binds Geniposide. *Molecules* **2017**, *22*.
43. Shuster, M. J.; Vaish, A.; Cao, H. H.; Guttentag, A. I.; McManigle, J. E.; Gibb, A. L.; Martinez-Rivera, M.; Nezarati, R. M.; Hinds, J. M.; Liao, W. S.; Weiss, P. S.; Andrews, A. M. Patterning Small-Molecule Biocapture Surfaces: Microcontact Insertion Printing vs. Photolithography. *Chem. Commun.* **2011**, *47*, 10641-10643.
44. Liao, W. S.; Cao, H. H.; Cheunkar, S.; Shuster, M. J.; Altieri, S. C.; Weiss, P. S.; Andrews, A. M. Small-Molecule Arrays for Sorting G-Protein-Coupled Receptors. *J. Phys. Chem. C* **2013**, *117*, 22362-22368.
45. Vaish, A.; Shuster, M. J.; Cheunkar, S.; Singh, Y. S.; Weiss, P. S.; Andrews, A. M. Native Serotonin Membrane Receptors Recognize 5-Hydroxytryptophan-Functionalized Substrates: Enabling Small-Molecule Recognition. *ACS Chem. Neurosci.* **2010**, *1*, 495-504.
46. Liao, W. S.; Cheunkar, S.; Cao, H. H.; Bednar, H. R.; Weiss, P. S.; Andrews, A. M. Subtractive Patterning *via* Chemical Lift-Off Lithography. *Science* **2012**, *337*, 1517-1521.
47. Cao, H. H.; Deshayes, S.; Nakatsuka, N.; Kasko, A. M.; Weiss, P. S.; Andrews, A. M. Enabling Multiplexed Small-Molecule Patterning *via* Pre-Functionalized Neurotransmitter Alkanethiols. *Submitted*, **2017**.
48. Schwartz, J. J.; Hohman, J. N.; Morin, E. I.; Weiss, P. S. Molecular Flux Dependence of Chemical Patterning by Microcontact Printing. *ACS Appl. Mater. Inter.* **2013**, *5*, 10310-10316.
49. Charles, P. T.; Stubbs, V. R.; Soto, C. M.; Martin, B. D.; White, B. J.; Taitt, C. R. Reduction of Non-Specific Protein Adsorption Using Poly(Ethylene) Glycol (PEG) Modified Polyacrylate Hydrogels in Immunoassays for Staphylococcal Enterotoxin B Detection. *Sensors (Basel)* **2009**, *9*, 645-655.
50. Wisniewski, N.; Reichert, M. Methods for Reducing Biosensor Membrane Biofouling. *Colloid Surf. B* **2000**, *18*, 197-219.
51. Xu, F. J.; Li, H. Z.; Li, J.; Teo, Y. H. E.; Zhu, C. X.; Kang, E. T.; Neoh, K. G. Spatially Well-Defined Binary Brushes of Poly(Ethylene Glycol)s for Micropatterning of Active Proteins on Anti-Fouling Surfaces. *Biosens. Bioelectron.* **2008**, *24*, 773-780.
52. Nojima, Y.; Iguchi, K.; Suzuki, Y.; Sato, A. The pH-Dependent Formation of PEGylated Bovine Lactoferrin by Branched Polyethylene Glycol (PEG)-*N*-Hydroxysuccinimide (NHS) Active Esters. *Biol. Pharm. Bull.* **2009**, *32*, 523-526.

53. Grumbach, I. M.; Veh, R. W. Sulpho-*N*-Hydroxysuccinimide Activated Long Chain Biotin. A New Microtitre Plate Assay for the Determination of Its Stability at Different pH Values and Its Reaction Rate with Protein Bound Amino Groups. *J. Immunol. Methods* **1991**, *140*, 205-210.
54. Sefah, K.; Shangguan, D.; Xiong, X. L.; O'Donoghue, M. B.; Tan, W. H. Development of DNA Aptamers Using Cell-SELEX. *Nat. Protoc.* **2010**, *5*, 1169-1185.
55. Cao, H. H.; Nakatsuka, N.; Serino, A. C.; Liao, W. S.; Cheunkar, S.; Yang, H. Y.; Weiss, P. S.; Andrews, A. M. Controlled DNA Patterning by Chemical Lift-Off Lithography: Matrix Matters. *ACS Nano* **2015**, *9*, 11439-11454.
56. Abendroth, J. M.; Nakatsuka, N.; Ye, M.; Kim, D.; Fullertor, E. E.; Andrews, A. M.; Weiss, P. S. Analyzing Spin Selectivity in DNA-Mediated Charge Transfer *via* Fluorescence Microscopy. *ACS Nano* **2017**, *11*, 7516-7526.
57. Kim, J.; Rim, Y. S.; Chen, H. J.; Cao, H. H.; Nakatsuka, N.; Hinton, H. L.; Zhao, C. Z.; Andrews, A. M.; Yang, Y.; Weiss, P. S. Fabrication of High-Performance Ultrathin In<sub>2</sub>O<sub>3</sub> Film Field-Effect Transistors and Biosensors Using Chemical Lift-Off Lithography. *ACS Nano* **2015**, *9*, 4572-4582.
58. Li, B. R.; Hsieh, Y. J.; Chen, Y. X.; Chung, Y. T.; Pan, C. Y.; Chen, Y. T. An Ultrasensitive Nanowire-Transistor Biosensor for Detecting Dopamine Release from Living PC12 Cells under Hypoxic Stimulation. *J. Am. Chem. Soc.* **2013**, *135*, 16034-16037.
59. Mannironi, C.; DiNardo, A.; Fruscoloni, P.; Tocchini Valentini, G. P. *In Vitro* Selection of Dopamine RNA Ligands. *Biochemistry* **1997**, *36*, 9726-9734.
60. Claridge, S. A.; Liao, W. S.; Thomas, J. C.; Zhao, Y. X.; Cao, H. H.; Cheunkar, S.; Serino, A. C.; Andrews, A. M.; Weiss, P. S. From the Bottom Up: Dimensional Control and Characterization in Molecular Monolayers. *Chem. Soc. Rev.* **2013**, *42*, 2725-2745.
61. Cao, H. H.; Nakatsuka, N.; Liao, W. S.; Serino, A. C.; Cheunkar, S.; Yang, H. Y.; Weiss, P. S.; Andrews, A. M. Advancing Biocapture Substrates *via* Chemical Lift-Off Lithography. *Chem Mater* **2017**, *29*, 6829-6839.
62. Lahiri, J.; Isaacs, L.; Tien, J.; Whitesides, G. M. A Strategy for the Generation of Surfaces Presenting Ligands for Studies of Binding Based on an Active Ester as a Common Reactive Intermediate: A Surface Plasmon Resonance Study. *Anal. Chem.* **1999**, *71*, 777-790.
63. Vanderah, D. J.; Vierling, R. J.; Walker, M. L. Oligo(Ethylene Oxide) Self-Assembled Monolayers, with Self-Limiting Packing Densities for the Inhibition of Nonspecific Protein Adsorption. *Langmuir* **2009**, *25*, 5026-5030.
64. Zuker, M. Mfold Web Server for Nucleic Acid Folding and Hybridization Prediction. *Nucleic Acids Res* **2003**, *31*, 3406-3415.

65. Shuster, M. J.; Vaish, A.; Szapacs, M. E.; Anderson, M. E.; Weiss, P. S.; Andrews, A. M. Biospecific Recognition of Tethered Small Molecules Diluted in Self-Assembled Monolayers. *Adv. Mater.* **2008**, *20*, 164-167.
66. Brandt, R. B.; Laux, J. E.; Yates, S. W. Calculation of Inhibitor  $K_i$  and Inhibitor Type from the Concentration of Inhibitor for 50% Inhibition for Michaelis-Menten Enzymes. *Biochem. Med. Metab. Biol.* **1987**, *37*, 344-349.
67. Ball, V.; Del Frari, D.; Toniazzo, V.; Ruch, D. Kinetics of Polydopamine Film Deposition as a Function of pH and Dopamine Concentration: Insights in the Polydopamine Deposition Mechanism. *J. Colloid Interf. Sci.* **2012**, *386*, 366-372.
68. Nakatsuka, N.; Andrews, A. M. Differentiating Siblings: The Case of Dopamine and Norepinephrine. *ACS Chem. Neurosci.* **2017**, *8*, 218-220.
69. Jhaveri, S.; Ellington, A. D. *In vitro Selection of RNA Aptamers to a Small Molecule Target*; John Wiley & Sons, Inc., 2002; Vol. Chapter 9, Unit 9.5.
70. Esser, K. H.; Marx, W. H.; Lisowsky, T. Maxxbond Ax: Optimized Regeneration Kit for Silica-Based Anion Exchange Resins. *Biotechniques* **2006**, *40*, 398-399.
71. Tan, S. C.; Yiap, B. C. DNA, RNA, and Protein Extraction: The Past and the Present. *J. Biomed. Biotechnol.* **2009**.
72. Verdolino, V.; Cammi, R.; Munk, B. H.; Schlegel, H. B. Calculation of  $pK$  Values of Nucleobases and the Guanine Oxidation Products Guanidinohydantoin and Spiroiminodihydantoin Using Density Functional Theory and a Polarizable Continuum Model. *J. Phys. Chem. B* **2008**, *112*, 16860-16873.

## Chapter VI

# Fabrication of High-Performance Ultrathin $\text{In}_2\text{O}_3$ Film Field-Effect Transistors and Biosensors Using Chemical Lift-Off Lithography



The information in this chapter was published in  
*ACS Nano* **2015**, 9, 4572-4582  
and has been reproduced here.

Authors: Kim, J.; Rim, Y. S.; Chen, H.; Cao, H. H.; Nakatsuka, N.;  
Hinton, H. L.; Zhao, C.; Andrews A. M.; Yang, Y.; Weiss, P.S.

## VI.A. Introduction

Field-effect transistors (FETs) have key advantages over optical or electrochemical platforms for biosensing applications, including low detection limits, real-time and label-free detection, and simple integration with standard semiconductor-device processing.<sup>1-4</sup> Biosensors based on FETs are typically constructed by immobilizing specific receptors on the surfaces of semiconducting channels. Upon specific interactions with target biomolecules, these receptors electrostatically gate the underlying channels and produce electronic signals such as changes in channel conductance and/or drain current. As the electronic signals of FET-based biosensors arise from the surface binding events between receptors and analytes, the sensitivity of devices is enhanced as the surface-to-volume ratio of the semiconducting channels increases. Therefore, nanomaterials with reduced dimensionalities and large surface areas are advantageous for the design of highly sensitive biosensors.

Notably, one-dimensional (1D) nanomaterials such as Si nanowires (SiNWs)<sup>5-10</sup> or carbon nanotubes (CNTs)<sup>11-17</sup> have been employed as the channel components of FET-based biosensors and shown to be highly effective in detecting biomolecules including proteins,<sup>5,8,9,12-15</sup> DNA,<sup>6,17</sup> viruses,<sup>18</sup> and neurotransmitters.<sup>7,10,19</sup> More recently, two-dimensional (2D) nanomaterials such as graphene<sup>20-24</sup> and molybdenum disulfide (MoS<sub>2</sub>)<sup>25,26</sup> have attracted attention for biosensing applications as they are composed of surfaces only and can thus provide remarkably large surface-to-volume ratios and high sensitivity.

One major challenge of using nanomaterials for FET-based biosensing applications is the complexity of the processes involved in their synthesis and integration into device

platforms. For instance, both SiNWs and CNTs are typically synthesized by chemical vapor deposition (CVD),<sup>27-30</sup> which requires precise control of the growth parameters to produce high-quality 1D nanomaterials suitable for FETs. In the case of CNTs, the CVD process usually produces a mixture of nanotubes with varying electrical properties, and additional purification steps are needed to separate from the mixture the metallic CNTs that are not compatible with FET channel materials.<sup>31-33</sup> For large-scale applications of 2D nanostructures, both graphene<sup>34-36</sup> and MoS<sub>2</sub><sup>37,38</sup> are typically grown by CVD as well. After growth, transfer steps are required that can leave undesirable polymer residues on surfaces that degrade device characteristics and/or the surface immobilization of receptors.<sup>39-42</sup>

Once nanomaterials are synthesized and placed on the desired substrates, lithography techniques are used to define device areas and to complete FET fabrication. Although conventional nanofabrication techniques, such as photolithography or electronbeam lithography, are effective in producing suitable electrode patterns for FET devices, they require the use of specialized equipment in clean, well-controlled environments. As such, there is a trade-off between spatial precision, cost, and throughput, limiting the scalability of high spatial precision patterning.

Here, we find that ultrathin (~4 nm), amorphous metal-oxide semiconductor films produced *via* simple sol-gel chemistry are effective for the fabrication of highly sensitive FET-based biosensors. Oxide semiconductor thin films were formed over large areas through a simple spin-coating process. This fabrication step was followed by functionalization with biologically receptive moieties through oxide surface chemistry attachment. To define the electrode patterns and to construct the devices, we employed



CLL<sup>43</sup> using SAMs of alkanethiols on Au as soft masks. Through covalent interactions formed at the interfaces between hydroxyl-terminated alkanethiol SAMs and “activated” PDMS stamps, thiol molecules were selectively removed from predefined areas, exposing the underlying bare Au surfaces for subsequent wet-etching.

Chemical lift-off lithography provides an efficient tool for high-throughput prototyping of FET devices over large areas without the use of sophisticated instruments, producing device features with high spatial precision suitable for the fabrication of micrometer- and submicrometer-scale devices. By combining ultrathin oxide semiconductor layers with CLL, we demonstrate simple and straightforward fabrication of highly sensitive biosensors toward the detection of the small-molecule neurotransmitter dopamine down to physiological subnanomolar concentrations.

## **VI.B. Experimental Methods**

### **VI.B.1. Materials**

The DNA aptamer for dopamine was synthesized by Integrated DNA Technologies, Inc. (Coralville, IA). The SYLGARD 184 was from Dow Corning Corporation and was used to make PDMS stamps throughout this work. All other chemicals were purchased from Sigma-Aldrich and used as received. Water was deionized before use ( $\sim 18.2 \text{ M}\Omega$ ) using a Milli-Q system (Millipore, Billerica, MA).

### **VI.B.2. Chemical Lift-Off Lithography**

Thin Au films (typically  $\sim 50 \text{ nm}$ ) were deposited on target substrates by electron-beam evaporation (CHA Industries, Fremont, CA) with Ti adhesion layers ( $5 \text{ nm}$ ). To deposit SAMs on Au surfaces, the substrates were immersed in  $1 \text{ mM}$  ethanolic solutions of 11-mercapto-1-undecanol and incubated overnight, unless described otherwise. The PDMS stamps with defined patterns were prepared over masters fabricated by standard photolithography or electron-beam lithography. The stamps were exposed to oxygen plasma (Harrick Plasma, Ithaca, NY) at a power of  $18 \text{ W}$  and an oxygen pressure of  $10 \text{ psi}$  for  $40 \text{ s}$  to yield fully hydrophilic reactive surfaces, and brought into conformal contact with the SAM-modified Au surfaces. After  $1 \text{ h}$ , unless described otherwise, the stamps were carefully removed from the substrates, and an aqueous solution of  $20 \text{ mM}$  iron nitrate and  $30 \text{ mM}$  thiourea was applied to the substrates to etch Au films selectively from the areas where the SAMs were removed. The Ti was removed from exposed areas using a  $1:2 \text{ (v/v)}$  solution of ammonium hydroxide and hydrogen peroxide. The substrates were rinsed with deionized water and dried under  $\text{N}_2$  before use.

### VI.B.3. Fabrication of Field-Effect Transistors and Biosensors

Chemical lift-off lithography was performed to pattern source and drain Au electrodes on a heavily doped silicon wafer covered with a 100 nm-thick thermally grown SiO<sub>2</sub> layer. Aqueous solutions of varying indium (III) nitrate hydrate (In(NO<sub>3</sub>)<sub>3</sub>·xH<sub>2</sub>O, 99.99%) concentrations were spin-coated onto the substrates at 3000 rpm for 30 s. The substrates were then prebaked at 100 °C for 5 min followed by thermal annealing at 250 °C for 1 h. For top-contact devices, indium oxide (In<sub>2</sub>O<sub>3</sub>) layers and Au thin films were deposited successively by spin-coating and electron-beam evaporation, respectively, and CLL was performed to pattern source and drain electrodes. To make biosensors, a DNA aptamer that recognizes dopamine was immobilized on In<sub>2</sub>O<sub>3</sub> layers with a top-contact device configuration.

Briefly, CLL was used to pattern interdigitated Au source and drain electrodes atop the In<sub>2</sub>O<sub>3</sub> layer deposited on SiO<sub>2</sub>/Si substrates. Substrate were then briefly exposed to oxygen plasma to remove the hydroxyl-terminated alkanethiols from the Au, followed by incubation in a 1 mM ethanolic solution of 1-dodecanethiol for 1 h. After thorough rinsing with ethanol, (3-aminopropyl)trimethoxysilane (APTMS) and trimethoxy(propyl)silane (PTMS) (1:9, v/v) were thermally evaporated onto the In<sub>2</sub>O<sub>3</sub> surface at 40 °C for 1 h, and substrates were immersed in a 1 mM solution of 3-maleimidobenzoic acid *N*-hydroxysuccinimide ester (MBS) dissolved in 1:9 (v/v) mixture of dimethyl sulfoxide (DMSO) and 1× PBS for 30 min. To anchor the DNA aptamer, substrates were rinsed with deionized water, immersed in a 1 μM solution of thiolated DNA in 1× PBS for 1 h, rinsed again with deionized water, and blown dry with N<sub>2</sub>.

#### VI.B.4. Characterization

Optical microscopy images were taken with an Olympus BX51M microscope. Atomic force microscopy imaging was performed on a Bruker Dimension Icon system using tapping mode. X-ray diffraction (XRD) and X-ray reflectivity (XRR) measurements were performed on a PANalytical X'Pert Pro system and a Bede D1 diffractometer, respectively. X-ray photoelectron spectra were collected on a Kratos Axis Ultra DLD system. Cyclic voltammetry was performed using a PAR EG&G 273A Potentiostat with an Ag/AgCl electrode, a platinum foil, and a platinum wire as a reference electrode, a counter electrode, and a working electrode, respectively. Measurements were performed in 0.1× PBS at a voltage sweep rate of 50 mV s<sup>-1</sup>. All electrical measurements were performed on a probe station equipped with an Agilent 4155C semiconductor analyzer. At least 10 devices were tested for each biosensing experiment, and the five best devices, in terms of stable (*i.e.*, low drift) baseline currents, were selected to obtain statistical data.

## VI.C. Results and Discussion

We employed  $\text{In}_2\text{O}_3$  as the channel material because its nanostructure has been shown to function effectively in biosensing platforms.<sup>14,44-46</sup> Moreover, thin films of  $\text{In}_2\text{O}_3$  can be formed *via* simple aqueous sol-gel chemistry, resulting in few organic contaminants and enabling lower temperature processing.<sup>47</sup> We dissolved varying amounts of an indium precursor, indium (III) nitrate hydrate in water and spin-coated the solutions onto heavily doped Si substrates covered with 100 nm-thick, thermally grown  $\text{SiO}_2$  dielectric layers.

As the indium precursor concentrations were increased, the color of the coated substrates changed from blue to light blue suggesting that the thickness of the deposited thin films increased. For the films prepared from solutions with low precursor concentrations ( $\leq 0.1$  M), the color change was barely noticeable. When examined under an optical microscope, however, we found that solutions containing less than 0.1 M of indium precursor produced large pinholes in the resulting thin films (left panel, Figure VI.1A), which can cause discontinuous electrical conduction and are thus not suitable for thin-film devices. We determined that an indium precursor concentration of 0.1 M was the lower limit for spin-coating of uniform  $\text{In}_2\text{O}_3$  films over large areas without pinholes (right panel, Figure VI.1A). Figure VI.1B and VI.1C show AFM images of the resulting thin films. Even though the apparent thickness of these films were only  $\sim 4$  nm (Figure VI.1B), they showed high uniformity over large areas ( $30\text{ }\mu\text{m} \times 30\text{ }\mu\text{m}$  in Figure VI.1C), and the root-mean-square roughness was calculated to be 0.4 nm.

We further examined these  $\text{In}_2\text{O}_3$  films using nondestructive X-ray metrology. Figure VI.1D shows an XRD pattern of an  $\text{In}_2\text{O}_3$  thin film prepared on a glass slide. Even after thermal annealing of the spin-coated film, no characteristic peak of  $\text{In}_2\text{O}_3$  was observed, suggesting that the

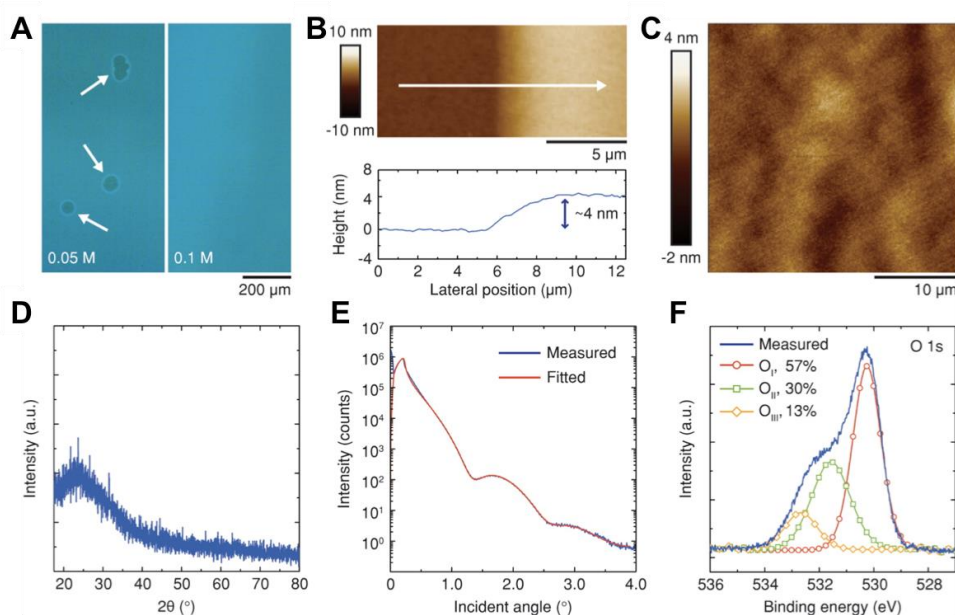


**Figure VI.1.** Sol-gel-processed  $\text{In}_2\text{O}_3$  ultrathin films. Simple spin-coating of indium precursor solutions followed by thermal annealing enabled uncomplicated deposition of  $\text{In}_2\text{O}_3$  layers with thickness measuring a few nanometers. (A) While a precursor solution containing 0.05 M of indium(III) nitrate produced a thin film with large pinholes (left, indicated by white arrows), a 0.1 M precursor solution produced a uniform thin film over large areas. (B,C) Atomic force microscope images of  $\text{In}_2\text{O}_3$  thin film produced from a 0.1 M precursor solution; the sol-gel process produced a uniform film over large areas, with (B) an apparent thickness of 4 nm and (C) a root-mean-square roughness of 0.4 nm. (D) No characteristic peaks were observed in the X-ray diffraction pattern, suggesting the amorphous nature of the thin film. (E) The thickness, mass density, and interface roughness of the sol-gel processed  $\text{In}_2\text{O}_3$  film were estimated to be 3.8 nm,  $5.90 \text{ g cm}^{-3}$ , and 0.4 nm, respectively, by fitting (red line) the X-ray reflectivity measurements (blue line) to a standard model. (F) The X-ray photoelectron O 1s spectrum of the ultrathin  $\text{In}_2\text{O}_3$  layer shows that most of the peak can be assigned to O in the oxide lattice ( $\text{O}_I$ : O in oxide lattice without vacancies,  $\text{O}_{II}$ : O in oxide lattice with vacancies), while only 13% of O can be assigned to unreacted metal hydroxide species ( $\text{O}_{III}$ ).

film was largely amorphous (a broad shoulder at around  $2\theta \approx 25^\circ$  corresponds to the background signal from the glass substrate). The thickness, mass density, and interface roughness of  $\text{In}_2\text{O}_3$  films deposited on  $\text{SiO}_2/\text{Si}$  substrates were extracted by fitting XRR curves to a standard model (Figure VI.1E). Film thicknesses were determined to be  $\sim 3.8 \text{ nm}$ , which agrees well with the apparent thickness measured by AFM (Figure VI.1B). The mass density of the films was estimated to be  $5.90 \text{ g cm}^{-3}$ , which is equivalent to 82.2%

of the theoretical value of structurally perfect  $\text{In}_2\text{O}_3$  crystals ( $7.18 \text{ g cm}^{-3}$ ). The roughness of the interface between  $\text{In}_2\text{O}_3$  and  $\text{SiO}_2$  was calculated to be  $\sim 0.4 \text{ nm}$ . In general, the interface roughness is indicative of the interface trap density, which has direct effects on the electron-transport properties of FET devices.<sup>48</sup> With an interface roughness below  $0.5 \text{ nm}$ , the  $\text{In}_2\text{O}_3$  films deposited on the  $\text{SiO}_2$  dielectric layers are expected to show good switching behavior, as demonstrated in subsequent experiments. Figure VI.1F shows the O 1s spectrum of the annealed  $\text{In}_2\text{O}_3$  films obtained by XPS. The spectrum was fit with and deconvoluted into three distinct peaks at 530.4, 531.5, and 532.6 eV, which correspond to O in the oxide lattice without vacancies ( $\text{O}_\text{I}$ ), O in the oxide lattice with vacancies ( $\text{O}_\text{II}$ ), and metal hydroxides ( $\text{O}_\text{III}$ ), respectively.<sup>47</sup> We found that most of the O atoms reside in the oxide lattice while only 13% of O was assigned to unreacted metal hydroxide species, which is comparable to  $\text{In}_2\text{O}_3$  films produced *via* organic-solvent-based approaches and annealed at high temperature.<sup>47</sup> On the basis of the XRD, XRR, and XPS measurements, we concluded that the aqueous-medium-based sol-gel process can produce, at relatively low temperatures, high-density amorphous  $\text{In}_2\text{O}_3$  ultrathin films that are suitable for electronic applications.

To construct FET devices using the sol-gel-processed  $\text{In}_2\text{O}_3$  films, we employed CLL as a high-throughput, large-scale tool to pattern Au source and drain contacts on  $\text{SiO}_2/\text{Si}$  substrates.<sup>43</sup> Figure VI.2A shows a schematic diagram depicting the CLL process. First, PDMS stamps with predesigned negative images of source-drain patterns were activated by oxygen plasma treatment and brought into conformal contact with hydroxyl-terminated alkanethiol SAMs of 11-mercapto-1-undecanol, deposited on Au surfaces (step 1). When the PDMS stamps were removed from the Au surfaces after 1 h of contact, thiol molecules

in direct contact with the reactive PDMS surfaces were selectively removed owing to condensation reactions between the hydroxyl groups of the PDMS surfaces and the SAMs (step 2). The remaining SAMs on the Au surfaces acted as soft masks against subsequent chemical reactions, where the exposed bare Au surfaces and underlying Ti adhesion layers were selectively removed by wet etching (step 3). Remaining SAM molecules were then removed using oxygen plasma treatment (step 4), and ultrathin  $\text{In}_2\text{O}_3$  layers were deposited on top of the electrode patterns *via* the sol-gel process (step 5). After thermal annealing,  $\text{In}_2\text{O}_3$  films outside the channel areas were removed by 1 M hydrochloric acid using photolithography-patterned masks (step 6).

Chemical lift-off lithography employs a strategy that is the inverse of conventional microcontact printing<sup>49</sup> as it leaves soft molecular masks on metal surfaces by subtractively patterning preformed SAMs. Compared to microcontact printing, which relies on the transfer of molecular inks from PDMS stamps to metal surfaces, both lateral diffusion and gas-phase deposition of ink molecules are avoided in CLL.<sup>50,51</sup> Thus, CLL produces high spatial precision, high-fidelity molecular masks that can be used to pattern underlying metal substrates. Figure VI.2B shows a photograph of 72 pairs of FET source-drain electrodes patterned over an area of  $0.25\text{ cm}^2$  using CLL. An optical microscope image of the Au patterns (Figure VI.2C) shows that the source and drain electrodes were well-defined and separated by channel gaps measuring a few micrometers.

While we typically incubated Au surfaces in thiol solutions overnight and left the PDMS stamps on the substrates for 1 h, we found that this process could be shortened significantly. The patterns obtained after 5 min of SAM deposition and a 5-min stamping process also showed clear definition, comparable to patterns produced with longer



processing times for the same spatial precision (Figure SE.1). The PDMS stamps could be used multiple times after simple rinsing and reactivation, reproducing patterns with similar qualities. A series of electrodes with varying channel lengths was also patterned on the same substrate for in-depth FET analysis (Figure VI.2D). Scanning electron microscope (SEM) images of the channel regions are shown in Figure SE.2.

Figure VI.2E and VI.2F show representative transfer and output characteristics of bottom-gate bottom-contact (BGBC)  $\text{In}_2\text{O}_3$  FET devices fabricated using CLL-patterned Au electrodes on  $\text{SiO}_2/\text{Si}$  substrates. In this structure, the channel width and length were 35 and 15  $\mu\text{m}$ , respectively, and heavily doped Si substrates were used as gate electrodes. Different annealing conditions were tested and optimized device performance was obtained after the  $\text{In}_2\text{O}_3$  thin films were annealed at 250  $^\circ\text{C}$  for 1 h (Figure SE.3). The optimized  $\text{In}_2\text{O}_3$  FETs showed high field-effect mobilities ( $\mu_{\text{sat}}$ ) of 11.5 ( $1.3 \text{ cm}^2 \text{ V}^{-1} \text{ s}^{-1}$ ) (averaged over 50 devices) and on/off current ratios ( $I_{\text{ON}}/I_{\text{OFF}}$ ) above  $10^7$ . These performance characteristics are comparable to FETs with thicker  $\text{In}_2\text{O}_3$  films fabricated *via* either organic-solvent-based sol-gel approaches<sup>52-55</sup> or sputtering<sup>56,57</sup> (Table SE1).

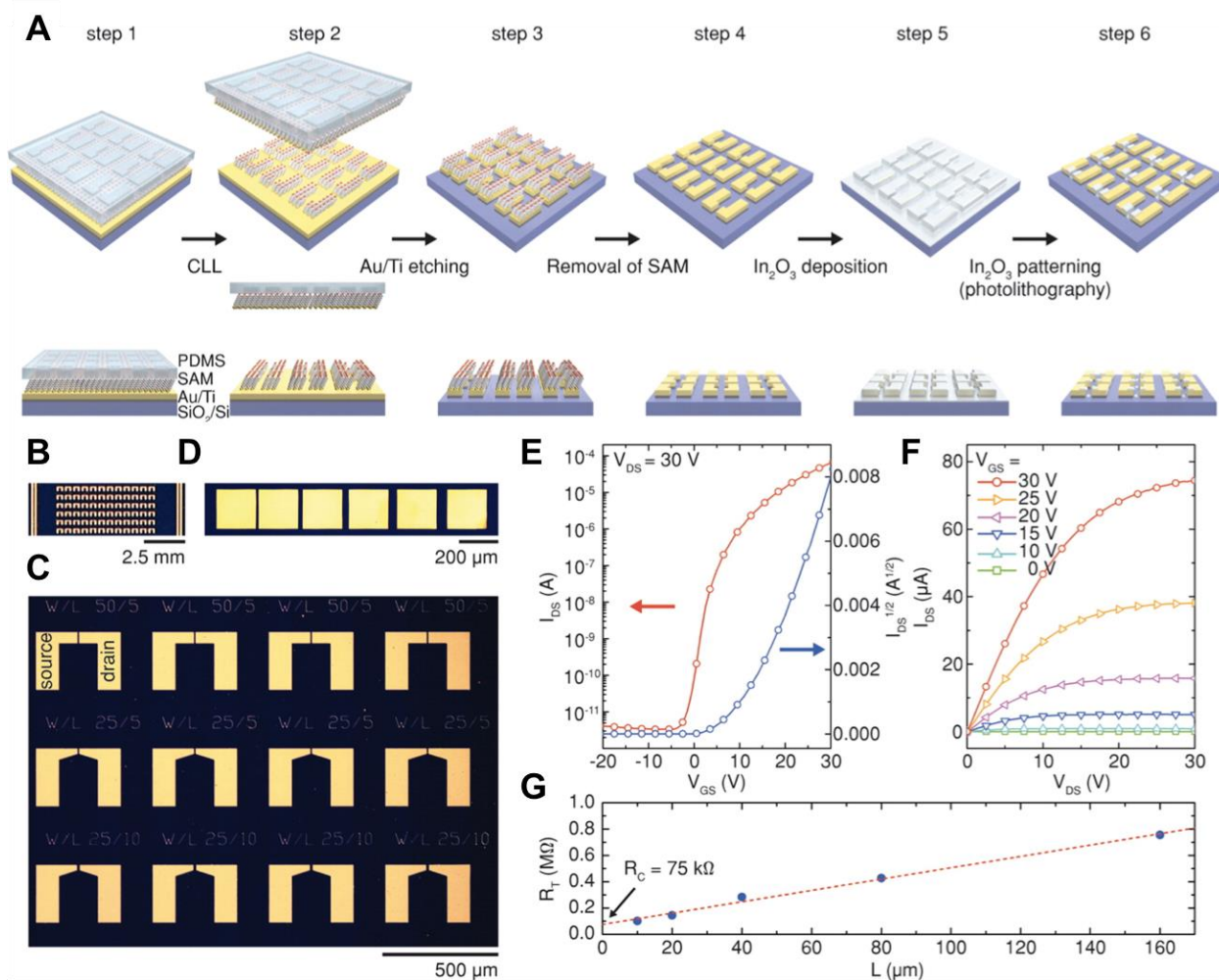


**Figure VI.2.** Field-effect transistor (FET) fabrication using chemical lift-off lithography. **(A)** Schematic illustration of FET fabrication steps using CLL. First, PDMS stamps with arrays of source and drain patterns were activated by oxygen plasma and brought into conformal contact with Au surfaces covered with SAMs of hydroxyl-terminated alkanethiols (step 1). Through a condensation reaction between the hydroxyl groups of the PDMS surfaces and the SAMs, alkanethiol molecules in direct contact with the PDMS surfaces were selectively removed (step 2), leaving molecular patterns that served as soft masks during the following wet-etching of Au and Ti (step 3). After the metals were etched from the unprotected areas, the SAMs were removed by oxygen plasma (step 4) and ultrathin  $\text{In}_2\text{O}_3$  layers were deposited through a sol-gel process (step 5). After thermal annealing,  $\text{In}_2\text{O}_3$  films outside the channel areas were removed by wet-etching using photolithography-patterned masks (step 6). **(B)** Photograph showing 72 FET device patterns produced by CLL on a 100 nm  $\text{SiO}_2$  layer on a Si substrate. **(C,D)** Optical microscope images of the CLL-produced device patterns over large areas showing **(C)** well-defined source and drain electrodes with channel gaps measuring a few micrometers and **(D)** a transmission line measurement (TLM) pattern with varying channel lengths. **(E)** Transfer and **(F)** output characteristics of the ultrathin  $\text{In}_2\text{O}_3$  film FETs constructed atop the CLL-produced device patterns; the FETs showed good device performance with  $n$ -type pinch-off behavior with  $\mu_{\text{sat}}$  of  $11.5 \pm 1.3 \text{ cm}^2 \text{ V}^{-1} \text{ s}^{-1}$  and  $I_{\text{ON}}/I_{\text{OFF}}$  of  $\sim 10^7$ . **(G)**  $R_{\text{C}}$  between  $\text{In}_2\text{O}_3$  and the Au electrodes was estimated to be  $\sim 75 \text{ k}\Omega$  using the TLM pattern shown in **(D)**.

The output characteristics of the FET devices (Figure VI.2F) showed *n*-type pinch-off behavior. The contact resistance (RC) between In<sub>2</sub>O<sub>3</sub> channels and Au electrodes was estimated by transmission-line measurements (TLMs; Figure VI.2G) using the pattern with varying channel lengths created by CLL (Figure VI.2D). Contact resistance was determined to be  $\sim 75 \text{ k}\Omega$ . We also fabricated bottom-gate top-contact (BGTC) In<sub>2</sub>O<sub>3</sub> FETs by performing CLL on Au/Ti deposited on top of the semiconducting layers (Figure SE.4). The BGTC FETs showed better device performance compared to BGBC FETs, with  $\mu_{\text{sat}} = 12.1 \pm 3.5 \text{ cm}^2 \text{ V}^{-1} \text{ s}^{-1}$  and  $I_{\text{ON}}/I_{\text{OFF}} \sim 10^8$ . This improved performance was attributed to more favorable energy-level alignment at the interface between the In<sub>2</sub>O<sub>3</sub> channels and the Ti adhesion layers.<sup>48</sup> Detailed device parameters of BGBC ultrathin In<sub>2</sub>O<sub>3</sub> film FETs processed under different annealing conditions and optimized BGTC devices are summarized in Table SE2.

Next, we scaled down the FET dimensions further and examined device performance of ultrathin In<sub>2</sub>O<sub>3</sub> film FETs with submicrometer-scale channel lengths. Field-effect transistor miniaturization is integral for high-density device integration and enables low-voltage, low-power device operation. In common laboratory settings, studies of FETs with submicrometer channel lengths are typically carried out with the aid of electron-beam lithography, which produces patterns with much finer features than photolithography. However, unlike photolithography, electron-beam lithography is a serial process and requires a considerable amount of time for patterning multiple devices over large areas. Chemical lift-off lithography enables facile prototyping of nanoscale devices as it enables parallel patterning of multiple devices over large areas with a spatial precision that can reach  $<20 \text{ nm}$ .<sup>43</sup>

Figure VI.3A shows 12 Au source-drain electrode pairs with sub-micrometer channel lengths produced by CLL on a SiO<sub>2</sub>/Si substrate. Bow-tie patterns with a large pad size were designed and used to ensure easy access by external electrodes. The top panels in Figure VI.3B and VI.3C show SEM images of the channel regions with gap lengths measuring 300 and 150 nm, respectively. High-magnification SEM images of the channel regions are shown in Figure SE.5. Transfer characteristics of ultrathin In<sub>2</sub>O<sub>3</sub> film FETs fabricated on the corresponding electrode patterns are shown in the bottom panels. Compared to devices with micrometer-scale channel lengths (Figure VI.2), the nm-gap FETs can be operated at a significantly lower drain voltage ( $V_{DS}$ ) of 4 V since the channel component of the series resistance scales down with decreasing channel lengths.

Field-effect transistors with channel lengths of 300 nm (Figure VI.3B) showed steep switching behavior with a subthreshold swing (SS) of  $0.3 \pm 0.1 \text{ V dec}^{-1}$ , which is significantly improved compared to the long-channel devices (Figure VI.2E;  $SS = 1.6 \pm 0.1 \text{ V dec}^{-1}$ ). We hypothesize that this behavior is due to the reduced number of charge traps along the lateral direction and a decrease in sheet resistance as the channel length was decreased. The values of  $\mu_{sat}$  and  $I_{ON}/I_{OFF}$  for these smaller FETs were  $0.6 \pm 0.3 \text{ cm}^2 \text{ V}^{-1} \text{ s}^{-1}$  and  $\sim 10^7$ , respectively. Further reduction of the channel length to 150 nm (Figure VI.3C) resulted in considerable degradation of device performance, with SS,  $\mu_{sat}$ , and  $I_{ON}/I_{OFF}$  values of  $0.6 \pm 0.1 \text{ V dec}^{-1}$ ,  $0.4 \pm 0.1 \text{ cm}^2 \text{ V}^{-1} \text{ s}^{-1}$ , and  $\sim 10^5$ , respectively. We attribute these adverse effects to drain-induced barrier lowering associated with short-channel FETs,<sup>48</sup> as evidenced by the negative shift in the turn-on voltage from -4 V (300 nm-channel FET) to -5 V (150 nm-channel FET). We expect that the performance of ultrathin In<sub>2</sub>O<sub>3</sub> film FETs with submicrometer channel lengths can be further improved by

employing advanced device architectures including lightly doped drains<sup>48</sup> or structures with double active layers.<sup>58</sup>

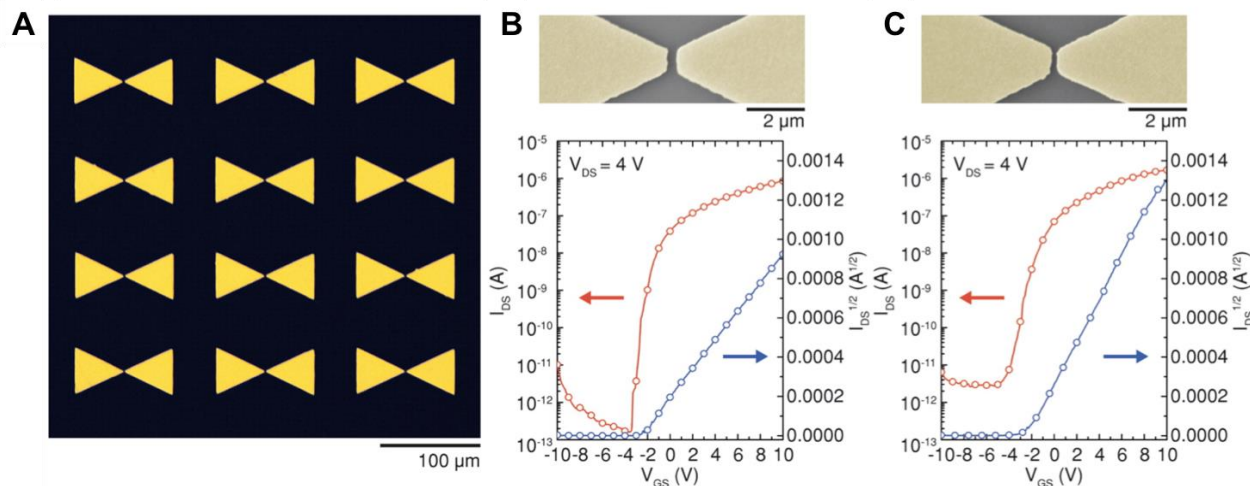


**Figure VI.3.** Fabrication of submicrometer-channel field-effect transistors using chemical lift-off lithography. (A) Bow-tie device patterns with submicrometer channel lengths produced by CLL. (B,C) The top panels show scanning electron micrographs of the channel regions of the CLL-produced device patterns, with gap lengths measuring (B) 300 nm and (C) 150 nm. Transfer characteristics of the ultrathin ( $\sim 4$  nm)  $\text{In}_2\text{O}_3$  film FETs fabricated atop the corresponding patterns are shown in the bottom panels. Compared to FETs with channel lengths measuring a few micrometers (Figure VI.2E), ultrathin  $\text{In}_2\text{O}_3$  film FETs with submicrometer channel lengths can be operated at much lower  $V_{\text{DS}}$ . Reduction of the channel length to (C) 150 nm led to considerable degradation in device performance because of the short-channel effect. The values of  $\mu_{\text{sat}}$ ,  $I_{\text{ON}}/I_{\text{OFF}}$ , and SS of (B) 300 nm-channel FETs were calculated to be  $0.6 \pm 0.3 \text{ cm}^2 \text{ V}^{-1} \text{ s}^{-1}$ ,  $\sim 10^7$ ,  $0.3 \pm 0.1 \text{ V dec}^{-1}$ , respectively, while those for (C) 150 nm-channel FETs were calculated to be  $0.4 \pm 0.1 \text{ cm}^2 \text{ V}^{-1} \text{ s}^{-1}$ ,  $\sim 10^5$ ,  $0.6 \pm 0.1 \text{ V dec}^{-1}$ , respectively.

As charge transport through sol-gel-processed  $\text{In}_2\text{O}_3$  thin films is confined within a few nanometers in the surface normal direction, electronic perturbation at the surface can significantly affect FET characteristics of the underlying metal oxide layer. Furthermore, various surface functionalization strategies available to metal oxides can be readily used to immobilize biospecific receptors on  $\text{In}_2\text{O}_3$  thin films for selective detection of target molecules.<sup>45</sup> Therefore, ultrathin  $\text{In}_2\text{O}_3$  layers can serve as platforms to construct highly sensitive and selective FET-based biosensors.

To test the ultrathin  $\text{In}_2\text{O}_3$  FETs fabricated by CLL for biosensing applications, we investigated molecular recognition of the neurotransmitter dopamine using a previously identified dopamine aptamer (Figure VI.4A).<sup>59-61</sup> We investigated dopamine as a prototypical analyte because (i) it is a key neurotransmitter involved in brain reward and movement circuitries; dopaminergic neurons are known to degenerate in Parkinson's disease,<sup>62-65</sup> and (ii) dopamine is a primary amine that carries a single positive charge at physiological pH, far less charge than that associated with biologically important macromolecular analytes such as proteins. Therefore, molecular recognition of dopamine at FET surfaces is expected to cause significantly less electronic perturbation than proteins. As such, dopamine is representative of an important class of biologically relevant small molecules that includes endogenous signaling molecules and drugs that are difficult to measure with simple devices.

To construct dopamine biosensors, we employed the BGTC structure that showed more favorable device characteristics (Table SE2). To obtain large active sensor areas and uniform current distribution, interdigitated source and drain electrodes were used for biosensors. We first deposited ultrathin  $\text{In}_2\text{O}_3$  layers on  $\text{SiO}_2/\text{Si}$  substrates, followed by Au/Ti depositions using electron-beam evaporation. The Au/Ti films were then patterned into interdigitated source and drain electrodes using CLL (Figure VI.4B). Subsequently, the hydroxyl-terminated alkanethiol SAMs used for CLL were removed by brief exposure to oxygen plasma, and 1-dodecanethiol was self-assembled on the Au surfaces to protect the electrodes from ensuing receptor immobilization. A thiol-terminated tethered DNA aptamer that recognizes dopamine, HS(CH<sub>2</sub>)<sub>6</sub>-5' -GTC TCT GTG TGC GCC AGA GAC ACT GGG GCA GAT ATG GGC CAG CAC AGA ATG AGG CCC-3' (Figure VI.4A),<sup>59-61</sup> was immobilized

on  $\text{In}_2\text{O}_3$  surfaces using APTMS and MBS as linkers to complete the biosensor fabrication. Organosilanes form SAMs on various metal oxide surfaces with in-plane cross-linked Si-O-Si networks promoting dense molecular packing.<sup>66-70</sup> As the size of DNA aptamers is on the order of a few nanometers, steric hindrance may prohibit effective ligand-receptor binding unless aptamers are well-separated.<sup>10</sup> Therefore, PTMS was co-deposited on  $\text{In}_2\text{O}_3$  surfaces and used as a spacer to optimize the surface density of aptamers for effective biosensing (see the Experimental Methods section).

Figure VI.4B shows a schematic illustration of the electrical measurement setup used for dopamine sensing experiments.  $0.1\times$  PBS (pH 7.4) was used as a liquid gate to detect signals effectively without severe Debye screening (Debye length  $\sim 2.3$  nm). The gate bias ( $V_{\text{GS}}$ ) was applied through a Pt wire. Specific amounts of dopamine in  $0.1\times$  PBS were injected into the electrolyte solution to set the dopamine concentrations in the liquid environment. To study the effect of the aptamer attachment to the channel surface, we first used highly doped Si substrates and 100 nm-thick  $\text{SiO}_2$  layers as a back gate and a dielectric layer, respectively, and examined the changes in FET characteristics in a dry state upon aptamer immobilization (Figure VI.4C). We found that the attachment of aptamers to the channel surfaces caused  $>10\times$  decreases in the drain currents and positive shifts in the turn-on voltages (from  $-19$  to  $-15$  V). We attributed these effects to the electrostatic gating effects of negatively charged DNA on the channel surfaces that result in decreases in carrier concentrations of the  $n$ -type  $\text{In}_2\text{O}_3$  layer. Upon incubation of these device in a 1 mM solution of dopamine for 1 h, the drain current partially recovered and the turn-on voltage shifted back to  $-18$  V.

Many, though not all, aptamers undergo significant conformational changes upon target binding, which should affect the conductance modulation of underlying channel layers substantially.<sup>71-75</sup> Since aptamers carry much greater charge than small molecules such as dopamine, their conformational changes are typically expected to dominate surface charge densities and surface charge density changes, as compared to the electrostatic gating effects of analytes. However, a previous study suggested that the dopamine-specific aptamer used in this work undergoes insufficient structural reorganization for electronic beacon approaches upon ligand binding.<sup>61</sup> Further studies will be needed to determine the specific charge redistribution and charge-sensing mechanisms of our dopamine aptamer-FET-based sensors, which will be critical to generalizing chemical sensing with these arrays.



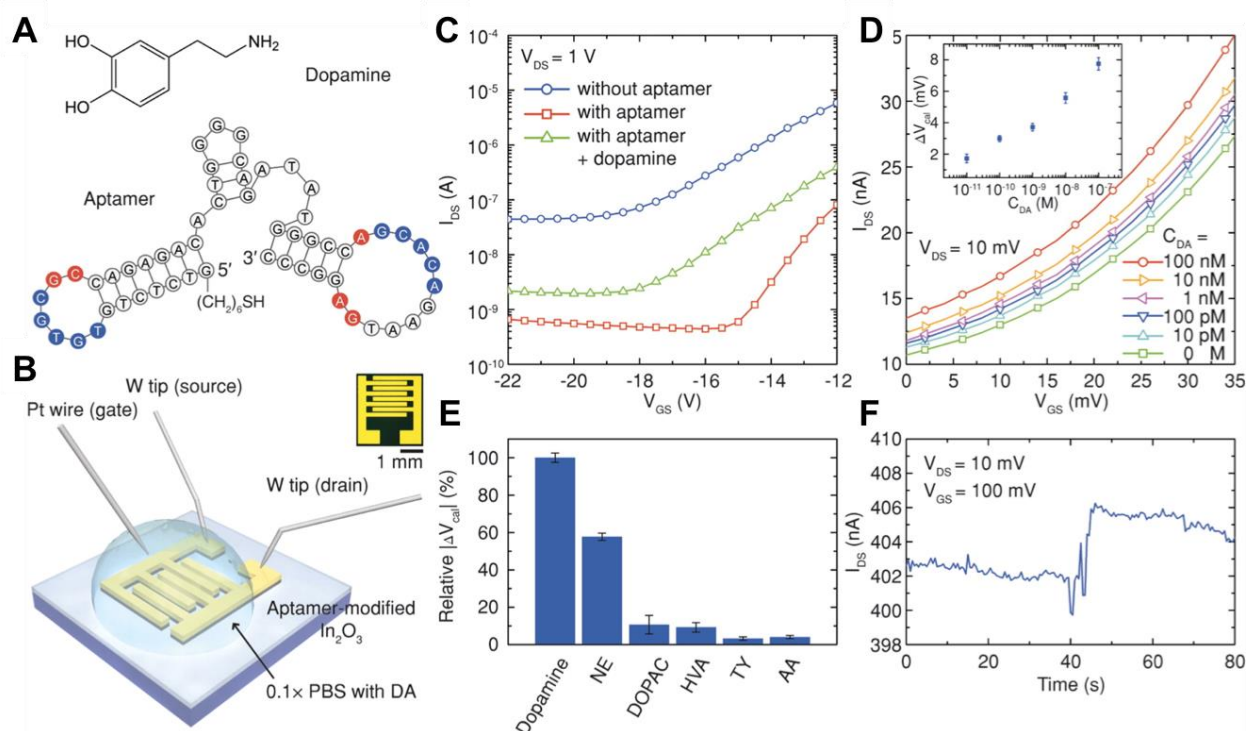


**Figure VI.4.** Aptamer- $\text{In}_2\text{O}_3$  biosensors for subnanomolar dopamine detection. The ultralow thickness of the sol-gel-processed  $\text{In}_2\text{O}_3$  enabled the construction of highly sensitive dopamine biosensors by immobilizing (A) a DNA aptamer (bottom) that had specific binding with dopamine (top) on the oxide surface. The complementary and invariant bases for dopamine binding are indicated in blue and red, respectively. (B) Schematic diagram of the sensing setup; the aptamer- $\text{In}_2\text{O}_3$  biosensors operated with a liquid gate. The inset shows an interdigitated electrode pattern, fabricated using chemical lift-off lithography, used for the biosensors. (C) Dry state, Si back-gating measurements show that upon immobilization of the aptamer on the oxide surface, the transfer characteristics of ultrathin  $\text{In}_2\text{O}_3$  film field-effect transistors (blue line) shifted downward (red line) and the turn-on voltage shifted toward positive values because of the electrostatic gating effect of negatively charged DNA on *n*-type  $\text{In}_2\text{O}_3$ . Positively charged dopamine binding to the aptamer partially recovered the drain current, with a shift of the turn-on voltage toward negative values (green line). (D) For the liquid-gate sensing experiments, the addition of dopamine to the liquid electrolyte also led to an increase in the drain current, and the linear working range of the aptamer- $\text{In}_2\text{O}_3$  biosensors was determined to be  $10^{-11}$ – $10^{-7}$  M (inset,  $\Delta V_{\text{cal}}$ : calibrated response). (E) Calibrated responses of the aptamer- $\text{In}_2\text{O}_3$  biosensors upon exposure to 1 nM each of ascorbic acid (AA), tyramine (TY), homovanillic acid (HVA), 3,4-dihydroxyphenylacetic acid (DOPAC), and norepinephrine (NE). (F) Real-time sensing recording of 100 pM dopamine in 0.1× PBS, showing an increase in current upon exposure.

Figure VI.4D shows the transfer characteristics of liquid-gated aptamer- $\text{In}_2\text{O}_3$  biosensors measured at various dopamine concentrations ( $C_{\text{DA}}$ ) in solution. As in the case of measurements in a dry state, using a back-gated FET (Figure VI.4C), exposure of the biosensors to dopamine in a liquid-gate setup resulted in increased drain current. As  $C_{\text{DA}}$

was increased from 10 pM to 100 nM, the transfer characteristics of the device continuously shifted upward. No significant redox behavior of dopamine was observed in our device operating range (Figure SE.6), and the leakage current through the 0.1× PBS electrolyte was confirmed to be negligible (Figure SE.7). While further increases of  $C_{DA}$  to 1  $\mu$ M or more resulted in continued upshift of the drain current, we found that nonspecific binding of dopamine to the channel surface became significant, and the drain current increased even without aptamer functionalization on the channel surface in this concentration range (see Supporting Information, Figure SE.8). To reduce device-to-device variations in sensor responses, the change in drain current was converted to a change in gate voltage (calibrated response,  $\Delta V_{cal}$ ),<sup>46</sup> and the linear working range of the aptamer- $\text{In}_2\text{O}_3$  biosensor was determined to be  $10^{-11}$ – $10^{-7}$  M, as shown in the inset of Figure VI.4D.

We also constructed devices using an aptamer with mutations at identified dopamine binding sites (mut-dopamine-aptamer,  $\text{HS}(\text{CH}_2)_6$ -5'-GTC TCT GTG TGC **TTC** AGA GAC ACT GGG GCA GAT ATG GGC CTG CAC AGA **ATT** TGG CCC-3', mutated bases are highlighted in bold), as well as DNA with a random base sequence (scrambled-DNA,  $\text{HS}(\text{CH}_2)_6$ -5'-CAT AAA TAC TAG GAT GTG CAT ACT TAG ACT GGA GAT TGT ATC CCT ACA CAC ACC CTA-3'). Upon exposure of devices functionalized with either of these aptamers to 10 nM dopamine in 0.1× PBS, we measured a  $\Delta V_{cal}$  of less than 15% of the responses measured at devices constructed using the correct aptamer sequence (Figure SE.9). These results strongly suggest that sensor responses are based on specific interactions between dopamine and its cognate aptamer.

To test the selectivity of the aptamer- $\text{In}_2\text{O}_3$  biosensors, we exposed devices to 1 nM solutions of other similarly structured small molecules found in the brain extracellular

environment.<sup>76</sup> Ascorbic acid (AA), tyramine (TY), homovanillic acid (HVA), 3,4-dihydroxyphenylacetic acid (DOPAC), and norepinephrine (NE) were dissolved in 0.1× PBS. Calibrated responses were then compared to responses to dopamine (Figure VI.4E). Although NE caused significant  $\Delta V_{\text{cal}}$  that reached  $58 \pm 2\%$  of the responses to dopamine, all other tested biomolecules were associated with relative responses that were below 10% of the dopamine response. Cross reactivity of this aptamer with NE has been previously observed and reported.<sup>10,61,77</sup> We note that dopamine, NE, and TY caused increases in the drain current while AA, HVA, and DOPAC caused decreases, as the former group of molecules carry positive charges at physiological pH while the latter carry negative charges.

Finally, we performed real-time detection of dopamine in 0.1× PBS. The drain current of the aptamer-In<sub>2</sub>O<sub>3</sub> device was continuously monitored at  $V_{\text{DS}} = 10$  mV and  $V_{\text{GS}} = 100$  mV while dopamine was introduced into the buffer solution. Figure VI.4F shows representative real-time sensing measurements obtained when the biosensor was exposed to a solution of 100 pM dopamine at  $t = 0$ . After a short delay associated with diffusion of dopamine to the channel surface, a sharp increase in drain current was observed. In comparison, the addition of buffer solution devoid of dopamine did not yield measurable changes in the drain current (data not shown).

#### VI.D. Conclusions and Prospects

A high-throughput and high spatial precision soft lithography technique, CLL, was employed to produce device patterns with both micrometer- and submicrometer-scale feature sizes over large areas. This patterning method can be integrated with other processes to produce electronic device and biosensor arrays. Here, we demonstrated that ultrathin  $\text{In}_2\text{O}_3$  layers, produced by simple aqueous sol-gel processing, can be used as semiconducting active layers to produce high-performance FETs and biosensors. The as-fabricated  $\text{In}_2\text{O}_3$  FETs showed effective device performance with  $\mu_{\text{sat}}$  exceeding  $10 \text{ cm}^2 \text{ V}^{-1} \text{ s}^{-1}$ . The ultrathin  $\text{In}_2\text{O}_3$  layers enabled construction of highly sensitive and selective aptamer-based biosensors capable of detecting subnanomolar concentrations of dopamine. The latter are more than sufficient to detect dopamine in the physiological range of basal extracellular brain levels.<sup>78</sup> Given this straightforward and effective device-fabrication strategy, we anticipate that CLL-patterned, sol-gel-processed metal-oxide FETs will enable platforms for the construction of both biological and non-biological sensors that can detect subtle yet important chemical perturbations at interfaces.

## **APPENDIX E**

# **Fabrication of High-Performance Ultrathin In<sub>2</sub>O<sub>3</sub> Film Field-Effect Transistors and Biosensors Using Chemical Lift-Off Lithography**

## **Supplementary Information**

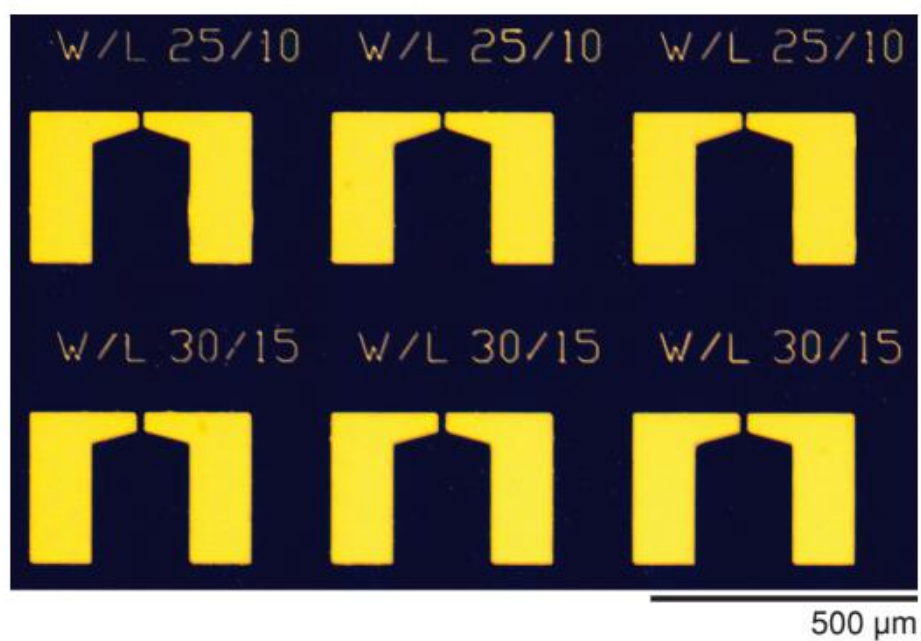


**Figure SE.1.** Field-effect transistor device patterns on a SiO<sub>2</sub>/Si substrate produced by chemical lift-off lithography with a short processing time (5 min self-assembled monolayer deposition, 5 min stamping time)

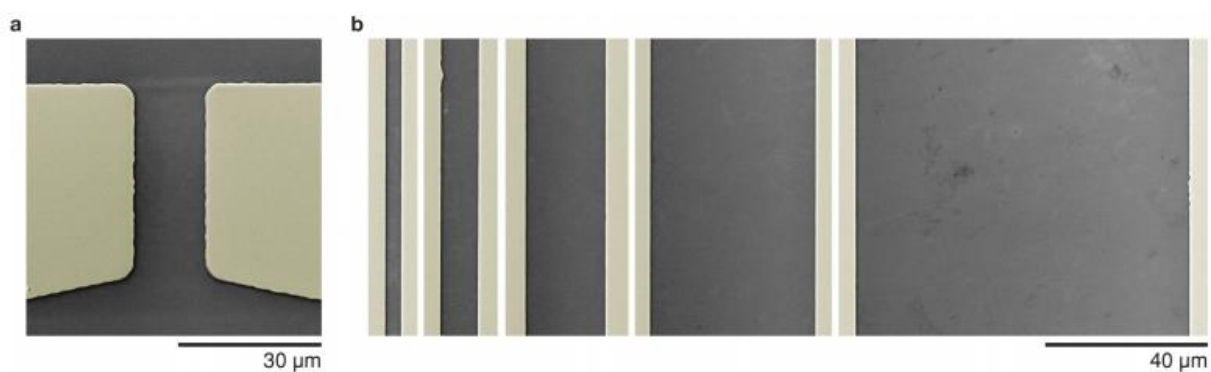


**Figure SE.2.** Scanning electron microscope images of channel regions. (a) A representative source-drain electrode pair used for device fabrication. (b) A transmission line measurement (TLM) pattern with varying channel lengths.

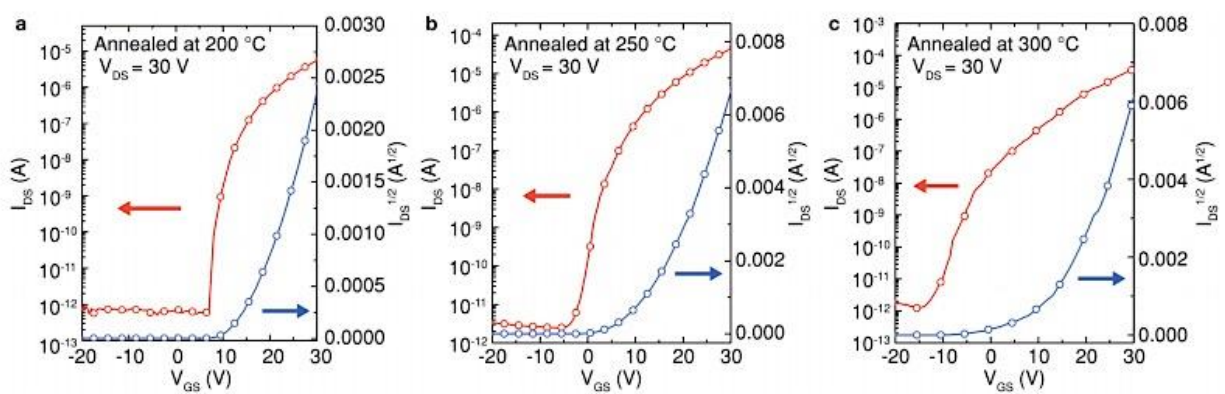


**Figure SE.3.** Bottom-gate bottom-contact field-effect transistor transfer characteristics of ultrathin  $\text{In}_2\text{O}_3$  layers annealed at (a) 200 °C, (b) 250 °C, and (c) 300 °C for 1 h.



Coating Method	Channel Thickness (nm)	$\mu_{\text{sat}}$ ( $\text{cm}^2 \text{V}^{-1} \text{s}^{-1}$ )	$I_{\text{ON}}/I_{\text{OFF}}$	SS ( $\text{V dec}^{-1}$ )	Ref.
Sol-gel	4	12	$10^7$	1.6	Our work
Sol-gel	30	0.7	$10^6$	5.7	S1
Sol-gel	25	2.24	$10^8$	0.45	S2
Sol-gel	6	7.5	$10^7$	N/A	S3
Sol-gel	30	3.37	$10^7$	N/A	S4
Sputtering	8	15.3	$10^8$	0.25	S5
Sputtering	10	15	$10^6$	N/A	S6

**Table SE.1.** Device performance of previously reported  $\text{In}_2\text{O}_3$  field-effect transistors.

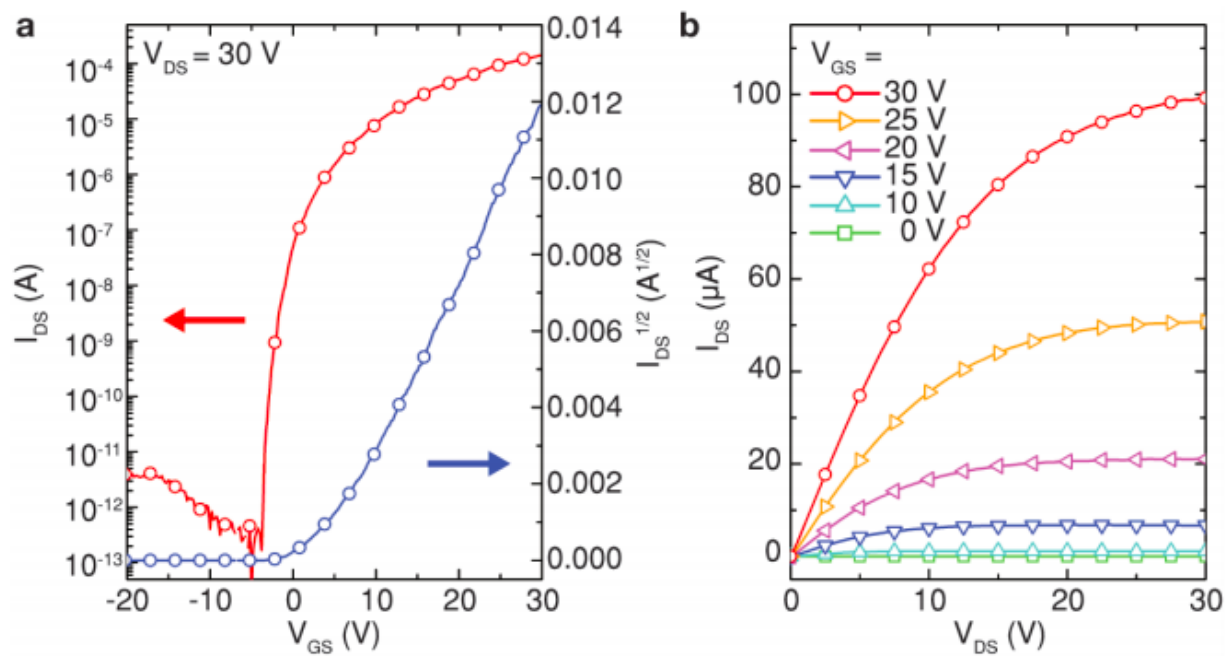


**Figure SE.4.** Bottom-gate top-contact field-effect transistor (a) transfer and (b) output characteristics of ultrathin  $\text{In}_2\text{O}_3$  layers.

Geometry	Annealing Temperature (°C)	$\mu_{\text{sat}}$ (cm <sup>2</sup> V <sup>-1</sup> s <sup>-1</sup> )	$I_{\text{ON}}/I_{\text{OFF}}$	SS (V dec <sup>-1</sup> )	$V_{\text{th}}$ (V) <sup>a</sup>
BGBC	200	2.3 ± 0.2	~10 <sup>6</sup>	1.2 ± 0.1	19.5 ± 2.1
BGBC	250	11.5 ± 1.3	~10 <sup>7</sup>	1.6 ± 0.1	15.6 ± 2.0
BGBC	300	10.4 ± 1.8	~10 <sup>7</sup>	2.7 ± 0.9	18.2 ± 1.2
BGTC	250	12.1 ± 3.5	~10 <sup>8</sup>	0.9 ± 0.2	9.5 ± 2.7

<sup>a</sup>Threshold voltage

**Table SE.2.** Summary of In<sub>2</sub>O<sub>3</sub> field-effect transistor device performance.

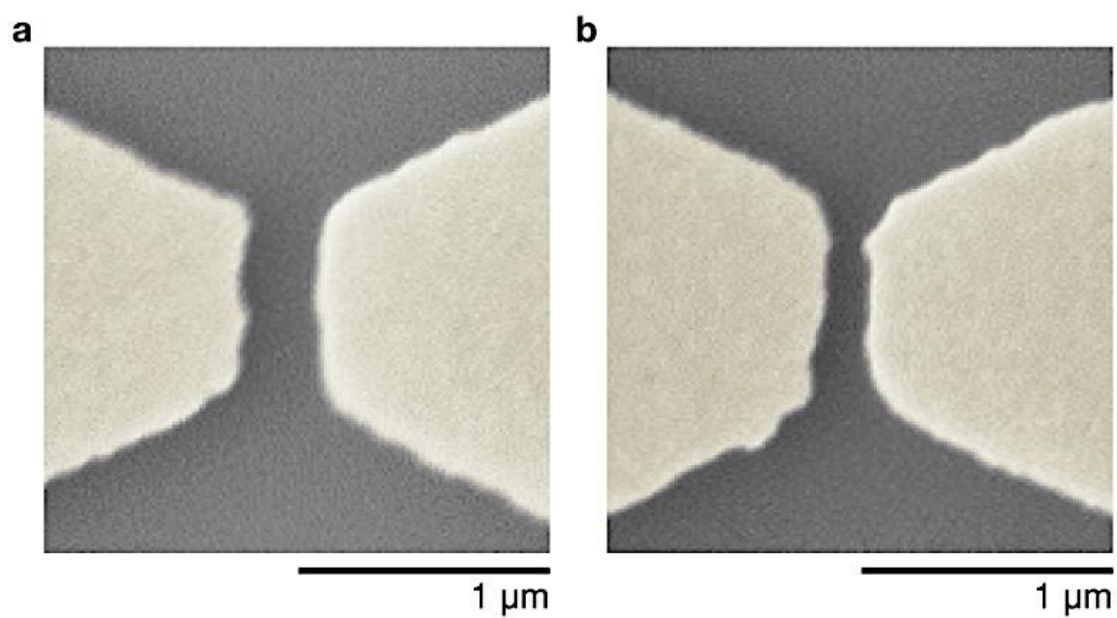


**Figure SE.5.** Scanning electron microscope images of sub-micrometer-channel devices with gap lengths measuring (a) 300 nm and (b) 150 nm.

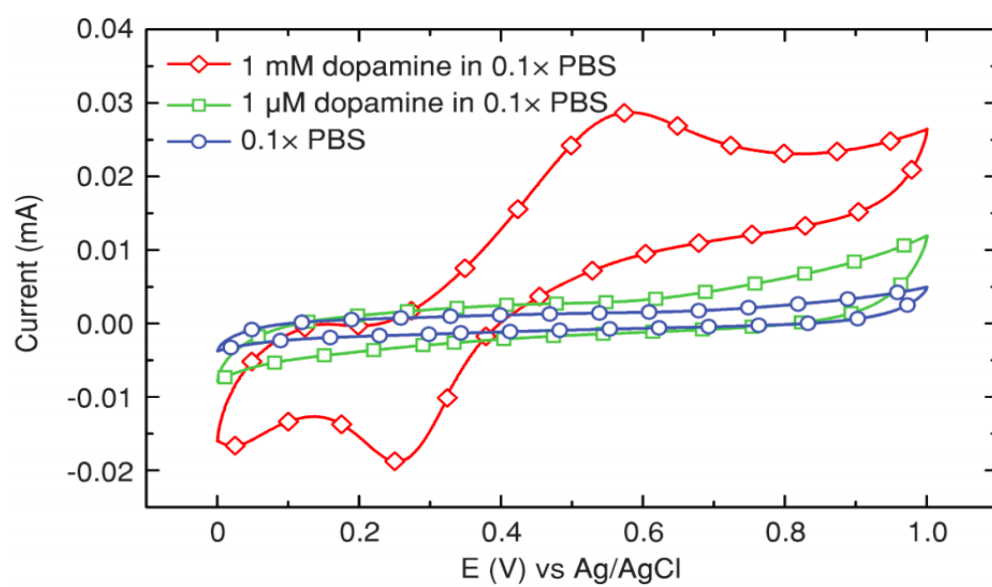


**Figure SE.6.** Cyclic voltammogram of a Pt wire in 0.1x PBS with (red:  $C_{DA} = 1$  mM, green:  $C_{DA} = 1$   $\mu$ M) or without (blue) dopamine.

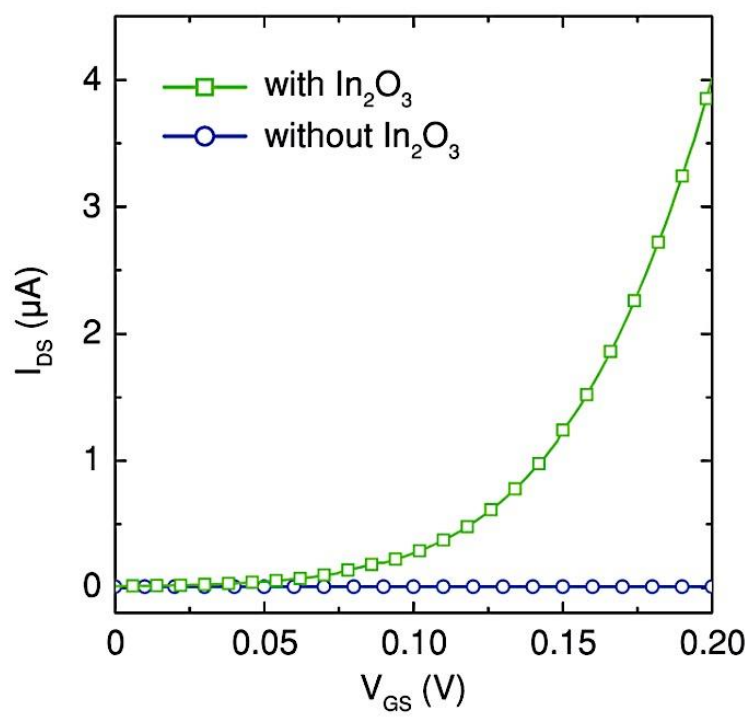


**Figure SE.7.** Transfer characteristics of devices with (green) or without (blue) the  $In_2O_3$  channel layer, confirming that the leakage current through a liquid electrolyte (blue) is negligible.

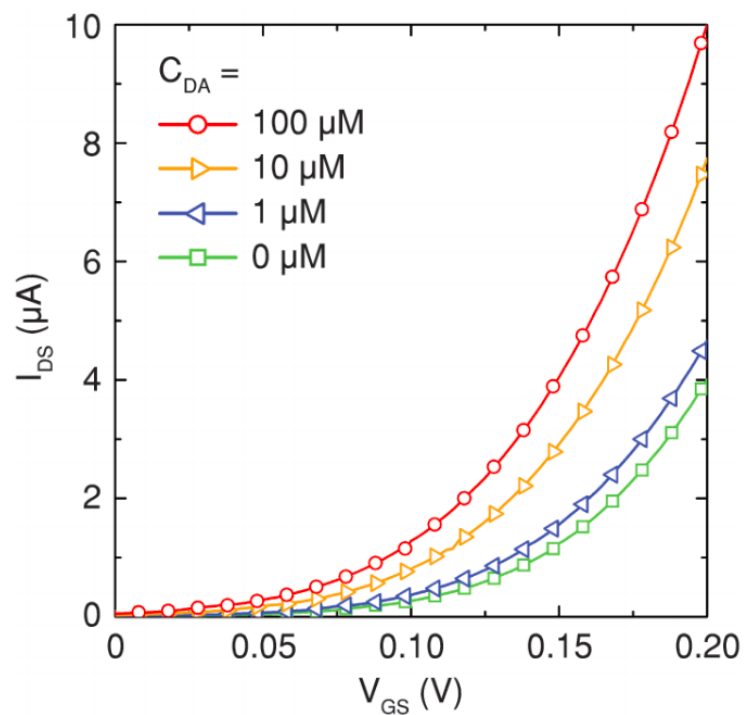


**Figure SE.8.** Transfer characteristics of  $\text{In}_2\text{O}_3$  field-effect transistors without aptamer immobilization. For  $C_{DA} \geq 1 \mu\text{M}$ , non-specific binding of dopamine on the channel surface becomes significant and causes upward shift in the drain current even without aptamer functionalization. No significant change in drain current was observed for  $C_{DA} \geq 1$

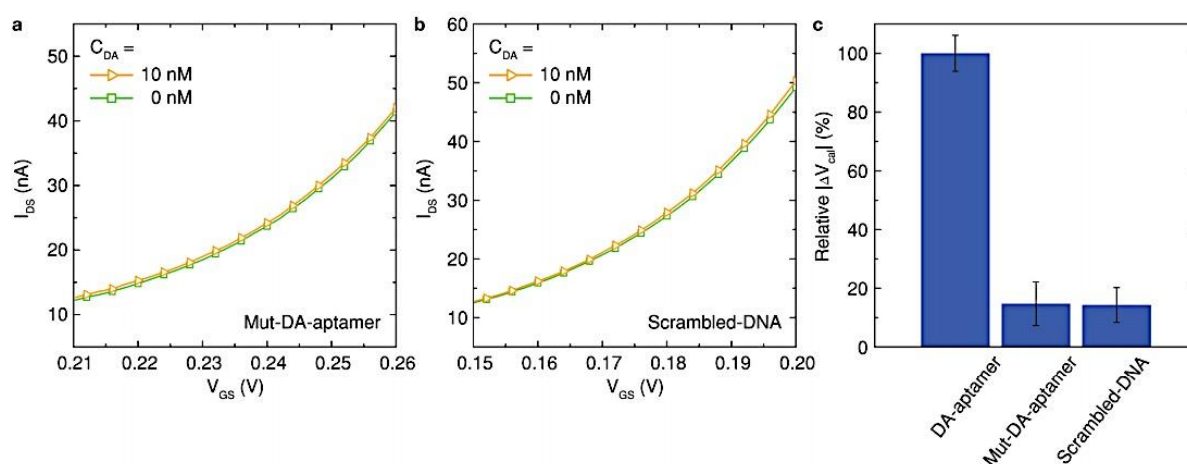


**Figure SE.9.** Transfer characteristics of  $\text{In}_2\text{O}_3$  field-effect transistors constructed using (a) an aptamer with mutations at the binding sites or (b) a DNA with a random base sequence. In both cases, the addition of 10 nM dopamine to  $0.1\times$  PBS induced only small changes in drain currents. (c)  $\Delta V_{cal}$  of both devices were measured to be less than 15% of the responses from devices constructed using the correct dopamine (DA) aptamer.



## References

1. Schoning, M. J.; Poghossian, A. Recent Advances in Biologically Sensitive Field-Effect Transistors (BioFETs). *Analyst* **2002**, *127*, 1137-1151.
2. Patolsky, F.; Lieber, C. M. Nanowire Nanosensors. *Mater. Today* **2005**, *8*, 20-28.
3. Allen, B. L.; Kichambare, P. D.; Star, A. Carbon Nanotube Field-Effect-Transistor-Based Biosensors. *Adv. Mater.* **2007**, *19*, 1439-1451.
4. Curreli, M.; Zhang, R.; Ishikawa, F. N.; Chang, H. K.; Cote, R. J.; Zhou, C.; Thompson, M. E. Real-Time, Label-Free Detection of Biological Entities Using Nanowire-Based FETs. *IEEE Trans. Nanotechnol.* **2008**, *7*, 651-667.
5. Cui, Y.; Wei, Q. Q.; Park, H. K.; Lieber, C. M. Nanowire Nanosensors for Highly Sensitive and Selective Detection of Biological and Chemical Species. *Science* **2001**, *293*, 1289-1292.
6. Hahm, J.; Lieber, C. M. Direct Ultrasensitive Electrical Detection of DNA and DNA Sequence Variations Using Nanowire Nanosensors. *Nano Lett.* **2004**, *4*, 51-54.
7. Wang, W. U.; Chen, C.; Lin, K. H.; Fang, Y.; Lieber, C. M. Label-Free Detection of Small-Molecule-Protein Interactions by Using Nanowire Nanosensors. *Proc. Natl. Acad. Sci. U. S. A* **2005**, *102*, 3208-3212.
8. Zheng, G. F.; Patolsky, F.; Cui, Y.; Wang, W. U.; Lieber, C. M. Multiplexed Electrical Detection of Cancer Markers with Nanowire Sensor Arrays. *Nat. Biotechnol.* **2005**, *23*, 1294-1301.
9. Stern, E.; Klemic, J. F.; Routenberg, D. A.; Wyrembak, P. N.; Turner-Evans, D. B.; Hamilton, A. D.; LaVan, D. A.; Fahmy, T. M.; Reed, M. A. Label-Free Immunodetection with CMOS-Compatible Semiconducting Nanowires. *Nature* **2007**, *445*, 519-522.
10. Li, B. R.; Hsieh, Y. J.; Chen, Y. X.; Chung, Y. T.; Pan, C. Y.; Chen, Y. T. An Ultrasensitive Nanowire-Transistor Biosensor for Detecting Dopamine Release from Living PC12 Cells under Hypoxic Stimulation. *J. Am. Chem. Soc.* **2013**, *135*, 16034-16037.
11. Besteman, K.; Lee, J. O.; Wiertz, F. G. M.; Heering, H. A.; Dekker, C. Enzyme-Coated Carbon Nanotubes as Single-Molecule Biosensors. *Nano Lett.* **2003**, *3*, 727-730.
12. Chen, R. J.; Bangsaruntip, S.; Drouvalakis, K. A.; Kam, N. W. S.; Shim, M.; Li, Y. M.; Kim, W.; Utz, P. J.; Dai, H. J. Noncovalent Functionalization of Carbon Nanotubes for Highly Specific Electronic Biosensors. *Proc. Natl. Acad. Sci. U. S. A* **2003**, *100*, 4984-4989.

13. So, H. M.; Won, K.; Kim, Y. H.; Kim, B. K.; Ryu, B. H.; Na, P. S.; Kim, H.; Lee, J. O. Single-Walled Carbon Nanotube Biosensors Using Aptamers as Molecular Recognition Elements. *J. Am. Chem. Soc.* **2005**, *127*, 11906-11907.
14. Tang, T.; Liu, X. L.; Li, C.; Lei, B.; Zhang, D. H.; Rouhanizadeh, M.; Hsiai, T.; Zhou, C. W. Complementary Response of In<sub>2</sub>O<sub>3</sub> Nanowires and Carbon Nanotubes to Low-Density Lipoprotein Chemical Gating. *Appl. Phys. Lett.* **2005**, *86*.
15. Maehashi, K.; Katsura, T.; Kerman, K.; Takamura, Y.; Matsumoto, K.; Tamiya, E. Label-Free Protein Biosensor Based on Aptamer-Modified Carbon Nanotube Field-Effect Transistors. *Anal. Chem.* **2007**, *79*, 782-787.
16. Kim, S. N.; Rusling, J. F.; Papadimitrakopoulos, F. Carbon Nanotubes for Electronic and Electrochemical Detection of Biomolecules. *Adv. Mater.* **2007**, *19*, 3214-3228.
17. Martinez, M. T.; Tseng, Y. C.; Ormategui, N.; Loinaz, I.; Eritja, R.; Bokor, J. Label-Free DNA Biosensors Based on Functionalized Carbon Nanotube Field Effect Transistors. *Nano Lett.* **2009**, *9*, 530-536.
18. Patolsky, F.; Zheng, G. F.; Hayden, O.; Lakadamyali, M.; Zhuang, X. W.; Lieber, C. M. Electrical Detection of Single Viruses. *Proc. Natl. Acad. Sci. U. S. A* **2004**, *101*, 14017-14022.
19. Alivisatos, A. P.; Andrews, A. M.; Boyden, E. S.; Chun, M.; Church, G. M.; Deisseroth, K.; Donoghue, J. P.; Fraser, S. E.; Lippincott-Schwartz, J.; Looger, L. L.; Masmanidis, S.; McEuen, P. L.; Nurmikko, A. V.; Park, H.; Peterka, D. S.; Reid, C.; Roukes, M. L.; Scherer, A.; Schnitzer, M.; Sejnowski, T. J.; Shepard, K. L.; Tsao, D.; Turrigiano, G.; Weiss, P. S.; Xu, C.; Yuste, R.; Zhuang, X. W. Nanotools for Neuroscience and Brain Activity Mapping. *ACS Nano* **2013**, *7*, 1850-1866.
20. Ohno, Y.; Maehashi, K.; Matsumoto, K. Label-Free Biosensors Based on Aptamer-Modified Graphene Field-Effect Transistors. *J. Am. Chem. Soc.* **2010**, *132*, 18012-18013.
21. Huang, Y. X.; Dong, X. C.; Shi, Y. M.; Li, C. M.; Li, L. J.; Chen, P. Nanoelectronic Biosensors Based on CVD Grown Graphene. *Nanoscale* **2010**, *2*, 1485-1488.
22. Yang, W. R.; Ratinac, K. R.; Ringer, S. P.; Thordarson, P.; Gooding, J. J.; Braet, F. Carbon Nanomaterials in Biosensors: Should You Use Nanotubes or Graphene? *Angew. Chem.* **2010**, *49*, 2114-2138.
23. Pumera, M. Graphene in Biosensing. *Mater. Today* **2011**, *14*, 308-315.
24. He, Q. Y.; Sudibya, H. G.; Yin, Z. Y.; Wu, S. X.; Li, H.; Boey, F.; Huang, W.; Chen, P.; Zhang, H. Centimeter-Long and Large-Scale Micropatterns of Reduced Graphene Oxide Films: Fabrication and Sensing Applications. *ACS Nano* **2010**, *4*, 3201-3208.

25. Sarkar, D.; Liu, W.; Xie, X. J.; Anselmo, A. C.; Mitragotri, S.; Banerjee, K. MoS<sub>2</sub> Field-Effect Transistor for Next-Generation Label-Free Biosensors. *ACS Nano* **2014**, *8*, 3992-4003.
26. Wang, L.; Wang, Y.; Wong, J. I.; Palacios, T.; Kong, J.; Yang, H. Y. Functionalized MoS<sub>2</sub> Nanosheet-Based Field-Effect Biosensor for Label-Free Sensitive Detection of Cancer Marker Proteins in Solution. *Small* **2014**, *10*, 1101-1105.
27. Morales, A. M.; Lieber, C. M. A Laser Ablation Method for the Synthesis of Crystalline Semiconductor Nanowires. *Science* **1998**, *279*, 208-211.
28. Hochbaum, A. I.; Fan, R.; He, R. R.; Yang, P. D. Controlled Growth of Si Nanowire Arrays for Device Integration. *Nano Lett.* **2005**, *5*, 457-460.
29. Fan, S. S.; Chapline, M. G.; Franklin, N. R.; Tombler, T. W.; Cassell, A. M.; Dai, H. J. Self-Oriented Regular Arrays of Carbon Nanotubes and Their Field Emission Properties. *Science* **1999**, *283*, 512-514.
30. Hata, K.; Futaba, D. N.; Mizuno, K.; Namai, T.; Yumura, M.; Iijima, S. Water-Assisted Highly Efficient Synthesis of Impurity-Free Single-Walled Carbon Nanotubes. *Science* **2004**, *306*, 1362-1364.
31. Hersam, M. C. Progress Towards Monodisperse Single-Walled Carbon Nanotubes. *Nat. Nanotechnol.* **2008**, *3*, 387-394.
32. Arnold, M. S.; Green, A. A.; Hulvat, J. F.; Stupp, S. I.; Hersam, M. C. Sorting Carbon Nanotubes by Electronic Structure Using Density Differentiation. *Nat. Nanotechnol.* **2006**, *1*, 60-65.
33. Zheng, M.; Jagota, A.; Strano, M. S.; Santos, A. P.; Barone, P.; Chou, S. G.; Diner, B. A.; Dresselhaus, M. S.; McLean, R. S.; Onoa, G. B.; Samsonidze, G. G.; Semke, E. D.; Usrey, M.; Walls, D. J. Structure-Based Carbon Nanotube Sorting by Sequence-Dependent DNA Assembly. *Science* **2003**, *302*, 1545-1548.
34. Sun, Z. Z.; Yan, Z.; Yao, J.; Beitler, E.; Zhu, Y.; Tour, J. M. Growth of Graphene from Solid Carbon Sources. *Nature* **2010**, *468*, 549-552.
35. Li, X. S.; Cai, W. W.; An, J. H.; Kim, S.; Nah, J.; Yang, D. X.; Piner, R.; Velamakanni, A.; Jung, I.; Tutuc, E.; Banerjee, S. K.; Colombo, L.; Ruoff, R. S. Large-Area Synthesis of High-Quality and Uniform Graphene Films on Copper Foils. *Science* **2009**, *324*, 1312-1314.
36. Bai, J. W.; Liao, L.; Zhou, H. L.; Cheng, R.; Liu, L. X.; Huang, Y.; Duan, X. F. Top-Gated Chemical Vapor Deposition Grown Graphene Transistors with Current Saturation. *Nano Lett.* **2011**, *11*, 2555-2559.

37. Lee, Y. H.; Zhang, X. Q.; Zhang, W. J.; Chang, M. T.; Lin, C. T.; Chang, K. D.; Yu, Y. C.; Wang, J. T. W.; Chang, C. S.; Li, L. J.; Lin, T. W. Synthesis of Large-Area MoS<sub>2</sub> Atomic Layers with Chemical Vapor Deposition. *Adv. Mater.* **2012**, *24*, 2320-2325.
38. Lee, Y. H.; Yu, L. L.; Wang, H.; Fang, W. J.; Ling, X.; Shi, Y. M.; Lin, C. T.; Huang, J. K.; Chang, M. T.; Chang, C. S.; Dresselhaus, M.; Palacios, T.; Li, L. J.; Kong, J. Synthesis and Transfer of Single-Layer Transition Metal Disulfides on Diverse Surfaces. *Nano Lett.* **2013**, *13*, 1852-1857.
39. Li, X. S.; Zhu, Y. W.; Cai, W. W.; Borysiak, M.; Han, B. Y.; Chen, D.; Piner, R. D.; Colombo, L.; Ruoff, R. S. Transfer of Large-Area Graphene Films for High-Performance Transparent Conductive Electrodes. *Nano Lett.* **2009**, *9*, 4359-4363.
40. Lee, Y.; Bae, S.; Jang, H.; Jang, S.; Zhu, S. E.; Sim, S. H.; Song, Y. I.; Hong, B. H.; Ahn, J. H. Wafer-Scale Synthesis and Transfer of Graphene Films. *Nano Lett.* **2010**, *10*, 490-493.
41. Lin, Y. C.; Lu, C. C.; Yeh, C. H.; Jin, C. H.; Suenaga, K.; Chiu, P. W. Graphene Annealing: How Clean Can It Be? *Nano Lett.* **2012**, *12*, 414-419.
42. Pirkle, A.; Chan, J.; Venugopal, A.; Hinojos, D.; Magnuson, C. W.; McDonnell, S.; Colombo, L.; Vogel, E. M.; Ruoff, R. S.; Wallace, R. M. The Effect of Chemical Residues on the Physical and Electrical Properties of Chemical Vapor Deposited Graphene Transferred to SiO<sub>2</sub>. *Appl. Phys. Lett.* **2011**, *99*.
43. Liao, W. S.; Cheunkar, S.; Cao, H. H.; Bednar, H. R.; Weiss, P. S.; Andrews, A. M. Subtractive Patterning *via* Chemical Lift-Off Lithography. *Science* **2012**, *337*, 1517-1521.
44. Ishikawa, F. N.; Chang, H. K.; Curreli, M.; Liao, H. I.; Olson, C. A.; Chen, P. C.; Zhang, R.; Roberts, R. W.; Sun, R.; Cote, R. J.; Thompson, M. E.; Zhou, C. W. Label-Free, Electrical Detection of the SARS Virus N-Protein with Nanowire Biosensors Utilizing Antibody Mimics as Capture Probes. *ACS Nano* **2009**, *3*, 1219-1224.
45. Curreli, M.; Li, C.; Sun, Y. H.; Lei, B.; Gundersen, M. A.; Thompson, M. E.; Zhou, C. W. Selective Functionalization of In<sub>2</sub>O<sub>3</sub> Nanowire Mat Devices for Biosensing Applications. *J. Am. Chem. Soc.* **2005**, *127*, 6922-6923.
46. Ishikawa, F. N.; Curreli, M.; Chang, H. K.; Chen, P. C.; Zhang, R.; Cote, R. J.; Thompson, M. E.; Zhou, C. W. A Calibration Method for Nanowire Biosensors to Suppress Device-to-Device Variation. *ACS Nano* **2009**, *3*, 3969-3976.
47. Hwang, Y. H.; Seo, J. S.; Yun, J. M.; Park, H.; Yang, S.; Park, S. H. K.; Bae, B. S. An 'Aqueous Route' for the Fabrication of Low-Temperature-Processable Oxide Flexible Transparent Thin-Film Transistors on Plastic Substrates. *NPG Asia Mater.* **2013**, *5*, 1-8.

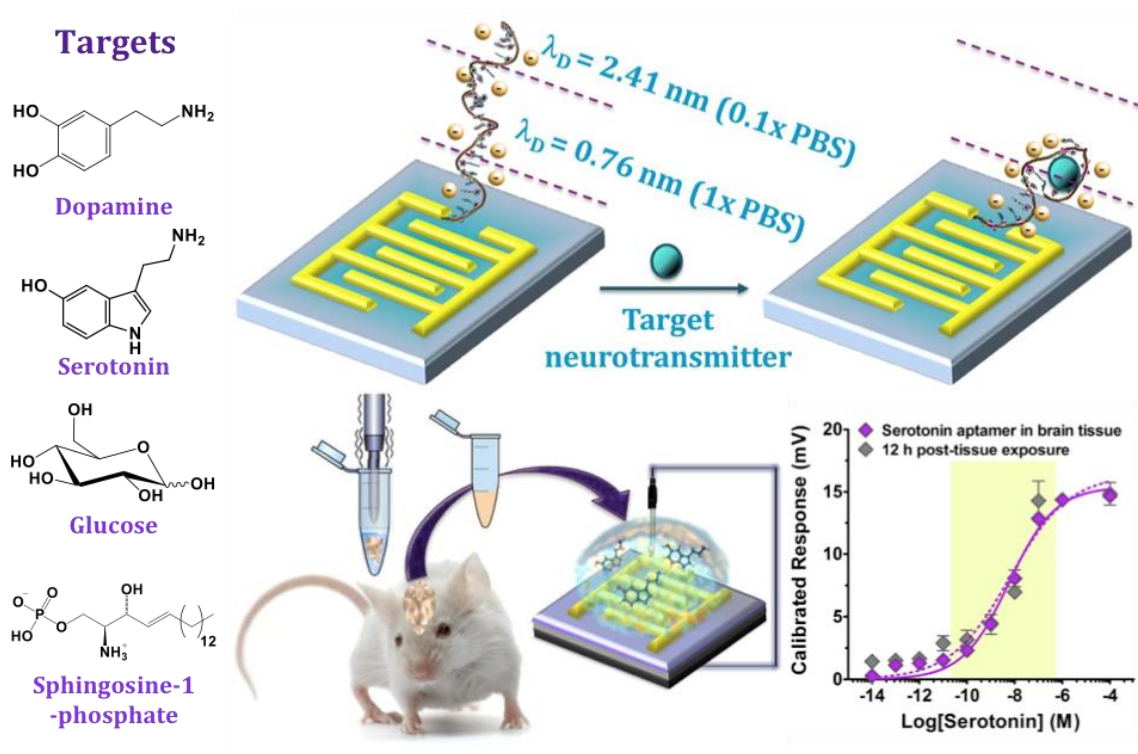
48. Sze, S. M.; Ng, K. K. *Physics of Semiconductor Devices*; Wiley-Interscience: Hoboken, JK, 2007.
49. Kumar, A.; Whitesides, G. M. Features of Gold Having Micrometer to Centimeter Dimensions Can Be Formed through a Combination of Stamping with an Elastomeric Stamp and an Alkanethiol Ink Followed by Chemical Etching. *Appl. Phys. Lett.* **1993**, *63*, 2002-2004.
50. Srinivasan, C.; Mullen, T. J.; Hohman, J. N.; Anderson, M. E.; Dameron, A. A.; Andrews, A. M.; Dickey, E. C.; Horn, M. W.; Weiss, P. S. Scanning Electron Microscopy of Nanoscale Chemical Patterns. *ACS Nano* **2007**, *1*, 191-201.
51. Braunschweig, A. B.; Huo, F. W.; Mirkin, C. A. Molecular Printing. *Nat. Chem.* **2009**, *1*, 353-358.
52. Kim, H. S.; Byrne, P. D.; Facchetti, A.; Marks, T. J. High Performance Solution-Processed Indium Oxide Thin-Film Transistors. *J. Am. Chem. Soc.* **2008**, *130*, 12580-12581.
53. Rim, Y. S.; Lim, H. S.; Kim, H. J. Low-Temperature Metal-Oxide Thin-Film Transistors Formed by Directly Photopatternable and Combustible Solution Synthesis. *ACS Appl. Mater. Inter.* **2013**, *5*, 3565-3571.
54. Choi, C. H.; Han, S. Y.; Su, Y. W.; Fang, Z.; Lin, L. Y.; Cheng, C. C.; Chang, C. H. Fabrication of High-Performance, Low-Temperature Solution Processed Amorphous Indium Oxide Thin-Film Transistors Using a Volatile Nitrate Precursor. *J. Mater. Chem. C* **2015**, *3*, 854-860.
55. Kim, M. G.; Kanatzidis, M. G.; Facchetti, A.; Marks, T. J. Low-Temperature Fabrication of High-Performance Metal Oxide Thin-Film Electronics *via* Combustion Processing. *Nat. Mater.* **2011**, *10*, 382-388.
56. Noh, J. H.; Ryu, S. Y.; Jo, S. J.; Kim, C. S.; Sohn, S. W.; Rack, P. D.; Kim, D. J.; Baik, H. K. Indium Oxide Thin-Film Transistors Fabricated by RF Sputtering at Room Temperature. *IEEE Electr. Device Lett.* **2010**, *31*, 567-569.
57. Jiao, Y.; Zhang, X. N.; Zhai, J. X.; Yu, X. K.; Ding, L. H.; Zhang, W. F. Bottom-Gate Amorphous In<sub>2</sub>O<sub>3</sub> Thin Film Transistors Fabricated by Magnetron Sputtering. *Electron. Mater. Lett.* **2013**, *9*, 279-282.
58. Rim, Y. S.; Chen, H. J.; Kou, X. L.; Duan, H. S.; Zhou, H. P.; Cai, M.; Kim, H. J.; Yang, Y. Boost up Mobility of Solution-Processed Metal Oxide Thin-Film Transistors *via* Confining Structure on Electron Pathways. *Adv. Mater.* **2014**, *26*, 4273-4278.
59. Mannironi, C.; DiNardo, A.; Fruscoloni, P.; Tocchini Valentini, G. P. *In Vitro* Selection of Dopamine RNA Ligands. *Biochemistry* **1997**, *36*, 9726-9734.

60. Walsh, R.; DeRosa, M. C. Retention of Function in the DNA Homolog of the RNA Dopamine Aptamer. *Biochem. Biophys. Res. Co.* **2009**, *388*, 732-735.
61. Farjami, E.; Campos, R.; Nielsen, J. S.; Gothelf, K. V.; Kjems, J.; Ferapontova, E. E. RNA Aptamer-Based Electrochemical Biosensor for Selective and Label-Free Analysis of Dopamine. *Anal. Chem.* **2013**, *85*, 121-128.
62. Giros, B.; Jaber, M.; Jones, S. R.; Wightman, R. M.; Caron, M. G. Hyperlocomotion and Indifference to Cocaine and Amphetamine in Mice Lacking the Dopamine Transporter. *Nature* **1996**, *379*, 606-612.
63. Kim, J. H.; Auerbach, J. M.; Rodriguez-Gomez, J. A.; Velasco, I.; Gavin, D.; Lumelsky, N.; Lee, S. H.; Nguyen, J.; Sanchez-Pernaute, R.; Bankiewicz, K.; McKay, R. Dopamine Neurons Derived from Embryonic Stem Cells Function in an Animal Model of Parkinson's Disease. *Nature* **2002**, *418*, 50-56.
64. Phillips, P. E. M.; Stuber, G. D.; Heien, M. L. A. V.; Wightman, R. M.; Carelli, R. M. Subsecond Dopamine Release Promotes Cocaine Seeking. *Nature* **2003**, *422*, 614-618.
65. Unger, E. L.; Eve, D. J.; Perez, X. A.; Reichenbach, D. K.; Xu, Y. Q.; Lee, M. K.; Andrews, A. M. Locomotor Hyperactivity and Alterations in Dopamine Neurotransmission Are Associated with Overexpression of A53T Mutant Human Alpha-Synuclein in Mice. *Neurobiol. Dis.* **2006**, *21*, 431-443.
66. Aswal, D. K.; Lenfant, S.; Guerin, D.; Yakhmi, J. V.; Vuillaume, D. Self Assembled Monolayers on Silicon for Molecular Electronics. *Anal. Chim. Acta* **2006**, *568*, 84-108.
67. Helmy, R.; Fadeev, A. Y. Self-Assembled Monolayers Supported on TiO<sub>2</sub>: Comparison of C<sub>18</sub>H<sub>37</sub>SiX<sub>3</sub> (X = H, Cl, OCH<sub>3</sub>), C<sub>18</sub>H<sub>37</sub>Si(CH<sub>3</sub>)<sub>2</sub>Cl, and C<sub>18</sub>H<sub>37</sub>PO(OH)<sub>2</sub>. *Langmuir* **2002**, *18*, 8924-8928.
68. Kim, J. S.; Park, J. H.; Lee, J. H.; Jo, J.; Kim, D. Y.; Cho, K. Control of the Electrode Work Function and Active Layer Morphology *via* Surface Modification of Indium Tin Oxide for High Efficiency Organic Photovoltaics. *Appl. Phys. Lett.* **2007**, *91*.
69. Chung, Y.; Verploegen, E.; Vailionis, A.; Sun, Y.; Nishi, Y.; Murmann, B.; Bao, Z. A. Controlling Electric Dipoles in Nanodielectrics and Its Applications for Enabling Air-Stable N-Channel Organic Transistors. *Nano Lett.* **2011**, *11*, 1161-1165.
70. Song, C. K.; Luck, K. A.; Zhou, N.; Zeng, L.; Heitzer, H. M.; Manley, E. F.; Goldman, S.; Chen, L. X.; Ratner, M. A.; Bedzyk, M. J.; Chang, R. P.; Hersam, M. C.; Marks, T. J. "Supersaturated" Self-Assembled Charge-Selective Interfacial Layers for Organic Solar Cells. *J. Am. Chem. Soc.* **2014**, *136*, 17762-17773.

71. Baker, B. R.; Lai, R. Y.; Wood, M. S.; Doctor, E. H.; Heeger, A. J.; Plaxco, K. W. An Electronic, Aptamer-Based Small-Molecule Sensor for the Rapid, Label-Free Detection of Cocaine in Adulterated Samples and Biological Fluids. *J. Am. Chem. Soc.* **2006**, *128*, 3138-3139.
72. Ferapontova, E. E.; Olsen, E. M.; Gothelf, K. V. An RNA Aptamer-Based Electrochemical Biosensor for Detection of Theophylline in Serum. *J. Am. Chem. Soc.* **2008**, *130*, 4256-4258.
73. Fan, C.; Plaxco, K. W.; Heeger, A. J. Electrochemical Interrogation of Conformational Changes as a Reagentless Method for the Sequence-Specific Detection of DNA. *Proc. Natl. Acad. Sci. U. S. A.* **2003**, *100*, 9134-9137.
74. Zuo, X.; Song, S.; Zhang, J.; Pan, D.; Wang, L.; Fan, C. A Target-Responsive Electrochemical Aptamer Switch (TREAS) for Reagentless Detection of Nanomolar ATP. *J. Am. Chem. Soc.* **2007**, *129*, 1042-1043.
75. Farjami, E.; Clima, L.; Gothelf, K.; Ferapontova, E. E. "Off-On" Electrochemical Hairpin-DNA-Based Genosensor for Cancer Diagnostics. *Anal. Chem.* **2011**, *83*, 1594-1602.
76. Singh, Y. S.; Sawarynski, L. E.; Dabiri, P. D.; Choi, W. R.; Andrews, A. M. Head-to-Head Comparisons of Carbon Fiber Microelectrode Coatings for Sensitive and Selective Neurotransmitter Detection by Voltammetry. *Anal. Chem.* **2011**, *83*, 6658-6666.
77. Zheng, Y.; Wang, Y.; Yang, X. R. Aptamer-Based Colorimetric Biosensing of Dopamine Using Unmodified Gold Nanoparticles. *Sensor Actuat. B-Chem* **2011**, *156*, 95-99.
78. Mathews, T. A.; Fedele, D. E.; Coppelli, F. M.; Avila, A. M.; Murphy, D. L.; Andrews, A. M. Gene Dose-Dependent Alterations in Extraneuronal Serotonin but Not Dopamine in Mice with Reduced Serotonin Transporter Expression. *J. Neurosci. Methods* **2004**, *140*, 169-181.

## Chapter VII

# Aptamer-Field-Effect Transistors Overcome Debye Length Limitations and Enable Small-Molecule Sensing



The information in this chapter is in preparation for *Science* and has been reproduced here.

Authors: Nakatsuka, N.; Yang, K. -A.; Xu, X.; Abendroth, J. M.; Zhao, C.; Cheung, K. M.; Zhu, B.; Rim, Y. S.; Yang, Y.; Weiss, P. S.; Stojanovic, M. N.; Andrews A. M.



## VII.A. Introduction

Field-effect transistors (FETs) modified with target-specific receptors provide means for direct electronic target detection.<sup>1,2</sup> Signal transduction and amplification in FET-based sensors are based on electrostatic gating of semiconductor channels by target-receptor complexes to produce changes in transconductance.<sup>3</sup> Two fundamental limitations have prevented widespread adoption of receptor-modified FETs. First, in solutions containing ions, the electric double layer shields semiconductor charge carriers limiting gating in response to recognition events. The extent of shielding, *i.e.*, the effective sensing distance, is characterized by the Debye length, which in physiological fluids, is <1 nm (Table SF.1).<sup>4</sup> Second, small target molecules with few or no charges have minimal impact on semiconductor transconductance, unless they trigger conformational changes in their receptors within or near the Debye length, or otherwise affect surface potentials.<sup>5</sup>

We overcome both of these obstacles by combining highly sensitive FETs with a specific type of oligonucleotide stem-loop receptor selected for adaptive target recognition (Figure VII.1A). Nanometer-thin In<sub>2</sub>O<sub>3</sub> FETs are produced by methods that facilitate nano- or microscale patterning and are scalable with respect to fabrication at high densities and for large numbers of devices.<sup>2,6</sup> Sensing *via* FETs is inherently nonlinear,<sup>5</sup> enabling target detection over larger and lower concentration ranges compared to equilibrium-based sensors.<sup>7</sup> Ultrathin metal-oxide FETs can be fabricated on flexible substrates for wearable<sup>8,9</sup> or chronically implantable devices. While others and we have previously used aptamers as receptors for FET devices, it is the unique combination of ligand-induced stem-loop conformational rearrangements involving negatively charged phosphodiester backbones together with associated counterions *and* close proximity to the surfaces of quasi-two-

dimensional FETs that enable signal transduction and amplification under biologically relevant conditions and for low-charge and neutral target molecules.

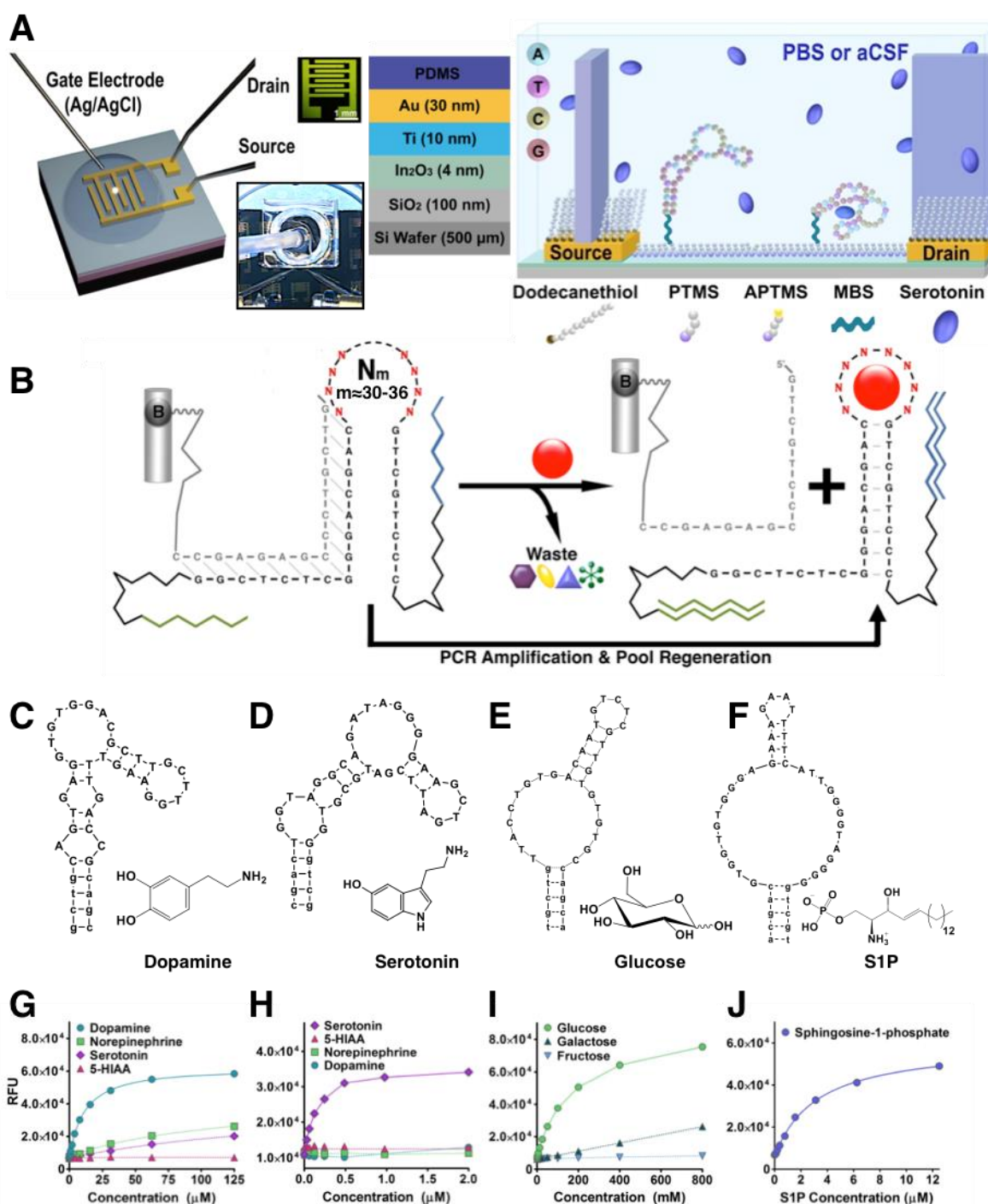


**Figure VII.1.** (A) Schematic of a field-effect transistor (FET), its fabrication, and surface chemistry to attach aptamers on  $\text{In}_2\text{O}_3$  semiconductor channels. (B) Oligonucleotide libraries ( $N_m$ , with random regions  $m \approx 30-36$  nucleotides, flanked by constant regions and primer regions for PCR amplification) were attached to agarose-streptavidin columns via biotinylated (B) complementary oligonucleotides. Exposure to targets (red sphere) causes elution of aptamers in which stems are stabilized. These sequences are preferentially amplified. Exposure to counter-targets (alternate shapes) eliminates cross-reactive sequences. (C) Dopamine ( $K_d = 150$  nM), (D) serotonin ( $K_d = 30$  nM), (E) glucose ( $K_d = 10$  mM), and (F) sphingosine-1-phosphate (S1P) ( $K_d = 190$  nM) aptamers were isolated. One advantage of solution-phase SELEX is that the resulting aptamers are directly turned into sensors. The complementary oligonucleotide is labeled with a quencher instead of biotin, while the aptamer is labeled with a fluorophore, leading to 'structure-switching'-like sensors with responses shown in (G-J). Fluorescence responses indicate selectivities of dopamine, serotonin, and glucose aptamers in the presence of specific vs. nonspecific targets. Fluorescence-concentration curves were obtained via competition with complementary strands and are the result of triplicate measurements with standard deviations too small to be visualized on the plots shown.

## **VII.B. Experimental Methods**

### **VII.B.1. Materials**

All chemicals were purchased from Sigma-Aldrich Co. (St. Louis, MO), unless otherwise noted below. Oligonucleotides were obtained from Integrated DNA Technologies (Coralville, IA). The SYLGARD 184 for fabricating PDMS wells was from Dow Corning Corporation (Midland, MI). Water was deionized before use (18.2 M $\Omega$ ) *via* a Milli-Q system (Millipore, Billerica, MA).

### **VII.B.2. Aptamer Selection**

Solution-phase selection of aptamer candidates was carried out using the following procedures and as previously described,<sup>10</sup> with modifications in oligonucleotides and PCR conditions as follows. (1) Random (N<sub>30</sub>) library 5'-GGA GGC TCT CGG GAC GAC-(N<sub>30</sub>)-GTC GTC CCG ATG CTG CAA TCG TAA-3', (2) Random (N<sub>36</sub>) library 5'-GGA GGC TCT CGG GAC GAC-(N<sub>36</sub>)-GTC GTC CCG CCT TTA GGA TTT ACA G-3', (3) forward-primer: 5'-GGA GGC TCT CGG GAC GAC-3', (4) reverse-primer for N<sub>30</sub> TTA CGA TTG CAG CAT CGG GAC G, (5) biotinylated reverse-primer for N<sub>30</sub> 5'-biotin- TTA CGA TTG CAG CAT CGG GAC G -3', (6) reverse-primer for N<sub>36</sub> 5'-CTG TAA ATC CTA AAG GCG GGA CGA C-3', (7) biotinylated reverse-primer for N<sub>36</sub> 5'-biotin-CTG TAA ATC CTA AAG GCG GGA CGA C-3', and (5) biotinylated column-immobilizing capture strand 5'-GTC GTC CCG AGA GCC ATA-BioTEG-3'.

Standard desalted oligonucleotides were used for the libraries, primers, and complementary strands. Modified oligonucleotides, *e.g.*, biotinylated, fluorophore-conjugated, were purified by reverse-phase high-performance liquid chromatography

(HPLC). All oligonucleotides were dissolved in nuclease-free water and stored at -20 °C. The PCR reactions were run with one cycle at 95 °C for 2 min, N cycles of [95 °C, 15 s → 60 °C, 30 s → 72 °C, 45 s], and one cycle at 72 °C for 2 min. Specific selection/counter-selection conditions are described below (Tables SF.2,3). Aptamers for serotonin, glucose, and S1P were selected in HEPES buffer at pH 7.5 while the dopamine aptamer was selected in PBS buffer with 2 mM MgCl<sub>2</sub> (Table SF.6). After adjusting the pH, HEPES buffer was filtered under vacuum using 0.22 µm filters (EMD Millipore Corp., Billerica, MA). Phosphate-buffered saline (PBS) was from Corning Inc. (Corning, NY), pH 7.4, with 2 mM MgCl<sub>2</sub> added.

#### **VII.B.3. Aptamer Fluorescence Assays**

Aptamer candidates were modified with fluorescein at their 5' ends (Figure SF.1a). Complementary strands were modified with dabcyI for quenching at the 3' ends. The concentrations of aptamers and complementary strands (Table SF.4) were determined empirically as per previous protocols.<sup>11</sup> Aptamer K<sub>d</sub> values were determined as per previously published methods.<sup>12</sup>

#### **VII.B.4. Aptamer-Functionalized Field-Effect Transistors**

To maximize channel surface-to-volume ratios, field-effect transistors (FETs) were fabricated with ultrathin (~4 nm) In<sub>2</sub>O<sub>3</sub> semiconductor films.<sup>2</sup> Aqueous solutions of indium(III) nitrate hydrate (In(NO<sub>3</sub>)<sub>3</sub> • xH<sub>2</sub>O, 99.999%) were spin-coated at 3000 rpm for 30 s onto heavily doped silicon wafers (University Wafer, Boston, MA) each having a 100- or 200 nm-thick thermally grown SiO<sub>2</sub> layer. Substrates were prebaked at 100°C for

5 min followed by thermal annealing at 350 °C for 3 h.<sup>13</sup> Interdigitated source and drain electrodes (width 1500 µm/length 80 µm, Figure SF.6) produced from 30 nm layers of Au over 10 nm Ti layers were patterned by standard photolithography. The Ti/Au layers were deposited by electron-beam evaporation on top of In<sub>2</sub>O<sub>3</sub> to obtain large transconductances and uniform current distributions.

To fabricate sensors, aptamers were immobilized on In<sub>2</sub>O<sub>3</sub>-exposed regions using a top-gate device configuration. Briefly, APTMS and PTMS (1:9 v/v ratio) were thermally evaporated using vapor-phase deposition onto In<sub>2</sub>O<sub>3</sub> surfaces at 40 °C for 1 h followed by incubation in 1 mM ethanolic solutions of 1-dodecanethiol for 1 h to passivate Au electrodes.

After rinsing with ethanol, substrates were immersed in 1 mM solutions of MBS dissolved in a 1:9 (v/v) mixture of DMSO and PBS for 30 min. The MBS crosslinks amine-terminated silanes to thiolated DNA aptamers. Aptamers were prepared for attachment to substrates by heating for 5 min at 95 °C in nuclease-free water followed by rapid cooling in an ice bath. Substrates were rinsed with deionized water and immersed in 1 µM solutions of thiolated DNA aptamers for 1 h, rinsed again with deionized water, and blown dry with N<sub>2</sub> gas.

Scrambled sequences with the same numbers and types of nucleotides as correct aptamer sequences but with pseudo-random orders were designed to investigate specific aptamer-target recognition *via* FETs (Table SF.5). Scrambled sequences were selected based on modeling (Mfold; <http://unafold.rna.albany.edu/?q=mfold>) to adopt significantly different secondary structures compared to the correct sequences.

### VII.B.5. Aptamer-Field-Effect Transistor Measurements

Soft-polymer PDMS wells were sealed on top of individual FETs to hold physiological buffers and targets. Phosphate-buffered saline (0.1× or 1× PBS), artificial cerebrospinal fluid (1× aCSF), HEPES buffer (1× HEPES), or Ringers solution (1× Ringers) were used as electrolyte solutions (Table SF.6). Commercially available Ag/AgCl reference electrodes (World Precision Instruments, Inc., Sarasota, FL) were placed in the solutions above the FETs. All FET measurements were performed on manual analytical probe stations (Signatone, Gilroy, CA) equipped with either an Agilent 4155C (Agilent Technologies, Santa Clara, CA) or Keithley 4200A (Tektronix, Beaverton, OR) semiconductor analyzer.

Source-drain current ( $I_{DS}$ ) transfer curves were obtained by sweeping the gate-bias voltage ( $V_{GS}$ ) from 0 to 400 mV while maintaining the drain voltage ( $V_D$ ) at 10 mV. Five consecutive sweeps were averaged for each transfer curve determined at each target or nontarget concentration. Calibrated responses were calculated to minimize device-to-device variation.<sup>14</sup> Briefly, the absolute sensor response ( $\Delta I$ ) that takes into account baseline subtraction was divided by the change in source-drain current with voltage sweep ( $\Delta I_{DS}/\Delta V_G$ ). This method relies on a correlation between absolute sensor responses and gate dependence in liquid-gate sensing set-ups.

#### **VII.B.6. *Ex Vivo* Sensing**

Brains lacking serotonin were from *Tph2* knockout mice provided by the laboratory of Donald Kuhn (Wayne State University, Detroit, MI). All procedures involving mice were pre-approved by the Wayne State University Institutional Animal Care and Use Committee. Mice were deeply anesthetized with pentobarbital and exsanguinated during cardiac perfusion with PBS. Brains were removed from the skulls and frozen at -70 °C, shipped to the University of California, Los Angeles on dry ice, and stored at -70 °C until use.

On the day of use, brains were thawed on ice and sectioned into quarters in the sagittal and rostrocaudal planes to facilitate homogenization. Each quarter was weighed and transferred to a 1.7-mL Eppendorf tube on ice. Ice-cold 1× aCSF was added to each tube (2 µL/mg tissue). Tissues were sonicated on ice using a VirTis Virsonic 600 ultrasonic cell disruptor (Gardiner, NY) with the microtip set at 4 and 50% duty, using 30-40 1-sec pulses. Homogenates were subdivided into aliquots (40 µL) for FET measurements. Serotonin was added to individual aliquots (10 fM-100 µM final concentrations). Aliquots were briefly vortexed prior to aptamer-FET measurements, which were carried out on six replicate samples per concentration.

#### **VII.B.7. Surface-Enhanced Raman Spectroscopy**

Localized surface-plasmon resonances, *i.e.*, hot spots, occurring in plasmonic nanostructures, significantly enhance Raman signals from adsorbed molecules. As such, surface-enhanced Raman spectroscopy (SERS) has been used to detect ultra-low target concentrations and even single molecules.<sup>15-17</sup> Additionally, SERS is sensitive to conformational changes associated with DNA-base interactions or molecular orientations



resulting in shifts in SERS spectra.<sup>18,19</sup> Halas and co-workers exploited SERS to monitor DNA aptamer interactions with target molecules and observed the appearance of unique peaks after specific binding.<sup>20</sup>

The Au nanoshells in surfactant (poly(4-vinylpyridine)) had silica cores with diameter  $83 \pm 5$  nm, Au-shell thickness  $30 \pm 7$  nm, and peak absorption at 660 nm in water, and were purchased from Nanocomposix Inc. (product number GSPN 660-25M, 0.05 mg/ml; San Diego, CA). The Au nanoshells were dispersed and centrifuged in acetone twice to remove surfactant. They were then washed with ethanol twice and re-dispersed in deionized water. Aliquots (40  $\mu$ l) of Au nanoshell dispersions were drop-cast onto clean glass slides and dried on a hotplate at 40 °C to form red ring-shaped films.<sup>21</sup> These “coffee” rings consisted of close-packed monolayers of Au nanoshells, as determined by SEM (Figure SF.3). Images were taken using a Zeiss Supra 40VP scanning electron microscope. The SERS substrates were made conductive by sputtering several nm of Au/Pt for SEM imaging.

Thiolated aptamers (5  $\mu$ M in nuclease-free water) were heated at 95 °C for 5 min and rapidly cooled in an ice bath to relax molecules into extended conformations.<sup>20,22</sup> Aptamers were then incubated overnight with Au nanoshell monolayers for self-assembly. A Renishaw inVia confocal Raman microscope was used to collect SERS spectra. A HeNe laser operating at 632.8 nm, in resonance with the absorption peak of Au nanoshells, was used for Raman excitation. The laser intensity was set at 25  $\mu$ W (0.5% of total power) to avoid damaging DNA. A 50 $\times$  objective was used to collect high-resolution spectra. Each spectrum was collected using a 20-s integration time, which was the accumulation of 10

spectra each with a 2-s exposure. A total of 20 spectra were collected for each sample and two replicate samples were tested for each condition.

#### **VII.B.8. Circular Dichroism Spectroscopy**

Spectral circular dichroism (CD) signatures are dominated by exciton interactions induced by stacking of hydrophobic bases in asymmetric helices. Therefore, the intensities and positions of the positive and negative peaks for oligonucleotides in sigmoidal CD spectra are sensitive to the extent of base stacking and orientations of dipole moments.<sup>23</sup>

Aptamer and target concentrations were 2  $\mu\text{M}$ <sup>20</sup> in 1× PBS, 1× aCSF, 1× aCSF without  $\text{Mg}^{2+}$  and  $\text{Ca}^{2+}$ , or 1× HEPES. To maintain the same overall ionic strength of 1× aCSF *sans* divalent cations, we adjusted the ionic strength using NaCl for CD and FET measurements. Aptamers were thermally treated as described above for SERS spectroscopy. Spectra were collected on a JASCO J-715 circular dichroism spectrophotometer at room temperature. Four scans were acquired per sample with 0.5 nm resolution, 1.0 nm bandwidth, a 4-s response time, and a 20 nm/min scan rate. Scans shown in the figures are average scans. Scans without targets were subtracted as background.

#### **VII.B.9. Statistics**

Data for fluorescence assays and FET calibrated responses are reported as means  $\pm$  standard deviations and were analyzed using GraphPad Prism 7.0 (GraphPad Software Inc., San Diego, CA). Concentration-dependent FET responses were analyzed by two-way analysis of variance (ANOVA) with concentration (repeated measure) and buffer/target condition as the independent variables. Omnibus statistics are in Table SF.7. Data for

counter-target selectivities were normalized to mean responses for correct targets and are reported as % calibrated responses. These data were analyzed by one-way ANOVA with omnibus statistics reported in Table SF.8. *Post hoc* comparisons were by Tukey's multiple comparisons. In all cases,  $P < 0.05$  was considered statistically significant.

### VII.C. Results and Discussion

Solution-phase selections that circumvent target tethering and are based on stem-loop closing were used to isolate receptors (Figure VII.1B),<sup>10,11</sup> with appropriate counter-selections (Tables SF.2,3). This protocol yields aptamers characterized by adaptive-loop binding. We isolated original receptors for dopamine, serotonin, glucose, and sphingosine-1-phosphate (S1P) (Figure VII.1C-F, Table SF.4). Dopamine was targeted because we had constructed devices using a previously reported dopamine aptamer<sup>24</sup> that required dilute ionic concentrations for FET sensing.<sup>2</sup> Serotonin was pursued as another important neurotransmitter target<sup>25</sup> having no publicly reported aptamers; we ultimately aim to distinguish serotonin from dopamine and other similarly structured molecules in measurements of brain intercellular signaling.<sup>26-28</sup> Glucose was selected as an example of an important small, neutral hydrophilic target with minimal associated companion ions. Aptamers interacting directly with glucose have not been reported (*cf.* aptamers for glucose sensors).<sup>11</sup> Additionally, S1P, which prevents chemotherapy associated apoptosis,<sup>29</sup> was chosen as a zwitterionic target. This endogenous lipid has good solubility (critical micelle concentration <10  $\mu$ M).

Fluorescence assays were used to characterize aptamer-target dissociation constants ( $K_d$ ) (Figure SF.1a). Selections led to high affinity aptamers for dopamine (150 nM) and serotonin (30 nM) (Figure SF.1b,c). Counter-selections eliminated interactions with similarly structured molecules (Figure VII.1G,H). Notably, the new dopamine aptamer does not recognize norepinephrine, in contrast to cross-reactivity encountered with the previously reported dopamine aptamer.<sup>2,24</sup> Poor selectivity is problematic for fast-scan cyclic voltammetry, the most common method for sensing

dopamine.<sup>26,30</sup> The affinity of the glucose aptamer (10 mM) (Figure SF.1d) and selectivity with respect to analogs (Figure VII.1I) were consistent with the hydrophobicity of the receptor.<sup>31</sup> The affinity of the S1P aptamer (180 nM) (Figure VII.1J, SF.1e) was not as high as that of a reported spiegelmer (4 nM).<sup>32</sup> However, our method of determining  $K_d$ <sup>12</sup> gives upper bounds, *i.e.*, affinities may be higher because additional conformations upon stem opening are not considered.

We initially functionalized FETs with dopamine or serotonin aptamers to investigate electronic small-molecule detection (Figure VII.1A). Despite sub-nanometer Debye screening lengths, aptamer-FETs responded to a wide range of target concentrations ( $10^{-14}$ - $10^{-9}$  M) in PBS (Figure VII.2A, SF.2a) or artificial cerebrospinal fluid (aCSF) (Figure VII.2B,C). Scrambled aptamer sequences (Table SF.5) produced negligible responses (Figure VII.2A-C, SF.2a). Even at physiological ionic concentrations ( $1\times$  PBS) and hence, a significantly smaller Debye length, FET responses for the new dopamine aptamer were more sensitive by three orders of magnitude compared to the previously reported dopamine aptamer in  $0.1\times$  PBS<sup>24</sup> (Figure VII.2A), due to improved molecular recognition associated with solution- vs. solid-phase selection approaches<sup>33</sup> and by-design adaptive aptamer conformational changes.

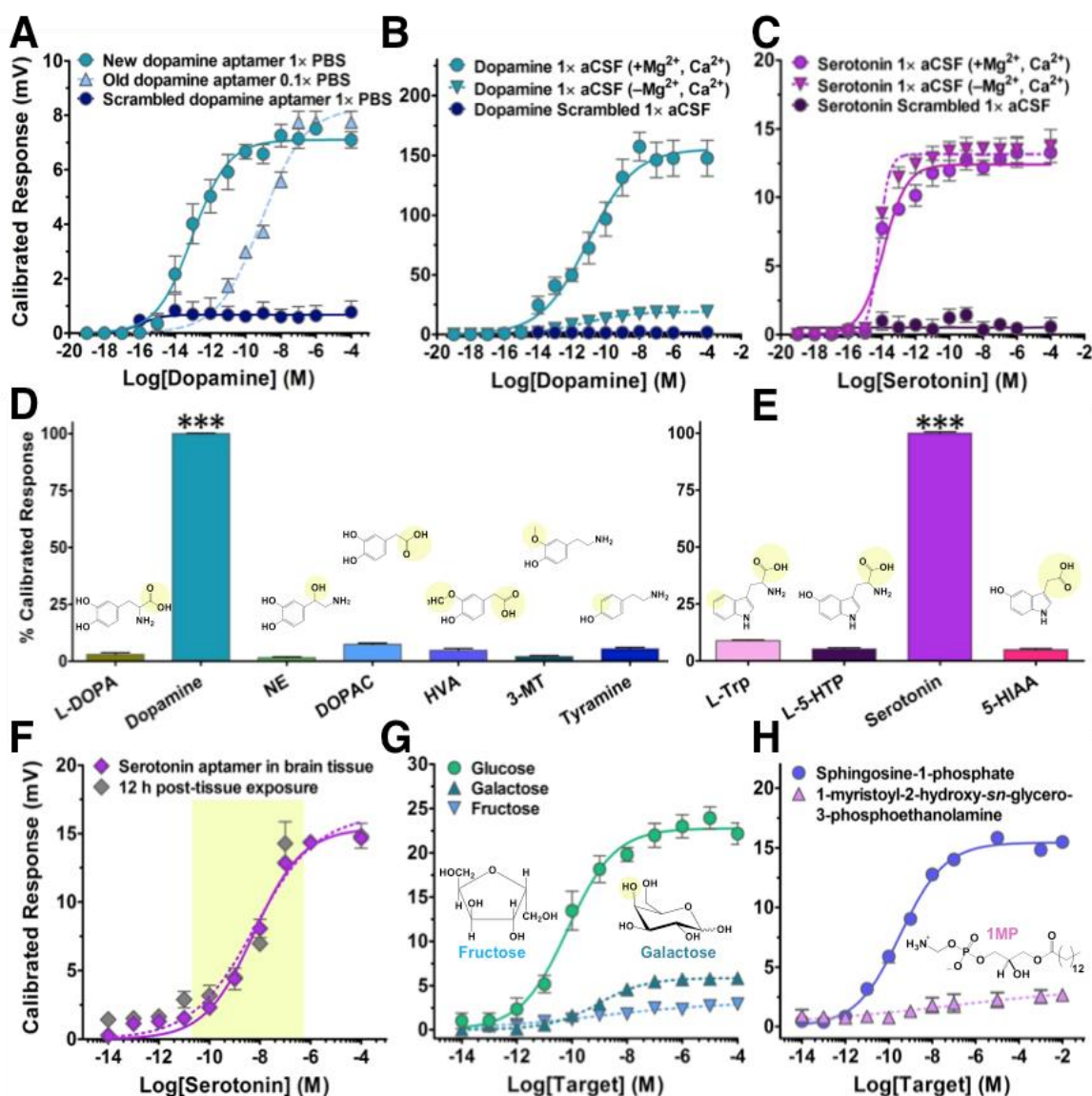


**Figure VII.2.** (A) Responses of field-effect transistor (FET) sensors functionalized with a new dopamine aptamer ( $K_d=150$  nM, 1× PBS) or its scrambled sequence, compared to FET responses with a previously reported dopamine aptamer ( $K_d=1$   $\mu$ M,<sup>24</sup> 0.1× PBS).<sup>2</sup> (B) FET responses to dopamine in artificial cerebrospinal fluid (aCSF) with or without divalent cations led to concentration-dependent responses for dopamine-aptamer-FETs. Negligible changes in calibrated responses occurred for scrambled dopamine sequences. (C) For serotonin-aptamer-FETs, serotonin in aCSF led to concentration-dependent responses, while scrambled serotonin sequences showed negligible responses. In contrast to dopamine-aptamer-FETs, divalent cations in aCSF did not affect serotonin responses. (D) Dopamine-aptamer-FET responses upon exposure to 100  $\mu$ M L-3,4-dihydroxyphenylalanine (L-DOPA), norepinephrine (NE), 3,4-dihydroxyphenylacetic acid (DOPAC), homovanillic acid (HVA), 3-methoxytyramine (3-MT), or tyramine were negligible compared to dopamine (10 nM). (E) Responses of serotonin-aptamer-FETs upon exposure to 100  $\mu$ M L-tryptophan (L-Trp), 5-hydroxytryptophan (L-5-HTP), or 5-hydroxyindoleacetic acid (5-HIAA) were negligible compared to serotonin (10 nM). (F) Concentration-dependent responses for serotonin-aptamer-functionalized FETs after exposure to brain tissue with increasing concentrations of serotonin. Responses were the same 12 h later. (G) Glucose sensing was carried out in HEPES buffer. Responses for glucose-aptamer-FETs were minimal or negligible for galactose or fructose, respectively. (H) Sphingosine-1-phosphate (S1P) aptamer-FETs showed concentration-dependent responses to S1P but not a phospholipid with similar epitopes. Error bars represent standard errors of the means with  $N=6$  (A-C, F-H) or  $N=3$  samples per group (D,E). \*\*\* $P<0.001$  vs. counter-targets.

Aptamer-FETs were selective for dopamine vs. structurally similar catecholamines, including L-DOPA, DOPAC, HVA, 3-methoxytyramine (3-MT), NE, and tyramine (Figure VII.2D). Serotonin-aptamer functionalized FETs showed high selectivity vs. indoleamines, *i.e.*, L-Trp, L-5-HTP, or 5-hydroxyindoleacetic acid (5-HIAA) (Figure VII.2E). Serotonin was also distinguished from other monoamine neurotransmitters (Figure SF.2b). To investigate the potential for sensing in native environments, increasing concentrations of serotonin were added to brain tissue homogenates lacking serotonin (Figure VII.2F).<sup>34</sup> Sensor performance was retested 12 h later in tissue; comparable responses were obtained indicating stable device performance. Electronic FET responses occurred over physiologically relevant serotonin concentrations (10 pM-100 nM),<sup>27</sup> suggesting the initial high sensitivity of aptamer-FETs can be used to offset losses often encountered in the presence of biological macromolecules.

Glucose-aptamer-FETs produced concentration-dependent responses to glucose (10 pM-10 nM) in HEPES buffer (Table SF.6), while responses to other six-carbon sugars were minimal (Figure VII.2G). The zwitterionic lipid S1P was detected from 10 pM-100 nM, with negligible responses to a nontarget lipid (1-myristoyl-2-hydroxy-*sn*-glycero-3-phosphoethanolamine) having similar epitopes (Figure VII.2H).

Aptamer-FET sensing enabled observations indicative of mechanisms. Transfer-curve characteristics, *i.e.*, source-drain current ( $I_{DS}$ ) vs. source-gate voltage ( $V_{GS}$ ), for dopamine- vs. serotonin-aptamer-FETs changed in opposite directions with increasing target concentrations in aCSF (Figure VII.3A,B). We hypothesize that upon dopamine capture, aptamer reorientation occurs such that a significant portion of the negatively charged backbone moves closer to the *n*-type semiconductor channel, increasing

electrostatic repulsion of charge carriers and decreasing transconductance, measured as target-related current responses (Figure VII.3C). In contrast, serotonin aptamers move predominantly away from channel surfaces upon target capture increasing transconductance (Figure VII.3D). Since dopamine and serotonin each have a single positive charge at physiological pH, these observations argue against signal transduction mechanisms based exclusively on target charge, as has been proposed,<sup>35</sup> and which would preclude detecting neutral targets (*vide infra*). Consistent with our mechanistic picture, increasing the distance from semiconductor surfaces by increasing stem lengths, led to decreases in FET-calibrated responses for glucose-aptamer-FETs (Figure VII.3E,F).



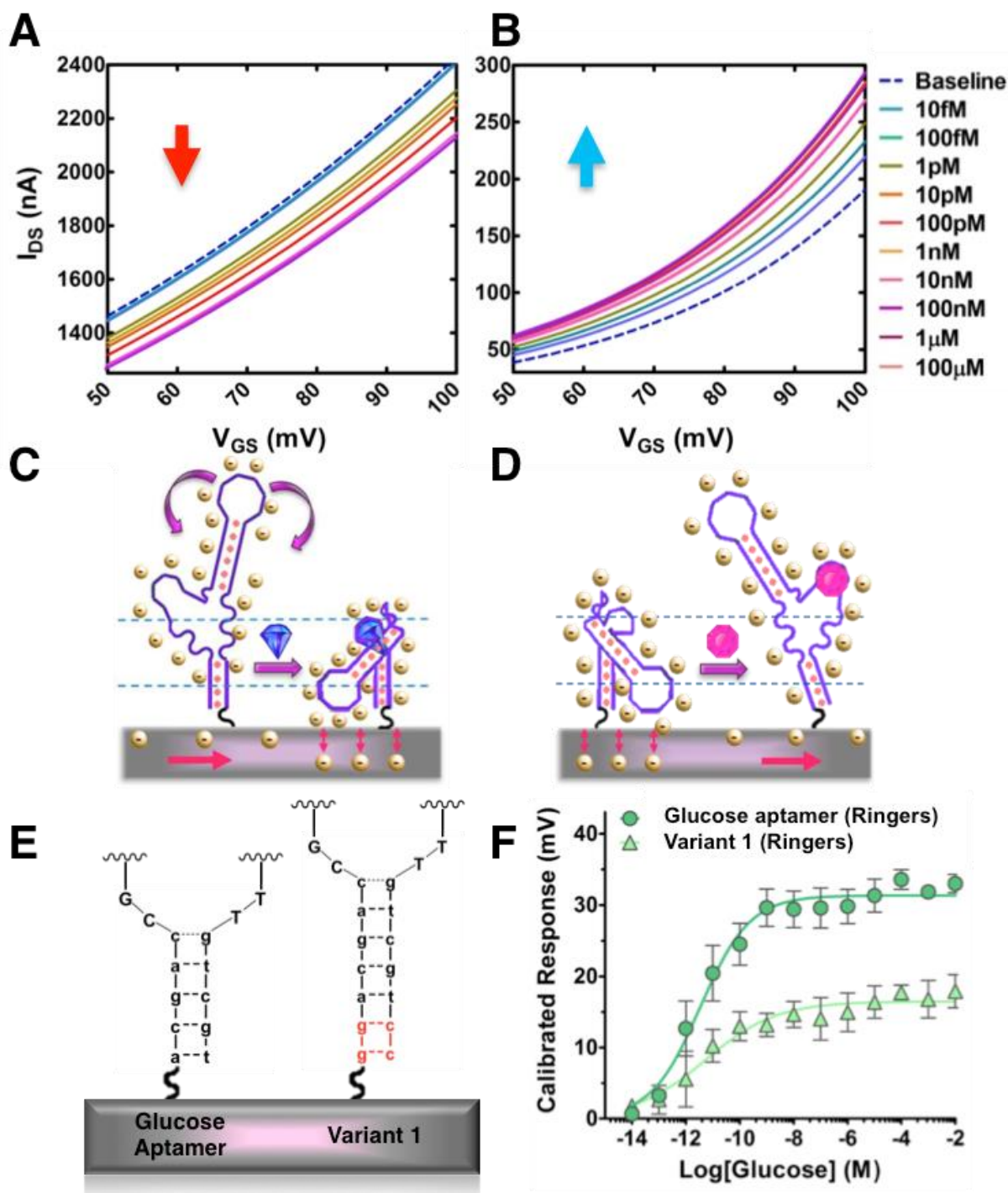


**Figure VII.3.** Mechanisms of aptamer-functionalized field-effect transistors (FETs). **(A,C)** Exposure of dopamine-aptamer-FETs to dopamine (1x aCSF) led to concentration-dependent *reductions* in source-drain currents, presumably associated with aptamer stem-loop structures folding in close proximity to semiconductor channels within or near the Debye length to deplete channels electrostatically. **(B,D)** For serotonin-aptamer-FETs, increasing concentrations of serotonin (1x aCSF) led to *increases* in source-drain currents. Here, target-mediated aptamer conformational changes are hypothesized to reorient serotonin aptamers away from FET semiconductor channels increasing transconductance. **(E)** For glucose-aptamer-FETs (**left**), *increasing* the distance from semiconductor surfaces by *increasing* the stem length (stem variants; **right**) resulted in **(F)** length-dependent *decreases* in FET calibrated responses (1x Ringers solution to mimic blood plasma ionic composition).

To investigate aptamer conformational changes further, we carried out SERS. Surface selection rules governing Raman enhancement modes predict that changes in the orientations of aptamers will be reflected in SERS spectra.<sup>20</sup> However, Raman signatures are enhanced only in close proximity to metal surfaces due to the short range of evanescent fields, with the strongest enhancements within 1 nm of surfaces.<sup>36</sup> We employed Au nanoshells as SERS substrates due to uniform and large hot spots (Figure SF.3), and high spectral reproducibility.<sup>37,38</sup> After dopamine, serotonin, glucose, or S1P were introduced, SERS spectra for the respective thiol-aptamer self-assembled monolayers exhibited complex pattern changes (Figure VII.4A-D). For all aptamers, SERS spectra were unchanged in the presence of nontarget compounds. Along with FET transconductances, changes in SERS spectra in response to aptamer-target association reflected large aptamer conformational changes, contractions or expansions of backbones, and/or rearrangements in the relative positions of aptamer stems in close proximity to semiconductors.

We carried out CD spectroscopy<sup>39,40</sup> to investigate specific conformational changes. Large changes in CD peak positions and relative intensities indicated formation of new structural motifs for dopamine and serotonin aptamers upon recognition of targets (Figure VII.4E,F) vs. nontargets (Figure SF.4a,b). A parallel G-quadruplex was indicated for dopamine-aptamer-target complexes (maxima shifted to 260 nm).<sup>23</sup> Spectral signatures consistent with the formation of an antiparallel G-quadruplex were observed for serotonin-aptamer-target complexes (minima shifted to 260 nm; maxima shifted to 290 nm). For glucose and S1P aptamers, target-induced changes in FET transconductances and SERS spectra, in the absence of large CD spectral shifts (Figure SF.4c,d), are consistent with all major DNA domains, *i.e.*, helices and single-stranded regions, being formed prior to target

binding. Here, adaptive binding occurs mostly through spatial rearrangement of existing secondary structures and companion ions.<sup>41</sup>

Mechanistic insight arose from another key observation. When sensing was carried out in the presence of  $Mg^{2+}$  and  $Ca^{2+}$  normally present in aCSF, FET responses were potentiated for dopamine but not serotonin, compared to *sans* divalent cations (Figure VII.2B,C). Similarly, large CD spectral shifts were observed for dopamine- but not serotonin-aptamer-target interactions in aCSF with  $Mg^{2+}$  and  $Ca^{2+}$  compared to their absence (Figure SF.4e,f). Some, though not all, stem-loop receptors require divalent cations<sup>42</sup> to adopt new target-induced secondary structures, which ultimately influence FET responses. Interestingly, FET transfer-curve characteristics changed in opposite directions with vs. without divalent cations for dopamine but not serotonin (Figure SF.5a,b,e,f). These findings further substantiate the hypothesis that divalent cations facilitate dopamine-aptamer target-induced conformational changes that orient phosphodiesterase backbones closer to FET surfaces (Figure VII.3C). Transfer-curve characteristics for glucose-aptamer-FET sensing in HEPES or Ringers indicate that predominant reorganizations upon target binding reorient aptamers away from semiconductor channels, similar to serotonin- and S1P-aptamers (Figure SF.5i-k).

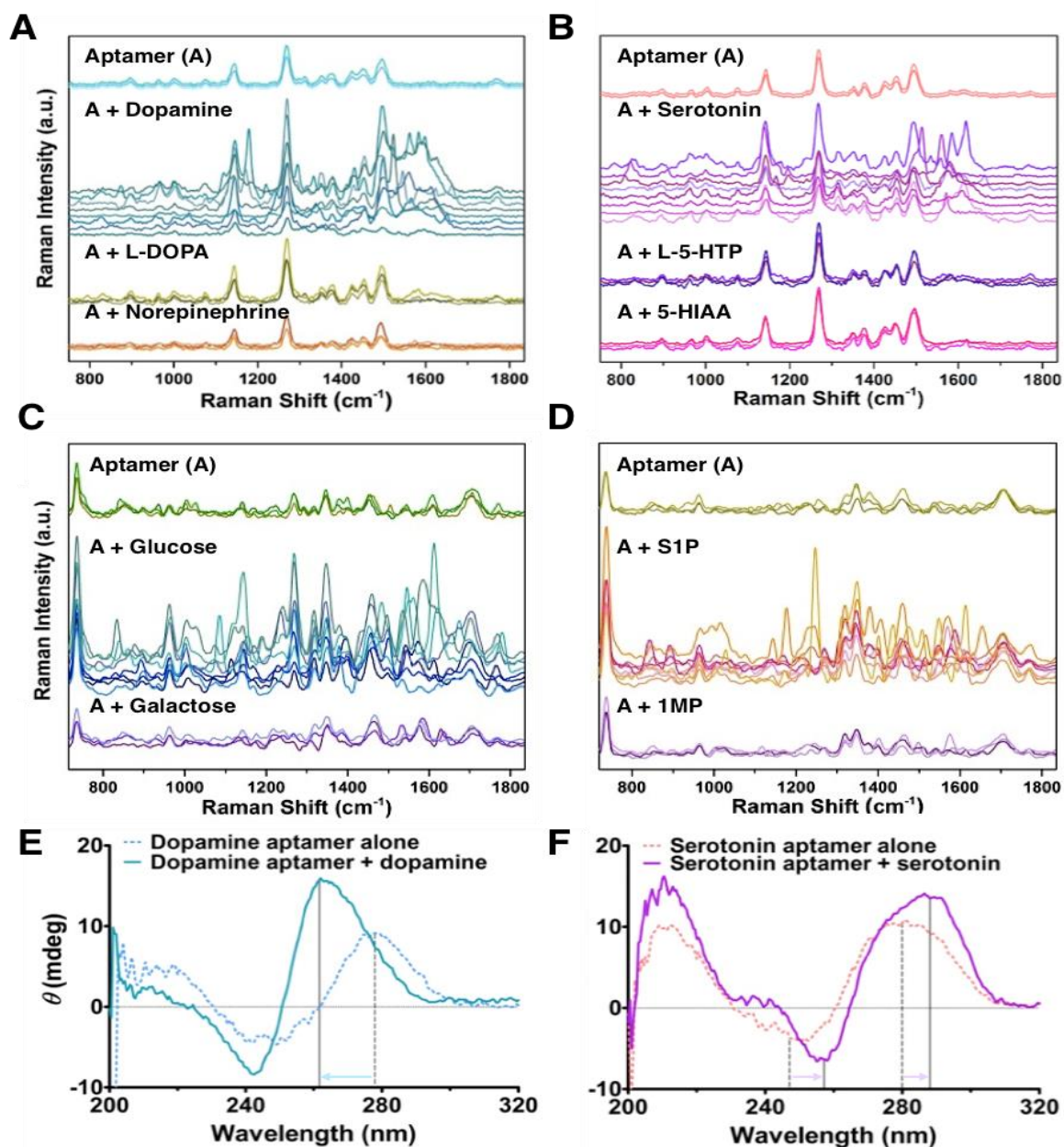


**Figure VII.4.** Surface-enhanced Raman spectra of (A) dopamine-, (B) serotonin-, (C) glucose-, or (D) S1P-aptamer-thiol monolayers on Au-nanoshells prior to exposure to targets, after correct target exposure, and following counter-target exposure. Spectral changes indicate aptamer conformational changes only in the presence of the matched targets. (E,F) Changes in secondary structures of aptamers upon target capture were investigated using circular dichroism spectroscopy. The dopamine aptamer showed significant shifts in the presence of dopamine indicating formation of a compact parallel G-quadruplex. By contrast, the serotonin aptamer showed a shift in peak positions upon serotonin addition indicating formation of an antiparallel G-quadruplex.

#### VII.D. Conclusions and Prospects

Ultrathin metal-oxide FETs coupled to conformationally mobile aptamers selectively detect low-charge and electroneutral targets over large, physiologically relevant concentration ranges, and where direct (and massively parallel) measurements preclude sample dilution or other sample manipulation.<sup>28,43</sup> Targets were detected orders of magnitude below aptamer  $K_d$ 's due to reorientation of negatively charged oligonucleotide receptors close to semiconductor surfaces. Aptamer affinities on FETs might be higher than measured by fluorescence assay because fluorophores and quenchers are not needed for target detection. However, even low receptor occupancy significantly and measurably affects transconductance in thin-film semiconductors such that target-receptor interactions are amplified.<sup>44</sup> Sensing under biologically relevant conditions occurred without the use of additional surface chemistries.<sup>45</sup> Unlike protein receptors (*e.g.*, antibodies), highly selective chemically synthesized nucleic acid receptors can be identified through *in vitro* selections/counter selections. Aptamer-receptors further enable fine tuning of binding affinities<sup>46,47</sup> and targeting of a wide variety of small (and large) molecules for electronic FET sensing.<sup>35</sup>

## **APPENDIX F**

### **Aptamer-Field-Effect Transistors Overcome Debye Length Limitations and Enable Small-Molecule Sensing**

#### **Supplementary Information**

$$\lambda_D = \sqrt{\frac{\epsilon_0 \epsilon_r K_B T}{2 N_a e^2 I}}$$

$\lambda_D$  is the Debye length  
 $\epsilon_0$  is the permittivity of free space  
 $\epsilon_r$  is the dielectric constant  
 $K_B$  is Boltzmann's constant  
 $T$  is temperature (Kelvin)  
 $N_a$  is Avogadro's number  
 $e$  is elementary charge  
 $I$  is the electrolyte ionic strength

Buffer	Ionic strength (mM)	Debye length (nm)
0.01x PBS	1.627	7.53
0.1x PBS	16.27	2.38
1.0x PBS	162.7	0.75
1.0x aCSF	159.5	0.74

**Table SF.1.** Debye lengths and hence, the ranges over which targets can be detected, increase substantially when physiological buffers (1.0x) buffers, such as phosphate-buffered saline (PBS) or artificial cerebrospinal fluid (aCSF), are diluted ten-fold (0.1x) or one-hundredfold (0.01x).

Target	SELEX/Counter-SELEX		
	Round	Target concentrations (no. of elutions)	Counter-target concentrations (no. of elutions)
<b>Dopamine</b> - SELEX with N <sub>36</sub> library - PBS + 2 mM MgCl <sub>2</sub>	1-2	100 µM (3)	No counter-SELEX
	3-4	100 µM (3)	Serotonin 100 µM (8)
	5	100 µM (3)	No counter-SELEX
	6	100 µM (3)	Serotonin 200 µM (8)
	7	100 µM (3)	Serotonin 200 µM (16)
	8	100 µM (3)	Tyrosine 100 µM (16)
	9	100 µM (3)	Tyrosine 200 µM (16)
	10	100 µM (3)	Tryptophan 200 µM (16)
	11	50 µM (3)	L-DOPA 200 µM (8)
	12	50 µM (3)	L-DOPA 200 µM (16)
	13	20 µM (3)	No counter-SELEX
	14-17	20 µM (3)	Serotonin 100 µM (16)
	18	20 µM (3)	Serotonin 20 µM (20)
<b>Serotonin</b> - SELEX with N <sub>36</sub> library - HEPES	1-4	100 µM (3)	No counter-SELEX
	5-6	100 µM (3)	Tryptophan 100 µM (8)
	7	100 µM (3)	Tryptophan 100 µM (16)
	8-9	50 µM (3)	No counter-SELEX
	10	50 µM (3)	Tryptophan 100 µM (8)
	11-12	50 µM (3)	Tryptophan 100 µM (16)
	13	25 µM (3)	No counter-SELEX
	14	25 µM (3)	Proline 100 µM (8)
	15	25 µM (3)	5-HIAA 50 µM (16)
	16-17	20 µM (3)	Melatonin 100 µM (16)
	18	20 µM (3)	Melatonin 100 µM (10) 5-HIAA 100 µM (10)
	19	10 µM (3)	Melatonin 200 µM (16)
	20	5 µM (3)	No counter-SELEX

**Table SF.2.** The SELEX/counter-SELEX processes used to identify the dopamine and serotonin aptamers investigated herein. Numbers of rounds of SELEX were determined empirically. Each elution was with 250 µL selection buffer.



Target	SELEX/Counter-SELEX		
	Round	Target concentrations (no. of elutions)	Counter-target concentrations (no. of elutions)
<b>Glucose</b> - SELEX with N <sub>30</sub> library - HEPES	1-5	100 mM (3)	No counter-SELEX
	6-7	50 mM (3)	Fructose, 100 mM (8)
	8-9	25 mM (3)	Galactose, 100 mM (8)
	10	25 mM (3)	Mixture of 100 mM fructose and 100 mM galactose (8)
	11-13	25 mM (3)	No counter-SELEX
	14	25 mM (3)	Fructose 100 mM (16) Galactose 100 mM (16)
	15	25 mM (3)	No counter-SELEX
<b>S1P</b> - SELEX with N <sub>36</sub> library - HEPES	1-2	50 $\mu$ M S1P-50 $\mu$ M CpRh (3)	No counter-SELEX
	3	25 $\mu$ M S1P-50 $\mu$ M CpRh (3)	No counter-SELEX
	4	25 $\mu$ M S1P-50 $\mu$ M CpRh (3)	CpRh, 50 $\mu$ M (6)
	5	25 $\mu$ M S1P-50 $\mu$ M CpRh (3)	CpRh, 100 $\mu$ M (6)
	6	25 $\mu$ M S1P-50 $\mu$ M CpRh (3)	No counter-SELEX
	7-11	25 $\mu$ M S1P-50 $\mu$ M CpRh (3)	No counter-SELEX
	12-14	25 $\mu$ M S1P-50 $\mu$ M CpRh (3)	CpRh, 100 $\mu$ M (16)
	15-16	50 $\mu$ M S1P-50 $\mu$ M CpRh (3)	CpRh, 100 $\mu$ M (16)
	17-18	50 $\mu$ M S1P-50 $\mu$ M CpRh (3)	CpRh, 100 $\mu$ M (24)
	19-20	50 $\mu$ M S1P-50 $\mu$ M CpRh (3)	CpRh, 100 $\mu$ M (16)
	<b>Note:</b> The original intended target was S1P-pentamethylcyclopentadienylrhodium(III) chloride dimer (CpRh) complex to develop a better epitope for the target. After isolating and characterizing the S1P aptamer, this aptamer was determined to be selective for S1P and not the complex.		

**Table SF.3.** The SELEX/counter-SELEX processes for the glucose and sphingosine-1-phosphate (S1P) aptamers investigated herein. Numbers of rounds of SELEX were determined empirically. Each elution was with 250  $\mu$ L selection buffer.

Aptamer	Strand	Sequence (5' → 3')	Concentration	Buffer
<b>Dopamine</b>	Sensor	/56-FAM/ CTC TCG GGA CGA CGC CAG TTT GAA GGT TCG TTC GCA GGT GTG GAG TGA CGT CGT CCC	50 nM	PBS
	Capture	CGT CGT CCC GAG AG/3Dab/	250 nM	
<b>Serotonin</b>	Sensor	/56-FAM/ CTC TCG GGA CGA CTG GTA GGC AGA TAG GGG AAG CTG ATT CGA TGC GTG GGT CGT CCC	50 nM	HEPES
	Capture	GTC GTC CCG AGA G/3Dab/	500 nM	
<b>Glucose</b>	Sensor	/56-FAM/CTC TCG GGA CGA CCG TGT GTG TTG CTC TGT AAC AGT GTC CAT TGT CGT CCC	50 nM	HEPES
	Capture	GGT CGT CCC GAG AG/3Dab/	250 nM	
<b>S1P</b>	Sensor	/56-FAM/CTC TCG GGA CGA CGT GGT GTG GGA GAA AGA ATT TTC ATT GGG GTA GGG GGT CGT CCC	50 nM	HEPES
	Capture	GTC GTC CCG AGA G/3Dab/	150 nM	

**Table SF.4.** Sequences of aptamers and complementary (capture) strands, and concentrations and buffers for fluorescence assays.

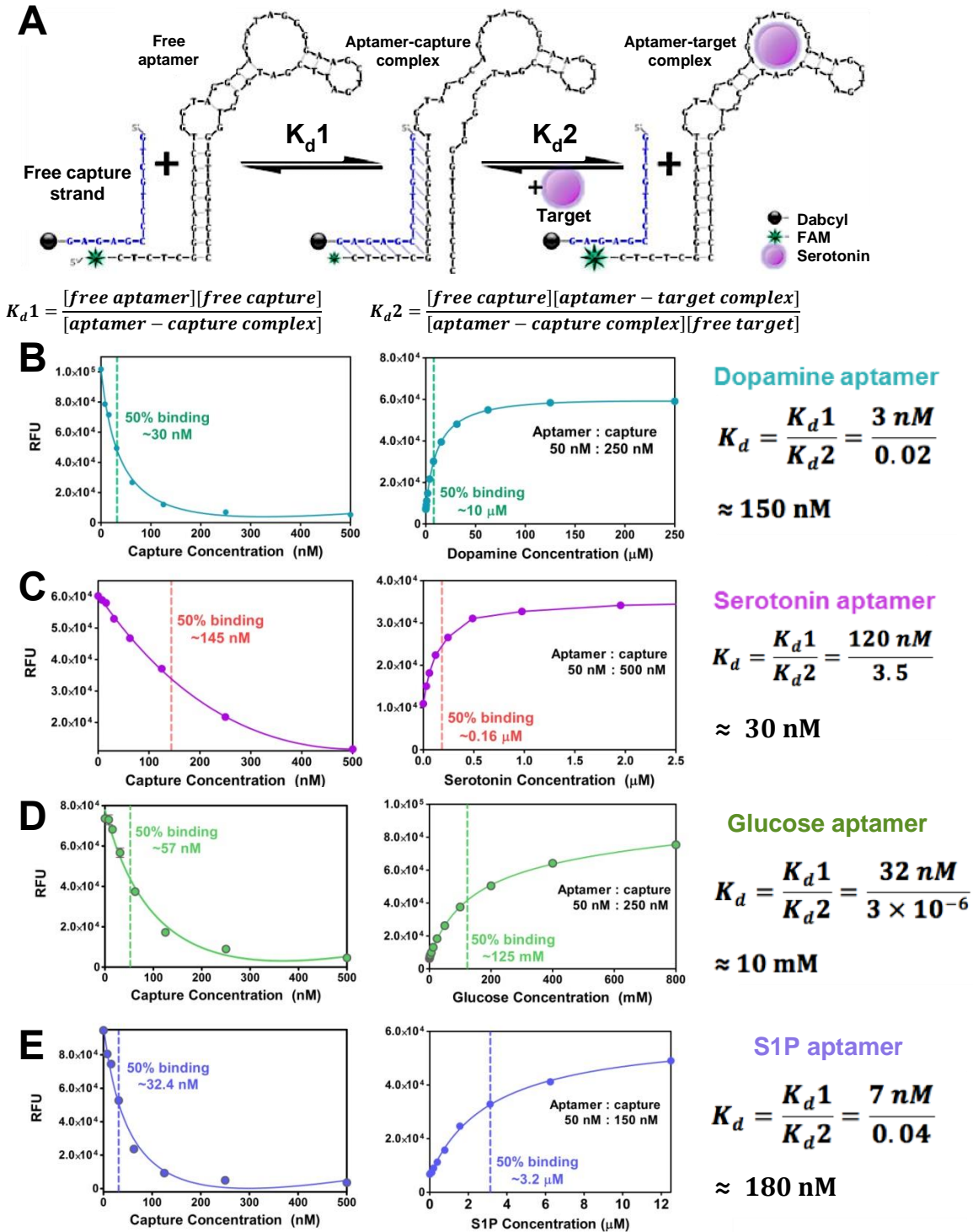


**Figure SF.1. (a)** Aptamers were incubated with increasing concentrations of complementary (capture) strands. Fluorescence quenching was used to determine  $K_d1$ . Upon target binding, aptamers fold inducing conformational changes that lead to dissociation from capture strands. Fluorescence in the presence of increasing target concentrations was used to determine  $K_d2$ . Fluorescence curves for **(b)** dopamine, **(c)** serotonin, **(d)** glucose, and **(e)** S1P aptamers. Dotted lines indicate half-maximal responses. Apparent dissociation constants ( $K_d$ ) were calculated as the ratio of  $K_d1/K_d2$ . Curves are the result of triplicate measurements with standard deviations too small to be visualized at the scales of these plots.

Serotonin Scrambled	5'-/5ThioMC6-D/CCCGGGAATTCCGGAATTGGGGCAATTGATGAGGGGGTCATGGG-3'
Dopamine Scrambled	5'-/5ThioMC6-D/AGTACGTCGATGCTCGATCAGTGGGCTAGGTGCGTAGCGGTCTG-3'

**Table SF.5.** Scrambled serotonin and dopamine aptamer sequences were determined after secondary structures were energy-minimized using Mfold, generating thermodynamically stable conformations contingent on base-sequence and external constraints, such as temperature and ionic conditions.

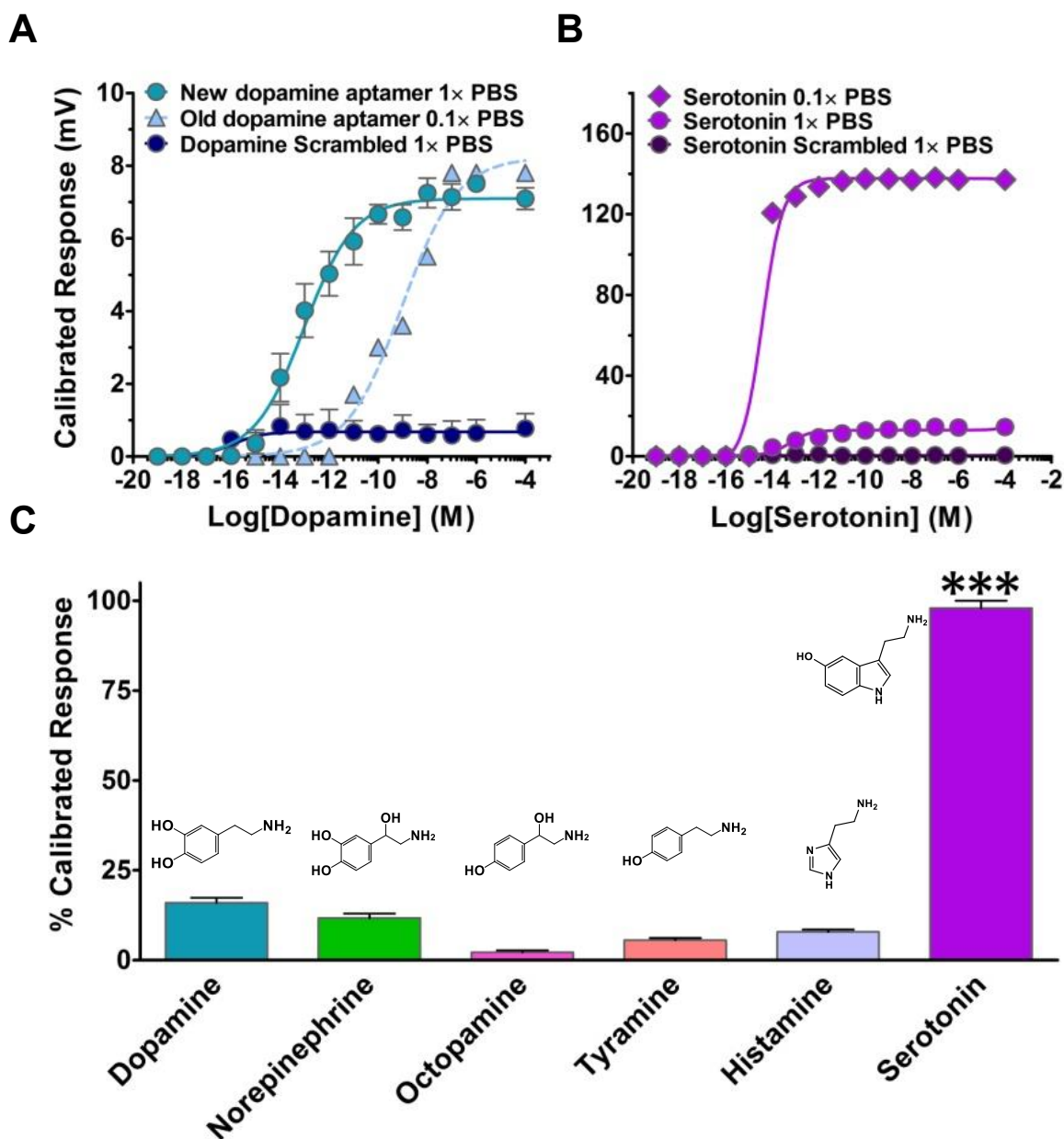


**Figure SF.2.** (a) Responses of FET sensors functionalized with the new dopamine aptamer ( $K_d=150$  nM, 1x PBS) or its scrambled sequence from Fig. 2A are replotted to visualize more clearly response magnitudes and to compare with previously reported FET responses obtained with the old dopamine aptamer ( $K_d=1$   $\mu$ M, 0.1x PBS). (b) Responses for serotonin-aptamer-FETs in 0.1x PBS were greatly increased over those in 1x PBS due to the increase in Debye length. Negligible changes in calibrated responses occurred for FETs functionalized with the scrambled serotonin sequence. (c) Serotonin-aptamer-FETs distinguished serotonin from other monoamine neurotransmitters. Error bars represent standard deviations for  $N=6$  (a,b) or  $N=3$  (c) FETs per condition. \*\*\* $P<0.001$  vs. counter-targets.

1x PBS	
Salt	Concentration (mM)
NaCl	137
KCl	2.7
Na <sub>2</sub> HPO <sub>4</sub>	10
KH <sub>2</sub> PO <sub>4</sub>	1.8
1x aCSF	
Salt	Concentration (mM)
NaCl	147
KCl	3.5
Na <sub>2</sub> HPO <sub>4</sub>	1.0
KH <sub>2</sub> PO <sub>4</sub>	2.5
CaCl <sub>2</sub>	1.0
MgCl <sub>2</sub>	1.2
1x HEPES	
Salt	Concentration (mM)
HEPES	20
NaCl	1000
MgCl <sub>2</sub>	10
KCl	5
1x Ringers	
Salt	Concentration (mM)
NaCl	147
KCl	4
CaCl <sub>2</sub>	2.25

**Table SF.6.** Ionic contents for phosphate-buffered saline (PBS), artificial cerebrospinal fluid (aCSF), HEPES, and Ringers buffers. The PBS and aCSF buffers were at pH 7.4. The HEPES buffer was adjusted to pH 7.5. Ringers solution was used as-purchased at pH 7.4.



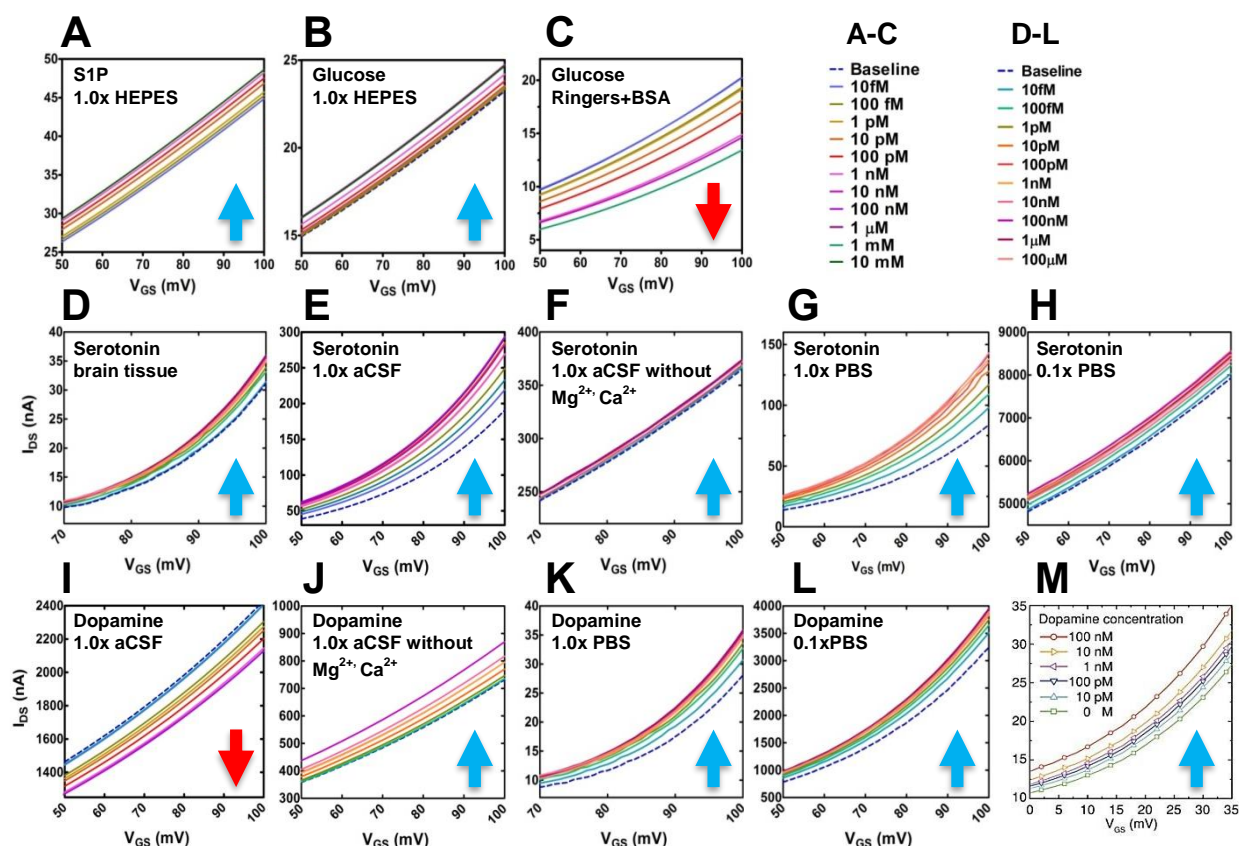


**Figure SF.3.** Exposure of (a) S1P- or (b) glucose-aptamer-FETs to S1P or glucose, respectively, led to concentration-dependent increases in source-drain currents. Target-mediated aptamer conformational changes are hypothesized to reorient glucose and S1P aptamers away from FET semiconductor channels facilitating transconductance. Exposure of (c) glucose-aptamer-FETs to glucose in Ringers solution with albumin, led to *decreasing* transfer curves as a function of increasing target concentration. The negatively charged albumin protein is hypothesized to increase electrostatic repulsion at the surface of the semiconducting channels. (d) Serotonin-aptamer-FET sensing of serotonin in brain tissue led to *increases* in source-drain currents, (e-h) as did exposure of serotonin-aptamer-FETs to serotonin under all buffer conditions. In contrast, exposure of dopamine-aptamer-FETs to dopamine (i) in 1.0x aCSF led to a *decrease* in source-drain current, (j-l) whereas, under all other buffer conditions, source-drain currents increased from baseline. (m) Regarding the previously reported dopamine aptamer on FETs, the source-drain current direction of change was the same as the new dopamine aptamer when both were measured in 0.1x PBS. This graph was reprinted with permission from reference 2. Copyright American Chemical Society, 2015.

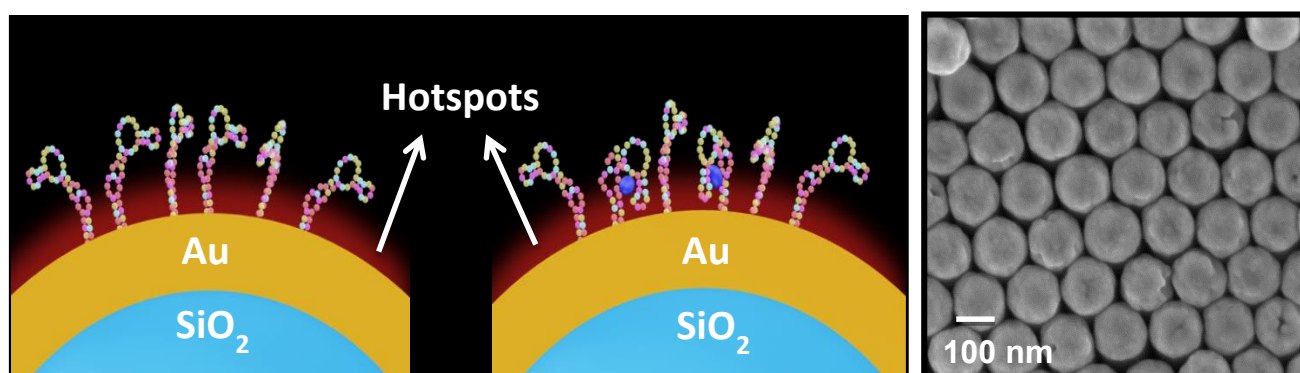


**Figure SF.4.** (Left) Schematic of thiolated aptamer self-assembled monolayers on Au nanoshells. Surface-enhanced Raman spectroscopy (SERS) was used for target detection. Conformational changes in aptamers induced by target molecule interactions altered aptamer vibrational modes within the hot spots of Au nanoshells. (Right) Scanning electron microscopy image of uniformly packed Au nanoshells used as SERS substrates.



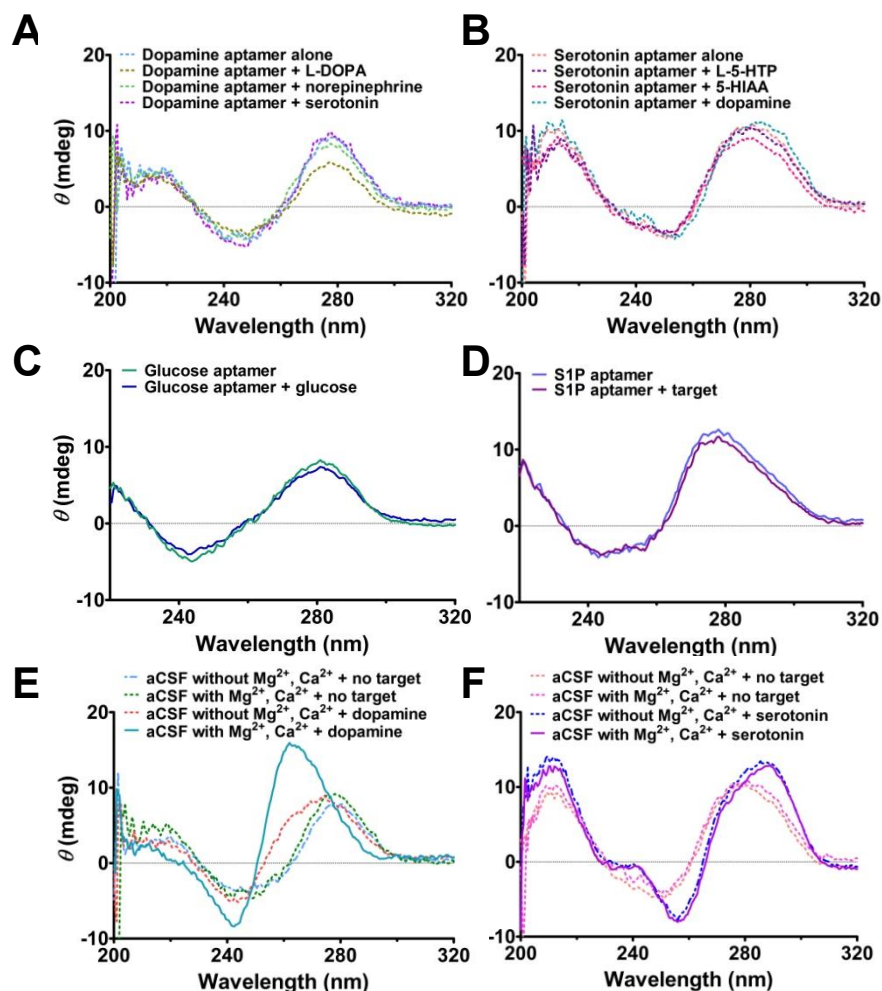


**Figure SF.5.** (a) Circular dichroism (CD) spectra showed minimal changes for the new dopamine aptamer in the presence of nonspecific targets. (b) Similarly, the serotonin aptamer showed minimal changes in CD spectra for nonspecific targets. (c,d) The CD spectra for glucose or S1P aptamers were unchanged upon target exposure suggesting that aptamer major secondary structural motifs are preformed and not dependent on the presence of targets for formation. (e,f) Changes in dopamine and serotonin aptamer secondary structures upon target capture in the presence or absence of divalent cations ( $Mg^{2+}$  and  $Ca^{2+}$ ) were investigated using CD spectroscopy. The serotonin aptamer showed similar spectra regardless of the presence of divalent cations suggesting little to no conformational dependence on these ions. By contrast, the new dopamine aptamer showed target-mediated amplification of its spectral shifts when divalent cations were included in artificial cerebral spinal fluid (aCSF). These findings illustrate that the secondary structure of this dopamine aptamer is influenced by the presence of  $Mg^{2+}$  and  $Ca^{2+}$ . For y-axes,  $\theta$  is ellipticity in millidegrees.

Figure	Interaction term	Condition	Concentration
<b>2A</b>	$F(28, 210) = 14806$ $P < 0.001$	$F(2, 15) = 17614$ $P < 0.001$	$F(14, 210) = 16949$ $P < 0.001$
<b>2B</b>	$F(28, 210) = 942$ $P < 0.001$	$F(2, 15) = 670$ $P < 0.001$	$F(14, 210) = 1343$ $P < 0.001$
<b>2C</b>	$F(28, 210) = 736$ $P < 0.001$	$F(2, 15) = 727$ $P < 0.001$	$F(14, 210) = 3378$ $P < 0.001$
<b>2F</b>	$F(9, 90) = 17$ $P < 0.001$	$F(1, 10) = 4$ $P < 0.01$	$F(9, 90) = 4057$ $P < 0.001$
<b>2G</b>	$F(40, 250) = 949$ $P < 0.001$	$F(4, 25) = 408$ $P < 0.001$	$F(10, 250) = 3916$ $P < 0.001$
<b>2H</b>	$F(10, 100) = 10694$ $P < 0.001$	$F(1, 10) = 864$ $P < 0.001$	$F(10, 100) = 16679$ $P < 0.001$
<b>S2A</b>	$F(10, 44) = 198$ $P < 0.001$	$F(10, 44) = 1295$ $P < 0.001$	$F(1, 44) = 2067$ $P < 0.001$
<b>S2B</b>	$F(28, 210) = 155911$ $P < 0.001$	$F(2, 15) = 209380$ $P < 0.001$	$F(14, 210) = 202054$ $P < 0.001$

**Table SF.7.** Concentration-dependent FET data were analyzed by two-way analysis of variance (ANOVA) with concentration (repeated measure) and buffer/target condition as the independent variables. In all cases, the omnibus statistics for the interaction terms and main effects were highly significant.

Figure	Target
2D	$F(6,14) = 10886; P < 0.001$
2E	$F(3,8) = 24085; P < 0.001$
S2C	$F(5,12) = 2836; P < 0.001$

**Table S8.** Dopamine- and serotonin-aptamer-FET responses to targets vs. counter-targets were significantly different as indicated by one-way ANOVAs.

## References

1. Cui, Y.; Wei, Q. Q.; Park, H. K.; Lieber, C. M. Nanowire Nanosensors for Highly Sensitive and Selective Detection of Biological and Chemical Species. *Science* **2001**, *293*, 1289-1292.
2. Kim, J.; Rim, Y. S.; Chen, H. J.; Cao, H. H.; Nakatsuka, N.; Hinton, H. L.; Zhao, C. Z.; Andrews, A. M.; Yang, Y.; Weiss, P. S. Fabrication of High-Performance Ultrathin In<sub>2</sub>O<sub>3</sub> Film Field-Effect Transistors and Biosensors Using Chemical Lift-Off Lithography. *ACS Nano* **2015**, *9*, 4572-4582.
3. Casal, P.; Wen, X. J.; Gupta, S.; Nicholson, T.; Wang, Y. J.; Theiss, A.; Bhushan, B.; Brillson, L.; Lu, W.; Lee, S. C. ImmunoFET Feasibility in Physiological Salt Environments. *Philos. T. R. Soc. A* **2012**, *370*, 2474-2488.
4. Vacic, A.; Criscione, J. M.; Rajan, N. K.; Stern, E.; Fahmy, T. M.; Reed, M. A. Determination of Molecular Configuration by Debye Length Modulation. *J. Am. Chem. Soc.* **2011**, *133*, 13886-13889.
5. Weiss, P. S.; Trevor, P. L.; Cardillo, M. J. Gas Surface Interactions on InP Monitored by Changes in Substrate Electronic-Properties. *J. Chem. Phys.* **1989**, *90*, 5146-5153.
6. Liao, W. S.; Cheunkar, S.; Cao, H. H.; Bednar, H. R.; Weiss, P. S.; Andrews, A. M. Subtractive Patterning *via* Chemical Lift-Off Lithography. *Science* **2012**, *337*, 1517-1521.
7. Shoorideh, K.; Chui, C. O. On the Origin of Enhanced Sensitivity in Nanoscale FET-Based Biosensors. *Proc. Natl. Acad. Sci. U. S. A.* **2014**, *111*, 5111-5116.
8. Rim, Y. S.; Bae, S. H.; Chen, H. J.; Yang, J. L.; Kim, J.; Andrews, A. M.; Weiss, P. S.; Yang, Y.; Tseng, H. R. Printable Ultrathin Metal Oxide Semiconductor-Based Conformal Biosensors. *ACS Nano* **2015**, *9*, 12174-12181.
9. Oh, J. Y.; Rondeau-Gagne, S.; Chiu, Y. C.; Chortos, A.; Lissel, F.; Wang, G. J. N.; Schroeder, B. C.; Kurosawa, T.; Lopez, J.; Katsumata, T.; Xu, J.; Zhu, C. X.; Gu, X. D.; Bae, W. G.; Kim, Y.; Jin, L. H.; Chung, J. W.; Tok, J. B. H.; Bao, Z. N. Intrinsically Stretchable and Healable Semiconducting Polymer for Organic Transistors. *Nature* **2016**, *539*, 411-415.
10. Yang, K. A.; Pei, R. J.; Stojanovic, M. N. *In Vitro* Selection and Amplification Protocols for Isolation of Aptameric Sensors for Small Molecules. *Methods* **2016**, *106*, 58-65.
11. Yang, K. A.; Barbu, M.; Halim, M.; Pallavi, P.; Kim, B.; Kolpashchikov, D. M.; Pecic, S.; Taylor, S.; Worgall, T. S.; Stojanovic, M. N. Recognition and Sensing of Low-Epitope Targets *via* Ternary Complexes with Oligonucleotides and Synthetic Receptors. *Nat. Chem.* **2014**, *6*, 1003-1008.

12. Hu, J. M.; Easley, C. J. A Simple and Rapid Approach for Measurement of Dissociation Constants of DNA Aptamers against Proteins and Small Molecules *via* Automated Microchip Electrophoresis. *Analyst* **2011**, *136*, 3461-3468.
13. Chen, H.; Rim, Y. S.; Wang, I. C.; Li, C.; Zhu, B.; Sun, M.; Goorsky, M. S.; He, X.; Yang, Y. Quasi-Two-Dimensional Metal Oxide Semiconductors Based Ultrasensitive Potentiometric Biosensors. *ACS Nano* **2017**, *11*, 4710-4718.
14. Ishikawa, F. N.; Curreli, M.; Chang, H. K.; Chen, P. C.; Zhang, R.; Cote, R. J.; Thompson, M. E.; Zhou, C. W. A Calibration Method for Nanowire Biosensors to Suppress Device-to-Device Variation. *ACS Nano* **2009**, *3*, 3969-3976.
15. Moskovits, M. Surface-Enhanced Raman Spectroscopy: A Brief Retrospective. *J. Raman Spectrosc.* **2005**, *36*, 485-496.
16. Doering, W. E.; Nie, S. M. Single-Molecule and Single-Nanoparticle SERS: Examining the Roles of Surface Active Sites and Chemical Enhancement. *J. Phys. Chem. B* **2002**, *106*, 311-317.
17. Le Ru, E. C.; Etchegoin, P. G. Single-Molecule Surface-Enhanced Raman Spectroscopy. *Annu. Rev. Phys. Chem.* **2012**, *63*, 65-87.
18. Otto, C.; Vandensteele, T. J. J.; Demul, F. F. M.; Greve, J. Surface-Enhanced Raman Spectroscopy of DNA Bases. *J. Raman Spectrosc.* **1986**, *17*, 289-298.
19. Pagba, C. V.; Lane, S. M.; Cho, H. S.; Wachsmann-Hogiu, S. Direct Detection of Aptamer-Thrombin Binding *via* Surface-Enhanced Raman Spectroscopy. *J. Biomed. Opt.* **2010**, *15*, 1-8.
20. Neumann, O.; Zhang, D. M.; Tam, F.; Lal, S.; Wittung-Stafshede, P.; Halas, N. J. Direct Optical Detection of Aptamer Conformational Changes Induced by Target Molecules. *Anal. Chem.* **2009**, *81*, 10002-10006.
21. Yunker, P. J.; Still, T.; Lohr, M. A.; Yodanis, C. L. Suppression of the Coffee-Ring Effect by Shape-Dependent Capillary Interactions. *Nature* **2011**, *476*, 308-311.
22. Barhoumi, A.; Zhang, D. M.; Halas, N. J. Correlation of Molecular Orientation and Packing Density in a dsDNA Self-Assembled Monolayer Observable with Surface-Enhanced-Raman Spectroscopy. *J. Am. Chem. Soc.* **2008**, *130*, 14040-14041.
23. Kypr, J.; Kejnovska, I.; Rencuk, D.; Vorlickova, M. Circular Dichroism and Conformational Polymorphism of DNA. *Nucleic Acids Research* **2009**, *37*, 1713-1725.
24. Walsh, R.; DeRosa, M. C. Retention of Function in the DNA Homolog of the RNA Dopamine Aptamer. *Biochem. Biophys. Res. Co.* **2009**, *388*, 732-735.

25. Altieri, S. C.; Yang, H.; O'Brien, H. J.; Redwine, H. M.; Senturk, D.; Hensler, J. G.; Andrews, A. M. Perinatal vs. Genetic Programming of Serotonin States Associated with Anxiety. *Neuropsychopharmacology* **2015**, *40*, 1456-1470.
26. Nakatsuka, N.; Andrews, A. M. Differentiating Siblings: The Case of Dopamine and Norepinephrine. *ACS Chem. Neurosci.* **2017**, *8*, 218-220.
27. Yang, H.; Thompson, A. B.; McIntosh, B. J.; Altieri, S. C.; Andrews, A. M. Physiologically Relevant Changes in Serotonin Resolved by Fast Microdialysis. *ACS Chem. Neurosci.* **2013**, *4*, 790-798.
28. Alivisatos, A. P.; Andrews, A. M.; Boyden, E. S.; Chun, M.; Church, G. M.; Deisseroth, K.; Donoghue, J. P.; Fraser, S. E.; Lippincott-Schwartz, J.; Looger, L. L.; Masmanidis, S.; McEuen, P. L.; Nurmikko, A. V.; Park, H.; Peterka, D. S.; Reid, C.; Roukes, M. L.; Scherer, A.; Schnitzer, M.; Sejnowski, T. J.; Shepard, K. L.; Tsao, D.; Turrigiano, G.; Weiss, P. S.; Xu, C.; Yuste, R.; Zhuang, X. Nanotools for Neuroscience and Brain Activity Mapping. *ACS Nano* **2013**, *7*, 1850-1866.
29. Perez, G. I.; Knudson, C. M.; Leykin, L.; Korsmeyer, S. J.; Tilly, J. L. Apoptosis-Associated Signaling Pathways Are Required for Chemotherapy-Mediated Female Germ Cell Destruction. *Nat. Med.* **1997**, *3*, 1228-1232.
30. Rodeberg, N. T.; Sandberg, S. G.; Johnson, J. A.; Phillips, P. E. M.; Wightman, R. M. Hitchhiker's Guide to Voltammetry: Acute and Chronic Electrodes for *in Vivo* Fast-Scan Cyclic Voltammetry. *ACS Chem. Neurosci.* **2017**, *8*, 221-234.
31. Ke, C.; Destecroix, H.; Crump, M. P.; Davis, A. P. A Simple and Accessible Synthetic Lectin for Glucose Recognition and Sensing. *Nat. Chem.* **2012**, *4*, 718-723.
32. Purschke, W. G.; Hoehlig, K.; Buchner, K.; Zboralski, D.; Schwoebel, F.; Vater, A.; Klusmann, S. Identification and Characterization of a Mirror-Image Oligonucleotide That Binds and Neutralizes Sphingosine 1-Phosphate, a Central Mediator of Angiogenesis. *Biochem. J.* **2014**, *462*, 153-162.
33. Vaish, A.; Shuster, M. J.; Cheunkar, S.; Singh, Y. S.; Weiss, P. S.; Andrews, A. M. Native Serotonin Membrane Receptors Recognize 5-Hydroxytryptophan-Functionalized Substrates: Enabling Small-Molecule Recognition. *ACS Chem. Neurosci.* **2010**, *1*, 495-504.
34. Angoa-Perez, M.; Kane, M. J.; Briggs, D. I.; Herrera-Mundo, N.; Sykes, C. E.; Francescutti, D. M.; Kuhn, D. M. Mice Genetically Depleted of Brain Serotonin Do Not Display a Depression-Like Behavioral Phenotype. *ACS Chem. Neurosci.* **2014**, *5*, 908-919.
35. Nakatsuka, N.; Weiss, P. S.; Stojanovic, M. N.; Andrews, A. M. Towards Electronic Biosensing *in Vivo*: Aptamer Field-Effect Transistors. *Chem. Rev.* **2017**, *submitted*.

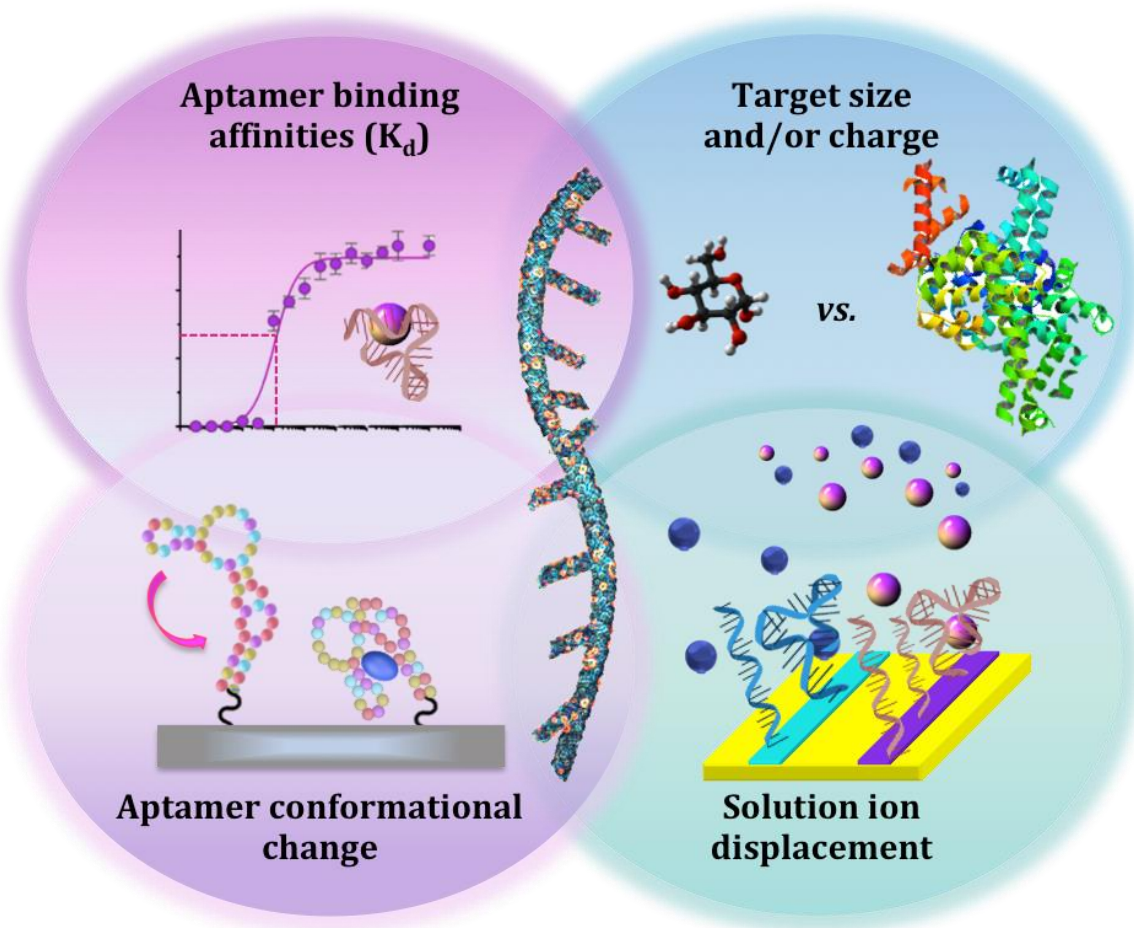
36. Masango, S. S.; Hackler, R. A.; Large, N.; Henry, A. I.; McAnally, M. O.; Schatz, G. C.; Stair, P. C.; Van Duyne, R. P. High-Resolution Distance Dependence Study of Surface-Enhanced Raman Scattering Enabled by Atomic Layer Deposition. *Nano Lett.* **2016**, *16*, 4251-4259.
37. Camden, J. P.; Dieringer, J. A.; Zhao, J.; Van Duyne, R. P. Controlled Plasmonic Nanostructures for Surface-Enhanced Spectroscopy and Sensing. *Acc. Chem. Res.* **2008**, *41*, 1653-1661.
38. Lal, S.; Grady, N. K.; Kundu, J.; Levin, C. S.; Lassiter, J. B.; Halas, N. J. Tailoring Plasmonic Substrates for Surface Enhanced Spectroscopies. *Chem. Soc. Rev.* **2008**, *37*, 898-911.
39. Liu, W.; Fu, Y.; Zheng, B.; Cheng, S.; Li, W.; Lau, T. C.; Liang, H. J. Kinetics and Mechanism of Conformational Changes in a G-Quadruplex of Thrombin-Binding Aptamer Induced by Pb<sup>2+</sup>. *J. Phys. Chem. B* **2011**, *115*, 13051-13056.
40. Nagatoishi, S.; Tanaka, Y.; Tsumoto, K. Circular Dichroism Spectra Demonstrate Formation of the Thrombin-Binding DNA Aptamer G-Quadruplex under Stabilizing-Cation-Deficient Conditions. *Biochem. Bioph. Res. Co.* **2007**, *352*, 812-817.
41. Nagai, Y.; Carbajal, J. D.; White, J. H.; Sladek, R.; Grutter, P.; Lennox, R. B. An Electrochemically Controlled Microcantilever Biosensor. *Langmuir* **2013**, *29*, 9951-9957.
42. Miyoshi, D.; Nakao, A.; Sugimoto, N. Structural Transition from Antiparallel to Parallel G-Quadruplex of d(G<sub>4</sub>T<sub>4</sub>G<sub>4</sub>) Induced by Ca<sup>2+</sup>. *Nucleic Acids Res.* **2003**, *31*, 1156-1163.
43. Biteen, J. S.; Blainey, P. C.; Cardon, Z. G.; Chun, M.; Church, G. M.; Dorrestein, P. C.; Fraser, S. E.; Gilbert, J. A.; Jansson, J. K.; Knight, R.; Miller, J. F.; Ozcan, A.; Prather, K. A.; Quake, S. R.; Ruby, E. G.; Silver, P. A.; Taha, S.; van den Engh, G.; Weiss, P. S.; Wong, G. C.; Wright, A. T.; Young, T. D. Tools for the Microbiome: Nano and Beyond. *ACS Nano* **2016**, *10*, 6-37.
44. Swager, T. M. The Molecular Wire Approach to Sensory Signal Amplification. *Acc. Chem. Res.* **1998**, *31*, 201-207.
45. Gao, N.; Gao, T.; Yang, X.; Dai, X. C.; Zhou, W.; Zhang, A. Q.; Lieber, C. M. Specific Detection of Biomolecules in Physiological Solutions Using Graphene Transistor Biosensors. *Proc. Natl. Acad. Sci. U. S. A.* **2016**, *113*, 14633-14638.
46. Ricci, F.; Valee-Belisle, A.; Simon, A. J.; Porchetta, A.; Plaxco, K. W. Using Nature's "Tricks" to Rationally Tune the Binding Properties of Biomolecular Receptors. *Acc. Chem. Res.* **2016**, *49*, 1884-1892.

47. Armstrong, R. E.; Strouse, G. F. Rationally Manipulating Aptamer Binding Affinities in a Stem-Loop Molecular Beacon. *Bioconjugate Chem.* **2014**, *25*, 1769-1776.



# Chapter VIII

## Mechanistic Investigations of Aptamer Field-Effect Transistor Sensing



The information in this chapter  
is an excerpt from a manuscript  
in preparation for *Chemical Reviews*.

Authors: Nakatsuka, N.; Weiss, P. S.; Andrews A. M.

## **VIII.A. Introduction**

The field of aptamer-FET sensing is a relatively new field. As such, there is, at present, a lack of unifying principles describing aptamer-FET sensing mechanisms. Potential mechanisms underlying bioFET sensing generally include signal contributions from substrates, recognition elements, and targets. Contributions from each of these sources have not been thoroughly deconvoluted and therefore, are incompletely understood and poorly exploited. As a result, I examine the current aptamer-FET literature from an agnostic viewpoint with the goal of extracting common themes and principles. In doing so, I acknowledge that some experimental designs and findings are not as strong as others, and some studies are not particularly well controlled or straightforwardly interpreted in the context of the broader literature.

Nonetheless, work described in previous chapters indicate the capabilities of aptamer FETs to detect small charged molecules, such as the neurotransmitters serotonin and dopamine, as well as neutral targets such as glucose. Measurable signals from aptamers binding neutral targets supports the hypothesis that negatively charged phosphodiester aptamer backbone rearrangements upon target recognition is a critical factor for FET signal responses. Future findings and time will eventually clarify understanding of each proposed mechanism and specific advantages and disadvantages of aptamer-FETs.

Reports on the use of aptamer-coupled FET sensors have been increasing over the last decade (Table VIII.1), although until now, only a limited number of target molecules have been detected using this approach. Two reviews highlight developments in materials design and fabrication of aptamer-FETs. The first, by Khung and Narducci focuses on

aptamer use with FETs based on 1D nanostructures.<sup>1</sup> The second, by Green and Norton evaluates insights into the nature of DNA-graphene interactions, and effects on sensors for detecting DNA, small molecules, and proteins.<sup>2</sup> In addition to 1D and 2D channel materials, diamond,<sup>3-5</sup> semiconductor,<sup>6-8</sup> and polymer<sup>9,10</sup> FETs have been coupled to aptamers.

One of the critical questions I try to answer below is how do aptamer-FETs detect analytes at concentrations that are orders of magnitude lower than aptamer-target dissociation constant ( $K_d$ ) values?<sup>7</sup> Fundamentally, target detection is expected to be related to aptamer-target affinity. In the simplest sense, higher aptamer binding affinities, *i.e.*, lower  $K_d$ 's, should be associated with lower detection limits. Yet, detection limits are also hypothesized to be associated with probe and target charges, which are related to molecular size, as more highly charged probes and targets will influence FET transconductance to a greater extent upon aptamer capture.

**Table VIII.1.**

Literature reports on aptamer field-effect transistor sensors as of September 2017.

Target	Size (kDa)	RNA/DNA	Aptamer K <sub>d</sub>	Ref	Detection limit	FET type	Ref
Potassium ion	0.04	DNA	500 nM	11,12	~1 nM	Silicon nanowires	11
Dopamine	0.15	DNA	1.7 $\mu$ M	13	10 pM	Silicon nanowires	14
Dopamine	0.15	DNA	1.7 $\mu$ M	13	10 pM	Indium oxide semiconductor	7
Mercury ions	0.2	DNA	~30 $\mu$ M	15	1.2 $\mu$ M	Graphene oxide on aluminum oxide gates	16
Mercury ions	0.2	DNA	470 nM	17	1 nM	Graphene oxide with gold nanoparticles	18,19
Bisphenol A	0.23	DNA	8.3 nM	20	10 fM	Aptamer sandwich-based carbon nanotubes	21
Bisphenol A	0.23	DNA	8.3 nM	20	1 fM	Multichannel carbon nanofibers	22
Tenofovir	0.29	DNA	~10 nM	23	1.2 nM	Metal-oxide semiconductor	24
Riboflavin	0.38	DNA	1.2 $\mu$ M	25	1 pM	Zinc oxide semiconductor	8
ATP	0.51	DNA	6 $\mu$ M	26	1 nM	Self-assembled monolayers on extended gate	27
ATP	0.51	DNA	6 $\mu$ M	26	10 pM	Graphene	28
Neuropeptide Y	4.27	DNA	~300 nM	29	10 nM	Silicon nanowires	30
HIV-1 Tat	11.5	RNA	120 pM	31	1 nM	Diamond	3
Lysozyme	14.3	DNA	31 nM	32	12 nM	Self-assembled monolayers on extended gate	33
Interferon-gamma	16.8	DNA	4 nM	34	83 pM	Graphene monolayers	35
PDGF	24.6	DNA	90 pM	36	1 nM	Diamond	4
PDGF	24.6	DNA	90 pM	36	5 fM	Polypyrrole-coated carbon nanofibers	37
Prostate-specific antigen	33	DNA	~30 nM	38	1 nM	Poly(ethylene glycol)-modified graphene	39
Thrombin	37.4	DNA	100 nM	40	10 nM	Single-walled carbon nanotubes	41
Thrombin	37.4	DNA	100 nM	40	50 nM (buffer), 170 nM	Polypyrrole nanotubes	9
Thrombin	37.4	DNA	100 nM	40	330 pM	Silicon nanowires	42
Thrombin	37.4	DNA	100 nM	40	20 pM	Carbon nanotubes	43
Thrombin	37.4	DNA	100 nM	40	6.7 nM	Self-assembled monolayers on extended gate	33
Thrombin	37.4	DNA	100 nM	40	10 nM	Graphene	44
VEGF	38.2	RNA	87 nM	45	100 pM	Silicon nanowires	45
VEGF	38.2	RNA	200 pM	46	400 fM	Polypyrrole nanotubes	10
VEGF	38.2	RNA	200 pM	46	100 fM	Polypyrrole-converted nitrogen-doped graphene	47
Insulin	58	DNA	35 nM	48	35 pM	Graphene	48
Protective antigen toxin	63	DNA	110 nM	49	1 nM	Single-walled carbon nanotubes	49
Protective antigen	83	DNA	8 nM	50	1.2 aM	Graphene	51
Carcinoembryonic antigen	~180	DNA	690 pM	52	~6 aM	Polypyrrole multi-dimensional nanotubes	53
Immunoglobulin E	190	DNA	3.6 nM	54	250 pM	Carbon nanotubes	55,56
Immunoglobulin E	190	DNA	3.6 nM	54	Not tested	Graphene	57
<i>Escherichia coli</i>	Cell ~1pg	RNA	N/A	N/A	3.1 x 10 <sup>3</sup> CFU/mL	Single-walled carbon nanotubes	58

I first examine relationships between aptamer dissociation constants, target sizes, and aptamer-FET detection limits. I divided the existing literature, summarized in Table VIII.1, into two categories of targets consisting of small (<1 kD) vs. large (>1 kD) targets (Figure VIII.1). Targets were separately analyzed based on size due to (1) limitations in identifying high affinity aptamers for small molecules<sup>59,60</sup> and (2) observations of target charge influencing biosensor detection limits for larger targets with higher charge densities. We excluded the last four targets in Table VIII.1 due to very large sizes (>100 kDa for carcinoembryonic antigen and immunoglobulin E) or unreported  $K_d$  (*Escherichia coli*). The trends were the same regardless of whether all data were included. Thus, I chose to visualize trends without extreme data points appearing to drive relationships.

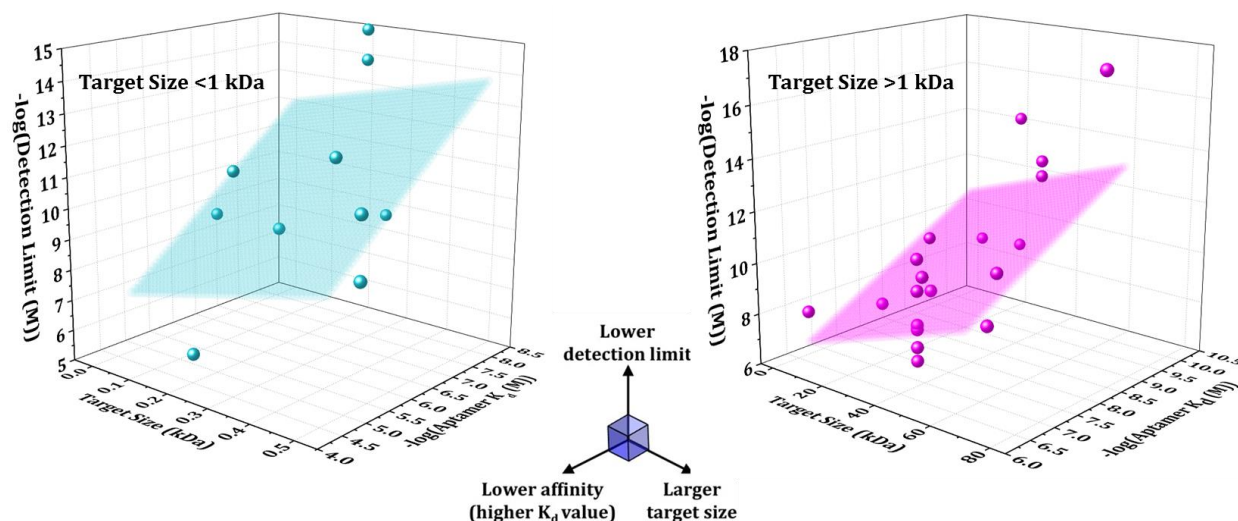


**Figure VIII.1.** Relationships between target sizes, aptamer dissociation constants ( $K_d$ ), and detection limits. The graph on the left shows data for targets <1 kDa. Targets >1 kDa are plotted on the right graph. The planes are best fits to the data (nonlinear surface fit, plane model, using the Levenberg Marquardt iteration algorithm in MatLab). Each plane correlates the three aptamer-FET parameters and is meant to guide the eye in visualizing relationships between these parameters.

I found that general trends for both classes of targets, regardless of FET platform, associated larger targets sizes with lower aptamer dissociation constants and thus, lower aptamer-FET limits of detection (Figure VIII.1). In many, though not all cases, detection limits were well below what was expected based on an equilibrium sensing model. As hypothesized generally for FET biosensors, aptamer-FETs appeared to have capabilities to detect target molecules at concentrations much lower than one order of magnitude below the aptamer dissociation constants. Aptamer dissociation constants determined in solution could differ from those characterizing aptamer-target binding when aptamers are immobilized on FETs. Also, aptamer dissociation constants reported for the same target varied across publications, depending on the technique used to determine  $K_d$  values.

## VIII.B. Other Detection Mechanisms of Aptamer Field-Effect Transistors

Beyond aptamer-target affinities and target charge/size, two additional factors emerge from the literature that appear to impact aptamer-FET feasibility and to influence detection sensitivity (particularly relative to translation to *in vivo* sensing). First, the smaller sizes of aptamers compared to antibodies have been hypothesized to facilitate capture of targets within or nearer to physiological Debye lengths. Since FET sensing mechanisms involve detecting changes in gate-electrode surface field potentials, it follows that the magnitude of target charge contributes to detectability, particularly for large targets such as proteins with high surface-charge densities. However, this does *not* explain the capacity of aptamer-FETs to detect small molecules or neutral targets, *e.g.*, potassium<sup>11</sup> and mercury ions,<sup>16,18,61</sup> dopamine,<sup>7,62</sup> and bisphenol A.<sup>22,63</sup> As such, a second hypothesized mechanism of aptamer-FETs involves conformational changes of the aptamers themselves upon target capture, whereby rearrangement of highly negatively charged aptamer phosphodiester backbones alters electric fields at the surfaces of FETs.<sup>8,37,48</sup>

### VIII.B.1. Effects of Target Charge in Aptamer-Field-Effect Transistor Sensing

Sensing *via* aptamer-FETs has been attributed to target binding occurring partly or wholly within Debye lengths at channel-surface/liquid interfaces, thereby bringing charged targets into close proximity of FET surfaces.<sup>33,64</sup> Matsumoto *et al.* posited that typical Debye lengths in low ionic strength (dilute) buffers at room temperature are ~5 nm.<sup>64</sup> We calculate the Debye length in dilute (0.1× or 1 mM) PBS (1.0 mM Na<sub>2</sub>HPO<sub>4</sub>, 0.18 mM KH<sub>2</sub>PO<sub>4</sub>, 0.27 mM KCl, 13.7 mM NaCl, pH 7.4 at 25 °C) to be 2.4 nm (Figure VIII.2A). This is in agreement with Kim *et al.*, who used a slightly higher concentration of NaCl in the

phosphate-buffered saline (15 mM *versus* 13.7 mM in our calculations) (Figure VIII.2B).<sup>51</sup>

The smaller sizes of aptamers result in their partial confinement within Debye lengths when target capture occurs, making them advantageous compared to larger protein-based recognition motifs where target binding may occur considerably outside of the Debye screening distance. Aptamer-target binding having the potential to occur closer to FET surfaces gives rise to the idea that target charge may be important in aptamer-FET sensing.

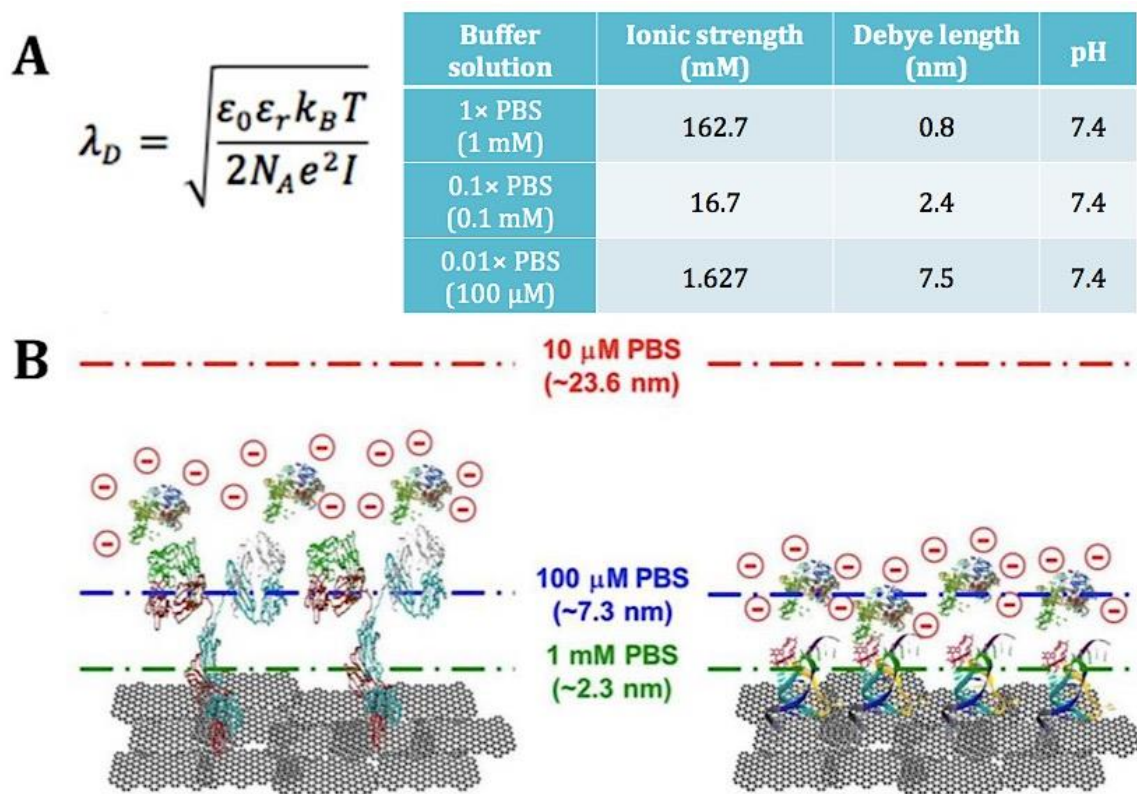


**Figure VIII.2.** Debye lengths in ionic solutions. (A) Debye length equation and typical lengths calculated for phosphate-buffered saline (PBS).  $\epsilon_0$  = permittivity of free space,  $\epsilon_r$  = water dielectric permittivity,  $k_B$  = Boltzmann constant,  $T$  = temperature (K),  $N_A$  = Avogadro's number,  $e$  = electron charge, and  $I$  = ionic strength of electrolyte (B) Schematic representation of Debye length and target capture from the work of Kim *et al.* Adapted with permission from ref. 51. Copyright 2013 Wiley.



In support of this hypothesis, Maehashi *et al.* tested biosensors targeting immunoglobulin E based on aptamer- vs. monoclonal antibody-modified carbon nanotube FETs.<sup>55</sup> The aptamer and antibody were reported to have similar  $K_d$ 's, yet an order of magnitude greater response was observed upon target binding for aptamer-modified FETs.<sup>55</sup> These results suggested that part of the large positively charged target protein was bound to the negatively charged aptamer in close proximity to the FET surface, resulting in a net positive charge change associated with the target-aptamer complex gating the semiconductor channel. Since the size of the antibody was  $\sim 10$  nm,<sup>65</sup> it was inferred that the target-antibody complex size would significantly exceed the Debye length and thus gate FETs to a lesser extent compared to the smaller aptamer. Below, we examine in greater detail the correlation between aptamer-FET detection limits and characteristics of targets, specifically size and charge.

### VIII.B.2. Detection of Large Charged Targets by Aptamer-Field-Effect Transistors

High molecular weight, highly charged protein targets are the common thread across the literature attributing aptamer-FET sensing to a mechanism involving target charge. In general, the larger the molecular weight of the target, the lower the detection limit for aptamer-FET devices (Figure VIII.1). Using aptamer-diamond-FETs, the smallest target protein sensed, the human immunodeficiency virus type 1 transactivator transcription factor (HIV-1 Tat; 12 kDa), was associated with a detection limit of 1 nM.<sup>3</sup> Sensing was conducted in 0.1× phosphate buffer saline at pH 7.4, where the Tat protein possesses a large number of positive charges associated with its rich arginine content.<sup>66</sup> Thus, Tat protein-associated charge in the accumulation layer of FET devices was postulated to result in changes in surface potential and thus, channel charge carrier densities.<sup>5</sup>

Thrombin, a popular target protein for testing bioFET functionality, has a molecular weight of 37 kDa—three times larger than HIV-1 Tat. Thrombin was detected *via* anti-thrombin aptamer-functionalized silicon-nanowire FETs at concentrations as low as 330 pM (Figure VIII.3A,B).<sup>42</sup> The isoelectric point of thrombin is 7.0-7.6 and the acetate buffer used for sensing had a pH of 5.4. Thus, thrombin was positively charged during capture.<sup>67</sup> The authors proposed that positively charged thrombin molecules effectively screen the negative charges of the anti-thrombin aptamer backbone, while also acting as concentrated sources of positive charge near FET surfaces to alter conductance in silicon-nanowire FETs.

A similar mechanism was suggested for a vascular endothelial growth factor (VEGF), a protein with a molecular weight of 38 kDa, which is upregulated in many tumors. The detection limit for VEGF was 400 fM using an anti-VEGF aptamer coupled to polypyrrole-

nanotube-FETs (Figure VIII.3C,D).<sup>10</sup> The isoelectric point of VEGF is 9.5 resulting in its being positively charged in the pH 7.5, 1× PBS used in this study. Although VEGF and thrombin have comparable molecular weights, VEGF was detected with 1000-fold greater sensitivity. This difference may be influenced by differences in VEGF vs. thrombin aptamer affinities (200 pM<sup>46</sup> vs. 100 nM,<sup>40</sup> respectively). Differences in surface charge densities between the two protein targets and in the inherent sensitivities of the FETs themselves (nanotubes vs. nanowires) may also contribute to varying sensitivities. Further, the buffer conditions differed for the two studies, which alters Debye lengths directly affecting high sensitivity sensing regimes. Despite problems associated with dissociating sensing modalities, increasing molecular mass of target proteins generally correlates with increased charge and thus, limits of detection (Figure VIII.1).

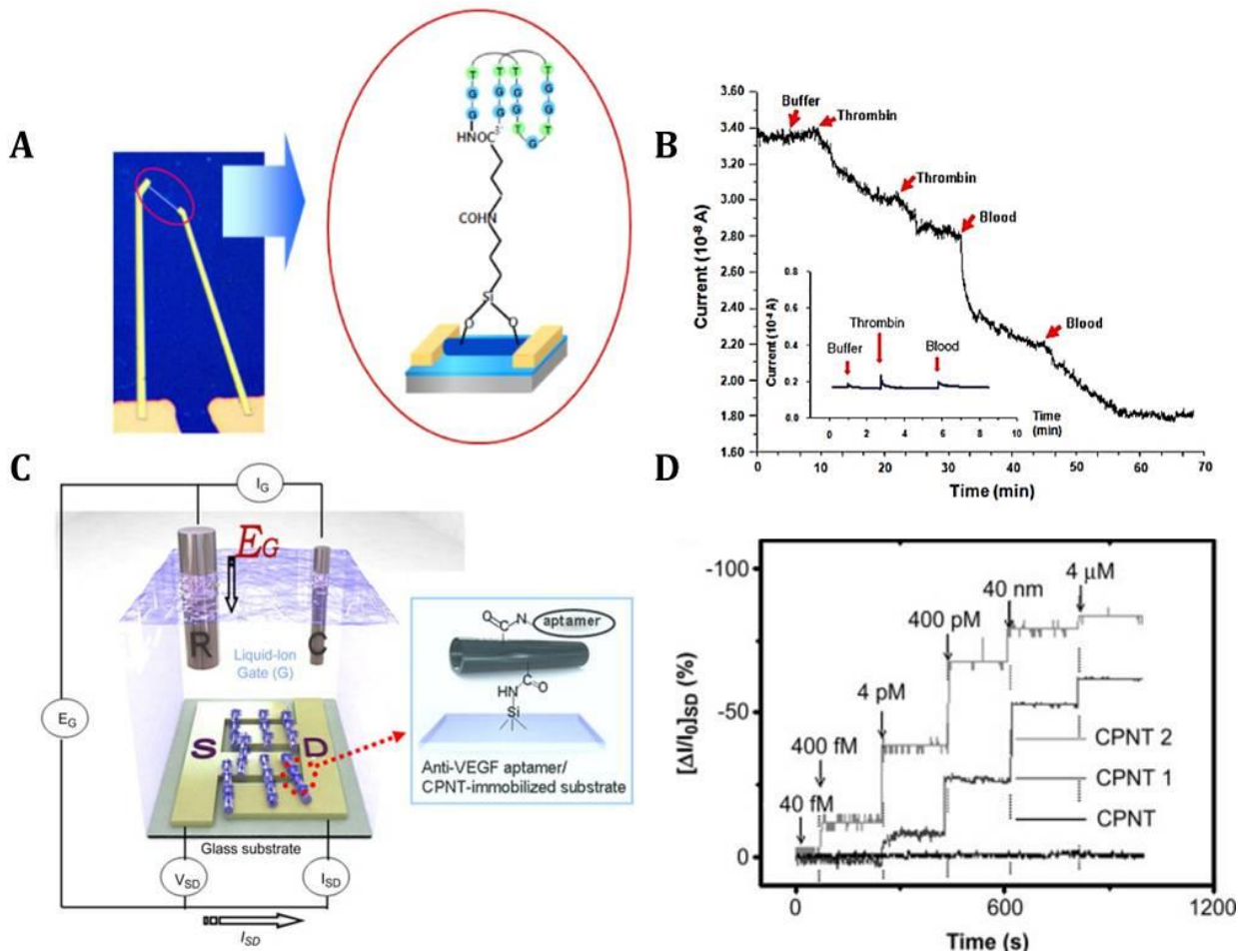


**Figure VIII.3.** Detection of large protein targets (thrombin and VEGF) using aptamer FETs. **(A)** An optical microscope image of anti-thrombin aptamers functionalized on silicon nanowires strung between gold electrodes in a FET biosensor. Magnified schematic representation on the right. **(B)** Real-time detection of thrombin and thrombin in blood. Inset shows FET responses without aptamers. **(C)** Illustration of carbon polypyrrole nanotube FETs functionalized with an anti-VEGF aptamer. **(D)** Real-time responses to various concentrations of VEGF with a  $\sim 400$  fM detection limit. Reproduced with permission from ref. 42 **(A,B)** and 10 **(C,D)**. Copyright 2009 IOP Publishing and 2010 Elsevier respectively.

Protective antigen (PA) (molecular weight 83 kDa), the cell-binding portion of anthrax toxin was detected at concentrations as low as 12 aM using graphene-based aptamer-FETs (Figure VIII.4A).<sup>51</sup> The PA was negatively charged in pH 7.4 PBS due to an isoelectric point of 5.6. Protective antigen is estimated to have overall dimensions of  $10 \text{ nm} \times 5 \text{ nm} \times 3 \text{ nm}$  and four domains,<sup>68</sup> each of which are highly negatively charged

compared to the 29-nucleotide PA-specific aptamer sequence. The phosphate buffer was 10  $\mu$ M for an estimated Debye length of  $\sim$ 24 nm (Figure VIII.2B).<sup>69</sup> Instead of shielding the negative charge of the aptamer backbone, bound PA molecules increased net negative charge near FET surfaces, especially when unhindered by a large Debye length.

The use of a dilute buffer facilitated comparison of sensing characteristics of aptamers vs. antibodies. The limit of detection of PA antibody-FETs was 12 fM compared to a 12 aM detection limit for PA aptamer-FETs. Moreover, the detection range of the antibody-FETs was three orders of magnitude compared to five orders of magnitude for the aptamer-FET configuration. The authors attributed improvements in aptamer-FET sensitivity to the higher affinity of the aptamer for its target, which they determined on FETs *via* Langmuir isotherms (antibody  $K_d$ =130 nM vs. aptamer  $K_d$ =2.3 fM).<sup>70</sup> Interestingly, the  $K_d$  for the same aptamer determined in solution *via* fluorophotometry with Cy3 dye-functionalized aptamers was  $\sim$ 8 nM.<sup>50</sup> This comparison emphasizes the dependence of  $K_d$  on the method of determination. The reasons for dissociation constants being orders of magnitude lower at the surface of FETs vs. in solution (a phenomenon that we also observe) have not been yet elucidated. While this comparative study of antibodies vs. aptamers as recognition elements is important, conducting comparisons in dilute ionic buffers leaves some questions unanswered. Whether lower concentrations of solution ions influences molecular recognition and binding conformations of biological molecular recognition elements on FET surfaces remains to be understood.

To investigate PA-aptamer-FET specificity, transfer characteristics upon exposure to dilute PBS containing a nontarget, carcinoembryonic antigen, were measured.<sup>51</sup> Lack of change in these current responses was interpreted as confirming aptamer specificity for PA. To test nonspecific binding, transfer characteristics of devices functionalized with linker molecules and without aptamers were tested. Here again, minimal responses were detected for PA in dilute PBS. The detection limit of PA-aptamer-FET sensing could be reduced another order of magnitude to 1.2 aM by the conjugation of gold

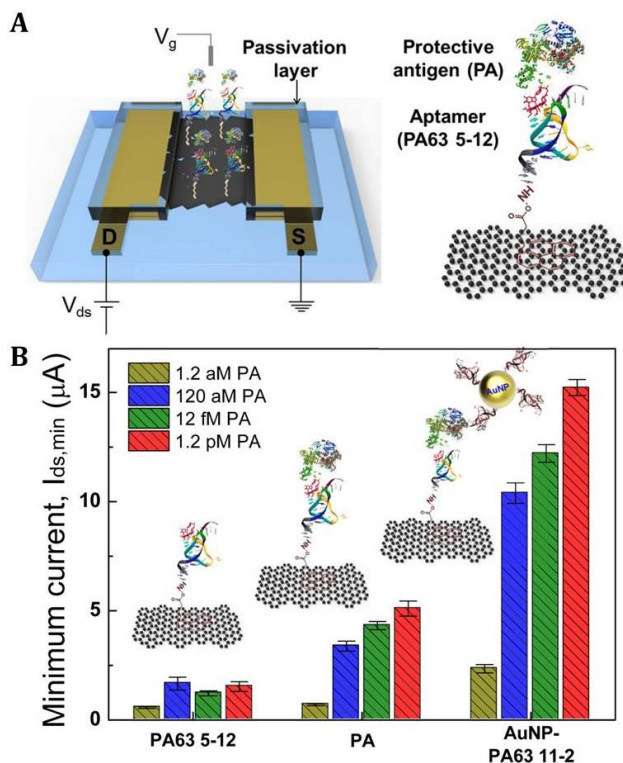


**Figure VIII.4.** Charge accumulation detection via graphene aptamer-FETs. (A) Schematic illustration of aptamers immobilized on graphene-FETs for the detection of protective antigen. (B) Changes in the minimum source-drain current when comparing the sizes of target molecules. Reproduced with permission from ref. 51. Copyright 2013 Wiley.

nanoparticles with secondary aptamers to sandwich PA molecules (Figure VIII.4B).<sup>51</sup> The authors ventured that further increases in net negative charge at FET surfaces due to secondary aptamer/gold nanoparticle capture contributed to improvements in the limit of detection.

This paper by Kim *et al.* exemplifies a number of key points.<sup>51</sup> Compared to antibodies, aptamers appeared to confer improved sensitivity and detection ranges. However, from this study, it was not clear whether lower detection limits were strictly due to higher aptamer affinity for target or the smaller size and high density of aptamer charge

redistribution, as hypothesized above. Regarding affinity, it is curious why the dissociation constant for aptamer-target binding is lower on FETs vs. in solution. Nonetheless, the literature pertaining to large target detection strongly supports that negatively, as well as positively charged protein targets can be sensed *via* aptamer FETs.

### VIII.B.3. Small-Molecule Sensing via Aptamer-Field-Effect Transistors

Unlike protein targets having large charge densities, small molecules have few/single charges or are neutral at physiological pH. Thus, target charge cannot affect charge accumulation to a large extent at FET surfaces when sensing small molecules. Small target molecules offer the opportunity to explore mechanisms of aptamer-FET sensing focused on the importance of aptamer conformational changes, which would enable small molecule detection *via* aptamer-FETs.

Anand *et al.* monitored potassium ion (0.04 kDa) efflux from  $\alpha$ -amino-3-hydroxy-5-methyl-4-isoxazolepropionic acid (AMPA)-stimulated cultured cortical neurons in real time using potassium-specific DNA aptamers tethered to silicon

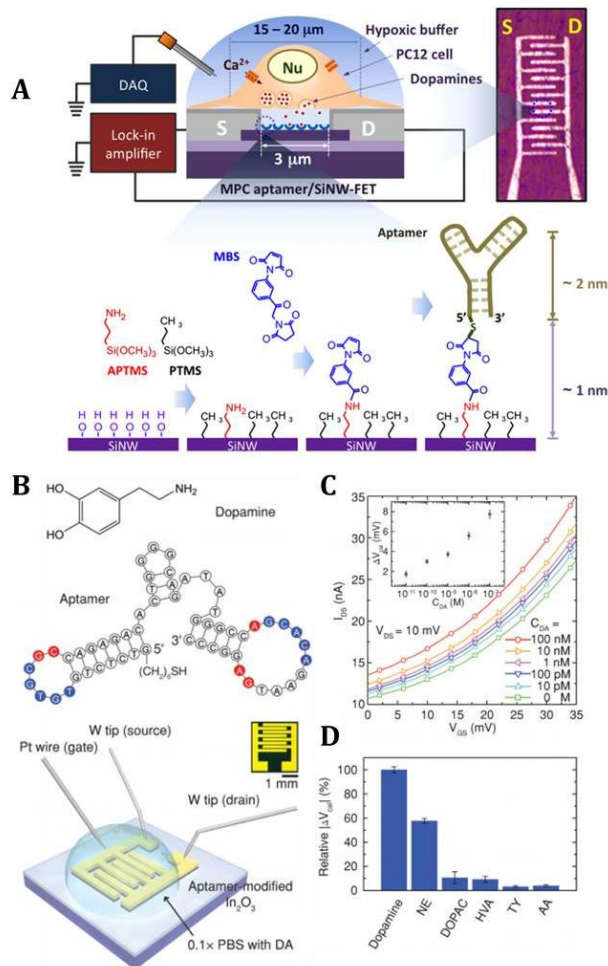


**Figure VIII.5.** Sensing the small-molecule neurotransmitter dopamine. (A) Illustration of the experimental setup for dopamine-aptamer modified silicon nanowire FETs for detecting exocytotic dopamine resulting from hypoxic stimulation of PC12 cells. An optical microscopy image of the device is shown on the top right and the immobilization strategy is below. (B) The dopamine aptamer used for both aptamer FET studies and the schematic for using thin film  $\text{In}_2\text{O}_3$  FETs are shown. (C) For liquid-gate sensing experiments, the addition of dopamine to the liquid electrolyte solution led to increases in the drain current; the linear working range was  $10^{-11}$  to  $10^{-7}$  M (inset shows the calibrated responses)(d) Selectivity is shown *via* calibrated responses of dopamine-aptamer  $\text{In}_2\text{O}_3$  sensors upon exposure to 1 nM each of ascorbic acid (AA), tyramine (TY), homovanillic acid (HVA), 3,4-dihydroxyphenylacetic acid (DOPAC), and norepinephrine (NE). Reprinted with permission from refs. 14 and 7. Copyright 2013 and 2015 American Chemical Society.



nanowire FETs.<sup>11</sup> The binding of AMPA to glutamate receptors activated associated ion channels facilitating sodium and potassium ion movement across cell membranes. By pretreating neurons with competitive AMPA-antagonists, AMPA-induced conductances were suppressed. Aptamer FETs showed 17-fold potassium selectivity vs. sodium, enabling sensing of potassium in mixtures with sodium in the background.

The small-molecule dopamine (0.15 kDa) has been detected by aptamer-FETs. Li and coworkers carried out *in vitro* studies using Si-nanowire-FETs to detect the release of dopamine from PC12 cells in response to hypoxic stimulation (Figure VIII.5A).<sup>14</sup> We have conducted dopamine sensing with a linear sensing range of 10 pM-100 nM in 0.1× PBS using In<sub>2</sub>O<sub>3</sub> thin-film-FETs<sup>7</sup> patterned using chemical lift-off lithography<sup>71</sup> (Figure VIII.5B-D). In both cases, a 57-base DNA aptamer<sup>13</sup> recognizing dopamine with a  $K_d$  of 0.7  $\mu$ M determined in solution *via* fluorescence anisotropy, was used for molecular recognition. Detection of dopamine, which has a single positive charge at physiological pH, by aptamer sequences each having 57 negative charges suggests that aptamer rearrangement is the predominant mechanism of sensing in this case.

For continuous, point-of-care, label-free therapeutic drug monitoring, DNA aptamers coupled to *n*-type metal-oxide semiconductor FET devices were used to monitor the small-molecule drug, tenofovir (0.29 kDa), with a detection limit of 1.2 nM over a linear range between 1 nM and 100 nM.<sup>24</sup> Tenofovir is an antiretroviral drug approved by the United States Food and Drug Administration for the treatment of patients with HIV infection or hepatitis B.<sup>72</sup> The authors demonstrated the capacity to monitor selective concentration changes in tenofovir in real time. These examples of detection of ions or small molecules using aptamer-FETs suggest that aptamer conformational rearrangements

are important for FET sensing, particularly for small/neutral targets. This mechanism further highlights a significant advantage of aptamers for molecular recognition compared to antibodies.<sup>73</sup>

### VIII.C. Aptamer Conformational Changes

Aptamers possess negatively charged phosphodiester backbones that can undergo target-induced secondary structural changes or backbone movements, with at least part of these rearrangements occurring in close proximity to FET surfaces. We hypothesize that a related mechanism of aptamer-FET sensing involves the concerted movement of solution electrolytes electrostatically associated with aptamer backbones and/or FET surfaces.<sup>74</sup> Uncharged targets that rearrange charged aptamers and displace electrolyte charge in near-surface regions upon recognition are hypothesized to be detectable by aptamer-FETs (a notion we recently tested).<sup>74</sup>

#### VIII.C.1. Flexibility of Aptamer Backbones

Hagen and co-workers explored the flexibility of a small-molecule riboflavin (0.38 kDa) aptamer<sup>25</sup> in the context of zinc-oxide-FET sensing.<sup>8</sup> The *mfold* program<sup>75</sup> had been used to model the secondary structure of riboflavin aptamers. Target molecule capture was predicted to result in more compact, looped structures bringing negatively charged aptamer backbones closer to sensor surfaces upon riboflavin recognition. This conformational change was hypothesized to result in a negative top-gating effect (termed the OFF-state in Figure VIII.6A).<sup>8</sup> The direction of electrical response was switched upon addition of ferrocene to the 5' end of the aptamer, which allowed injection of electrons from the ferrocene into the semiconductor (termed as the ON state in Figure VIII.6B). One note is that while *mfold* is a useful tool to predict aptamer secondary structures, this tool does *not* capture the target binding-induced conformational changes that aptamers

undergo when tethered to FET surfaces (where there are presumably fewer degrees of freedom).

Contributions to sensing mechanisms associated with rearrangement of aptamer backbones has also been suggested for large target molecules. Although platelet-derived growth factor (PDGF) is a 25 kDa positively charged protein at physiological pH, Jun and co-workers attributed highly sensitive (5 fM) detection of PDGF to structural rearrangements of aptamers upon specific

binding when coupled to polypyrrole-functionalized carbon nanotubes.<sup>37</sup> The change in negative charge density at the aptamer-FET interface was hypothesized to be responsible for changes in FET currents. Similarly, Hao *et al.* highlighted the folding of negatively charged aptamer backbones into compact and stable antiparallel or parallel G-quadruplex conformations upon binding the target molecule, insulin (58 kDa).<sup>48</sup> In their work, graphene-based conducting channels were functionalized with guanine-rich insulin-specific aptamers. Insulin binding promoted G-quadruplex conformation-switching that was hypothesized to bring negatively charged insulin and DNA strands into close proximity with the graphene surface. These changes were hypothesized to cause disturbances in carrier concentrations in bulk graphene.

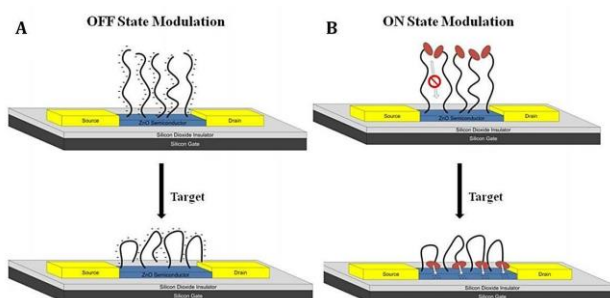


**Figure VIII.6.** When some aptamers bind their targets, they adopt new secondary structural motifs, which in many cases involve looped and more compact structures, as shown in this schematic for a riboflavin aptamer. **(A)** The secondary structure of the riboflavin aptamer brings the negative charges of the DNA backbone closer to the surface of the semiconductor and has a negative top-gating effect on the device resulting in a decrease in current (OFF state). **(B)** The addition of an electron-donating molecule such as ferrocene to the 5' end of the DNA enables the injection of electrons into the semiconductor resulting in increases in current upon riboflavin binding (ON state). Reproduced with permission from ref. 8. Copyright 2011 Multidisciplinary Digital Publishing Institute.

The literature reviewed (*vide supra*) highlights the ability of aptamer-FETs to exploit target-induced aptamer conformational changes within close proximity to sensor surfaces. Aptamer backbone rearrangements enable substantial charge redistribution for detectable responses even for small molecules such as riboflavin.<sup>8</sup> However, when sensing larger targets such as PDGF or insulin, it is difficult to deconvolute whether highly charged targets or negatively-charged aptamer backbone rearrangement, or a combination of both, is responsible for rearrangement of charge distribution.

### **VIII.C.2. Extent of Aptamer Conformational Changes**

An aptamer folding-based mechanism and the predictability of nucleic acid secondary structure suggest the possibility of manipulating binding interactions between aptamers and their targets to advantage.<sup>76</sup> With this strategy in mind, an additional contribution to the observed trends in detection with respect to target size involves the extent of conformational changes that aptamers undergo upon target recognition. As discussed, detection sensitivity is expected to correlate with intrinsic binding affinities between aptamers and their targets. For aptamers to have high affinities, they often require large target surface areas for recognition.<sup>77</sup> Thus, for protein targets having large surface areas, even aptamers with relatively rigid secondary structures should be amenable for sensing.

A thrombin-binding aptamer that has been studied extensively<sup>78-80</sup> serves as an example of FET sensing using an aptamer with a rigid secondary structure. This thrombin aptamer structure has been well characterized *via* NMR<sup>81-84</sup> and X-ray crystallography,<sup>85-87</sup> showing that it folds into an anti-antiparallel chair-like quadruplex structure in the absence of target.<sup>88,89</sup> The minimal conformational change that occurs when the anti-thrombin

aptamer binds positively charged thrombin in solution supports the idea that sensing mechanisms relying on high target affinity and/or charge can predominate with aptamers having limited conformational rearrangements upon target binding. The detection limits of anti-thrombin aptamer functionalized FETs are in the high picomolar to nanomolar range (Table VIII.1), which may be due to the limited rearrangement of this aptamer backbone.

For small target-molecule FET sensing, larger conformational changes associated with aptamer backbone rearrangement may be more critical compared to sensing of larger and more highly charged protein targets. As an example, a mercury-binding aptamer captures mercury ions between mismatched thymine residues in hybridized DNA, resulting in a folded hairpin structure (Figure VIII.7A).<sup>61</sup> This conformational change was exploited for mercury ion sensing using *p*-type semiconductor aptamer-FETs by two different groups.<sup>18,61</sup>

Bao and co-workers used organic thin-film transistors with 5,5'-bis-(7-dodecyl-9H-fluoren-2-yl)-2,2'-bithiophene as the semiconductor modified with gold nanoparticles to provide modular attachment points for functionalization with the mercury-specific aptamer. Using this system, they observed increases in current upon target binding, which they attributed to aptamer folding associated with mercury-ion capture.<sup>168</sup> These authors posited that increased negative charge density at FET surfaces due to rearrangement of the aptamer backbone induces a field effect in which excess holes in the semiconducting channel accumulate at the surface. The upward band bending makes the surface more *p*-type than the bulk, leading to a higher majority charge carrier density and an increase in conductance.

Alternatively, using reduced graphene oxide FETs coated with gold nanoparticles for mercury aptamer functionalization, Chang *et al.* explained increases in currents upon exposure to mercury ions instead to accumulation of  $\text{Hg}^{2+}$  on device surfaces upon target capture (Figure VIII.7B).<sup>61</sup> Interestingly, the sign of the source-drain current change was *opposite* with the incorporation of a passivation layer consisting of a 2 nm aluminum oxide ( $\text{Al}_2\text{O}_3$ ) film on the graphene oxide surface (Figure VIII.7C).<sup>61</sup> This layer was incorporated to prevent free ions as charge carriers in solution from contacting FET surfaces and contributing to conductivity changes, while also minimizing semiconductor degradation. Coating with a passivation layer was suggested to minimize conductivity changes due to conduction effects of solution ions and doping effects. Thus, the  $\text{Al}_2\text{O}_3$  layer was hypothesized to enable deconvolution of direct electrostatic gating effects from the accumulation of positively charged  $\text{Hg}^{2+}$  at the surface.

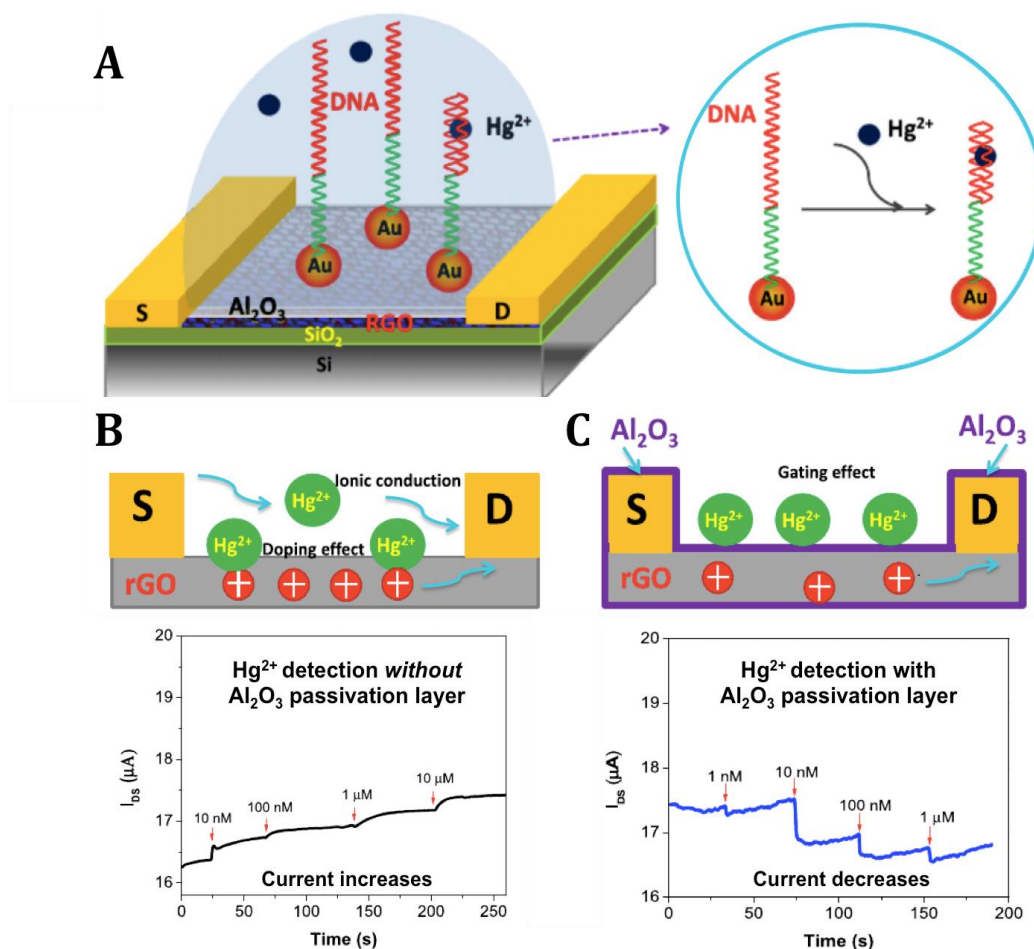


**Figure VIII.7.** (A) Schematic illustration of the Al<sub>2</sub>O<sub>3</sub> passivation layer on the reduced graphene oxide (RGO) transistor functionalized with Hg<sup>2+</sup>-specific aptamers functionalized on Au nanoparticles (left). Schematic of the interaction between Hg<sup>2+</sup> and the DNA aptamer resulting in a hairpin conformation (right). (B) Doping effect and ionic conduction on the RGO FET sensor without a passivation layer, which resulted in an *increase* in source-drain current upon target exposure. (C) Gating effect of the RGO FET sensor with Al<sub>2</sub>O<sub>3</sub> passivation layer, resulting in a *decrease* in source-drain current upon Hg<sup>2+</sup> recognition. Reproduced with permission from ref. 61 Copyright 2015 Elsevier.

These findings emphasize the importance of systematic interrogation of aptamer-FET sensing mechanisms associated with FET materials and functionalization/passivation chemistries, as well as the other parameters discussed above and below, to formulate more encompassing and unified theories of sensing mechanisms and understanding of the relative contributions of different (and sometimes competing) mechanisms.



### VIII.C.3. Detecting Aptamer-Target Conformational Changes

Investigation of aptamer conformational changes more specifically support the likelihood of structural rearrangements as influencing detection mechanisms and limits of detection in FET sensing. Modifications of aptamers with fluorophores have been used to detect aptamer conformational changes *via* fluorescence quenching or Förster-resonance energy transfer (FRET) between two tethered fluorescent reporters.<sup>90</sup> For example, cocaine was detected quantitatively by fluorescence quenching upon aptamer conformational changes associated with cocaine recognition (Figure VIII.8A).<sup>91</sup> In this work, shortening one stem of the three-way junction of a cocaine-binding aptamer resulted in junction destabilization. Cocaine binding closes the aptamer stem resulting in stabilization of the three-way junction. Thus, labeling one stem with the fluorophore, fluorescein, and the other with the quencher, dabcyI, the cocaine aptamer conformational change upon target binding enabled fluorescence quenching measurements.

Aptamers functioning as molecular switches to transduce binding events have enabled real-time monitoring in complex biological environments.<sup>92,93</sup> Using the same cocaine aptamer described above,<sup>91</sup> reversible cocaine binding was detected electrochemically at gold electrodes (Figure VIII.8B).<sup>94</sup> One aptamer end was thiolated to enable self-assembly on gold. The other (free) aptamer end was modified with a methylene blue redox indicator. Binding-induced aptamer conformational changes increased the proximity of methylene blue moieties with the gold electrode producing an increase in electrode current due to increased electron transfer.<sup>92</sup> For electrochemical sensors, aptamer sequences designed to undergo large conformational changes in the presence of targets have been shown to improve sensitivity and limits of detection.<sup>95-97</sup>

Halas and colleagues used label-free SERS to investigate aptamer interactions with target molecules in the context of aptamer structural rearrangements (Figure VIII.8C,D).<sup>98</sup> This technique utilizes localized surface plasmon resonance to significantly enhance Raman signals of molecules adsorbed on plasmonic nanostructures.<sup>99</sup> Conformational changes of biomolecules can be tracked by SERS *via* significant changes in the spectra caused by various DNA-base interactions or orientation changes of the molecules.<sup>100,101</sup> Nanoshell-based substrates with high densities of uniformly distributed hotspots for SERS field enhancement were used due to spot-to-spot and sample-to-sample spectral reproducibility.<sup>102</sup> Spectral responses arising from cocaine aptamer<sup>91</sup> binding to cocaine were discriminated from weaker responses associated with aptamer binding to nonspecific targets benzocaine or caffeine.

Further evidence that changes in SERS spectra result from aptamer conformational changes has been obtained using CD spectroscopy, which detects changes in biomolecule secondary structure, including that of aptamers.<sup>103-105</sup> The CD spectra of the anti-cocaine aptamer before and after target introduction (Figure VIII.8E) showed that thermal treatment eliminates misfolds in the aptamer secondary structure, while target molecule interactions induce aptamer refolding, consistent with the SERS results.<sup>98</sup>

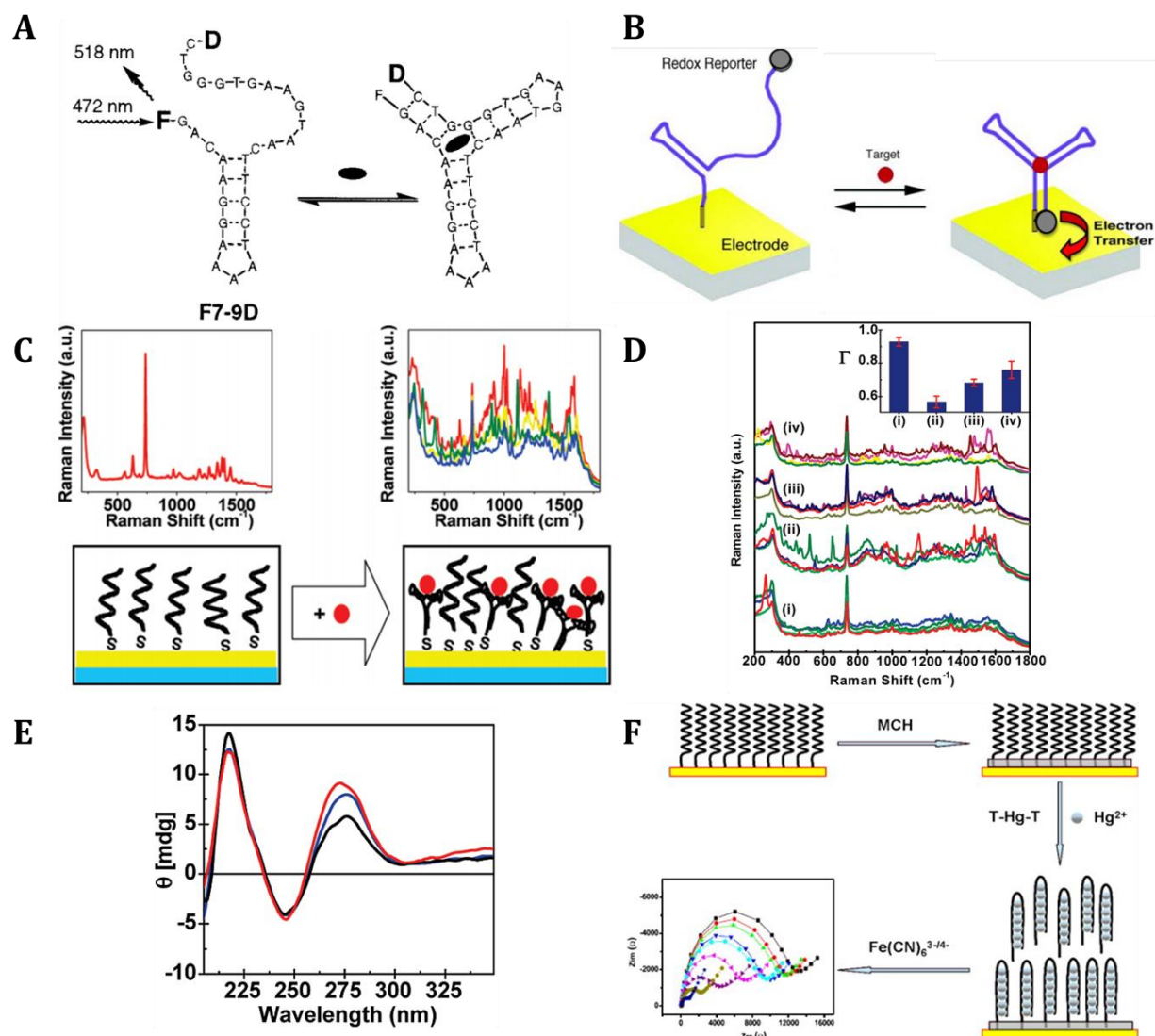


**Figure VIII.8.** Alternate detection strategies for aptamer-target capture. **(A)** Sensor F7-9D signals the presence of cocaine in solution by aptamer conformational changes that change the proximity of the 5' and 3' ends (F=fluorescein, D=dabcyi). The open structure of the aptamer is also predicted by secondary structure prediction programs. **(B)** Electrochemical aptamer-beacons undergo binding-induced "folding" of RNA or DNA oligonucleotides, which can be monitored electrochemically *via* changes in electron transfer between an attached redox tag and a supporting electrode. **(C)** Thermal treatment is used to eliminate aptamer secondary structure prior to monolayer formation on nanoshell substrates. Conformational changes in the aptamer induced by target molecule interactions are monitored by surface-enhanced Raman spectroscopy (SERS). **(D)** SERS spectra of an anticocaine aptamer (i) alone, (ii) with cocaine, (iii) with benzocaine, and (iv) with caffeine. **Inset:** cross-correlation SERS spectra demonstrate that differential target binding induces spectral variation by reintroducing aptamer hairpin structure. Error bars represent one standard deviation. **(E)** The CD spectra of an anticocaine aptamer showing a structural transition from a folded state (red) or hairpin state (blue) to an extended single-stranded state (black). **(F)** Schematic representation of electrochemical detection of mercury ions using Faradaic impedance. Reproduced with permission from refs. 91, 94, 98, 107. Copyright 2001 American Chemical Society, 2011 Elsevier, 2009 American Chemical Society, and 2009 Elsevier, respectively.

Similarly, Perlin and co-workers used CD spectroscopy to analyze the folding of azole-specific aptamers functionalized to graphene-based FETs for monitoring antifungal drugs.<sup>106</sup> In particular, CD spectroscopy was performed in the presence of targets and salts, such as magnesium chloride, which are known to affect DNA secondary structure. The formation of G-quadruplexes was hypothesized based on multiple stretches of guanine residues present in the aptamer sequence. Spectra with maxima at 260 nm and minima at 240 nm characteristic of G-quadruplexes were observed. Furthermore, the intensities of the spectral peaks changed upon addition of magnesium chloride indicative of secondary structure stabilization *via* divalent cation association.

Electrochemical impedance spectroscopy, which can be used to monitor changes in molecular charge densities, has been used to investigate conformational changes of a mercury-binding DNA aptamer composed solely of thymine bases and assembled on gold electrodes (Figure VIII.8F).<sup>107</sup> Coordination between mercury ions and thymines in DNA results in the folding of linear aptamers into hairpin-like structures.<sup>108,109</sup> These conformational changes increase steric (base stacking) and coulombic (repulsion of phosphodiester backbone) forces between adjacent sequences,<sup>110</sup> changing DNA charge densities on the electrode surfaces. Concentrations of mercury ions were quantitatively determined by following interfacial changes using impedance spectroscopy. The ability to design aptamer sequences that undergo large conformational changes to enhance signal detection emphasizes a critical advantage of aptamers as recognition elements.

### VIII.D. Solution Ion Displacement at Transistor Surfaces

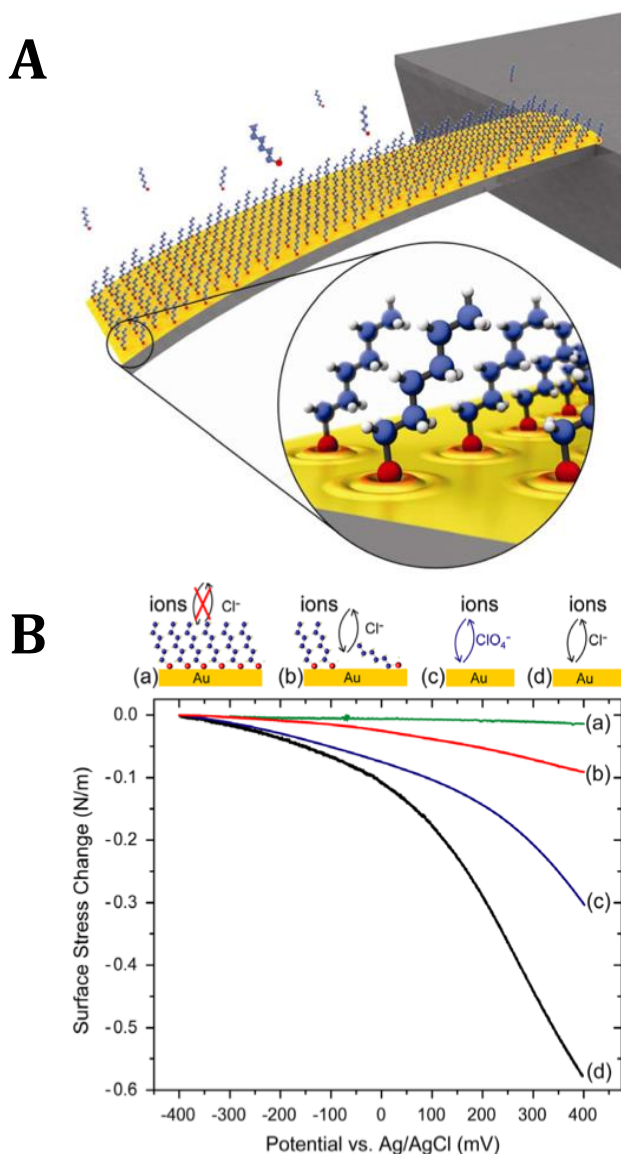


**Figure VIII.9.** Charge detection *via* surface-functionalized microcantilevers **(A)** Schematic illustration of an alkanethiol self-assembled monolayer (SAM) on a gold-coated microcantilever. **Inset:** close-up view of hexanethiol molecules adsorbed on the gold surface, highlighting the redistribution of the electronic structure of the gold surface due to the creation of the Au–S bond. **(B)** Changes in the surface stress as a function of electrode potential in 100 mM NaCl of **(a)** a SAM-modified Au-coated cantilever, **(b)** defective SAM, **(c)** base Au in 100 mM HClO<sub>4</sub>, and **(d)** bare Au in 100 mM NaCl. Reproduced with permission from ref. 115. Copyright 2010 IOP Publishing.

In addition to gating effects associated with rearrangements of negatively charged oligonucleotide backbones, we hypothesize that interactions between solution ions and FET semiconductor surfaces are an important aspect of aptamer-FET sensing mechanisms.

While this mechanism has not been specifically investigated in the context of aptamer-FETs, it is suggested by microcantilever sensors, which are nanoscale systems that transduce charge rearrangement at surfaces.<sup>111-114</sup>

Here, a microcantilever is the working electrode in a three-electrode electrochemical system (Figure VIII.9A).<sup>115</sup> Cantilever deflection, monitored by reflection of a laser spot, is measured as a

function of the applied potential, which causes redistribution of ions at the cantilever-solution interface. Changes in surface stress are dependent on electrochemically controlled adsorption/desorption of species onto the cantilever gold-coated surfaces.

Surface stress depends not only on the adsorbed molecules, but on solution ions present at the gold surface (Figure VIII.9B).<sup>115</sup> When comparing a defect-containing self-assembled monolayer to a defect-free tightly-packed monolayer, stress increased in the former due to exposure of the underlying gold surface to chloride or other ions in solution.<sup>115,116</sup> Furthermore, stress is modulated by the strength of adsorption based on anion identity. For a given potential change, the change in charge density at the gold surface for particular electrolyte concentrations determines the capacitance of the metal/solution interface and the resulting surface stress.<sup>117</sup> Ion adsorption and desorption can be controlled *via* electrochemical potential or blocked by surface passivation.<sup>116</sup>

Aptamers as receptors were incorporated into cantilever-based sensors by Savran and co-workers.<sup>118</sup> Their system consisted of two cantilevers, the first was the sensor cantilever functionalized with aptamers for *Thermus aquaticus* (Taq) DNA polymerase, an enzyme frequently used in the polymerase chain reaction. The second was the reference cantilever functionalized with a nonspecific sequence. The difference in deflection between the two cantilevers was used to quantify specific binding.

A decade later, Lennox, Grutter, and co-workers used aptamers targeting *L*-argininamide tethered to microcantilevers in a systematic study of *competition* between charged species for surface sites.<sup>119</sup> Cantilever deflections, measured optically, were induced by changes in surface charge densities mediated by adsorption and desorption of ions in response to changes in the applied potential. Electrochemical control of chloride

ions ( $\text{Cl}^-$ ) adsorbed onto gold sensing surfaces in a potential-dependent manner<sup>120,121</sup> was used to manipulate the density of ions close to and at the cantilever surface. The *L*-argininamide aptamer undergoes a conformational change to a more compact state upon binding to its cognate ligand.<sup>122</sup> Compared to the relaxed state, the compact aptamer-target complex produces additional areas on the gold surface for  $\text{Cl}^-$  adsorption. Thus, stress-induced changes observed upon changing the applied potential likely derive from competition between different charged adsorbates, including  $\text{Cl}^-$ , surface-bound aptamers, and buffer components.<sup>119</sup> Since surface-stress change at cantilevers is proportional to the available and accessible gold surface area, optimal densities of surface-tethered recognition elements were needed for large signal responses. Covering the surface with a densely packed monolayer of thiolated single-stranded oligonucleotides prevented ions from reaching the surface and as a consequence, large changes in surface stress were not observed.<sup>115</sup>

Cantilever-based systems illustrate that solution ions redistribute at sensing surfaces in response to aptamer conformational changes and applied potentials. They also point to the complexity of the mechanisms at work. To optimize FET sensor design, three-dimensional mathematical modeling and simulations can allow calculations of physically relevant quantities, such as electrostatic potential, and electron and hole densities in devices.<sup>123-125</sup> Reed and co-workers have calculated charge concentrations in the biofunctionalized boundary at semiconductor-electrolyte interfaces using the PROPKA algorithm.<sup>126</sup> The simulation models the screening of biomolecules by free ions in liquid using a sensitivity factor. These authors calculated the charge state of the target molecule, PSA, using a screening factor and computed effective surface-charge densities.<sup>127,128</sup>

Simulations that take into account each of the different surface-charge contributors, including oligonucleotide recognition elements and their conformational changes, ions in solution, and Debye length screening effects, will be beneficial for quantifying the contributions of the various charged species to aptamer-FET mechanisms.

For sensing large protein targets with high surface-charge densities, changes in surface field potentials are likely detectable with high sensitivity due to a combination of target charge, recognition element-target affinity, recognition element conformational changes, and changes in the densities of associated solution ions. For small-molecule targets, only the latter three mechanisms are hypothesized to contribute substantially to target detection. The capacity of aptamers, having preformed and stable secondary structures and/or lacking large conformational rearrangements upon target recognition, to transduce signals from small molecule binding led to our hypothesis that highly negatively charged aptamer backbones and their associated counterions may be sufficient to amplify minimal conformational changes *via* solution ion redistribution.



### VIII.E. Conclusions and Prospects

There are critical areas where systematic investigation is anticipated to advance aptamer-FET sensing in general, and specifically for *in vivo* applications. Additional studies involving structural and electronic modeling will be useful for deconvoluting the relative contributions of each of the mechanisms discussed to sensing *via* aptamer-FETs, *i.e.*, aptamer-target affinity, target charge, aptamer conformational changes, solution ion displacement, and combinations thereof. I hypothesize that when detecting large, highly charged protein targets, which are orders of magnitude larger than aptamer recognition elements, that aptamer affinity and target charge predominate transconductance mechanisms. By contrast, aptamer-FET sensing of small molecules or ions with few or no charges, which by themselves do not significantly impact overall charge distributions at FET surfaces, suggests that aptamer affinity and conformational changes can predominate, in combination with solution ion displacement/rearrangement, particularly in high ionic strength environments.

Rationally designed experiments that deconvolute individual mechanisms will be key to improving fundamental understanding, as well as improving and exploiting aptamer-FETs to advantage. Conformational changes of aptamers upon target binding can be investigated by spectroscopic methods, such as circular dichroism, surface-enhanced Raman spectroscopy, impedance spectroscopy, electrochemistry, and fluorescence measurements, the latter using aptamers modified with fluorophores and/or quenchers. Specific aptamer-target combinations can be developed<sup>129</sup> and used to improve predictive understanding of aptamer-FET sensing mechanisms and to optimize aptamer-FETs for

specific targets, target concentration ranges, and sensing milieus, including *in vivo* environments.

Another area of importance involves carrying out *in vitro* experiments under conditions that better simulate important aspects of complex *in vivo* environments. I note that of the aptamer-FET papers reviewed, most involve sensing in dilute buffers that are *not* representative of the high ionic strength conditions to which sensors are exposed *in vivo*. While FET-based biosensors are generally promising, their implementation *in vivo* and in clinical diagnostics has been largely prevented by fundamental limitations related to Debye length issues. The use of aptamers offers a generalizable solution to this longstanding and well-recognized problem.<sup>74</sup>

To realize biological and biomedical applications, including those *in vivo*, aptamer selectivity will need to be improved to detect targets in the presence of structurally similar molecules and high-concentration interferents present in physiological fluids. Multiple controls for targets and recognition elements will be essential for verifying the functionality and specificity of aptamer-FETs. To investigate specific recognition, single-point-mutation sequences known to abrogate target recognition (or scrambled aptamers) can be used as controls and on devices destined for *in vivo* implantation (for subtractive/on-device referenced sensing). For target selectivity, investigation of sensor responses to similarly structured target precursors and/or metabolites and high-concentration matrix molecules, *e.g.*, ascorbate, uric acid, will enable interference and nonspecific recognition to be understood and mitigated.

Although I did not focus on the influence of FET materials and designs, it will also be necessary to carry out rationally designed studies using different types of FETs to

understand and to exploit mechanisms of aptamer-FET sensing fully, as device design contributes to detection limits and other performance characteristics of importance for *in vivo* applications. Combining intelligent aptamer design and state-of-the-art materials for FET fabrication have significant potential for *in vivo* sensing of difficult targets, including many physiologically important small molecules involved in signaling pathways. Systematic delineation of the mechanistic aspects of interactions between aptamers and their targets, both small and large, will enable rational optimization of aptamer-FET biosensors for implementation *in vivo*.

## References

1. Khung, Y. L.; Narducci, D. Synergizing Nucleic Acid Aptamers with 1-Dimensional Nanostructures as Label-Free Field-Effect Transistor Biosensors. *Biosens. Bioelectron.* **2013**, *50*, 278-293.
2. Green, N. S.; Norton, M. L. Interactions of DNA with Graphene and Sensing Applications of Graphene Field-Effect Transistor Devices: A Review. *Anal. Chim. Acta.* **2015**, *853*, 127-142.
3. Ruslinda, A. R.; Tanabe, K.; Ibori, S.; Wang, X. F.; Kawarada, H. Effects of Diamond-FET-Based RNA Aptamer Sensing for Detection of Real Sample of HIV-1 Tat Protein. *Biosens. Bioelectron.* **2013**, *40*, 277-282.
4. Ruslinda, A. R.; Tajima, S.; Ishii, Y.; Ishiyama, Y.; Edgington, R.; Kawarada, H. Aptamer-Based Biosensor for Sensitive PDGF Detection Using Diamond Transistor. *Biosens. Bioelectron.* **2010**, *26*, 1599-1604.
5. Kawarada, H.; Ruslinda, A. R. Diamond Electrolyte Solution Gate FETs for DNA and Protein Sensors Using DNA/RNA Aptamers. *Phys. Status Solidi A* **2011**, *208*, 2005-2016.
6. Landheer, D.; Aers, G.; McKinnon, W. R.; Deen, M. J.; Ranuarez, J. C. Model for the Field Effect from Layers of Biological Macromolecules on the Gates of Metal-Oxide-Semiconductor Transistors. *J. Appl. Phys.* **2005**, *98*, 44701-44716.
7. Kim, J.; Rim, Y. S.; Chen, H. J.; Cao, H. H.; Nakatsuka, N.; Hinton, H. L.; Zhao, C. Z.; Andrews, A. M.; Yang, Y.; Weiss, P. S. Fabrication of High-Performance Ultrathin In<sub>2</sub>O<sub>3</sub> Film Field-Effect Transistors and Biosensors Using Chemical Lift-Off Lithography. *ACS Nano* **2015**, *9*, 4572-4582.
8. Hagen, J. A.; Kim, S. N.; Bayraktaroglu, B.; Leedy, K.; Chavez, J. L.; Kelley-Loughnane, N.; Naik, R. R.; Stone, M. O. Biofunctionalized Zinc Oxide Field Effect Transistors for Selective Sensing of Riboflavin with Current Modulation. *Sensors (Basel)* **2011**, *11*, 6645-6655.
9. Yoon, H.; Kim, J. H.; Lee, N.; Kim, B. G.; Jang, J. A Novel Sensor Platform Based on Aptamer-Conjugated Polypyrrole Nanotubes for Label-Free Electrochemical Protein Detection. *ChemBioChem* **2008**, *9*, 634-641.
10. Kwon, O. S.; Park, S. J.; Jang, J. A High-Performance VEGF Aptamer Functionalized Polypyrrole Nanotube Biosensor. *Biomaterials* **2010**, *31*, 4740-4747.
11. Anand, A.; Liu, C. R.; Chou, A. C.; Hsu, W. H.; Ulaganathan, R. K.; Lin, Y. C.; Dai, C. A.; Tseng, F. G.; Pan, C. Y.; Chen, Y. T. Detection of K<sup>+</sup> Efflux from Stimulated Cortical Neurons by an Aptamer-Modified Silicon Nanowire Field-Effect Transistor. *ACS Sens.* **2017**, *2*, 69-79.

12. Huang, C. C.; Chang, H. T. Aptamer-Based Fluorescence Sensor for Rapid Detection of Potassium Ions in Urine. *Chem. Commun.* **2008**, 1461-1463.
13. Walsh, R.; DeRosa, M. C. Retention of Function in the DNA Homolog of the RNA Dopamine Aptamer. *Biochem. Bioph. Res. Co.* **2009**, 388, 732-735.
14. Li, B. R.; Hsieh, Y. J.; Chen, Y. X.; Chung, Y. T.; Pan, C. Y.; Chen, Y. T. An Ultrasensitive Nanowire-Transistor Biosensor for Detecting Dopamine Release from Living PC12 Cells under Hypoxic Stimulation. *J. Am. Chem. Soc.* **2013**, 135, 16034-16037.
15. Ono, A.; Togashi, H. Highly Selective Oligonucleotide-Based Sensor for Mercury(II) in Aqueous Solutions. *Angew. Chem. Int. Ed.* **2004**, 43, 4300-4302.
16. Sharon, E.; Liu, X. Q.; Freeman, R.; Yehezkeli, O.; Willner, I. Label-Free Analysis of Thrombin or Hg<sup>2+</sup> Ions by Nucleic Acid-Functionalized Graphene Oxide Matrices Assembled on Field-Effect Transistors. *Electroanalysis* **2013**, 25, 851-856.
17. Wang, Z.; Heon Lee, J.; Lu, Y. Highly Sensitive "Turn-On" Fluorescent Sensor for Hg<sup>2+</sup> in Aqueous Solution Based on Structure-Switching DNA. *Chem. Commun.* **2008**, 6005-6007.
18. Hammock, M. L.; Sokolov, A. N.; Stoltenberg, R. M.; Naab, B. D.; Bao, Z. A. Organic Transistors with Ordered Nanoparticle Arrays as a Tailorable Platform for Selective, *in Situ* Detection. *ACS Nano* **2012**, 6, 3100-3108.
19. Chang, J.; Zhou, G.; Gao, X.; Mao, S.; Cui, S.; Ocola, L. E.; Yuan, C.; Chen, J. Real-Time Detection of Mercury Ions in Water Using a Reduced Graphene Oxide/DNA Field-Effect Transistor with Assistance of a Passivation Layer. *Sens. Biosensing. Res.* **2015**, 5, 97-104.
20. Jo, M.; Ahn, J. Y.; Lee, J.; Lee, S.; Hong, S. W.; Yoo, J. W.; Kang, J.; Dua, P.; Lee, D. K.; Hong, S.; Kim, S. Development of Single-Stranded DNA Aptamers for Specific Bisphenol a Detection. *Oligonucleotides* **2011**, 21, 85-91.
21. Lee, J.; Jo, M.; Kim, T. H.; Ahn, J. Y.; Lee, D. K.; Kim, S.; Hong, S. Aptamer Sandwich-Based Carbon Nanotube Sensors for Single-Carbon-Atomic-Resolution Detection of Non-Polar Small Molecular Species. *Lab Chip* **2011**, 11, 52-56.
22. Kim, S. G.; Lee, J. S.; Jun, J.; Shin, D. H.; Jang, J. Ultrasensitive Bisphenol A Field-Effect Transistor Sensor Using an Aptamer-Modified Multichannel Carbon Nanofiber Transducer. *ACS Appl. Mater. Inter.* **2016**, 8, 6602-6610.
23. Kammer, M. N.; Olmsted, I. R.; Kussrow, A. K.; Morris, M. J.; Jackson, G. W.; Bornhop, D. J. Characterizing Aptamer Small Molecule Interactions with Backscattering Interferometry. *Analyst* **2014**, 139, 5879-5884.

24. Aliakbarinodehi, N.; Jolly, P.; Bhalla, N.; Miodek, A.; De Micheli, G.; Estrela, P.; Carrara, S. Aptamer-Based Field-Effect Biosensor for Tenofovir Detection. *Sci. Rep.* **2017**, *7*, 44409.
25. Lauhon, C. T.; Szostak, J. W. RNA Aptamers That Bind Flavin and Nicotinamide Redox Cofactors. *J. Am. Chem. Soc.* **1995**, *117*, 1246-1257.
26. Huizenga, D. E.; Szostak, J. W. A DNA Aptamer That Binds Adenosine and ATP. *Biochemistry* **1995**, *34*, 656-665.
27. Goda, T.; Miyahara, Y. A Hairpin DNA Aptamer Coupled with Groove Binders as a Smart Switch for a Field-Effect Transistor Biosensor. *Biosens. Bioelectron.* **2012**, *32*, 244-249.
28. Mukherjee, S.; Meshik, X.; Choi, M.; Farid, S.; Datta, D.; Lan, Y.; Poduri, S.; Sarkar, K.; Batteredne, U.; Huang, C. E.; Wang, Y. Y.; Burke, P.; Dutta, M.; Strosio, M. A. A Graphene and Aptamer Based Liquid Gated FET-Like Electrochemical Biosensor to Detect Adenosine Triphosphate. *IEEE Trans. Nanobiosci.* **2015**, *14*, 967-972.
29. Mendonsa, S. D.; Bowser, M. T. *In Vitro* Selection of Aptamers with Affinity for Neuropeptide Y Using Capillary Electrophoresis. *J. Am. Chem. Soc.* **2005**, *127*, 9382-9383.
30. Banerjee, S.; Hsieh, Y. J.; Liu, C. R.; Yeh, N. H.; Hung, H. H.; Lai, Y. S.; Chou, A. C.; Chen, Y. T.; Pan, C. Y. Differential Releases of Dopamine and Neuropeptide Y from Histamine-Stimulated PC12 Cells Detected by an Aptamer-Modified Nanowire Transistor. *Small* **2016**, *12*, 5524-5529.
31. Yamamoto, R.; Katahira, M.; Nishikawa, S.; Baba, T.; Taira, K.; Kumar, P. K. R. A Novel RNA Motif That Binds Efficiently and Specifically to the Tat Protein of HIV and Inhibits the Trans-Activation by Tat of Transcription *in Vitro* and *in Vivo*. *Genes Cells* **2000**, *5*, 371-388.
32. Kirby, R.; Cho, E. J.; Gehrke, B.; Bayer, T.; Park, Y. S.; Neikirk, D. P.; McDevitt, J. T.; Ellington, A. D. Aptamer-Based Sensor Arrays for the Detection and Quantitation of Proteins. *Anal. Chem.* **2004**, *76*, 4066-4075.
33. Goda, T.; Miyahara, Y. Label-Free and Reagent-Less Protein Biosensing Using Aptamer-Modified Extended-Gate Field-Effect Transistors. *Biosens. Bioelectron.* **2013**, *45*, 89-94.
34. Tuleuova, N.; Jones, C. N.; Yan, J.; Ramanculov, E.; Yokobayashi, Y.; Revzin, A. Development of an Aptamer Beacon for Detection of Interferon-Gamma. *Anal. Chem.* **2010**, *82*, 1851-1857.

35. Farid, S.; Meshik, X.; Choi, M.; Mukherjee, S.; Lan, Y.; Parikh, D.; Poduri, S.; Baterdene, U.; Huang, C. E.; Wang, Y. Y.; Burke, P.; Dutta, M.; Strosio, M. A. Detection of Interferon Gamma Using Graphene and Aptamer Based FET-Like Electrochemical Biosensor. *Biosens. Bioelectron.* **2015**, *71*, 294-299.
36. Pendergrast, P. S.; Marsh, H. N.; Grate, D.; Healy, J. M.; Stanton, M. Nucleic Acid Aptamers for Target Validation and Therapeutic Applications. *J. Biomol. Tech.* **2005**, *16*, 224-234.
37. Jun, J.; Lee, J. S.; Shin, D. H.; Jang, J. Aptamer-Functionalized Hybrid Carbon Nanofiber FET-Type Electrode for a Highly Sensitive and Selective Platelet-Derived Growth Factor Biosensor. *ACS Appl. Mater. Inter.* **2014**, *6*, 13859-13865.
38. Savory, N.; Abe, K.; Sode, K.; Ikebukuro, K. Selection of DNA Aptamer against Prostate Specific Antigen Using a Genetic Algorithm and Application to Sensing. *Biosens. Bioelectron.* **2010**, *26*, 1386-1391.
39. Gao, N.; Gao, T.; Yang, X.; Dai, X. C.; Zhou, W.; Zhang, A. Q.; Lieber, C. M. Specific Detection of Biomolecules in Physiological Solutions Using Graphene Transistor Biosensors. *P. Natl. Acad. Sci. U.S.A.* **2016**, *113*, 14633-14638.
40. Pasternak, A.; Hernandez, F. J.; Rasmussen, L. M.; Vester, B.; Wengel, J. Improved Thrombin Binding Aptamer by Incorporation of a Single Unlocked Nucleic Acid Monomer. *Nucleic Acids Res.* **2011**, *39*, 1155-1164.
41. So, H. M.; Won, K.; Kim, Y. H.; Kim, B. K.; Ryu, B. H.; Na, P. S.; Kim, H.; Lee, J. O. Single-Walled Carbon Nanotube Biosensors Using Aptamers as Molecular Recognition Elements. *J. Am. Chem. Soc.* **2005**, *127*, 11906-11907.
42. Kim, K. S.; Lee, H. S.; Yang, J. A.; Jo, M. H.; Hahn, S. K. The Fabrication, Characterization and Application of Aptamer-Functionalized Si-Nanowire FET Biosensors. *Nanotechnology* **2009**, *20*, 1-6.
43. Pacios, M.; Martin-Fernandez, I.; Borriase, X.; del Valle, M.; Bartroli, J.; Lora-Tamayo, E.; Godignon, P.; Perez-Murano, F.; Esplandiú, M. J. Real Time Protein Recognition in a Liquid-Gated Carbon Nanotube Field-Effect Transistor Modified with Aptamers. *Nanoscale* **2012**, *4*, 5917-5923.
44. Saltzgaber, G.; Wojcik, P.; Sharf, T.; Leyden, M. R.; Wardini, J. L.; Heist, C. A.; Adenuga, A. A.; Remcho, V. T.; Minot, E. D. Scalable Graphene Field-Effect Sensors for Specific Protein Detection. *Nanotechnology* **2013**, *24*, 1-5.
45. Lee, H. S.; Kim, K. S.; Kim, C. J.; Hahn, S. K.; Jo, M. H. Electrical Detection of VEGFs for Cancer Diagnoses Using Anti-Vascular Endothelial Growth Factor Aptamer-Modified Si Nanowire FETs. *Biosens. Bioelectron.* **2009**, *24*, 1801-1805.

46. Green, L. S.; Jellinek, D.; Bell, C.; Beebe, L. A.; Feistner, B. D.; Gill, S. C.; Jucker, F. M.; Janjic, N. Nuclease-Resistant Nucleic-Acid Ligands to Vascular-Permeability Factor Vascular Endothelial Growth-Factor. *Chem. Biol.* **1995**, *2*, 683-695.
47. Kwon, O. S.; Park, S. J.; Hong, J. Y.; Han, A. R.; Lee, J. S.; Lee, J. S.; Oh, J. H.; Jang, J. Flexible FET-Type VEGF Aptasensor Based on Nitrogen-Doped Graphene Converted from Conducting Polymer. *ACS Nano* **2012**, *6*, 1486-1493.
48. Hao, Z.; Zhu, Y.; Wang, X.; Rotti, P. G.; DiMarco, C.; Tyler, S. R.; Zhao, X.; Engelhardt, J. F.; Hone, J.; Lin, Q. Real-Time Monitoring of Insulin Using a Graphene Field-Effect Transistor Aptameric Nanosensor. *ACS Appl. Mater. Inter.* **2017**, *9*, 27504-27511.
49. Cella, L. N.; Sanchez, P.; Zhong, W. W.; Myung, N. V.; Chen, W.; Mulchandani, A. Nano Aptasensor for Protective Antigen Toxin of Anthrax. *Anal. Chem.* **2010**, *82*, 2042-2047.
50. Choi, J. S.; Kim, S. G.; Lahousse, M.; Park, H. Y.; Park, H. C.; Jeong, B.; Kim, J.; Kim, S. K.; Yoon, M. Y. Screening and Characterization of High-Affinity ssDNA Aptamers against Anthrax Protective Antigen. *J. Biomol. Screen.* **2011**, *16*, 266-271.
51. Kim, D. J.; Park, H. C.; Sohn, I. Y.; Jung, J. H.; Yoon, O. J.; Park, J. S.; Yoon, M. Y.; Lee, N. E. Electrical Graphene Aptasensor for Ultra-Sensitive Detection of Anthrax Toxin with Amplified Signal Transduction. *Small* **2013**, *9*, 3352-3360.
52. Hashemi Tabar, G. R.; Smith, L. C. DNA Aptamers Selected as Molecular Probes for Diagnosis of Cancerous Cells. *World Appl. Sci. J.* **2010**, *8*, 16-21.
53. Park, J. W.; Na, W.; Jang, J. One-Pot Synthesis of Multidimensional Conducting Polymer Nanotubes for Superior Performance Field-Effect Transistor-Type Carcinoembryonic Antigen Biosensors. *RSC Adv.* **2016**, *6*, 14335-14343.
54. Liss, M.; Petersen, B.; Wolf, H.; Prohaska, E. An Aptamer-Based Quartz Crystal Protein Biosensor. *Anal. Chem.* **2002**, *74*, 4488-4495.
55. Maehashi, K.; Katsura, T.; Kerman, K.; Takamura, Y.; Matsumoto, K.; Tamiya, E. Label-Free Protein Biosensor Based on Aptamer-Modified Carbon Nanotube Field-Effect Transistors. *Anal. Chem.* **2007**, *79*, 782-787.
56. Maehashi, K.; Matsumoto, K.; Takamura, Y.; Tamiya, E. Aptamer-Based Label-Free Immunosensors Using Carbon Nanotube Field-Effect Transistors. *Electroanalysis* **2009**, *21*, 1285-1290.
57. Ohno, Y.; Maehashi, K.; Matsumoto, K. Label-Free Biosensors Based on Aptamer-Modified Graphene Field-Effect Transistors. *J. Am. Chem. Soc.* **2010**, *132*, 18012-18013.



58. So, H. M.; Park, D. W.; Jeon, E. K.; Kim, Y. H.; Kim, B. S.; Lee, C. K.; Choi, S. Y.; Kim, S. C.; Chang, H.; Lee, J. O. Detection and Titer Estimation of *Escherichia Coli* Using Aptamer-Functionalized Single-Walled Carbon-Nanotube Field-Effect Transistors. *Small* **2008**, *4*, 197-201.
59. Ruscito, A.; DeRosa, M. C. Small-Molecule Binding Aptamers: Selection Strategies, Characterization, and Applications. *Front. Chem.* **2016**, *4*, 14.
60. McKeague, M.; Derosa, M. C. Challenges and Opportunities for Small Molecule Aptamer Development. *J. Nucleic Acids* **2012**, *2012*, 1-20.
61. Chang, J.; Zhou, G.; Gao, X.; Mao, S.; Cui, S.; Ocola, L. E.; Yuan, C.; Chen, J. Real-Time Detection of Mercury Ions in Water Using a Reduced Graphene Oxide/DNA Field-Effect Transistor with Assistance of a Passivation Layer. *Sens. Biosensing. Res.* **2015**, *5*, 97-104.
62. Li, B. R.; Hsieh, Y. J.; Chen, Y. X.; Chung, Y. T.; Pan, C. Y.; Chen, Y. T. An Ultrasensitive Nanowire-Transistor Biosensor for Detecting Dopamine Release from Living PC12 Cells under Hypoxic Stimulation. *J. Am. Chem. Soc.* **2013**, *135*, 16034-16037.
63. Lee, J.; Jo, M.; Kim, T. H.; Ahn, J. Y.; Lee, D. K.; Kim, S.; Hong, S. Aptamer Sandwich-Based Carbon Nanotube Sensors for Single-Carbon-Atomic-Resolution Detection of Non-Polar Small Molecular Species. *Lab Chip* **2011**, *11*, 52-56.
64. Matsumoto, K.; Maehashi, K.; Ohno, Y.; Inoue, K. Recent Advances in Functional Graphene Biosensors. *J. Phys. D Appl. Phys.* **2014**, *47*, 1-6.
65. Kane, P. M.; Holowka, D.; Baird, B. Cross-Linking of IgE-Receptor Complexes by Rigid Bivalent Antigens Greater Than 200Å in Length Triggers Cellular Degranulation. *J. Cell Biol.* **1988**, *107*, 969-980.
66. Shojania, S.; O'Neil, J. D. HIV-1 Tat Is a Natively Unfolded Protein - The Solution Conformation and Dynamics of Reduced HIV-1 Tat-(1-72) by NMR Spectroscopy. *J. Biol. Chem.* **2006**, *281*, 8347-8356.
67. Thompson, A. R.; Enfield, D. L.; Ericsson, L. H.; Legaz, M. E.; Fenton, J. W. Human Thrombin - Partial Primary Structure. *Arch. Biochem. Biophys.* **1977**, *178*, 356-367.
68. Petosa, C.; Collier, R. J.; Klimpel, K. R.; Leppla, S. H.; Liddington, R. C. Crystal Structure of the Anthrax Toxin Protective Antigen. *Nature* **1997**, *385*, 833-838.
69. Stern, E.; Wagner, R.; Sigworth, F. J.; Breaker, R.; Fahmy, T. M.; Reed, M. A. Importance of the Debye Screening Length on Nanowire Field Effect Transistor Sensors. *Nano Lett.* **2007**, *7*, 3405-3409.
70. Squires, T. M.; Messinger, R. J.; Manalis, S. R. Making It Stick: Convection, Reaction and Diffusion in Surface-Based Biosensors. *Nat. Biotechnol.* **2008**, *26*, 417-426.

71. Liao, W. S.; Cheunkar, S.; Cao, H. H.; Bednar, H. R.; Weiss, P. S.; Andrews, A. M. Subtractive Patterning *via* Chemical Lift-Off Lithography. *Science* **2012**, *337*, 1517-1521.
72. Dienstag, J. L. Hepatitis B Virus Infection. *N. Engl. J. Med.* **2008**, *359*, 1486-1500.
73. Song, S. P.; Wang, L. H.; Li, J.; Zhao, J. L.; Fan, C. H. Aptamer-Based Biosensors. *Trend. Anal. Chem.* **2008**, *27*, 108-117.
74. Nakatsuka, N.; Yang, K. A.; Xu, X.; Abendroth, J. M.; Zhao, C. Z.; Zhu, B.; Chen, H.; Rim, Y. S.; Yang, Y.; Weiss, P. S.; Stojanovic, M. N.; Andrews, A. M. Aptamer Field-Effect Transistors Overcome Debye Length Limitations and Enable Small-Molecule Sensing. *submitted* **2017**.
75. Zuker, M. Mfold Web Server for Nucleic Acid Folding and Hybridization Prediction. *Nucleic Acids Res.* **2003**, *31*, 3406-3415.
76. Schoukroun-Barnes, L. R.; White, R. J. Rationally Designing Aptamer Sequences with Reduced Affinity for Controlled Sensor Performance. *Sensors (Basel)* **2015**, *15*, 7754-7767.
77. Thivianathan, V.; Gorenstein, D. G. Aptamers and the Next Generation of Diagnostic Reagents. *Proteom. Clin. Appl.* **2012**, *6*, 563-573.
78. Diclescu, V. C.; Chiorcea-Paquim, A. M.; Eritja, R.; Oliveira-Brett, A. M. Thrombin-Binding Aptamer Quadruplex Formation: AFM and Voltammetric Characterization. *J. Nucleic Acids* **2010**, *2010*, 1-8.
79. del Toro, M.; Gargallo, R.; Eritja, R.; Jaumot, J. Study of the Interaction between the G-Quadruplex-Forming Thrombin-Binding Aptamer and the Porphyrin 5,10,15,20-Tetrakis-(*N*-Methyl-4-Pyridyl)-21, 23H-Porphyrin Tetratosylate. *Anal. Biochem.* **2008**, *379*, 8-15.
80. Kelly, J. A.; Feigon, J.; Yeates, T. O. Reconciliation of the X-Ray and NMR Structures of the Thrombin-Binding Aptamer d(GGTTGGTGTGGTTGG). *J. Mol. Biol.* **1996**, *256*, 417-422.
81. Schultze, P.; Macaya, R. F.; Feigon, J. Three-Dimensional Solution Structure of the Thrombin-Binding DNA Aptamer d(GGTTGGTGTGGTTGG). *J. Mol. Biol.* **1994**, *235*, 1532-1547.
82. Mao, X. A.; Marky, L. A.; Gmeiner, W. H. NMR Structure of the Thrombin-Binding DNA Aptamer Stabilized by Sr<sup>2+</sup>. *J. Biomol. Struct. Dyn.* **2004**, *22*, 25-33.
83. Marathias, V. M.; Bolton, P. H. Structures of the Potassium-Saturated, 2:1, and Intermediate, 1:1, Forms of a Quadruplex DNA. *Nucleic Acids Res.* **2000**, *28*, 1969-1977.

84. Macaya, R. F.; Schultze, P.; Smith, F. W.; Roe, J. A.; Feigon, J. Thrombin-Binding DNA Aptamer Forms a Unimolecular Quadruplex Structure in Solution. *P. Natl. Acad. Sci. USA* **1993**, *90*, 3745-3749.
85. Russo Krauss, I.; Merlino, A.; Randazzo, A.; Novellino, E.; Mazzarella, L.; Sica, F. High-Resolution Structures of Two Complexes between Thrombin and Thrombin-Binding Aptamer Shed Light on the Role of Cations in the Aptamer Inhibitory Activity. *Nucleic Acids Res.* **2012**, *40*, 8119-8128.
86. Padmanabhan, K.; Tulinsky, A. An Ambiguous Structure of a DNA 15-Mer Thrombin Complex. *Acta Crystallogr. D* **1996**, *52*, 272-282.
87. Padmanabhan, K.; Padmanabhan, K. P.; Ferrara, J. D.; Sadler, J. E.; Tulinsky, A. The Structure of Alpha-Thrombin Inhibited by a 15-Mer Single-Stranded-DNA Aptamer. *J. Biol. Chem.* **1993**, *268*, 17651-17654.
88. Chi, C. W.; Lao, Y. H.; Li, Y. S.; Chen, L. C. A Quantum Dot-Aptamer Beacon Using a DNA Intercalating Dye as the FRET Reporter: Application to Label-Free Thrombin Detection. *Biosens. Bioelectron.* **2011**, *26*, 3346-3352.
89. Cai, B. B.; Yang, X. T.; Sun, L. D.; Fan, X. M.; Li, L. Y.; Jin, H. W.; Wu, Y.; Guan, Z.; Zhang, L. R.; Zhang, L. H.; Yang, Z. J. Stability and Bioactivity of Thrombin Binding Aptamers Modified with *D*-/*L*-Isothymidine in the Loop Regions. *Org. Biomol. Chem.* **2014**, *12*, 8866-8876.
90. Wang, R. E.; Zhang, Y.; Cai, J.; Cai, W.; Gao, T. Aptamer-Based Fluorescent Biosensors. *Curr. Med. Chem.* **2011**, *18*, 4175-4184.
91. Stojanovic, M. N.; de Prada, P.; Landry, D. W. Aptamer-Based Folding Fluorescent Sensor for Cocaine. *J. Am. Chem. Soc.* **2001**, *123*, 4928-4931.
92. Swensen, J. S.; Xiao, Y.; Ferguson, B. S.; Lubin, A. A.; Lai, R. Y.; Heeger, A. J.; Plaxco, K. W.; Soh, H. T. Continuous, Real-Time Monitoring of Cocaine in Undiluted Blood Serum *via* a Microfluidic, Electrochemical Aptamer-Based Sensor. *J. Am. Chem. Soc.* **2009**, *131*, 4262-4266.
93. Ferguson, B. S.; Hoggarth, D. A.; Maliniak, D.; Ploense, K.; White, R. J.; Woodward, N.; Hsieh, K.; Bonham, A. J.; Eisenstein, M.; Kippin, T. E.; Plaxco, K. W.; Soh, H. T. Real-Time, Aptamer-Based Tracking of Circulating Therapeutic Agents in Living Animals. *Sci. Transl. Med.* **2013**, *5*, 213ra165.
94. Plaxco, K. W.; Soh, H. T. Switch-Based Biosensors: A New Approach Towards Real-Time, *in Vivo* Molecular Detection. *Trends Biotechnol.* **2011**, *29*, 1-5.
95. White, R. J.; Rowe, A. A.; Plaxco, K. W. Re-Engineering Aptamers to Support Reagentless, Self-Reporting Electrochemical Sensors. *Analyst* **2010**, *135*, 589-594.

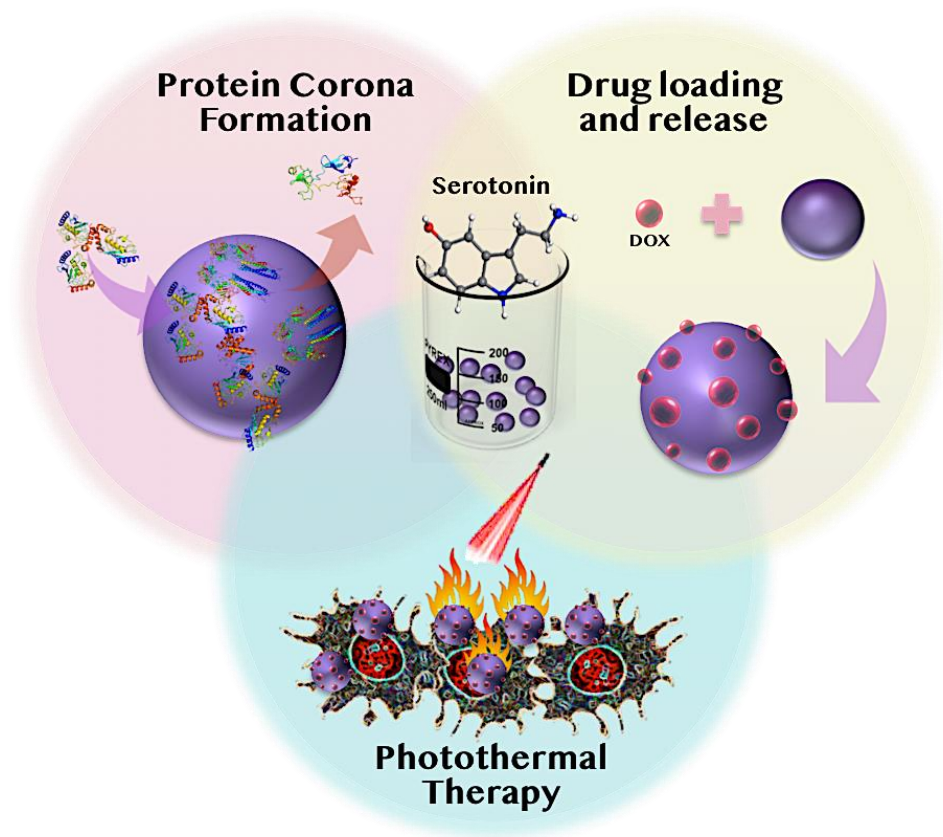
96. White, R. J.; Plaxco, K. W. Engineering New Aptamer Geometries for Electrochemical Aptamer-Based Sensors. *P. Soc. Photo-Opt. Ins.* **2009**, 7321, 1-13.
97. Schoukroun-Barnes, L. R.; Wagan, S.; White, R. J. Enhancing the Analytical Performance of Electrochemical RNA Aptamer-Based Sensors for Sensitive Detection of Aminoglycoside Antibiotics. *Anal. Chem.* **2014**, 86, 1131-1137.
98. Neumann, O.; Zhang, D. M.; Tam, F.; Lal, S.; Wittung-Stafshede, P.; Halas, N. J. Direct Optical Detection of Aptamer Conformational Changes Induced by Target Molecules. *Anal. Chem.* **2009**, 81, 10002-10006.
99. Moskovits, M. Surface-Enhanced Raman Spectroscopy: A Brief Retrospective. *J. Raman Spectrosc.* **2005**, 36, 485-496.
100. Barhoumi, A.; Zhang, D.; Tam, F.; Halas, N. J. Surface-Enhanced Raman Spectroscopy of DNA. *J. Am. Chem. Soc.* **2008**, 130, 5523-5529.
101. Otto, C.; Vandentweel, T. J. J.; Demul, F. F. M.; Greve, J. Surface-Enhanced Raman-Spectroscopy of DNA Bases. *J. Raman Spectrosc.* **1986**, 17, 289-298.
102. Lal, S.; Grady, N. K.; Kundu, J.; Levin, C. S.; Lassiter, J. B.; Halas, N. J. Tailoring Plasmonic Substrates for Surface Enhanced Spectroscopies. *Chem. Soc. Rev.* **2008**, 37, 898-911.
103. Mukerji, I.; Williams, A. P. UV Resonance Raman and Circular Dichroism Studies of a DNA Duplex Containing an A<sub>3</sub>T<sub>3</sub> Tract: Evidence for a Premelting Transition and Three-Centered H-Bonds. *Biochemistry* **2002**, 41, 69-77.
104. Johnson, N. P.; Baase, W. A.; von Hippel, P. H. Low-Energy Circular Dichroism of 2-Aminopurine Dinucleotide as a Probe of Local Conformation of DNA and RNA. *P. Natl. Acad. Sci. U.S.A.* **2004**, 101, 3426-3431.
105. Saenger, W.; Hunter, W. N.; Kennard, O. DNA Conformation Is Determined by Economics in the Hydration of Phosphate Groups. *Nature* **1986**, 324, 385-388.
106. Wiedman, G. R.; Zhao, Y.; Mustaev, A.; Ping, J.; Vishnubhotla, R.; Johnson, A. T. C.; Perlin, D. S. An Aptamer-Based Biosensor for the Azole Class of Antifungal Drugs. *mSphere* **2017**, 2, 1-10.
107. Cao, R. G.; Zhu, B.; Li, J. J.; Xu, D. S. Oligonucleotides-Based Biosensors with High Sensitivity and Selectivity for Mercury Using Electrochemical Impedance Spectroscopy. *Electrochem. Commun.* **2009**, 11, 1815-1818.
108. Hoang, C. V.; Oyama, M.; Saito, O.; Aono, M.; Nagao, T. Monitoring the Presence of Ionic Mercury in Environmental Water by Plasmon-Enhanced Infrared Spectroscopy. *Sci. Rep.* **2013**, 3, 1-6.

109. Liu, S. J.; Nie, H. G.; Jiang, J. H.; Shen, G. L.; Yu, R. Q. Electrochemical Sensor for Mercury(II) Based on Conformational Switch Mediated by Interstrand Cooperative Coordination. *Anal. Chem.* **2009**, *81*, 5724-5730.
110. Liu, C. W.; Huang, C. C.; Chang, H. T. Control over Surface DNA Density on Gold Nanoparticles Allows Selective and Sensitive Detection of Mercury(II). *Langmuir* **2008**, *24*, 8346-8350.
111. Ibach, H. The Role of Surface Stress in Reconstruction, Epitaxial Growth and Stabilization of Mesoscopic Structures. *Surf. Sci. Rep.* **1997**, *29*, 195-263.
112. Haiss, W. Surface Stress of Clean and Adsorbate-Covered Solids. *Rep. Prog. Phys.* **2001**, *64*, 591-648.
113. Smetanin, M.; Viswanath, R. N.; Kramer, D.; Beckmann, D.; Koch, T.; Kibler, L. A.; Kolb, D. M.; Weissmuller, J. Surface Stress-Charge Response of a (111)-Textured Gold Electrode under Conditions of Weak Ion Adsorption. *Langmuir* **2008**, *24*, 8561-8567.
114. Tabard-Cossa, V.; Godin, M.; Beaulieu, L. Y.; Grutter, P. A Differential Microcantilever-Based System for Measuring Surface Stress Changes Induced by Electrochemical Reactions. *Sensor Actuat. B-Chem.* **2005**, *107*, 233-241.
115. Godin, M.; Tabard-Cossa, V.; Miyahara, Y.; Monga, T.; Williams, P. J.; Beaulieu, L. Y.; Lennox, R. B.; Grutter, P. Cantilever-Based Sensing: The Origin of Surface Stress and Optimization Strategies. *Nanotechnology* **2010**, *21*.
116. Juluri, B. K.; Kumar, A. S.; Liu, Y.; Ye, T.; Yang, Y. W.; Flood, A. H.; Fang, L.; Stoddart, J. F.; Weiss, P. S.; Huang, T. J. A Mechanical Actuator Driven Electrochemically by Artificial Molecular Muscles. *ACS Nano* **2009**, *3*, 291-300.
117. Tabard-Cossa, V.; Godin, M.; Burgess, I. J.; Monga, T.; Lennox, R. B.; Grutter, P. Microcantilever-Based Sensors: Effect of Morphology, Adhesion, and Cleanliness of the Sensing Surface on Surface Stress. *Anal. Chem.* **2007**, *79*, 8136-8143.
118. Savran, C. A.; Knudsen, S. M.; Ellington, A. D.; Manalis, S. R. Micromechanical Detection of Proteins Using Aptamer-Based Receptor Molecules. *Anal. Chem.* **2004**, *76*, 3194-3198.
119. Nagai, Y.; Carbajal, J. D.; White, J. H.; Sladek, R.; Grutter, P.; Lennox, R. B. An Electrochemically Controlled Microcantilever Biosensor. *Langmuir* **2013**, *29*, 9951-9957.
120. Lipkowski, J.; Shi, Z. C.; Chen, A. C.; Pettinger, B.; Bilger, C. Ionic Adsorption at the Au(111) Electrode. *Electrochim. Acta* **1998**, *43*, 2875-2888.

121. Hinnen, C.; Rousseau, A.; Parsons, R.; Reynaud, J. A. Comparison between the Behavior of Native and Denatured DNA at Mercury and Gold Electrodes by Capacity Measurements and Cyclic Voltammetry. *J. Electroanal. Chem.* **1981**, *125*, 193-203.
122. Guo, X. H.; Liu, Z. Q.; Liu, S. Y.; Bentzley, C. M.; Bruist, M. F. Structural Features of the L-Argininamide-Binding DNA Aptamer Studied with ESI-FTMS. *Anal. Chem.* **2006**, *78*, 7259-7266.
123. Heitzinger, C.; Mauser, N. J.; Ringhofer, C. Multiscale Modeling of Planar and Nanowire Field-Effect Biosensors. *SIAM J. Appl. Math.* **2010**, *70*, 1634-1654.
124. Baumgartner, S.; Heitzinger, C. Existence and Local Uniqueness for 3D Self-Consistent Multiscale Models of Field-Effect Sensors. *Commun. Math. Sci.* **2012**, *10*, 693-716.
125. Baumgartner, S.; Vasicek, M.; Bulyha, A.; Heitzinger, C. Optimization of Nanowire DNA Sensor Sensitivity Using Self-Consistent Simulation. *Nanotechnology* **2011**, *22*.
126. Baumgartner, S.; Heitzinger, C.; Vacic, A.; Reed, M. A. Predictive Simulations and Optimization of Nanowire Field-Effect PSA Sensors Including Screening. *Nanotechnology* **2013**, *24*.
127. Bas, D. C.; Rogers, D. M.; Jensen, J. H. Very Fast Prediction and Rationalization of pKa Values for Protein-Ligand Complexes. *Proteins* **2008**, *73*, 765-783.
128. Olsson, M. H.; Sondergaard, C. R.; Rostkowski, M.; Jensen, J. H. PROPKA3: Consistent Treatment of Internal and Surface Residues in Empirical pK<sub>a</sub> Predictions. *J. Chem. Theory Comput.* **2011**, *7*, 525-537.
129. Stojanovic, M. N.; Green, E. G.; Semova, S.; Nikic, D. B.; Landry, D. W. Cross-Reactive Arrays Based on Three-Way Junctions. *J. Am. Chem. Soc.* **2003**, *125*, 6085-6089.

## Chapter IX

# Polyserotonin Nanoparticles as Multifunctional Nanomaterials for Biomedical Applications



The information in this chapter is in preparation for *ACS Applied Materials and Interfaces* and has been reproduced here.

Authors: Nakatsuka, N.; Hasani-Sadrabadi, M. M.;  
Cheung, K. M.; Young, T. D.; Bahlakeh, G.;  
Moshaverinia, A.; Weiss, P. S.; Andrews A. M.

## IX.A. Introduction

Challenges associated with implementing nanoparticles *in vivo* arise from poor understanding and control of surface interactions at the nano-bio interface.<sup>1</sup> Immediately following dispersion within physiological fluids, nanoparticles are coated with proteins to form a protein corona,<sup>2,3</sup> which then determines particle physicochemical properties.<sup>4,5</sup> The corona defines the biological identity of the nanoparticles, which directly manifest in interactions with cells and thus, influences critical parameters including cytotoxicity<sup>6,7</sup> and endocytosis into specific cells.<sup>8-11</sup> Therefore, the protein corona of nanoparticles must be optimized prior to implementation for specific biomedical applications.<sup>12-14</sup>

Polydopamine (PDA) nanoparticles<sup>15</sup> have been used for a variety of biomedical applications in drug delivery,<sup>16-18</sup> cancer therapeutics,<sup>19-21</sup> antimicrobial applications,<sup>22,23</sup> bone and tissue engineering,<sup>24-26</sup> and cell adhesion and patterning.<sup>27,28</sup> Despite these demonstrations *in vitro* for biomedical applications, most have failed to be translated successfully *in vivo*.<sup>29</sup> This challenge may arise from the protein corona surrounding PDA nanoparticles, which remains to be thoroughly characterized, resulting in nanoparticle-protein interactions with undesired effects. The high adhesive properties of PDA that are permissive of the coating of any material,<sup>30</sup> may in fact lead to promiscuous protein coatings that cause delivery and uptake issues depending on specific targets. While drug delivery capabilities of PDA-based nanoparticles have been shown,<sup>16,17,21,31,32</sup> the structure and mechanism of dopamine polymerization have not yet been elucidated and thus, surface interactions between adsorbed drug molecules and the nanoparticle surface remains to be investigated.<sup>33</sup>



Inspired by PDA-based nanoparticles, we designed and developed novel nanoparticles based on the autoxidation of serotonin monomers. Serotonin, when left in basic pH conditions, self-assembles into nanoparticles. In addition to facile synthesis, oxidized serotonin showed reduced adhesive properties compared to PDA. We compare the protein corona that adheres to the surface of polyserotonin vs. PDA nanoparticles to investigate how different protein-nanoparticle interactions may lead to unique *in vivo* applications. We explore the potential of polyserotonin nanoparticles as multifunctional nanomaterials for use in cancer therapeutics by testing photothermal properties, drug loading and release, and biocompatibility with stem cell lines. To improve understanding of molecular interactions at nano-bio interfaces, we employed molecular and quantum dynamic simulations to model the loading of a chemotherapeutic drug doxorubicin (DOX). This work suggests that serotonin-based nanoplatforms can serve as versatile scaffolds for combined, synergistic chemo- and photothermal cancer therapeutics, while exhibiting reduced nonspecific adhesion of proteins encountered *in vivo*.

## **IX.B. Experimental Methods**

### **IX.B.1. Materials**

Gold films (100 nm) overlaying titanium (10 nm) on Si substrates (Au/Si) were purchased from Platypus Technologies (Madison, WI). Serotonin hydrochloride, dopamine hydrochloride, doxorubicin hydrochloride, Tris-HCl,  $\text{KH}_2\text{PO}_4$ , and  $\text{K}_2\text{HPO}_4$  (phosphate buffer components) were purchased from Sigma-Aldrich (St. Louis, MO). Dulbecco's Modified Eagle Medium (DMEM) and Pierce bicinchoninic acid (BCA) Protein Assay Kit were purchased from Thermo Fisher Scientific (Canoga Park, CA). Deionized water ( $\sim 18 \text{ M}\Omega$ ) was obtained from a Millipore water purifier (Billerica, MA).

Young (18–25 years old) healthy male individuals undergoing third molar extractions were selected for extraction of gingival and dental pulp tissues. All procedures involving human tissues were pre-approved by the Institutional Review Boards for protection of human subjects' research (IRB # BUA6510). Gingival mesenchymal stem cells (GMSCs) and dental pulp stem cells (DPSCs) were isolated and cultured according to published protocols.<sup>34,35</sup> Human bone marrow mesenchymal stem cells (hBMMSCs) were purchased from Lonza Inc. (Walkersville, MD). Flow cytometry (BD Biosciences, San Jose, CA) was used to determine stem cell surface markers STRO-1 and CD146. Cells from passage four were used in all the experiments.

### **IX.B.2. Serotonin and Dopamine Nanoparticle Synthesis**

Serotonin hydrochloride (2 mg/mL) was incubated in phosphate buffer (0.70 mM  $\text{KH}_2\text{PO}_4$ , 500 mM  $\text{K}_2\text{HPO}_4$ , pH 9.5) for 5 days to produce polyserotonin nanoparticles. Polydopamine nanoparticles were synthesized *via* an oxidation and self-polymerization dispersion

polymerization procedure.<sup>17,19,32</sup> Briefly, dopamine hydrochloride was dissolved in Tris-HCl buffer (10mM, pH 8.5) and the mixture was stirred in the dark for 16 h to polymerize dopamine at room temperature.

### **IX.B.3. Characterization**

#### **IX.B.3.a. UV-visible Spectroscopy**

Absorbance measurements were performed using an Evolution 600 UV-visible spectrophotometer (Thermo Scientific).

#### **IX.B.3.b. Dynamic Light Scattering and Zeta Potential**

Dynamic light scattering (DLS) and Zeta potential measurements were performed at pH 7.4 using a Zetasizer (Zetasizer 3000HS, Malvern Instruments Ltd., Worcestershire, UK). Measurements were conducted in backscattering mode at an angle of 173° for diluted polyserotonin nanoparticle suspensions in water at 37 °C.

#### **IX.B.3.c. Scanning Electron Microscopy**

Polyserotonin nanoparticles were centrifuged and washed three times in deionized water, drop-cast onto Au/Si substrates, and incubated overnight. The substrates were rinsed with deionized water and blown dry with nitrogen gas prior to imaging. Samples were imaged with a JEOL JSM-6700F field emission scanning electron microscope with a 3 kV accelerating potential.

#### **IX.B.3.d. Atomic Force Microscopy**

Particles were imaged by AFM using a Bruker Dimension Icon Scanning Probe Microscope (SPM). The topography and mechanical properties of these particles were simultaneously measured using the PeakForce Quantitative Nanomechanical Property Mapping (PeakForce QNM) mode. ScanAsyst-Air cantilevers (Bruker, spring constant =  $0.4 \pm 0.1$  N/m) were used for all of the measurements. The peak force set point was chosen and adjusted automatically through the ScanAsyst® imaging mode.

#### **IX.B.3.e. X-ray Photoelectron Spectroscopy**

An AXIS Ultra DLD X-ray photoelectron spectrometer (Kratos Analytical Inc., Chestnut Ridge, NY, USA) was used for elemental surface analysis. The spectrometer uses a monochromatic Al KR X-ray source with a 200  $\mu\text{m}$  circular spot size and ultrahigh vacuum ( $10^{-9}$  Torr). Spectra were acquired at a pass energy of 160 eV for survey spectra and 20 eV for high-resolution spectra of C 1s, O 1s, and N 1s, regions using a 300 ms dwell time. For both scan types, 15 kV was applied with an emission of 10 mA. Three scans were performed for survey spectra and 10 scans for each of the high-resolution spectra.

#### **IX.B.3.f. Protein Corona**

Protein corona experiments were performed as reported previously.<sup>36,37</sup> Briefly, venous blood was obtained from ten healthy donors. Plasma was separated, and protein aggregates were removed by ultracentrifugation. Nanoparticles were incubated with human plasma under gentle shaking for 3 h, separated using ultracentrifugation at 20,000x g for 1 h, and then washed three times. Proteins were then eluted after dissolving

nanoparticles by reducing the pH to 3.0 and shaking the solution for 30 min. Protein concentration was assessed *via* micro BCA protein assays.

Afterwards, proteins were digested following reported protocols.<sup>38</sup> Quantitative analysis of protein samples was performed by liquid-chromatography mass-spectrometry (LC-MS). A LTQ Orbitrap XL Mass Spectrometer (Thermo Fisher Scientific) coupled with Eksigent NanoLC-2D HPLC and autosampler was used after 10-fold dilution of digested protein samples in 0.1% formic acid. The experimental details were as reported by Schöttler *et al.*<sup>36</sup> Mass spectra were collected over a  $m/z$  range of 300-2000 Da. All samples were analyzed in triplicate to quantify the amounts of each protein adsorbed on nanoparticle surfaces.

#### **IX.B.3.g. Cell Viability**

Standard 3-(4,5-dimethylthiazol-2-yl)-2,5-diphenyltetrazolium bromide (MTT) colorimetric assays were conducted using human bone-marrow mesenchymal stem cells, hBMMSCs, GMSCs, DPSCs, and a cervical cancer cell line, HeLa cells, to examine the cytotoxicity of the fabricated nanoparticles. To determine cell cytotoxicity/viability, the cells were plated at densities of 10,000 cells per well in 96-well plates and incubated overnight at 37°C in an incubator maintained at 5% CO<sub>2</sub>. Cells were then incubated with nanoparticles over a concentration range of 1–400 µg/mL. The culture medium was discarded after 24 or 48 h and cells were washed with PBS (pH 7.4) followed by incubation for 2 h with 100 µL of MTT solution in DMEM (500 µg/mL in phosphate buffer pH 7.4). The medium containing MTT was replaced with 150 µL of dimethyl sulfoxide (DMSO) in each well.

After shaking the plates for 10 min, the absorbance values of the wells were recorded with a microplate reader (Bio-Tek Synergy HT, Winooski, VT, USA) at a wavelength of 570 nm. The control culture medium contained no nanoparticles. All measurements were performed at room temperature. The spectrophotometer was calibrated to zero absorbance using control culture medium containing no cells. The relative cell viability (%) related to the control wells, containing cell culture medium without nanoparticles, was calculated as:

$$[A]_{\text{test}}/[A]_{\text{control}} \times 100,$$

where  $[A]_{\text{test}}$  was absorbance of the test sample and  $[A]_{\text{control}}$  was absorbance of the control sample.

#### **IX.B.3.h. *In Vitro* Drug Release**

To determine *in vitro* drug release profiles, lyophilized DOX-loaded polyserotonin nanoparticles (1 mg) were dispersed in 1 mL of 1× PBS (pH 7.4). The solutions were placed in a 3500 Da MWCO dialysis cartridge (Thermo Scientific, Waltham, MA, USA). Cartridges were then immersed in 1 L of PBS and gently shaken at 37 °C in a water bath. At predetermined intervals, buffered solutions were collected and replaced with equivalent volumes of fresh PBS. The DOX concentrations were measured by UV spectrophotometry at 430 nm.

Concentrations were evaluated over a linear concentration range. In this range, the percent deviation from theoretical value was found to be less than 5% and coefficients of linearity remained greater than 0.96 using clean DOX standards. The DOX concentrations were corrected for sampling effects according to the following equation:

$$C_n^l = C_n[V_T/(V_T - V_S)](C_{n-1}^l/C_{n-1})$$

where  $C_n^l$  is the corrected concentration of the  $n^{\text{th}}$  sample,  $C_n$  is the measured concentration of DOX in the  $n^{\text{th}}$  sample,  $C_{n-1}$  is the measured concentration of the  $(n-1)^{\text{th}}$  sample,  $V_T$  is the volume of receiver fluid,  $V_S$  represents the volume of the sample drawn (1 mL), and  $C_{n-1}^l$  is the corrected concentration of the  $(n-1)^{\text{th}}$  sample. Loading efficiencies of the nanoparticles were determined by applying the following equation:

$$\text{DOX Loading efficiency} = (\text{DOX adsorbed to nanoparticles} / \text{initial amount of DOX}) \times 100\%.$$

### **IX.B.3.i. Photothermal Therapy**

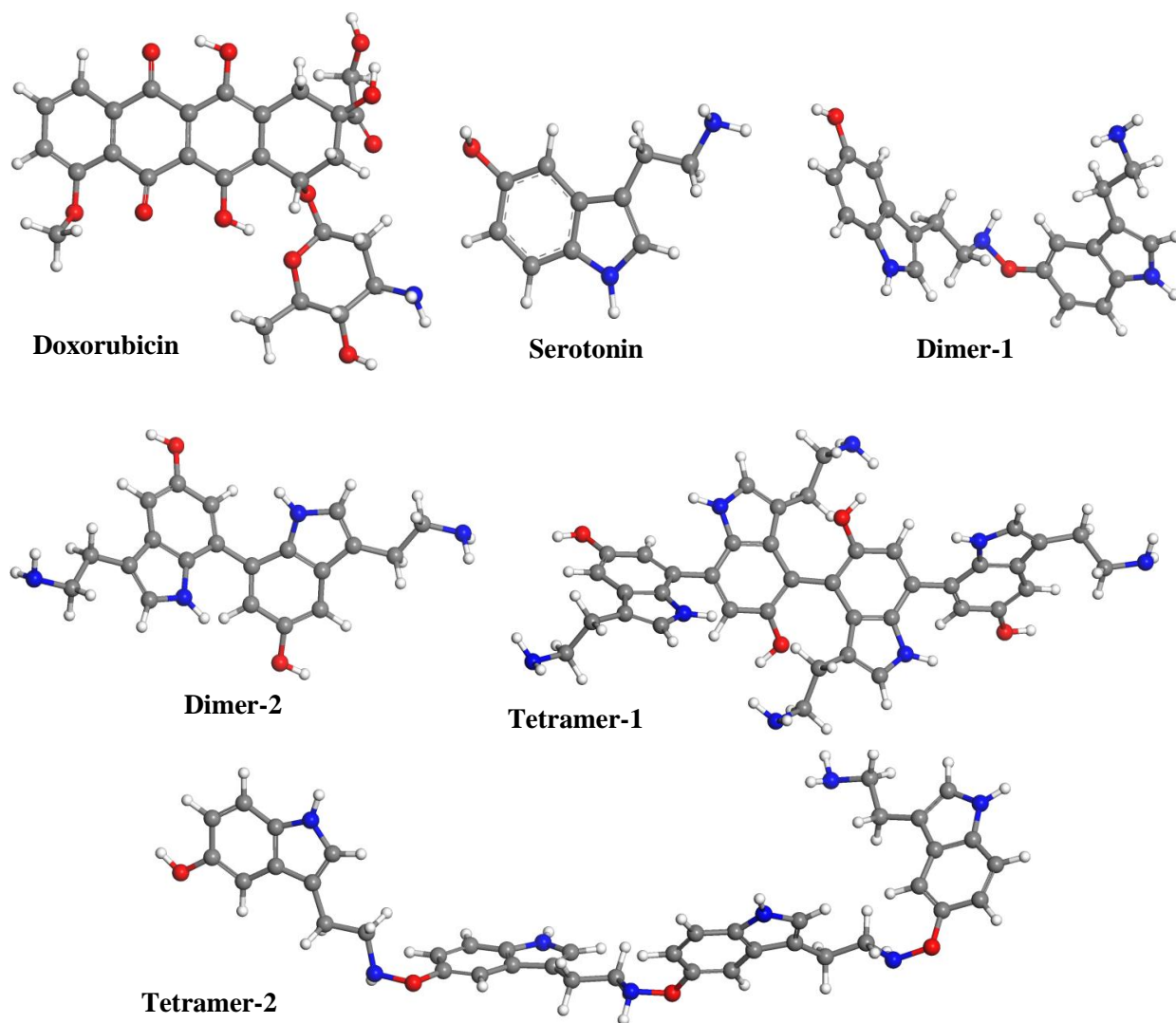
A thermal imaging camera (FLIR Systems; Nashua, NH, USA) was used to record near-infrared laser irradiation-induced increases in temperature (808 nm; 1.5 W·cm<sup>-2</sup>). For photothermal ablation of cancer cells, HeLa cells were seeded in tissue culture dishes at a density of 40,000 cells/cm<sup>2</sup> and were cultured for 24 h at 37 °C in an incubator maintained at 5% CO<sub>2</sub> until 80% confluence. Next, the medium was replaced with nanoparticle-containing medium (25-400 mg/ml). After incubation for 4 h, the cells were rinsed three times with PBS to remove free nanostructures. Fresh medium was added and then laser light at 808 nm; 1.5 W·cm<sup>-2</sup> with a 250-nm diameter spot-size was irradiated for 6 min. Cell viability was characterized by using the live/dead assay and MTT assay as described above.

#### **IX.B.4. Theoretical Details**

##### **IX.B.4.a. Quantum Mechanics Computations**

To explore DOX affinity for polyserotonin nanoparticles, *ab initio* quantum mechanics (QM) computations employing density functional theory (DFT) methods were applied. The molecular structures of DOX and serotonin are displayed in Scheme IX.1. As illustrated, a number of oxygenated and nitrogenous moieties are present in DOX and serotonin. Accordingly, to examine interactions between the functional groups of DOX and serotonin, five different starting DOX-serotonin clusters were constructed. These hybrid clusters were subjected to geometry optimization based on DFT calculations. Within DFT computations, the electronic exchange-correlation interactions were taken into account using two different levels of M06-2X<sup>39</sup> and B3LYP in conjunction with the 6-311G(d,p) basis function.<sup>40-42</sup> Lowest energy geometries were utilized to determine the partial atomic charges of DOX and serotonin, and their binding energies. The electrostatic potential (ESP) based method, ChelpG, was adopted to analyze the partial charges of geometry-optimized DOX and serotonin for subsequent use in classical atomistic molecular dynamics (MD) simulations.<sup>43</sup> All QM computations were done using the Gaussian 09 suite of programs.<sup>44</sup>





**Scheme IX.1.** The B3LYP/6-311G(d,p) optimized geometries of DOX and serotonin and its constructed two dimers and two tetramers chosen for theoretical QM calculations and MD simulations. The atomic color code is: carbon gray, oxygen red, hydrogen white, and nitrogen blue.

#### IX.B.4.b. Construction of Serotonin Surfaces

Besides first-principles QM computations, classical MD simulations were applied to examine DOX-polyserotonin affinity at a larger atomic scale. As the structure of polyserotonin is not understood, in addition to serotonin, two different dimers (designated as dimer-1 and dimer-2) and two different tetramers (called tetramer-1 and tetramer-2) based on the serotonin structure were built to represent polyserotonin. The minimum

energy structures of these dimers and tetramers resulting from DFT/B3LYP/6-311G(d,p) are demonstrated in Scheme IX.1.

To construct surfaces of serotonin, serotonin dimers, and serotonin tetramers, their corresponding energy-minimized structures derived from QM calculations were utilized. First, a serotonin cell consisting of 100 serotonin molecules, two serotonin dimer cells each containing 50 molecules of respective dimer, and two amorphous cells for serotonin tetramers including 25 serotonin tetramers were generated at a lower density of  $0.5 \text{ g}\cdot\text{cm}^{-3}$  using Materials Studio software.<sup>45</sup> These five simulation cells were energy minimized by Smart minimizer algorithm for 2000 steps and then subjected to NPT MD simulations performed for 250 ps at 1 atm and 300 K. Afterwards, a vacuum space of approximately 30 Å was placed above all equilibrated cells in a direction normal to the surface, that is the z-axis.

#### **IX.B.4.c. Molecular Dynamics Simulations**

To conduct MD simulations, the DFT-optimized DOX geometry was first placed over all five simulation cells at larger distances from each surface. The cells containing serotonin-based adsorbent and DOX adsorbate are depicted in Figure SG.1 Before MD simulations, the potential energy of these cells was minimized by applying the Smart minimizer algorithm for 2000 steps. Subsequently, MD simulations were executed on optimized cells in the NVT ensemble (N is the number of particles in the system; V is the system volume; T is the absolute temperature) for 300 ps at room temperature. Both optimization and dynamics simulations were carried out using the Forcite module, as available in the Materials Studio software.<sup>45</sup>

Except for the partial atomic charges elucidated from *ab initio* QM computations, all other potential energy parameters required for the calculations of bonded and non-bonded interactions of DOX and serotonin (*i.e.*, monomer, dimers, and tetramers) were taken from the COMPASS (condensed-phase optimized molecular potentials for atomistic simulation studies) force field.<sup>46,47</sup> During MD simulations, both van der Waals and electrostatic interactions were modeled by the Ewald summation scheme. The velocity Verlet method with a time step of 1 fs was applied for the integration of Newton's equation of motion.<sup>48</sup>

## **IX.C. Results and Discussion**

### **IX.C.1. Synthesis and Characterization of Polyserotonin Nanoparticles**

For the synthesis of polyserotonin nanoparticles, we incubated serotonin monomers under alkaline conditions (2 mg/mL in phosphate buffer, pH 9.5) for one to five days (Figure IX.1A). While this method did not require the addition of a catalyst, the kinetics of polyserotonin nanoparticle formation appeared substantially slower than dopamine polymerization, which has been reported to be on the order of minutes.<sup>49</sup> Conventionally, dopamine nanoparticles are synthesized by the oxidation and self-polymerization of dopamine in a mixture containing water, ethanol, and ammonia at room temperature.<sup>20</sup> Similarly to PDA formation,<sup>50</sup> the oxidation process of serotonin can be monitored *via* the appearance of a UV absorption peak with time, coupled with a color change of the solution from colorless to dark brown (Figure IX.1B). Serotonin incubated under mildly acidic conditions (pH 6) did not show additional absorption peaks or solution color change even after 5 days.

The size distribution of polyserotonin nanoparticles was visualized by SEM (Figure IX.1C). The average particle size was ~440 nm after 5 days of incubation determined by DLS measurements (Figure IX.1D). A polydispersity index of 0.06 indicated single size modes with minimal aggregates.<sup>51</sup> The zeta potential of the serotonin nanoparticles showed a sharp peak at approximately -45 mV, indicative of an overall negative surface charge (Figure IX.1E). Serotonin monomers have two protonation sites, an aliphatic amino group and an aromatic hydroxyl moiety with  $pK_a$  values of 9.97 and 10.73 respectively.<sup>52,53</sup> Since the serotonin nanoparticles were synthesized at a pH of 9.5, which is close to the  $pK_a$  of the amino group of serotonin, we predicted these particles to be composed of a mixture

of cationic (protonated amino group) and neutral (deprotonated amino group) serotonin. However, we observed a negative surface charge for these serotonin nanoparticles.

The zeta-potential of dopamine-melanin films has been shown to -40 mV similar to the polyserotonin nanoparticles.<sup>54</sup> Dopamine has similar  $pK_a$  values as serotonin – two phenolic hydroxyl groups with  $pK_a$  values of 9.44 and 12.8 and a primary amine with  $pK_a$  10.75.<sup>55</sup> The negative zeta-potential for dopamine-melanin films is hypothesized to originate from the dissociation of the quinone imine and catechol groups at a pH of 8.5.<sup>54,56,57</sup> Thus, while the mechanism by which serotonin monomers cluster to form spherical nanoparticles is not clear, we hypothesize that serotonin undergoes a similar polymerization process to rationalize the resulting negative surface charge.

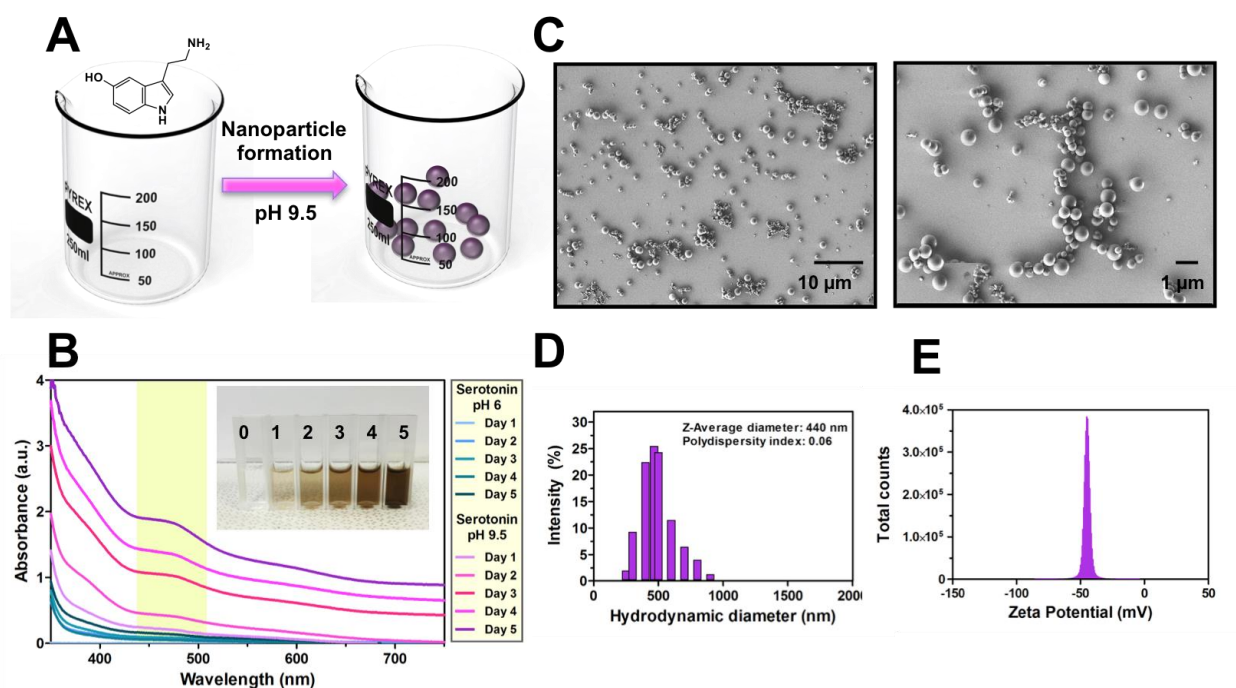


**Figure IX.1.** (A) Schematic illustration of the synthesis process of polyserotonin nanoparticles (not to scale). (B) UV-vis spectra for aqueous solutions of serotonin incubated at either pH 6 or pH 9.5 over 5 days with a photograph of cuvettes containing samples at each time point under basic conditions. (C) SEM images of polyserotonin nanoparticles. (D) Average sizes of polyserotonin nanoparticles determined to be 440 nm *via* dynamic light scattering with a polydispersity index of 0.06. (E) Zeta-potential of polyserotonin nanoparticles.

X-ray photoelectron spectroscopy was performed to identify the composition and chemical bonding of the polyserotonin nanoparticles. Serotonin hydrochloride incubated in acidic buffer (phosphate buffer, pH 6.5) to hinder polymerization-preceding oxidation, was used to investigate the differences in the chemical bonding characteristics of monomeric serotonin vs. oxidized serotonin that form nanoparticles. The lack of serotonin nanoparticle formation at mildly acidic pH, even after five days was confirmed *via* SEM (Figure SG.2). The elements present in monomeric serotonin, (carbon, oxygen, and nitrogen), appear in the respective spectra for the base-treated nanoparticles (Figure IX.2A,B).

The C 1s regions for both the serotonin monomers and nanoparticles can be fit with four peaks corresponding to C-H/C-NH<sub>2</sub> (285 eV), C-O/C-N (286 eV), C=O/C=N (288 eV), and  $\pi \rightarrow \pi^*$  (291 eV) species.<sup>49,58</sup> While the basic peak shapes for both these spectra are similar, the peak intensities corresponding to oxygen functional groups are more dominant in the nanoparticle case, suggesting that serotonin was indeed oxidized. The O 1s regions for both samples can be fit with two peaks corresponding to O=C (531 eV) and O-C (533 eV) species.<sup>49,58</sup> It should be noted that the additional peak at 535 eV, seen in Figure IX.2E, is an overlap from the Na KLL auger peak.<sup>58</sup> While the N 1s regions for both the serotonin monomers and nanoparticles have peaks corresponding to R-NH<sub>2</sub> (402 eV) and R-NH-R (400 eV), there are additional peaks corresponding to =N-R (399 eV) and oxidized nitrogen functionalities (403 eV) for the polyserotonin nanoparticles.<sup>58-60</sup> Together, these additional peaks show that serotonin is oxidized and likely polymerizes to form nanoparticles.

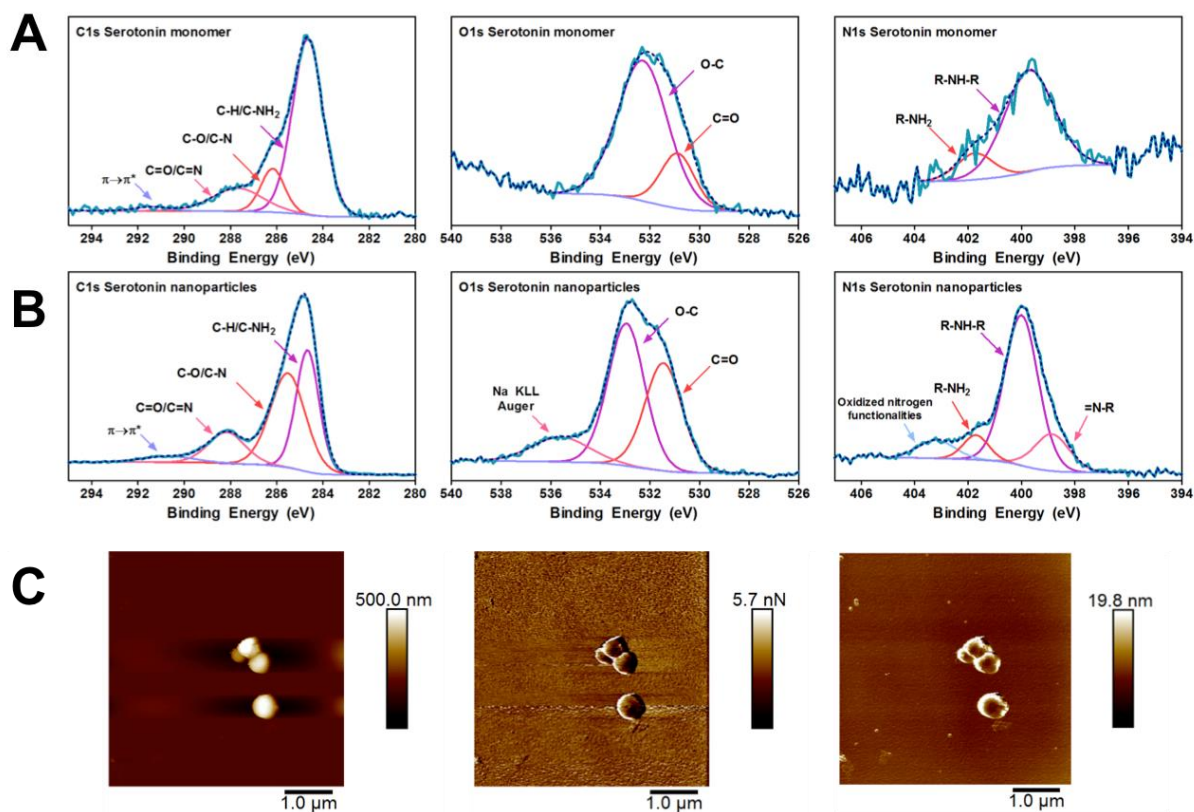


**Figure IX.2.** Characterization of polyserotonin nanoparticles. **(A)** XPS spectra for the C 1s, O 1s, and N 1s peak for serotonin incubated at acidic pH to prevent nanoparticle formation. **(B)** XPS spectra for the C 1s, O 1s, and N 1s peaks for serotonin incubated at basic pH to induce polymerization and nanoparticle formation. Fitted curves are labeled with corresponding species. The dashed line in the spectra represents the global envelopes corresponding to the sum of the Gaussian-Lorentzian peaks used to fit the spectra. **(C)** Atomic force microscopy of serotonin nanoparticles showing height, adhesion, and deformation.

Additionally, we visualized the polyserotonin nanoparticles using peak-force atomic force microscopy (PF-AFM), an intermittent contact mode used to measure the topography and nanomechanical properties of materials. The AFM topography map in Figure IX.2C shows polyserotonin nanoparticles having approximately 500 nm diameters. These measured diameters are consistent with those measured *via* SEM and DLS. We also used PF-AFM to measure the adhesion force, the force required to retract an AFM tip from a surface, of the polyserotonin nanoparticles in comparison to PDA nanoparticles. As shown in the adhesion maps of polyserotonin nanoparticles (Figure IX.2C) and PDA nanoparticles

(Figure SG.3), the difference in adhesion, between the nanoparticles and the Au substrate is approximately four times greater for PDA compared to that of the polyserotonin nanoparticles. Thus, these adhesion maps suggest that PDA is significantly more adhesive than the polyserotonin nanoparticles. The greater adhesion for PDA is likely due to the availability of functional groups, such as the catechol, post-polymerization.

### **IX.C.2. Protein Corona**

One of the main criteria in selecting nanoparticles for biomedical applications is their level of interaction with proteins in biological environments. Interfacial interactions of nanoparticles with various blood proteins alters therapeutic functionality in an unpredictable manner.<sup>61</sup> In 2007, the term “protein corona” emerged to depict the spontaneous self-assembly and layering of proteins onto nanoparticle surfaces.<sup>3</sup> Despite nanoparticle surface functionalization strategies aimed at reducing protein adsorption, there is currently no strategy to fully eliminate protein corona formation.<sup>62</sup> We hypothesized that the reduced adhesive properties of polyserotonin nanoparticles compared to dopamine nanoparticles would influence protein corona formation on the surfaces of these nanoparticles.

To assess differences in adhesive properties between PDA vs. polyserotonin nanoparticles and to investigate whether surface adhesion influences protein adsorption directly, we analyzed the adsorption of over 100 proteins using LC-MS. Depending on the nature of each protein and the nanoparticle surfaces, some proteins associated weakly and quickly dissociated (soft corona), while others bound strongly and irreversibly (hard corona).<sup>3,63</sup> Polyserotonin nanoparticles adsorbed about 60% less identified plasma



proteins in comparison to PDA nanoparticles, possibly due to the lower surface adhesion as determined by the AFM results (Figure IX.2G and SG1).

Fibrinogen, a coagulation protein, was found to be the major plasma component in the hard corona for both serotonin and dopamine-based nanoparticles (Figure IX.3). High adsorption levels of fibrinogen have been reported for hydrophilic nanoparticle surfaces and amine-modified quantum dots,<sup>64</sup> at significantly higher quantities than other adhesion proteins.<sup>65</sup> Fibrinogen surface adhesion is problematic for *in vivo* delivery because it triggers activation of the immune system *via* hemostasis and leukocyte activation.<sup>66,67</sup>

Serum albumin was the protein with the second highest surface adsorption for both serotonin and PDA-based nanoparticles. Bovine serum albumin has been used to coat the surfaces of drug delivery carriers to form “stealth” nanoparticles with prolonged blood circulation times.<sup>68</sup> Preformed albumin coronas have also been shown to be a strategic way to decrease nonspecific adsorption of other immune-triggering proteins and to decrease the clearance rate of nanoparticles.<sup>69,70</sup> Thus, having a high surface coverage of serum albumin may in fact be advantageous for the nanoparticles. The complement system is the first line of defense against foreign materials that causes inflammation and damage to the host.<sup>71,72</sup> Relatively low levels of complement proteins adsorbed on the surface of both polyserotonin and PDA nanoparticles, which may result in longer blood circulation times for these nanoparticles.<sup>73</sup>

Coating nanoparticles with the hydrophilic polymer, polyethylene glycol (PEG), has been shown to impart steric stabilization and to reduce surface adhesion of blood proteins, thereby prolonging circulation half-lives *in vivo*.<sup>74</sup> To this end, we coated polyserotonin nanoparticles with PEG *via* incubation of nanoparticles with PEG-SH at basic pH (~8.5) for

24 h. As shown in Figure IX.3, PEGylation of polyserotonin nanoparticles reduced total protein adsorption levels by a factor of three. Post PEGylation, fibrinogen adhesion was reduced by ~85%, which suggests that PEGylated polyserotonin nanoparticles may evoke reduced immunological responses when exposed to *in vivo* environments.

Clusterin, a lipoprotein, was found to be the major protein in the hard corona of PEGylated polyserotonin nanoparticles. High levels of clusterin adsorption were previously reported for other PEGylated<sup>36,75</sup>, silica<sup>38</sup>- and lipid-based<sup>76</sup> nanoparticles. It has been reported that clusterin adhesion on the surface of PEGylated nanoparticles induced the stealth effect and inhibited nanoparticle uptake by phagocytes.<sup>77</sup> Thus immunotoxicity can be mitigated or augmented depending on the type of nanoparticle and adsorbed plasma proteins.<sup>78</sup> Analyzing the protein corona of three different nanoparticle compositions demonstrated the importance of investigating nano-bio interfaces at nanoparticle surfaces, which will enable choices of delivery vehicles depending on the targeting application and experimental design.

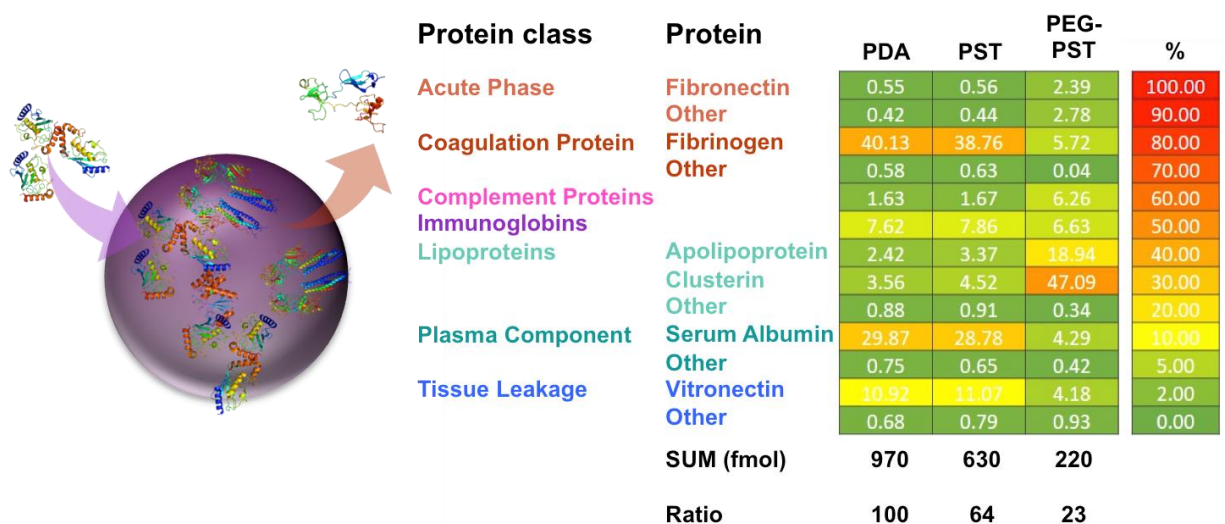


**Figure IX.3.** Schematic of presumptive interactions with plasma proteins and polyserotonin (PST) nanoparticles (left). Heat map of the adsorbed proteins on PDA, PST, and PEGylated PST nanoparticles, evaluated by proteomic mass spectrometry and ordered based on their abundances (right). Average from triplicate measurements are illustrated in femtomoles. Percentages of identified proteins are grouped according to biological class.

### IX.C.3. Cell Viability

Polyserotonin nanoparticles were incubated with three different types of human-derived stem cells (*i.e.*, hBMMSCs, GMSCs, and DPSCs) to assess the biocompatibility. Stem cells were incubated with nanoparticles at different concentrations, ranging from 1 to 400  $\mu\text{g}\cdot\text{ml}^{-1}$  to investigate polyserotonin nanoparticle cytotoxicity. A standard MTT assay was used to measure cell viability at two different time points, 24 h and 48 h. As shown in Figure IX.4, even after 72 h of culturing, a viability of >90% was achieved at lower concentrations (1-25  $\mu\text{g}\cdot\text{ml}^{-1}$ ) of polyserotonin nanoparticles. At elevated concentrations (>25  $\mu\text{g}\cdot\text{ml}^{-1}$ ), reduced viability was observed after 72 h of culture. However, even at this time point, polyserotonin nanoparticles displayed lower cytotoxicity ( $P<0.01$ ) than their dopamine counterparts (~90% cell viability for polyserotonin nanoparticles vs. ~80% viability for PDA nanoparticles at high concentrations (100 mg/mL; Figure SG.4)).

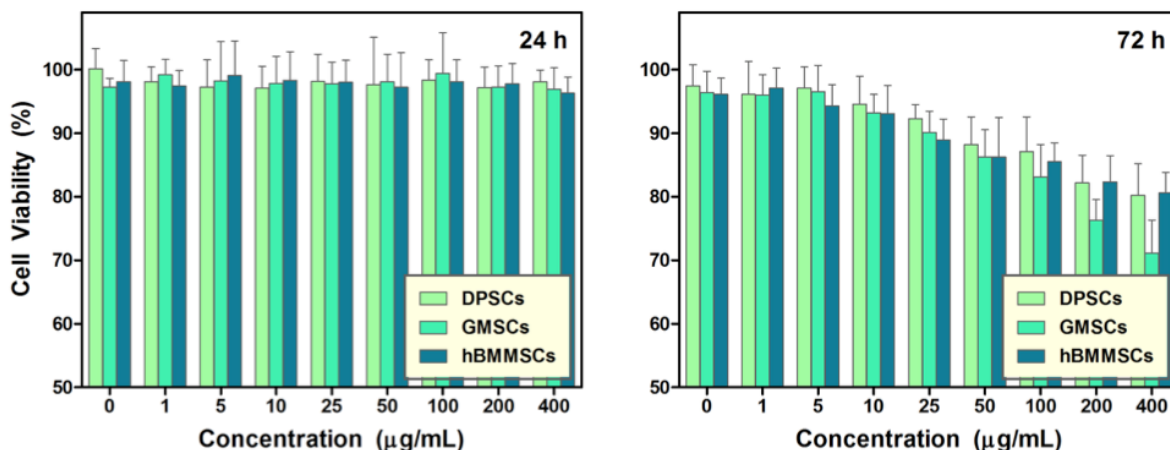


**Figure IX.4.** Cellular viability of human bone-marrow mesenchymal stem cell (hBMSCs), gingival-derived mesenchymal stem cell (GMSCs), and human dental pulp stem cells (DPSCs) after incubation with different concentrations of serotonin-based nanoparticles after 24 h (left) and 72 h (right).

#### IX.C.4. *In Vitro* Drug Release and Photothermal Therapy

Mild photothermal heating ( $\sim 45^{\circ}\text{C}$ ) has been shown to improve treatment efficacy by enhancing cellular uptake of chemotherapeutics or triggering intracellular drug release from nanocarriers without causing cell necrosis.<sup>79,80</sup> Near-Infrared (NIR)-triggered nano-drug carriers have been extensively explored for cancer combination therapy.<sup>81</sup> It has been reported that PDA-based nanoparticles can kill cancerous cells and suppress tumor growth *via* photothermal effects by NIR irradiation.<sup>20</sup> We investigated whether polyserotonin nanoparticles display a similar effect.

Figure IX.5A shows the change in the temperature of the DMEM media over time during laser irradiation at different polyserotonin nanoparticle concentrations. The maximum temperature change for the PBS media was less than  $5^{\circ}\text{C}$  for samples without polyserotonin nanoparticles. Samples with polyserotonin nanoparticles ( $>100 \mu\text{g}\cdot\text{ml}^{-1}$ ) showed temperature increases of more than  $20^{\circ}\text{C}$  after NIR irradiation, as shown in Figure IX.5B. We observed that the temperature increase was higher for PDA nanoparticles

(Figure SG.5) compared to polyserotonin nanoparticles. This may be due to the higher degree of polymerization in the case of PDA nanoparticles.

In addition to targeted heat therapy, we explored the drug loading and delivery capabilities of polyserotonin nanoparticles. Doxorubicin is an anticancer chemotherapeutic drug, extensively used for the treatment of solid tumors and acute leukemias.<sup>82</sup> Akin to PDA nanoparticles, polyserotonin nanoparticles can be used for DOX loading by means of surface adsorption *via*  $\pi$ - $\pi$  stacking and hydrophobic interactions (Figure IX.5C).<sup>19,32,83</sup> Comparative studies of the loading efficiencies of PDA vs. polyserotonin nanoparticles are shown in Figure SG.6. The *in vitro* drug release profiles of DOX-loaded polyserotonin nanoparticles in PBS (37 °C) at different pHs are shown in Figure IX.5D. At pH 7.4, polyserotonin nanoparticles exhibited slow DOX release over a time span of 100 h.

However, polyserotonin nanoparticles exhibited high sensitivity to changes in pH. At pH 6.5 (mimicking tumor microenvironments) and at pH 5.5 (mimicking intracellular lysosomal pH) polyserotonin nanoparticles showed significantly faster release profiles compared to pH 7.4. This result is promising for localized cancer therapy delivery where the loaded drug will not be fully released from the surface of the polyserotonin nanoparticles while in circulation, but can be liberated upon reaching acidic tumor microenvironments.

Polyserotonin nanoparticles thus have the potential to be used as combination cancer therapeutic agents *via* photothermal effects, as well as efficient loading and release of the anticancer drug DOX. A critical requirement for an improved cancer therapeutic is the ability to maximize lethal effects at tumor cell sites. We examined the toxicity of unloaded vs. DOX-loaded polyserotonin nanoparticles with and without laser irradiation.

Similar to cell viability results previously performed with stem cells lines (Figure IX.4), polyserotonin nanoparticles alone showed no cytotoxic effects for HeLa cells, even at high concentrations (200  $\mu\text{g/mL}$ ). However, DOX-loaded polyserotonin nanoparticles reduced cellular viability significantly in a concentration-dependent manner (Figure IX.5E).

Laser irradiation of PDA nanoparticles has been shown to ablate tumors completely *via* localized increases in temperature.<sup>84</sup> Upon irradiation with the NIR laser, the death rate of cancer cells significantly increased and was dependent on polyserotonin nanoparticle concentrations. Effects were more highly pronounced at higher polyserotonin nanoparticle concentrations and were more notable for DOX-loaded polyserotonin nanoparticles, which showed about 80% cytotoxicity at a concentration of 50  $\mu\text{g}\cdot\text{mL}^{-1}$  of nanoparticles. Figure IX.5F shows the estimated half maximal inhibitory concentrations ( $IC_{50}$ ) for serotonin-based nanotherapeutics. While polyserotonin nanoparticles alone were nontoxic, a synergistic cytotoxic effect of DOX-loaded nanoparticles post-laser exposure was found to reduce the required doses of the nanotherapeutic by 40% and 100% compared to DOX or laser treatment alone, respectively.

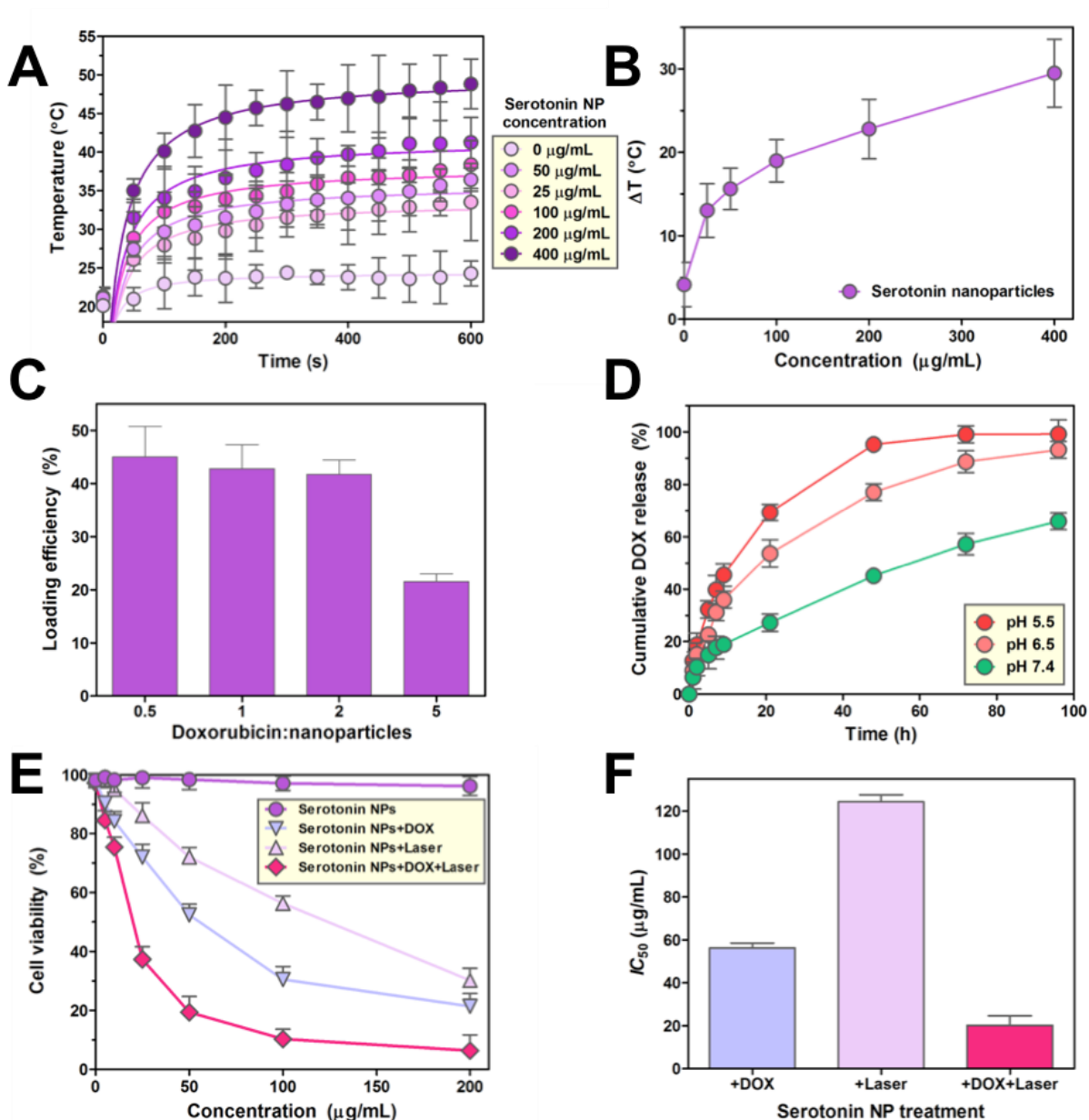


**Figure IX.5.** (A) *In vitro* heat generation in PBS suspensions containing various concentrations of serotonin-based nanoparticles after NIR-irradiation (808 nm laser; 3 W·cm<sup>-2</sup>; 10 min). (B) Temperature change (ΔT) over a period of 10 min for various concentrations of serotonin-based nanoparticles (NPs) after NIR-irradiation. (C) Loading efficiency of DOX (DOX) on the surface of PST nanoparticles at different initial drug contents. (D) Cumulative *in vitro* release profiles of DOX from serotonin-based nanoparticles in PBS solution at different pH values mimicking tumor microenvironments (pH 6.5) and intracellular lysosomal environments (pH 5.5). (E) MTT-based cell viability assay of HeLa cells after 24 h of exposure to DOX-loaded and unloaded polyserotonin nanoparticles as a function of concentration at 37 °C. The effect of laser exposure and combinatorial treatment (DOX-loaded nanoparticles + laser exposure) on cellular viability of HeLa cells is also demonstrated. (F) Estimated half maximal inhibitory concentrations (IC<sub>50</sub>) for serotonin-based nanotherapeutics.

### IX.C.5. Molecular and Quantum Dynamics

To obtain electronic-/atomic-level details regarding the interactions responsible for DOX adsorption to serotonin-based nanostructures, theoretical electronic QM computations and all-atom MD simulations were performed. Figure IX.6A depicts the final geometry-optimized DOX-serotonin clusters extracted from DFT computations at the M06-2X/6-311G(d,p) level. According to these lowest energy geometries, it is evident that different DOX functional groups, including hydroxyl (-OH), carbonyl (-C=O), and amine (-NH<sub>2</sub>), were involved in intermolecular hydrogen bonding interactions with the hydroxyl and primary amine groups of serotonin. This theoretical outcome substantiates the central role of hydrogen bonding interactions in DOX adhesion to polyserotonin nanoparticle surfaces. Furthermore, it can be seen that in one of the hybrid clusters, the aromatic backbone of serotonin is aligned with a parallel orientation relative to the aromatic heterocycles of DOX, implying the presence of  $\pi$ - $\pi$  interactions between DOX and serotonin.

In addition to visualized interactions, the DOX-serotonin binding affinity was probed quantitatively by computing the binding energy term ( $\Delta E_{binding}$ ), expressed as follows:  $\Delta E_{binding} = E_{cluster} - (E_{DOX} + E_{serotonin})$ . In this expression,  $E_{cluster}$  is the potential energy of the optimized DOX-serotonin clusters, and  $E_{DOX}$  and  $E_{serotonin}$  represent the potential energies of the isolated DOX and serotonin molecules respectively. The computed  $\Delta E_{binding}$  for all hybrid clusters, as well as the binding energies determined from the B3LYP/6-311(d,p) theory level are presented in Figure IX.6A. All  $\Delta E_{binding}$  energies were found to be negative, which validates DOX-serotonin interactions.



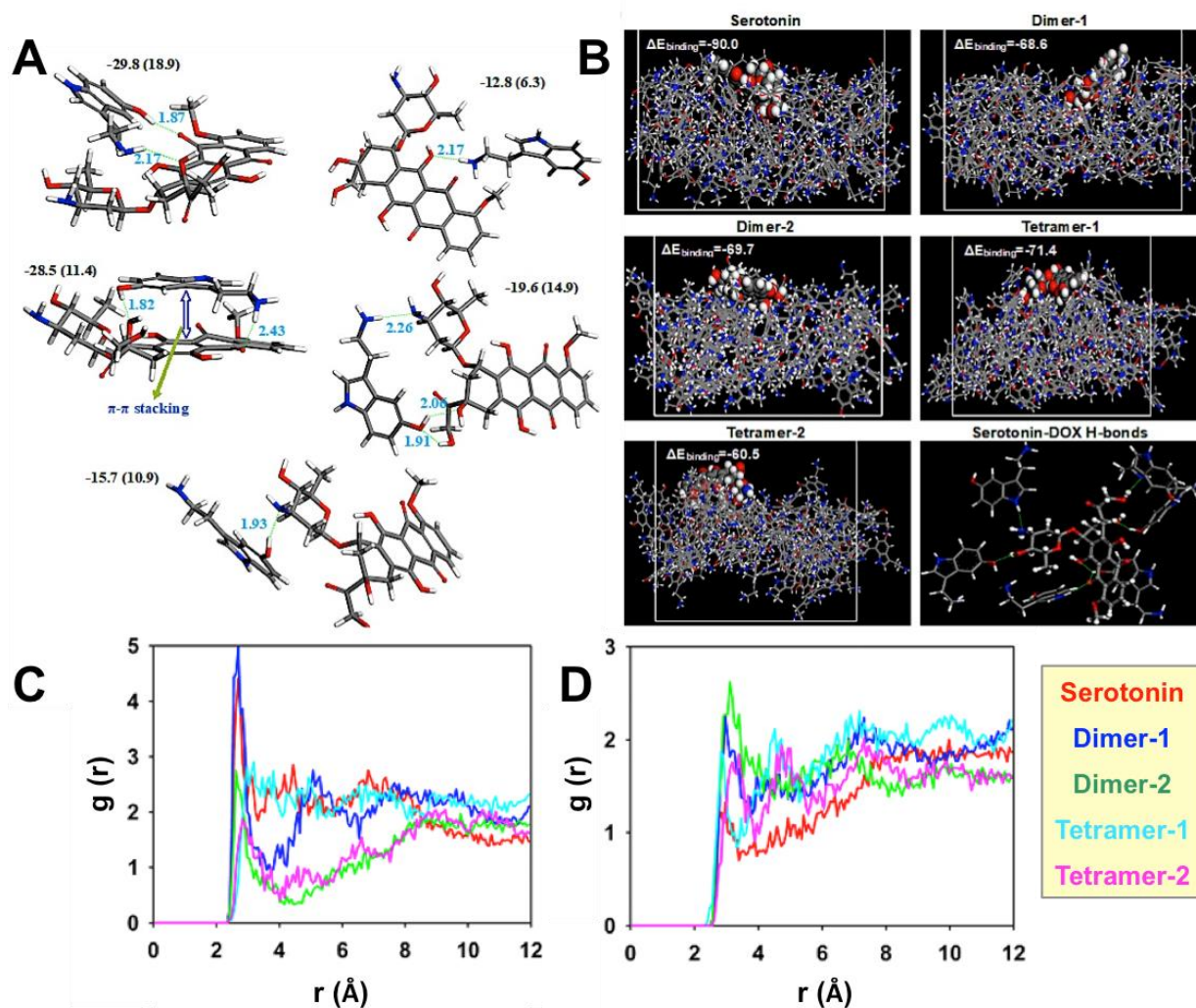


**Figure IX.6.** Investigation of molecular interactions between serotonin-based clusters and the drug molecule, doxorubicin (DOX). **(A)** The DFT/M06-2X/6-311G(d,p) optimized geometries of different DOX-serotonin clusters. The hydrogen-bonds are shown as green dashed line and their lengths are in angstroms (Å). The computed binding energies are in kcal/mol. The data in parentheses indicate the binding energies derived from DFT/B3LYP/6-311G(d,p) theory level. **(B)** The side views of final snapshots of a DOX molecule on the surface of monomeric serotonin and its two dimers and two tetramers were obtained from molecular dynamic simulations. The DOX molecule is displayed in CPK style. The hydrogen-bonding interactions of surface-bound DOX with serotonin molecules are shown as green dashed line. Radial distribution functions of oxygen atoms in DOX with **(C)** oxygen and **(D)** nitrogen atoms in serotonin and its two dimers and two tetramers are shown.

To examine the adsorption tendency of DOX to the serotonin clusters, atomistic MD simulations were also performed. Figure IX.6B visualizes the final structures of DOX over the surfaces of serotonin and its dimers and tetramers, which were obtained from the last step of the MD simulations. When these snapshots were compared with corresponding

initial cells (Figure SG.1), it was noted that the DOX distance relative to all serotonin substrates was significantly reduced, which suggests the tendency of DOX molecules to adsorb on all of the investigated surfaces. Adsorption of DOX on serotonin and serotonin cluster (dimer and tetramer) surfaces was also confirmed by the computed negative binding energy values, as listed in the Figure IX.6B. Based on the  $\Delta E_{binding}$  data, the strongest adhesion occurred over the serotonin surface, and the adhesion level of DOX bound to the serotonin dimers and tetramers were in the same level. To gain in-depth insight into DOX interaction behavior at the interface, the simulation snapshot for the serotonin surface was further inspected and the results are displayed in Figure IX.6. From this closer examination, it was observed that the serotonin molecules surrounding the DOX contributed to hydrogen bonding interactions, which, in line with the QM results, further point to the major role of hydrogen bonding interactions upon DOX adsorption on serotonin and polyserotonin surfaces.

Radial distribution functions (RDFs, also called pair correlation functions  $g(r)$ ) were analyzed<sup>85</sup> to understand DOX interactions with polyserotonin nanoparticle surfaces. The RDF analysis was done for oxygen atoms in DOX with regards to oxygen and nitrogen heteroatoms in serotonin monomers, dimers, and tetramers (Figure IX.6C,D). As shown in Figure IX.6C, the RDFs of DOX oxygen atoms towards the serotonin monomer, dimer, and tetramer O atoms showed a heightened first peak, particularly for the serotonin and dimer-1 at 2.62-2.97 Å. These peak positions are within the distances required for hydrogen-bonding interactions<sup>85</sup> between oxygenated sites in DOX and serotonin species.

Similarly, the DOX O atom RDFs relative to nitrogen atoms of serotonin and its dimers and tetramers possessed a high peak but of lower intensity at larger distances. As a

result, the oxygenated DOX fragments are also involved in interfacial H-bonds with nitrogenous groups of serotonin-based species. These RDF results are in agreement with geometry-optimized DOX-serotonin clusters achieved from QM computations. Visualized MD snapshots further suggest DOX loading on polyserotonin nanoparticle surfaces through H-bonding interactions.

The theoretical computations that propose that H-bonding interactions are the primary mechanism of DOX loading, rationalize differences in the rates of DOX release from the polyserotonin nanoparticles at lower pH values mimicking tumor and intracellular lysosomal microenvironments (pH 6.5 and 5.5, respectively). Disruption of hydrogen bonding networks at acidic pH may be the cause behind faster drug release, advantageous for targeted delivery of DOX.<sup>86</sup> Investigating molecular interactions between available surface functional groups of polyserotonin nanoparticles and drug molecules such as DOX, will determine what classes of drugs can be loaded on the polyserotonin nanoparticle surfaces for targeted drug delivery applications.

#### **IX.D. Conclusions and Prospects**

Polyserotonin nanoparticles were discovered as a new multifunctional nanomaterial with potential for combined photothermal and chemotherapy in cancer treatment. Therapeutic properties of polyserotonin nanoparticles, such as drug loading efficiency and photothermal capabilities, are comparable in some aspects to PDA-based nanoparticles. However, by conducting protein corona measurements to investigate the nano-bio interface of polyserotonin nanoparticles with serum proteins, we observed significantly reduced (~80%) overall protein adsorption compared to PDA-based nanoparticles after functionalizing the surface of polyserotonin nanoparticles with poly(ethylene) glycol molecules. In particular, the adsorption of immune triggering serum proteins such as fibrinogen was significantly reduced. Further, polyserotonin nanoparticles showed improved biocompatibilities with three stem cell lines over longer time periods. These are critical properties making small-molecule polymerized nanoparticles viable candidates as novel cancer therapeutics and suggesting the potential of polyserotonin nanoparticles for future clinical applications.

## **APPENDIX G**

# **Polyserotonin Nanoparticles as Multifunctional Nanomaterials for Biomedical Applications**

## **Supplementary Information**

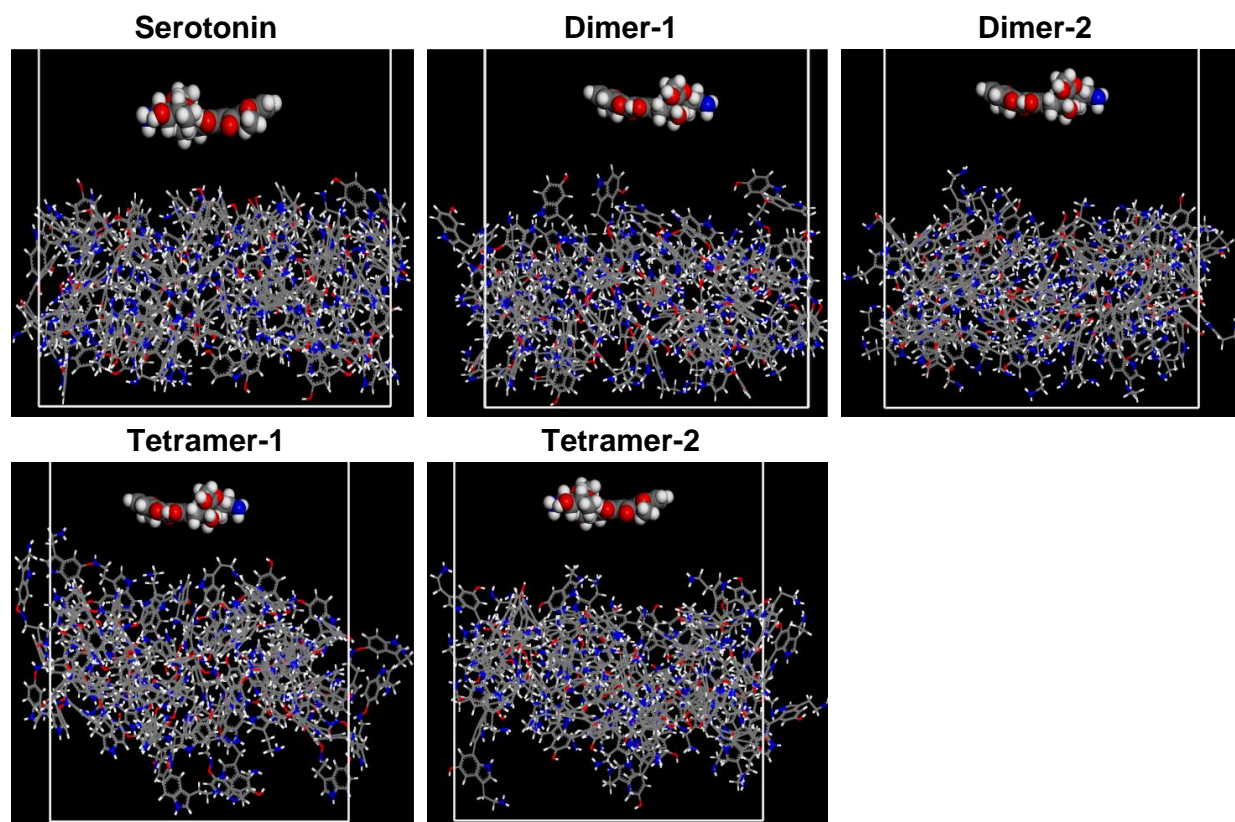


**Figure SG.1.** The side views of initial snapshots of doxorubicin over surfaces of serotonin and its two dimers and two tetramers. The doxorubicin molecule is shown in CPK style. The atomic color code is: carbon gray, oxygen red, hydrogen white, and nitrogen blue.

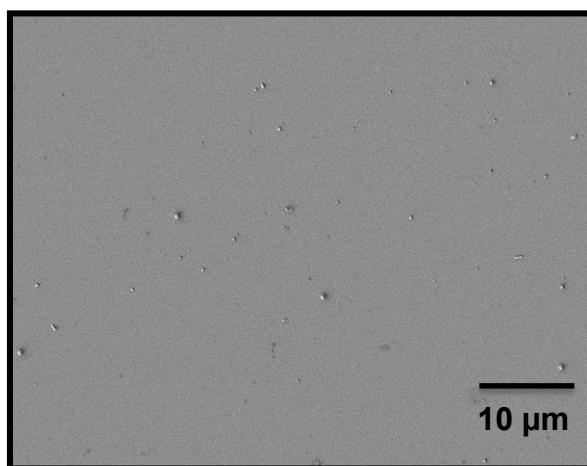


**Figure SG.2.** Scanning electron microscope image of serotonin hydrochloride incubated in acidic buffer (pH 6.5) to hinder polymerization. Lack of serotonin nanoparticle formation was confirmed after five days.

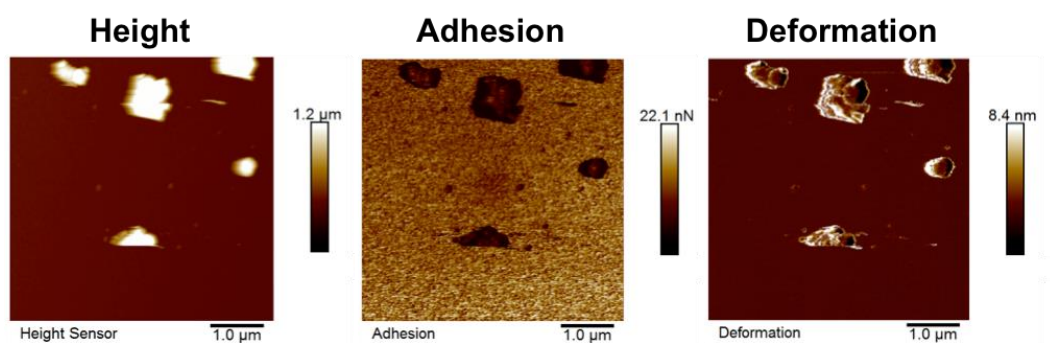


**Figure SG.3.** Atomic force microscopy images of polymerized dopamine for comparison of adhesive properties with serotonin nanoparticles.



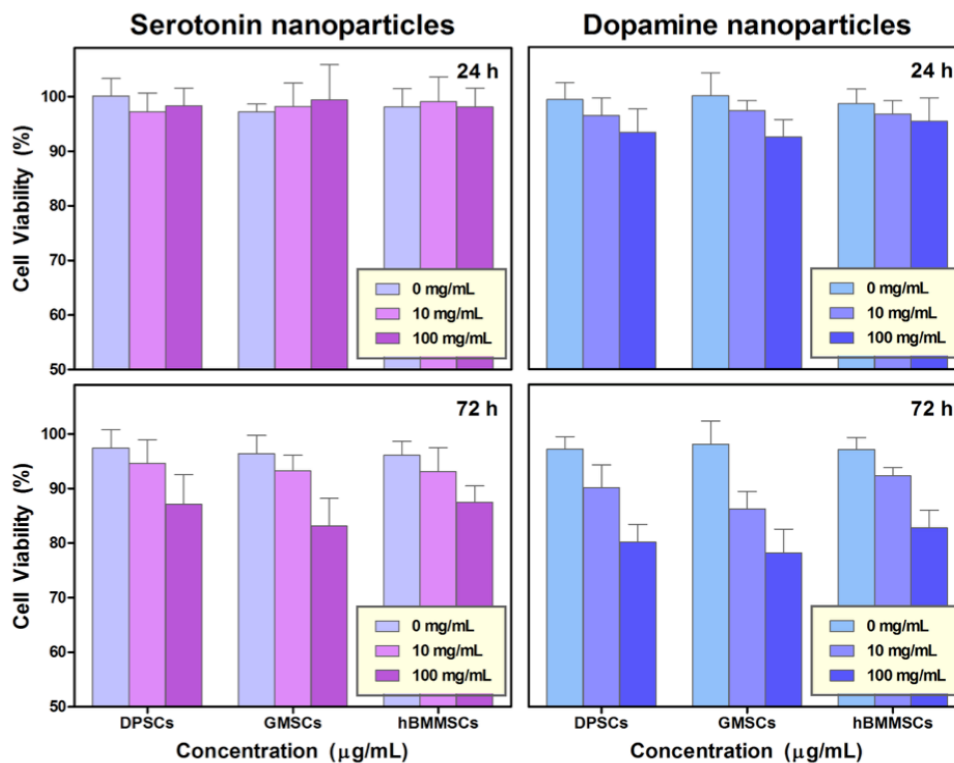


**Figure SG.4.** Cellular viability of human bone-marrow mesenchymal stem cell, (hBMMSCs), gingival-derived mesenchymal stem cell (GMSCs), human dental pulp stem cells (DPSCs) after incubation with two concentrations of serotonin- (**left**) and dopamine- (**right**) based nanoparticles after 24 h (**upper panels**) and 72 h (**lower panels**).

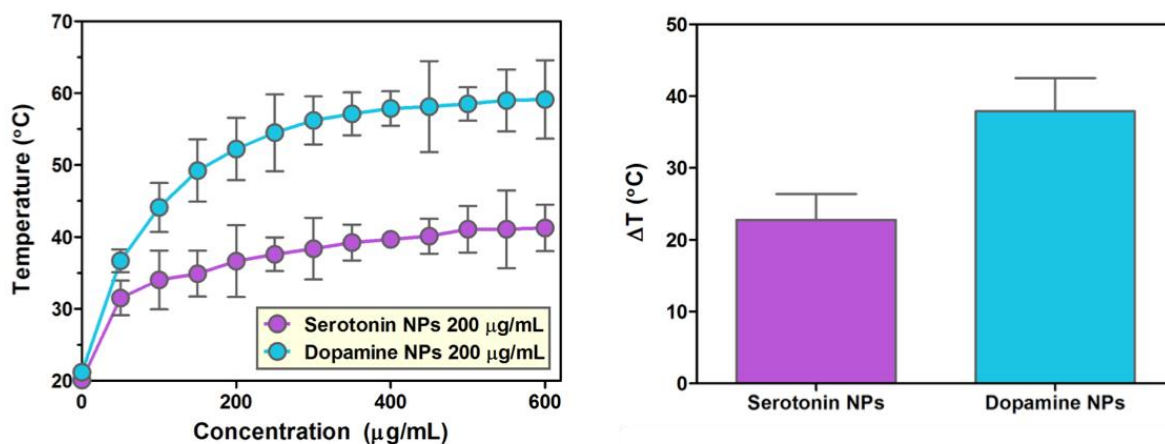


**Figure SG.5.** *In vial* heat generation in PBS suspensions containing PST and PDA nanoparticles at 200  $\mu\text{g}\cdot\text{mL}^{-1}$  after NIR-irradiation (808-nm laser; 3  $\text{W}\cdot\text{cm}^{-2}$ ) for 10 min. (Left) Temperature change ( $\Delta T$ ) over a period of 10 min for PST and PDA-based nanoparticles after NIR-irradiation at constant concentration of 200  $\mu\text{g}\cdot\text{mL}^{-1}$  (Right).

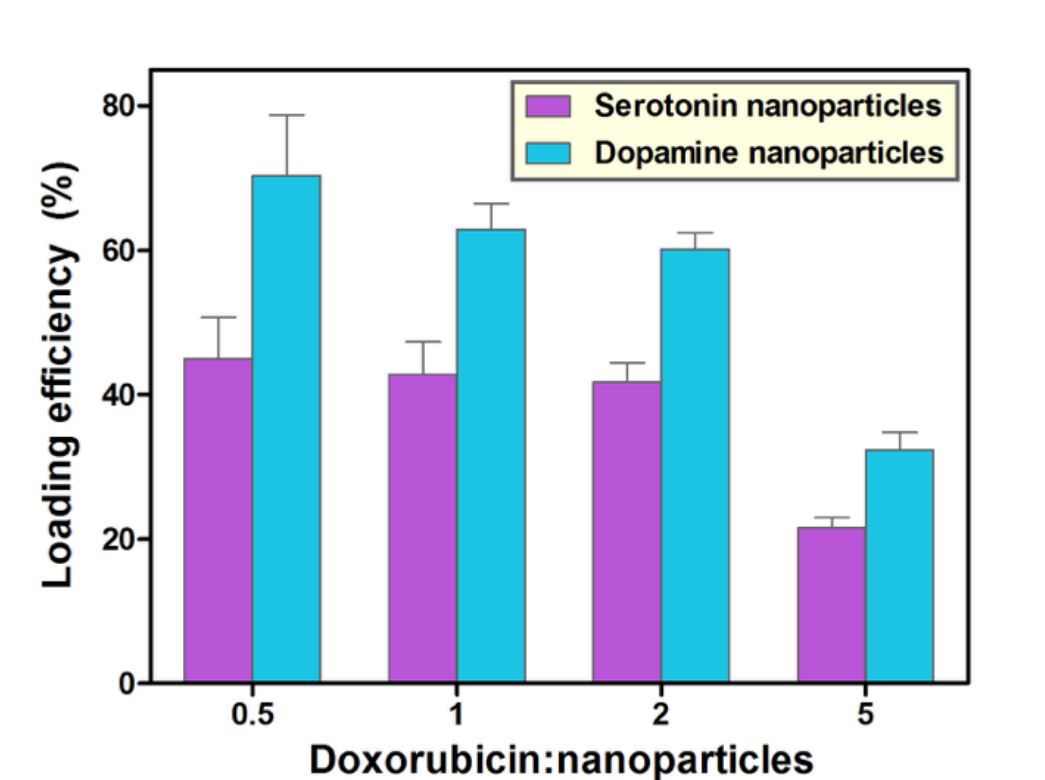


**Figure SG.6.** Loading efficiently of Doxorubicin on surface of PST and PDA nanoparticles at different initial drug contents.

## References

1. Ritz, S.; Schottler, S.; Kotman, N.; Baier, G.; Musyanovych, A.; Kuharev, J.; Landfester, K.; Schild, H.; Jahn, O.; Tenzer, S.; Mailander, V. Protein Corona of Nanoparticles: Distinct Proteins Regulate the Cellular Uptake. *Biomacromolecules* **2015**, *16*, 1311-1321.
2. Walczyk, D.; Bombelli, F. B.; Monopoli, M. P.; Lynch, I.; Dawson, K. A. What the Cell "Sees" in Bionanoscience. *J. Am. Chem. Soc.* **2010**, *132*, 5761-5768.
3. Cedervall, T.; Lynch, I.; Lindman, S.; Berggard, T.; Thulin, E.; Nilsson, H.; Dawson, K. A.; Linse, S. Understanding the Nanoparticle-Protein Corona Using Methods to Quantify Exchange Rates and Affinities of Proteins for Nanoparticles. *P. Natl. Acad. Sci. U.S.A.* **2007**, *104*, 2050-2055.
4. Tenzer, S.; Docter, D.; Kuharev, J.; Musyanovych, A.; Fetz, V.; Hecht, R.; Schlenk, F.; Fischer, D.; Kiouptsi, K.; Reinhardt, C.; Landfester, K.; Schild, H.; Maskos, M.; Knauer, S. K.; Stauber, R. H. Rapid Formation of Plasma Protein Corona Critically Affects Nanoparticle Pathophysiology. *Nat. Nanotechnol.* **2013**, *8*, 772-781.
5. Rocker, C.; Potzl, M.; Zhang, F.; Parak, W. J.; Nienhaus, G. U. A Quantitative Fluorescence Study of Protein Monolayer Formation on Colloidal Nanoparticles. *Nat. Nanotechnol.* **2009**, *4*, 577-580.
6. Kim, J. A.; Salvati, A.; Aberg, C.; Dawson, K. A. Suppression of Nanoparticle Cytotoxicity Approaching *in Vivo* Serum Concentrations: Limitations of *in Vitro* Testing for Nanosafety. *Nanoscale* **2014**, *6*, 14180-14184.
7. Saha, K.; Moyano, D. F.; Rotello, V. M. Protein Coronas Suppress the Hemolytic Activity of Hydrophilic and Hydrophobic Nanoparticles. *Mater. Horizons* **2014**, *1*, 102-105.
8. Walkey, C. D.; Chan, W. C. W. Understanding and Controlling the Interaction of Nanomaterials with Proteins in a Physiological Environment. *Chem Soc. Rev.* **2012**, *41*, 2780-2799.
9. Hellstrand, E.; Lynch, I.; Andersson, A.; Drakenberg, T.; Dahlback, B.; Dawson, K. A.; Linse, S.; Cedervall, T. Complete High-Density Lipoproteins in Nanoparticle Corona. *FEBS J.* **2009**, *276*, 3372-3381.
10. Fleischer, C. C.; Payne, C. K. Nanoparticle-Cell Interactions: Molecular Structure of the Protein Corona and Cellular Outcomes. *Acc. Chem. Res.* **2014**, *47*, 2651-2659.
11. Fleischer, C. C.; Payne, C. K. Secondary Structure of Corona Proteins Determines the Cell Surface Receptors Used by Nanoparticles. *J. Phys. Chem. B* **2014**, *118*, 14017-14026.

12. Kah, J. C. Y.; Chen, J.; Zubietta, A.; Hamad-Schifferli, K. Exploiting the Protein Corona around Gold Nanorods for Loading and Triggered Release. *ACS Nano* **2012**, *6*, 6730-6740.
13. Cifuentes-Rius, A.; de Puig, H.; Kah, J. C. Y.; Borros, S.; Hamad-Schifferli, K. Optimizing the Properties of the Protein Corona Surrounding Nanoparticles for Tuning Payload Release. *ACS Nano* **2013**, *7*, 10066-10074.
14. Walkey, C. D.; Olsen, J. B.; Song, F. Y.; Liu, R.; Guo, H. B.; Olsen, D. W. H.; Cohen, Y.; Emili, A.; Chan, W. C. W. Protein Corona Fingerprinting Predicts the Cellular Interaction of Gold and Silver Nanoparticles. *ACS Nano* **2014**, *8*, 2439-2455.
15. Lee, H.; Dellatore, S. M.; Miller, W. M.; Messersmith, P. B. Mussel-Inspired Surface Chemistry for Multifunctional Coatings. *Science* **2007**, *318*, 426-430.
16. Ho, C. C.; Ding, S. J. The pH-Controlled Nanoparticles Size of Polydopamine for Anti-Cancer Drug Delivery. *J. Mater. Sci.* **2013**, *24*, 2381-2390.
17. Liu, R.; Guo, Y. L.; Odusote, G.; Qu, F. L.; Priestley, R. D. Core-Shell Fe<sub>3</sub>O<sub>4</sub> Polydopamine Nanoparticles Serve Multipurpose as Drug Carrier, Catalyst Support and Carbon Adsorbent. *ACS Appl. Mater. Inter.* **2013**, *5*, 9167-9171.
18. Zhong, X. Y.; Yang, K.; Dong, Z. L.; Yi, X.; Wang, Y.; Ge, C. C.; Zhao, Y. L.; Liu, Z. Polydopamine as a Biocompatible Multifunctional Nanocarrier for Combined Radioisotope Therapy and Chemotherapy of Cancer. *Adv. Funct. Mater.* **2015**, *25*, 7327-7336.
19. Dong, Z. L.; Gong, H.; Gao, M.; Zhu, W. W.; Sun, X. Q.; Feng, L. Z.; Fu, T. T.; Li, Y. G.; Liu, Z. Polydopamine Nanoparticles as a Versatile Molecular Loading Platform to Enable Imaging-Guided Cancer Combination Therapy. *Theranostics* **2016**, *6*, 1031-1042.
20. Liu, Y. L.; Ai, K. L.; Liu, J. H.; Deng, M.; He, Y. Y.; Lu, L. H. Dopamine-Melanin Colloidal Nanospheres: An Efficient near-Infrared Photothermal Therapeutic Agent for *in Vivo* Cancer Therapy. *Adv. Mater.* **2013**, *25*, 1353-1359.
21. Sasikala, A. R. K.; GhavamiNejad, A.; Unnithan, A. R.; Thomas, R. G.; Moon, M.; Jeong, Y. Y.; Park, C. H.; Kim, C. S. A Smart Magnetic Nanoplatfrom for Synergistic Anticancer Therapy: Manoeuvring Mussel-Inspired Functional Magnetic Nanoparticles for pH Responsive Anticancer Drug Delivery and Hyperthermia. *Nanoscale* **2015**, *7*, 18119-18128.
22. Cong, Y.; Xia, T.; Zou, M.; Li, Z. N.; Peng, B.; Guo, D. Z.; Deng, Z. W. Mussel-Inspired Polydopamine Coating as a Versatile Platform for Synthesizing Polystyrene/Ag Nanocomposite Particles with Enhanced Antibacterial Activities. *J. Mater. Chem. B* **2014**, *2*, 3450-3461.

23. Lu, Z. S.; Xiao, J.; Wang, Y.; Meng, M. *In Situ* Synthesis of Silver Nanoparticles Uniformly Distributed on Polydopamine-Coated Silk Fibers for Antibacterial Application. *J. Colloid Interf. Sci.* **2015**, *452*, 8-14.
24. Ko, E.; Yang, K.; Shin, J.; Cho, S. W. Polydopamine-Assisted Osteoinductive Peptide Immobilization of Polymer Scaffolds for Enhanced Bone Regeneration by Human Adipose-Derived Stem Cells. *Biomacromolecules* **2013**, *14*, 3202-3213.
25. Luo, R. F.; Tang, L. L.; Zhong, S.; Yang, Z. L.; Wang, J.; Weng, Y. J.; Tu, Q. F.; Jiang, C. X.; Huang, N. *In Vitro* Investigation of Enhanced Hemocompatibility and Endothelial Cell Proliferation Associated with Quinone-Rich Polydopamine Coating. *ACS Appl. Mater. Inter.* **2013**, *5*, 1704-1714.
26. Gao, X.; Song, J. L.; Ji, P.; Zhang, X. H.; Li, X. M.; Xu, X.; Wang, M. K.; Zhang, S. Q.; Deng, Y.; Deng, F.; Wei, S. C. Polydopamine-Templated Hydroxyapatite Reinforced Polycaprolactone Composite Nanofibers with Enhanced Cytocompatibility and Osteogenesis for Bone Tissue Engineering. *ACS Appl. Mater. Inter.* **2016**, *8*, 3499-3515.
27. Chien, H. W.; Tsai, W. B. Fabrication of Tunable Micropatterned Substrates for Cell Patterning *via* Microcontact Printing of Polydopamine with Poly(Ethylene Imine)-Grafted Copolymers. *Acta Biomater.* **2012**, *8*, 3678-3686.
28. Sun, K.; Xie, Y. Y.; Ye, D. K.; Zhao, Y. Y.; Cui, Y.; Long, F.; Zhang, W.; Jiang, X. Y. Mussel-Inspired Anchoring for Patterning Cells Using Polydopamine. *Langmuir* **2012**, *28*, 2131-2136.
29. Caracciolo, G.; Farokhzad, O. C.; Mahmoudi, M. Biological Identity of Nanoparticles *in Vivo*: Clinical Implications of the Protein Corona. *Trends Biotechnol.* **2017**, *35*, 257-264.
30. Lynge, M. E.; van der Westen, R.; Postma, A.; Stadler, B. Polydopamine - A Nature-Inspired Polymer Coating for Biomedical Science. *Nanoscale* **2011**, *3*, 4916-4928.
31. Wang, X. Y.; Zhang, J. S.; Wang, Y. T.; Wang, C. P.; Xiao, J. R.; Zhang, Q.; Cheng, Y. Y. Multi-Responsive Photothermal-Chemotherapy with Drug-Loaded Melanin-Like Nanoparticles for Synergetic Tumor Ablation. *Biomaterials* **2016**, *81*, 114-124.
32. Li, W. Q.; Wang, Z. G.; Hao, S. J.; He, H. Z.; Wan, Y.; Zhu, C. D.; Sun, L. P.; Cheng, G.; Zheng, S. Y. Mitochondria-Targeting Polydopamine Nanoparticles to Deliver Doxorubicin for Overcoming Drug Resistance. *ACS Appl. Mater. Inter.* **2017**, *9*, 16794-16803.
33. Liebscher, J.; Mrowczynski, R.; Scheidt, H. A.; Filip, C.; Hadade, N. D.; Turcu, R.; Bende, A.; Beck, S. Structure of Polydopamine: A Never-Ending Story? *Langmuir* **2013**, *29*, 10539-10548.

34. Seo, B.-M.; Miura, M.; Gronthos, S.; Bartold, P. M.; Batouli, S.; Brahimi, J.; Young, M.; Robey, P. G.; Wang, C. Y.; Shi, S. Investigation of Multipotent Postnatal Stem Cells from Human Periodontal Ligament. *The Lancet* **2004**, *364*, 149-155.
35. Gronthos, S.; Mankani, M.; Brahimi, J.; Robey, P. G.; Shi, S. Postnatal Human Dental Pulp Stem Cells (DPSCs) *in Vitro* and *in Vivo*. *Proc. Natl. Acad. Sci. U. S. A.* **2000**, *97*, 13625-13630.
36. Schöttler, S.; Becker, G.; Winzen, S.; Steinbach, T.; Mohr, K.; Landfester, K.; Mailänder, V.; Wurm, F. R. Protein Adsorption Is Required for Stealth Effect of Poly(Ethylene Glycol)- and Poly(Phosphoester)-Coated Nanocarriers. *Nat. Nanotechnol.* **2016**, *11*, 372-377.
37. Palchetti, S.; Colapicchioni, V.; Digiacomo, L.; Caracciolo, G.; Pozzi, D.; Capriotti, A. L.; La Barbera, G.; Laganà, A. The Protein Corona of Circulating PEGylated Liposomes. *Biochim. Biophys. Acta* **2016**, *1858*, 189-196.
38. Tenzer, S.; Docter, D.; Rosfa, S.; Wlodarski, A.; Kuharev, J.; Rekić, A.; Knauer, S. K.; Bantz, C.; Nawroth, T.; Bier, C.; Sirirattanapan, J.; Mann, W.; Treuel, L.; Zellner, R.; Maskos, M.; Schild, H.; Stauber, R. H. Nanoparticle Size Is a Critical Physicochemical Determinant of the Human Blood Plasma Corona: A Comprehensive Quantitative Proteomic Analysis. *ACS Nano* **2011**, *5*, 7155-7167.
39. Zhao, Y.; Schultz, N. E.; Truhlar, D. G. Design of Density Functionals by Combining the Method of Constraint Satisfaction with Parametrization for Thermochemistry, Thermochemical Kinetics, and Noncovalent Interactions. *J. Chem. Theory Comput.* **2006**, *2*, 364-382.
40. Becke, A. D. Density-Functional Thermochemistry. III. The Role of Exact Exchange. *J. Chem. Phys.* **1993**, *98*, 5648-5652.
41. Lee, C.; Yang, W.; Parr, R. G. Development of the Colle-Salvetti Correlation-Energy Formula into a Functional of the Electron Density. *Phys. Rev. B* **1988**, *37*, 785-789.
42. McLean, A. D.; Chandler, G. S. Contracted Gaussian Basis Sets for Molecular Calculations. I. Second Row Atoms, Z=11-18. *J. Chem. Phys.* **1980**, *72*, 5639-5648.
43. Breneman, C. M.; Wiberg, K. B. Determining Atom-Centered Monopoles from Molecular Electrostatic Potentials. The Need for High Sampling Density in Formamide Conformational Analysis. *J. Comput. Chem.* **1990**, *11*, 361-373.
44. Frisch, M.; Trucks, G.; Schlegel, H. B.; Scuseria, G.; Robb, M.; Cheeseman, J.; Scalmani, G.; Barone, V.; Mennucci, B.; Petersson, G.; Gaussian, Inc., Wallingford CT: 2009.
45. Accelrys Software Inc., S. D., 2009.

46. Sun, H. Compass: An Ab Initio Force-Field Optimized for Condensed-Phase Applications Overview with Details on Alkane and Benzene Compounds. *J. Phys. Chem. B* **1998**, *102*, 7338-7364.
47. Sun, H.; Ren, P.; Fried, J. The Compass Force Field: Parameterization and Validation for Phosphazenes. *Comput. Theor. Polym. Sci.* **1998**, *8*, 229-246.
48. Swope, W. C.; Andersen, H. C.; Berens, P. H.; Wilson, K. R. A Computer Simulation Method for the Calculation of Equilibrium Constants for the Formation of Physical Clusters of Molecules: Application to Small Water Clusters. *J. Chem. Phys.* **1982**, *76*, 637-649.
49. Zangmeister, R. A.; Morris, T. A.; Tarlov, M. J. Characterization of Polydopamine Thin Films Deposited at Short Times by Autoxidation of Dopamine. *Langmuir* **2013**, *29*, 8619-8628.
50. Mazario, E.; Sanchez-Marcos, J.; Menendez, N.; Herrasti, P.; Garcia-Hernandez, M.; Munoz-Bonilla, A. One-Pot Electrochemical Synthesis of Polydopamine Coated Magnetite Nanoparticles. *RSC Adv.* **2014**, *4*, 48353-48361.
51. Nobbmann, U.; Morfesis, A. Light Scattering and Nanoparticles. *Mater. Today* **2009**, *12*, 52-54.
52. Pratuangdejkul, J.; Nosoongnoen, W.; Guerin, G. A.; Loric, S.; Conti, M.; Launay, J. M.; Manivet, P. Conformational Dependence of Serotonin Theoretical pK<sub>a</sub> Prediction. *Chem. Phys. Lett.* **2006**, *420*, 538-544.
53. Rudnick, G.; Kirk, K. L.; Fishkes, H.; Schuldiner, S. Zwitterionic and Anionic Forms of a Serotonin Analog as Transport Substrates. *J. Biol. Chem.* **1989**, *264*, 14865-14868.
54. Bernsmann, F.; Frisch, B.; Ringwald, C.; Ball, V. Protein Adsorption on Dopamine-Melanin Films: Role of Electrostatic Interactions Inferred from Zeta-Potential Measurements versus Chemisorption. *J. Colloid Interf. Sci.* **2010**, *344*, 54-60.
55. Li, Y. X.; Li, J.; Shangguan, E.; Li, Q. M. The Effect of Acidity, Hydrogen Bond Catalysis and Auxiliary Electrode Reaction on the Oxidation Peak Current for Dopamine, Uric Acid and Tryptophan. *Anal. Methods* **2015**, *7*, 2636-2644.
56. Bernsmann, F.; Ponche, A.; Ringwald, C.; Hemmerle, J.; Raya, J.; Bechinger, B.; Voegel, J. C.; Schaaf, P.; Ball, V. Characterization of Dopamine-Melanin Growth on Silicon Oxide. *J. Phys. Chem. C* **2009**, *113*, 8234-8242.
57. Szpoganicz, B.; Gidanian, S.; Kong, P.; Farmer, P. Metal Binding by Melanins: Studies of Colloidal Dihydroxyindole-Melanin, and Its Complexation by Cu(II) and Zn(II) Ions. *J. Inorg. Biochem.* **2002**, *89*, 45-53.



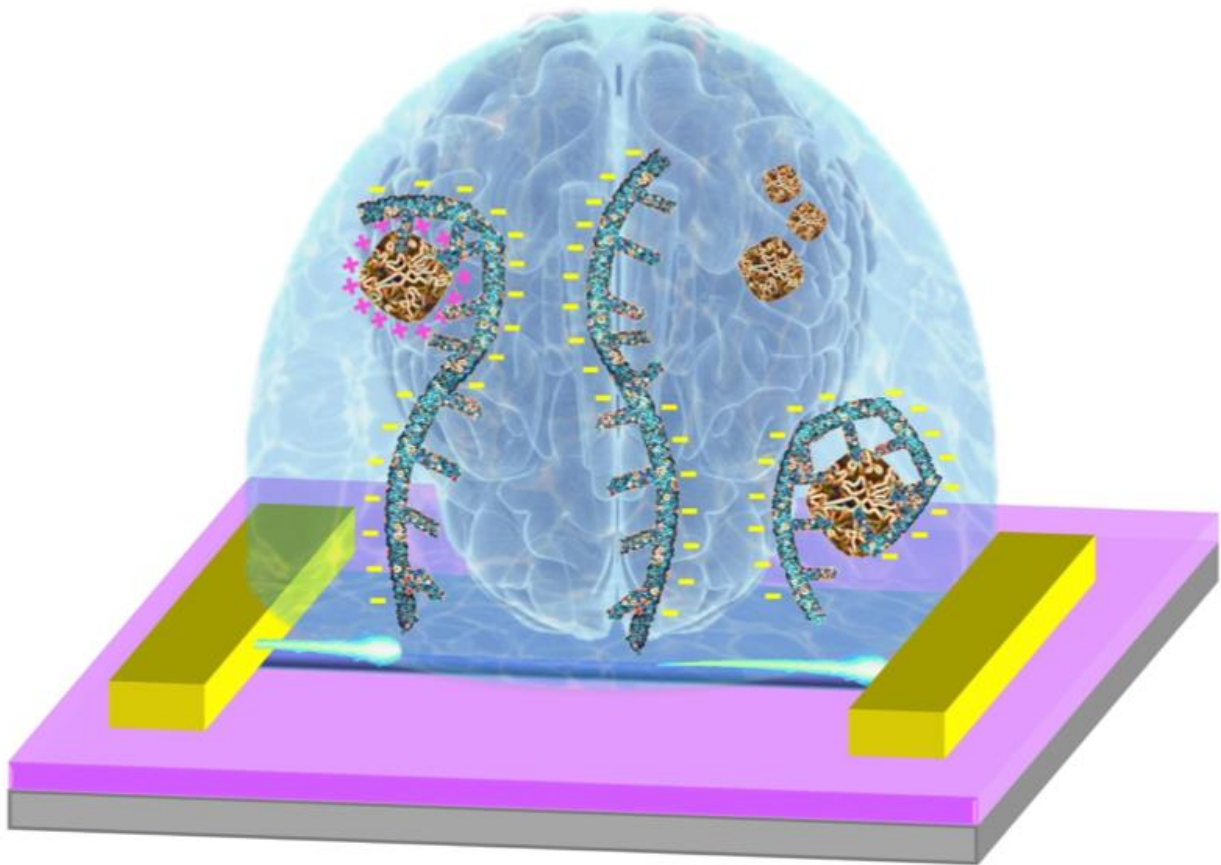
58. Han, X. F.; Zhang, L.; Li, C. Z. Preparation of Polydopamine-Functionalized Graphene-Fe<sub>3</sub>O<sub>4</sub> Magnetic Composites with High Adsorption Capacities. *RSC Adv.* **2014**, *4*, 30536-30541.
59. Noel, S.; Liberelle, B.; Robitaille, L.; De Crescenzo, G. Quantification of Primary Amine Groups Available for Subsequent Biofunctionalization of Polymer Surfaces. *Bioconjugate Chem.* **2011**, *22*, 1690-1699.
60. Chambrion, P.; Suzuki, T.; Zhang, Z. G.; Kyotani, T.; Tomita, A. XPS of Nitrogen-Containing Functional Groups Formed During the C-NO Reaction. *Energ. Fuel* **1997**, *11*, 681-685.
61. Hadjidemetriou, M.; Kostarelos, K. Nanomedicine Evolution of the Nanoparticle Corona. *Nat. Nanotechnol.* **2017**, *12*, 288-290.
62. Pelaz, B.; del Pino, P.; Maffre, P.; Hartmann, R.; Gallego, M.; Rivera-Fernandez, S.; de la Fuente, J. M.; Nienhaus, G. U.; Parak, W. J. Surface Functionalization of Nanoparticles with Polyethylene Glycol: Effects on Protein Adsorption and Cellular Uptake. *ACS Nano* **2015**, *9*, 6996-7008.
63. Wang, H. X.; Shang, L.; Maffre, P.; Hohmann, S.; Kirschhofer, F.; Brenner-Weiss, G.; Nienhaus, G. U. The Nature of a Hard Protein Corona Forming on Quantum Dots Exposed to Human Blood Serum. *Small* **2016**, *12*, 5836-5844.
64. Walkey, C. D.; Chan, W. C. W. Understanding and Controlling the Interaction of Nanomaterials with Proteins in a Physiological Environment. *Chem. Soc. Rev.* **2012**, *41*, 2780-2799.
65. Horbett, T. A. Principles Underlying the Role of Adsorbed Plasma-Proteins in Blood Interactions with Foreign Materials. *Cardiovasc. Pathol.* **1993**, *2*, 137-148.
66. Lundqvist, M.; Stigler, J.; Elia, G.; Lynch, I.; Cedervall, T.; Dawson, K. A. Nanoparticle Size and Surface Properties Determine the Protein Corona with Possible Implications for Biological Impacts. *P. Natl. Acad. Sci. U.S.A.* **2008**, *105*, 14265-14270.
67. Lishko, V. K.; Podolnikova, N. P.; Yakubenko, V. P.; Yakovlev, S.; Medved, L.; Yadav, S. P.; Ugarova, T. P. Multiple Binding Sites in Fibrinogen for Integrin Alpha-M beta-2 (Mac-1). *J. Biol. Chem.* **2004**, *279*, 44897-44906.
68. Mariam, J.; Sivakami, S.; Dongre, P. M. Albumin Corona on Nanoparticles - A Strategic Approach in Drug Delivery. *Drug Deliv.* **2016**, *23*, 2668-2676.
69. Cifuentes-Rius, A.; de Puig, H.; Kah, J. C.; Borros, S.; Hamad-Schifferli, K. Optimizing the Properties of the Protein Corona Surrounding Nanoparticles for Tuning Payload Release. *ACS Nano* **2013**, *7*, 10066-10074.

70. Mortimer, G. M.; Butcher, N. J.; Musumeci, A. W.; Deng, Z. J.; Martin, D. J.; Minchin, R. F. Cryptic Epitopes of Albumin Determine Mononuclear Phagocyte System Clearance of Nanomaterials. *ACS Nano* **2014**, *8*, 3357-3366.
71. Rybak-Smith, M. J.; Sim, R. B. Complement Activation by Carbon Nanotubes. *Adv. Drug Deliv. Rev.* **2011**, *63*, 1031-1041.
72. Sim, R. B.; Tsiftoglou, S. A. Proteases of the Complement System. *Biochem. Soc. Trans.* **2004**, *32*, 21-27.
73. Mirshafiee, V.; Mahmoudi, M.; Lou, K.; Cheng, J.; Kraft, M. L. Protein Corona Significantly Reduces Active Targeting Yield. *Chem. Commun.* **2013**, *49*, 2557-2559.
74. Allen, T. M.; Hansen, C.; Martin, F.; Redemann, C.; Yau-Young, A. Liposomes Containing Synthetic Lipid Derivatives of Poly(Ethylene Glycol) Show Prolonged Circulation Half-Lives *in Vivo*. *Biochim. Biophys. Acta* **1991**, *1066*, 29-36.
75. Mahmoudi, M.; Lynch, I.; Ejtehadi, M. R.; Monopoli, M. P.; Bombelli, F. B.; Laurent, S. Protein–Nanoparticle Interactions: Opportunities and Challenges. *Chem. Rev.* **2011**, *111*, 5610-5637.
76. Goppert, T. M.; Muller, R. H. Adsorption Kinetics of Plasma Proteins on Solid Lipid Nanoparticles for Drug Targeting. *Int. J. Pharm.* **2005**, *302*, 172-186.
77. Aoyama, M.; Hata, K.; Higashisaka, K.; Nagano, K.; Yoshioka, Y.; Tsutsumi, Y. Clusterin in the Protein Corona Plays a Key Role in the Stealth Effect of Nanoparticles against Phagocytes. *Biochem. Biophys. Res. Commun.* **2016**, *480*, 690-695.
78. Lee, Y. K.; Choi, E. J.; Webster, T. J.; Kim, S. H.; Khang, D. Effect of the Protein Corona on Nanoparticles for Modulating Cytotoxicity and Immunotoxicity. *Int. J. Nanomedicine* **2015**, *10*, 97-113.
79. Yan, H.; Teh, C.; Sreejith, S.; Zhu, L. L.; Kwok, A.; Fang, W. Q.; Ma, X.; Nguyen, K. T.; Korzh, V.; Zhao, Y. L. Functional Mesoporous Silica Nanoparticles for Photothermal-Controlled Drug Delivery *in Vivo*. *Angew. Chem. Int. Edit.* **2012**, *51*, 8373-8377.
80. Song, G. S.; Liang, C.; Gong, H.; Li, M. F.; Zheng, X. C.; Cheng, L.; Yang, K.; Jiang, X. Q.; Liu, Z. Core-Shell MnSe@Bi<sub>2</sub>Se<sub>3</sub> Fabricated *via* a Cation Exchange Method as Novel Nanotheranostics for Multimodal Imaging and Synergistic Thermoradiotherapy. *Adv. Mater.* **2015**, *27*, 6110-6117.
81. Zou, L. L.; Wang, H.; He, B.; Zeng, L. J.; Tan, T.; Cao, H. Q.; He, X. Y.; Zhang, Z. W.; Guo, S. R.; Li, Y. P. Current Approaches of Photothermal Therapy in Treating Cancer Metastasis with Nanotherapeutics. *Theranostics* **2016**, *6*, 762-772.
82. Yang, F.; Teves, S. S.; Kemp, C. J.; Henikoff, S. Doxorubicin, DNA Torsion, and Chromatin Dynamics. *Biochim. Biophys. Acta* **2014**, *1845*, 84-89.

83. Mrowczynski, R.; Jurga-Stopa, J.; Markiewicz, R.; Coy, E. L.; Jurga, S.; Wozniak, A. Assessment of Polydopamine Coated Magnetic Nanoparticles in Doxorubicin Delivery. *RSC Adv.* **2016**, *6*, 5936-5943.
84. Li, C. Y.; Liu, Z. J.; Yao, P. Gold Nanoparticles Coated with a Polydopamine Layer and Dextran Brush Surface for Diagnosis and Highly Efficient Photothermal Therapy of Tumors. *RSC Adv.* **2016**, *6*, 33083-33091.
85. Bahlakeh, G.; Mahdi Hasani-Sadrabadi, M.; Jacob, K. I. Morphological and Transport Characteristics of Swollen Chitosan-Based Proton Exchange Membranes Studied by Molecular Modeling. *Biopolymers* **2017**, *107*, 5-19.
86. Bae, J. E.; Kim, I. J.; Nam, K. H. Disruption of the Hydrogen Bonding Network Determines the pH-Induced Non-Fluorescent State of the Fluorescent Protein ZsYellow by Protonation of Glu221. *Biochem. Biophys. Res. Commun.* **2017**, *493*, 562-567.

## Chapter X

### Implementing Aptamer–Field Effect Transistors *in Vivo* — Perspectives



## **X.A. Introduction**

My thesis work began with the overarching goal to develop, to fabricate, and to validate next-generation *in vivo* sensors for monitoring neurotransmitters to investigate central nervous system interneuronal signaling in the brain. Neurotransmitter sensing at the spatiotemporal resolution pertinent to intrinsically encoded information will transform our fundamental understanding of brain function. These breakthroughs will elucidate how neurotransmitter flux relate to complex behavior and brain disorders for discovering new treatments and prevention strategies. The biosensing I conducted by coupling serotonin and dopamine-specific aptamers to FET platforms showed excellent sensing characteristics, and I believe we are now on a strong path towards realizing *in vivo* neurochemical sensors based on aptamer-FETs.

Continuous, real-time tracking of neurotransmitters *in vivo* would enhance our capacity to detect, to monitor, and to devise treatment strategies in a patient-specific manner. To understand the connection between physiological processes, pharmacokinetics, and toxicology, aptamer-FET platforms will need to function in living animals (and humans) performing behavioral tasks. However, several challenges have impeded continuous *in vivo* monitoring of biomolecules. First, for continuous measurements, sensors cannot rely on batch processing that includes wash or separation steps.<sup>1</sup> Second, for *in vivo* measurements, sensors must remain stable under prolonged exposure to diverse, high-salt, complex matrices, such as urine or blood.<sup>2</sup> *In vivo* conditions can reduce specific binding of targets due to nonspecific adsorption of proteins, lipids, and cells.<sup>3,4</sup> Finally, under *in vivo*

conditions, sensors must achieve sufficient sensitivity, selectivity, and dynamic range over physiologically meaningful concentrations and time scales.<sup>5</sup>

With the aforementioned challenges that accompany continuous real-time monitoring of biomolecules in an environment as complex as the brain, answering the call of the BRAIN Initiative to revolutionize the next generation of neuroscience tools is an ambitious endeavor. While serotonin and dopamine sensing using macroscopic transistors in a milieu that mimic *in vivo* environments is highly promising, there are still many obstacles that we must overcome. The work presented here has built on over a decade of research conducted in our groups by many postdoctoral fellows and graduate students, myself included.

Our work began with a vision to isolate artificial receptors with enhanced selectivities and tunable binding affinities that could remain stable under physiological conditions for long periods of time. Our aim to discover artificial receptors in the form of aptamers inspired the birth of the “neurochip” project. At the time, neurochips were necessary to identify high-affinity neurotransmitter-specific aptamers, which did not exist due to shortcomings of conventional SELEX methods.<sup>6,7</sup> Many steps formed the foundation for the design rules we now employ. Our groups pioneered chemical patterning tools to enable multiplexed patterning of small molecules on planar substrates.<sup>8,9</sup> To design and to develop *functional* screening platforms, optimization of surface chemistries to tether small-molecule neurotransmitters to substrates while mimicking endogenous molecules in biological milieu was critical.<sup>10,11</sup>

Our collaboration with the Stojanović group at Columbia University, which provided us with novel high-affinity serotonin and dopamine aptamers, enabled me to apply what I had learned about surface chemistry optimization to functionalize novel aptamers onto the semiconducting surfaces of  $\text{In}_2\text{O}_3$  thin-film FETs. The current aim of this project involves the fabrication of miniaturized arrays with multiplexed aptamer-FET sensors on the surface of silicon microprobes to measure multiple analytes simultaneously *in vivo*. Multiplexed aptamer FETs have the potential for the comprehensive mapping of many signaling molecules that are released, taken-up, or degraded during brain activity. Future work will focus on targeting neurochemicals chosen to embody structural diversity as shown in Figure X.1. With the exception of dopamine, glutamate, and acetylcholine, there are no methods currently to measure these diverse neurochemical targets in real time, *in vivo*.

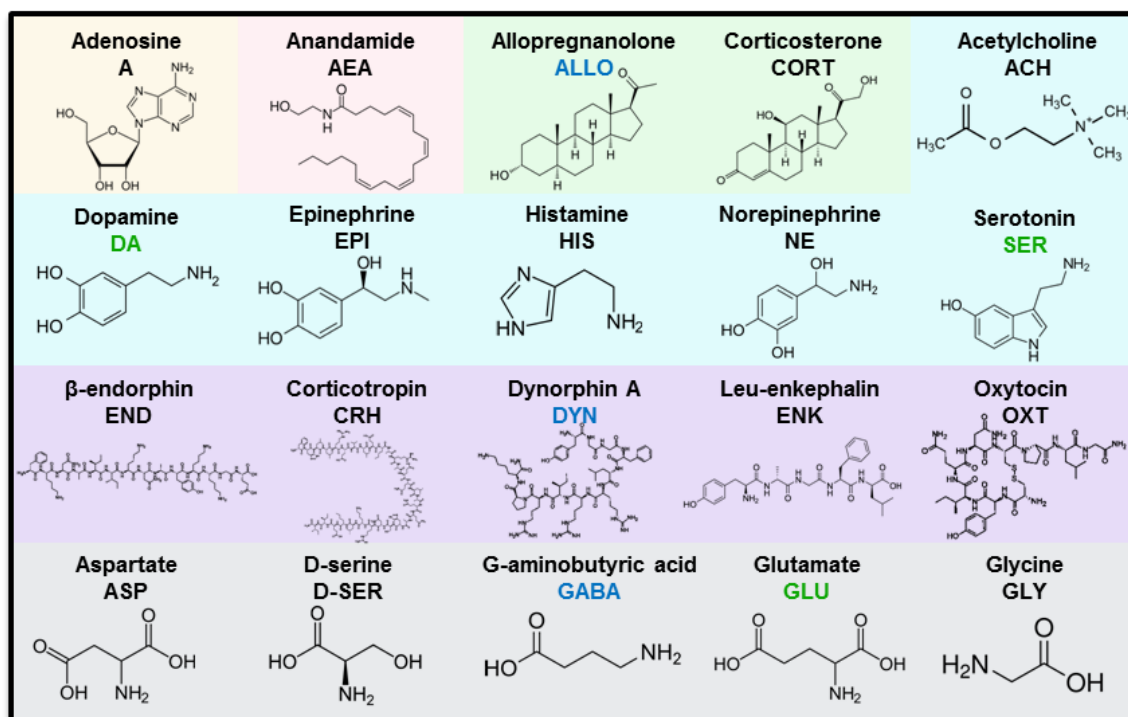


**Figure X.1.** Names, abbreviations, and structures for neurochemical targets. Chemical classes are nucleic acid (yellow), lipid (pink), steroid (green), aromatic amine (blue), peptide (purple), and amino acid (grey).

As an initial design, we imagine prototype, micron-scale aptamer-FET arrays coupled to implantable, micromachined, multi-electrode array (MEA) silicon microprobes designed by Wassum, Monbouquette, Maidment, and co-workers, with optimal spatiotemporal resolution (Figure X.2A).<sup>12-14</sup> Their enzyme-based silicon microprobes have been used to detect cortically evoked glutamate in ventral striatum in anesthetized rats<sup>14</sup> and stress-induced glutamate release in awake rats.<sup>13</sup> Multiplexing has been demonstrated by incorporating enzymatic glutamate electrodes and amperometric sensors for dopamine onto the same microprobe.<sup>15</sup>

Once we optimize the initial design with microscale FETs replacing planar metal electrodes previously used on the microprobes, our preliminary goal will be to obtain measurements from three aptamer-FETs on the surface of a microprobe



with one solid-state reference electrode (Figure X.2B). Two aptamer-FETs will be functionalized with target-specific aptamers, and one will be functionalized with a scrambled sequence as a background reference for the target-specific aptamer-FETs. Ultimately, we envision scaling up to ~100 aptamer-FET device arrays per probe, with which we anticipate sensing up to ten analytes simultaneously, each with their own self-reference controls. Device wiring from >1000 electrodes *via* external connections to electronics has already been demonstrated (Figure X.2C).<sup>16-18</sup>

Arrays of aptamer FETs on the surface of microprobes for *in vivo* measurements will complement other efforts to measure action potentials or intracellular  $\text{Ca}^{2+}$  concentrations, associated with synaptic signaling, from large numbers of neurons. Thus, aptamer-FET arrays will contribute to cumulative data, that will be computationally deciphered in expectation of uncovering emergent properties of information coding within neural circuitry.

I conclude by discussing the current state of aptamer *in vivo* demonstrations, which is promising for the realization of future aptamer-FET-array microprobes. Then, I will examine the challenges to translate aptamer-FETs for *in vivo* sensing. Device architectures must be first optimized in scaling down the dimensions of the transistors, as device performance depends on channel width and shape, electrode contact to the semiconducting channel, and passivation of electrode surfaces.<sup>19-21</sup>

To approach the spatiotemporal resolution needed to reveal information encoding, it will be crucial to obtain the kinetic parameters of aptamer-target binding that will be one limiting factor in real-time measurements. The capacity to

select aptamers with various dissociation constants suggests the capacity to engineer appropriate  $k_{\text{off}}$  values for fast sensing. Once aptamer sequences are isolated for multiple targets of interest, they will need to be multiplexed at specific locations on the surfaces of implantable microprobes with microscale precision. Finally, for biosensors to function *in vivo* for long periods of time to extract extensive information, sensor stability and biocompatibility in complex environments must be considered.

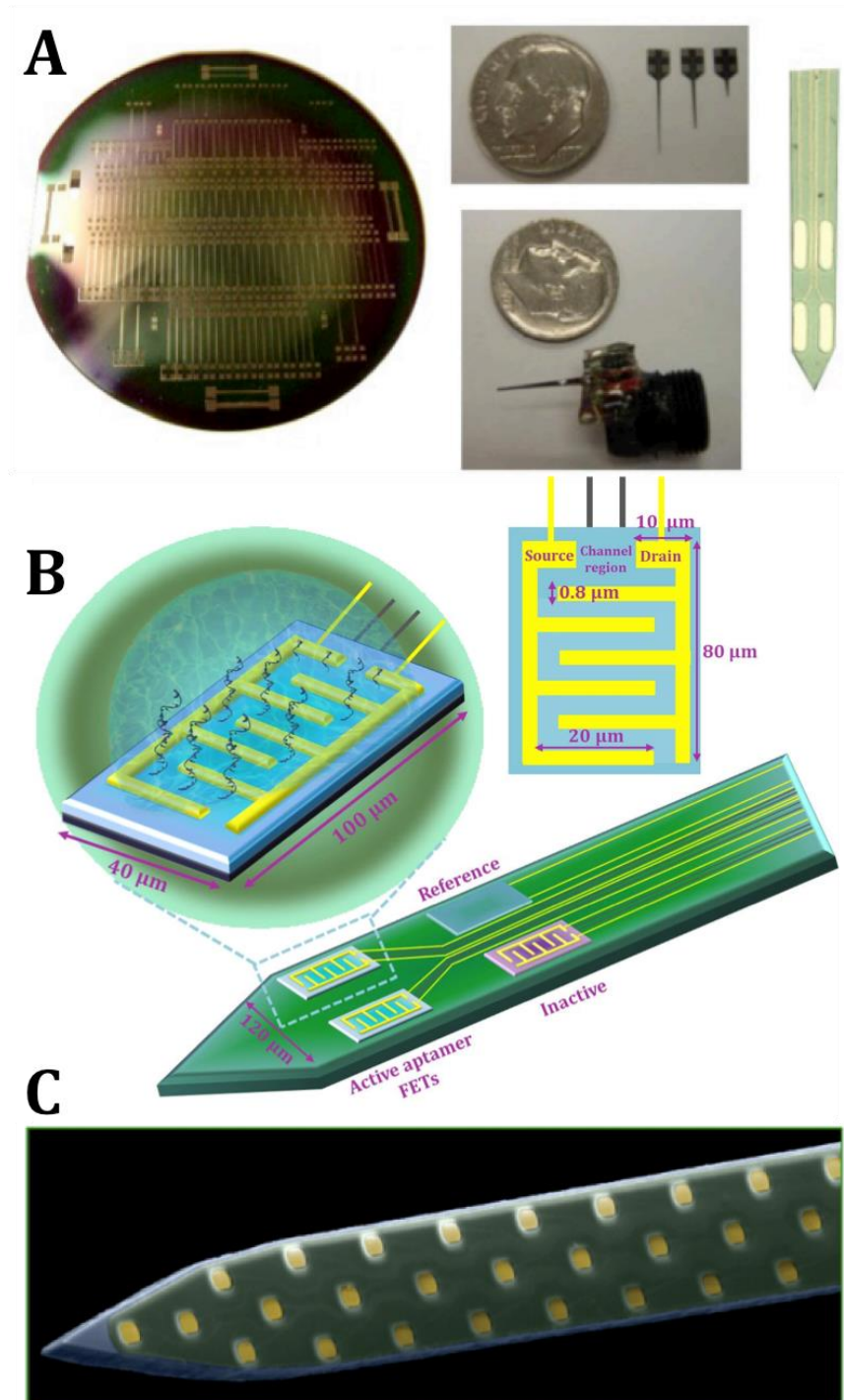


**Figure X.2.** (A) Fabrication of silicon microprobes on 150  $\mu\text{m}$  thick 4"-silicon wafers to produce 150 probes/wafer. Variable shaft lengths (2, 6, 9 mm) enable brain implantation at various depths. Prototype microelectrode sites are 40  $\mu\text{m}$  x 120  $\mu\text{m}$ . (B) Schematic of aptamer FET-microprobe device. Initial devices will be produced with two active FETs functionalized with correct sequence aptamers, one inactive FET for self-referencing with a scrambled sequence aptamer, and one solid-state reference electrode. (C) Multi-site electrodes fabricated lithographically for high-density electrophysiological recordings that can be adapted for neurochemical measurements. Each recording site is 100  $\mu\text{m}^2$ . Electrodes can be replaced with FETs and functionalized with aptamers for multiplexed sensing. Reproduced with permission from refs. 14 and 18. Copyright 2008 Multidisciplinary Digital Publishing Institute and 2011 PLoS ONE respectively.

## **X.B. Aptamers *in Vivo***

An example of aptamers for *in vivo* monitoring involves electrochemical aptamer-based sensors.<sup>22</sup> Plaxco and coworkers fabricated electrodes with biocompatible polysulfone membranes to limit surface biofouling. These electrodes were inserted *via* a catheter into the jugular veins of anesthetized rats.<sup>23</sup> Real-time concentrations of doxorubicin and several aminoglycoside antibiotics were monitored over 5 h in ambulatory animals enabling pharmacokinetic analyses. The aptamers cross-reacted with the different drugs, which was less of an issue for therapeutic monitoring where specific drugs are administered. However, cross-reactivity will be problematic for monitoring endogenous substances, emphasizing the importance of negative selections in the SELEX process to produce selective aptamers.<sup>24,25</sup>

Langer and Kohane reported strategies for the light-triggered control of aptamer activity and biodistribution *in vivo*.<sup>26</sup> The capacity of an AS1411 aptamer that binds with high affinity and selectivity to nucleolin,<sup>27-29</sup> which is overexpressed on cell membranes of several types of cancer cells, was blocked *via* hybridization with a photo-cleavable complementary oligonucleotide. Nude mice bearing 4T1 tumors were administered nucleolin-targeting fluorophore-labeled aptamers intravenously. Irradiation at the tumor site liberated the aptamer from the duplex, leading to binding. Within 2 h of injection, fluorescence was detected specifically at tumor sites.

In another *in vivo* demonstration, Shi *et al.* designed a switch-based fluorescence-activated aptamer probe for detecting leukemia cell lines where aptamer recognition of lymphoblastic leukemia cells was associated with an

increase in fluorescence, allowing for the sensitive and specific detection of cancer cells.<sup>30</sup> Furthermore, aptamers that bind to PDGF have been covalently attached to mesenchymal stem cell membranes.<sup>31</sup> Using intravital microscopy, PDGF added to cell cultures or secreted by neighboring cells was detected quantitatively at the single-cell level using these aptamers.

Similarly, single protein detection has been achieved *in vivo* in live cell samples using non-covalent conjugation of aptamers to near-infrared emissive single-walled carbon nanotubes.<sup>32</sup> Aptamer-tethered nanotubes were used to detect the proteins RAP-1, a small GTPase, and HIV-1 integrase from *Escherichia coli* (bacteria) and *Pichia pastoris* (yeast), respectively. Protein binding to the aptamers produced an optical signal in the near-infrared optical window where photo-scattering in biological samples is low, enabling detection of single proteins.<sup>33</sup> This setup allowed real-time monitoring of protein export on a single-cell level from living cells.

Aptamers as receptors for *in vivo* sensing are advantageous because of their inherent biocompatibility. In 2004, the U.S. Food and Drug Administration approved pegaptanib sodium, clinically known as *Macugen*, an anti-vascular endothelial growth factor RNA aptamer for the treatment of neovascular age-related macular degeneration that causes vision loss.<sup>34</sup> The approval of *Macugen* demonstrated that aptamers have significant potential for therapeutic applications.<sup>35</sup> Today, therapeutic aptamers appear increasingly promising with several candidates currently undergoing clinical trials for diseases ranging from cancer and heart disease to type II diabetes,<sup>36</sup> and many more candidates in the pipeline.<sup>37</sup>

### **X.C. Resolution, Kinetic Measurements, and Multiplexing**

For biosensors to detect transient, *in vivo* events occurring on second to millisecond time scales, it will be critical to consider the temporal resolution of aptamer-target recognition and signal transduction.<sup>38</sup> Typically, a temporal resolution of 1-15 s for multi-cell domains and millisecond timescales for single-cell signaling events are needed.<sup>39,40</sup> These temporal considerations will require engineering aptamers that have fast ( $\sim 0.05$ -1 s<sup>-1</sup>)  $k_{\text{off}}$  rates<sup>41,42</sup> to enable rapid, real-time monitoring of analyte fluxes.

Regarding spatial resolution, in the brain, communication occurs at nanometer distances for synaptic release events,<sup>43</sup> but over longer distances and *via* multi-cellular circuits for volume transmission and neurohormone signaling. Spatial considerations will require scaling FETs to the small sizes associated with the biological compartments where sampling will occur. Hence, we aim to miniaturize aptamer-FET arrays on implantable microprobes to approach the spatial resolution needed to investigate localized neurotransmitter fluxes in the brain. Newly sized transistor geometries will be optimized for high transconductance (increased output current) *via* three parameters: the intrinsic mobility of the semiconductor material, the capacitance in physiological environments, and channel width.

Precise temporal measurements are challenging with the current aptamer-FET system using static fluid on the surfaces of the aptamer-FETs. In unstirred solutions for high-affinity target-binding interactions, such as enzyme-linked immunosorbent assays (ELISA), the signal is not simply an indicator of the chemical processes of association and dissociation of the target binding to the surface-

tethered receptor.<sup>44</sup> The generated signal is also the result of these chemical processes combined with convection and diffusion of bulk analyte flow.<sup>45</sup> Therefore, response times increase due to the formation of a boundary diffusion layer that hinders analyte binding to the surface-tethered receptors.

In the past decade, several developments in microfluidic-based immunosorbent assays have been reported to circumvent problems associated with extracting rate constants from conventional immunoassays.<sup>46-51</sup> Nevertheless, these methods still require incubation and are unable to measure dynamic changes in analyte concentrations in real time. One strategy to improve analyte capture and detection is to incorporate mixing elements (*e.g.*, ultrasonic transducers that generate acoustic waves, embedded microelectrodes for electrophoretic mixing) to accelerate the diffusion process in microfluidic devices.<sup>52-54</sup> Integrating microfluidics with mixing elements that have been validated for enzymatic systems may allow the measurement of precise kinetic rate constants to optimize aptamer-FET real-time measurements.

Aptamer-FET biosensors have shown highly sensitive responses four to six orders of magnitude lower than the dissociation constants of the recognition elements calculated in-solution *via* fluorescence quenching.<sup>55</sup> These expansive sensing ranges were unexpected based on equilibrium sensing that has the greatest sensitivity an order of magnitude on each side of the  $K_d$ . The high sensitivity achieved with current high-affinity aptamers allows us to investigate aptamers with higher  $K_d$  values (lower affinities) and with increased rates of target dissociation ( $k_{off}$ ), so as to improve temporal resolution.

For simultaneous analyte detection in real time, biosensors will need to be multiplexed, also necessitating FET miniaturization.<sup>56</sup> Nanoscale surface patterning techniques will be useful in terms of achieving high feature resolution for side-by-side interrogation of multiple targets or the same target at multiple locations.<sup>9,57</sup> An important issue in multiplexing is addressing different recognition elements upon integration into electronic devices.

As an example, Mayer, Keating, and co-workers used off-chip functionalization and confined electric fields to assemble different populations of DNA-functionalized nanowires to specific on-chip locations while maintaining DNA hybridization capacities (Figure X.3).<sup>58</sup> We have used microfluidics for independent functionalization of different parts of substrates.<sup>11,59</sup> Other nanopatterning techniques, such as chemical lift-off lithography,<sup>9,60</sup> dip-pen nanolithography,<sup>61</sup> polymer-pen lithography,<sup>62</sup> and nano-pipetting,<sup>63,64</sup> can be used for patterned surface functionalization.<sup>65-68</sup>



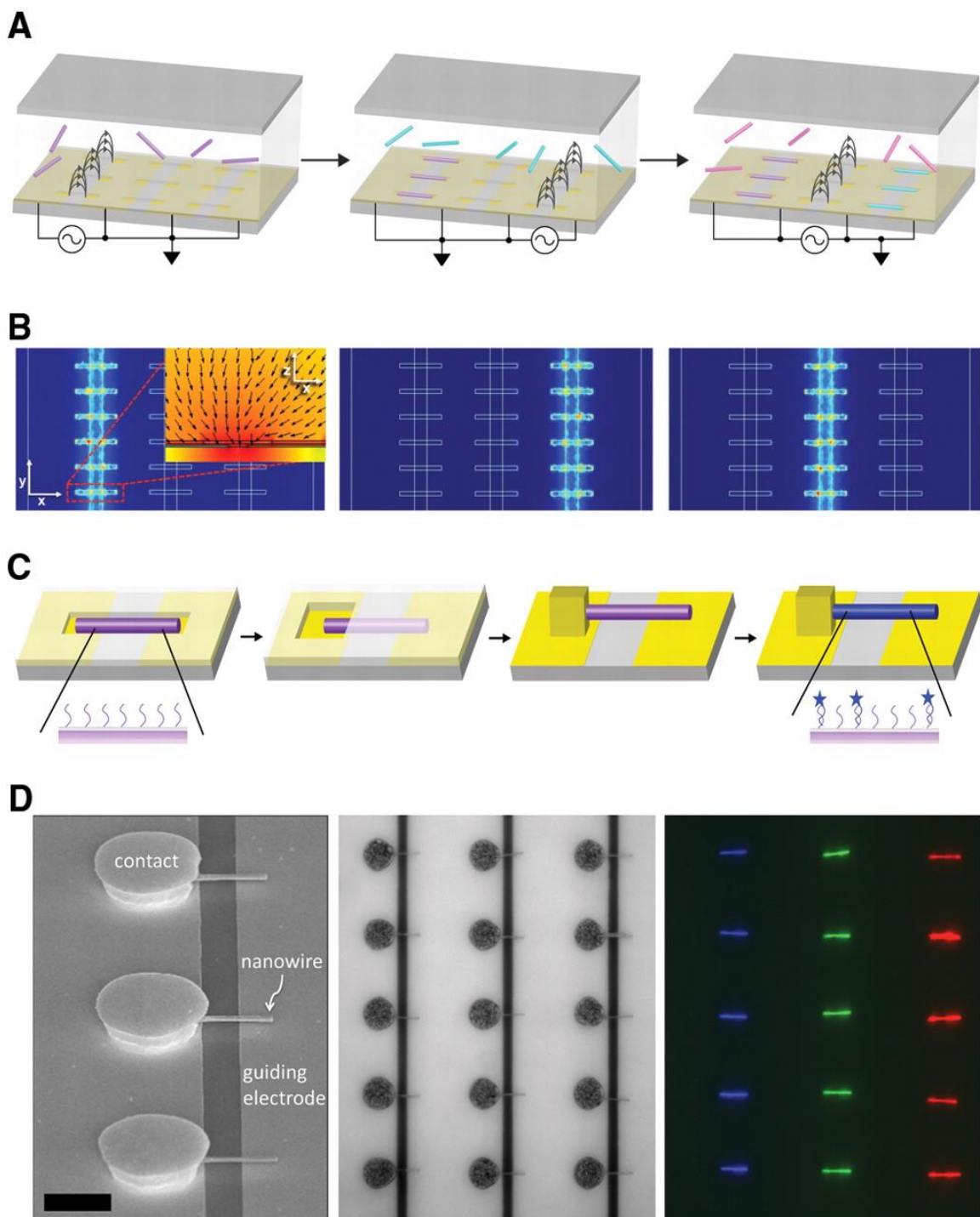


**Figure X.3.** Fabrication of multi-sequence DNA-coated nanowire device arrays. **(A)** Assembly process. Suspensions of nanowires functionalized with different DNA sequences were injected sequentially, and directed to microwells in specific columns. **(B)** Simulated spatial electrical-field gradient during assembly. Contour plots show  $\nabla|E|^2$  measured at the surface of the microwells; scale is  $10^{10}$  (blue) to  $10^{18}$  (red)  $V^2/m^3$ . **(Inset)** Cross-sectional view of one microwell **(C)** Schematic for post-assembly device integration. **(D)** **(left)** Scanning electron microscope, **(center)** optical reflectance, and **(right)** fluorescence images after incubation with labeled complementary targets. Scale bar indicates 5 mm. Reproduced with permission from ref. 58. Copyright 2009 The American Association for the Advancement of Science.

#### **X.D. *In Vivo* Device Stability and Biocompatibility**

Biocompatibility and biostability need to be addressed for sensors to perform reliably and reproducibly in research animals or humans over days to weeks to months, and even years.<sup>69-71</sup> Sensors should minimally perturb the *in vivo* environment, and the *in vivo* environment should not adversely affect sensor performance.<sup>72</sup> Three specific aspects encompass requirements associated with chronic sensing paradigms. The first involves the effects of implanted aptamer-FET devices on local host responses.<sup>73</sup> Second, and related, is the degradation of biosensor components by inflammatory responses.<sup>74,75</sup> The third aspect is biofouling, *i.e.*, the adhesion of biological molecules on sensor surfaces resulting in poor sensor performance or failure.<sup>76</sup>

A review by Kozai *et al.* highlights the limitations of implantable biosensors for probing neurochemical processes and general difficulties associated with maintaining long-term biosensor performance (Figure X.4).<sup>77</sup> The physical insertion of a probe into brain (or other) tissue causes local penetration injury, which initiates progressive inflammatory responses.<sup>78</sup> Inflammation alters the physiochemical environment in which sensing occurs, leading to sensor inaccuracy, instability, and often, failure. The authors emphasize that understanding the biological processes underlying tissue responses to implanted devices at the cellular and molecular levels will enable strategies for improving signal sensitivity and longevity.<sup>79-82</sup> Similarly, Gunasekera *et al.* outlined challenges for chronic recordings using intracortical recording interfaces, which are critical components of brain computer interfaces.<sup>69</sup> In addition to inflammation upon device insertion, these authors

identified critical issues including glial scarring, neurodegeneration, neurotoxicity, and neural cell death.<sup>83,84</sup>

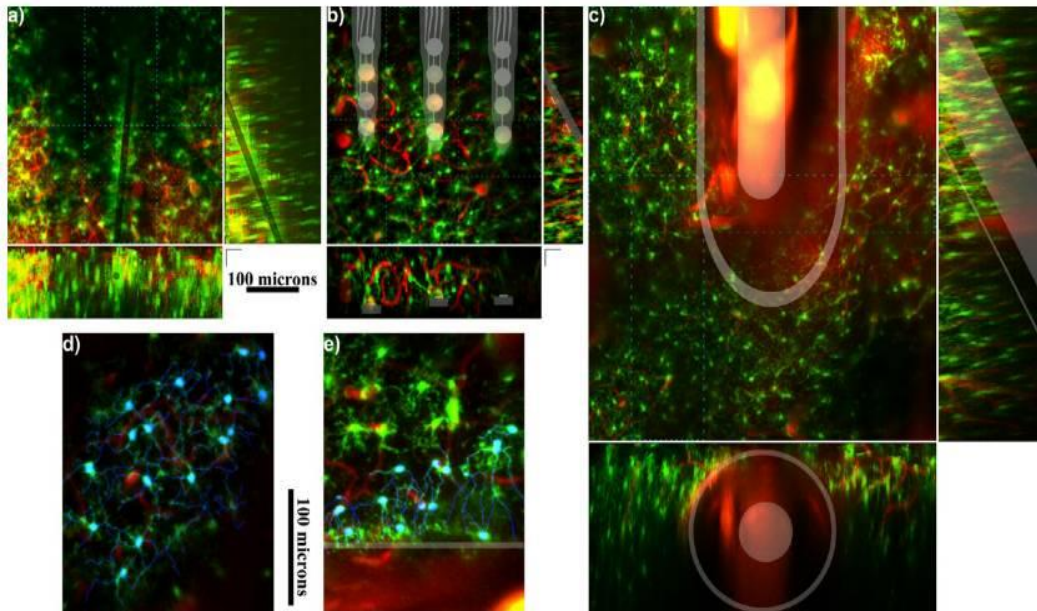


**Figure X.4.** Limitations of implantable biosensors—microglia activation after electrode implantation. Microglia (green), blood-brain barrier (red), and devices (gray). (A–C) Z-stack projections, as well as front and side view reconstructions of the dashed boxed regions are shown for: (A) parylene insulated carbon fiber electrodes, (B) planar silicon electrodes, and (C) microdialysis probes. (D) Ramified (normal) microglia show radial projections or processes indicated by blue traces. (E) Microglia adjacent to a microdialysis probe edge (gray) can be seen to retract processes that are oriented away from the probe, and to extend processes oriented toward the probe surface. Reproduced with permission from ref. 77. Copyright 2015 American Chemical Society.

Therefore, in addition to device failure, it will be important to consider tissue damage that measurement devices cause. A design that has been envisioned incorporates wireless technology to enable reductions in the sizes of implanted devices minimizing tissue strain and damage.<sup>85</sup> Furthermore, simultaneous damage monitoring of surrounding tissue, such as by two-photon microscopy, magnetic resonance imaging (MRI), or computerized tomography (CT), will be advantageous for prolonging chronic recordings *in vivo* and evoking timely therapeutic interventions.<sup>86,87</sup>

Progress has been made in the area of “transient” electronics for *in vivo* sensors and therapeutic devices.<sup>88-92</sup> Biodegradable power sources for *in vivo* biomechanical energy harvesting<sup>93</sup> and brain sensors that enable wireless data collection, including measurements of pressure, temperature, motion, and pH with bioresorbable platforms have been developed.<sup>94</sup> Designing and engineering these characteristics into *in vivo* aptamer-FET sensors could improve prospects for long-term monitoring and human use. For example, it may be possible to use aptamer-FETs in closed-loop monitoring configurations *in vivo* to guide refinement of deep-brain stimulation parameters and localization for treating advanced/refractory neurodegenerative or neuropsychiatric disorders.

## **X.E. Conclusions and Prospects**

While the primary goal is to realize aptamer-FET biosensors to elucidate brain function, we are striving to demonstrate, in parallel, the applicability of aptamer-FETs for a wide range of chemical targets regardless of size, charge, or chemical functionalities for future sensing *in vivo*. The capacity to sense small-molecule targets ranging from neurotransmitters (dopamine and serotonin) to neutral molecules (glucose) and zwitterionic species (sphingosine-1-phosphate) in complex environments (*i.e.* brain tissue and serum) indicate that aptamer-FETs may be a universal platform for producing electronic biosensors specialized for virtually *any* small molecule. With improved solution-phase *in vitro* selection techniques, high-affinity DNA aptamers can be isolated for diverse targets of clinical importance. As such, aptamer-FETs generalized for clinically relevant biomarkers can be foreseen to revolutionize biomedicine.

## References

1. Plaxco, K. W.; Soh, H. T. Switch-Based Biosensors: A New Approach Towards Real-Time, *in Vivo* Molecular Detection. *Trends Biotechnol.* **2011**, *29*, 1-5.
2. Gaster, R. S.; Hall, D. A.; Nielsen, C. H.; Osterfeld, S. J.; Yu, H.; Mach, K. E.; Wilson, R. J.; Murmann, B.; Liao, J. C.; Gambhir, S. S.; Wang, S. X. Matrix-Insensitive Protein Assays Push the Limits of Biosensors in Medicine. *Nat. Med.* **2009**, *15*, 1327-1332.
3. Vaisocherova, H.; Brynda, E.; Homola, J. Functionalizable Low-Fouling Coatings for Label-Free Biosensing in Complex Biological Media: Advances and Applications. *Anal. Bioanal. Chem.* **2015**, *407*, 3927-3953.
4. Meyers, S. R.; Grinstaff, M. W. Biocompatible and Bioactive Surface Modifications for Prolonged *in Vivo* Efficacy. *Chem. Rev.* **2012**, *112*, 1615-1632.
5. Rong, G.; Corrie, S. R.; Clark, H. A. *In Vivo* Biosensing: Progress and Perspectives. *ACS Sens.* **2017**, *2*, 327-338.
6. Ruscito, A.; DeRosa, M. C. Small-Molecule Binding Aptamers: Selection Strategies, Characterization, and Applications. *Front. Chem.* **2016**, *4*.
7. McKeague, M.; Derosa, M. C. Challenges and Opportunities for Small Molecule Aptamer Development. *J. Nucleic Acids* **2012**, *2012*, 748913.
8. Shuster, M. J.; Vaish, A.; Cao, H. H.; Guttentag, A. I.; McManigle, J. E.; Gibb, A. L.; Martinez, M. M.; Nezarati, R. M.; Hinds, J. M.; Liao, W. S.; Weiss, P. S.; Andrews, A. M. Patterning Small-Molecule Biocapture Surfaces: Microcontact Insertion Printing vs. Photolithography. *Chem. Commun.* **2011**, *47*, 10641-10643.
9. Liao, W. S.; Cheunkar, S.; Cao, H. H.; Bednar, H. R.; Weiss, P. S.; Andrews, A. M. Subtractive Patterning *via* Chemical Lift-Off Lithography. *Science* **2012**, *337*, 1517-1521.
10. Vaish, A.; Shuster, M. J.; Cheunkar, S.; Singh, Y. S.; Weiss, P. S.; Andrews, A. M. Native Serotonin Membrane Receptors Recognize 5-Hydroxytryptophan-Functionalized Substrates: Enabling Small-Molecule Recognition. *ACS Chem. Neurosci.* **2010**, *1*, 495-504.
11. Liao, W. S.; Cao, H. H.; Cheunkar, S.; Shuster, M. J.; Altieri, S. C.; Weiss, P. S.; Andrews, A. M. Small-Molecule Arrays for Sorting G-Protein-Coupled Receptors. *J. Phys. Chem. C* **2013**, *117*, 22362-22368.

12. Tolosa, V. M.; Wassum, K. M.; Maidment, N. T.; Monbouquette, H. G. Electrochemically Deposited Iridium Oxide Reference Electrode Integrated with an Electroenzymatic Glutamate Sensor on a Multi-Electrode Array Microprobe. *Biosens. Bioelectron.* **2013**, *42*, 256-260.
13. Wassum, K. M.; Tolosa, V. M.; Tseng, T. C.; Balleine, B. W.; Monbouquette, H. G.; Maidment, N. T. Transient Extracellular Glutamate Events in the Basolateral Amygdala Track Reward-Seeking Actions. *J. Neurosci.* **2012**, *32*, 2734-2746.
14. Wassum, K. M.; Tolosa, V. M.; Wang, J. J.; Walker, E.; Monbouquette, H. G.; Maidment, N. T. Silicon Wafer-Based Platinum Microelectrode Array Biosensor for near Real-Time Measurement of Glutamate *in Vivo*. *Sensors (Basel)* **2008**, *8*, 5023-5036.
15. Tseng, T. T. C.; Monbouquette, H. G. Implantable Microprobe with Arrayed Microsensors for Combined Amperometric Monitoring of the Neurotransmitters, Glutamate and Dopamine. *J. Electroanal. Chem.* **2012**, *682*, 141-146.
16. Shobe, J. L.; Claar, L. D.; Parhami, S.; Bakhurin, K. I.; Masmanidis, S. C. Brain Activity Mapping at Multiple Scales with Silicon Microprobes Containing 1,024 Electrodes. *J. Neurophysiol.* **2015**, *114*, 2043-2052.
17. Sadek, A. S.; Karabalin, R. B.; Du, J. G.; Roukes, M. L.; Koch, C.; Masmanidis, S. C. Wiring Nanoscale Biosensors with Piezoelectric Nanomechanical Resonators. *Nano Lett.* **2010**, *10*, 1769-1773.
18. Du, J. G.; Blanche, T. J.; Harrison, R. R.; Lester, H. A.; Masmanidis, S. C. Multiplexed, High Density Electrophysiology with Nanofabricated Neural Probes. *PLoS One* **2011**, *6*.
19. Javey, A.; Guo, J.; Wang, Q.; Lundstrom, M.; Dai, H. J. Ballistic Carbon Nanotube Field-Effect Transistors. *Nature* **2003**, *424*, 654-657.
20. Shirak, O.; Shtempluck, O.; Kotchakov, V.; Bahir, G.; Yaish, Y. E. High Performance Horizontal Gate-All-around Silicon Nanowire Field-Effect Transistors. *Nanotechnology* **2012**, *23*.
21. Rajan, N. K.; Routenberg, D. A.; Chen, J.; Reed, M. A. 1/f Noise of Silicon Nanowire BioFETs. *IEEE Electr. Device Lett.* **2010**, *31*, 615-617.
22. Swensen, J. S.; Xiao, Y.; Ferguson, B. S.; Lubin, A. A.; Lai, R. Y.; Heeger, A. J.; Plaxco, K. W.; Soh, H. T. Continuous, Real-Time Monitoring of Cocaine in Undiluted Blood Serum *via* a Microfluidic, Electrochemical Aptamer-Based Sensor. *J. Am. Chem. Soc.* **2009**, *131*, 4262-4266.

23. Arroyo-Curras, N.; Somerson, J.; Vieira, P. A.; Ploense, K. L.; Kippin, T. E.; Plaxco, K. W. Real-Time Measurement of Small Molecules Directly in Awake, Ambulatory Animals. *Proc. Natl. Acad. Sci. U. S. A.* **2017**, *114*, 645-650.
24. Yang, K. A.; Pei, R. J.; Stefanovic, D.; Stojanovic, M. N. Optimizing Cross-Reactivity with Evolutionary Search for Sensors. *J. Am. Chem. Soc.* **2012**, *134*, 1642-1647.
25. Stojanovic, M. N.; Green, E. G.; Semova, S.; Nikic, D. B.; Landry, D. W. Cross-Reactive Arrays Based on Three-Way Junctions. *J. Am. Chem. Soc.* **2003**, *125*, 6085-6089.
26. Li, L.; Tong, R.; Chu, H.; Wang, W.; Langer, R.; Kohane, D. S. Aptamer Photoregulation *in Vivo*. *Proc. Natl. Acad. Sci. U. S. A.* **2014**, *111*, 17099-17103.
27. Soundararajan, S.; Chen, W.; Spicer, E. K.; Courtenay-Luck, N.; Fernandes, D. J. The Nucleolin Targeting Aptamer AS1411 Destabilizes *Bcl-2* Messenger RNA in Human Breast Cancer Cells. *Cancer Res.* **2008**, *68*, 2358-2365.
28. Reyes-Reyes, E. M.; Teng, Y.; Bates, P. J. A New Paradigm for Aptamer Therapeutic AS1411 Action: Uptake by Macropinocytosis and Its Stimulation by a Nucleolin-Dependent Mechanism. *Cancer Res.* **2010**, *70*, 8617-8629.
29. Soundararajan, S.; Wang, L.; Sridharan, V.; Chen, W.; Courtenay-Luck, N.; Jones, D.; Spicer, E. K.; Fernandes, D. J. Plasma Membrane Nucleolin Is a Receptor for the Anticancer Aptamer AS1411 in MV4-11 Leukemia Cells. *Mol. Pharmacol.* **2009**, *76*, 984-991.
30. Shi, H.; He, X.; Wang, K.; Wu, X.; Ye, X.; Guo, Q.; Tan, W.; Qing, Z.; Yang, X.; Zhou, B. Activatable Aptamer Probe for Contrast-Enhanced *in Vivo* Cancer Imaging Based on Cell Membrane Protein-Triggered Conformation Alteration. *Proc. Natl. Acad. Sci. U. S. A.* **2011**, *108*, 3900-3905.
31. Zhao, W.; Schafer, S.; Choi, J.; Yamanaka, Y. J.; Lombardi, M. L.; Bose, S.; Carlson, A. L.; Phillips, J. A.; Teo, W.; Droujinine, I. A.; Cui, C. H.; Jain, R. K.; Lammerding, J.; Love, J. C.; Lin, C. P.; Sarkar, D.; Karnik, R.; Karp, J. M. Cell-Surface Sensors for Real-Time Probing of Cellular Environments. *Nat. Nanotechnol.* **2011**, *6*, 524-531.
32. Landry, M. P.; Ando, H.; Chen, A. Y.; Cao, J. C.; Kottadiel, V. I.; Chio, L.; Yang, D.; Dong, J. Y.; Lu, T. K.; Strano, M. S. Single-Molecule Detection of Protein Efflux from Microorganisms Using Fluorescent Single-Walled Carbon Nanotube Sensor Arrays. *Nat. Nanotechnol.* **2017**, *12*, 368-377.



33. Iverson, N. M.; Barone, P. W.; Shandell, M.; Trudel, L. J.; Sen, S.; Sen, F.; Ivanov, V.; Atolia, E.; Farias, E.; McNicholas, T. P.; Reuel, N.; Parry, N. M.; Wogan, G. N.; Strano, M. S. *In Vivo* Biosensing via Tissue-Localizable Near-Infrared-Fluorescent Single-Walled Carbon Nanotubes. *Nat. Nanotechnol.* **2013**, *8*, 873-880.
34. Ruckman, J.; Green, L. S.; Beeson, J.; Waugh, S.; Gillette, W. L.; Henninger, D. D.; Claesson-Welsh, L.; Janjic, N. 2'-Fluoropyrimidine RNA-Based Aptamers to the 165-Amino Acid Form of Vascular Endothelial Growth Factor (VEGF<sub>165</sub>). Inhibition of Receptor Binding and VEGF-Induced Vascular Permeability through Interactions Requiring the Exon 7-Encoded Domain. *J. Biol. Chem.* **1998**, *273*, 20556-20567.
35. Ng, E. W. M.; Shima, D. T.; Calias, P.; Cunningham, E. T.; Guyer, D. R.; Adamis, A. P. Pegaptanib, a Targeted Anti-VEGF Aptamer for Ocular Vascular Disease. *Nat. Rev. Drug Discov.* **2006**, *5*, 123-132.
36. Sundaram, P.; Kurniawan, H.; Byrne, M. E.; Wower, J. Therapeutic RNA Aptamers in Clinical Trials. *Eur. J. Pharm. Sci.* **2013**, *48*, 259-271.
37. Maier, K. E.; Levy, M. From Selection Hits to Clinical Leads: Progress in Aptamer Discovery. *Mol. Ther. Methods Clin. Dev.* **2016**, *5*, 16014.
38. Pellerin, L.; Magistretti, P. J. Neuroscience. Let There Be (NADH) Light. *Science* **2004**, *305*, 50-52.
39. Beyene, A. G.; McFarlane, I. R.; Pinals, R. L.; Landry, M. P. Stochastic Simulation of Dopamine Neuromodulation for Implementation of Fluorescent Neurochemical Probes in the Striatal Extracellular Space. *ACS Chem. Neurosci.* **2017**, *8*, 2275-2289.
40. Clark, R. A.; Zerby, S. E.; Ewing, A. G. Electrochemistry in Neuronal Microenvironments. *Electroanal. Chem.* **1998**, *20*, 227-294.
41. Drabovich, A.; Berezovski, M.; Krylov, S. N. Selection of Smart Aptamers by Equilibrium Capillary Electrophoresis of Equilibrium Mixtures (ECEEM). *J. Am. Chem. Soc.* **2005**, *127*, 11224-11225.
42. Drabovich, A. P.; Berezovski, M.; Okhonin, V.; Krylov, S. N. Selection of Smart Aptamers by Methods of Kinetic Capillary Electrophoresis. *Anal. Chem.* **2006**, *78*, 3171-3178.
43. Wilson, G. S.; Gifford, R. Biosensors for Real-Time *in Vivo* Measurements. *Biosens. Bioelectron.* **2005**, *20*, 2388-2403.
44. Chaiken, I.; Rose, S.; Karlsson, R. Analysis of Macromolecular Interactions Using Immobilized Ligands. *Anal. Biochem.* **1992**, *201*, 197-210.

45. Porstmann, T.; Kiessig, S. T. Enzyme-Immunoassay Techniques - An Overview. *J. Immunol. Methods* **1992**, *150*, 5-21.
46. Chen, C. H.; Sarkar, A.; Song, Y. A.; Miller, M. A.; Kim, S. J.; Griffith, L. G.; Lauffenburger, D. A.; Han, J. Enhancing Protease Activity Assay in Droplet-Based Microfluidics Using a Biomolecule Concentrator. *J. Am. Chem. Soc.* **2011**, *133*, 10368-10371.
47. Hou, C. L.; Herr, A. E. Ultrashort Separation Length Homogeneous Electrophoretic Immunoassays Using On-Chip Discontinuous Polyacrylamide Gels. *Anal. Chem.* **2010**, *82*, 3343-3351.
48. Lee, J. H.; Cosgrove, B. D.; Lauffenburger, D. A.; Han, J. Microfluidic Concentration-Enhanced Cellular Kinase Activity Assay. *J. Am. Chem. Soc.* **2009**, *131*, 10340-10341.
49. Nie, S.; Henley, W. H.; Miller, S. E.; Zhang, H.; Mayer, K. M.; Dennis, P. J.; Oblath, E. A.; Alarie, J. P.; Wu, Y.; Oppenheim, F. G.; Little, F. F.; Uluer, A. Z.; Wang, P. D.; Ramsey, J. M.; Walt, D. R. An Automated Integrated Platform for Rapid and Sensitive Multiplexed Protein Profiling Using Human Saliva Samples. *Lab Chip* **2014**, *14*, 1087-1098.
50. Rissin, D. M.; Kan, C. W.; Campbell, T. G.; Howes, S. C.; Fournier, D. R.; Song, L.; Piech, T.; Patel, P. P.; Chang, L.; Rivnak, A. J.; Ferrell, E. P.; Randall, J. D.; Provuncher, G. K.; Walt, D. R.; Duffy, D. C. Single-Molecule Enzyme-Linked Immunosorbent Assay Detects Serum Proteins at Sub-femtomolar Concentrations. *Nat. Biotechnol.* **2010**, *28*, 595-599.
51. Bange, A.; Halsall, H. B.; Heineman, W. R. Microfluidic Immunosensor Systems. *Biosens. Bioelectron.* **2005**, *20*, 2488-2503.
52. Hu, G. Q.; Gao, Y. L.; Li, D. Q. Modeling Micropatterned Antigen-Antibody Binding Kinetics in a Microfluidic Chip. *Biosens. Bioelectron.* **2007**, *22*, 1403-1409.
53. Meijer, H. E. H.; Singh, M. K.; Kang, T. G.; den Toonder, J. M. J.; Anderson, P. D. Passive and Active Mixing in Microfluidic Devices. *Macromol. Symp.* **2009**, *279*, 201-209.
54. Lee, C. Y.; Chang, C. L.; Wang, Y. N.; Fu, L. M. Microfluidic Mixing: A Review. *Int. J. Mol. Sci.* **2011**, *12*, 3263-3287.
55. Nakatsuka, N.; Yang, K. A.; Xu, X.; Abendroth, J. M.; Zhao, C. Z.; Zhu, B.; Chen, H.; Rim, Y. S.; Yang, Y.; Weiss, P. S.; Stojanovic, M. N.; Andrews, A. M. Aptamer Field-Effect Transistors Overcome Debye Length Limitations and Enable Small-Molecule Sensing. *submitted* **2017**.

56. Tang, H. Y.; Ali-Khan, N.; Echan, L. A.; Levenkova, N.; Rux, J. J.; Speicher, D. W. A Novel Four-Dimensional Strategy Combining Protein and Peptide Separation Methods Enables Detection of Low-Abundance Proteins in Human Plasma and Serum Proteomes. *Proteomics* **2005**, *5*, 3329-3342.
57. Cao, H. H.; Nakatsuka, N.; Serino, A. C.; Liao, W. S.; Cheunkar, S.; Yang, H. Y.; Weiss, P. S.; Andrews, A. M. Controlled DNA Patterning by Chemical Lift-Off Lithography: Matrix Matters. *ACS Nano* **2015**, *9*, 11439-11454.
58. Morrow, T. J.; Li, M. W.; Kim, J.; Mayer, T. S.; Keating, C. D. Programmed Assembly of DNA-Coated Nanowire Devices. *Science* **2009**, *323*, 352-352.
59. Hou, X.; Zhang, Y. S.; Santiago, G. T. D.; Alvarez, M. M.; Ribas, J.; Jonas, S. J.; Weiss, P. S.; Andrews, A. M.; Aizenberg, J.; Khademhosseini, A. Interplay between Materials and Microfluidics. *Nat. Rev. Mater.* **2017**, *2*.
60. Kim, J.; Rim, Y. S.; Chen, H. J.; Cao, H. H.; Nakatsuka, N.; Hinton, H. L.; Zhao, C. Z.; Andrews, A. M.; Yang, Y.; Weiss, P. S. Fabrication of High-Performance Ultrathin In<sub>2</sub>O<sub>3</sub> Film Field-Effect Transistors and Biosensors Using Chemical Lift-Off Lithography. *ACS Nano* **2015**, *9*, 4572-4582.
61. Piner, R. D.; Zhu, J.; Xu, F.; Hong, S. H.; Mirkin, C. A. "Dip-Pen" Nanolithography. *Science* **1999**, *283*, 661-663.
62. Huo, F. W.; Zheng, Z. J.; Zheng, G. F.; Giam, L. R.; Zhang, H.; Mirkin, C. A. Polymer Pen Lithography. *Science* **2008**, *321*, 1658-1660.
63. Smith, R. K.; Lewis, P. A.; Weiss, P. S. Patterning Self-Assembled Monolayers. *Prog. Surf. Sci.* **2004**, *75*, 1-68.
64. Saavedra, H. M.; Mullen, T. J.; Zhang, P. P.; Dewey, D. C.; Claridge, S. A.; Weiss, P. S. Hybrid Strategies in Nanolithography. *Rep. Prog. Phys.* **2010**, *73*, 1-40.
65. Love, J. C.; Estroff, L. A.; Kriebel, J. K.; Nuzzo, R. G.; Whitesides, G. M. Self-Assembled Monolayers of Thiolates on Metals as a Form of Nanotechnology. *Chem. Rev.* **2005**, *105*, 1103-1169.
66. Claridge, S. A.; Schwartz, J. J.; Weiss, P. S. Electrons, Photons, and Force: Quantitative Single-Molecule Measurements from Physics to Biology. *ACS Nano* **2011**, *5*, 693-729.
67. Derkus, B. Applying the Miniaturization Technologies for Biosensor Design. *Biosens. Bioelectron.* **2016**, *79*, 901-913.

68. Liu, X.; Carbonell, C.; Braunschweig, A. B. Towards Scanning Probe Lithography-Based 4D Nanoprinting by Advancing Surface Chemistry, Nanopatterning Strategies, and Characterization Protocols. *Chem. Soc. Rev.* **2016**, *45*, 6289-6310.
69. Gunasekera, B.; Saxena, T.; Bellamkonda, R.; Karumbaiah, L. Intracortical Recording Interfaces: Current Challenges to Chronic Recording Function. *ACS Chem. Neurosci.* **2015**, *6*, 68-83.
70. Alba, N. A.; Du, Z. J.; Catt, K. A.; Kozai, T. D.; Cui, X. T. *In Vivo* Electrochemical Analysis of a PEDOT/MWCNT Neural Electrode Coating. *Biosensors (Basel)* **2015**, *5*, 618-646.
71. Kozai, T. D.; Catt, K.; Li, X.; Gugel, Z. V.; Olafsson, V. T.; Vazquez, A. L.; Cui, X. T. Mechanical Failure Modes of Chronically Implanted Planar Silicon-Based Neural Probes for Laminar Recording. *Biomaterials* **2015**, *37*, 25-39.
72. Onuki, Y.; Bhardwaj, U.; Papadimitrakopoulos, F.; Burgess, D. J. A Review of the Biocompatibility of Implantable Devices: Current Challenges to Overcome Foreign Body Response. *J. Diabetes Sci. Technol.* **2008**, *2*, 1003-1015.
73. Williams, D. F. A Model for Biocompatibility and Its Evaluation. *J. Biomed. Eng.* **1989**, *11*, 185-191.
74. Hannan, M. A.; Mutashar, S.; Samad, S. A.; Hussain, A. Energy Harvesting for the Implantable Biomedical Devices: Issues and Challenges. *Biomed. Eng. Online* **2014**, *13*, 79-102.
75. Rogers, J. A. Electronics for the Human Body. *J. Am. Med. Assoc.* **2015**, *313*, 561-562.
76. Wisniewski, N.; Moussy, F.; Reichert, W. M. Characterization of Implantable Biosensor Membrane Biofouling. *Fresen. J. Anal. Chem.* **2000**, *366*, 611-621.
77. Kozai, T. D. Y.; Jaquins-Gerstl, A. S.; Vazquez, A. L.; Michael, A. C.; Cui, X. T. Brain Tissue Responses to Neural Implants Impact Signal Sensitivity and Intervention Strategies. *ACS Chem. Neurosci.* **2015**, *6*, 48-67.
78. Kozai, T. D. Y.; Marzullo, T. C.; Hooi, F.; Langhals, N. B.; Majewska, A. K.; Brown, E. B.; Kipke, D. R. Reduction of Neurovascular Damage Resulting from Microelectrode Insertion into the Cerebral Cortex Using *in Vivo* Two-Photon Mapping. *J. Neural Eng.* **2010**, *7*, 1-12.
79. Nesbitt, K. M.; Jaquins-Gerstl, A.; Skoda, E. M.; Wipf, P.; Michael, A. C. Pharmacological Mitigation of Tissue Damage During Brain Microdialysis. *Anal. Chem.* **2013**, *85*, 8173-8179.

80. Potter, K. A.; Buck, A. C.; Self, W. K.; Capadona, J. R. Stab Injury and Device Implantation within the Brain Results in Inversely Multiphasic Neuroinflammatory and Neurodegenerative Responses. *J. Neural Eng.* **2012**, *9*, 1-14.
81. Woolley, A. J.; Desai, H. A.; Otto, K. J. Chronic Intracortical Microelectrode Arrays Induce Non-Uniform, Depth-Related Tissue Responses. *J. Neural Eng.* **2013**, *10*, 1-11.
82. Zhang, J.; Liu, Y. S.; Jaquins-Gerstl, A.; Shu, Z.; Michael, A. C.; Weber, S. G. Optimization for Speed and Sensitivity in Capillary High Performance Liquid Chromatography. The Importance of Column Diameter in Online Monitoring of Serotonin by Microdialysis. *J. Chromatogr. A* **2012**, *1251*, 54-62.
83. McConnell, G. C.; Rees, H. D.; Levey, A. I.; Gutekunst, C. A.; Gross, R. E.; Bellamkonda, R. V. Implanted Neural Electrodes Cause Chronic, Local Inflammation That Is Correlated with Local Neurodegeneration. *J. Neural Eng.* **2009**, *6*, 1-12.
84. Saxena, T.; Karumbaiah, L.; Gaupp, E. A.; Patkar, R.; Patil, K.; Betancur, M.; Stanley, G. B.; Bellamkonda, R. V. The Impact of Chronic Blood-Brain Barrier Breach on Intracortical Electrode Function. *Biomaterials* **2013**, *34*, 4703-4713.
85. Fu, X.; Chen, W.; Ye, S.; Tu, Y.; Tang, Y.; Li, D.; Chen, H.; Jiang, K. A Wireless Implantable Sensor Network System for *in Vivo* Monitoring of Physiological Signals. *IEEE Trans. Inf. Technol. Biomed.* **2011**, *15*, 577-584.
86. Kozai, T. D. Y.; Vazquez, A. L.; Weaver, C. L.; Kim, S. G.; Cui, X. T. *In vivo* Two-Photon Microscopy Reveals Immediate Microglial Reaction to Implantation of Microelectrode through Extension of Processes. *J. Neural Eng.* **2012**, *9*, 1-17.
87. Zhang, H. N.; Patel, P. R.; Xie, Z. X.; Swanson, S. D.; Wang, X. D.; Kotov, N. A. Tissue-Compliant Neural Implants from Microfabricated Carbon Nanotube Multilayer Composite. *ACS Nano* **2013**, *7*, 7619-7629.
88. Dagdeviren, C.; Hwang, S. W.; Su, Y. W.; Kim, S.; Cheng, H. Y.; Gur, O.; Haney, R.; Omenetto, F. G.; Huang, Y. G.; Rogers, J. A. Transient, Biocompatible Electronics and Energy Harvesters Based on ZnO. *Small* **2013**, *9*, 3398-3404.
89. Hwang, S. W.; Song, J. K.; Huang, X.; Cheng, H. Y.; Kang, S. K.; Kim, B. H.; Kim, J. H.; Yu, S.; Huang, Y. G.; Rogers, J. A. High-Performance Biodegradable/Transient Electronics on Biodegradable Polymers. *Adv. Mater.* **2014**, *26*, 3905-3911.
90. Wang, C. H.; Hsieh, C. Y.; Hwang, J. C. Flexible Organic Thin-Film Transistors with Silk Fibroin as the Gate Dielectric. *Adv. Mater.* **2011**, *23*, 1630-1634.

91. Irimia-Vladu, M.; Troshin, P. A.; Reisinger, M.; Schwabegger, G.; Ullah, M.; Schwoediauer, R.; Mumyatov, A.; Bodea, M.; Fergus, J. W.; Razumov, V. F.; Sitter, H.; Bauer, S.; Sariciftci, N. S. Environmentally Sustainable Organic Field Effect Transistors. *Org. Electron.* **2010**, *11*, 1974-1990.
92. Kim, D. H.; Viventi, J.; Amsden, J. J.; Xiao, J. L.; Vigeland, L.; Kim, Y. S.; Blanco, J. A.; Panilaitis, B.; Frechette, E. S.; Contreras, D.; Kaplan, D. L.; Omenetto, F. G.; Huang, Y. G.; Hwang, K. C.; Zakin, M. R.; Litt, B.; Rogers, J. A. Dissolvable Films of Silk Fibroin for Ultrathin Conformal Bio-Integrated Electronics. *Nat. Mater.* **2010**, *9*, 511-517.
93. Gross, R. A.; Kalra, B. Biodegradable Polymers for the Environment. *Science* **2002**, *297*, 803-807.
94. Kang, S. K.; Murphy, R. K. J.; Hwang, S. W.; Lee, S. M.; Harburg, D. V.; Krueger, N. A.; Shin, J. H.; Gamble, P.; Cheng, H. Y.; Yu, S.; Liu, Z. J.; McCall, J. G.; Stephen, M.; Ying, H. Z.; Kim, J.; Park, G.; Webb, R. C.; Lee, C. H.; Chung, S. J.; Wie, D. S.; Gujar, A. D.; Vemulapalli, B.; Kim, A. H.; Lee, K. M.; Cheng, J. J.; Huang, Y. G.; Lee, S. H.; Braun, P. V.; Ray, W. Z.; Rogers, J. A. Bioresorbable Silicon Electronic Sensors for the Brain. *Nature* **2016**, *530*, 71-76.